ASME
SETTING THE STANDARD

Journal of Engineering for Gas Turbines and Power

Published Quarterly by ASME

VOLUME 129 • NUMBER 4 • OCTOBER 2007

Transactions of the ASME, Journal of Engineering for Gas Turbines and Power (ISSN 0742-4795) is published quarterly (Jan., April, July, Oct.) by The American Society of Mechanical Engineers, Three Park Avenue, New York, NY 10016. Periodicals postage paid at New York, NY and additional mailing offices. POSTMASTER: Send address changes to Transactions of the ASME, Journal of Engineering for Gas Turbines and Power, c/o THE AMERICAN SOCIETY OF MECHANICAL ENGINEERS, 22 Law Drive, Box 2300, Fairfield, NJ 07007-2300.
CHANGES OF ADDRESS must be received at Society headquarters seven weeks before they are to be effective. Please send old label and new address.
STATEMENT from By-Laws. The Society shall not be responsible for statements or opinions advanced in papers or ... printed in its publications (B7.1, par. 3).

TECHNICAL PAPERS

(Contents continued on inside back cover)

This journal is printed on acid-free paper, which exceeds the ANSI Z39.48-1992 specification for permanence of paper and library materials. ♾™
♻ 85% recycled content, including 10% post-consumer fibers.

(Contents continued)

Journal of Engineering for Gas Turbines and Power OCTOBER 2007

Volume 129, Number 4

(Contents continued on facing page)

Journal of Engineering for Gas Turbines and Power OCTOBER 2007

Volume 129, Number 4

TECHNICAL BRIEF

DISCUSSION

The ASME Journal of Engineering for Gas Turbines and Power is abstracted and indexed in the following:

AESIS (Australia's Geoscience, Minerals, & Petroleum Database), Applied Science & Technology Index, Aquatic Sciences and Fisheries Abstracts, Civil Engineering Abstracts, Compendex (The electronic equivalent of Engineering Index), Computer & Information Systems Abstracts, Corrosion Abstracts, Current Contents, Engineered Materials Abstracts, Engineering Index, Enviroline (The electronic equivalent of Environment Abstracts), Environment Abstracts, Environmental Science and Pollution Management, Fluidex, INSPEC, Mechanical & Transportation Engineering Abstracts, Mechanical Engineering Abstracts, METADEX (The electronic equivalent of Metals Abstracts and Alloys Index), Pollution Abstracts, Referativnyi Zhurnal, Science Citation Index, SciSearch (The electronic equivalent of Science Citation Index), Shock and Vibration Digest

Buoyancy-Induced Flow in Open Rotating Cavities

J. Michael Owen
University of Bath,
Bath, BA2 7AY, UK

Hans Abrahamsson

Klas Lindblad

Volvo Aero Corporation,
46181 Trollhättan, Sweden

Buoyancy-induced flow can occur in the cavity between the co-rotating compressor disks in gas-turbine engines, where the Rayleigh numbers can be in excess of 10^{12}. *In most cases the cavity is open at the center, and an axial throughflow of cooling air can interact with the buoyancy-induced flow between the disks. Such flows can be modeled, computationally and experimentally, by a simple rotating cavity with an axial flow of air. This paper describes work conducted as part of ICAS-GT, a major European research project. Experimental measurements of velocity, temperature, and heat transfer were obtained on a purpose-built experimental rig, and these results have been reported in an earlier paper. In addition, 3D unsteady CFD computations were carried out using a commercial code (Fluent) and a RNG k-ε turbulence model. The computed velocity vectors and contours of temperature reveal a flow structure in which, as seen by previous experimenters, "radial arms" transport cold air from the center to the periphery of the cavity, and regions of cyclonic and anticyclonic circulation are formed on either side of each arm. The computed radial distribution of the tangential velocity agrees reasonably well with the measurements in two of the three cases considered here. In the third case, the computations significantly overpredict the measurements; the reason for this is not understood. The computed and measured values of Nu for the heated disk show qualitatively similar radial distributions, with high values near the center and the periphery. In two of the cases, the quantitative agreement is reasonably good; in the third case, the computations significantly underpredict the measured values.* [DOI: 10.1115/1.2719260]

1 Introduction

Figure 1 shows a simplified diagram of a high-pressure compressor rotor through the center of which is an axial flow of air that is used downstream for turbine cooling. When the cooling air has a lower temperature than the rotating surfaces (as is the case for steady-state engine operation), buoyancy-induced flow can occur in the cavity between the disks.

In contrast to the open cavity considered above, in some engines the cavity is closed: the air is enclosed by the rotating disks and by inner and outer cylindrical surfaces. For the case where the outer surface is hotter than the inner one, King et al. [1] showed that Rayleigh-Bénard convection could occur, as shown in Fig. 2. For a rotating inviscid fluid, a radial velocity is only possible if there is a circumferential gradient of pressure; without this, the flow would be thermally stratified and convection could not take place. Counter-rotating cyclonic and anticyclonic vortices, with their axes parallel to the axis of rotation, respectively, create regions of low and high pressure; these provide the circumferential pressure gradients that allow convection to occur.

The main features of the flow in the open system can be modeled by the simplified rotating cavities shown in Fig. 3. Most of the experimental work to date has been conducted with either a central inlet or with an annular inlet for the cooling air. In the latter case, the inner cylinder rotates at the same speed as the disks; in an engine, it usually rotates at a slower speed. In the open cavities, the axial throughflow tends to induce a toroidal circulation near the center, and buoyancy-induced flow occurs at the outer radii.

An experimental project on an open cavity has recently been published [2]. The work was carried out as part of a major European research project, entitled "The Internal Cooling Air Systems of Gas Turbines" (ICAS-GT). The project, which was sponsored by the European Commission, ran from 1998 to 2000 and involved ten gas turbine companies and four universities. The University of Bath carried out experiments in a rotating cavity with an annular inlet (as shown in Fig. 3(*b*)), and Volvo Aero Corporation conducted computations of the flow in the system.

This paper describes the computational method used and presents comparisons between the computed and measured results. The principal objectives are to improve the understanding of these complex rotating flows and to see if CFD codes are capable of providing predictions that could be used in the design of internal-air systems in gas turbines.

Section 2 is a brief review of some relevant research; Sec. 3 describes the experimental apparatus; Sec. 4 outlines the computational method; and Sec. 5 discusses comparisons between computations and measurements. The principal conclusions are summarized in Sec. 6.

2 Review of Previous Work

Although the paper concentrates on open cavities, it is useful to consider some of the published research on closed systems. Bohn et al. [3–6] made heat transfer measurements in a sealed rotating annulus (with $a/b=0.35$ and 0.52) where the heat flow could be either axial (from a hot to a cold disk) or radial (from a hot outer cylinder to a cold inner one). For the radial case, they correlated their Nusselt number, for Rayleigh numbers up to 10^{12}, by $\mathrm{Nu} \propto \mathrm{Ra}^c$, where the constant c was approximately 0.2. Sun et al. [7] used an unsteady 3D CFD code, with no Reynolds averaging or turbulence model, to compute the flow in a sealed annulus with a radial heat flow. Their computed Nusselt numbers were in good agreement with the correlations of Bohn et al.

King et al. [1] used unsteady 2D and 3D CFD codes, with no Reynolds averaging, to compute the heat transfer in a sealed annulus with a radial heat flow for $\mathrm{Ra} \leq 10^9$. The computed streamlines showed that Rayleigh-Bénard convection occurred, with cyclonic and anticyclonic vortices in the r-φ plane. The time-averaged Nusselt numbers were in good agreement with correlations for a stationary cavity (with the gravitational accel-

Contributed by the International Gas Turbine Institute of ASME for publication in the JOURNAL OF ENGINEERING FOR GAS TURBINES AND POWER. Manuscript received June 19, 2006; final manuscript received January 11, 2007. Review conducted by Dilip R. Ballal. Paper presented at the ASME Turbo Expo 2006: Land, Sea and Air (GT2006), May 8–11, 2006. Barcelona, Spain. Paper No. GT2006-91134.

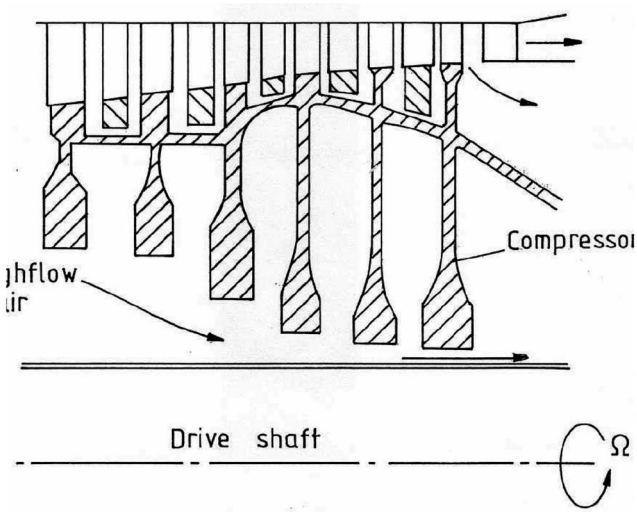

Fig. 1 Simplified diagram of high-pressure compressor rotor with axial throughflow

eration replaced by the centripetal acceleration), but they were significantly higher than the correlations of Bohn et al.; the reason for this overestimate of Nu was not understood.

The Sussex group [8–13] made measurements and computations for an open cavity (with $a/b \approx 0.1$) with an axial throughflow of cooling air. There was no central shaft or cylinder, and the outer cylindrical surface and/or the disks could be heated.

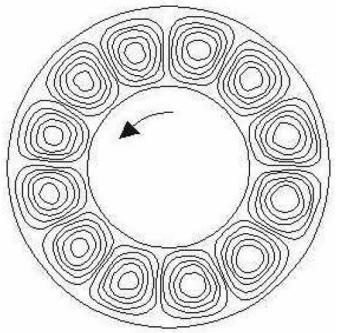

Fig. 2 Rayleigh-Bénard vortices in a closed rotating cavity

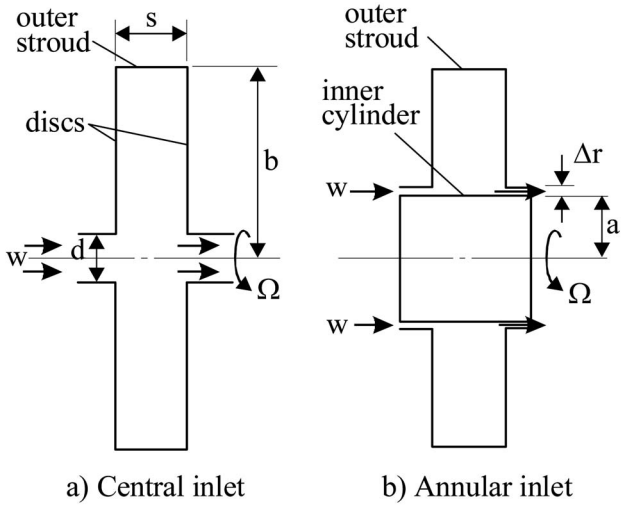

Fig. 3 Rotating cavity with axial throughflow of cooling air

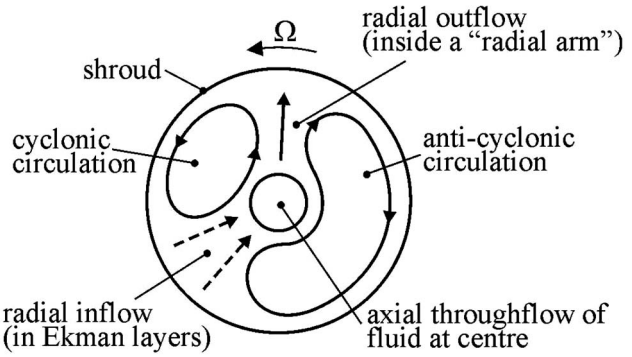

Fig. 4 Schematic of flow structure in a heated rotating cavity with an axial throughflow of cooling air

Farthing et al. [8] carried out flow visualization and LDA (laser-Doppler anemometry) studies in both isothermal and heated cavities. In isothermal cavities [14] with large gap ratios ($G > 0.4$), the axial throughflow generated a powerful toroidal vortex, the strength of which decreased as the Rossby number Ro decreased. Depending on the values of G and Ro, axisymmetric and non-axisymmetric vortex breakdown were observed in the central jet.

When one or both of the disks were heated, the flow in the cavity became non-axisymmetric, and cyclonic and anticyclonic vortices were observed, as shown schematically in Fig. 4. Farthing et al. used the so-called linear equations for rotating flows to explain that, as stated above, the cyclonic and anticyclonic circulation generated the circumferential pressure gradient that is needed to produce a radial flow inside the core of fluid between the disks. In particular, they observed a "radial arm" that convected cold air from the center to the periphery of the cavity. The core of fluid precessed at an angular speed (Ω_c say) slightly less than that of the disks; the ratio of Ω_c/Ω decreased as the temperature difference between the disks and the cooling air increased.

Owen and Powell [2] made measurements in an open cavity, where $a/b = 0.4$ and $G = 0.2$, in which one of the disks was heated. LDA and heat transfer measurements were made for $1.4 \times 10^3 < \mathrm{Re}_z < 5 \times 10^4$ and $4 \times 10^5 < \mathrm{Re}_\phi < 3.2 \times 10^6$. Spectral analysis of the LDA measurements revealed a multicell structure comprising one, two, or three pairs of vortices. As found in the experiments of Farthing et al., the core of fluid between the disks precessed at an angular speed, Ω_c, less than that of the disks, and Ω_c/Ω decreased as the temperature of the heated disk increased. At the smaller values of Re_z, the measured Nusselt numbers were consistent with buoyancy-induced flow; at the larger values of Re_z, the effect of the axial throughflow became dominant.

Tian et al. [15] computed the flow and heat transfer in a rotating cavity based on the geometry of Farthing et al. Their 3D, steady, turbulent computations showed that the flow structure comprised two parts: Rayleigh-Bénard convection at the larger radii, and forced convection in the central region. The computations suggested that there is a critical Rayleigh number above which the flow becomes unstable and time dependent.

Johnson et al. [16] investigated the stability characteristics of variable-density swirling flow in rotating cavities. Using a narrow-gap approximation for inviscid flow, they produced criteria for the necessary and sufficient conditions for stability. When the rotating surfaces are colder than the "cooling air" (such as at take-off in an aeroengine) the flow is stably stratified: the axial throughflow cannot penetrate very far into the cavity and the resulting convective heat transfer is relatively low. Conversely, when the rotating surfaces are hotter than the air (at cruise and landing), the flow is unstable, the axial flow can readily enter the cavity, and the heat transfer is increased as a consequence.

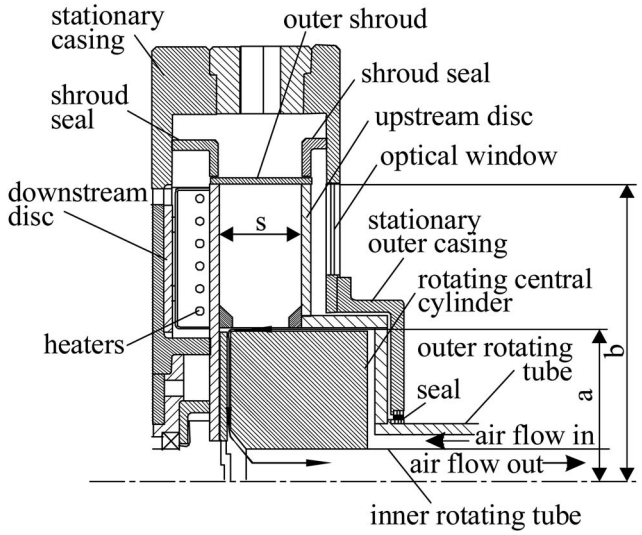

Fig. 5 Schematic of Bath rotating-cavity rig

3 Experimental Setup

The experimental apparatus and instrumentation are described below; more details are given in [2].

4 Experimental Rig

The Bath rotating-cavity rig is shown in Fig. 5. The salient dimensions of the cavity were $a=150$ mm, $b=371$ mm, $\Delta r=4.8$ mm, and $s=75.2$ mm ($x_a=a/b=0.40$, $G=s/b=0.20$).

The downstream disk was made from 10 mm thick steel, the back face of which was radiantly heated by a 21 kW stationary electric heater, and the front (cavity-side) face was covered by a 1 mm thick glass-fiber mat in the outer surface of which ten RDF fluxmeters and ten thermocouples were embedded. The upstream disc, which was 12 mm thick, was made from transparent polycarbonate. The outer shroud was made from 5 mm thick glass-fiber composite, the inner surface of which was thermally insulated by a 5 mm thick layer of Rohacell foam. The inner cylinder, which was made from Rohacell foam, rotated synchronously with the two disks and the shroud. So-called cobs, also made from Rohacell foam, were attached to the two disks; the cobs crudely modeled the geometry of compressor disks, and they also provided annular passages at inlet to and outlet from the cavity to encourage the air to enter and leave in the axial direction.

The rotating cavity and heater unit were enclosed by a stationary steel casing, designed to withstand a differential pressure of 3 bar. A window, in the upstream side of the casing, provided optical access for LDA measurements. Cooling air for the cavity, and pressurising air for the outer casing, was supplied by a Bellis & Morcom compressor with a maximum output of around 1 kg/s at 4 bar absolute pressure. The cooling air was supplied, via stationary piping and an inlet volute, into the annular space between the rotating inner and outer tubes. The air then flowed radially outward through the axial and radial clearances between the rotating inner cylinder and the upstream disc. After flowing axially through the cavity, the air left the system, via the axial clearance between the inner cylinder and the downstream disk, through the rotating inner tube from where it flowed into a stationary tube. Radial vanes, attached to the upstream and downstream radial faces of the inner cylinder, ensured that the air entered the system with solid-body rotation.

Owing to stress considerations, the maximum speed of the polycarbonate disk was limited to 1500 rev/min. The cavity was rotated by means of a combination of two thyristor-controlled dc motors (not shown in Fig. 5), with a total output of 26 kW, and the rotational speed of the cavity could be controlled to ±1 rev/min. A toothed-belt and pulley system was used to transfer the power from the motors to the upstream and downstream discs; a layshaft ensured corotation of the two disks.

5 Instrumentation

As stated above, there were ten thermocouples and ten fluxmeters on the front (cavity-side) surface of the heated downstream disk. (Owing to failures, and to the fact that insulating foam covered some of the instrumentation, not all the fluxmeters were serviceable.) The signals from the rotating instrumentation were brought out through a 52-channel silver/silver-graphite slip-ring unit. The voltages were then measured using a computer-controlled solartron data-logger and digital voltmeter with a resolution of ±1 μV. The uncertainty of the thermocouple measurements was estimated to be ±0.3°C. It was necessary to correct the measured heat fluxes for radiation from the heated disk to the unheated surfaces. Owen and Powell [2] suggested that their approximate black-body correction could result in an overestimate in the Nusselt numbers; a positive bias of Nu=50 could occur in the results presented here.

The temperatures of the air at inlet to and outlet from the system were measured using total-temperature probes inserted in the stationary tubing upstream and downstream, respectively, of the rig. The voltage outputs from the total-temperature probes were measured using the data-logger. No instrumentation was attached to the shroud or to the inner cylinder, both of which were sensibly adiabatic, or to the polycarbonate disk, which was quasi-adiabatic.

The flow rates of the cooling air and sealing air were measured using orifice plates made to British Standards BS1042, and the estimated uncertainty was ±3% of the measured flow rate. The absolute pressures of the air, and the pressure drop across the orifice plates, were measured using a pair of absolute and differential pressure transducers multiplexed by a Scanivalve system, the outputs of which were recorded on the data-logger.

The LDA system used a 4W Spectra-Physics argon-ion laser, the beam of which was transmitted to the optics through a fibre-optics cable with an efficiency of around 50%. The TSI optics, which were configured in a single-component back-scatter mode, were mounted on an x-y traversing table, allowing movement in the radial and axial directions. By turning the transmitting optics through 90 deg, it was possible to measure either the radial or the tangential component of velocity. The transmitting optics included a Bragg cell, which allowed frequency shifts of up to 40 MHz, and the beam spacing was 50 mm, which, with a 250 mm focal-length lens, produced an optical probe volume around 1.4 mm long and 0.14 mm diameter. The Doppler signal from the receiving optics was processed by a TSI IFA-750 burst-correlator, which could handle frequencies up to 90 MHz with signal-to-noise ratios as low as −5 dB. Micron-sized oil particles for the LDA measurements were injected into the cooling-air supply upstream of the rotating tubes in the rig. The estimated uncertainty in the velocity measurements was $0.01\Omega r$.

6 Computational Method

The geometry and computational mesh for the Bath rig is shown in Fig. 6. The final mesh had a total of 2,600,000 cells, with 6500 in the r-z plane and 400 in the tangential direction. A mesh study showed that it was important to have many cells in the tangential (φ) direction in order to resolve the thin radial arms referred to above. Nonuniform grid spacing was used to ensure that the values of y^+ for the grid points nearest the walls were less than unity.

The 3D unsteady compressible CFD simulations were computed, in the rotating frame of reference, using the commercial CFD code Fluent with a segregated implicit solver (SIMPLE). Second-order space-discretization, PRESTO pressure-discretization, and second-order implicit time-stepping were used.

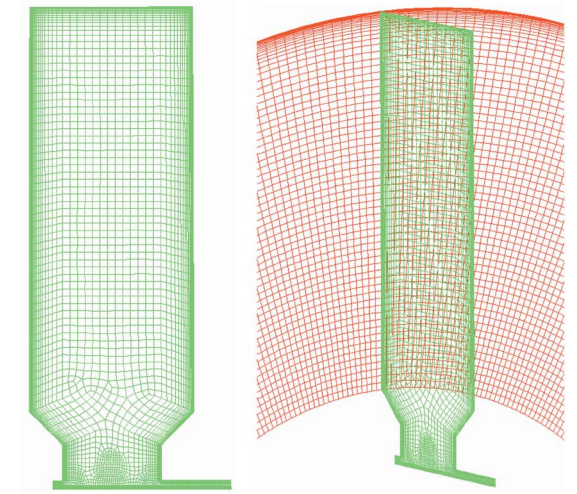

Fig. 6 Geometry and grid of CFD model

Table 1 Test matrix for the experiments

Experiment	($\div 10^6$)	Re_z ($\div 10^4$)	Ro
2	0.430	0.303	0.674
5	1.57	0.164	0.100
6	1.63	0.295	0.173

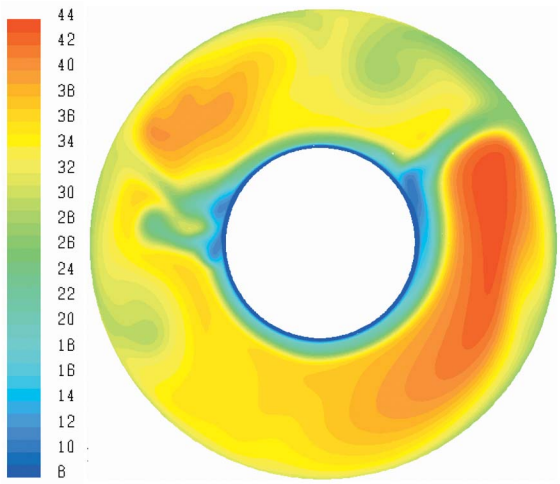

Fig. 8 Computed contours of ΔT_c (K) in mid-axial plane for experiment 2 ($Re_\phi/10^6=0.43$, $Re_z/10^4=0.303$)

The renormalized group (RNG) k-ε turbulence model was chosen, and different time steps and numbers of subiterations per time step were investigated. Before starting to collect results, the computation was run for a significant time, monitoring the integrated heat flux on the heated wall, to ensure that the final solutions were independent of the initial conditions.

The CFD analysis was run on a Linux PC cluster of 8 to 16 CPUs, and the computations took about 1 week to complete.

7 Computational Results

The CFD analyses were performed for the three experimental cases given in Table 1, and the radial distributions of ΔT (where $\Delta T=T_s-T_i$) for the heated disk are shown in Fig. 7.

Figures 8 and 9 respectively show computed contours of ΔT_c (where $\Delta T_c=T_c-T_i$) in the mid-axial r-φ plane, at $z/s=0.5$, for experiments 2 and 5. It should be noted that, as discussed below, the flow patterns changed with time, and the contours and vectors shown in Figs. 8–13 were the final ones computed.

It can be seen in Fig. 8, for experiment 2, that the axial throughflow of cooling air creates a circular ring of cold fluid (colored

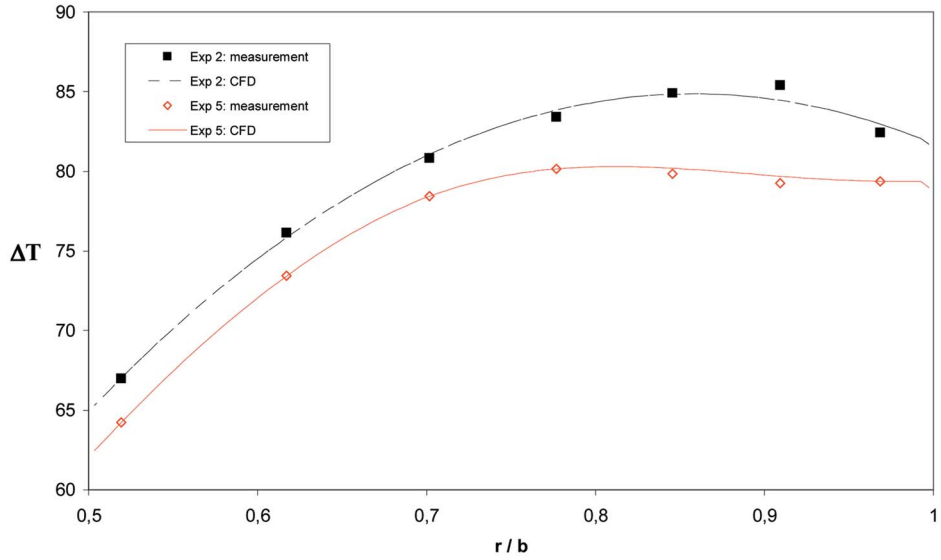

Fig. 7 Radial distribution of ΔT (K) for heated disk

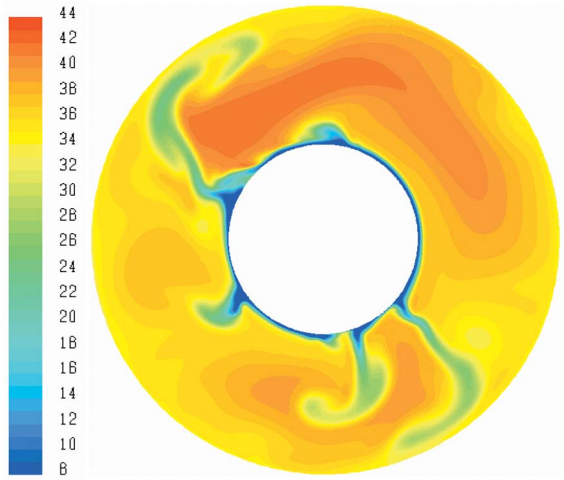

Fig. 9 Computed contours of ΔT_c (K) in mid-axial plane for experiment 5 ($Re_\phi/10^6=1.57$, $Re_z/10^4=0.164$)

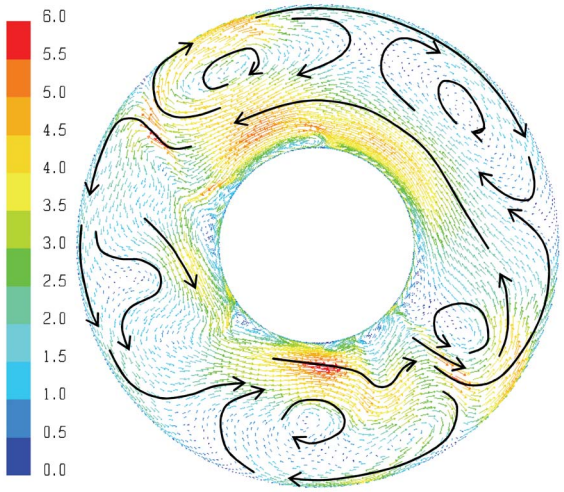

Fig. 11 Computed velocity vectors in mid-axial plane for experiemt 5 ($Re_\phi/10^6=1.57$, $Re_z/10^4=0.164$)

blue) at the center of the cavity. Radial arms (green), similar to the one shown in Fig. 4, transport some of the fluid from the center to the periphery of the cavity, creating a thin layer of cold air (green) adjacent to the unheated shroud. For experiment 2, two distinct radial arms are clearly visible, and this is in agreement with the two-cell structure that was observed experimentally. To the right of each radial arm is a region of high temperature (red), which, as discussed below, is caused by air that is convected from the heated disk into the fluid core.

The contours for experiment 5 in Fig. 9 are more complex. Several large and small radial arms can be seen, and to the right of each one is a high-temperature region. For this case, the experimental observations were unable to determine the number of cells. It is interesting to observe that the ring of cold air that can be seen near the center of Fig. 8 for experiment 2 is much larger than that in Fig. 9 for experiment 5. This is consistent with the findings of Farthing et al. [8] that the radial extent of the toroidal vortex, created by the throughflow, decreased as Ro decreased: for experiments 2 and 5, Ro=0.674 and 0.100, respectively.

Figures 10 and 11 show the computed velocity vectors, in the mid-axial r-φ plane, corresponding to the temperature contours discussed above. Some "streamlines" are superposed on the vectors so that the general flow structure can be seen more clearly. Colored contours, corresponding to the magnitude (in m/s) of the vectors, are used to show regions where the velocity is large relative to the rotating disks.

The radial outflows that separate regions of cyclonic and anticyclonic circulation in Fig. 10 correspond to the radial arms shown in Fig. 8. Although it cannot be seen from this figure, the axial width of the radial arms is the same as the spacing between the two cobs. To the right of the radial arms the circulation is cyclonic which, as noted by King et al. [1], corresponds to a region of low pressure in the core. In this region, air flows axially from the heated disk into the core, raising the temperature of the fluid in the mid-axial plane, as shown in Fig. 8. Conversely, in the anticyclonic zones to the left of the radial arms, the high pressure will create an axial flow towards the heated disk.

In a stationary fluid, a vertical plane plume of hot air creates vortices on either side. In a rotating fluid, a radial plume, or radial arm, of cold air creates a cyclonic and an anticyclonic vortex on either side and, as stated above, these vortices produce the circumferential gradient of pressure needed for the plume to penetrate radially into the rotating fluid. In Fig. 9, several embryonic radial arms can be seen, each with its associated pair of vortices, cir-

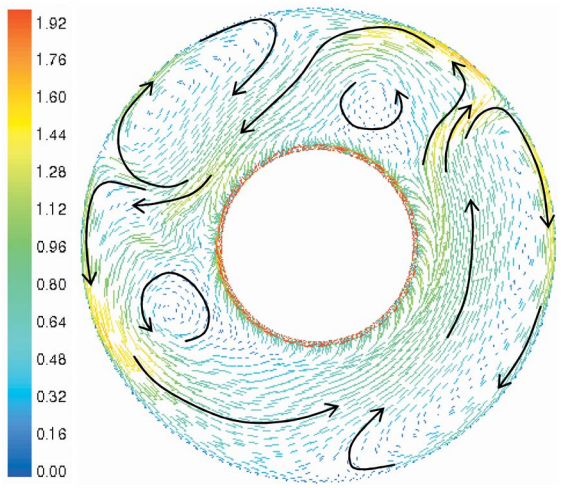

Fig. 10 Computed velocity vectors in mid-axial plane for experiment 2 ($Re_\phi/10^6=0.43$, $Re_z/10^4=0.303$)

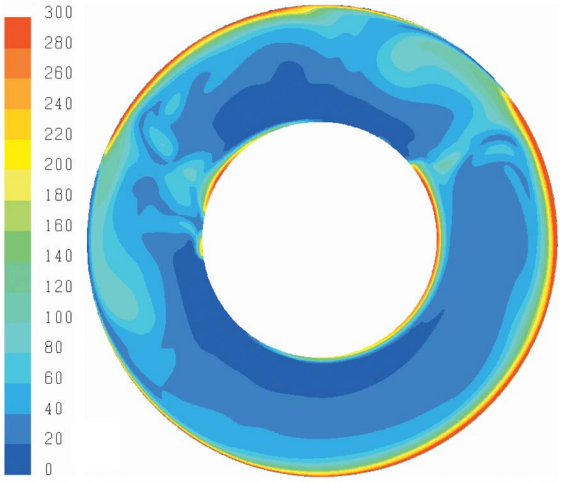

Fig. 12 Computed contours of Nusselt number for experiment 2 ($Re_\phi/10^6=0.43$, $Re_z/10^4=0.303$)

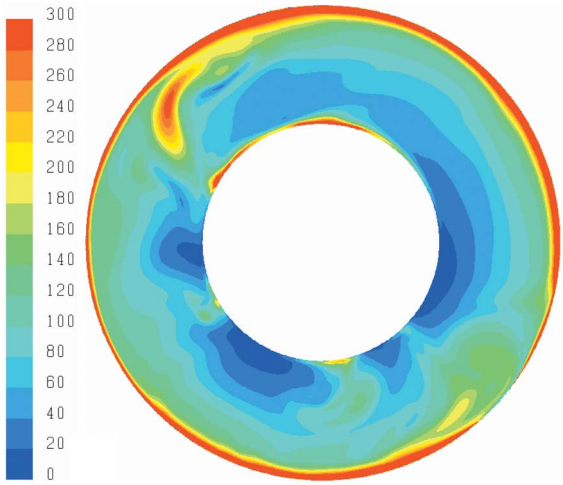

Fig. 13 Computed contours of Nusselt number for experiment 5 ($Re_\phi/10^6=1.57$, $Re_z/10^4=0.164$)

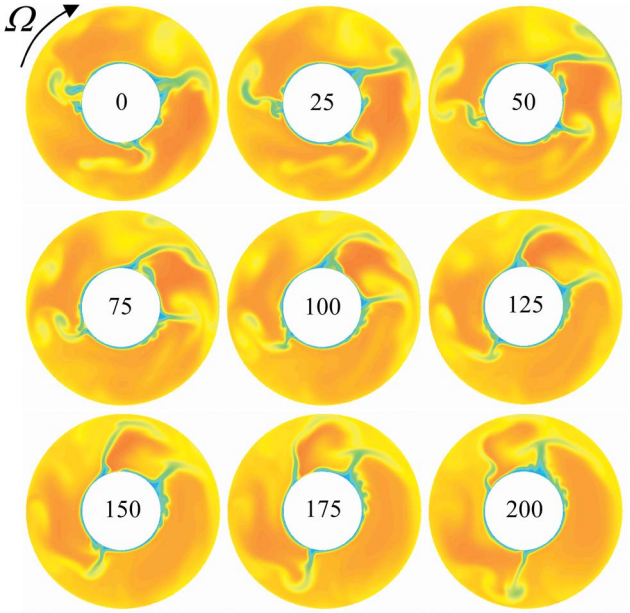

Fig. 15 Computed time-sequence of contours of ΔT_c in mid-axial plane for experiment 5 ($Re_\phi/10^6=1.57$, $Re_z/10^4=0.164$). Time in ms.

cumferentially to both left and right. There are also large values of Nu in Fig. 12 near the center where the axial throughflow impinges on the heated disk. Owing to the more complex flow structure in experiment 5, the similarity between the contours in Figs. 9 and 13 is less obvious.

Figures 14 and 15 show a time-sequence of computed contours of ΔT_c in the mid-axial plane for experiments 2 and 5, respectively. The temperature scale for the contours is the same as that shown in Figs. 8 and 9.

In Fig. 14 it can be seen that, although the overall flow structure is virtually invariant with time, the two radial arms rotate in the opposite sense to the rotation of the disks. This is consistent with the experimental measurements, in a *stationary frame of reference*, which show that the core of fluid rotates at a slower speed than the disks. Figure 15 shows that the core of fluid for experiment 5 rotates in the opposite sense to the disks, but the overall flow structure varies more with time than that for experiment 2.

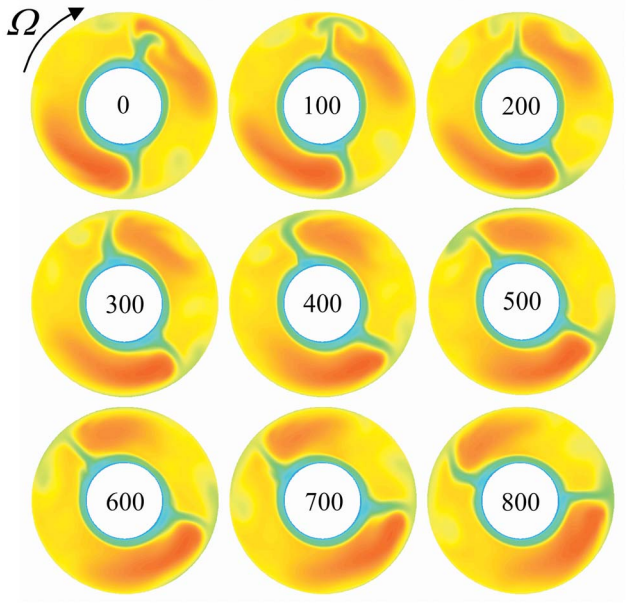

Fig. 14 Computed time-sequence of contours of ΔT_c in mid-axial plane for experiment 2 ($Re_\phi/10^6=0.43$, $Re_z/10^4=0.303$). Time in ms.

Figure 16 shows the comparison between the computed and measured radial distribution of $V_\phi/\Omega r$ in the mid-axial plane for experiments 2, 5, and 6. It should be noted that the measured velocities at a fixed radius were time-average values in a stationary frame of reference; as the core was rotating, these measured values were, in effect, both time and circumferential averages. The computations were made in the rotating frame, and the displayed velocities are circumferential averages at the last time step; the computed circumferential averages were found to agree well with time averages.

Bearing in mind the 1% uncertainty in the measured velocities, the computed distributions for experiments 2 and 6 show reasonable agreement with the measurements. The measured velocities of Farthing et al. [8] showed that $V_\phi/\Omega r \geq 1$ in the core of an isothermal cavity and, as a result of the toroidal vortex, which is discussed above, a maximum value of $V_\phi/\Omega r$ occurred near the center of the cavity, and this maximum value decreased as Ro decreased. This effect is consistent with the computations shown in Fig. 16: a computed maximum in $V_\phi/\Omega r$ occurs near the center ($x=0.4$) for experiment 2, where Ro=0.674, but not for experiments 5 and 6, where Ro=0.100 and 0.173, respectively.

The measured velocities for experiment 5 are significantly smaller than the computations. In the experiments of Farthing et al. [8], the values of $V_\phi/\Omega r$ at the larger radii of the heated cavity were mainly greater than 0.9. This was the also the case for around half of the 24 experiments reported by Owen and Powell [2]. In the other half, the measured values were similar to those shown in Fig. 16 for experiment 5, and these unusually low values for the core rotation did not appear to correlate with Re_ϕ, Re_z, or Ro. The differences between the computations and measurements for experiment 5 are not understood: either there were unknown experimental errors in the measurements or the low values were caused by a physical phenomenon, such as vortex breakdown, that was not captured by the computations.

Figure 17 shows the comparison between the computed and measured radial distribution of Nu for experiments 2, 5, and 6. The measured values of Nu were time-average values made by fluxmeters located at fixed locations on the rotating heated disk.

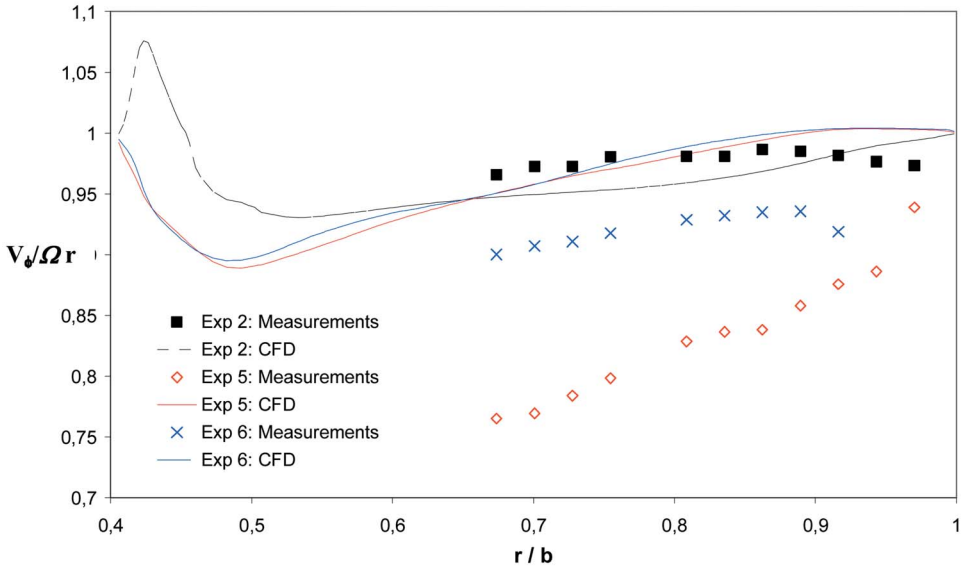

Fig. 16 Computed and measured radial distributions of $V_\phi/\Omega r$ in mid-axial plane for experiment 2 ($Re_\phi/10^6=0.43$, $Re_z/10^4=0.303$), experiment 5 ($Re_\phi/10^6=1.57$, $Re_z/10^4=0.164$), and experiment 6 ($Re_\phi/10^6=1.63$, $Re_z/10^4=0.173$)

The computed values represent circumferential space averages of the last time step; the computed circumferential averages were found to agree well with time averages.

In all three cases, the computations and measurements show similar qualitative radial distributions: the higher values of Nu measured near the center and shroud are captured by the computations. As stated above, the measured Nusselt numbers could be biased by the approximate radiation correction; this could result in a significant experimental overestimate of the true values of Nu. Bearing in mind the experimental uncertainties, the quantitative agreement is reasonably good for experiments 2 and 5, but the computations significantly underpredict the measurements for experiment 6; the underprediction is much greater than the maximum bias (Nu=50) in the measured values of Nu. It is possible that a conjugate solution, taking account of the radiation to and from the heated disk, could produce more accurate computations of Nu, but this has yet to be tried.

8 Conclusions

3D unsteady CFD analysis of the flow and heat transfer in a rotating cavity with an axial throughflow of cooling air have been performed using a commercial CFD code (Fluent) incorporating an RNG k-ε turbulence model. The CFD results have been compared with velocity and heat transfer measurements made in a rotating cavity rig in which one of the two disks was heated.

The computed contours of temperature and velocity vectors reveal a flow structure in which, as seen by previous experimenters, radial arms transport cold air from the center to the periphery of the cavity, and regions of cyclonic and anticyclonic circulation are formed on either side of each arm. In the regions of cyclonic circulation, where the pressure is low in the core, axial flow from the hot disk creates regions of high temperature in the core. The impingement of the radial arms on the shroud, and of the axial

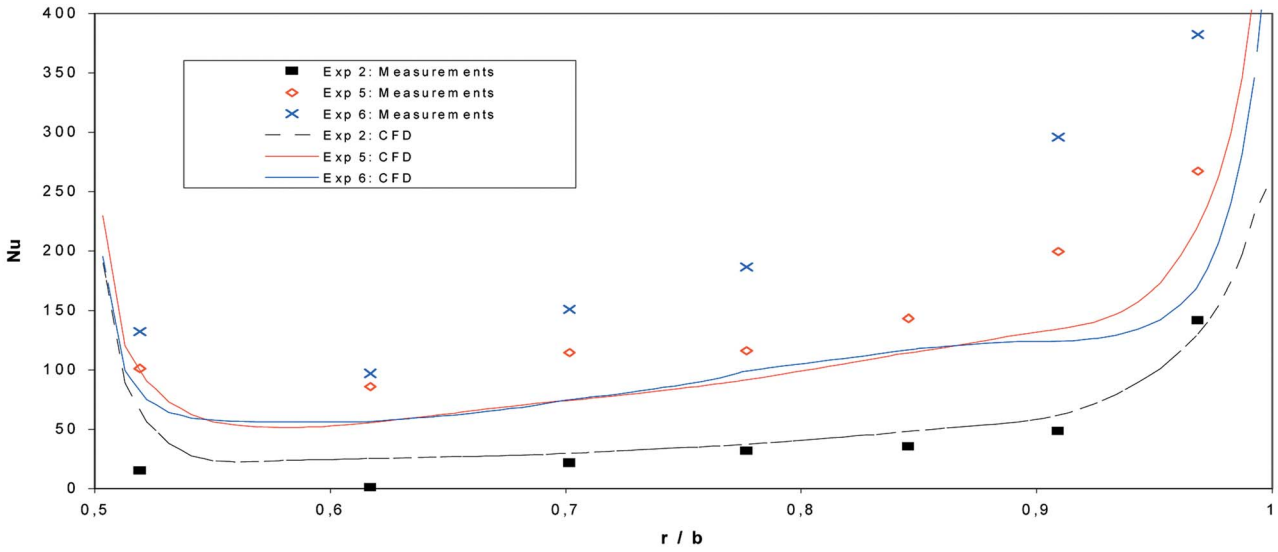

Fig. 17 Computed and measured radial distributions of Nu for experiment 2 ($Re_\phi/10^6=0.43$, $Re_z/10^4=0.303$), experiment 5 ($Re_\phi/10^6=1.57$, $Re_z/10^4=0.164$), and experiment 6 ($Re_\phi/10^6=1.63$, $Re_z/10^4=0.173$)

throughflow on the central region of the heated disk, creates regions of high heat transfer at the large and small radii of the disk.

The computed radial distribution of $V_\phi/\Omega r$ at $z/s=0.5$ agrees reasonably well with the measurements in two of the three cases considered here. In the third case, the computations significantly overpredict the measurements; the reason for this is not understood.

The computed and measured values of Nu for the heated disk show qualitatively similar radial distributions, with high values near the center and the periphery. In two of the cases, the quantitative agreement is reasonably good. In the third case, the computations significantly underpredict the measured values.

The research has been successful in helping to understand the flow physics, but more work is required before the engine designer can depend solely on CFD codes to predict buoyancy-induced flow in rotating cavities.

Acknowledgment

The authors wish to acknowledge the support of the other consortium partners in the ICAS-GT project and to thank the European Commission for helping to fund this work. We also thank Jon Powell for obtaining the experimental measurements used in this paper and Per Birkestad for help with some of the computations. We are also grateful to the reviewers for their helpful and constructive comments.

Nomenclature

a = inner radius of cavity (radius of inner cylinder)
b = outer radius of cavity
d = diameter of circular inlet
$\tilde{g}$ = acceleration
G = s/b, gap ratio
Gr = $\tilde{g}L^3\beta\Delta T/\nu^2$, Grashof number
k = thermal conductivity
L = characteristic length
$\dot{m}$ = mass flow rate
n = number of vortex pairs
Nu = $qL/k\Delta T$, Nusselt number
Pr = ν/α, Prandtl number
q = heat flux
r = radius
Ra = PrGr, Rayleigh number
Re_ϕ = $\Omega b^2/\nu$, rotational Reynolds number
Re_z = WL/ν, axial Reynolds number
Ro = $W/\Omega a$, Rossby number
s = axial gap between disks
t = time
T = absolute static temperature
T_c = temperature in core at $z/s=0.5$
T_i = inlet temperature
T_s = surface temperature of heated disk
V_r, V_ϕ = radial, tangential components of velocity in stationary frame of reference
W = bulk-average axial velocity at inlet
x = r/b, nondimensional radius
x_a = a/b, radius ratio of cavity
z = axial distance from heated disk
α = thermal diffusivity
β = T_i^{-1}, volume expansion coefficient
Δr = radial clearance between disks and inner cylinder
ΔT = $T_s - T_i$, disk temperature difference
ΔT_c = $T_c - T_i$, core temperature difference
μ = dynamic viscosity
φ = tangential coordinate
ν = kinematic viscosity
ρ = density
Ω = angular speed of cavity
Ω_c = angular speed of air

References

[1] King, M. P., Wilson, M., and Owen, J. M., 2007, "Rayleigh-Benard Convection in Open and Closed Rotating Cavities," ASME J. Eng. Gas Turbines Power, **129**, pp. 305–311.
[2] Owen, J. M., and Powell, J., 2006, "Buoyancy-Induced Flow in a Heated Rotating Cavity," ASME J. Eng. Gas Turbines Power, **128**, pp. 128–134.
[3] Bohn, D., Dibelius, G. H., Deuker, E., and Emunds, R., 1994, "Flow Pattern and Heat Transfer in a Closed Rotating Annulus," ASME J. Turbomach., **116**, pp. 542–547.
[4] Bohn, D., Deuker, E., Emunds, R., and Gorzelitz, V., 1995, "Experimental and Theoretical Investigations of Heat Transfer in Closed Gas Filled Rotating Annuli, ASME J. Turbomach., **117**, pp. 175–183.
[5] Bohn, D., Edmunds, R., Gorzelitz, V., and Kruger, U., 1996, "Experimental and Theoretical Investigations of Heat Transfer in Closed Gas-Filled Rotating Annuli II," ASME J. Turbomach., **118**, pp. 11–19.
[6] Bohn, D., and Gier, J., 1998, "The Effect of Turbulence on the Heat Transfer in Closed Gas-Filled Rotating Annuli," ASME J. Turbomach., **120**, pp. 824–830.
[7] Sun, X., Kilfoil, A., Chew, J. W., and Hills, N. J., 2004, "Numerical Simulation of Natural Convection in Stationary and Rotating Cavities," ASME Paper No. GT2004-53528.
[8] Farthing, P. R., Long, C. A., Owen, J. M., and Pincombe, J. R., 1992, "Rotating Cavity With Axial Throughflow of Cooling Air: Flow Structure, ASME J. Turbomach., **114**, pp. 237–246.
[9] Farthing, P. R., Long, C. A., Owen, J. M., and Pincombe, J. R., 1992, "Rotating Cavity With Axial Throughflow of Cooling Air: Heat Transfer," ASME J. Turbomach., **114**, pp. 229–236.
[10] Long, C. A., 1994, "Disk Heat Transfer in a Rotating Cavity With an Axial Throughflow of Cooling Air," Int. J. Heat Fluid Flow, **15**, pp. 307–316.
[11] Long, C. A., Morse, A. P., and Tucker, P. G., 1997, "Measurement and Computation of Heat Transfer in High Pressure Compressor Drum Geometries With Axial Throughflow," ASME J. Turbomach., **119**, pp. 51–60.
[12] Long, C. A., and Tucker, P. G., 1994, "Numerical Computation of Laminar Flow in a Heated Rotating Cavity With an Axial Throughflow of Air," Int. J. Numer. Methods Heat Fluid Flow, **4**, pp. 347–365.
[13] Long, C. A., and Tucker, P. G., 1994, "Shroud Heat Transfer Measurements From a Rotating Cavity With an Axial Throughflow of Air," ASME J. Turbomach., **116**, pp. 525–534.
[14] Owen, J. M., and Pincombe, J. R., 1979, "Vortex Breakdown in a Rotating Cylindrical Cavity," J. Fluid Mech., **90**, pp. 109–127.
[15] Tian, S., Tao, Z., Ding, S., and Xu, G., 2004, "Investigation of Flow and Heat Transfer in a Rotating Cavity With Axial Throughflow of Cooling Air," ASME Paper No. GT2004-53525.
[16] Johnson, B. V., Lin, J. D., Daniels, W. A., and Paolillo, R., 2004, "Flow Characteristics and Stability Analysis of Variable-Density Rotating Flows in Compressor-Disk Cavities," ASME Paper No. GT2004-54279.

Francesco Fantozzi
e-mail: fanto@unipg.it

Simone Colantoni
e-mail: simone_colantoni@unipg.it

Department of Industrial Engineering,
University of Perugia,
Via G. Duranti 67,
06125 Perugia, Italy

Pietro Bartocci
Biomass Research Center,
University of Perugia,
Via M. Iorio 8,
06125 Perugia, Italy
e-mail: bartocci@crbnet.it

Umberto Desideri
Department of Industrial Engineering,
University of Perugia,
Via G. Duranti 67,
06125 Perugia, Italy
e-mail: umberto.desideri@unipg.it

Rotary Kiln Slow Pyrolysis for Syngas and Char Production From Biomass and Waste—Part I: Working Envelope of the Reactor

A microscale electrically heated rotary kiln for slow pyrolysis of biomass and waste was designed and built at the University of Perugia. The reactor is connected to a wet scrubbing section, for tar removal, and to a monitored combustion chamber to evaluate the lower heating value of the syngas. The system allows the evaluation of gas, tar, and char yields for different pyrolysis temperatures and residence times. The feeding screw conveyor and the kiln are rigidly connected; therefore, a modification of the flow rate implies a modification of the inside solid motion and of residence time. The paper provides the theoretical and experimental calculation of the relationships between residence time and flow rate used to determine the working envelope of the reactor as a function of the feedstock bulk density and moisture content, given the actual heat rate of the electric heaters. The methodology is extendable to any rotary kiln reactor with a rigidly connected feeding screw conveyor, given its geometric and energetic specifications. Part II of the paper will extend the energy balance, also introducing the yields of pyrolysis products. [DOI: 10.1115/1.2720521]

Keywords: biomass, pyrolysis, rotary kiln, residence time, syngas, tar, char

Introduction

Residual energy sources, such as biomass and waste (B&W), may contribute effectively to meeting the Kyoto Protocol targets by reducing both the recourse to fossil fuels and the volume of waste to dispose of. Toward this aim, the University of Perugia has developed the integrated pyrolysis recuperated plant (IPRP) technology [1,2], which allows B&W energy conversion on microscale in order to achieve sustainability for small communities. The advantages of distributed generation from residuals are, namely, the reduction of the local impact of the plant, of the harvesting process, and obviously of transmission losses. A pilot IPRP plant was built at the Terni facility of the University of Perugia [3]. The core of the 70 kW_{el} power plant is a rotary kiln pyrolyzer previously designed and built with the help of data provided by a laboratory scale, electrically heated, rotary kiln that was designed and built, to this aim, at the University of Perugia [4]. The main characteristic of the laboratory pyrolizer is that the rotary kiln and the feeding screw conveyor are rigidly connected, so they must rotate together. The laboratory pyrolizer is briefly described in the following section. The present paper describes the theoretical and experimental activity that was carried out to determine the working envelope of the reactor, as a function of biomass humidity and density, through a mass and energy balance.

Pyrolysis

Biomass pyrolysis is the thermal decomposition of wood, which is made up of cellulose, hemicellulose, and lignin. Cellulose decomposition takes place at about 325–400°C; the mechanism of cellulose decomposition as studied by Kilzer and Broido [5] may be described as a sequence of events, such as dehydration of cellulose (200–280°C), depolymerization of cellulose (280–340°C) and formation of volatiles, and decomposition of hydrocellulose into gases and char residue via exothermic reaction (320°C). The volatiles formed during reaction, also known as tars, consist mainly of levoglucosans. Primary and secondary reactions of cellulose pyrolysis can be modeled according to Di Blasi [6].

Hemicelluloses heated in a nitrogen atmosphere in a differential thermal analysis study [7] show an initial endothermic process, caused by bond-water loss, followed by exothermic processes, beginning at about 180°C and reaching a peak at 255°C; therefore, hemicelluloses are the first compounds in wood to be thermally degraded. According to Kudo and Yoshida [8], lignin decomposition begins at about 280°C, with a maximum occurring between 350°C and 450°C. The degradation is completed at 500°C.

Browne [9] divides the pyrolysis processes into four zones, or temperature ranges, all of which can be present simultaneously in wood of appreciable thickness:

- Zone A, below 200°C, in which only noncombustible gases, primarily water vapor, are produced. Dehydration of sorbed water is complete.
- Zone B, from 200° to 280°C, in which the reactions are endothermic, and the products are almost entirely nonflammable.
- Zone C, from 280° to 500°C, in which active pyrolysis takes place under exothermic conditions, leading to secondary reactions among the products. The products are largely combustible (carbon monoxide, methane, etc.), and include the highly flammable tars in the vapor state.
- Zone D, above 500°C, in which the residue consists primarily of charcoal, which provides an extremely active site for further secondary reactions, therefore acting as a catalyst.

Temperature is therefore a very important parameter in pyrolysis reaction because it influences both quantity and quality of the

Contributed by the International Gas Turbine Institute of ASME for publication in the JOURNAL OF ENGINEERING FOR GAS TURBINES AND POWER. Manuscript received July 11, 2006; final manuscript received January 4, 2007. Review conducted by Dilip R Ballal. Paper presented at the ASME Turbo Expo 2006: Land, Sea and Air (GT2006), May 8–11, 2006, Barcelona, Spain, Paper No. GT2006-90818.

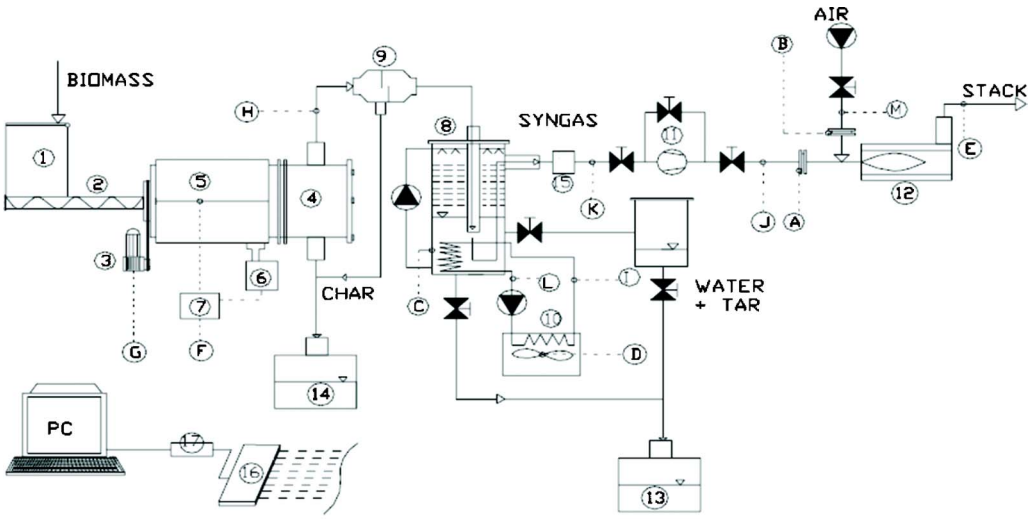

Number	Items	Letter	Measures and Controls
1	Hopper	A	Flow measure
2	Screw conveyor	B	Flow measure
3	Engine gear and chain	C	Temperature measure
4	Kiln discharge section	D	Fan Control
5	Electrical heaters	E	Temperature measure
6	Power Controller	F	Temperature Control
7	PID	G	Rotational Speed Control
8	Gurgler and scrubber	H	Temperature measure
9	De-ashing device	I	Temperature measure
10	Cooling Radiator	J	Temperature measure
11	Compressor	K	Temperature measure
12	Burner LHV measure	L	Temperature measure
13	Tars stockage	M	Temperature measure
14	Char stockage		
15	Filter and demister		
16	I/O interface		
17	Data Acquisition Board		

Fig. 1 Test bench layout [1]

products obtained. About this topic, Bridgwater [10] asserts that for fast pyrolysis the lower limit on wood decomposition is approximately 435°C for obtaining acceptable liquid yields of at least 50% with low reaction times.

Thus, a "time-temperature history" can be a good approach for a preliminary analysis of a pyrolysis reactor.

Residence time in a pyrolysis reactor is also a key parameter to ensure that the reaction happens, needing to be greater than the reaction time. Moreover, temperature is also influenced by radiative and convective transport, internal conduction, and chemical reactions; residence time depends on the path that particles follow inside the reactor, which depends on particle density, gravity, size, heat capacity, and rotational speed of the kiln.

In this paper an experimental analysis on mean residence time of biomass in a rotary kiln reactor, and preliminary results of an energy balance, are used to individuate which is the optimal rotational speed for the rotary kiln pyrolyzer, as a function of biomass characteristics; namely, humidity content and bulk density.

Test Bench Layout

To support the ongoing activities on pyrolysis at the University of Perugia, with particular reference to the IPRP demonstrative unit design and realization [3], a laboratory rotary kiln pyrolyzer was designed and built. With reference to Fig. 1, and to Ref. [4] for a detailed description, the pyrolyzer is basically organized into three main components:

- the pyrolyzer;
- the syngas cleaning section;
- the syngas burner.

The feeding section consists of an airtight hopper connected to a screw conveyor, while the rotary kiln is made of an AISI 304 steel pipe provided with ceramic external heaters to provide the reactor and its content with the energy required to reach pyrolysis temperature. An electric motor, through a gear and a chain, keeps rotating both the kiln and the screw conveyor, which are rigidly connected. The rotary kiln enters a coaxial stationary cylinder to discharge pyrolysis products (char and gas).

The gaseous phase (composed by syngas and tar vapors) passes through a cleaning section; namely, a calm chamber, for char particulate elimination, and a humid quencher-scrubber, made of a cylinder full of water through which the gas gurgles, condensing water and tar vapors. Fine particulate, light tars, and water pass to a secondary vessel and are eventually discharged. Heavy tars accumulate in the bottom of the main vessel.

The syngas burner is monitored in terms of both syngas flow

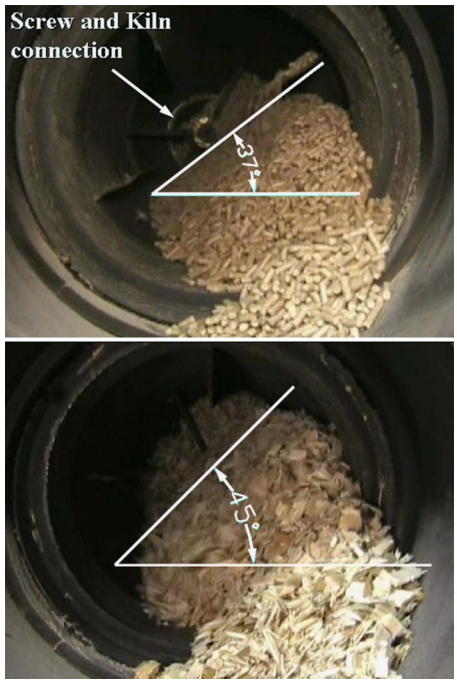

Fig. 2 Graphic—experimental calculation of the dynamic angle of repose for pellet (above) and wood chips (below)

and air flow; temperatures are also measured before and after the combustion, so that a mass and energy balance can be carried out to evaluate the LHV of the gas.

Objectives

The residence time of the feedstock in the reactor is a very important parameter in pyrolysis process because it determines the energy received by the biomass at a given heating rate. This parameter strongly influences the yield of the products given the humidity content and the size of the biomass. In rotary kilns, residence time is usually a function of the mean volumetric flow and of the rotational speed of the kiln. In this particular case, the two quantities are not independent variables because the screw conveyor is rigidly connected to the kiln (Fig. 2); therefore, they both rotate at the same speed. The rotational speed (n) of the screw conveyor therefore determines the feed rate and the bed depth inside the kiln, which have a direct effect on mass and energy balance. The rotational speed of the kiln (n) determines the motion of particles inside the kiln, directly affecting both heat transfer and residence time. For a given heat rate, and where rotational speed is directly related to volumetric flow, as in our case, it is essential to determine the optimal rotational speed (n) that guarantees that enough energy reaches the feedstock before it exits the reactor. This energy is obviously a function of feedstock characteristics.

When the rotary kiln and screw conveyor are not rigidly connected, it is possible to change the rotational speed of the reactor without affecting the feed rate and consequently the bed depth inside the kiln, which directly determines the transverse motion of the particles. The rotational speed as a function of feedstock characteristics may be addressed as the working envelope of the kiln reactor, which is the aim of the present paper.

Methodology

The transverse motion that assures a correct mass and heat transfer for the pyrolysis process is the so-called rolling motion [11–13]. It is possible to evaluate the particle trajectory under this solid bed condition by means of equilibrium equations that describe mean excursion time, which is the average time required by a particle to pass through the reactor, and mean volumetric flow, as a function of rotational speed and biomass and reactor characteristics. However, they require correction with experimental data obtainable through the *technique of tracers*. This analysis also provides the minimum rotational speed value ($n_{\min}$) that guarantees rolling motion.

Eventually, a balance between the energy supplied by shell heaters and the energy required to bring biomass to pyrolysis initial conditions, provides the maximum rotational speed ($n_{\max}$) as a function of the physical characteristics of the material (moisture, bulk density), and also the minimum residence time.

Table 1 Geometrical characteristics of the reactor

External diameter (cm)	32.5
Internal diameter (cm)	31.9
Thickness (cm)	0.3
Length (cm)	100.0

Solids' Transverse Motion

In this first part of the work, an analysis of the dynamics of solid materials in the bed is carried out. Different types of motion can develop in a rotary kiln, but only rolling motion is desirable for a good pyrolysis.

In this motion regime, the bed material may be divided into two regions: a thinner active layer and a thicker stagnant one. The rolling motion is characterized by a uniform flow of the particles inside the active layer, while particles in the stagnant region are carried upward by the rotating wall, until they enter the active layer and roll again.

This motion assures a mixing of the solid bed, which optimizes mass and heat transfer thus accelerating pyrolysis reactions. MET (of the solids through the reactor) and MVF (or mass flow) are directly affected by:

- characteristics of the feedstock (dynamical angle of repose);
- geometric characteristic of the reactor (roughness of the inside wall, exit dam, internal structures);
- operating parameters (kiln slope and rotational speed).

MET and MVF can be determined theoretically from the analysis of solids particle motion inside the reactor. Models in the Literature can be subdivided into two groups:

- axial distribution model, in which solid particles are considered like an ideal fluid [14];
- particle trajectory model, in which solid particles are considered like a granular substance [15].

This paper focuses on vector analysis of gravity-induced axial displacement of a solid particle in a single rolling step [16], which is based on PTM. The trajectory of a single particle is traced under the hypothesis of the rolling bed, while MET and MVF are, respectively, shown in Eqs. (1) and (2)

$$\mathrm{MET} = \frac{L \sin \theta_d}{2\pi R n(\tan \alpha + \cos \theta_d \tan \bar{\beta})\cos^2 \bar{\beta}} \tag{1}$$

$$\mathrm{MVF} = \frac{4}{3} n \pi \cos^2 \bar{\beta} \left(\frac{\tan \alpha}{\sin \theta_d} + \cot \theta_d \tan \bar{\beta} \right) (2Rh_0 - h_0^2)^{3/2} \tag{2}$$

as in [16], where L is the axial length and R the internal radius of the reactor, while θ_d is the dynamical angle of repose, α the kiln slope, h_0 the inlet depth of solid bed, and $\bar{\beta}$ the averaged bed slope. The mean mass flow is the product of MVF and bulk density ρ. The geometrical characteristics of the reactor are reported in Table 1.

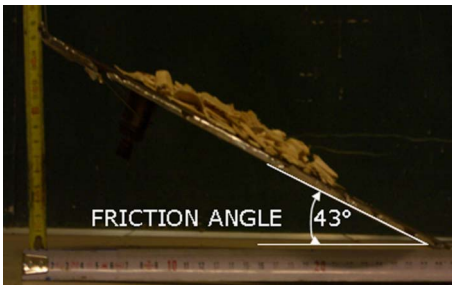

Fig. 3 Graphic—experimental calculation of the friction angle for wood chips

No dam at the outlet section, and a horizontal kiln ($\alpha=0$) were considered. Friction characteristics were determined experimentally for two different feedstocks, namely, chips and pellet, as follows.

The dynamic angle of repose influences the transport and the mixing of solids into the reactor and it can be considered constant in rolling motion. The dynamic angle of repose was calculated on multiple images of the rolling bed motion through a 3D rendering software (Fig. 2). Results show very low data scattering and are consistent with the ones provided by the rotary drum method [17].

Similarly, wall friction factor μ_W was calculated tilting a surface with the same roughness of the reactor and previously covered with the material. The angle at which solids fall is the friction angle (Fig. 3). The values of the wall friction factor, reported in Table 2, show that the cylindrical shape of pellet favors their fall along the inclined surface, while the tabulate shape of wood chips increases adhesion.

Checking of Rolling Motion. Equations (1) and (2) are valid for a rolling motion which, according to [11], requires the following conditions:

- $10^{-4} < \mathrm{Fr} < 10^{-2}$
- $f > 0.1$
- $\mu_W > \mu_{WC}$

where Fr is the Froude Number, f is the filling degree, μ_W is the wall friction coefficient, and μ_{WC} is the critical wall friction coefficient.

Check of Froude Number. The Froude number is the ratio of centrifugal force to gravity

$$\mathrm{Fr} = \frac{\omega^2 R}{g} \tag{3}$$

Therefore, for $D=0.319$ m, rolling motion is always possible in the range of 0.75 rpm to 7.5 rpm, which includes the chosen working condition.

Check of Filling Degree. According to [11], the filling degree is defined as the portion of the cylinder cross section occupied by the bed; it is determined through the filling angle as follows

Table 2 Feedstock characteristics

Material	Shape	Bulk density (kg/m^3)	Middle size (mm)	Dynamic angle of repose (deg)	Friction factor μ_W	Average bed slope $\bar{\beta}$ (deg)
Pellet	Cylindrical	650	Φ6×20	37±2%	0.61	8.10
Wood chips	Tabulate	200	15×40×5	45±2%	0.93	5.82

Table 3 Filling degree of the kiln at inlet and outlet for pellet and wood chips

		Bed depth (cm)	ε (deg)	f	Check rolling motion $f>0.1$
Pellet	H_{in}	13.0	158.68	0.380	Yes
	H_{ex}	2.0	58.00	0.026	No
Wood chips	H_{in}	18.5	161.00	0.600	Yes
	H_{ex}	8.0	120.20	0.200	Yes

$$f = \frac{1}{\pi}\left(\frac{\varepsilon}{2} - \sin\frac{\varepsilon}{2}\cos\frac{\varepsilon}{2}\right) \tag{4}$$

where ε represents the bed angle of the circular segment occupied with solids and it is obtained as follows

$$\varepsilon(z) = 2\cos^{-1}\left(1 - \frac{H(z)}{R}\right) \tag{5}$$

where $H(z)$ is the solid bed's depth as a function of z, which represents the kiln axis. The height of the bed was measured at the inlet and outlet of the kiln for both pellet and wood chips, and results are shown in Table 3.

Results show that the rolling motion condition is always verified for wood chips, while pellets tend to reduce their tendency to roll the farther they proceed into the kiln. The 0.1 limit for the filling degree is therefore crossed at the very end of the kiln and may be raised by introducing a dam at the end.

Hence, it may be concluded that the rolling motion condition is verified.

Check of Wall Friction Coefficient. The critical wall friction coefficient (μ_{WC}), may be defined as

$$\mu_{WC} = \frac{2\sin^3\frac{\varepsilon}{2}\sin\theta_d}{3\pi f(1+\mathrm{Fr})} \tag{6}$$

which leads to the results highlighted in Table 4.

Rolling motion is therefore verified also with respect to friction.

Results and Discussions

The aim of Part I of this paper is to define the working envelope of the rotary kiln from the particle motion point of view without any heat applied. Therefore, possible alterations of a particle when heated, such as stickiness, as well as tendencies to swell and to agglomerate, are neglected.

MET and MVF must be calculated once the system has reached steady state condition; that is, when feed rate and output of the materials are the same. Toward this aim, the mass flow was measured by collecting samples every minute and weighting them with an electronic balance. Steady state was assumed to be reached when the difference between two consecutive samples was negligible (<0.5%). Results are shown in Fig. 4.

Values obtained for steady state mass flow are shown in Table 5 together with values obtained from screw conveyor theory: a good agreement is detectable.

MET was also experimentally evaluated through the technique of tracers [18], assuming the hypothesis of a normally distributed

Table 4 Wall friction coefficient for pellets and wood chips

	μ_W	μ_{WC}	$\mu_W > \mu_{WC}$
Pellet	0.61	0.37	Yes
Wood chips	0.93	0.43	Yes

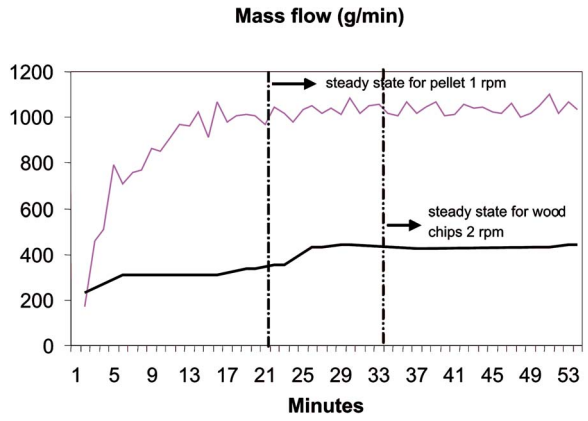

Fig. 4 Steady state mass flow for pellet and wood chips

excursion time. Once steady state was reached, 60 tracers were introduced inside the reactor, each tracer being a particle of material colored with paint, as shown in Fig. 5.

Tracers were divided into three groups, colored with different paints (red, blue, green), and each group was inserted at a different time. The inlet time of each group of tracers was recorded, as well as the number of exit tracers in each time interval. With these data, the mean value and variance of MET were calculated as follows:

$$\mathrm{MET} \approx \sum_{i=1}^{I} t_i E(\Delta t_i) \tag{7}$$

$$\sigma^2 \approx \sum_{i=1}^{I} (t_i - \mathrm{MET})^2 E(\Delta t_i) \tag{8}$$

where t is the MET of the ith sampling interval of amplitude Δt_i, I is the number of sampling intervals, and E is the number of tracers in the interval normalized to the total number.

Data obtained are shown in Figs. 6 and 7.

Table 5 Steady state mass and volumetric flow for pellets and wood chips

	Pellet	Wood chips
Bulk density (kg/m^3)	650	200
n (rpm)	1	2
Time necessary to get the steady state (min)	22	34
Mass flow (kg/min)	1.028	0.437
Volumetric flow (dm^3/min)	1.580	2.180
Screw conveyor mass flow (kg/min)	1.030	0.431
$Q=\rho\pi(D_{SC})^2 p\varphi n/4$		

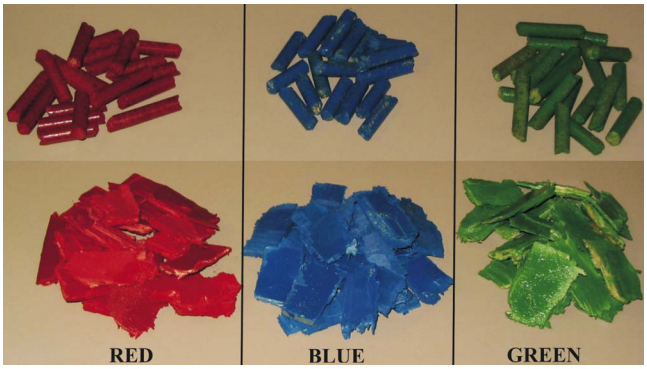

Fig. 5 Colored tracers for MET evaluation

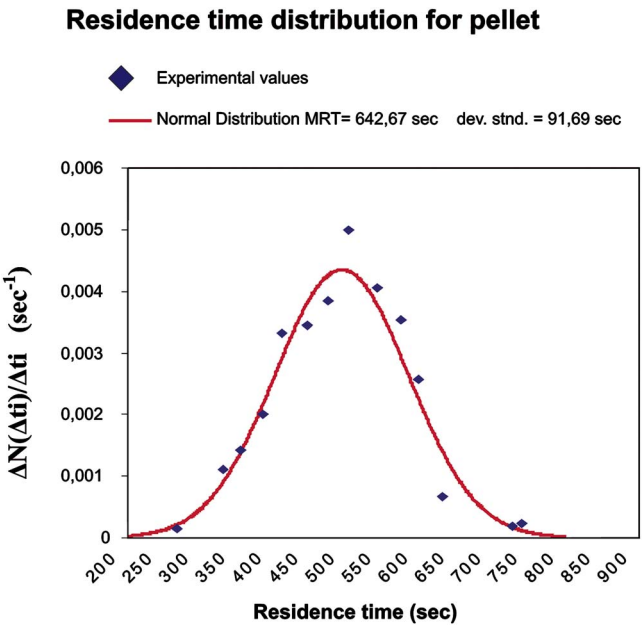

Fig. 6 MET normal distribution for pellets

Table 6 shows the comparison between theoretical values (PTM) and experimental values for MET and MVF. Results show an average underestimation of MET ranging from 30% for pellet to 40% for wood chips.

The difference may be due to having discarded the interaction between particles and kiln surface. In particular, the presence of internal ribs slows down the flow, especially when the feedstock is not of regular shape. This explains also why the underestimation is higher for chips than for pellets.

Correction coefficients were then introduced to meet experimental results as shown in Table 6. The magnitude of the correction coefficients, and therefore of the error committed on the evaluation of MET, points out the necessity of experimental verification of real values of MET for best design and control of kiln reactors.

Residence time distribution for wood chips

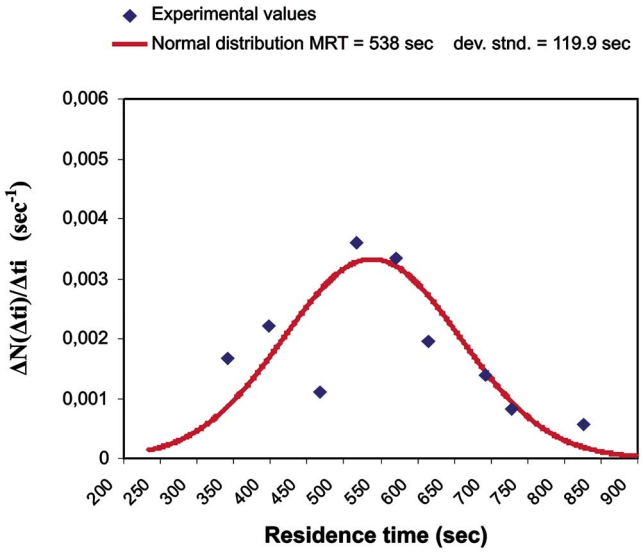

Fig. 7 MET normal distribution for wood chips

Table 6 Comparison between theoretical values (PTM) and experimental values for MET and MVF

	MET_{PTM} (s)	MET_{EXP} (s)	ε_t $\left(\frac{MET_{EXP}}{MET_{PTM}}\right)$	MVF_{PTM} (dm^3/min)	MVF_{EXP} (dm^3/min)	ε_f $\left(\frac{MVF_{EXP}}{MVF_{PTM}}\right)$
Pellet	439.8	642.7	1.46	2.26	1.58	0.70
Wood chips	305.4	538.2	1.76	3.30	2.18	0.66

Kiln Working Envelope

According to Browne [9] endothermic reactions of wood pyrolysis start at about 200°C, that is almost the same activation temperature of hemicellulose (~180°C) [7]. Therefore, assuming a pyrolysis starting temperature of 200°C, energy supplied by the electrically heated ceramic shells equals the energy required to heat the biomass from ambient temperature to 200°C plus the energy absorbed by the water content of biomass to reach the same temperature (also considering evaporation)

$$P\eta = \mathrm{MVF}\,\rho C(T_s - T_a) + m\,\mathrm{MVF}\,\rho\Delta h \tag{9}$$

where P is the electric power provided by heaters, η is the heat exchange efficiency (experimentally evaluated in a drying test), C is the specific heat of the biomass, m is the moisture content, and Δh is the water enthalpy variation. Considering data provided in Table 7 and introducing Eq. (2) into Eq. (9), the resulting equation will provide the required rotational speed as a function of biomass humidity and bulk density.

The above-derived relation may be plotted in a 3D surface that depicts the maximum rotational speed required to start pyrolysis, as a function of biomass humidity and bulk density.

The upper limit of 3 rpm corresponds to the maximum rotational speed of the reactor when the frequency provided by the inverter of the motor is 50 Hz.

The lower limit for rotational speed is imposed by the rolling motion conditions and does not depend on material characteristics. The surface in Fig. 8 is therefore valid only above 0.75 rpm (plane surface in Fig. 8) if rolling motion is desired. Under these conditions pyrolysis can start only for materials with a very low humidity content (for wood chips the humidity has to be less than 50%, but for a material with a higher bulk density, i.e., 600 kg/m^3, humidity reaches almost 0%). In order to use feedstocks with higher water content, the uncoupling of the screw conveyor from the kiln is then required. On the other hand, a kiln designed with a lower diameter would have a higher representative surface, therefore a higher rolling motion limit (Fig. 9).

Conclusions

The working envelope of the laboratory kiln pyrolyzer of the University of Perugia was determined with a theoretical and experimental approach. The kiln utilizes a single electrical engine for the rotation of both the screw conveyor and the kiln, and the working envelope is a 3D surface that provides rotational speed as a function of biomass humidity and bulk density.

Table 7 Constant values used in the energy balance

Parameter	Value	Source
P (kW)	7.5	Measured
η	0.7	Measured
T_s (K)	473	Assumed
T_a (K)	293	Assumed
C (kJ/kgK)	2.567	[19]
Δh (kJ/kg)	2790	Assumed

To this aim, the mean excursion time was calculated, but the theoretical approach did not provide reliable results and an experimental validation was necessary. Results show that when a rolling motion is required, only dry biomass must be used; otherwise, it is necessary to uncouple screw and kiln. If the coupling is desired for economical reasons and energy saving, the kiln must be designed with a smaller value of internal diameter. In Part II of this work, the energy balance (9) will be further developed introducing a pyrolysis model that takes into account the reactions and the yields of products. Eventually, the energy balance will provide the yields of products as a function of rotational speed.

Acknowledgment

The authors gratefully acknowledge the contribution of S. Massoli, who performed the experimental tests, and Dr. A. Giovannozzi for graphical editing and useful discussions.

Nomenclature

- B&W = biomass and waste
- C = specific heat, J/kg K
- D = diameter, m
- DTA = differential thermal analysis
- E = number of tracers in the sampling interval normalized to the total number
- Fr = Froude number
- I = number of sampling intervals
- L = axial length, m
- LHV = lower heating value, MJ/kg
- MET = mean excursion time, s
- MVF = mean volumetric flow dm^3/min
- P = electric power, W
- PTM = particle trajectory model
- R = internal radius of the reactor, m
- T = temperature, K
- F = filling degree of kiln reactor
- g = gravity acceleration, m/s^2

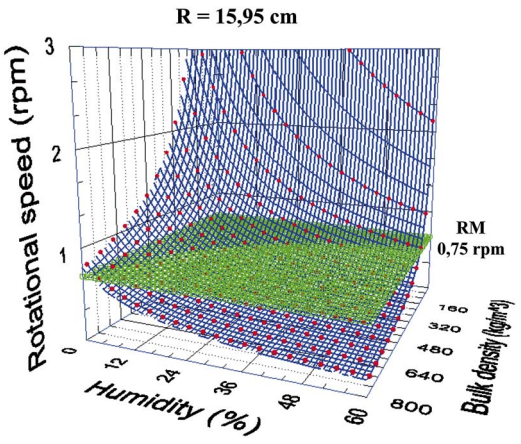

Fig. 8 Working envelope of the reactor

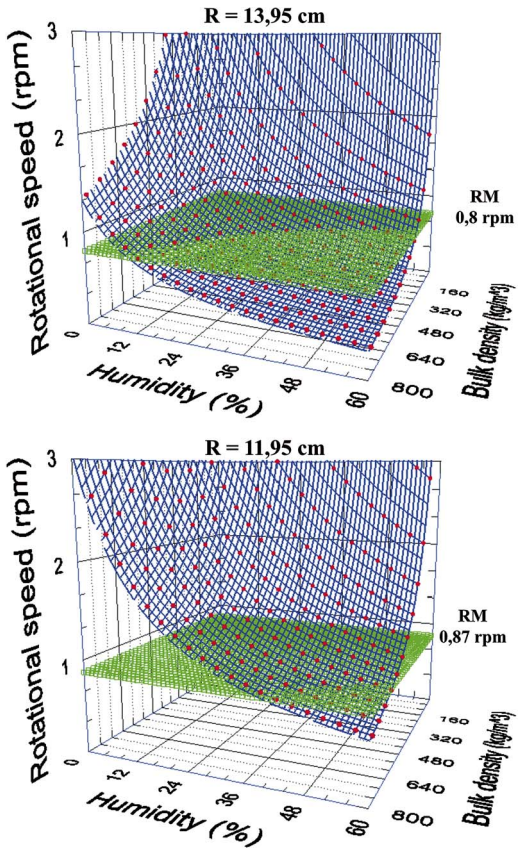

Fig. 9 Working envelope of the reactor for different internal diameters of rotary kiln

h = depth of solid bed, m
m = moisture, %
n = rotational speed, rpm
p = step of the propeller, m

Symbols

Δh = enthalpy variation, J/kg
Δt = amplitude of the sampling interval, s
α = kiln slope, deg
β = averaged bed slope, deg
$\varepsilon/2$ = filling angle of kiln reactor, deg
η = heat exchange efficiency
θ = angle of repose, deg
μ = friction coefficient
σ = variance, s
ρ = bulk density, kg/dm^3
φ = filling degree of screw conveyor
ω = rotational speed, rad/s

Subscripts

SC = screw conveyor
W = wall
WC = wall critical
a = Ambient
d = Dynamic
i = ith sampling interval
o = inlet
s = pyrolysis starting

References

[1] Fantozzi, F., D'Alessandro, B., and Bidini, G., 2003, "IPRP—Integrated Pyrolysis Regenerated Plant—Gas Turbine and Externally Heated Rotary-Kiln Pyrolysis as a Biomass and Waste Energy Conversion System. Influence of Thermodynamic Parameters," Proc. Inst. Mech. Eng., Part A, **217**, pp. 519–527.

[2] Fantozzi, F., D'Alessandro, B., and Desideri, U., 2005, "IPRP—Integrated Pyrolysis Regenerated Plant—An Efficient and Scalable Concept for Gas Turbine Based Energy Conversion From Biomass and Waste," ASME J. Eng. Gas Turbines Power, **127**, pp. 348–357.

[3] Bidini, G., Moriconi, A., Rossi, D., and Fantozzi, F., 2004, "IPRP–Integrated Pyrolysis Regenerated Plant—Rotary Kiln Pyrolyzer and Microturbine for Distributed Energy Conversion From Biomass a 70 kW Demonstration Unit in Central Italy," *2nd World Conference on Biomass for Energy, Industry and Climate Protection*, Rome, Italy, May 10–14.

[4] Fantozzi, F., and Desideri, U., 2004, "Micro Scale Slow Pyrolysis Rotary Kiln for Syngas and Char Production From Biomass and Waste," *2nd World Conference on Biomass for Energy, Industry and Climate Protection*, Rome, Italy, May 10–14.

[5] Kilzer, F.J., and Broido, A., 1965, "Speculations on the Nature of Cellulose Pyrolysis," Pyrodynamics, **2**, pp. 151–163.

[6] Di Blasi, C., 1996, "Influences of Model Assumptions on the Predictions of Cellulose Pyrolysis in the Heat Transfer Controlled Regime," Fuel, **75**(1), pp. 58–66.

[7] Domansky, R., and Rendos, F., 1962, "On the Pyrolysis of Wood and its Components," Holz Roh-Werkst., **20**, pp. 473–476.

[8] Kudo, K., and Yoshida, E., 1957, "On the Decomposition Process of Wood Constituents in the Course of Carbonization. I. The Decomposition of Carbohydrate and Lignin in Mizunara (Quercus Crispula Blume) Wood," Mokuzai Gakkaishi, **3**(4), pp. 125–127.

[9] Browne, F. L., 1958, "Theories on the Combustion of Wood and its Control," U.S. Forest Prod. Lab., Rep. 2136, Madison, WI., p. 59.

[10] Bridgwater, A. V., 1999, "Principles and Practice of Biomass Fast Pyrolysis Processes for Liquids," J. Anal. Appl. Pyrolysis, **51**, pp. 3–22.

[11] Mellmann, J., 2001, "The Transverse Motion of Solids in Rotating Cylinders - Forms of Motion and Transition Behaviour," Powder Technol., **118**, pp. 251–270.

[12] Reuter, G., 1975, "Das Transport - und Mischverhalten von Drehrohrofenmoller bei der Erzeugung von Eisenschwamm," Ph.D. dissertation, RWTH Aachen, Germany.

[13] Cross, M., 1979, "The Transverse Motion of Solids Moving Through Rotary Kilns," Powder Technol., **22**, pp. 187–190.

[14] Danckwerts, P. V., 1953, "Continuous Flow Systems—Distribution of Residence Times," Chem. Eng. Sci., **2**, pp. 1–13.

[15] Saeman, W. C., 1951, "Passage of Solids Through Rotary Kilns—Factors Affecting Time of Passage," Chem. Eng. Prog., **47**, pp. 508–514.

[16] Li, S.-Q., Yan, J.-H., Li, R.-D., Chi, Y., and Cen, K.-F., 2002, "Axial Transport and Residence Time of MSW in Rotary Kilns—Part II. Theoretical and Optical Analyses," Powder Technol., **126**, pp. 228–240.

[17] Henein, H., Brimacombe, J. K., and Watkinson, A. P., 1983, "Experimental Study of Transverse Bed Motion in Rotary Kilns," Metall. Trans. B, **14B**, pp. 191–204.

[18] Li, S.-Q., Yan, J.-H., Li, R.-D., Chi, Y., and Cen, K.-F., 2002, "Axial Transport and Residence Time of MSW in Rotary Kilns Part I. Experimental," Powder Technol., **126**, pp. 217–227.

[19] Koufopanos, C. A., Papayannakos, N., Maschio, G., and Lucchesi, A., 1991, "Modelling of the Pyrolysis of Biomass Particles. Studies on Kinetics, Thermal and Heat Transfer Effects," Can. J. Chem. Eng., **69**, pp. 907–915.

Rotary Kiln Slow Pyrolysis for Syngas and Char Production From Biomass and Waste — Part II: Introducing Product Yields in the Energy Balance

Francesco Fantozzi
e-mail: fanto@unipg.it

Simone Colantoni
e-mail: simone_colantoni@unipg.it

Department of Industrial Engineering,
University of Perugia,
Via G. Duranti 67,
06125 Perugia, Italy

Pietro Bartocci
Biomass Research Center,
University of Perugia,
Via M. Iorio 8,
06125 Perugia, Italy
e-mail: bartocci@crbnet.it

Umberto Desideri
Department of Industrial Engineering,
University of Perugia,
Via G. Duranti 67,
06125 Perugia, Italy
e-mail: umberto.desideri@unipg.it

A microscale electrically heated rotary kiln for slow pyrolysis of biomass and waste was designed and built at the University of Perugia. The reactor is connected to a wet scrubbing section, for tar removal, and to a monitored combustion chamber to evaluate the lower heating value of the syngas. The system allows the evaluation of gas, tar, and char yields for different pyrolysis temperature and residence time. The feeding screw conveyor and the kiln are rigidly connected; therefore a modification of the flow rate implies a modification of the inside solid motion and of residence time. Part I of the paper describes the theoretical and experimental evaluation of the working envelope of the reactor, that is, rotational speed as a function of feedstock density and humidity content, to obtain pyrolysis conditions inside the kiln. This paper describes the development and resolution of an energy balance of the reactor under pyrolysis conditions. Once the rotational speed n is fixed, the aim of the balance is to obtain the yield of wood biomass pyrolysis products such as syngas, tar, and char. Results can be used to choose the correct rotational speed of kiln and feeding screw before doing the real pyrolysis test.
[DOI: 10.1115/1.2720539]

Keywords: biomass, pyrolysis, syngas, tar, char, residence time, rotary kiln, energy balance

Introduction

Residual energy sources, such as biomass and waste (B&W), may contribute effectively to meeting the Kyoto Protocol targets by reducing both the recourse to fossil fuels and the volume of waste to dispose of. Toward this aim, the University of Perugia has developed the integrated pyrolysis recuperated plant (IPRP) technology [1,2], which allows B&W energy conversion on microscale in order to achieve sustainability for small communities. The advantages of distributed generation from residuals are, namely, the reduction of the local impact of the plant, of the harvesting process, and obviously of transmission losses. A pilot IPRP plant was built at the Terni facility of the University of Perugia [3]. The core of the 70 kW_{el} power plant is a rotary kiln pyrolyzer that was designed and built with the help of the data provided by a laboratory scale, electrically heated, rotary kiln previously designed and built, to this aim, at the University of Perugia [4]. The laboratory pyrolyzer was briefly described in Part I of this work [5], pointing out the peculiarity of its having the feeding screw mechanically connected to the kiln; therefore, both rotate at the same speed. In the first part of this work, a theoretical and experimental activity was carried out to determine mean residence time inside the kiln and mean mass flow, as a function of the rotating speed of the kiln and of biomass characteristics (humidity and bulk density). This was used to determine the minimum rotational speed required to maintain optimal rolling motion inside the bed and the maximum value above which pyrolysis does not start because the heat available is not sufficient. The aim of this second part of the work is to introduce a biomass pyrolysis model into the energy balance to obtain the yield of pyrolysis product as a function of rotational speed and as before of biomass humidity content and bulk density.

Energy Balance

In Part I of this work, biomass pyrolysis was considered starting at a temperature of 200°C. Below this temperature, the external energy supplied is used to heat biomass from ambient temperature to 200°C and to heat and vaporize the humidity present in the biomass by means of Eq. (1)

$$P\eta = \mathrm{MVF}\ \rho C_B(T_s - T_a) + \%m\ \mathrm{MVF}\ \rho\Delta h \tag{1}$$

where P is the electric power provided to heaters, η is the heat exchange efficiency, C_B is the specific heat of the biomass, $\%m$ is the moisture content, and Δh is the water enthalpy variation. This balance provides the pyrolysis retention time (PRT) inside the kiln, that is, the time necessary to obtain starting pyrolysis conditions, as a function of rotational speed, humidity content, and bulk density of the feedstock.

When PRT is smaller than the overall kiln residence time (RT), that is, the time required for a particle to pass through the whole kiln, the biomass begins to decompose into gas, tar, and char with a mechanism that will be described in the following section.

In this case there exists a time interval (RT–PRT) in which the energy provided by the electrical heaters will be partly used to decompose the biomass, partly to heat residual dry biomass and water vapor, and partly to heat pyrolysis product as described in the energy balance of the kiln (Eq. (2))

Contributed by the International Gas Turbine Institute of ASME for publication in the JOURNAL OF ENGINEERING FOR GAS TURBINES AND POWER. Manuscript received July 11, 2006; final manuscript received January 5, 2007. Review conducted by Dilip R. Ballal. Paper presented at the ASME Turbo Expo 2006: Land, Sea and Air (GT2006), May 8–11, 2006, Barcelona, Spain. Paper No. GT2006-90819.

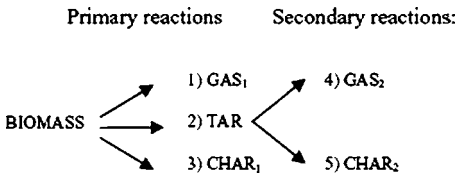

Fig. 1 Simplified scheme for biomass pyrolysis as derived from [10]

$$E_S = E_G + E_T + E_C + Q_G + Q_T + Q_C + Q_B + Q_V \tag{2}$$

where

E_S=External energy supplied from time equal to pyrolysis retention time
E_G=Energy used up for gas production
E_T=Energy used up for tar production
E_C=Energy used up for char production
Q_G=Energy absorbed to warm up the gas produced
Q_T=Energy absorbed to warm up the tar produced
Q_C=Energy absorbed to warm up the char produced
Q_B=Energy absorbed to warm up the residual dry biomass
Q_V=Energy absorbed to warm up the vapor

Pyrolysis

To evaluate the energy required by the pyrolysis reaction, we will refer to the kinetic scheme shown in Fig. 1 derived from [6–10]. According to [10], the primary reaction is the thermal degradation of biomass into gas, tar, and char; eventually, when the temperature reaches a higher value, with reference to Fig. 1, tar decomposes into gas and char in secondary reactions. The first three reactions are endothermic, while the fourth and fifth are exothermic. According to Browne [11], primary reactions for wood begin at about 200°C, while the secondary exothermic reactions begin at about 280°C, in which active pyrolysis takes place under exothermic conditions. The energies required to carry out the above reactions may be expressed as the product of the mass produced and the heat of reaction: hence, they may be calculated through five equations in the form.

$$E_i = H_i m_i \tag{3}$$

where the index i refers to the five reactions; E and m are, respectively, the energy required by, or released from, the ith reaction and the mass produced, while H is the heat of reaction (positive for i=1 to 3 and negative for i=4 to 5). The yields of the different products (ranging from 1 to 5), and the contemporary diminution of biomass, are a function of both time and temperature. Mass variation with time may be expressed as shown in Eq. (4) according to [10]

Table 1 Physical characteristics of wood chips and rotational speed range for rolling motion as derived from [5]

Material	Bulk density (kg/m^3)	Moisture (%)	n_{max} (rpm)	n_{min} (rpm)
Wood chips	200	10	1.97	0.25

$$\begin{cases} \dfrac{dm_B}{dt} = -(k_1 + k_2 + k_3)m_B \\ \dfrac{dm_1}{dt} = k_1 m_B \\ \dfrac{dm_2}{dt} = k_2 m_B - (k_4 + k_5)m_2 \\ \dfrac{dm_3}{dt} = k_3 m_B \\ \dfrac{dm_4}{dt} = k_4 m_2 \\ \dfrac{dm_5}{dt} = k_5 m_2 \end{cases} \tag{4}$$

The dependence on temperature is intrinsically introduced with the equilibrium constants k_i of primary (k_1, k_2, k_3) and secondary (k_4, k_5) reactions. They may be expressed with the Arrhenius correlation

$$k_i = A_i e^{-E_i/(RT)} \quad i = 1 \ldots 5 \tag{5}$$

in which A is the frequency factor, E is the activation energy, R is the gas constant, and T is the temperature at which the reaction takes place. Considering an infinitesimal time interval dT in which the temperature may be kept constant, Eqs. (4) can be integrated assuming as initial conditions:

(1) for primary reactions (t=0):

$$\begin{cases} m_B = m_0 \\ m_1 = m_2 = m_3 = 0 \end{cases} \tag{6}$$

(2) for secondary reactions (t=t^*, where t^* is the time corresponding to a T=280°C, that is, the temperature at which the secondary exothermic reactions begin):

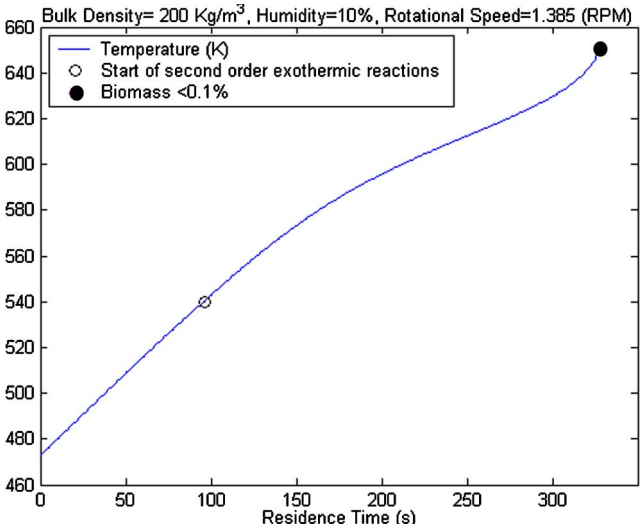

Fig. 2 Temperature as a function of residual time after PRT (ρ=200 kg/m^3; %m=10%; 1.385 rpm)

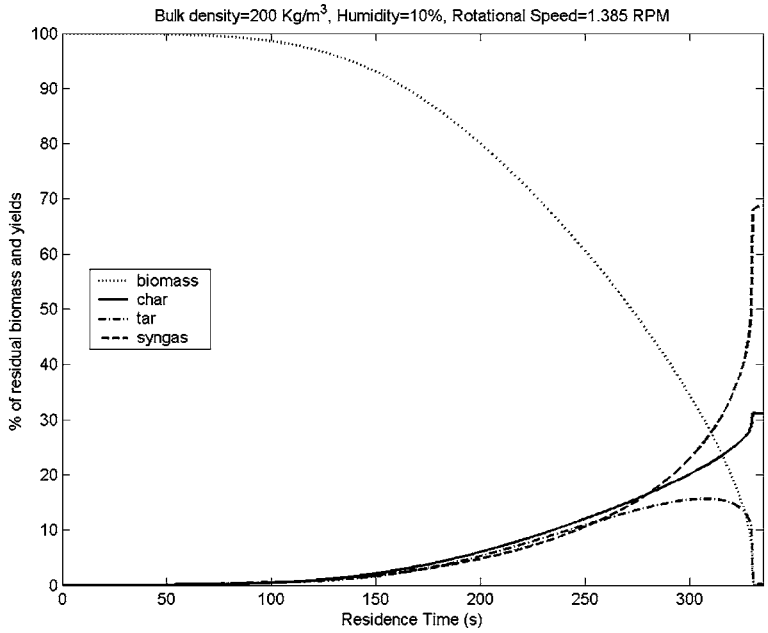

Fig. 3 Residual dry biomass and pyrolysis products yields as function of residual time after PRT (ρ=200 kg/m^3; %m=10%; 1.385 rpm)

$$\begin{cases} m_4 = 0 \\ m_5 = 0 \end{cases} \tag{7}$$

Heating Terms

The heat required to warm up the yields may be expressed as

$$Q_j = \int \int dm_j C_j dT \quad j = G,T,C \tag{8}$$

The index j refers to gas, tar, and char, and the infinitesimal masses dm_j, which experience the temperature excursion dT, are expressed as in Eq. (9) directly derived from the solution of Eq. (4)

$$dm_G = dm_1 + dm_4 = (k_1 m_B + k_4 m_2)dt$$

$$dm_T = (k_2 m_B + (k_4 + k_5)m_2)dt$$

$$dm_C = dm_3 + dm_5 = (k_3 m_B + k_5 m_2)dt \tag{9}$$

The heat absorbed to warm up the residual biomass is expressed as

$$Q_B = m_0 C_B (T - 473\ \text{K}) - \int \int (k_1 + k_2 + k_3) m_B C_B dt dT \tag{10}$$

The heat absorbed from water vapor (Q_V) to warm up from 473 K to the temperature T is easily derived from steam tables.

Solving

Equations (10) and (8) are double-integrals in time and temperature, and their ranges are

$$0 < t < (\text{RT} - \text{PRT}); \quad 473\ \text{K} < \text{Temp} < T$$

The left side of the energy balance (2) is only a function of the residence time, while the right member is a function of both residence time and temperature. This balance was solved in MATLAB® environment for each given rotational motion of the kiln and for a range of rotational speed between rolling motion condition (lower limit) and the maximum value, where PRT is coincident with RT.

The software outputs the temperature trend of the biomass inside the kiln, as it proceeds from the PRT instant until it exits the kiln, and also the yield of pyrolysis products.

The energy balance was carried out for wood chips. This material was studied in Part I of the work, in which the maximum and minimum values of rotational speed were determined (Table 1). Table 2 shows the constant values used to solve the system of equations.

Results and Discussion

Figure 2 shows the time evolution of temperature at a rotational speed of 1.385 rpm, which is the maximum rotational speed that still allows a complete pyrolysis process for the infinitesimal mass dm within the length span of the reactor; that is, when pyrolysis is complete at the outlet of the reactor.

Table 2 Constant values used in the energy balance

Parameter	Value	References
$P(W)$	7500	Experimentally determined
η	0.7	Experimentally determined
H_1=H_2= H_3(kJ/kg)	420	Di Blasi [12]
H_4=H_5 (kJ/kg)	−40	Liden et al. [13]
A_1 (s^{-1})	1.44×10^4	Thurner and Mann [14]
A_2 (s^{-1})	4.13×10^6	Thurner and Mann [14]
A_3 (s^{-1})	7.38×10^5	Thurner and Mann [14]
A_4 (s^{-1})	4.28×10^6	Liden et al. [13]
A_5 (s^{-1})	1×10^5	Di Blasi [12]
E_1 (kJ/mol)	88.6	Thurner and Mann [14]
E_2 (kJ/mol)	112.7	Thurner and Mann [14]
E_3 (kJ/mol)	106.5	Thurner and Mann [14]
E_4 (kJ/mol)	107.5	Liden et al. [13]
E_5 (kJ/mol)	107.5	Di Blasi [12]
R (J/mol K)	8.314	
C_B (J/kg K)	2567	Fantozzi et al. [5]
C_T (J/kg K)	2500	Di Blasi [13]
C_G (J/kg K)	1100	Di Blasi [13]
C_C (J/kg K)	1000	Di Blasi [13]

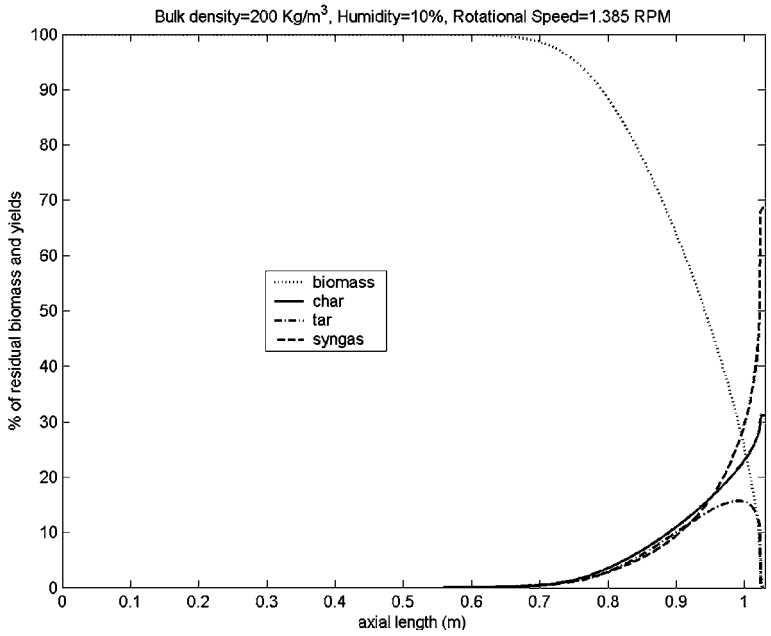

Fig. 4 Residual dry biomass and pyrolysis products yields as function of axial length (ρ=200 kg/m^3; %m=10%; 1.385 rpm)

The curve shows the presence of two flexions. The first one, approximately at 150 s, is caused by the beginning of primary reactions, that are endothermic, hence increasing absorbed energy for product formation and decreasing the T rise rate. The second flexion, approximately at 270 s, is caused by a lower amount of biomass available (which tends dramatically to zero in the last sections of the reactor) while the same heating rate is provided: a temperature increase in the feedstock is therefore experienced.

The maximum value of temperature reached is 650 K after 325 s; it is obvious that for longer residence times the temperature will still be growing, but the chemical reactions will be completed by then.

Figure 3 shows the time evolution of biomass and pyrolysis products as a function of residual time after PRT; that is, RT – PRT. To pyrolyze all initial biomass m_0 in the chosen conditions at least 360 s are required, which corresponds to a rotational speed of about 1.385 rpm. This result shows that pyrolysis of wood chips with a humidity content of 10% and a bulk density of 200 kg/m^3 is consistent with the range of rotational speed imposed by rolling motion conditions (see Table 1). The time evolution of tar yield shows a growing trend which gradually diminishes as secondary reactions begin (second flexion, Fig. 2). As the thermal degradation of tar in gas and char proceeds during sec-

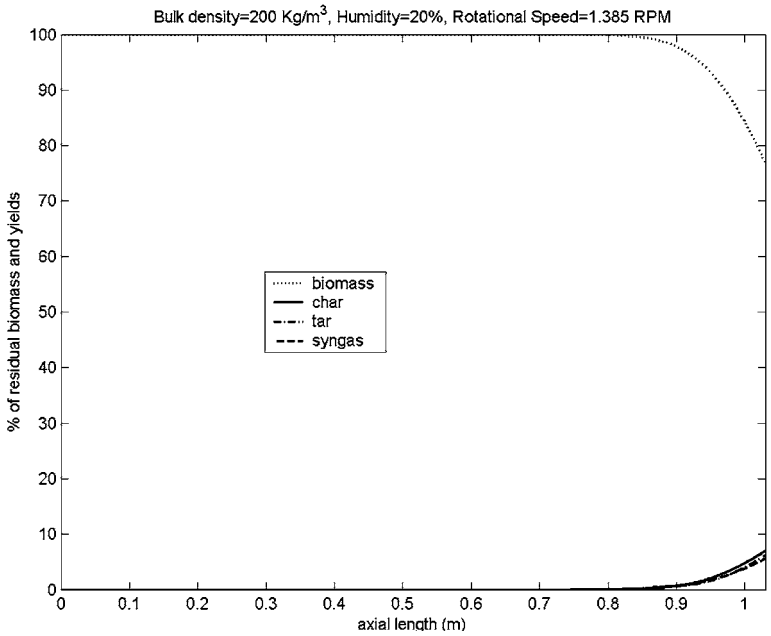

Fig. 5 Residual dry biomass and pyrolysis products yields as function of axial length (ρ=200 kg/m^3; %m=20%; 1.385 rpm)

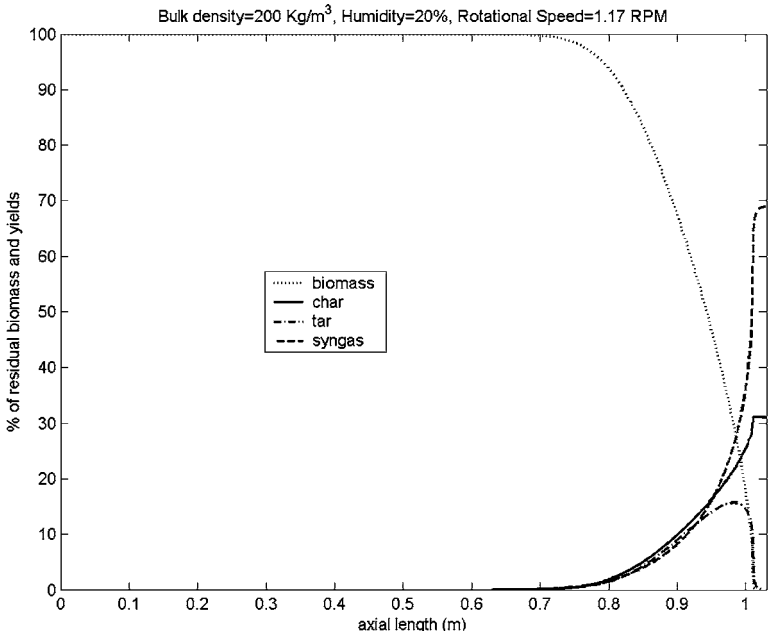

Fig. 6 Residual dry biomass and pyrolysis products yields as function of axial length (ρ=200 kg/m^3; %m=20%; 1.17 rpm)

ondary reactions the curve inverts the trend and a maximum value of about 15.6% (time=330 s, temperature=630 K) is present; eventually, tar is consumed and reaches zero.

The time evolution of char and gas are both increasing, until a maximum value of ~31% for char and ~67% for syngas is reached when biomass and tar have completely reacted. These curves are consistent with trends available in the literature [16,17].

Figure 4 shows the same curves as a function of the axial length of the reactor. It can be noticed that since pyrolysis is complete approximately at outlet of the kiln, the yields of pyrolysis products remain constant and a complete biomass conversion is achieved. As stated in Table 1 and referring to Fig. 4, for rotational speeds above the maximum value (1.97 rpm) pyrolysis does not begin, while values below 1.385 rpm are not necessary because the complete conversion of biomass is achieved at this speed.

Figure 5 shows that increasing the humidity of the biomass (from 10% (wb) to 20% (wb)) at the same rotational speed (n =1.385 rpm), results in a pyrolysis process far from completion. A lower value of the rotational speed (1.17 rpm), as shown in Fig. 6, is therefore necessary to pyrolyze the more humid feedstock. Similarly a humidity of 30% (wb) needs a rotational speed of 1 rpm to pyrolize the whole feedstock (data not shown in figure).

Similar trends are observed when increasing bulk density for a

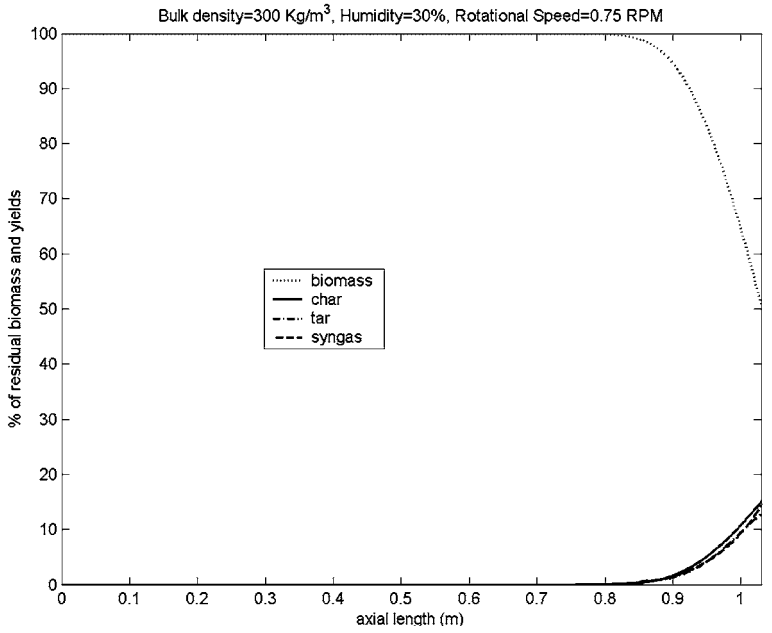

Fig. 7 Residual dry biomass and pyrolysis products yields as function of axial length (ρ=300 kg/m^3; %m=30%; 0.75 rpm)

given humidity (with a bulk density of 300 kg/m^3 and a humidity content of 10% (wb), a rotational speed of 0.94 rpm is required to pyrolize the whole feedstock). For a higher bulk density (300 kg/m^3) and a higher humidity content (30% (wb)) at the lower limit of rotational speed (0.75 rpm), imposed by rolling motion conditions, it is not possible to pyrolyze the whole feedstock (Fig. 7).

Conclusions

The working envelope of the laboratory kiln pyrolyzer of the University of Perugia was determined with a theoretical and experimental approach. The kiln utilizes a single engine for the rotation of the screw conveyor and the kiln which therefore rotate at the same speed. A pyrolysis model adapted from the literature was developed in a MATLAB® environment giving results consistent with literature data. The model was eventually inserted into the energy balance of the kiln in order to obtain pyrolysis products as a function of biomass humidity and bulk density. Data show that increasing the humidity (or the bulk density) of biomass results into a lower value of rotational speed if a complete pyrolysis of the feedstock is required; however, the rolling motion lower limit should not be trespassed if an optimal heat exchange and kiln efficiency are required. A powerful tool for operational optimization of a rotary kiln pyrolysis reactor in off-design conditions was then obtained. Considering the extreme variability of residual fuels characteristics, the software may be also used for on-line speed adjusting. Further developments of the work will consider the tuning of the model and eventual experimental verification with data from the test bench.

Nomenclature

A = frequency factor, s^{-1}
C = specific heat, kJ/kg K
E = activation energy, kJ/mol
H = heat of reaction, kJ/kg
MVF = mean volumetric flow, m^3/s
P = power, kW
PRT = pyrolysis retention time, s
Q = heat, kJ
R = gas constant, kJ/mol K
RT = residence time, s
T = temperature, K
h = enthalpy, kJ/kg
k = equilibrium constants, s^{-1}
m = mass, kg
$\%m$ = moisture content
n = rotational speed, rpm
t = time, s
wb = wet basis

Symbols

ρ = bulk density, kg/m^3
η = efficiency

Subscripts

B = biomass
C = char
G = gas
S = supplied
T = tar
V = vapor
a = ambient conditions
i = index
s = starting pyrolysis
0 = initial conditions
1 = gas from biomass
2 = tar from biomass
3 = char from biomass
4 = gas from tar
5 = char from tar

Acknowledgment

The authors gratefully acknowledge the contribution of many students and graduates. Among them, particular thanks go to A. Babbini, Dr. A. Giovannozzi, and G. Nocentini.

References

[1] Fantozzi, F., D'Alessandro, B., and Bidini, G., 2003, "IPRP — Integrated Pyrolysis Regenerated Plant — Gas Turbine and Externally Heated Rotary-Kiln Pyrolysis as a Biomass and Waste Energy Conversion System. Influence of Thermodynamic Parameters," Proc. Inst. Mech. Eng., Part A, **217**, pp. 519–527.

[2] Fantozzi, F., D'Alessandro, B., and Desideri, U., 2005, "IPRP — Integrated Pyrolysis Recuperated Plant — An Efficient and Scalable Concept for Gas Turbine Based Energy Conversion From Biomass and Waste," ASME J. Eng. Gas Turbines Power, **127**, pp. 348–357.

[3] Bidini, G., Moriconi, A., Rossi, D., and Fantozzi, F., 2004, "IPRP — Integrated Pyrolysis Recuperated Plant Rotary Kiln Pyrolyzer and Microturbine for Distributed Energy Conversion From Biomass — A 70 kW Demonstration Unit in Central Italy," *2nd World Conference on Biomass for Energy, Industry and Climate Protection*, Rome, Italy, May 10–14.

[4] Fantozzi, F., and Desideri, U., 2004, "Micro Scale Slow Pyrolysis Rotary Kiln for Syngas and Char Production From Biomass and Waste," *2nd World Conference on Biomass for Energy, Industry and Climate Protection*, Rome, Italy, May 10–14.

[5] Fantozzi, F., Desideri, U., Bartocci, P., and Colantoni, S., 2007, "Rotary Kiln Slow Pyrolysis for Syngas and Char Production From Biomass and Waste—Part I: Working Envelope of the Reactor," ASME J. Eng. Gas Turbines Power, **129**, pp. 901–907.

[6] Thurner, F., and Mann, U., 1981, "Kinetic Investigation of Wood Pyrolysis," I&EC Process Des. Dev., **20**, pp. 482–488.

[7] Shafizadeh, F., and Chin, P. P. S., 1977, "Thermal Deterioration of Wood," ACS Symp. Ser., **43**, pp. 57–81.

[8] Chan, W. R., Kelbon, M., and Krieger, B. B., 1985, "Modelling and Experimental Verification of Physical and Chemical Processes During Pyrolysis of Large Biomass Particle," Fuel, **64**, pp. 1505–1513.

[9] Font, R., Marcilla, A., Verdu, E., and Devesa, J., 1990, "Kinetics of the Pyrolysis of Almond Shells and Almond Shells Impregnated With $CoCl_2$ in a Fluidized Bed Reactor and in a Pyroprobe 100," Ind. Eng. Chem. Res., **29**, pp. 1846–1855.

[10] Di Blasi, C., 1996, "Heat, Momentum, and Mass Transport Through a Shrinking Biomass Particle Exposed to Thermal Radiation," Chem. Eng. Sci., **51**(7), pp. 1121–1132.

[11] Browne, F. L., 1958, "Theories on the Combustion of Wood and its Control," U.S. Forest Prod. Lab., Rep. 2136, Madison, WI, p. 59.

[12] Di Blasi, 1993, "Analysis of Convection and Secondary Reaction Effects Within Porous Solid Fuels Undergoing Pyrolysis," Combust. Sci. Technol., **90**, pp. 315–340.

[13] Liden, A. G., Berruti, F., and Scott, D. S., 1988, "A Kinetic Model for the Production of Liquids From the Flash Pyrolysis of Biomass," Chem. Eng. Commun., **65**, pp. 207–221.

[14] Thurner, F., and Mann, U., 1981, "Kinetic Investigation of Wood Pyrolysis," I&EC Process Des. Dev., **20**, pp. 482–488.

[15] Di Blasi, C., 1997, "Influences of Physical Properties on Biomass Devolatilization Characteristics," Fuel, **76**(10), pp. 957–964.

[16] Demirbas, A., 2005, "Pyrolysis of Round Beech Wood in Irregular Heating Rate Conditions," J. Anal. Appl. Pyrolysis, **73**, pp. 39–43.

[17] Demirbas, A., 1998, "Kinetics for Non-Isothermal Flash Pyrolysis of Hazelnut Shell," Bioresour. Technol., **66**, pp. 247–252.

Liquid Fuel Combustion Using Heat Recirculation Through Annular Porous Media

E. Ryan Newburn[1]
School of Aerospace and Mechanical Engineering,
University of Oklahoma,
Norman, OK 73019

Ajay K. Agrawal[2]
Fellow ASME
Department of Mechanical Engineering,
University of Alabama,
Tuscaloosa, AL 35487

A counter-flow annular heat recirculating burner was designed for lean prevaporized, premixed combustion. Prior to entering the combustor, the reactants are passed through a porous media-filled preheating annulus surrounding the combustor. Kerosene is dripped by gravity onto the porous media and vaporized by the heat conducted through the combustor wall. Experiments were conducted to evaluate heat transfer and combustion performance at various equivalence ratios, heat release rates, and inlet air temperatures. Results show low CO emissions over a range of equivalence ratios. NOx emissions were high at high heat release rates, indicating inadequate prevaporization and premixing of fuel with air. Heat recirculation and heat loss characteristics are presented at various operating conditions. [DOI: 10.1115/1.2719259]

Introduction

The mixing of fuel and air is the key component of combustor design. In a typical gas turbine, the liquid fuel is atomized by an injector before combustion occurs in the primary zone. The injector must provide fine atomization resulting in small fuel droplets and excellent dispersion. In a spray with fine droplets, a significant portion of the fuel evaporates to form fuel/air premixture, which burns at the temperature determined by the local fuel/air ratio. The flame temperature of the resulting fuel lean (or fuel rich) mixtures is significantly lower than the stoichiometric flame temperature. Alternatively, in a coarse spray, the fuel evaporates slowly and, hence, a major portion of the fuel burns in droplet combustion (or diffusion) mode, which produces high flame temperatures and consequently high NOx levels through the thermal NOx mechanism. Moreover, the fuel pyrolysis is enhanced in the droplet combustion mode to result in large amounts of soot. The spray dispersion characteristics impact the distribution of fuel/air ratio, which also affect the NOx emissions. Thus, the liquid fuel injector must be designed to form fine droplets, which are dispersed to produce a uniform fuel/air ratio distribution across the combustor [1]. Recent concepts to enhance fuel/air mixture uniformity include lean-premixed/prevaporized (LPP) combustion [2,3] and lean direct injection (LDI) combustion [4,5].

The underlying principle of the LPP combustion concept is to supply homogeneous fuel/air mixture to operate the combustor near the lean flammability limit. A premixer is used to achieve complete evaporation and mixing of fuel and air upstream of the combustion zone. Lean combustion not only eliminates soot emissions but also reduces the heat radiated to the liner wall(s). The main drawback of the LPP concept is the long residence time required for fuel evaporation and fuel/air premixing, which can cause autoignition or flashback, especially at higher compression ratios [6]. Lean blowout and acoustic resonance are other problems associated with lean premixed (LPM) combustion. In the LDI concept, the fuel is injected directly into the air stream to produce lean fuel/air mixture prior to combustion. Good atomization and vigorous fuel/air mixing are key requirements of this approach. Samuelsen and McDonnel [4] developed an LDI design consisting of an airblast radial injector and a mixing region dubbed as the "quarl." A multipoint LDI concept has been investigated by NASA and Parker Hannifin [5]. The spray nozzles etched on a thin sheet of material were used for multipoint injection. Multipoint injection provided more uniform distribution of fuel/air ratio into the combustor.

In the present study, a design concept involving porous inert media filled annulus around the combustor is utilized to recirculate energy from the reaction zone to prevaporize and preheat the reactants. The porous media are intended to increase the heat transfer from the product gases to the reactants and also to promote mixing between fuel and air. The concept of recirculating energy from the reaction zone to the reactants in the so-called "excess enthalpy flame" was proposed by Wienberg [7,8]. Lloyd and Wienberg [9] demonstrated a Swiss roll style burner design to achieve LPM combustion of gaseous fuels at very low equivalence ratios. Kotani and Takeno [10] used a combustion chamber filled with alumina tubes to transfer heat from the flame zone to the reactants. By introducing a solid medium in the reaction zone, they demonstrated the extension of the lean stability limit of methane at low flow rates. Another method to recirculate energy from the flame to the reactants involves the use of porous inert media (PIM) to stabilize the flame [11–14]. Recently, Marbach and Agrawal [15] compared natural gas flames stabilized on the surface and inside the PIM at identical conditions. They found that the lean blow off (LBO) limit and the NOx and CO emissions were lower for combustion inside the PIM compared to those on PIM surface, suggesting greater heat recirculation for the former case. Heatly and Agrawal [16] found lower LBO limit for prevaporized, premixed combustion of kerosene inside PIM.

Few studies have been conducted on combustion of liquid fuels using porous inert media. Kaplan and Hall [17] investigated vaporization and combustion of a heptane spray in a porous ceramic burner. The heat recirculated from the flame by the porous media caused sufficient prevaporization and premixing to support combustion, although the operating range was narrow. Tseng and Howell [18] showed that the droplet size of the injected fuel did not affect combustion, so long as the droplets were completely vaporized before reaching the combustion zone. Jungai and Narongsak [19] utilized porous media strictly as a preheating device, rather than a flame holder. Kerosene was dripped by gravity onto porous media heated by a downstream flame. The swirling flame observed in their experiment yielded low CO emissions, but NOx emissions were high: 60–70 ppm at $\phi=0.7-0.55$ and energy release rates of $Q=2.62$ to 3.49 kW. Marbach and Agrawal [20] showed that increasing the mixing length improved emissions

[1]Presently at General Electric Company, GE Aviation, Evandale, OH.
[2]Corresponding author.

Contributed by the International Gas Turbine Institute of ASME for publication in the JOURNAL OF ENGINEERING FOR GAS TURBINES AND POWER. Manuscript received October 26, 2005; final manuscript received January 21, 2007. Review conducted by Dilip R Ballal. Paper presented at the ASME Turbo Expo 2005: Land, Sea and Air (GT2005), June 6–9, 2005, Reno, NV. Paper No. GT2005-68588.

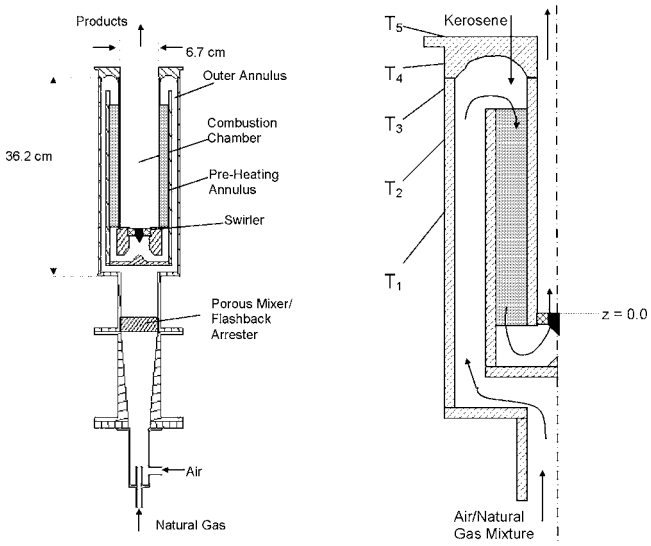

Fig. 1 System configuration: overall system (Left), combustor details (Right)

performance of kerosene flames in a combustor using porous inert media. Recently, Liedtke et al. [21] presented a combustor design for micro-turbines that utilized a concentric-tubes setup with reactants entering through the inner tube and product gases exiting through the annulus. Heat from product gases was recovered to evaporate the fuel oil sprayed onto the inner tube surface.

The present combustor system has features similar to those of Liedtke et al. [21]. Previously, Newburn and Agrawal [22] conducted experiments using this burner operated on methane. They showed low CO and NOx emissions and lower LBO limits, compared to typical swirl-stabilized combustion systems. The objective of present work is to obtain heat transfer and combustion performance of the proposed burner design operated on kerosene.

Experimental Setup

Figure 1 shows a schematic drawing of the experimental setup. Air entered through the inlet section and mixed with natural gas (at the start of burner operation) in a diffuser with a porous piece to promote mixing. The burner system consists of three concentric stainless steel tubes resulting in two annular spaces. Natural gas and air entered through the outer annulus before turning into the preheating annulus surrounding the combustor chamber. The preheating annulus was filled with stainless steel beads of 0.48 cm diameter. Liquid kerosene was fed by a peristaltic pump into a tubular ring positioned at the top of the preheating annulus. The kerosene was dripped by gravity through 12 equidistant holes around the ring onto the stainless steel beads. The kerosene was prevaporized and premixed with air in the annulus filled with steel beads. Furthermore, the premixed reactants were preheated by heat transfer through the combustor wall before entering the combustor chamber through a swirler with a centerbody. The product gases from the swirl-stabilized combustor exit to the atmosphere at ambient pressure. Key dimensions of the burner system are provided in Table 1. The dimensions of the burner and beads were chosen to demonstrate the concept and, hence, no geometric optimization studies were carried out.

The air was supplied by a compressor, dried, and then measured by a laminar flow element calibrated for 0 to 300 standard liters per minute (slm). An electrical heater was used to preheat air to the desired inlet temperature. The temperature on the exterior surface of the system was monitored by K-type thermocouples at five locations (shown in Fig. 1). Table 1 lists thermocouple locations measured with respect to the combustor inlet plane (z=0.0 in Fig. 1). A K-type thermocouple was used to measure temperature at the inlet of the system and the combustion chamber. The product gas temperature was measured at the combustor exit plane using an R-type thermocouple, which was mounted on a traversing system. No measurements were taken inside the porous media. Temperature measurements are reported without corrections for heat conduction or radiation. The gas samples were taken by a quartz sampling-probe with a tapered tip to quench reactions. The product gases passed through an ice bath and driers before CO and NOx emissions were measured by electrochemical analyzers. Table 2 summarizes the measurement uncertainties. The measurements were taken for equivalence ratio, ϕ, starting at 0.58 and reduced in 0.025 decrements, until the lean blow off (LBO). The equivalence ratio was varied by maintaining the airflow rate constant as the fuel flow rate was varied. The combustor was started on natural gas until steady state was reached. Then, the natural gas

Table 1 Key dimensions of the burner

Component	Dimensions (cm)
Combustion chamber	L=27.9 ID=6.7 OD=7.0
Preheating annulus	L=25.9 ID=7.0 OD=10.2
Outer annulus	L=36.2 ID=11.4 OD=13.4
Exterior thermocouple locations (measured from the combustor inlet plane, z=0.0 cm)	z_1=7.6 z_2=17.8 z_3=22.9 z_4=25.4 z_5=27.9

Table 2 Measurement uncertainties

Instrument/ Quantity	n	Precision	Bias	Uncertainty
Gas analyzer	5	1 ppm	2 ppm	2.2 ppm
Thermocouple	5	2.5°C	2.2°C	3.3°C
Fuel flow	5	0.2 slm	0.6 slm	0.63 slm
Air flow	5	1 slm	3 slm	3.2 slm

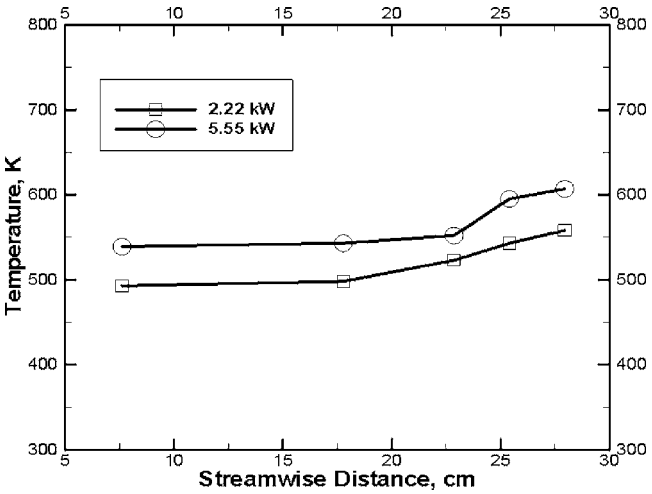

Fig. 2 Exterior surface temperature profiles at steady state for ϕ=0.57.

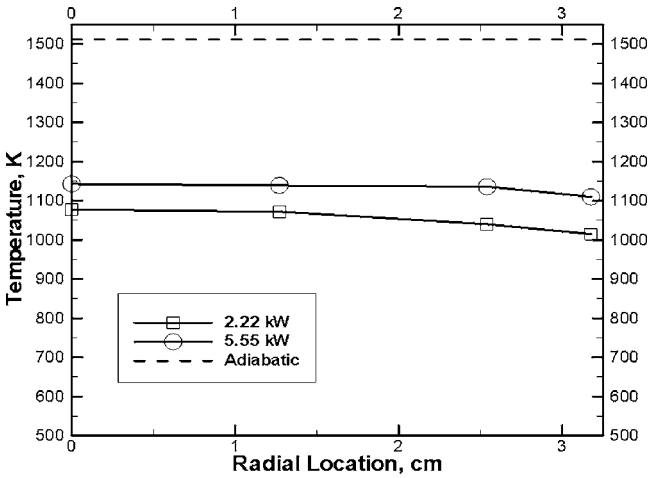

Fig. 3 Radial temperature profile at the combustor exit (z =27.2 cm)

flow rate was reduced to nearly the LBO limit and the peristaltic pump was turned on to provide the desired flow rate of kerosene. Next, the natural gas flow rate was reduced gradually, until the system operated only on kerosene.

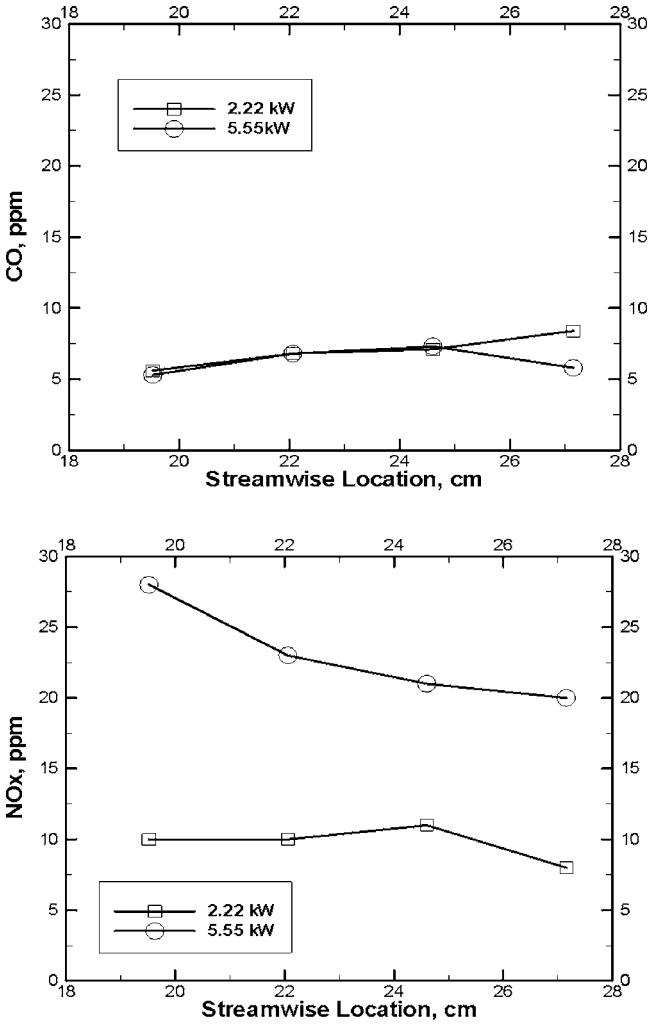

Fig. 4 Emissions in the streamwise direction at r=0.0 cm: (*a*) CO (top) and (*b*) NOx (bottom)

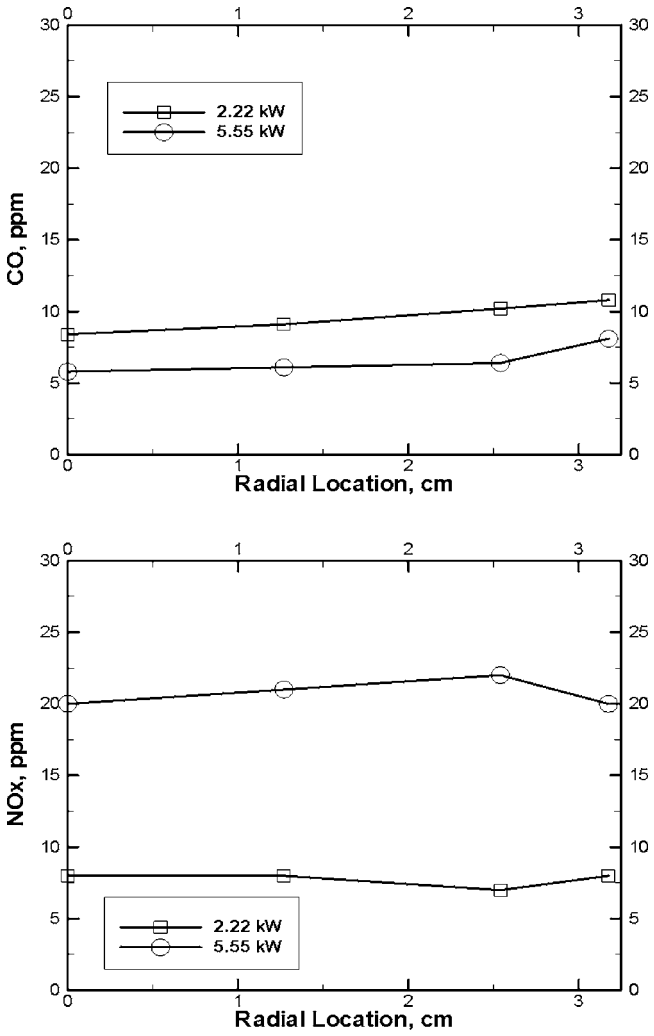

Fig. 5 Emissions profiles at the combustor exit plane: (*a*) CO (top) and (*b*) NOx (bottom)

Results and Discussion

First, experiments were conducted to determine steady-state characteristics of the burner system operated on kerosene. Measurements were taken at two heat release rates, Q=2.22 and 5.55 kW, for a constant equivalence ratio, ϕ=0.57. The kerosene was represented by n-dodecane and complete combustion of fuel with air was assumed to compute the equivalence ratio from the measured oxygen concentration in the products. Figure 2 presents the temperature profile on the exterior surface of the burner system after steady state was reached. At steady state, the absolute temperature was within 2% of the previous reading at all measurement locations in the 5 min recording interval. Results show that the surface temperature is constant along much of the system length, with a slight rise observed near the burner exit. Increasing the heat release rate increased the surface temperature by about 50 K, indicating higher heat loss (in kW) at the higher heat release rate. The product gas temperature measured at the combustor exit plane for different heat release rates is shown in Fig. 3. Measurements show that the temperature is uniform across the combustor exit, except for a slight dip near the wall. Moreover, the product gas temperature is higher for the higher heat release case. Even though the net heat loss is higher for Q=5.5 kW, the product temperature is higher because a larger fraction of heat released is retained within the system. For both cases, the product gas temperature is below the calculated adiabatic flame temperature,

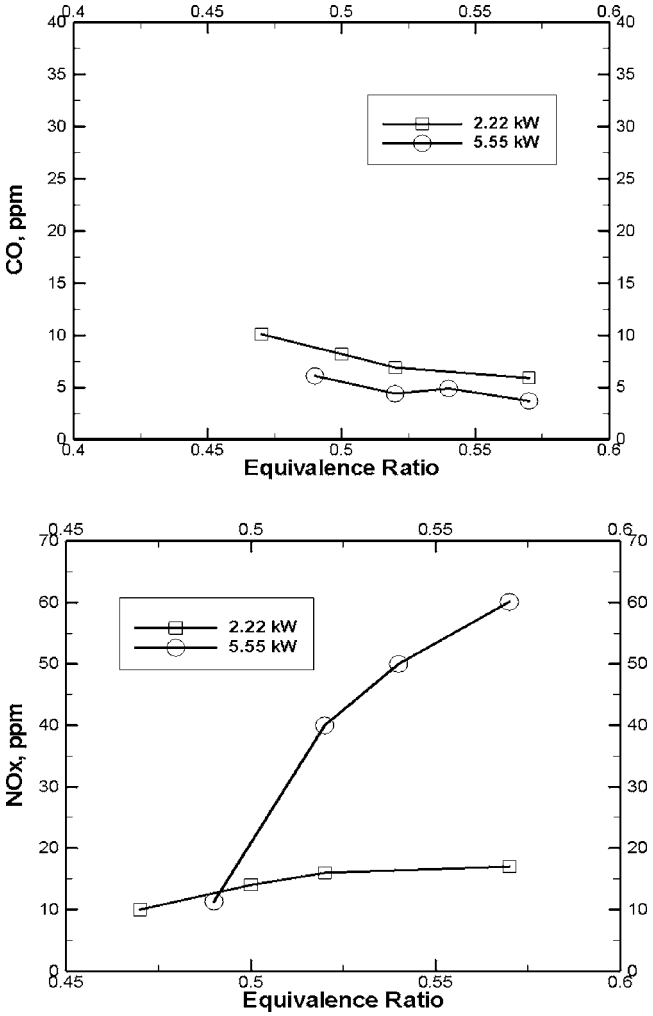

Fig. 6 Emissions versus equivalence ratio in the center point at the combustor exit plane: (*a*) CO (top) and (*b*) NOx (bottom)

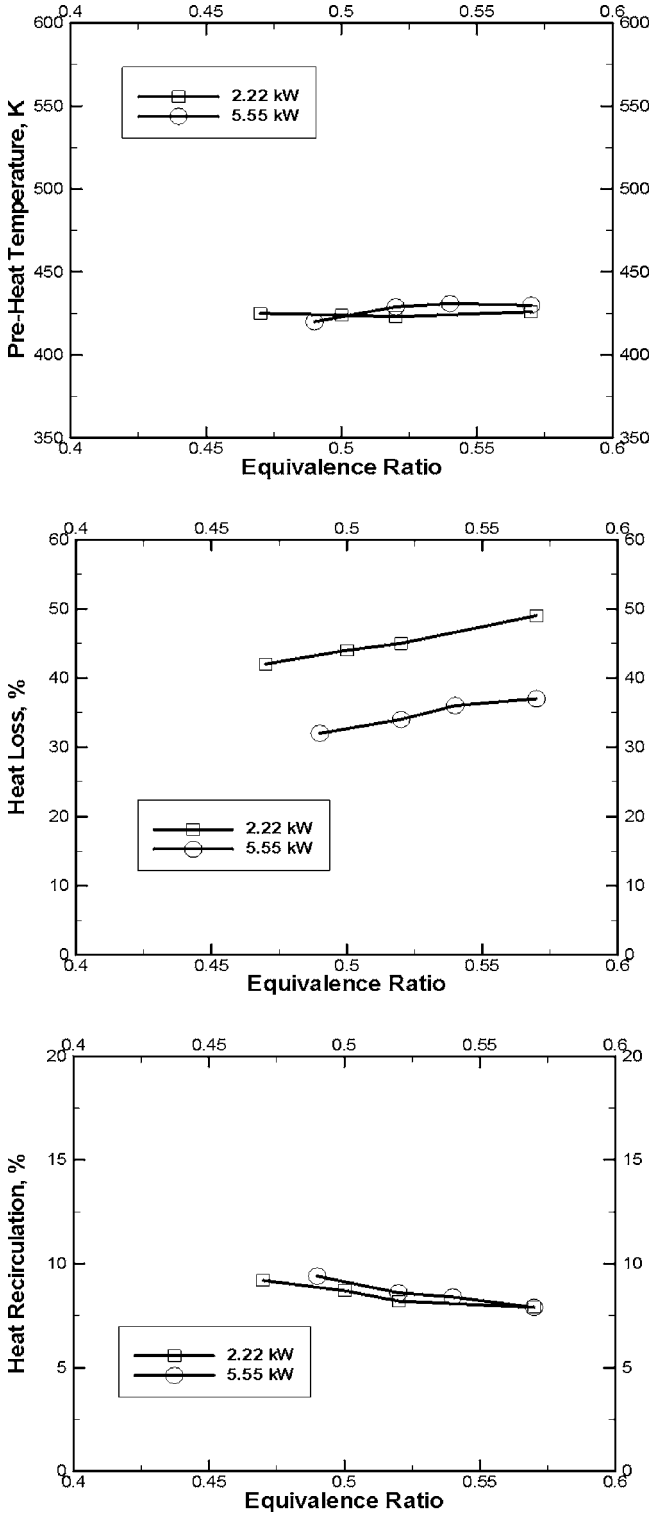

Fig. 7 (*a*) Preheat temperature, (*b*) percent heat loss, and (*c*) percent heat recirculation

which is also shown in Fig. 3. Flame temperature lower than the adiabatic value signifies heat loss to the surroundings, which is an undesirable feature of the present design. However, it is anticipated that the heat loss may be minimized by optimizing geometric parameters and by properly insulating the exterior surface of the burner system.

Emissions measurements were taken to determine completeness and uniformity of combustion. Figure 4(*a*) presents CO concentration in the streamwise direction at the combustor centerline. All CO measurements are less than 10 ppm, indicating nearly complete combustion for both heat release rates. The NOx emissions for the two heat release rates are shown in Fig. 4(*b*). For $Q=2.22$ kW, the NOx concentrations are within 10 ppm along the combustor length. However, significantly higher NOx values are observed for $Q=5.5$ kW. Visual observation of the flame in this case revealed localized regions with features of a diffusion flame. Thus, the fuel is not completely prevaporized and premixed with air, within the limited residence time at high heat release rates (and, hence, high fuel and air flow rates) available in the preheating annulus. Results suggests that a fuel injection system producing fine droplets will be required to ensure prevaporization and premixing of fuel with air, especially at high heat release rates. The decreasing trend of NOx concentration in the flow direction is attributed to local mixing of products generated at stoichiometric and lean conditions. Radial profiles of CO and NOx emissions at the combustor exit plane are shown in Fig. 5. Both CO and NOx emission profiles show little variation, indicating uniformity at the combustor exit plane. Once again, NOx concentrations are more pronounced at the higher heat release rate.

Emissions measurements were taken at various equivalence ratios obtained by fixing the fuel flow rate (in ml/min) and varying the air flow rate. Figure 6 shows CO concentration varying between 4 and 10 ppm, indicating that CO emissions are independent of the heat release rate and equivalence ratio, within the

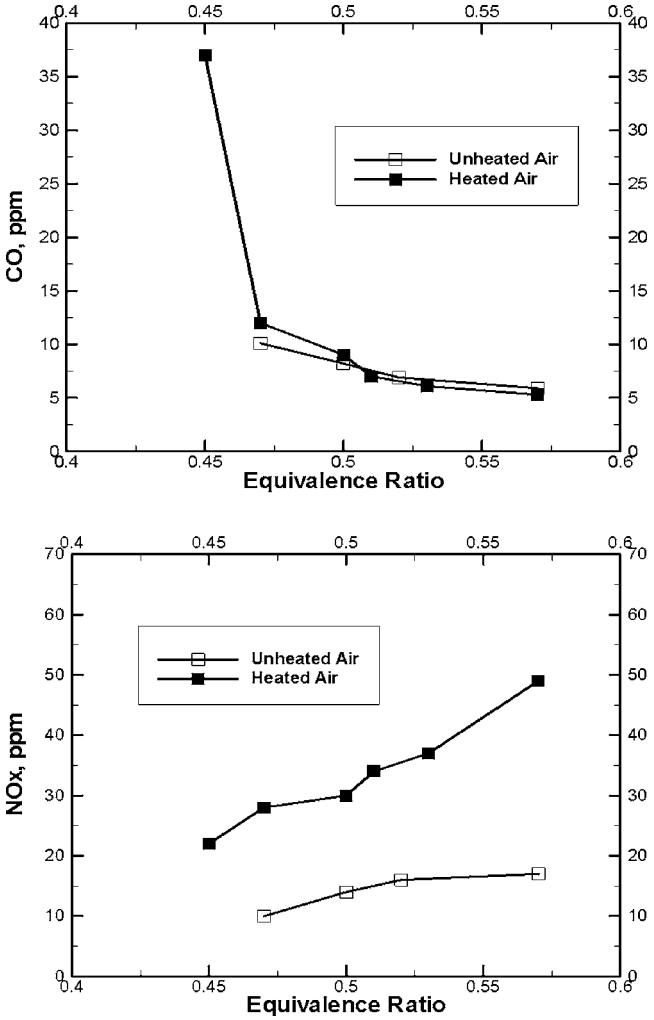

Fig. 8 Effect of inlet air temperature: (*a*) CO (top) and (*b*) NOx (bottom)

range of the experiment. The NOx emissions increased with increasing equivalence ratio, because of the greater importance of the thermal NOx mechanism. At high heat release rate, inadequate prevaporization of fuel resulting in localized diffusion flames has caused high NOx emissions, as discussed previously. The data points at the lowest equivalence ratio represent the LBO limit, which is higher for the higher heat release case.

Thermal characteristics of the system are presented in terms of preheat temperature, percent heat loss, and percent heat recirculation. The preheat temperature refers to the value measured upstream of the combustor at the swirler inlet. The heat loss was defined as the difference between the enthalpy of the products at the adiabatic flame temperature, T_{ad}, and the enthalpy of products at the temperature measured at the exit plane, T_{ex}. The percent heat loss was taken as a percentage of the lower heating value of the fuel, or the difference between the enthalpies of the products and reactants at the reference temperature shown below.

$$Q_{loss} = \frac{[H_P(T_{ad}) - H_P(T_{ex})]}{[H_P(T_{ref}) - H_R(T_{ref})]} \tag{1}$$

Heat recirculation was defined as the difference between the enthalpy of the reactants at the temperature measured at the combustor inlet, T_{cin}, and the enthalpy of the reactants at the system inlet temperature, T_{in}. The percent heat recirculation was calculated as follows.

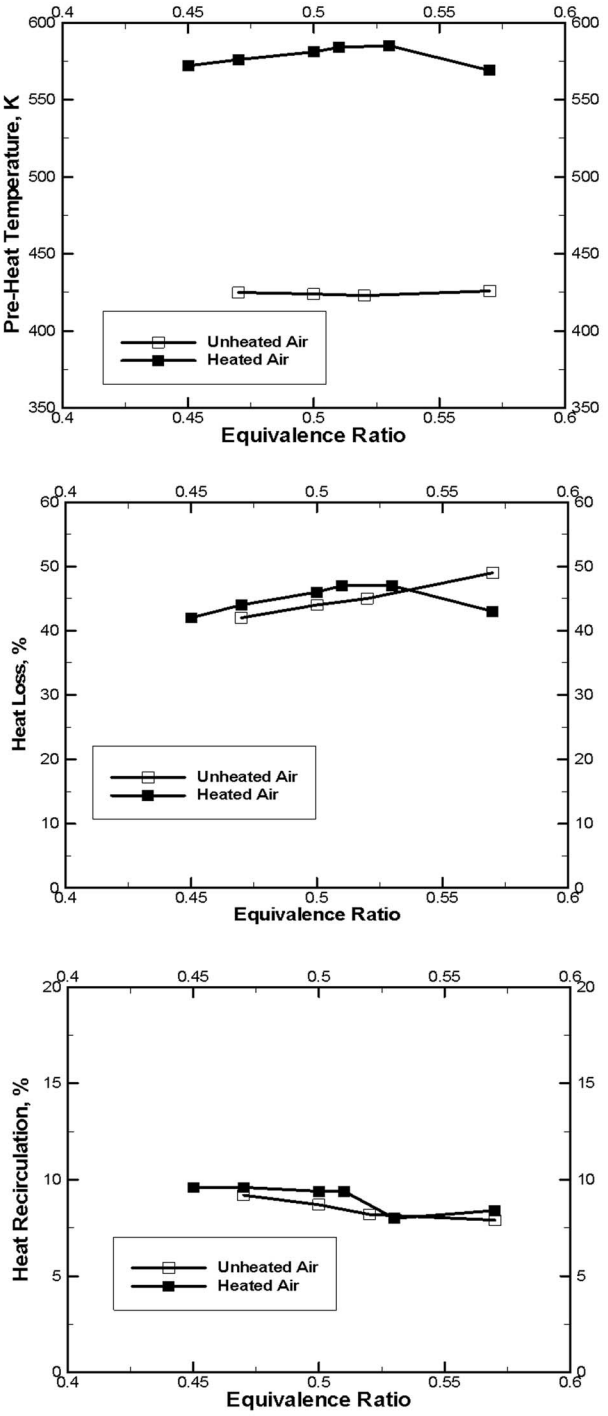

Fig. 9 Effect of air temperature on (*a*) Pre-heat temperature, (*b*) percent heat loss, (*c*) percent heat recirculation

$$Q_{recir} = \frac{[H_R(T_{cin}) - H_R(T_{in})]}{[H_P(T_{ref}) - H_R(T_{ref})]} \tag{2}$$

Figure 7(*a*) shows a preheat temperature of about 425 K, which is independent of ϕ and heat release rate. Figure 7(*b*) shows that the percent heat loss from the exterior surfaces depended on both equivalence ratio and heat release rate. High flame temperatures at higher equivalence ratios contributed to increased percent heat loss. The percent heat loss is much higher for the lower heat

release rate. The heat recirculation, shown in Fig. 7(*c*), is about 10%, and it decreased with increasing equivalence ratio because of the higher heat loss to the surroundings.

Next, experiments were conducted using inlet air preheated to 430 K by an electrical heater. Figure 8 shows nearly the same CO emissions using unheated and heated air. The NOx emissions increased with heated air because of the rise in the flame temperature increasing reaction rates of the thermal NOx mechanism. Higher inlet air temperature produced higher reactant temperature before combustion, as shown in Fig. 9(*a*). Figures 9(*b*) and 9(*c*) show that air temperature had little effect on percent heat loss or percent heat recirculation.

Conclusions

A heat recirculating combustor with a porous media filled annular preheating section was designed and tested using kerosene. The system was shown to produce low emissions by operating in lean prevaporized, premixed combustion mode using room temperature air. However, the prevaporization and premixing with air was incomplete at higher heat release rates because of the smaller residence time in the preheating annulus. Visual examination after the experiment revealed no fuel coking in the porous media annulus. It is believed that coking is avoided in the present system because of the low temperature and presence of air in the preheat region. The present design shows potential to effectively recirculate energy generated in the combustion zone to improve combustion of liquid fuels. However, practical implementation of this approach will require a fuel injection system producing finer droplets, a burner with optimized geometry to reduce heat loss to the surroundings, and insulation on the exterior surface to further reduce the heat loss.

Acknowledgment

This work was supported by the U.S. Army Research Laboratory and the U.S. Army Research Office under Grant No. DAAD 190210082 with Dr. David Mann serving as the technical monitor.

Nomenclature

H_P = enthalpy of products
H_R = enthalpy of reactants
Q_l = heat loss
Q_r = heat recirculated
r = radial coordinate
T_{ad} = adiabatic flame temperature
T_{cin} = combustor inlet temperature
T_{ex} = temperature at the combustor exit plane
T_{in} = system inlet temperature
z = streamwise coordinate
ϕ = equivalence ratio

References

[1] Razdan, M. K., 1999, "Fuel/Air Preparation in the Design of Low Emissions Gas Turbine Combustion Systems," *NATO RTO Meeting Proceedings 14 on Gas Turbine Combustion Emissions and Alternative Fuels*, Lisbon, Portugal, October 12–16, 1998, Paper No. 34.
[2] Ripplinger, Th., Zarzalis, N., Meikis, G., Hassa, C., and Brandt, M., 1999, "NOx Reduction by Lean Premixed Prevaporized Combustion," *NATO RTO Meeting Proceedings 14 on Gas Turbine Combustion Emissions and Alternative Fuels*, Lisbon, Portugal, October 12–16, 1998, Paper No. 7.
[3] Wedlock, M. I., Tilston, J. R., and Seoud, R. E., 1999, "The Design and Evaluation of a Piloted Lean Burn, Premixed, Prevaporized Combustor," *NATO RTO Meeting Proceedings 14 on Gas Turbine Combustion Emissions and Alternative Fuels*, Lisbon, Portugal, October 12–16, 1998, Paper No. 23.
[4] Samuelsen, S., and McDonell, V., 1999, "Advanced Fuel Injection Strategies for High Performance gas Turbine Engines," *NATO RTO Meeting Proceedings 14 on Gas Turbine Combustion Emissions and Alternative Fuels*, Lisbon, Portugal, October 12–16, 1998, Paper No. 24.
[5] Tacina, R. R., Wey, C., Laing, P., and Mansour, A., 2001, "A Low NOx Lean-Direct Injection, Multipoint Integrated Module Combustor Concept for Advanced Aircraft Gas Turbines," Clean Air Conference, Portugal.
[6] Lefebvre, A. H., 1995, "The Role of Fuel Preparation in Low-Emission Combustion," ASME J. Eng. Gas Turbines Power, **117**, pp. 617–654.
[7] Weinberg, F. J., 1971, "Combustion Temperatures: The Future?" Nature (London), **223**, p. 239–241.
[8] Hardesty, D. R., and Wienberg, F. J., 1974, "Burners Producing Large Excess Enthalpies" Combust. Sci. Technol., **8**, pp. 201–214.
[9] Lloyd, S. A., and Wienberg, F. J., 1974, "A Burner for Mixtures of Very Low Heat Content," Nature (London), **251**, pp. 47–49.
[10] Kotani, Y., and Takeno, T., 1982, "An Experimental Study on Stability and Combustion Characteristics of an Excess Enthalpy Flame," Proc. Combust. Inst., **19**, pp. 1503–1509.
[11] Sathe, S. B., Kulkarni, M. R., Peck, R. E., and Tong, T. W., 1990, "An Experimental and Theoretical Study of Porous Radiant Burner Performance," Proc. Combust. Inst., **23**, pp. 1011–1018.
[12] Howell, J. R., Hall, M. J., and Ellzey, J. L., 1996, "Combustion of Hydrocarbon Fuels Within Porous Inert Media," Prog. Energy Combust. Sci. **22**, pp. 121–145.
[13] Mital, R., Gore, J. P., and Viskanta, R., 1997, "A Study of the Structure of Submerged Reaction Zone in Porous Ceramic Radiant Burners," Combust. Flame, **111**, pp. 175–184.
[14] Trimis, D., Durst, F., Pickenäcker, Ó., and Pickenäcker, K., 1997, "Porous Medium Combustor Versus Combustion Systems With Free Flames," *Proceedings From the 2nd Intl. Symposium on Heat Transfer Enhancement and Energy Conservation*, ISHTEEC, Guangzhou, China, June 16–19, pp. 339–345.
[15] Marbach, T. L., and Agrawal, A. K., 2003, "Experimental Study of Surface and Interior Combustion Using Composite Porous Media," ASME Paper No. GT2003-38713.
[16] Heatly, R. J., and Agrawal, A. K., 2003, "Combustion of Pre-Vaporized, Pre-Mixed Fuel Using Porous Inert Media," *AIAA/ASME/SAE/ASEE Joint Propulsion Conference*, Vol. 39, AIAA Paper No. AIAA-2003-5089.
[17] Kaplan, M., and Hall, M., 1995, "The Combustion of Liquid Fuels Within a Porous Media Radiant Burner," Exp. Therm. Fluid Sci., **11**, pp. 13–20.
[18] Tseng, C., and Howell, J., 1996, "Combustion of Liquid Fuels in a Porous Radiant Burner," Combust. Sci. Technol., **112**, pp. 141–161.
[19] Jugjai, S., and Narongsak, W., 2002, "The Combustion of Liquid Fuels Using a Porous Medium," Exp. Therm. Fluid Sci., **26**, pp. 15–23.
[20] Marbach, T., and Agrawal, A., 2003, "Fuel Vaporization and Combustion With the Use of Porous Inert Media," *AIAA/ASME/SAE/ASEE Joint Propulsion Conference*, Vol. 39, AIAA Paper No. AIAA-2003-5090.
[21] Liedtke, O., Schulz, A., and Wittig, S., 2003, "Emission Performance of a Micro Gas Turbine LPP-Combustor With Fuel Film Evaporation," ASME Paper No. GT2003-38697.
[22] Newburn, E. R., and Agrawal, A., 2005, "Lean Premixed Combustion Using Heat Recirculation Through Annular Porous Media," 43rd AIAA Aerospace Sciences Meeting and Exhibit, AIAA Paper No. 2005-0934.

Numerical Simulation of Liquid Jet Atomization Including Turbulence Effects

Huu P. Trinh
Engineering Directorate,
NASA—Marshall Space Flight Center,
Huntsville, AL 35812
e-mail: Huu.P.Trinh@nasa.gov

C. P. Chen[1]
e-mail: cchen@che.uah.edu

M. S. Balasubramanyam

Department of Chemical & Materials Engineering,
University of Alabama in Huntsville,
Huntsville, AL 35899

*This paper describes numerical implementation and validation of a newly developed hybrid model, T-blob/T-TAB, into an existing computational fluid dynamics (CFD) program for primary and secondary breakup simulation of liquid jet atomization. This model extends two widely used models, the Kelvin-Helmholtz (KH) instability of Reitz (the "blob" model) (1987, Atomization Spray Technol., **3**, pp. 309–337) and the Taylor-Analogy-Breakup (TAB) secondary droplet breakup of O'Rourke and Amsden (1987, SAE Technical Paper No. 872089) to include liquid turbulence effects. In the primary breakup model, the level of the turbulence effect on the liquid breakup depends on the characteristic scales and flow conditions at the liquid nozzle exit. Transition to the secondary breakup was modeled based on energy balance, and an additional turbulence force acted on parent drops was modeled and integrated into the TAB governing equation. Several assessment studies are presented, and the results indicate that the existing KH and TAB models tend to underpredict the product drop size and spray angle, whereas the current model provides superior results when compared to the measured data.*
[DOI: 10.1115/1.2747253]

Keywords: atomization, spray, secondary breakup, numerical modeling

Introduction

Atomization of liquid jet into a gaseous surrounding plays an important role in combustion dynamics of many industrial power and propulsion systems. Jet inertia, aerodynamic forces, as well as the surface tension all contribute to the liquid stream breakup process. In addition, the turbulence behavior inside the liquid jet also contributes to the jet disintegration. Often the geometrical sharpness of the injection nozzle inlet, along with appropriate flow conditions, can create cavitations inside the nozzle. The collapse of this cavitation can generate a flow fluctuation, leading to a more aggressive disintegration of the liquid jet. Traditional spray atomization models, such as the Kelvin-Helmholtz (KH) instability model of Reitz [1], the TAB of O'Rourke and Amsden [2], and some enhanced models [3,4], did not account for the liquid turbulence effects. Recently, Nishimura and Assanis [5] developed a phenomenological cavitation model in which the liquid turbulence motion within the injector was formed by the bubble collapse and the fluid turbulence motion. Their model was applied to the primary breakup regime. Considering the nozzle exit turbulence conditions of diesel sprays, Huh et al. [6] proposed a scheme taking into account two independent mechanisms, wave growth and turbulence in the atomization process. The turbulence is characterized partially by the injection nozzle geometry, whereas the wave growth is derived from the KH instability theory. The aforementioned models were formulated with semi-empiricism. More recently, several efforts using sophisticated numerical approaches have been performed in modeling the detailed turbulent flow fields in the liquid and gas during the atomization process. In the large eddy simulation (LES) spray modeling of Apte et al. [7], a stochastic approach for droplet breakup taking into account a range of product droplet sizes was developed for modeling of secondary breakup regime. De Villiers et al. [8] applied LES to resolve the primary atomization under more realistic operating conditions found in diesel engines. These methods have a real potential of providing a complete physical description of the liquid jet breakup with minimum assumptions; however, they require submicron spatial elements in size and picoseconds in time steps to properly predict the atomizing sprays at the high-velocity injection conditions. Consequently, grid mesh size and the considered physical domain must be taken care of so that the computational time and memory storage requirements can be manageable. At the present time, they are still too expensive and generally impractical in terms of computational time and power requirements for engineering calculation applications. Hence, the engineering analysis and design of the liquid spray devices must still rely on phenomenological engineering models.

Based on two widely used models, Reitz's primary atomization (blob) [1] and the Taylor-Analogy-Breakup (TAB) [2] secondary droplet breakup, a hybrid T-blob/T-TAB model was recently developed by Trinh and Chen [9] to include liquid-phase turbulence effects in both primary and secondary breakup regimes. The "hybrid" model is used to explicitly differentiate between the primary and secondary breakup mechanisms that occur in different regimes. The hybrid model can account for the flow conditions inside the injector hole, such as liquid turbulence levels, which is important for atomization at high injection pressure. The approaches described in [5,6,10,11] are hybrid models. In hybrid models, transitions of the primary breakup to secondary breakup models were incorporated. However, the switching criteria are somewhat arbitrary (see Ref. [10]). In the primary breakup model of Trinh and Chen [9], the T-blob model, the level of the turbulence effect on the liquid breakup depends on the characteristic time scales and the initial flow conditions. This treatment offers a competitive contribution of liquid turbulence and perturbed surface wave physical phenomena on the liquid breakup process. For the secondary breakup, T-TAB, an additional turbulence force acted on parent drops is modeled and integrated into the TAB governing equation. The "switching" and drop size formation from the primary to secondary breakup regime is estimated based on the energy balance before and after the breakup occurrence. The turbulence energy is also considered in this process. Detailed

[1]Corresponding author.

Contributed by the Internal Combustion Engine Division of ASME for publication in the JOURNAL OF ENGINEERING FOR GAS TURBINES AND POWER. Manuscript received November 3, 2005; final manuscript received March 20, 2007. Review conducted by Margaret Wooldridge.

model development and theoretical formulations, as well as several fundamental test cases and energy budget calculations were described in [9] for simple prescribed flow fields (one-way coupling) to validate several model coefficients. Model constants associated with this phenomenological model were also determined based on pure one-way Lagrangian study in [9]. In order for the model to be applied to broader engineering applications, the model has to be tested in two-way coupled atomization/spray systems. This paper focuses on incorporating this newly developed hybrid phenomenological T-blob/T-TAB model into a computational fluid dynamics (CFD) methodology based on Eulerian (gas)-Lagrangian (liquid) two-way coupling formulation [12] for complicated injector liquid-atomization and spray simulation. Several assessment studies with comparison to available measured data are conducted. This effort may be considered as a closure of our model development.

Model Description

Detailed development and theoretical foundation of T-blob/T-TAB model was described in [9]. Only the final forms of the model are summarized here.

T-blob Model for Primary Breakup. In this model, the drop breakup rate and the mean drop size are given by

$$\frac{da}{dt} = -\left[\frac{a}{\tau} - C_a\left(\frac{L_w}{\tau_w} - \frac{L_t}{\tau_t}\right)\right], \quad \text{when} \quad r_p \ll a \tag{1}$$

$$r_p = \frac{r_w r_t}{(1-c_t)r_t + c_t r_w} \tag{2}$$

The characteristic length scale L_w and time scale τ_w are associated with the droplet surface wave instability. These two scales along with τ and C_a are formulated from the original "blob" model [1] as: $L_w=\Lambda$, $\tau_w=a/\Lambda\Omega$, $\tau=3.726B_1 a/\Lambda\Omega$ and $C_a=B_0/3.726B_1$. The turbulence characteristic length scale L_t and time scales τ_t were derived based on analytical solution of the k-ε turbulence model

$$\tau_t = \tau_t^o + 0.0828t \tag{3}$$

$$L_t = L_t^0\left(1 + \frac{0.0828t}{\tau_t^0}\right)^{0.457} \tag{4}$$

The time t is counted from the time at which the parent drop leaves the injection nozzle exit. The initial turbulence length scale L_t^0 and time scale τ_t^0 are evaluated from the initial turbulent kinetic energy k_t^0 and its corresponding dissipation rate ε_t^0 at the injector exit,

$$L_t^0 = c_\mu \frac{(k_t^0)^{3/2}}{\varepsilon_t^0}, \quad \tau_t^0 = c_\mu \frac{k_t^0}{\varepsilon_t^0}; \quad \text{where} \quad c_\mu = 0.09$$

The initial turbulent kinetic energy k_t^0 and its corresponding dissipation rate ε_t^0 can be modeled [13] as

$$k_t^0 = \frac{U^2}{8L/D}\left[\frac{1}{C_d^2} - K_c - (1-s^2)\right] \tag{5}$$

$$\varepsilon_t^0 = K_\varepsilon \frac{U^3}{2L}\left[\frac{1}{C_d^2} - K_c - (1-s^2)\right] \tag{6}$$

with $K_\varepsilon=0.27$. The velocity U is the liquid velocity at the injection nozzle, which has length L, and diameter D. The discharge coefficient, the loss coefficient due to the nozzle entrance sharpness, and the downstream-to-upstream contraction area ratio of the injection nozzle are represented by C_d, K_c, and s, respectively. The parent drop would no longer strip its mass to create the product drop when the parent drop radius a is less than the radius, r_p, of the product droplet. In Eq. (2), determination of the radius r_w associated with the wave motion follows the original formula of [1]; and the value of r_t, as well as weighting coefficients can be found in [9]. Along with the inclusion of the turbulence effect on the primary atomization process, the subject phenomenon also is transitioned to the secondary droplet breakup model, the T-TAB model. The required initial velocity fluctuation quantity of the product drops right after their formation was obtained by examining the energy conservation during the primary breakup process. By equating the change in the energies of the parent drop with the energy of the product drops, the turbulent kinetic energy for the product drop was derived [9] and used to estimate the initial velocity fluctuation for the secondary breakup process, which is discussed next.

T-TAB Model for Secondary Breakup. To account for liquid turbulence effect, the original TAB model was modified to

$$\ddot{y} = \frac{C_F}{C_b}\frac{\rho_g}{\rho_l}\frac{W^2}{r_p^2} + C_t\frac{\varepsilon_o}{C_b^2 r_p^2}\left[\frac{k}{k_o}\right]^{C_\varepsilon}\dot{y}^{-1} - C_k\frac{\sigma}{\rho_l r_p^3}y - C_d\frac{\mu_l}{\rho_l r_p^2}\dot{y} \tag{7}$$

Except for the second term on the right-hand side, Eq. (7) is the same as the governing equation of the TAB model. Again, Ref. [9] should be consulted for detailed derivation of this model. To estimate the post-breakup drop size, a similar method as used in the TAB model is employed for the calculation of Sauter mean radius (SMR):

$$\text{SMR} = \frac{4\pi r_p^3 \sigma}{E_{\text{par}} - \frac{\pi}{6} r_p^5 \rho_l \dot{y}^2} \tag{8}$$

Based on the conservation principle, the initial turbulent kinetic energy (k_0) and dissipation rate (ε_0), in Eq. (7), of the new drop were formulated [9]. E_{par} in Eq. (8) is the total energy of the original drop prior to the breakup and is determined from the original TAB model.

Model Implementation

For primary atomization using T-blob model, the liquid is assumedly injected in a form of "blob" parcels containing spherical drops with their initial size equal to the nozzle exit dimension. The computational approach for the primary atomization proposed by Reitz [1] is adopted in the present study. Extra relations representing the turbulence are described here. The initial turbulence quantities are estimated based on Eqs. (5) and (6). Values of the turbulence characteristic scales are then calculated from these turbulence values. An individual parcel is tracked at each time step, and change in "blob" drop size is also determined using Eq. (1). Next, the mass stripped from the parent drops is computed and formed into a new product drop parcel. The primary breakup of the blob drops continues until their size reduces to the dimension of the product drops. It is not necessary to create a new parcel in each computational time step. For the purpose of saving computer memory and computational time, the stripped mass would be accumulated until certain criteria are met. Then, a new parcel is added to the computations and its drop size is calculated from Eq. (2). The criterion of forming a new parcel varies among authors. For instance, Reitz [1] defined the creation of a new parcel when the accumulated mass had exceeded 3% of the original parcel mass, whereas Huh et al. [6] used the value of 10%. It was found that at least for the test cases of interest, the computational results from theses two criteria are not much different, although the number of parcels in the computational domain varies considerably. In the original CFD-ACE+ [14], a new parcel is created when the number of product drops is $>20\%$ of the ones in the parent. In the present study, the initial turbulent kinetic energy of the product drops is estimated from the energy conservation formulation described in [9]. When this estimated energy is $<0.1\%$ of the kinetic energy of the droplet motion, it is assumed that the turbulence motion within the droplet becomes insignificant. Then, no turbulence is considered in the secondary breakup for subject droplet,

Table 1 Test cases and measured data used in the computation

Case	H-1	H-2	H-3	K
Nozzle diameter (mm)		0.3		0.24
Ambient gas	Nitrogen	Nitrogen	Nitrogen	Nitrogen
Ambient pressure (MPa)	1.1	3	5	2.17
Ambient temperature (K)	298	298	298	298
Density (kg/m^3)	12.36	33.7	56.17	24.51
Liquid fuel	Diesel	Diesel	Diesel	Diesel
Density (kg/m^3)	840	840	840	840
Viscosity (Kg/ms)	2.9×10^{-3}	2.9×10^{-3}	2.9×10^{-3}	5.0×10^{-3}
Surface tension (N/m)	2.05×10^{-2}	2.05×10^{-2}	2.05×10^{-2}	2.06×10^{-2}
Injection velocity (m/s)	102	90.3	86.41	133.81
Initial turbulence quantity				
Kinetic energy (m^2/s^2)	2.88×10^{2}	2.26×10^{2}	3.94×10^{1}	5.22×10^{2}
Dissipation rate of kinetic energy (m^2/s^3)	1.06×10^{8}	7.34×10^{7}	1.22×10^{7}	3.14×10^{8}
Average Weber number of primary atomization	940.93	2010.68	3068.81	2556.43
Average drop diameter on 2nd droplet breakup (mm)	0.05	0.05	0.05	0.05
Average Weber number of secondary atomization	156.82	335.11	511.47	535.19
Reference		Hiroyasu et al. [5]		Koo [17]

and the classical TAB model is employed. Otherwise, the drops would be considered for the secondary breakup with the turbulence effects that are described in the Results and Discussion.

While the parcels produced from the primary atomization are continuously tracked in the Lagrangian coordinate system, they are also considered for the secondary breakup, which is governed by Eq. (7). This equation is solved in the same way as the classical TAB model [2] but using the finite difference method since its exact analytical solution does not exist. To develop the finite difference formulation for Eq. (7), it is convenient to define a new set of coefficients for this equation as follows:

$$C_1 = \frac{C_F}{C_b}\frac{\rho_g}{\rho_l}\frac{W^2}{r_p^2}, \quad C_2 = C_t\frac{\varepsilon_o}{C_b^2 r_p^2}\left[\frac{k}{k_o}\right]^{C_\varepsilon}, \quad C_3 = C_k\frac{\sigma}{\rho_l r_p^3},$$

$$C_4 = C_d\frac{\mu_l}{\rho_l r_p^2},$$

By substituting the above coefficients, Eq. (7) becomes

$$\ddot{y} = C_1 + C_2\dot{y}^{-1} - C_3 y - C_4\dot{y} \tag{9}$$

In contrast to the TAB model, an exact solution cannot be obtained since it contains an extra nonlinear term (second term on the right-hand side). Instead, a second-order finite central difference scheme in a time step was used [13]. The deformation displacement y is computed at every time step. The secondary breakup assumedly occurs when y approaches 1. Then, the product drop size is calculated from Eq. (8). At the same time, its initial turbulence quantities are estimated [9]. Again, the new product drops are continuously tracked until they leave the computational domain. When the product drop size is smaller than the Kolmogorov length scale, the turbulence activity of the new drop is no longer considered. In this case, the present model would recover the classical TAB model.

The T-blob/T-TAB model was incorporated into the CFD-ACE+ [14] program for two-way gas-liquid atomization calculations. This code, together with its liquid spray module, solves the equations of steady state as well as transient flow with chemically reactive fluid dynamics and droplet spray. The governing equations and the numerical solution method are discussed in [14] and are only described briefly here. The Navier-Stokes equations and RNG (renormalized group) k-ε turbulence model for a gas phase are solved with a finite volume method. A time-marching with a high-order accurate explicit scheme is employed in the transient calculation. For spray, numerical parcels of drops are tracked in a Lagrangian framework. The parcel represents an ensemble of identical drops occupied in the same space at a given time. Subsequently, the spray properties at each point are described by statistically sampling the spray parcels. The drop parcels exchange mass, momentum, and energy with the gas through source terms in the Navier-Stokes equations.

Results and Discussion

Several relevant test cases selected from available research publications for performing numerical simulations are shown in Table 1. Variations in the predictions from the two classical KH and TAB models and the present models are also examined. The two-dimensional axisymmetric flow of a cylindrical liquid jet located at the centerline of the computational domain is simulated. It should be noted that the current version of CFD-ACE+ does not have collision/coalescence models. Because of the observation of these phenomena [15], a module was written [13] to compute the droplet collision and coalescence based on model of [16]. The time-transient liquid jet breakup and the ambient gas behavior are computed for an incremental time step, Δt, of 2.5×10^{-6} s. The spray trajectory is tracked in the Lagrangian coordinate system. A different time step, which is normally smaller, is applied for this coordinate system. CFD-ACE+ recalculates this time step continuously based on criteria of preassigned maximum allowable changes in drop velocity and diameter. The Lagrangian tracking time step used in the simulations for this study ranges from 1/3 to 1/10 of Δt. It should be noted that a solution sensitivity study for various numerical parameters, such as grid mesh size, time step values, etc., has been performed [13] prior to obtaining the results of this investigation.

The spray tip penetrations from the exit port into the ambient gas for test cases H-1 and H-2 are plotted in Fig. 1 as a function of time. Both predictions from the T-blob/T-TAB and KH/TAB are similar. Nearly straight lines of the tip penetration curves at the beginning indicate that the tip velocity of the liquid jets remains almost constant. Once the jet is fully converted into droplets, the surface area of the spray nose is radially expanded because of droplet's radial momentum components. The jet speed is also reduced due to aerodynamic force and drag. Hence, the penetration curve has a smaller slope at the later time. Furthermore, the results also reveal that the spray penetrates at faster rate into a lower-pressure gas. In comparison to measurements, the tip penetrations in both cases are slightly underpredicted with analytical models at the beginning of the spray; however, they are overpredicted some-

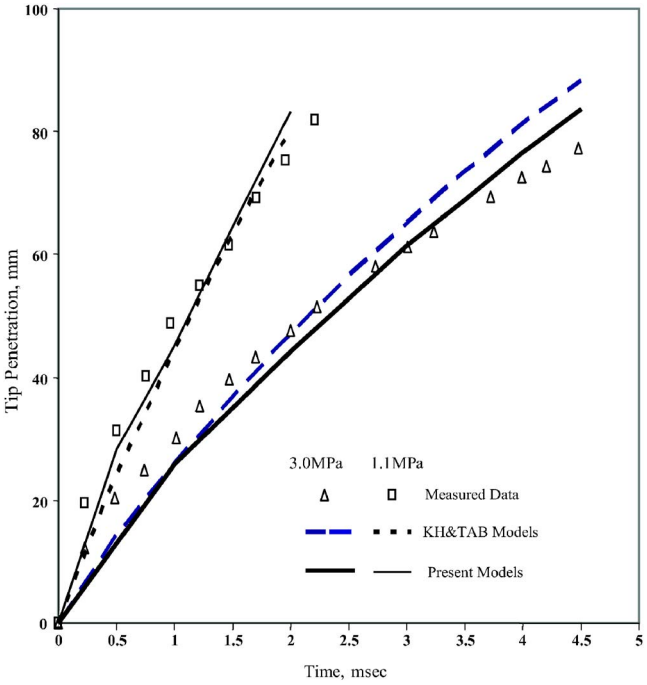

Fig. 1 Comparison between numerical and measured tip penetration

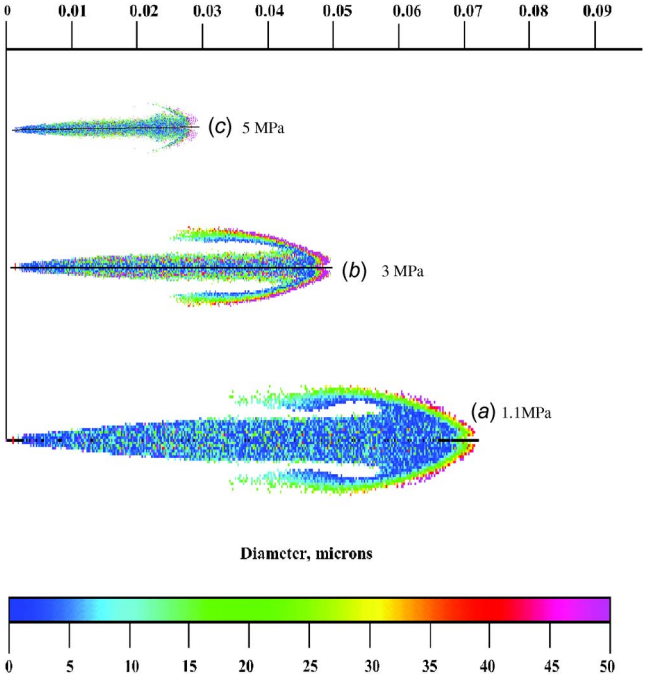

Fig. 3 Predicted variations in spray shape, tip penetration, and drop size at t=2.5 ms due to different back pressures using the T-blob/T-TAB model: (*a*) 1.1 MPa, (*b*) 3 MPa, and (*c*) 5 MPa

what at the later time. Overall, the computational results show a close agreement with the experimental data. Variations in the spray angle due to different ambient gas pressures for test cases H-1–H-3 are depicted in Fig. 2. This angle is a global parameter used to characterize the radial expansion of the spray. For an axisymmetric case this angle, as shown in Fig. 2, is formed by the two opposite tangent lines drawn along the spray envelop. The results portray higher back pressure with a larger radial expansion of the spray. A further examination of the atomization modeling suggests that the radial product drop velocity is related to the wavelength and its maximum growth rate. The values of these parameters, however, are dependent on the liquid-to-gas density ratio. Consequently, higher gas pressure would result in a larger radial-to-axial velocity ratio and a wider spray angle. In comparison to the results of the KH/TAB models, a favorable larger spray angle is predicted by the present models. As stated in [9], the T-blob model estimates considerably larger product drop sizes than the KH model, which leads to the prediction of a stronger radial momentum. Consequently, liquid drops are spread outward more in the T-blob model when compared to the predictions provided by the KH models. As shown in Fig. 2, a better agreement with the measured data is obtained with the present models.

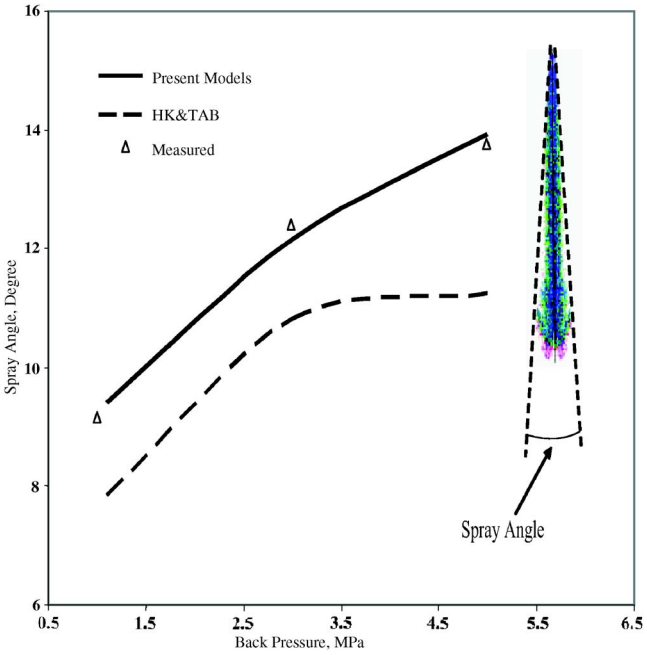

Fig. 2 Variations in spray angles versus back pressure

The computed spray shapes and tip penetrations from the present models are displayed in Fig. 3 for three different back pressure conditions after 2.5 ms of liquid injection. It should be noted that the injection velocity is higher for a lower back-pressure condition. Hence, the spray tip penetrates faster into a lower-pressure environment, although the drag increases on the periphery of the spray contour. This phenomenon leads to parcels containing small drops being dragged into the wake behind the tip region, which clearly can be observed in Figs. 3(*a*) and 3(*b*). It is also interesting to note that larger drops appear on the spray tip as well as on the peripheral regions near the tip. Generally, large drops carry a stronger momentum, which decays less than their smaller drop counterparts. Hence, the large drops tend to travel faster downstream than the smaller drops do. In addition, large drops found in these regions reflect the effect of drop coalescences. The coalescence is more pronounced in an elevated gas pressure. As illustrated in Fig. 3(*c*), a larger drop size can be observed in the tip region at higher ambient pressures. Weber numbers for primary and secondary droplet breakups are also estimated and listed in Table 1. In secondary atomization regimes, We numbers are much smaller. In phenomenological modeling, detailed breakup regimes, such as column breakup, bag breakup, multimode breakup, shear breakup, catastrophic breakup, etc., were not separately modeled. Based on the We number calculated and Oh number used, the secondary breakup is within the shear breakup regime where the aerodynamic force dominantly causes the droplet breakup process.

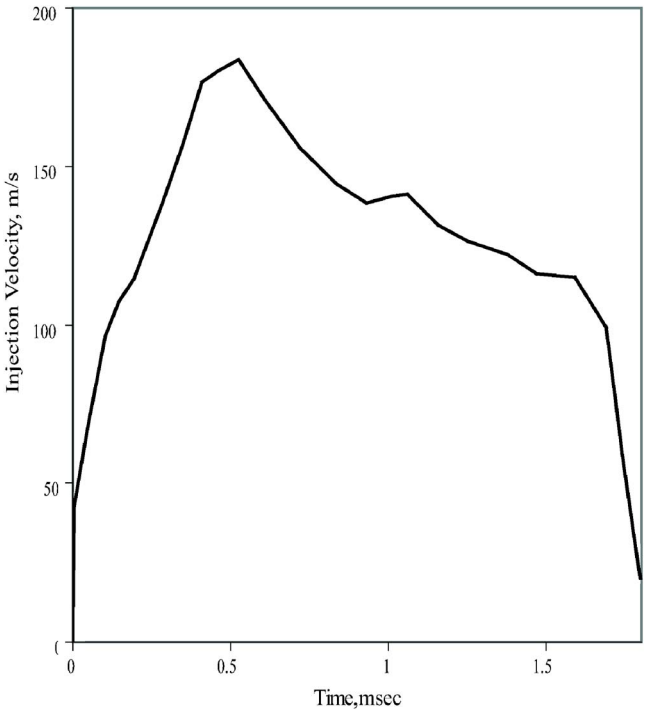

Fig. 4 Fuel injection velocity used in simulation for test case K

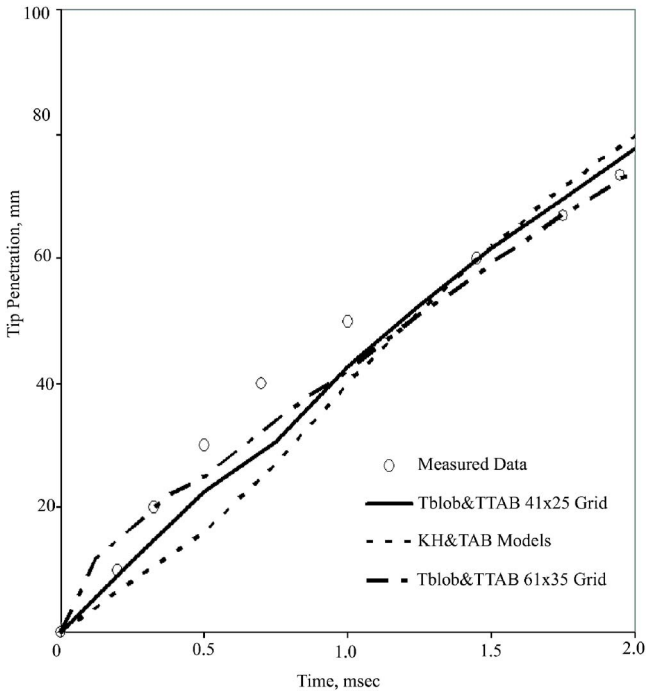

Fig. 5 Predicted and measured spray tip penetration for test case K

The following results are collected from numerical simulations of test case K (see Table 1). This test case is selected to evaluate the atomization models because of its available measured drop size data. In the experiment, Koo [17] measured diesel sprays with a phase/Doppler particle analyzer (PDPA) system. In general, a PDPA can recognize only a defined range of droplet diameters due to digital processing hardware limitations. Normally, the ratio of the largest observable droplet to the smallest observable droplet cannot exceed 35. Regarding to this experiment, the instrument was set to measure drop sizes from 1.8 μm to 246 μm. It should be noted that the liquid fuel injection was driven by a cyclic pumping system for which the mass injection rate is no longer constant. To simulate more realistically the inlet flow conditions, the transient injection velocity profile reported by Koo [17], as shown in Fig. 4, is utilized in the computations. Similar to the previous computational cases, this test case is simulated also for the transient flow field conditions with $\Delta t = 2.5 \times 10^{-6}$ s. It should be noted that the present simulation utilizes the RANS approach to obtain the mean velocity field of the gas phase. For statistically nonstationary flows, which were investigated experimentally by Koo [17] in this case, the interpretation of the averaging process is the ensemble averaging; thus, the RANS formulation is justified for the statistically transient case as indicated by the injector inlet condition of Fig. 4. The predicted spray tip penetration and the measured data are presented in Fig. 5, as are the grid-refinement comparative results. With finer grids packed in the near nozzle region, the spray seemed to be "denser" and penetrate further into the gaseous environment. This is the general shortcoming of Eulerian-Lagrangian approach utilizing particulate "point source" assumption within the Eulerian grids [10,18]. Extremely fine grids cannot be used. Within certain grid density, the spray exhibits similar behavior. The predictions of this test case, made with both the KH/TAB and present models, are slightly lower than the measurement at the beginning of the injection; however, the predicted curves approach the experimental data at a later time. It is noted that Koo [17] reported the spray penetration length from the beginning of the injection to the time of 1.5 ms, while the computation continues to 3.0 ms. In general, both the predicted tip penetrations are similar and their values are in reasonable agreement with the experimental data. Figure 6 displays the simulated spray shapes along with the photographs recorded at several time intervals in the experiment. In comparison to the photographs, the simulated spray penetrates with a slightly shorter distance into the ambient gas than the actual distance depicted from the photographs initially; however, the predictions improve significantly afterward. These results also reflect the same assessment of the tip penetration comparison shown in Fig. 5. It is also interesting to observe the degree of the spray being spread laterally and its tip shape. All the models predict a similar radial expansion of the spray for all considered time intervals and are compared reasonably well to their photographic counterparts. However, the numerical simulations display the tip profile more like a conical shape with parcels containing large drops rather than a round tip shown in the photographs. Since the momentum of these large drops is degrading much less than the one of the small drops, the large drops move faster downstream than the smaller drops. Therefore, the moving motion of the large drops creates the appearance of the conical shape at the tip. A series of the computational cases have been conducted to examine the tip shape variation for different initial spray angles. The analysis suggests that the spray tip head-end changes to a round shape and does not penetrate into the ambient gas as deep when increasing the initial spray angle. The tip variation analysis is not addressed in detail here, since it is not a main focus in this study. Further detailed drop-size comparisons between the predictions and the measurements are presented in Figs. 7 and 8. Figure 7 reveals the drop sizes recorded at three axial locations along the center line of the spray, which are identified in Fig. 7(*a*). The results indicate that the jet, with an initial diameter of 240 μm, breaks up into relatively large drops along the centerline. Their product drop diameters range from 100 μm to 200 μm at the stations of $x = 10$ mm and 20 mm (Figs. 7(*b*) and 7(*c*)). These results suggest that the primary breakup process is dominant in these regions. Further downstream, the drops undergo the secondary atomization, which generates smaller drops. Figure 7(*d*) exhibits drops of 20–50 μm dia at the $x = 60$ mm station. It should also be noted that the fuel injection cycle for this test case is complete at 1.77 ms; therefore, the drop sizes shown in Figs. 7(*b*) and 7(*c*)

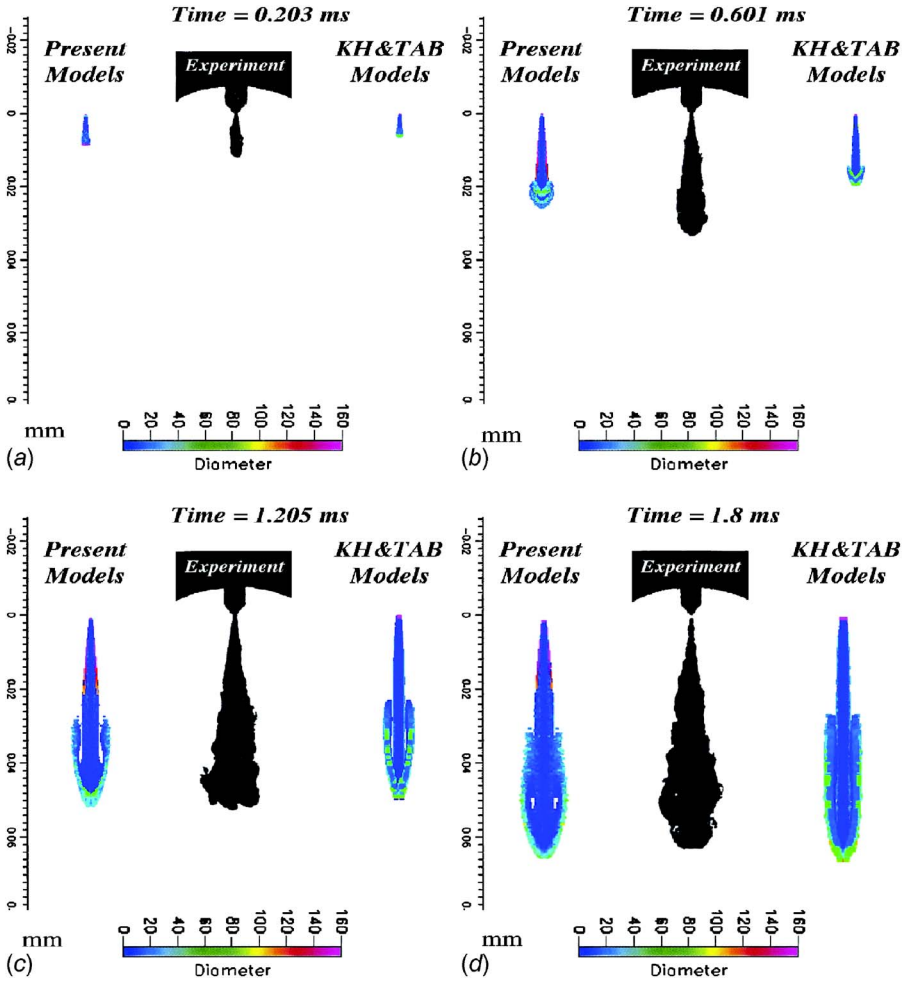

Fig. 6 Simulations and photographs of case K: (*a*) *t*=0.203 ms, (*b*) 0.601 ms, (*c*) 1.205 ms, and (*d*) 1.8 ms

also reflect this end period at which the small drops are registered. In Fig. 7(*b*), the effect of finer grid within this region is also observed. As discussed earlier, the finer grid system seems to see "more" droplets even when the spray has been terminated (after 2 ms). The small drops recorded after 1.77 ms are formed because of the small injection rate at the tail end of the injection cycle, as well as the small drops lagging behind in the spray motion. In general, the predictions from the present models are in good agreement with the measured data. In contrast, the KH and TAB models underpredict the drop size for stations of $x=10$ mm and 20 mm; however, their predictions are improved significantly at the $x=60$ mm station. This observation is consistent with earlier results in [9]. The results also show that the KH model predicts generally smaller drop sizes than the T-blob model. Figure 8 displays the drop sizes at three off-centerline locations $[x,y]$ shown in Fig. 8(*a*). For the location at [10, 0.5], the measurement registered relatively large drops, the diameters of which are ranging from 30 μm to 180 μm with a random order in time. Similar to the results shown in Fig. 7, the smaller drops are also observed after the end of the injection cycle at $t=1.77$ ms. The present model predictions capture large drops intermittently at certain short time intervals; however, both the KH/TAB and T-blob/T-TAB atomization models project typically a much smaller drop size than the measurement portrayed. In other words, the CFD simulation indicates that the secondary droplet breakup process takes place at this location but not the primary breakup. The drop diameter at [10, 1.5] and [30, 2] in Figs. 8(*c*) and 8(*d*), respectively, varies from 20 μm to 50 μm. This suggests that considerably smaller drops appear on the spray periphery and their presence in this outermost region forms the shape of the spray. Furthermore, since the drop sizes at these locations are relatively small, the secondary droplet breakup occurs mostly in these regions. This assessment is consistent with the observation of Koo [17] in his measured data analysis. He concluded that the small droplets in the periphery of the spray are not those directly injected from the nozzle. The small droplets from the nozzle travel much slower than the large droplets, which are produced in the primary breakup; hence, they cannot maintain the spray shape observed in the experiments without the appearance of drops formed by the secondary breakup mechanism. It is interesting to note that the simulation with the KH and TAB models has a limited number of parcels and no parcel tracked at [30, 2] and [10, 1.5], as shown in Figs. 8(*c*) and 8(*d*), respectively. Again, this examination reconfirms the display in Fig. 2 that the spray angle predicted by the classical KH and TAB models is a little smaller than the actual angle. In the present model, the numerical simulation captures droplets at [10, 1.5] and [30, 2] only in a short time span, and the predicted drop sizes at this interval are close to the measured data.

Conclusions

We have successfully implemented a newly developed hybrid T-blob/T-TAB atomization model into an existing CDA-ACE+ code for simulation of liquid jet atomization using two-way Eulerian-Lagrangian method. A drop collision and coalescence

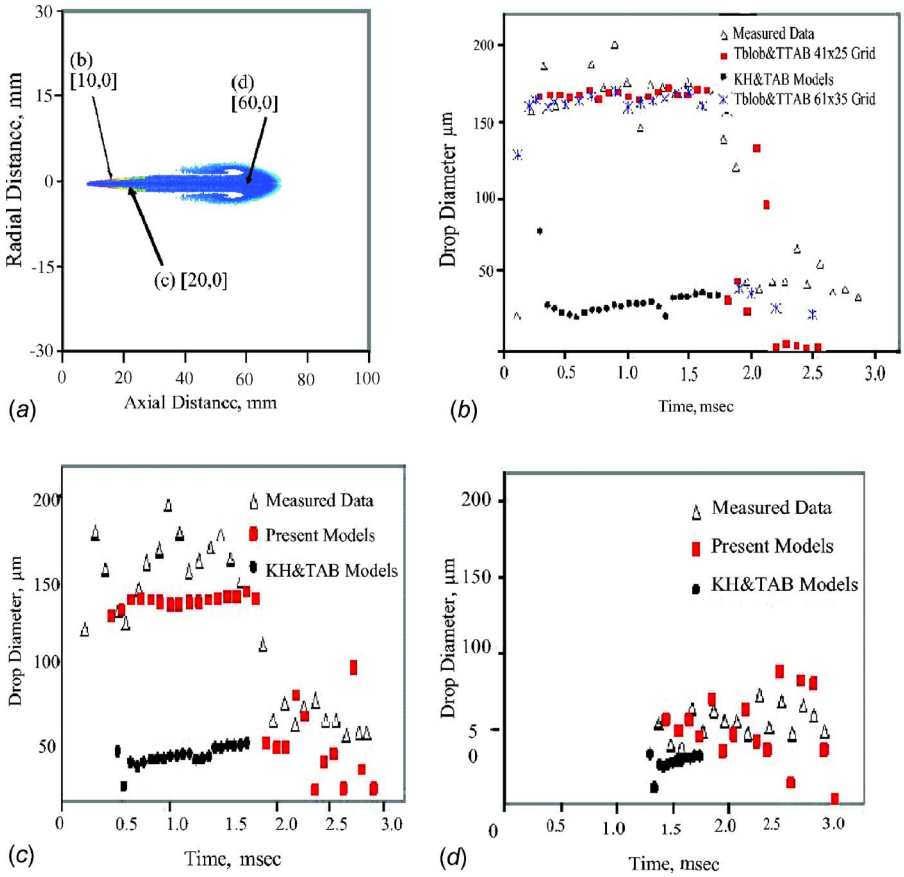

Fig. 7 Drop size distributions along spray center line for test case K

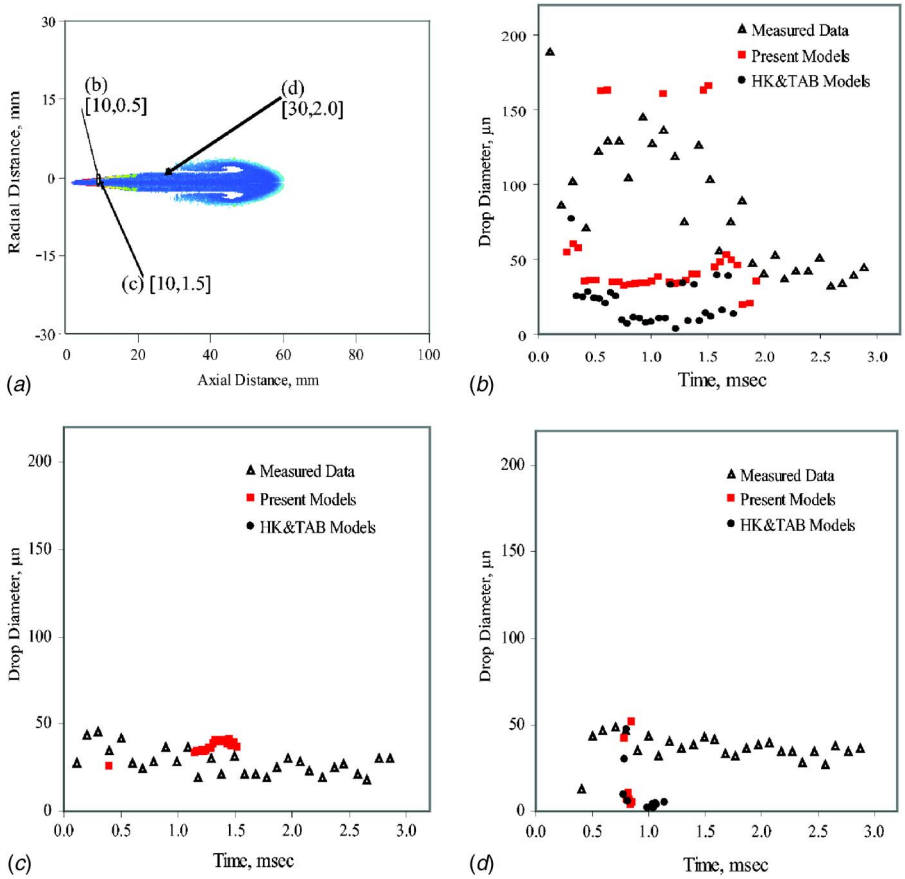

Fig. 8 Off-centerline drop size distributions for test case K

model [15] has also been incorporated into the ACE+ code to provide more realistic simulations. Assessments of the new model have been performed against two experimental studies and several observations and conclusions can be drawn as follows:

1. In general, the CFD simulations are able to capture similar spray structures observed in the experiments. The spray tip penetration lengths as well as the appearances of large drops at the spray tips, which are predicted from the two sets of the KH/TAB and T-blob/T-TAB atomization models, are comparable to the measured data. However, the KH and TAB models estimate smaller spray angles for the test cases H-1–H-3 than the measurements indicate.
2. For the test case K, the drop measurements and the predictions indicate that small drops created from the secondary breakup appear in the outermost regions of the spray. Hence, this breakup mechanism is responsible for the radial expansion of the spray. These drops then form the profile of the spray. On the other hand, the drops on centerline of the spray are relatively large. Furthermore, the appearance of large drops at the spray tips may result from drop coalescence. In addition, the strong momentum of the large drops allows them to travel ahead downstream.
3. In summary, for test case K, the CFD simulation using the KH and TAB models tends to underpredict the drop size of the spray, while it is able to capture reasonably the liquid spray structure. On the other hand, the present models predict comparable drop sizes, as seen in the measured data. Overall, the predicted results from the present models do agree reasonably with the experimental data.

Acknowledgment

This research is supported by NASA Marshall Space Flight Center in Huntsville, Alabama under a full-time study program. Technical consultations of Dr. D.S. Crocker, Dr. B. Zuo, and Dr. S. Kim of CFD Research Corporations in this study are acknowledged. Finally, helpful assistance of librarians at Redstone Scientific Information Center in Huntsville, Alabama is appreciated.

Nomenclature

a = radius of *blob* or parent drop
B_0 = constant (=0.61)
B_1 = constant (=10.0)
C_a = constant ($=B_o/3.726B_1$)
C_b = constant (=1/2)
C_d = discharge coefficient of injection nozzle; constant used in Eq. (9)
C_F = constant (=1/3)
C_{jet} = constant (=10)
C_k = constant (=8)
C_t = empirical constant involving turbulence force
C_ε = turbulence constant (=1.92)
c_t = weighting parameter associated with turbulence motion
c_w = weighting parameter associated with surface motion
D = diameter of injection nozzle
E = term associated with energy
k = turbulence kinetic energy per unit mass in the k-ε model
k_t = turbulent kinetic energy
K_c = loss coefficient due to nozzle inlet geometry
K_ε = turbulence constant (=0.27)
L = length of injection nozzle
L_w = characteristic length scale associated with surface motion
L_t = characteristic length scale associated with turbulence
Oh = Ohnesorge number ($\text{We}_1^{0.5}/\text{Re}_1$)
r_p = radius of a parent drop used in the secondary breakup formulations
r_t = radial length scale associated with turbulence motion
r_w = radial length scale associated with surface wave motion
s = contraction area ratio of injection nozzle
SMR = Sauter-mean radius of product drop
t = time
U = liquid jet injection velocity
W = relative drop velocity with respect to local gas velocity
We = Weber number ($\rho_g W^2 r_p/\sigma$)
y = nondimensional parameter of distortion displacement ($\zeta/C_b r_p$)

Greek Letters

Λ = wave length of fastest growing wave
ρ = density
σ = surface tension coefficient
ε = dissipation rate of turbulence kinetic energy per unit mass
τ = time associated with surface wave motion
τ_w = characteristic time scale associated with surface wave motion ($a/\Lambda\Omega$)
τ_t = characteristic time scale associated with turbulence
μ = molecular viscosity
ω = angular frequency
ζ = radial cross-sectional change of drop from its equilibrium position
Ω = maximum wave growth rate

Subscripts

0 = initial value
g = value of ambient gas
l = value of liquid phase
t = parameter associated with turbulence
w = parameter associated with surface wave motion

Superscripts

o = initial value
$\cdot$ = first derivative with respect to time
$\cdot\cdot$ = secondary derivative with respect to time

References

[1] Reitz, R. D., 1987, "Modeling Atomization Processes in High-Pressure Vaporizing Sprays," Atomization Spray Technol., **3**, pp. 309–337.
[2] O'Rourke, P. J., and Amsden, A. A., 1987, "The Tab Method for Numerical Calculation of Spray Droplet Breakup," SAE Technical Paper No. 872089.
[3] Tanner, F. X., 1998, "Liquid Jet Atomization and Drop Breakup Modeling of Non-Evaporation Diesel Fuel Sprays," SAE Trans. J. Engines, **106**(3), pp. 127–140.
[4] Tanner, F. X., 2003, "A Cascade Atomization and Drop Breakup Model for the Simulation of High-Pressure Liquid Jets," SAE Paper No. 01-1044.
[5] Nishimura, A., and Assanis, D. N., 2000, "A Model for Primary Atomization Based on Cavitation Bubble Collapse Energy," *Proc. of ICLASS 2000*, Pasadena, CA, July 16-20, pp. 1249–1256.
[6] Huh, K. Y., Lee, E., and Koo, J. Y., 1998, "Diesel Spray Atomization Model Considering Nozzle Exit Turbulence Conditions," Atomization Sprays, **8**, pp. 453–469.
[7] Apte, S. V., Gorokhovski, M., and Moin, P., 2003, "LES of Atomizing Spray With Stochastic Modeling of Secondary Breakup," Int. J. Multiphase Flow, **29**, pp. 1503–1522.
[8] De Villiers, E., Gosman, A. D., and Weller, H. G., 2004, "Large Eddy Simulation of Primary Diesel Spray Atomization," 2004 SAE International, SAE Paper No. 2004-01-0100.
[9] Trinh, H. P., and Chen, C. P., 2006, "Development of Liquid Jet Atomization and Breakup Models Including Turbulence Effects," Atomization Sprays, **16**, pp. 907–932.
[10] Bianchi, G. M., Pelloni, P., Corcione, F. E., Allocca, L., and Luppino, F., 2001, "Modeling Atomization of High-Pressure Diesel Sprays," ASME J. Eng. Gas Turbines Power, **123**, pp. 419–427.

[11] Arcoumanis, C., and Gavaises, M., 1998, "Linking Nozzle Flow With Spray Characteristics in a Diesel Fuel Injection System," Atomization Sprays, **8**, pp. 307–347.
[12] Chen, C. P., Shang, H. M., and Jiang, Yu, 1992, "An Efficient Pressure-Velocity Coupling Method for Two-Phase Gas-Droplet Flows," Int. J. Numer. Methods Fluids, **15**, pp. 233–245.
[13] Trinh, H. P., "Modeling of Turbulence Effect on Liquid Jet Atomization," Ph.D. Dissertation, University of Alabama in Huntsville, 2004.
[14] CFD Research, 2003, CFD-ACE+ Theory Manual, CFD Research Corporation, Huntsville, AL.
[15] Hiroyasu, H., and Kadota, T., 1974, "Fuel Droplet Size Distribution in Diesel Combustion Chamber," SAE Paper No. 740715.
[16] O'Rourke, P. J., and Bracco, F. V., 1980, "Modeling of Drop Interactions in Thick Spray and Comparision With Experiments," *Stratified Charge Auto Engineering Conference*, Institute of Mechanical Engineering Publications, pp. 101–106.
[17] Koo, J., 1991, "Characteristics of a Transient Diesel Fuel Spray," Ph.D. dissertation, University of Wisconsin-Madison.
[18] Salman, H., and Soteriou, M., 2004, "Lagrangian Simulation of Evaporating Droplet Sprays," Phys. Fluids, **16**, pp. 4601–4622.

Analysis of Combustion Induced Vortex Breakdown Driven Flame Flashback in a Premix Burner With Cylindrical Mixing Zone

F. Kiesewetter

M. Konle[1]
e-mail: konle@td.mw.tum.de

T. Sattelmayer

Lehrstuhl für Thermodynamik,
Technische Unversität München,
D-85748 Garching, Germany

In earlier experimental studies of the authors a previously unknown mechanism leading to flame flashback—combustion induced vortex breakdown (CIVB)—was discovered in premixed swirl burners. It exhibits the sudden formation of a recirculation bubble in vortical flows, which propagates upstream into the mixing zone after the equivalence ratio has exceeded a critical value. This bubble then stabilizes the chemical reaction and causes overheat with subsequent damage to the combustion system. Although it was shown earlier that the sudden change of the macroscopic character of the vortex flow leading to flashback can be qualitatively computed with three-dimensional as well as axisymmetric two-dimensional URANS-codes, the proper prediction of the flashback limits could not be achieved with this approach. For the first time, the paper shows quantitative predictions using a modified code with a combustion model, which covers the interaction of chemistry with vortex dynamics properly. Since the root cause for the macroscopic breakdown of the flow could not be explained on the basis of experiments or CFD results in the past, the vorticity transport equation is employed in the paper for the analysis of the source terms of the azimuthal component using the data delivered by the URANS-model. The analysis reveals that CIVB is initiated by the baroclinic torque in the flame and it is shown that CIVB is essentially a two-dimensional effect. As the most critical zone, the upstream part of the bubble was identified. The location and distribution of the heat release in this zone governs whether or not a flow field is prone to CIVB.
[DOI: 10.1115/1.2747259]

Introduction

Flame flashback into the mixing section deteriorates the reliability of premix burners, as premature heat release causes burner overheat with subsequent failure of the entire combustion system. Since these reliability problems are becoming more severe with increasing air pressure as well as air and flame temperature, the improvement of the existing knowledge concerning flashback phenomena is crucial. Three mechanisms leading to undesired flame propagation upstream are widely known and well understood: If the turbulent flame speed is higher than the turbulent burning velocity flashback will occur in the core flow. Upstream propagation of the flame will be initiated in the wall boundary layer, if the velocity gradient falls below a critical value. Violent combustion instabilities can also lead to sudden transitions of the flame position from the combustor into the premix duct. In an experimental investigation of a gas turbine burner without centerbody [1–3] a fourth mechanism was explicitly observed for the first time: *Combustion Induced Vortex Breakdown* (CIVB) is a previously unknown form of flashback, which can occur only in premixed swirling flames. Typically, the flame propagation driven by CIVB through the entire mixing section occurs during the increase of the equivalence ratio or the reduction of the mixture mass flow [1]. Flame flashback due to CIVB differs substantially from the other three forms, as the heat release alters the flow field in the vortex core almost totally.

Figure 1 shows a sketch of the experimental setup [1]. The swirl burner consists of a conical swirler followed by an optically accessible cylindrical tube. It is attached to a combustor with a considerably larger cross section. In the experiments, the reactants were externally premixed to avoid any equivalence ratio fluctuations. The mixture entered the tubular section of 75 mm diameter via the ports in the swirl generator as well as via a small annular gap near the centerline. This gap mass flow is only a few percent of the mass flow passing the swirl generator. In normal operation, the vortex breaks down downstream of the burner exit plane and forms an internal recirculation zone (IRZ) [4] in the combustion chamber. The IRZ transports heat and active chemical species from the burnt region upwards to the tip of the flame and serves in this way as aerodynamic flameholder.

Fritz [1] and Kröner [2] used several measurement techniques for the investigation of the flow and the reaction zone during flashback, particularly laser induced fluorescence (LIF) for the location of the flame front, laser Doppler anemometry (LDA) for the measurement of the velocity field and chemiluminescence recorded with a UV intensified high speed camera for the tracking of the flame motion. In Fig. 2 an example of the recorded series of flame chemiluminescence pictures is shown. It proves that the flashback took place in the center of the flow, although the flow velocity in normal operation was more than four times the turbulent flame velocity. Since no reaction was observed near the walls and the thermoacoustic velocity oscillations were very low in the tests, Fritz and Kröner [1] concluded that they had detected a previously unknown flashback mechanism. Their measurements showed that the heat release of the flame located in the combustor suddenly leads to the combustion induced vortex breakdown in the tube with the formation of an upward traveling bubble acting as the permanent flame ignition source. Figure 3 shows four snapshots taken during flashback to illustrate the appearance of the

[1]Corresponding author.

Contributed by the International Gas Turbine Institute (IGTI) of ASME for publication in the JOURNAL OF ENGINEERING FOR GAS TURBINES AND POWER. Manuscript received June 7, 2006; final manuscript received April 3, 2007. Review conducted by Nader Rizk.

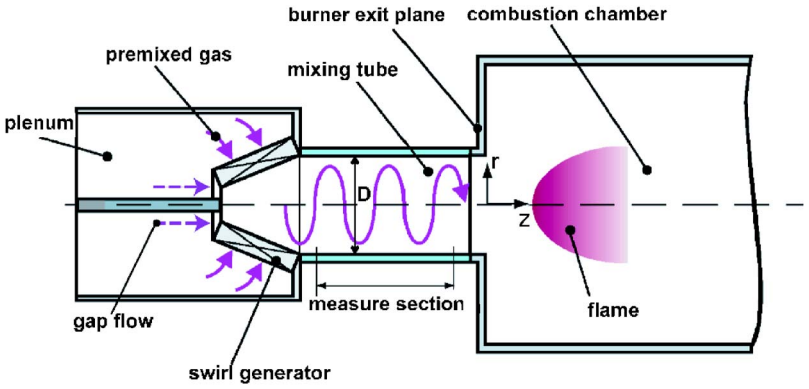

Fig. 1 Experimental setup employed for the CIVB studies

phenomenon. In this displayed computation the simulated flashback occured due to the increase of the equivalence ratio from $\Phi=0.83$ to $\Phi=0.91$.

Qualitative numerical simulations published previously [5] have proven that the basic features of CIVB can be captured numerically with CFD computations. Fritz showed earlier that the propagation velocity of the bubble can be properly calculated with a global model based on mass and momentum conservation [6]. Kröner was able to correlate the flashback limits for a wide range of methane-hydrogen mixtures [3] successfully. The form of the correlation he developed reveals that the heat release in the propagating bubble is governed by the balance between turbulent mixing and flame quenching.

Since the application of the vortex transport equation is somewhat particular in numerical combustion studies, Sec. 2 introduces the relationships required for the analysis of the URANS data, before in Sec. 3 the models used for the CIVB computations are described. Finally, Sec. 4 presents the results and their interpretation before the conclusions are listed in Sec. 5.

Theory

Vorticity Transport Equation. Although the vortex transport equation can be used for the computation of flows (e.g. [7]), in CFD studies of combusting turbulent flows, mostly the Navier-Stokes equations are employed for this purpose. The computations of the flow during flashback presented below were also computed on this basis, but for the analysis of the results, the vortex transport equation was preferred, as this method provides a substantially deeper insight into vortex phenomena than the discussion in terms of the Navier-Stokes equations [8–10],

$$\frac{D\boldsymbol{\omega}}{Dt} = \frac{\partial}{\partial t}(\boldsymbol{\omega}) + (\mathbf{U}\cdot\nabla)\boldsymbol{\omega} = (\boldsymbol{\omega}\cdot\nabla)\mathbf{U} - \boldsymbol{\omega}(\nabla\cdot\mathbf{U}) + \frac{1}{\rho^2}(\nabla\rho\times\nabla p) \tag{1}$$

Equation (1) describes the inviscid transport of vorticity ω. On the right-hand side of the equation the first term represents the effect of stretching and tilting of vortices, the second describes the volume expansion due to heat release, and the third term accounts for the baroclinic torque. While the first term is caused by the flow field and, therefore, exists also in the isothermal case, the other two occur only in the reacting case and are generated by the heat release in the flame. Contributions of viscous diffusion and dissipation [10] are of minor influence and have therefore been neglected.

Azimuthal Vorticity. The components of the vorticity vector are given by

$$\zeta = \frac{1}{r}\frac{\partial(rV)}{\partial r}$$

$$\xi = -\frac{\partial V}{\partial z}$$

$$\eta = \frac{\partial U}{\partial z} - \frac{\partial W}{\partial r}$$

with the components ζ, ξ, and η in the axial, radial, and azimuthal direction. U is the radial, V is the tangential, and W is the axial velocity. These three relationships indicate that vorticity produces additional velocity in the flow field. The occurrence of vortex

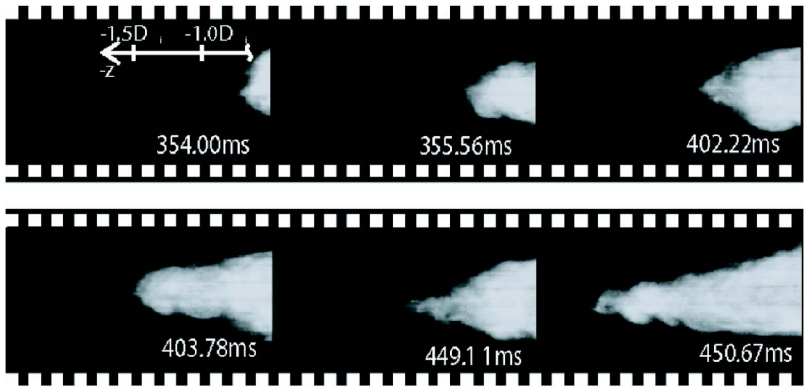

Fig. 2 Flame position during sudden vortex breakdown in the tubular burner section (from high speed films recorded with a UV-intensified camera)

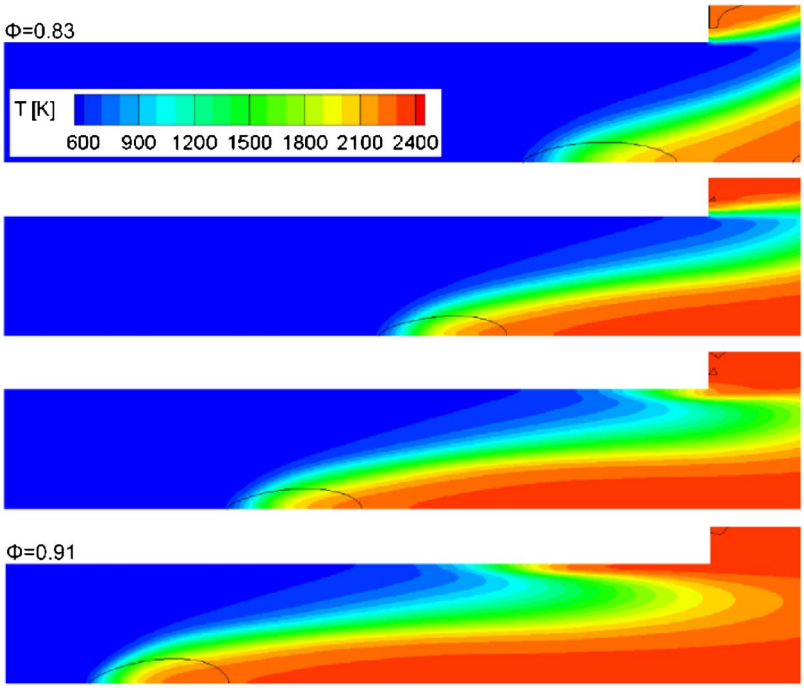

Fig. 3 Numerical simulation of a flashback occurring by the increase of Φ =0.83 to Φ=0.91

breakdown is closely linked to the generation of axial velocity w_{ind} in the opposite direction of the main flow. For the purpose of the data analysis presented below only the azimuthal vorticity is important, because only this component induces this negative axial velocity in the case of rotational symmetry according to the law of Biot-Savart [11],

$$w_{ind}(z) = \frac{1}{2}\int_{-\infty}^{\infty}\int_{0}^{\infty}\frac{r^{*2}\eta(r^*,z^*)}{[r^{*2}+(z-z^*)^2]^{3/2}}dr^*dz^* \qquad (2)$$

In the nonreacting case as well as in all cases with flame stabilization in the combustor, the location of the upstream end of the recirculation bubble is the result of the balance between the axial flow and the induced velocity w_{ind} against the main flow. A more detailed explanation is provided in [4].

Numerical Simulation

Numerical Approach. In the URANS calculations the second order LRR Reynolds stress turbulence model was used and for combustion modeling the Schmid model [12] was employed. This numerically robust combustion model was selected on the basis of the encouraging results reported in the literature for a wide range of premixed flames [12] also covering the thickended flame regime, which is of particular relevance for the precise prediction of the CIVB limits. Furthermore, it does not require any adjustment of free parameters [5]. Tests revealed that the measured thickness of the turbulent reaction zone in normal operation was predicted properly, indicating that the ratio between the turbulent and the chemical time scale was realistically determined.

Simplified Two-Dimensional Models. For two reasons a simplified two-dimensional model was implemented. On the one hand, full three-dimensional CIVB calculations are computationally expensive. Thus, it was required to reduce to two dimensions, before parametric studies covering the variations of the premixed methane-air mass flow, the equivalence ratio, and the preheat temperature could be accomplished. On the other hand, the comparison of the results from the two-dimensional axisymmetric model with the full model allows the assessment of the question, to what extent the observed flame propagation is governed by three-dimensional effects.

As a first step, a limited number of CIVB computations were done with the full three-dimensional model. After their successful validation with experimental data these computational results were used as inflow and reference data for the following reduced models. Then a swirl source was implemented, which produces profiles corresponding to these reference data [5]. In a further simplifying step, a 2D-axisymmetric model with fixed profiles taken from the three-dimensional computations at the inlet was developed. Because this last version has the drawback of constraining vortex dynamics and cannot simulate the feedback of the propagation flame on the flow in the swirl generator, flame flashback cannot propagate through the entire tube as experimentally observed.

Figure 4 shows the axial velocity fields of the nonreacting flow computed with the full 3D and the 2D axisymmetric model with fixed inlet profiles. The conditions for these simulations were 70 g/s total mass flow with a gap mass flow of 0.5 g/s on the axis (see Fig. 1). A comparison of the results indicates that the simplifications have negligible influence. Additional studies of the reacting case proved that the observed constraint does not negatively influence the capability of the simplest model to compute flashback limits as well as the initial bubble propagation after the transition of the flow. For this reason and due to its high computational effectiveness the simplest form of the model is best suited for parametric studies and it was selected for most of the flashback computations, which delivered the results presented subsequently.

Sensitivity Analysis. The quantitative prediction of the CIVB flashback limits turned out to be challenging. The CIVB phenomenon reacts extremely sensitive on even small changes of the velocity field of the vortex flow particularly near the centerline. For example, the annular gap mass flow (see Fig. 1) influences the nonreacting velocity field considerably and indirectly influences

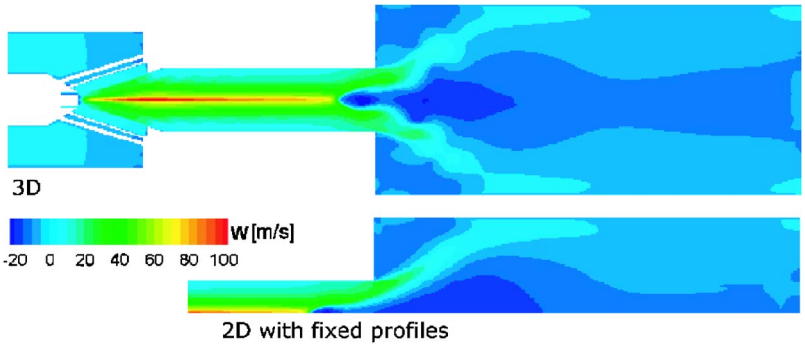

Fig. 4 Comparison of numerical results obtained with the full 3D model and the axisymmetric 2D model

flame flashback due to CIVB. Figure 5 shows this effect: A reduction of approximately 35% of this gap mass flow leads already to a substantial shift of the recirculation bubble into the vortex tube.

Fritz [1] and Kröner [3] detected that each configuration is either flashback safe or exhibits CIVB at a critical equivalence ratio, and they showed that small changes of the velocity distribution in the vortex core may lead to a transition from one case to the other. For the comparison of both cases with the 2D axisymmetric model the tangential velocity profile of a stable configuration was slightly modified to obtain an unstable case. Both profiles follow closely the results of the three-dimensional computations. Figure 6 shows the axial and tangential velocity components W and V for these two cases. While the axial velocity distribution and the turbulent quantities at the inlet remain unchanged, the moderate increase of the tangential velocity V of approximately 5% near the vortex core creates the unstable configuration.

Results

Distribution of the Azimuthal Vorticity. In order to illustrate the influence of the three source terms of the right term of Eq. (1) all three terms were separately calculated using the URANS data. Figure 7 shows the results for a stable operating point and allows us to evaluate the contributions of the three source terms in detail. The solid black line and the dotted line show the position of the recirculation bubble and the position of the reaction zone, respec-

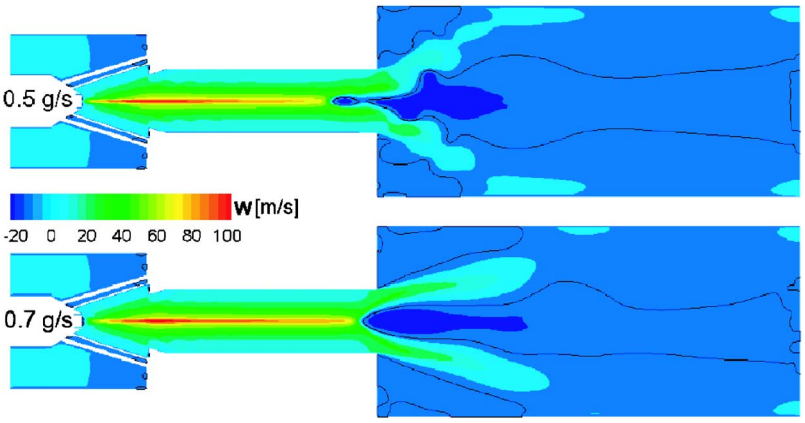

Fig. 5 Model sensitivity regarding the annular gap mass flow (total mass flow 70 g/s)

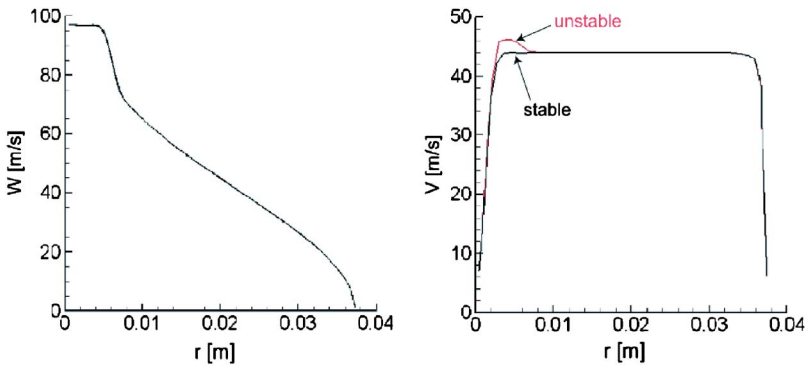

Fig. 6 Velocity profiles employed for the CIVB analysis. The slight increase of the tangential velocity V near the centerline converts the stable configuration in a CIVB prone case.

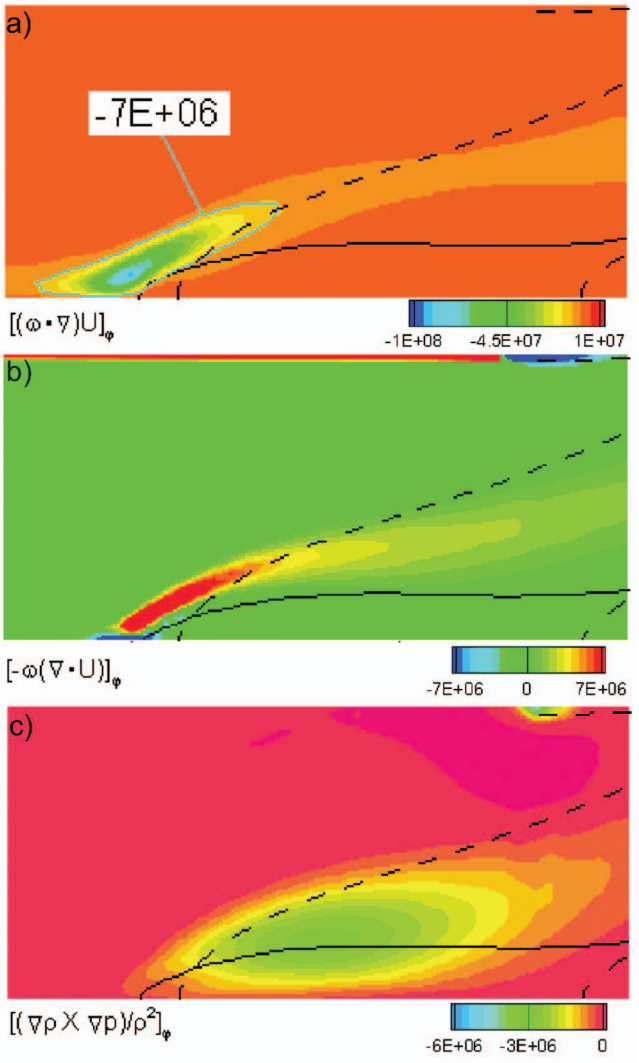

Fig. 7 The source term of the azimuthal vorticity transport equation in the stable regime near the flashback limit: (*a*) stretching/tilting; (*b*) volume expansion; (*c*) baroclinic torque

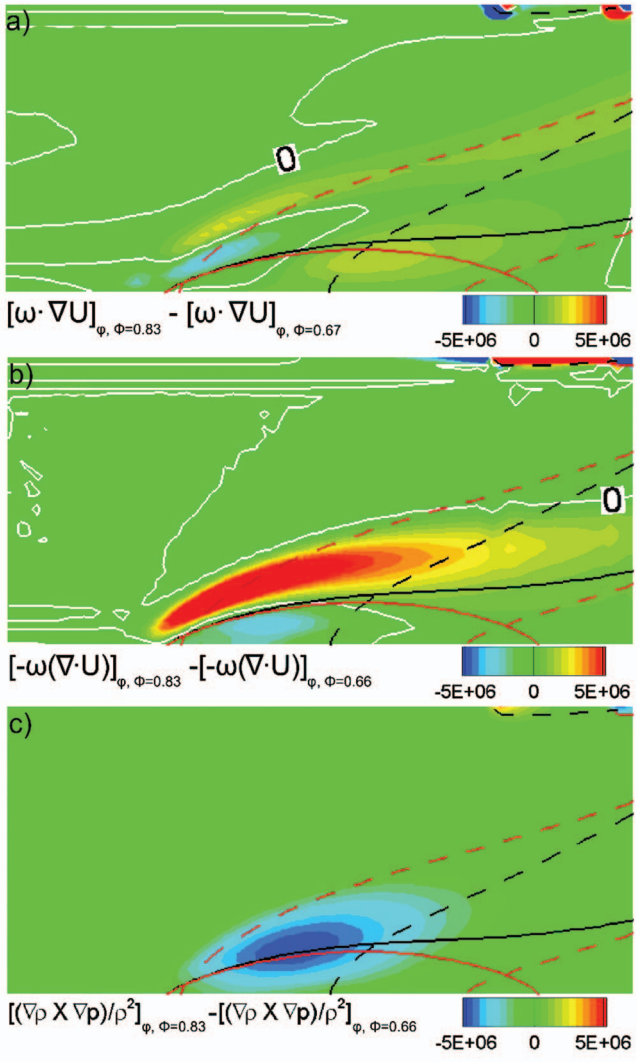

Fig. 8 Influence of the equivalence ratio change from Φ =0.67 (black lines) to Φ=0.83 (red lines): (*a*) stretching/tilting; (*b*) volume expansion; (*c*) baroclinic torque

tively. The comparison shows that in absolute numbers the stretching/tilting term due to streamline widening dominates over the other combustion related terms representing the volume expansion and the baroclinic torque, but from this order of magnitude a comparison cannot be concluded, whose term is responsible for flame flashback. Interestingly, the calculation of the difference of the stretching/tilting term, which occurs when the equivalence ratio is increased from $\Phi=0.67$ to $\Phi=0.83$ (Fig. 8(*a*)) is very small compared to the differences seen for the two other source terms. This indicates that the influence of the first term regarding the generation of flashback is negligible and leads to the conclusion that CIVB is initiated by one of the two other source terms. A deeper analysis revealed two adverse effects that are generated by the heat release: The volume expansion mainly creates positive azimuthal vortictity in a narrow region upstream of the recirculation zone, whereas the baroclinic torque is responsible for negative vorticity production in a wider area along the boundary of the recirculation zone. As CIVB requires additional combustion generated negative vorticity and positive vorticity leads to a downstream shift of the stagnation point, only the baroclinic torque stimulates the CIVB phenomenon, whereas the expansion tends to stabilize the flow.

These findings are illustrated for an example in greater detail in Fig. 8, which shows the sensitivity of each of the three source terms regarding a step of the equivalence ratio. The differences obtained when the equivalence ratio is increased towards the CIVB flashback limit are plotted. As already mentioned, the change of the azimuthal vorticity production caused by stretching/tilting is almost negligible. Of particular importance, however, is the local distribution of the last two combustion-related components (Figs. 8(*b*) and 8(*c*)). The volume expansion reduces in the existing negative azimuthal vorticity outside of the recirculation substantially but also leads to the local production of some negative vorticity inside. This negative vorticity is moderate compared to the negative vorticity generation by the baroclinic torque in a larger zone along the recirculation zone boundary. In conclusion, the occurrence of CIVB is closely linked to a flame generated baroclinic torque, which is only in flashback prone configurations large enough for the generation of a propagating bubble.

Turbulence-Chemistry Interaction. In order to further analyze the differences encountered in the stable and unstable cases the streamlines near the recirculation bubble were investigated. Figure 9 shows the streamline distribution for the following cases in one common plot:

$\Phi=0.67$, stable configuration (black line)

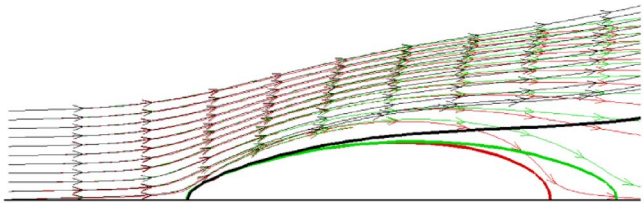

Fig. 9 Streamlines for $\Phi=0.67$ and for $\Phi=0.83$

$\Phi=0.83$ for the CIVB safe configuration
$\Phi=0.83$ for the CIVB prone configuration

For the ease of comparison the coordinate systems for all three cases have been mapped such that the three stagnation points are shifted to the common origin of the plot. Interestingly, both configurations, the CIVB safe and the CIVB prone case, do not show any differences upstream of the bubble. For this reason, the different behavior of the stable and the unstable configuration does not result from different levels of stretching/tilting and the causes for initiating CIVB in the unstable case are differences of the flow downstream of the stagnation point.

The earlier studies mentioned in the Introduction already revealed that the local heat release is governed by the interaction of turbulence and chemical reactions, which can be expressed in terms of the Damköhler number Da,

$$\mathrm{Da} = \frac{\tau_t}{\tau_c} \tag{3}$$

where τ_t is the characteristic time for the turbulent flow and τ_c is the characteristic chemical time for the reaction [13]. Small Damköhler numbers indicate that quenching of the reaction is relevant, whereas the chemical reaction is fast enough to prevent local quenching in zones of larger Da. Figures 10 and 11 show the distribution of the Damköhler number extracted from the Schmid model [12] in the form of isolines for both cases. Both figures show a zone of low Da near the stagnation point outside as well as inside the recirculation zones. However, the locations of the low Da zones with respect to the stagnation point as well as their sizes are considerably different for the two cases. In the stable configuration the smaller quenching zone near the stagnation point generates a shift of the flame position upstream and thus does not allow the generation of sufficient negative azimuthal vorticity (Fig. 10). However, in the unstable case (Fig. 11) the flame displacement downstream due to the stronger quenching permits a level of negative vorticity production, which is sufficient for the formation of a propagating bubble.

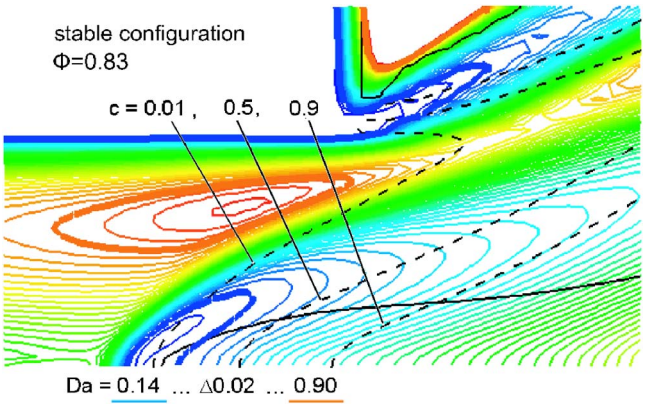

Fig. 10 Interaction between turbulence and chemistry, stable configuration (c: reaction progress)

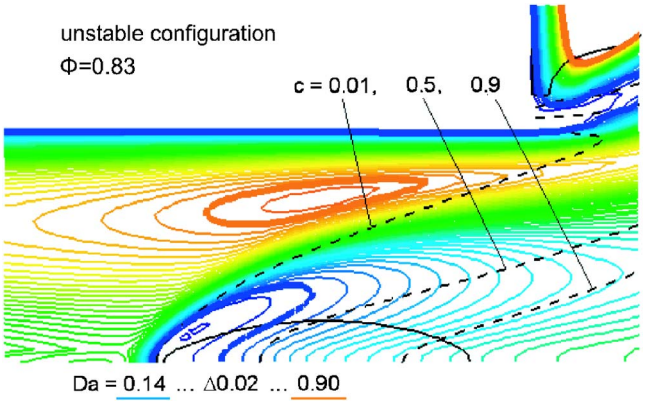

Fig. 11 Interaction between turbulence and chemistry, unstable configuration (c: reaction progress)

Validation. Figures 12 and 13 show a comparison of the computational results with experimental data taken from [1–3]. Figure 12 displays the axial velocity at different radial positions near the propagating bubble tracked during flashback and shows a remarkable quality of the simulation.

The most serious criterion for the verification of the simulation quality is the validation of the observed flame flashback limits. Figure 13 displays the numerically and experimentally determined equivalence ratios, which separate the stable regime from the re-

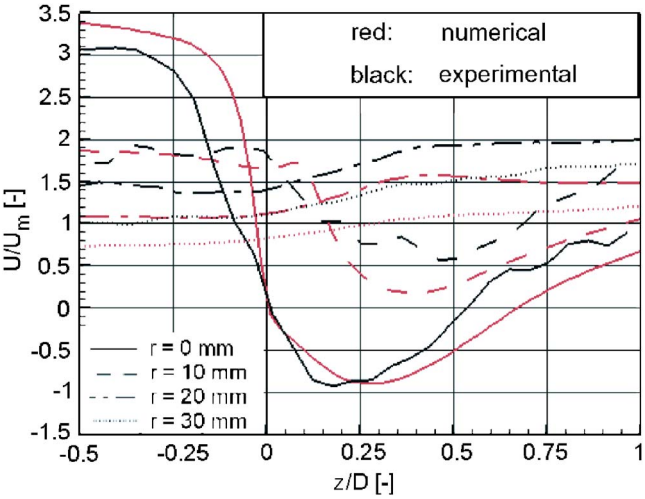

Fig. 12 Comparison of experimental and numerical results: velocity profiles in the propagating bubble

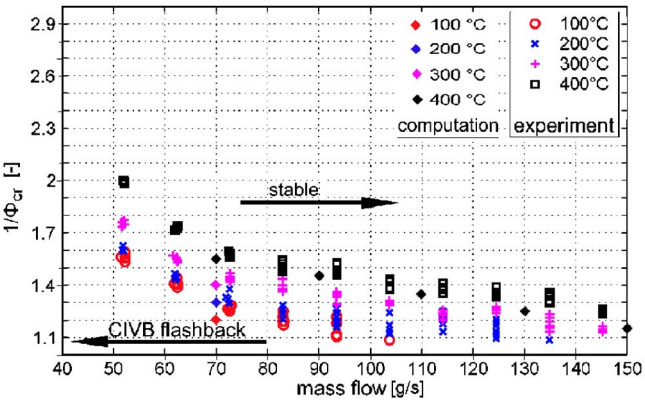

Fig. 13 Comparison of experimental and numerical results: flashback limits

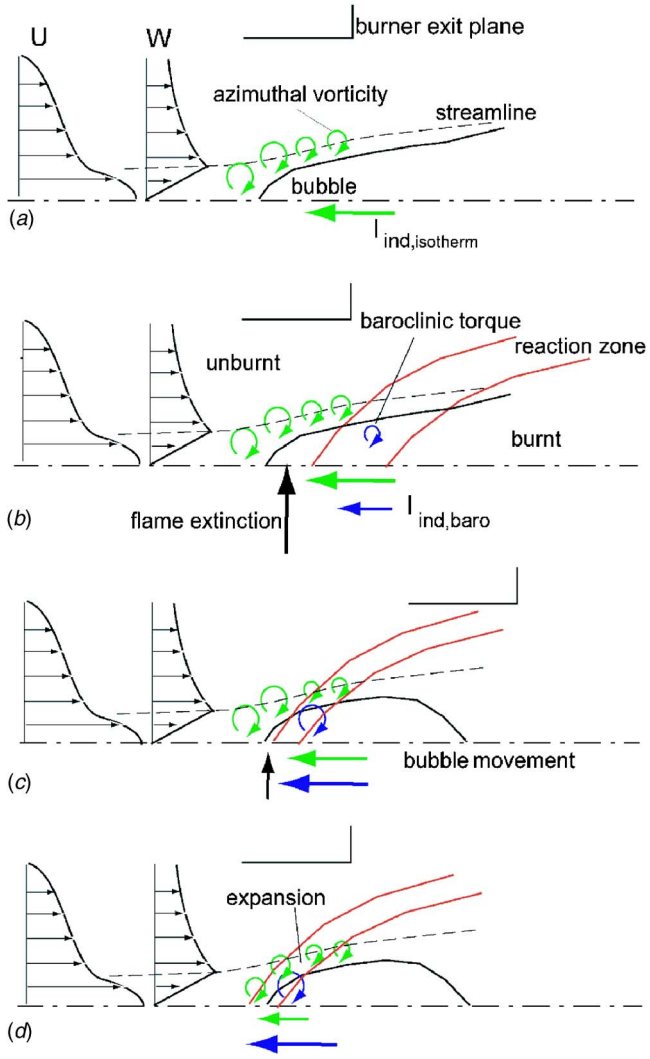

Fig. 14 Sketch of the effects leading to Combustion Induced Vortex Breakdown

gime with CIVB driven flame flashback. The comparison shows that the experimental values from [1] are predictable with a high level of accuracy. Both the effect of the mass flow, as well as the influence of the preheat temperature are well reproduced.

Effects Leading to CIVB Driven Flashback. The analysis of the CFD results on the basis of the source terms of the vorticity transport equation presented above provides the basis for the explanation of the root cause for the observed sudden occurrence of CIVB driven flame flashback of premixed, highly turbulent methane-air flames. The relevant effects are illustrated schematically in Figs. 14, which splits the process into four characteristic steps.

(a) In the nonreacting case the flow field induces the internal recirculation zone at the transition from the vortex tube into the combustor. This process is governed by stretching and tilting of the vortices due to streamline widening normal to the main flow direction. The bubble position results from the balance between the flow field and the isothermally induced force $I_{\mathrm{ind,isotherm}}$ against the main flow direction.

(b) In the reacting case the baroclinic torque in the reaction zone contributes to the generation of negative vorticity inside the bubble. This second contribution to the azimuthal vorticity induces additional negative axial velocity. The bubble reaches a new position slightly further upstream and a stable steady-state is reached also in the reacting case.

(c) If the equivalence ratio is further increased, the reaction zone will become more compact and the flame will move upstream with respect to the location of the recirculation zone. Due to the concentration of the reaction near the stagnation point the generation of negative azimuthal vorticity by the baroclinic torque will also increase. Exceeding a critical value can lead to an unstable situation. If the flame can be prevented from releasing substantial heat upstream of the recirculation zone, the levels of negative vorticity production and induced velocity w_{ind} required for the formation of a closed and propagating bubble will be achieved and the final flashback will be initiated.

(d) Of particular importance for the occurrence of the CIVB driven flame flashback is the existence of a distance between the upstream flame envelope and the location of the stagnation point. If the reaction zone is able to pass the stagnation point in upstream direction, the volume expansion upstream of the recirculation zone generates positive azimuthal vorticity and thus positive velocity, which stabilizes the flow. This stable situation cannot be reversed by further equivalence ratio increases. Although the baroclinic torque becomes stronger, the reduction of the total induction by positive vorticity production inhibits the motion of the stagnation point and thus the initiation of CIVB.

The decisive difference between the stable and unstable configuration is as follows: In the stable case the flame quenching upstream of the bubble is weaker than in the unstable configuration (Figs. 5, 10, and 11). Thus the flame reaches and even passes the stagnation point in an upstream direction for the stable case. This leads to further volume expansion upstream of the bubble which prevents the flame from generating the necessary level of induction of negative axial velocity. In contrast, the unstable configuration reaches the required induction level and CIVB driven flame flashback occurs suddenly after the critical equivalence ratio has been exceeded.

Conclusions

Using a hybrid approach consisting of URANS-computations and the data analysis on the basis of the source terms of the vorticity transport equation, the effects leading to *Combustion Induced Vortex Breakdown*, a special type of flashback, were explained. In addition, the CIVB flashback limits were quanitatively modeled for the first time with remarkable precision. The main conclusions from the analysis are as follows:

(a) The flame changes the vorticity of the flow field due to its volume expansion and the baroclinic torque.

(b) The baroclinic torque in the flame is responsible for CIVB driven flashback, as only this term produces considerable levels of negative axial velocity in the vortex core.

(c) If the flame releases considerable heat upstream of the stagnation point of the recirculation zone, the volume expansion stabilizes the vortex flow and prevents CIVB.

(d) The high accuracy of the results indicates that the combustion model of Schmid is well suited for the computation of the reacting flow during CIVB driven flame flashback near the quenching limit.

(e) CIVB driven flame flashback in swirl burners is essentially a two-dimensional phenomenon, which can be well reproduced in two-dimensional URANS computations.

(f) The sudden occurrence of CIVB driven flame flashback is governed by the spatial distribution of the turbulent and chemical time scales in the core of the vortex flow.

These conclusions point out that any condition changes, which provide an upstream repositioning of the flame, can increase the danger of CIVB driven flame flashback. To verify this important implication the authors will carry out experiments as well as numerical calculations on a new burner geometry prone to CIVB flashback. This will confirm the geometry independence of the shown results and clearify the significance of the swirl form and level for burner stability [14].

Nomenclature

D = mixing tube diameter, m
$\mathbf{U}$ = velocity vector, m/s
U = radial velocity, m/s
V = tangential velocity, m/s
W = axial velocity, m/s
c = reaction progress
p = pressure, Pa
r = radial coordinate, m
t = time, s
w_{ind} = induced axial velocity, m/s
z = axial coordinate, m
Φ = equivalence ratio
ρ = density, $\mathrm{kg/m^3}$
η = azimuthal vorticity, 1/s
τ_c = chemical time scale, s
τ_t = turbulent time scale, s
$\boldsymbol{\omega}$ = vorticity vector, 1/s
ξ = radial vorticity, 1/s
ζ = axial vorticity, 1/s

References

[1] Fritz, J., Kröner, M., and Sattelmayer, T., 2004, "Flashback in a Swirl Burner With Cylindrical Premixing Zone," ASME J. Eng. Gas Turbines Power, **126**, pp. 276–283.
[2] Kröner, M., Fritz, J., and Sattelmayer, T., 2003, "Flashback Limits for Combustion Induced Vortex Breakdown in a Swirl Burner," ASME J. Eng. Gas Turbines Power, **125**, pp. 693–700.
[3] Kröner, M., Sattelmayer, T., Fritz, J., Kiesewetter, F., and Hirsch, C., 2006, "Flame Propagation in Swirling Flows-Effect of Local Extinction on the Combustion Induced Vortex Breakdown," Combust. Sci. Technol., **179**, pp. 1385–1416.
[4] Burmberger, S., Hirsch, C., and Sattelmayer, T., 2006, "Design Rules for the Velocity Field of Vortex Breakdown Swirl Burners," ASME Paper No. GT2006–90495.
[5] Kiesewetter, F., Hirsch, C., Fritz, J., Kröner, M., and Sattelmayer, T., 2003, "Two-Dimensional Flashback Simulation in Strongly Swirling Flows," ASME Paper No. GT2003–38395.
[6] Fritz, J., 2003, "Flammenrückschlag Durch Verbrennungsinduziertes Wirbelaufplatzen," dissertation, Lehrstuhl für Thermodynamik, TU-München, http://www.td.mw.tum.de/tum-td/de/forschung/dissertationen/download/G2003/fritz.pdf.
[7] Qian, L., 2001, "A Vorticity-Based Method for Incompressible Unsteady Viscous Flows," J. Comput. Phys., **172**, pp. 515–542.
[8] Darmofal, D. L., 1993, "The Role of Vorticity Dynamics in Vortex Breakdown," AIAA Paper No. 93–3036, 24th Fluid Dynamic Conference.
[9] Brown, G. L., and Lopez, J. M., 1990, "Axisymmetric Vortex Breakdown: Part 2 Physical Mechanisms," J. Fluid Mech., **221**, pp. 553–576.
[10] Hasegawa, T., Nishiki, S., and Michikami, S., 2001, "Mechanism of Flame Propagation Along a Vortex Tube," IUTAM Symposium on Geometry and Statistics of Turbulence, Kluwer Academic, pp. 235–240.
[11] Panton, R. L., 1996, *Incompressible Flow*, Wiley-Interscience, New York.
[12] Schmid, H. P., Habisreuther, P., and Leuckel, W., 1998, "A Model for Calculating Heat Release in Premixed Turbulent Flames," Combust. Flame, **113**, pp. 79–91.
[13] Borghi, R., 1984, "On the Structure of Turbulent Premixed Flames," C. Bruno and C. Casci, eds., *Recent Advances in Aeronautical Science*, Pergamon, London.
[14] Konle, M., Komarek, T., and Sattelmayer, T., 2007, "Conditioned PIV-PLIF-Measurements of CIVB Driven Flashback With 1 kHz Repetition Rate," *Proceedings of European Combustion Meeting* Chania, Greece, The Combustion Institute.

Ignition of Lean Methane-Based Fuel Blends at Gas Turbine Pressures

Eric L. Petersen[1]
e-mail: petersen@mail.ucf.edu

Joel M. Hall

Schuyler D. Smith

Jaap de Vries

Mechanical, Materials & Aerospace Engineering,
University of Central Florida,
P.O. Box 162450,
Orlando, FL 32816

Anthony R. Amadio

Mark W. Crofton

Space Materials Laboratory,
The Aerospace Corporation,
El Segundo, CA 90245

Shock-tube experiments and chemical kinetics modeling were performed to further understand the ignition and oxidation kinetics of lean methane-based fuel blends at gas turbine pressures. Such data are required because the likelihood of gas turbine engines operating on CH_4*-based fuel blends with significant* ($>10\%$) *amounts of hydrogen, ethane, and other hydrocarbons is very high. Ignition delay times were obtained behind reflected shock waves for fuel mixtures consisting of* CH_4, CH_4/H_2, CH_4/C_2H_6, *and* CH_4/C_3H_8 *in ratios ranging from 90/10% to 60/40%. Lean fuel/air equivalence ratios* ($\phi=0.5$) *were utilized, and the test pressures ranged from 0.54 to* 30.0 atm. *The test temperatures were from* 1090 K *to* 2001 K. *Significant reductions in ignition delay time were seen with the fuel blends relative to the* CH_4*-only mixtures at all conditions. However, the temperature dependence (i.e., activation energy) of the ignition times was little affected by the additives for the range of mixtures and temperatures of this study. In general, the activation energy of ignition for all mixtures except the* CH_4/C_3H_8 *one was smaller at temperatures below approximately*1300 K ($\sim$27 kcal/mol) *than at temperatures above this value* ($\sim$41 kcal/mol). *A methane/hydrocarbon–oxidation chemical kinetics mechanism developed in a recent study was able to reproduce the high-pressure, fuel-lean data for the fuel/air mixtures. The results herein extend the ignition delay time database for lean methane blends to higher pressures* (30 atm) *and lower temperatures* (1100 K) *than considered previously and represent a major step toward understanding the oxidation chemistry of such mixtures at gas turbine pressures. Extrapolation of the results to gas turbine premixer conditions at temperatures less than* 800 K *should be avoided however because the temperature dependence of the ignition time may change dramatically from that obtained herein.* [DOI: 10.1115/1.2720543]

Introduction

For several years now, natural gas has been widely used as a fuel for stationary power generation gas turbine engines [1]. Although composed primarily of methane, natural gases can contain from a few percent up to as much as 18% of other gases, depending on the international source [2]. These natural gas impurities are usually higher-order hydrocarbons such as ethane and propane. Composition variations in native and foreign natural gases can cause changes in the combustion chemistry, emissions formation, and stability, among other concerns [3–5].

However, in the near future, power generation gas turbines may be required to burn ever more exotic gaseous fuel blends in addition to indigenous natural gas. Typical fuel blends can include potentially high concentrations ($>10\%$) of hydrogen and even larger concentrations of hydrocarbons than what are common in natural gases. In addition to changes in the heating value of the fuel blends, significant changes in the ignition chemistry occur when gases such as H_2 and C_2H_6 are added to methane. According to previous studies, even a few percent of higher-order hydrocarbons can greatly accelerate the ignition process of a methane-based fuel [2]. Even larger changes in the combustion chemistry may then occur if the methane-based fuel were to contain significant levels of hydrogen or hydrocarbons. Such chemical effects can have dramatic impacts on existing gas turbine combustors designed to operate on natural gases typical of those found, for example, in the United States. These concerns are complicated by the fact that few data exist on the fundamental effects of fuel composition variation at the fuel/air mixture ratios, temperatures, and pressures of interest to the designers of power generation gas turbines.

Ignition delay time is a fundamental parameter often used to provide chemical time scale information for the improvement of chemical kinetics models. In a gas turbine application, the term "autoignition" refers to a problem specific to engines employing premixed combustion wherein the mixture might "autoignite" prior to reaching the main burner. The term "ignition" in the present paper refers to the more general kinetic definition and is therefore not limited to the relatively low temperatures seen in the premixer region of gas turbines ($<$800 K, typically). Ignition delay time measurements at relatively higher temperatures ($>$1100 K) are nonetheless useful for gas turbines because they are used for the improvement of chemical kinetics mechanisms that can be used for all regimes, and the kinetics at the higher temperatures of the main burner may be of importance to flame speed predictions, dynamics, and emissions predictions.

With these issues and concerns in mind, the authors are conducting a research program to study ignition delay times and related chemical kinetics over a wide range of fuel composition, mixture stoichiometry, temperature, and pressure. The present paper concentrates on fuel blends and conditions of most concern to the present generation of gas turbines, namely undiluted fuel-lean mixtures ($\phi=0.5$) at pressures up to 25 atm for fuel blends that contain mostly methane ($>60\%$). Gases blended with methane in the present study include hydrogen, ethane, and propane. Presented first is a background review of the existing literature on ignition-delay time measurements and the chemical kinetics of methane-based fuel blends, followed by details on the current

[1]Corresponding author.

Contributed by the International Gas Turbine Institute of ASME for publication in the JOURNAL OF ENGINEERING FOR GAS TURBINES AND POWER. Manuscript received July 17, 2006; final manuscript received January 2, 2007. Review conducted by Philip C. Malte. Paper presented at the ASME Turbo Expo 2005: Land, Sea, and Air (GT2005), Reno, NV, USA, June 6–9, 2005, Paper No. GT2005-68517.

shock-tube experiments. The results of the experiments for each additive are then summarized, and the methane-only results are compared to an improved methane oxidation chemical kinetics model designed for the higher-pressure, fuel-lean conditions of this study.

Background

As summarized by Spadaccini and Colket [2], methane ignition and oxidation have been the subjects of many shock-tube investigations. The strong interest in methane is because of its practical significance as a fuel and because methane's oxidation chemistry is important in the combustion of all other hydrocarbons. While the chemical kinetics of CH_4 ignition are considered well known at high temperatures (>1300 K) and pressures near or below 1 atm, the kinetics of CH_4 ignition at pressures greater than atmospheric, lower temperatures, and lower dilution levels are much less known. Some high-pressure shock-tube methane ignition data are available from the studies of Tsuboi and Wagner (3–300 atm) [6], Petersen et al. (1–480 atm) [7,8], and more recently by Zhukov et al. [9] and Huang et al. (16–40 atm) [10].

Petersen and co-workers [7] presented a correlation of methane ignition delay times over the wide range of pressures in their experiments

$$\tau_{ign} = 4.05 \times 10^{-15}[CH_4]^{0.33}[O_2]^{-1.05} \exp(51.8/RT) \quad (1)$$

where the ignition delay time (τ_{ign}) is in seconds; the activation energy (E) is 51.8 kcal/mol; R is the universal gas constant; T is the temperature in K; and the concentrations are given in mol/cm^3. The correlation in Eq. (1) is valid for T =1400–2050 K, ϕ=0.5–2.0, and concentrations up to $[CH_4]$ $=3.6\times10^{-5}$ mol/cm^3; $[O_2]=3.6\times10^{-5}$ mol/cm^3; and $[M]=3.6$ $\times10^{-3}$ mol/cm^3; the overall pressure dependence is $P^{-0.72}$.

Some shock-tube ignition data are available for methane mixed with other species, driven mainly by the importance of minor components in natural gas combustion. Cheng and Oppenheim [11] performed a study exploring combinations of H_2 and CH_4. They looked at a wide range of CH_4/H_2 blends and stoichiometry, with the % H_2 varying from 0% to 100%. For all cases, the argon dilution was 90% by volume, and the pressure ranged from 1 atm to 3 atm. Lifshitz et al. [12] looked at the effect of small levels of hydrogen addition on methane ignition. Krishnan et al. [13] conducted a study of CH_4 ignition when combined with the next smallest hydrocarbon fuel, acetylene. They tested mixtures ranging from 100% CH_4 to 100% C_2H_2 for equivalence ratios (ϕ) of 0.5, 1.0, and 2.0; with Ar dilutions near 90%; and pressures from 1 atm to 4 atm.

Because of the importance of ethane and other alkanes as trace species in natural gas, a few shock-tube studies have been performed to examine CH_4/alkane ignition [14–16]. Crossley et al. [14] tested small levels of C_2H_6, C_3H_8, C_4H_{10}, and C_5H_{12} additives to a base stoichiometric concentration of 3.5% CH_4 and 7% O_2 in Ar. Their reflected-shock pressures ranged from 6 atm to 10 atm. Similarly, Eubank et al. [15] and Zellner et al. [16] studied small additions of ethane, propane, and butane to stoichiometric methane oxidation, but for relatively dilute mixtures (96–99% Ar) at about 4 atm. Frenklach and Bornside [17] concentrated on additions of 0.19–1.9% propane to a mixture of 9.5% CH_4/19.0% O_2/Ar, and Higgin and Williams [18] examined the effect of n-butane on the lean ignition of CH_4–O_2–Ar mixtures. In addition to H_2, Lifshitz et al. [12] also looked at the effect of small levels of C_3H_8 on methane ignition.

Spadaccini and Colket in their comprehensive article [2] proposed a correlation of their own ignition delay time data for methane blends with small levels of hydrocarbons that generalizes all additives by one concentration term, [HC]

$$\tau_{ign} = 1.77 \times 10^{-14}[CH_4]^{0.66}[O_2]^{-1.05}[HC]^{-0.39} \exp(37.1/RT) \quad (2)$$

The hydrocarbons tested included ethane, propane, and n-butane. As expected, increasing hydrocarbon concentration leads to decreased τ_{ign}. The overall pressure dependence is $P^{-0.78}$, and the correlation is valid for temperatures between 1300 and 2000 K, pressures from 3 atm to 15 atm, and ϕ=0.43–1.25.

Nonshock-tube studies of methane ignition in mixtures with H_2 and other hydrocarbons have also been performed. For example, Griffiths et al. [19] measured autoignition temperatures of CH_4/C_2H_6 and CH_4/n-C_4H_{10} mixtures in a spherical reaction vessel at atmospheric pressures, and Naber et al. [20] studied autoignition for various natural gas blends in a constant-volume reaction vessel. Methane-based mixture variations were explored in more practical settings by Jones and Leng [21] in a natural gas-fired pulsed combustor and by Flores et al. [4,5] in a model gas turbine combustor.

All of these studies demonstrated the accelerating effects of hydrogen and higher-order hydrocarbons on methane ignition. However, the focus of most of them was on stoichiometric methane oxidation; they were highly diluted; they were at pressures less than 10 atm; and, relatively small levels of additive were tested in most cases, corresponding to the levels seen in common natural gas blends. Nonetheless, no shock-tube data are available that cover simultaneously the pressures, stoichiometry, and wide ranges of additive/methane ratio of interest to the present study.

Many studies have also been performed on the chemical kinetics modeling of methane ignition and oxidation, but the key reactions and overall mechanisms have been validated mostly at higher temperatures and lower pressures. A good example of the state-of-the-art in CH_4 oxidation modeling is the latest mechanism from the Gas Research Institute (GRI), GRI-Mech 3.0 [22]. Some methane oxidation models have been applied to available high-pressure CH_4 ignition data, including those of Li and Williams [23], Petersen et al. [24], and Huang et al. [10]. The latter two are based on the core GRI mechanism.

Modeling the addition of higher-order hydrocarbons to methane combustion requires the addition of reactions that have been validated for the kinetics of the particular hydrocarbon(s). The first attempt to model the ignition chemistry of methane/ethane mixtures was the landmark study by Westbrook [25]. His model was validated against the entire range of available ignition data from pure methane to pure ethane. Westbrook and Pitz [26] later considered the effects of propane addition using an improved model. A reduced kinetics mechanism based on the ignition of CH_4/C_2H_6 blends was developed by Gardiner et al. [27], and modeling to support constant-volume autoignition experiments was performed by Griffiths et al. [19] and Naber et al. [20]. More recently, Khalil and Karim [28] assembled a kinetics model to look at the effects of natural gas variation on ignition in diesel engines.

Many models for higher-order hydrocarbons exist in the literature, and all of these models have subsets for methane oxidation. However, not all such models were tested against the conditions and mixtures of interest herein, so applying them to situations outside of where they were optimized should be done with caution. The approach herein was to utilize a mechanism from a recent study and apply it to the experimental data to help elucidate further insight and to determine the validity of the model for the ignition delay times.

Experiment

A helium-driven shock tube with a 16.2-cm-diameter, 10.7-m-long driven section was employed in the ignition experiments. The shock-tube facility and techniques used to measure ignition delay times are discussed in more detail elsewhere [29,30] and will be briefly reviewed here. All experiments were performed behind reflected shock waves, and ignition times were monitored from an endwall location. The delay times were inferred from a

Table 1 Mixtures and compositions used in the present study

Mixture	Blend	X_{CH4}	X_{H2}	X_{C2H6}	X_{C3H8}	X_{O2}	X_{N2}
1	100% CH_4	0.0525	—	—	—	0.2098	0.7377
2	100% CH_4	0.0500	—	—	—	0.2000	0.7500
3	80/20% CH_4/H_2	0.0466	0.0117	—	—	0.1978	0.7439
4	60/40% CH_4/H_2	0.0420	0.0280	—	—	0.1950	0.7350
5	90/10% CH_4/C_2H_6	0.0419	—	0.0047	—	0.2003	0.7531
6	70/30% CH_4/C_2H_6	0.0288	—	0.0123	—	0.2015	0.7574
7	80/20% CH_4/C_3H_8	0.0311	—	—	0.0077	0.2020	0.7592

PCB 134A pressure transducer and a photomultiplier tube (Hamamatsu 1P21) detector monitoring CH^* chemiluminescence through a 430 mm±5 nm bandpass filter. Pressure and CH^* emission were also measured from a sidewall window port, but since the sidewall measurements for the undiluted fuel/air mixtures herein are prone to gas dynamic effects, the sidewall data were not used to determine τ_{ign} [8]. A combination of lexan and Al diaphragms was employed to achieve reflected-shock pressures from 0.5 atm to 30 atm. Ultimate pressures before each experiment were approximately 1×10^{-5} Torr. As shown in Petersen et al. [30], the uncertainty in the test temperature when the temperature is obtained by measuring the speed of incident wave in the authors' facility is less than 15 K for the conditions herein.

Seven different mixtures were studied. Each of the mixtures was at a fuel-lean, fuel-to-air equivalence ratio of or near 0.5, and three different gaseous species were mixed individually with the methane/air mixtures: hydrogen, ethane, and propane. Table 1 summarizes the mixture compositions. Two levels of additive for each CH_4/additive blend were chosen to cover a general range of conditions rather than to target certain mixtures expected in the field. The equivalence ratios were based on the total carbon and hydrogen content of the fuel blends rather than just on the base methane since the non-CH_4 species percentage was in all cases 10% or more of the blend. The gas purities were as follows: ultrahigh purity O_2 (99.9995%), ultrahigh purity nitrogen (99.9995%), research grade CH_4, H_2, and C_2H_6, and 99.98% C_3H_8. Uncertainties in the mixture compositions listed in Table 1 are less than 1% of each minor constituent and less than 0.2% for the nitrogen.

Figure 1 provides typical CH^* emission and pressure time histories for two different pressure extremes: Fig. 1(*a*) presents data from a lower-pressure test with a reflected-shock pressure of 0.92 atm, and Fig. 1(*b*) presents data from a higher-pressure test with a pressure of 23.8 atm. For both pressure extremes, ignition is marked by the rapid increase in the CH^* signal. Since CH^* chemiluminescence has been shown to be a good marker of ignition in shock-tube studies of hydrocarbon oxidation [31], τ_{ign} is defined herein as the sudden rise in CH^*, as shown in Figs. 1(*a*) and 1(*b*). Provided in Table 2 is a summary of all ignition data from this study. The maximum uncertainty in τ_{ign} is 10% of the stated values. Because the CH^* formation and corresponding pressure rise are nearly step functions at the time of ignition for the undiluted mixtures herein, endwall emission and endwall pressure measurement yield identical results for ignition delay time, as seen in Fig. 1(*b*). Any integration of the light signal from the endwall port due to reaction at different locations in the tube does not affect the determination of ignition for such exothermic mixtures. The following four sections present and discuss the data, grouped by additive species.

Methane Mixtures

Methane-only fuels at two different $CH_4/O_2/N_2$ ratios, both with fuel-lean equivalence ratios near 0.5, were studied at pressures between 0.54 atm and 23.8 atm and temperatures from 1243 K to 2001 K. These experiments were conducted to compare the current experimental techniques and results with established high-temperature methane ignition studies and to provide additional methane oxidation data at higher pressures and intermediate temperatures.

Figure 2 presents the lower-pressure data corresponding to Mixture 1. These data are compared to the master correlation of Petersen et al. [7] presented above as Eq. (1). The agreement between the present data and the overall methane ignition correlation covering a wide range of ϕ and concentration is quite good. The Mixture 1 data in Fig. 1 follow an activation energy trend of 41.5 kcal/mol. Table 3 summarizes the activation energies for each mixture and for each temperature and pressure range as appropriate.

The data in Fig. 2 span a pressure range of 0.54–0.92 atm but are plotted as a line of constant pressure at the average pressure of 0.72 atm. Each τ_{ign} data point that is not at this average pressure is plotted with a pressure adjustment to the average pressure using a $P^{-0.75}$ dependence. The same pressure dependence was used to plot all the data in this study; the actual pressures for each data point are listed in Table 2. This pressure dependence is based on

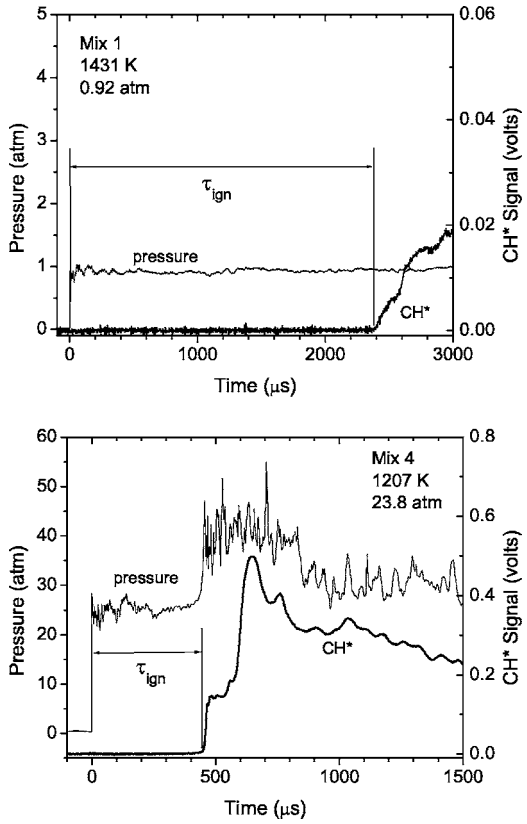

Fig. 1 Sample endwall pressure and CH^* chemiluminescence traces and definition of ignition delay time: (*a*) lower pressure experiment; and (*b*) higher pressure experiment

Table 2 Ignition delay time data and experimental conditions

Mixture	T (K)	P (atm)	τ_{ign} (μs)
1	1431	0.92	2369
	1451	0.80	1951
100% CH_4	1526	0.74	978
	1611	0.79	430
	1673	0.73	284
	1854	0.55	106
	2001	0.54	56
	1452	8.41	385
2	1290	10.3	1815
	1312	10.8	1116
100% CH_4	1361	10.8	818
	1399	10.4	548
	1407	10.6	569
	1477	11.6	268
	1535	10.9	145
	1548	10.5	135
	1625	11.1	69
	1243	22.5	1318
	1283	23.8	937
	1289	22.4	814
	1367	20.8	525
	1416	20.0	271
	1442	20.5	243
	1460	19.8	215
	1490	18.0	146
	1533	19.0	101
	1537	18.6	112
	1606	16.7	64
	1659	16.5	43
3	1141	25.1	1827
	1251	23.8	684
80/20% CH_4/H_2	1305	21.7	416
	1355	21.3	242
	1383	20.2	185
	1440	19.9	113
	1459	19.0	96
	1553	18.2	35
4	1132	25.0	1094
	1170	25.3	582
60/40% CH_4/H_2	1201	25.0	437
	1207	23.8	452
	1228	23.7	378
	1316	22.7	173
	1345	21.6	80
	1353	30.0	77
	1392	20.5	69
	1409	20.6	53
5	1155	24.9	1446
	1181	25.2	1127
90/10% CH_4/C_2H_6	1232	24.7	717
	1281	23.3	588
	1296	22.4	422
	1330	21.7	276
	1379	21.0	166
	1399	21.5	142
	1429	20.0	113
	1532	19.4	40
6	1091	24.5	1164
	1187	25.6	493
70/30% CH_4/C_2H_6	1195	22.8	378
	1244	24.1	245
	1267	22.0	197
	1327	21.5	130
	1359	19.9	87
	1402	18.5	53
	1437	18.8	35
7	1189	11.1	1323
	1222	11.3	941
80/20% CH_4/C_3H_8	1353	11.1	183
	1447	13.8	54
	1497	13.2	34
	1531	12.8	25
	1615	11.8	12

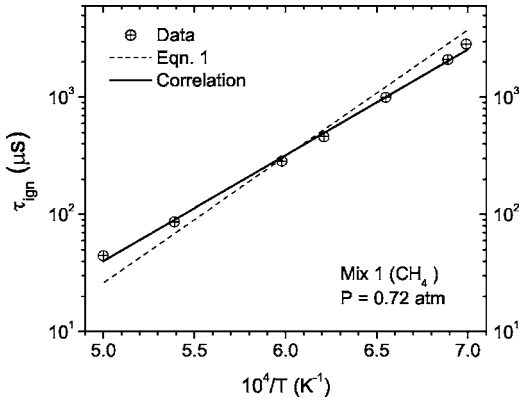

Fig. 2 Ignition delay times for methane-only Mixture 1 at lower pressure. Comparison is with the correlation of Petersen et al. [7] (Eq. (1)) and correlation of current data.

the average between the master correlation presented in Eq. (1) (−0.72) and the methane/HC correlation in Eq. (2) (−0.78).

Similar agreement is seen in Fig. 3 between the current Mixture 2 data at elevated pressures and the overall correlation of Eq. (1). Note however that Eq. (1) is only valid for temperatures greater than 1400 K, so it is only plotted over that temperature range. At lower temperatures, the slopes of the ignition delay time curves at constant pressure get smaller due to the shift in kinetics that occurs at lower temperatures and higher pressures. In the 19.4-atm data, the activation energy at lower temperatures is 26.2 kcal/mol, in contrast to the value of 40.1 kcal/mol for the higher-temperature data.

Petersen et al. [8,24] observed comparable activation energies at intermediate temperatures for a fuel-lean (ϕ=0.4) mixture at pressures from 44 atm to 161 atm. Their average value was 27.8 kcal/mol. The similarity between the activation energies at the higher temperatures over a wide range of pressures (i.e., about 41 kcal/mol, Table 3) and between the E values at the lower temperatures over a similar range of pressures (i.e., about 27 kcal/mol) indicates that the kinetics in the two temperature regions are fairly independent of pressure (although the temperature at which transition between the two regions tends to occur appears to be pressure dependent [24]). Of course, the transition in activation energy is slightly more gradual than that implied in Fig. 2 (and in other figures herein) but is shown in that fashion for presentation purposes to emphasize the shift in kinetics. Provided in the "Kinetics Modeling" section are further details on the chemical kinetics in the different temperature and pressure regions.

Table 3 Ignition activation energies for each set of data

Mixture	Blend	T (K)	P_{avg} (atm)	E (kcal/mol)
1	100% CH_4	1431–2001	0.7	41.5
2	100% CH_4	1407–1625	10.8	44.4
2	100% CH_4	1290–1407	10.8	36.1
2	100% CH_4	1367–1659	19.9	40.1
2	100% CH_4	1243–1367	19.9	26.2
3	80/20% CH_4H_2	1141–1553	21.1	41.4
4	60/40% CH_4H_2	1316–1409	23.3	45.1
4	60/40% CH_4H_2	1132–1228	23.3	31.1
5	90/10% $CH_4C_2H_6$	1296–1532	22.4	42.1
5	90/10% $CH_4C_2H_6$	1155–1296	22.4	25.4
6	70/30% $CH_4C_2H_6$	1267–1437	22.0	40.2
6	70/30% $CH_4C_2H_6$	1091–1267	22.0	28.9
7	80/20% $CH_4C_3H_8$	1189–1615	12.2	41.9

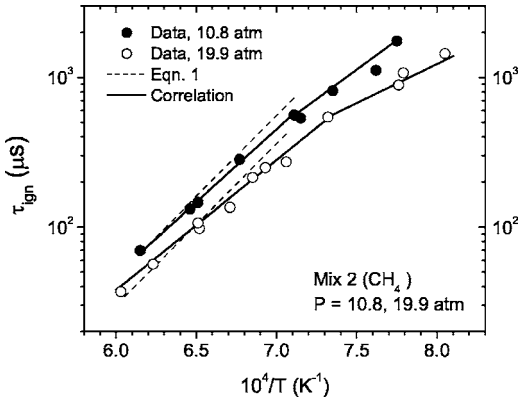

Fig. 3 Results for CH_4-only Mixture 2 at two different average pressures: 10.8 atm and 19.9 atm. Comparison is with correlation of Petersen et al. [7] (Eq. (1)) and correlation of current data.

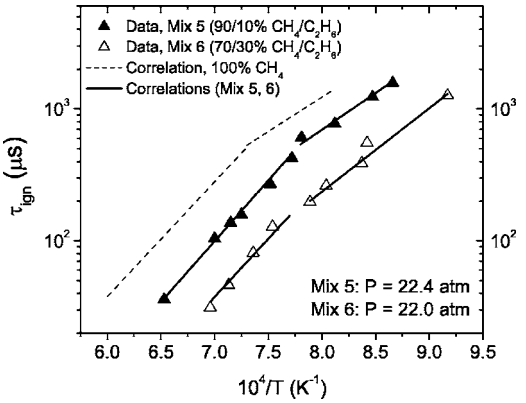

Fig. 5 Ignition delay times for the methane/ethane blends in comparison to the methane-only data at similar pressures

Methane–Hydrogen Mixtures

Two CH_4/H_2 blends were studied, with ratios of 80/20 and 60/40 (Table 1). Both mixtures had fuel/air equivalence ratios of 0.5. The shock-tube data cover a range of pressures near 21 atm (i.e., 18.2–25.1 atm) and temperatures from 1141 K to 1553 K. These data are shown in Fig. 4 in a plot of τ_{ign} versus $1/T$. Also shown in Fig. 4 are the results from the methane-only experiments for a similar pressure range, shown in the form of correlation lines (Mixture 2, 19.4 atm).

Two observations are most notable in the hydrogen blends. The first observation is that the addition of H_2 reduced the ignition delay time significantly when compared to the methane-only fuel. For example, the 20% H_2 addition decreased reaction times by a factor of 3, and the 40% addition by nearly a factor of 10. This is not unexpected, however, and the effect increases with increasing level of H_2 in the fuel blend [11]. The second observation is that the hydrogen addition did not seem to shift the dominant kinetic regimes for the range of mixtures studied thus far; that is, the activation energies of the ignition delay time curves in Fig. 4 differ very little from the CH_4-only mixture over comparable temperature ranges (Table 3). The E value at higher temperatures for Mixture 3 is 41.4 kcal/mol as compared to ≈41 kcal/mol for Mixtures 1 and 2. Similarly, at lower temperatures, Mixture 4 has a 31.1-kcal/mol activation energy as compared to similar values for Mixture 2 (26.2 kcal/mol) and from the literature (27.8 kcal/mol) [8].

Methane–Ethane Mixtures

Figure 5 summarizes the ignition delay time results for the ethane blends. Two fuel-lean (ϕ=0.5) mixtures were studied, one with a CH_4/C_2H_6 ratio of 90/10 and one with a ratio of 70/30 (Table 1). A temperature range from 1091 K to 1532 K and pressures from 18.5 to 25.6 were tested behind reflected shock waves. Similar results were observed for the ethane mixtures as were seen in the hydrogen blends: the addition of C_2H_6 decreased ignition times but with similar activation energies as the CH_4-only mixtures. As seen in Fig. 5, a 10% addition of ethane decreased τ_{ign} by a factor of three, and a 30% addition decreased it by a factor of ten over the range of conditions in this work. At higher temperatures, the activation energy slopes were 42.1 kcal/mol and 40.2 kcal/mol for Mixtures 5 and 6, respectively (Table 3). At lower temperatures, the activation energies were found to be 25.4 kcal/mol and 28.9 kcal/mol, respectively.

Methane–Propane Mixtures

One methane fuel blend containing 20% propane (Mixture 7, Table 1) was studied at an average pressure of 12.2 atm (Table 2). Ignition delay times were measured at reflected-shock temperatures ranging from 1189 K to 1615 K. An Arrhenius plot of the resulting ignition times is contained in Fig. 6. When compared to the methane-only results at a similar pressure (10.8 atm), the propane addition again speeds up the ignition process but with the same temperature dependence.

The ignition activation energy of the Mixture 7 data is 41.9 kcal/mol, and the addition of 20% C_3H_8 resulted in a six

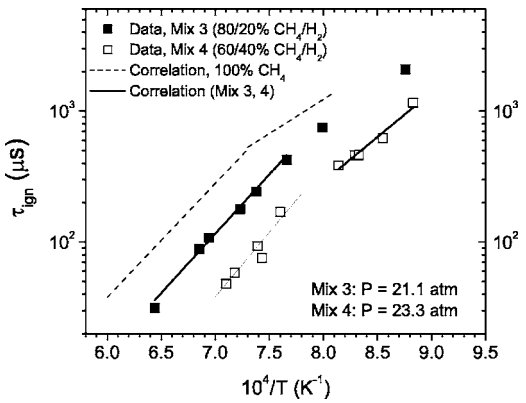

Fig. 4 Ignition delay times for the methane/hydrogen blends in comparison to the methane-only data at similar pressures

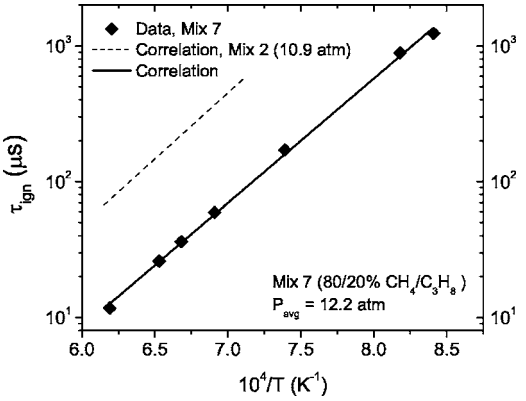

Fig. 6 Measured ignition delay times for the methane/propane blend in comparison to the methane-only data at similar pressures

times reduction in τ_{ign} at 12.2 atm over the range of temperatures studied. Interestingly, no shift in temperature dependence was observed for Mixture 7 at the pressures studied, even for temperatures below 1200 K. The differences in hydrocarbon content and their effects on the chemical kinetics of methane blend ignition can be further elucidated by the use of comprehensive chemical kinetics modeling. The groundwork for such kinetics modeling for the conditions of this study is presented in the following section.

Kinetics Modeling

While the data presented in this study constitute a fundamental basis for understanding the high-pressure ignition of CH_4/Air mixtures at intermediate-to-high temperatures, extension of these results to various working conditions would be impractical, or even impossible, were new experiments necessary for every new application. To aid in the extrapolation of these data, and in the understanding of the detailed combustion chemistry, a kinetics mechanism that suitably predicts the ignition delay times of the methane–air mixtures at the conditions of interest is needed. Curran and co-workers have recently developed just such a model as presented in detail by Petersen et al. [32].

The comprehensive kinetics mechanism contains 663 reversible reactions and 116 species and has been shown to accurately reproduce shock-tube ignition data at elevated pressures for methane/hydrocarbon mixtures (in fact, the mechanism is based in part on the data presented herein when they were originally presented in the conference version of this paper). Ignition delay times were determined from the mechanism using CHEMKIN [33] and the same definition of ignition described above for the experimental pressure traces, assuming a constant-volume combustion process. For the gas turbine operating conditions considered herein, i.e., fuel-lean and 20–30 atm, a large portion of the methyl oxidation occurs through methoxy and methyl–peroxy channels as follows.

$$CH_3 + O_2 \leftrightarrows CH_3O_2$$

$$CH_3O + CH_3 \leftrightarrows CH_4 + CH_2O$$

$$CH_3O_2 + CH_3 \leftrightarrows CH_3O + CH_3O$$

$$CH_3O_2 + HO_2 \leftrightarrows CH_3O_2H + O_2$$

Other important reactions for the conditions and mixtures herein include the ignition promoting reaction at lower temperatures

$$OH + OH(+M) \leftrightarrows H_2O_2(+M)$$

and the ignition-suppressing reactions

$$CH_3 + CH_3(+M) \leftrightarrows C_2H_6(+M)$$

$$H + O_2 + N_2 \leftrightarrows HO_2 + N_2$$

Figure 7 shows the relative significance of the most influential reactions at the conditions studied in terms of ignition-time sensitivities for the methane-only mixture 2 at a pressure of 20 atm and two representative temperatures, 1290 K and 1490 K. The sensitivity of τ_{ign} to each rate coefficient was defined as $S=-\partial\tau/\partial k_i$ so that a positive sensitivity indicates a faster ignition (lower τ_{ign}) with increasing k_i. Reactions shown are those with the largest sensitivity coefficients and from certain third-body pressure-dependent reactions included in the mechanism [32]. As shown, the sensitivity of τ_{ign} to the methyl recombination reaction rivals or even exceeds its sensitivity to the classic chain branching reaction

$$H + O_2 \leftrightarrows OH + O$$

Although this reaction was found by Petersen et al. [24] to be less significant in fuel-rich methane mixtures at elevated pressures, the excess oxygen available in the present experiments consumes a large portion of the H atoms available in the radical pool and is a primary ignition promoter.

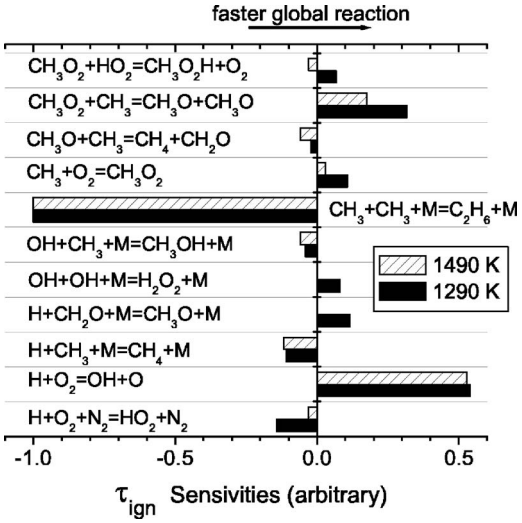

Fig. 7 Ignition–time sensitivity spectra for two target conditions. Reactions shown are those with the largest sensitivity coefficients of the current model [32]: for Mixture 2 (CH_4/Air, ϕ=0.5). Sensitivity to the H+O_2 chain branching step is shown for comparison.

As seen in Fig. 8(*a*), the model agrees quite well with the methane-only ignition data from Mixture 2. Also shown for com-

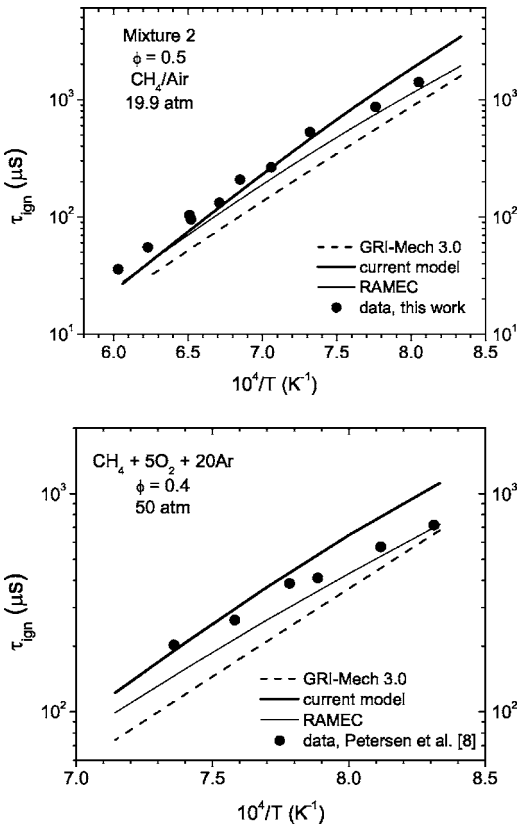

Fig. 8 Numerical simulations for fuel-lean, pure-CH_4/air mixtures at elevated pressure. Models include GRI-Mech 3.0 [22], RAMEC [24], and that adopted by the current study [32]: (*a*) Mixture 2, CH_4/Air, ϕ=0.5, 19.9 atm; and (*b*) Mixture 1 from Petersen et al. [8], CH_4/O_2/Ar, ϕ=0.4, 50 atm.

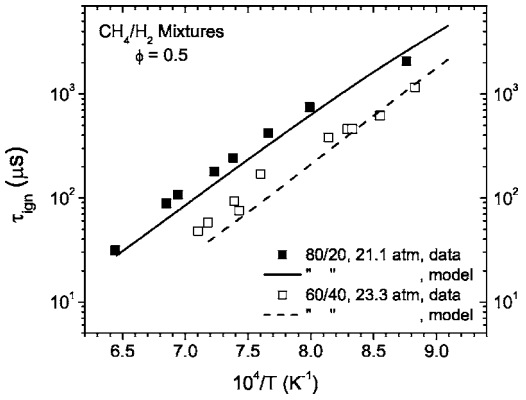

Fig. 9 Comparison between model [32] and experiment for mixtures of methane and hydrogen in air (Mixtures 3 and 4)

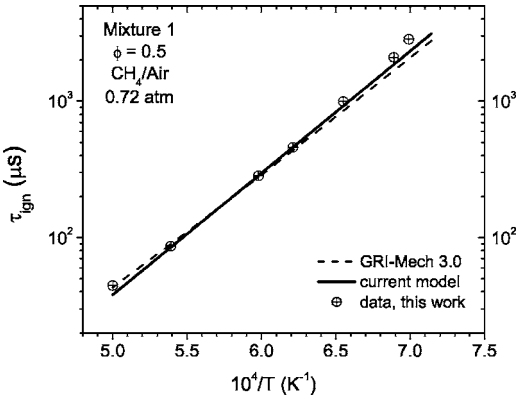

Fig. 11 Model and experiment at low-pressure, high-temperature conditions. As expected, both the model adopted herein [32] and GRI-Mech 3.0 agree favorably with the data and each other at conditions where the latter model was formulated.

parison are the predictions of GRI-Mech 3.0 and RAMEC [24] for the same data. As expected, GRI-Mech 3.0 does not capture the higher-pressure ignition trends since it was designed using mostly lower-pressure data. At the even higher-pressure, fuel-lean conditions of Petersen et al. [8], i.e., 50 atm, the current model performs favorably, as shown in Fig. 8(*b*).

Presented in Figs. 9 and 10 are the results of the model when applied to the ignition conditions of the CH_4/H_2 and CH_4/C_2H_6 blends, respectively. For both the hydrogen and ethane additives, the model predicts well the reduction in ignition delay time with the volumetric percentage of each additive. Note that the model also produces similar ignition delay time slopes between the two levels of additive, as observed in the data for the conditions herein but underestimates the ignition delay time slightly, particularly at the higher temperatures. Finally, Fig. 11 shows that the model also performs well in the region where GRI-Mech 3.0 is known to work best, that is lower pressures and higher temperatures. Both the current model and GRI-Mech 3.0 perform similarly when compared to the 0.72-atm CH_4-only data for Mixture 1.

Discussion

When comparing the ignition delay time results from the various mixtures, the ability of the nonmethane species to accelerate the ignition process increases not only with increasing levels of a particular species, but also with increasing levels of hydrocarbons in general. For example, there was a factor-of-three decrease in τ_{ign} for a 20% H_2 addition (Fig. 4), but a similar decrease was seen with only a 10% C_2H_6 addition (Fig. 5) at pressures near 20 atm. A 20% propane addition led to a factor-of-six decrease in τ_{ign} at a pressure near 10 atm (Fig. 6). Other investigators observed similar trends with modest additive levels (<10% additive)

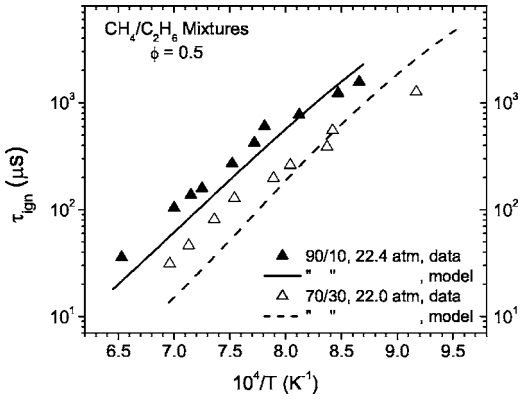

Fig. 10 Comparison between model [32] and experiment for mixtures of methane and ethane in air (Mixtures 5 and 6)

[2,14–16]. One would expect that in the limit of a methane/ethane (or other additive) blend, for example, the extreme values for ignition time would be situated between the pure CH_4 and the pure C_2H_6 (or other HC) cases. The effects would be further complicated if several hydrocarbon species were present simultaneously.

Although the experiments covered significant levels of additives in the methane-based fuel blends, the activation energy trends observed in Figs. 4–6 indicate that the radical production channels of all the mixtures are most likely still dominated by the methane chemistry. The acceleration of the CH_4 ignition process with small-to-moderate levels of additional fuel species points to the fact that the other fuels are merely supplying extra radicals to the preignition radical pool; the dominant radicals and their formation pathways are otherwise the same as for pure methane oxidation. Upon addition of even greater volumetric percentages of non-CH_4 fuels, the chemistry at some point would shift to that of the other fuel. For example, the higher-temperature activation energy of ethane ignition is lower than that of methane, i.e., 28 kcal/mol for C_2H_6 [34] versus 41 kcal/mol for CH_4 (Table 3) at $\phi=0.5$, so a reduction in E for fuel-blend ignition would be expected with levels of C_2H_6 greater than those studied herein. Elucidation of such effects is important to understanding the ignition chemistry of fuel blends and requires further study.

Deeper insight into each of these issues can be gained from the chemical kinetics modeling. Covering the range from 100% CH_4 to 100% other hydrocarbon(s) requires kinetics data and corresponding reaction mechanisms and submechanisms for methane as well as for each of the other hydrocarbons. The present paper shows that the model of Curran et al. [32] performs well for the mixtures and conditions herein and can form a useful start for more detailed analysis of the effects of higher-order hydrocarbons and hydrogen on the ignition of methane-based fuels. Problems such as autoignition in premixed systems require accurate data and kinetics mechanisms for temperatures as low as 700 K at gas turbine pressures [1]. It should be noted that the ignition data and kinetics modeling trends presented above should not be extrapolated to the much lower temperatures of interest to the specific problem of "autoignition" in premixed systems (<800 K). The temperature dependence of the ignition delay time at temperatures less than about 1100 K is expected to change dramatically relative to what it is for the intermediate temperatures of this study, leading to overprediction of the ignition time at compressor discharge temperatures.

The experiments and modeling extend the database of methane-based oxidation beyond previous studies, which focused primarily on either methane-only mixtures or on lower-pressure natural gas

mixtures with relatively small levels of other hydrocarbons. The present study focused on higher-pressure, fuel-lean mixtures with additive levels as high as 40% of the fuel blend. However, a thorough study of the ignition behavior and the development of appropriate chemical kinetics mechanisms for every possible combination of CH_4 with H_2, C_2H_6, C_3H_8, and other hydrocarbons requires an even broader range of mixtures and conditions. Ignition experiments covering the range of 100% methane to 100% additive, stoichiometry from fuel lean to fuel rich, combinations of multiple additives, pressures from subatmospheric to 30+ atm, and temperatures below 1100 K are required. To cover such a broad array of parameters, an optimization approach has been developed by the authors [35–37]. The resulting matrices of mixtures and conditions build upon the experimental database and theoretical foundation developed herein.

Conclusions

Over 50 experiments on the ignition of methane-based fuel blends at gas turbine conditions were conducted behind reflected shock waves. Seven different fuel-lean fuel/air mixtures were investigated: two CH_4-only blends, two CH_4/H_2 blends (80/20 and 60/40), two CH_4/C_2H_6 blends (90/10 and 70/30), and one CH_4/C_3H_8 blend (80/20). Ignition was deduced from endwall pressure measurements and CH^* chemiluminescence measurements taken from an optical port located in the shock-tube endwall. The temperatures in the experiments ranged from 1090 K to 2001 K, and pressures from 0.54 atm up to 25.3 atm were covered, with emphasis on pressures in the 19–25 atm range.

Each of the mixtures produced ignition delay time data with activation energies that were well correlated. In general, the ignition delay times decreased with increasing volumetric percentage of additive and carbon–atom content, but no significant changes in the activation energies were observed when compared to the methane-only results. A chemical kinetics model presented in a separate study was compared to the data and was seen to capture the ignition trends of the data both in absolute magnitude and in the effect of increasing levels of hydrogen and hydrocarbons.

Acknowledgment

This work was supported primarily by a University Turbine Systems Research grant from the South Carolina Institute of Energy Studies, Contract No. 04-01-SR114, with Dr. Richard Wenglartz as program monitor. Partial support also came from The Aerospace Corporation. The authors gratefully acknowledge the assistance of Carrol Gardner (Aerospace) in performing some of the experiments and Matthew Drake (UCF) for his help in the background literature search.

References

[1] Lefebvre, A. H., 1999, *Gas Turbine Combustion*, 2nd ed., Taylor & Francis, Philadelphia, PA.
[2] Spadaccini, L. J., and Colket, M. B., III, 1994, "Ignition Delay Characteristics of Methane Fuels," Prog. Energy Combust. Sci., **20**, pp. 431–460.
[3] Naber, J. D., Siebers, D. L., Di Julio, S. S., and Westbrook, C. K., 1994, "Effects of Natural Gas Composition on Ignition Delay Under Diesel Conditions," Combust. Flame, **99**, pp. 192–200.
[4] Flores, R. M., Miyasato, M. M., McDonell, V. G., and Samuelsen, G. S., 2001, "Response of a Model Gas Turbine Combustor to Variation in Gaseous Fuel Composition," J. Eng. Gas Turbines Power, **123**, pp. 824–831.
[5] Flores, R. M., McDonell, V. G., and Samuelsen, G. S., 2003, "Impact of Ethane and Propane Variation in Natural Gas on Performance of a Model Gas Turbine Combustor," J. Eng. Gas Turbines Power, **125**, pp. 701–708.
[6] Tsuboi, T., and Wagner, H. Gg., 1974, "Homogeneous Thermal Oxidation of Methane in Reflected Shock Waves," Proc. Combust. Inst., **15**, pp. 883–890.
[7] Petersen, E. L., Röhrig, M., Davidson, D. F., Hanson, R. K., and Bowman, C. T., 1996, "High-Pressure Methane Oxidation Behind Reflected Shock Waves," Proc. Combust. Inst., **26**, pp. 799–806.
[8] Petersen, E. L., Davidson, D. F., and Hanson, R. K., 1999, "Ignition Delay Times of Ram Accelerator CH_4/O_2/Diluent Mixtures," J. Propul. Power, **15**, pp. 82–91.
[9] Zhukov, V. P., Sechenov, V. A., and Starikovskii, A. Yu., 2003, "Spontaneous Ignition of Methane-Air Mixtures in a Wide Range of Pressures," Combust., Explos. Shock Waves, **30**, pp. 487–495.
[10] Huang, J., Hill, P. G., Bushe, W. K., and Munshi, S. R., 2004, "Shock-Tube Study of Methane Ignition Under Engine-Relevant Conditions: Experiments and Modeling," Combust. Flame, **136**, pp. 25–42.
[11] Cheng, R. K., and Oppenheim, A. K., 1984, "Autoignition in Methane-Hydrogen Mixtures," Combust. Flame, **58**, pp. 125–139.
[12] Lifshitz, A., Scheller, K., Burcat, A., and Skinner, G. B., 1971, "Shock-Tube Investigation of Ignition in Methane-Oxygen-Argon Mixtures," Combust. Flame, **16**, pp. 311–321.
[13] Krishnan, K. S., Ravikumar, R., and Bhaskaran, K. A., 1983, "Experimental and Analytical Studies on the Ignition of Methane-Acetylene Mixtures," Combust. Flame, **49**, pp. 41–50.
[14] Crossley, R. W., Dorko, E. A., Scheller, K., and Burcat, A., 1972, "The Effect of Higher Alkanes on the Ignition of Methane-Oxygen-Argon Mixtures in Shock Waves," Combust. Flame, **19**, pp. 373–378.
[15] Eubank, C. S., Rabinowitz, M. J., Gardiner, W. C. Jr., and Zellner, R. E., 1981, "Shock-Initiated Ignition of Natural Gas-Air Mixtures," Proc. Combust. Inst., **18**, pp. 1767–1774.
[16] Zellner, R., Niemitz, K. J., Warnatz, J., Gardiner, W. C., Jr., Eubank, C. S., and Simmie, J. M., 1983, "Hydrocarbon Induced Acceleration of Methane-Air Ignition," Prog. Aeronaut. Astronaut., **88**, pp. 252–272.
[17] Frenklach, M., and Bornside, D. E., 1984, "Shock-Initiated Ignition in Methane-Propane Mixtures," Combust. Flame, **56**, pp. 1–27.
[18] Higgin, R. M. R., and Williams, A., 1969, "A Shock-Tube Investigation of the Ignition of Lean Methane and n-Butane Mixtures With Oxygen," Proc. Combust. Inst., **12**, pp. 579–590.
[19] Griffiths, J. F., Coppersthwaite, D., Phillips, C. H., Westbrook, C. K., and Pitz, W. J., 1990, "Auto-Ignition Temperatures of Binary Mixtures of Alkanes in a Closed Vessel: Comparisons Between Experimental Measurements and Numerical Predictions," Proc. Combust. Inst., **23**, pp. 1745–1752.
[20] Naber, J. D., Siebers, D. L., Di Julio, S. S., and Westbrook, C. K., 1994, "Effects of Natural Gas Composition on Ignition Delay Under Diesel Conditions," Combust. Flame, **99**, pp. 192–200.
[21] Jones, H. R. N., and Leng, J., 1994, "The Effect of Hydrogen and Propane Addition on the Oxidation of a Natural Gas-Fired Pulsed Combustor," Combust. Flame, **99**, pp. 404–412.
[22] Smith, G. P., Golden, D. M., Frenklach, M., Moriarty, N. W., Eiteneer, B., Goldenberg, M., Bowman, C. T., Hanson, R. K., Song, S., Gardiner, W. C., Lissianski, V. V., and Qin, Z., GRI-Mech 3.0, http://www.me.berkeley.edu/gri-mech/
[23] Li, S. C., and Williams, F. A., 2002, "Reaction Mechanisms for Methane Ignition," J. Eng. Gas Turbines Power, **124**, pp. 471–480.
[24] Petersen, E. L., Davidson, D. F., and Hanson, R. K., 1999, "Kinetics Modeling of Shock-Induced Ignition in Low-Dilution CH_4/O_2 Mixtures at High Pressures and Intermediate Temperatures," Combust. Flame, **117**, pp. 272–290.
[25] Westbrook, C. K., 1979, "An Analytical Study of the Shock Tube Ignition of Mixtures of Methane and Ethane," Combust. Sci. Technol., **20**, pp. 5–17.
[26] Westbrook, C. K., and Pitz, W. J., 1983, "Effects of Propane on Ignition of Methane-Ethane-Air Mixtures," Combust. Sci. Technol., **33**, pp. 315–319.
[27] Gardiner, W. C. Jr., Lissianski, V. V., and Zamanski, V. M., 1995, "Reduced Chemical Reaction Mechanism of Shock-Initiated Ignition of Methane and Ethane Mixtures With Oxygen," *Shock Waves at Marseille II, Proceedings of the 19th International Symposium on Shock Waves*, R. Brun, and L. Z. Dumitrescu, (eds.), Springer, Berlin, pp. 155–160.
[28] Khalil, E. B., and Karim, G. A., 2002, "A Kinetic Investigation of the Role of Changes in the Composition of Natural Gas in Engine Applications," J. Eng. Gas Turbines Power, **124**, pp. 404–411.
[29] Kalitan, D. M., Hall, J. M., and Petersen, E. L., 2005, "Ignition and Oxidation of Ethylene-Oxygen-Diluent Mixtures With and Without Silane Addition," J. Propul. Power, **21**, pp. 1045–1056.
[30] Petersen, E. L., Rickard, M. J. A., Crofton, M. D., Abbey, E. D., Traum, M. J., and Kalitan, D. M., 2005, "A Facility for Gas- and Condensed-Phase Measurements Behind Shock Waves," Meas. Sci. Technol., **16**, pp. 1716–1729.
[31] Hall, J. M., Rickard, M. J. A., and Petersen, E. L., 2005, "Comparison of Characteristic Time Diagnostics for Ignition and Oxidation of Fuel/Oxidizer Mixtures Behind Reflected Shock Waves," Combust. Sci. Technol., **177**, pp. 455–483.
[32] Petersen, E. L., Kalitan, D. M., Simmons, S. L., Bourque, G., Curran, H. J., and Simmie, J. M., 2007, "Methane/Propane Oxidation at High Pressures: Experimental and Detailed Chemical Kinetic Modeling," Proc. Combust. Inst., **31**, pp. 447–454.
[33] Kee, R. J., Rupley, F. M., Miller, J. A., Coltrin, M. E., Grcar, J. F., Meeks, E., Moffat, H. K., Lutz, A. E., Dixon-Lewis, G., Smooke, M. D., Warnatz, J., Evans, G. H., Larson, R. S., Mitchell, R. E., Petzold, L. R., Reynolds, W. C., Caracotsios, M., Stewart, W. E., Glarborg, P., Wang, C., and Adigun, O., 2004, *Chemkin Collection*, *Release 4.0*, Reaction Design, Inc., San Diego, CA.
[34] de Vries, J., Hall, J. M., Simmons, S. L., Rickard, M. J. A., Kalitan, D. M., and Petersen, E. L., 2007, "Ethane Ignition and Oxidation Behind Reflected Shock Waves," Combust. Flame, in press.
[35] Petersen, E. L., and de Vries, J., 2005, "Measuring the Ignition of Fuel Blends Using a Design of Experiments Approach," AIAA Paper No. 2005-1165.
[36] de Vries, J., and Petersen, E. L., 2005, "Design and Validation of a Reduced Test Matrix for the Autoignition of Gas Turbine Fuel Blends," ASME Paper No. IMECE2005-80040.
[37] de Vries, J., and Petersen, E. L., 2007, "Autoignition of Methane-Based Fuel Blends Under Gas Turbine Conditions," Proc. Combust. Inst., **31**, pp. 3163–3171.

Nonlinear Breakup Model for a Liquid Sheet Emanating From a Pressure-Swirl Atomizer

Ashraf A. Ibrahim

Milind A. Jog[1]
e-mail: Milind.Jog@uc.edu

Department of Mechanical, Industrial, and Nuclear Engineering,
598 Rhodes Hall,
P.O. Box 210072,
University of Cincinnati,
Cincinnati, OH 45221

Predictions of breakup length of a liquid sheet emanating from a pressure-swirl (simplex) fuel atomizer have been carried out by computationally modeling the two-phase flow in the atomizer coupled with a nonlinear analysis of instability of the liquid sheet. The volume-of-fluid (VOF) method has been employed to study the flow field inside the pressure-swirl atomizer. A nonlinear instability model has been developed using a perturbation expansion technique with the initial amplitude of the disturbance as the perturbation parameter to determine the sheet instability and breakup. The results for sheet thickness and velocities from the internal flow solutions are used as input in the nonlinear instability model. Computational results for internal flow are validated by comparing film thickness at exit, spray angle, and discharge coefficient with available experimental data. The predictions of breakup length show a good agreement with semiempirical correlations and available experimental measurements. The effect of elevated ambient pressure on the atomizer internal flow field and sheet breakup is investigated. A decrease in air core diameter is obtained at higher ambient pressure due to increased liquid-air momentum transport. Shorter breakup lengths are obtained at elevated air pressure. The coupled internal flow simulation and sheet instability analysis provides a comprehensive approach to modeling sheet breakup from a pressure-swirl atomizer.
[DOI: 10.1115/1.2747263]

Keywords: sheet breakup, atomization, computational modeling

Introduction

Pressure-swirl atomizers or simplex atomizers are used for liquid fuel injection in a variety of combustion systems including aircraft engines, marine engines, land-based gas turbine combustors as well as industrial oil fired furnaces. Also, pressure swirl atomizers are being considered for direct injection spark ignition engines or gasoline direct injection engines. Pressure swirl atomizers are easy to manufacture even in small sizes, provide good atomization quality, and have low clogging tendencies [1]. Figure 1 shows a schematic of simplex atomizer geometry. In a simplex atomizer, the fuel is forced under high pressure to enter a swirl chamber through tangential inlet slots. As a result of the swirling motion (centrifugal forces) within the swirl chamber, the pressure decreases towards the center axis. Due to the lower pressure near the center axis, an air-core is formed along the centerline. Once the liquid sheet exits the atomizer and moves away from the atomizer, waves are formed at the inner and the outer surface of the sheet and the sheet becomes unstable. The difference between the velocity of the sheet and the surrounding air or gas causes aerodynamic forces that amplify the waves on the sheet. The waves grow until they reach critical amplitude and cause sheet breakup. The internal flow characteristics in pressure-swirl atomizers are important, because they govern the characteristics of the sheet formed at the discharge orifice including the axial, tangential, and radial velocity, and the sheet thickness.

To reduce emissions, it is critical to design fuel atomizers that can produce sprays with predetermined droplet size distribution at the desired combustor locations to enhance the mixing process between the fuel and the air. It is well-known that the characteristics of the liquid sheet emanating from the atomizer depend on the atomizer geometry and the inlet flow conditions [1–5]. As such, a comprehensive approach to modeling of atomization from a pressure-swirl atomizer must include determination of the flow field inside the atomizer, evaluation of the characteristics of the liquid sheet exiting from the atomizer, and modeling of the sheet instability and breakup. Earlier studies that follow such comprehensive approaches have relied on a linear analysis of sheet stability [6–8]. Cousin et al. [6] have used a simplified model for the internal flow by treating it as single phase and have not taken the air core into account. Liao et al. [7] have presented a comprehensive model to predict the performance of a simplex atomizer. They have predicted the internal flow and properties of the liquid sheet emanating from the atomizer with the Arbitrary-Lagrangian-Eulerian (ALE) method, followed by a linear instability analysis to determine the mean drop diameter resulting from sheet breakup. Using experimental data for breakup length, their predictions of mean drop diameter agree reasonably well with experimental data for large scale prototype atomizer. Ibrahim et al. [8] have investigated the effect of liquid swirl velocity profile on mean droplet diameter predictions for simplex atomizers. Their mean drop size predictions match well with experimental measurements. Once again, they have used known values of breakup length from experimental measurements in their model to predict mean droplet diameter. The linear stability theory used in these studies can predict the onset of instability but is unable to predict the sheet deformation to breakup due to the underlying assumption of infinitesimal perturbation magnitude. Therefore to predict the performance of a simplex atomizer, a nonlinear model is needed that can determine the annular sheet evolution to breakup and provide the sheet breakup length.

In this paper, we have computationally determined the pressure-swirl atomizer internal flow field using the volume-of-fluid (VOF) method. A nonlinear instability model is then developed to determine the sheet instability and the breakup length. The results for sheet thickness and velocities from the internal flow solution are used as input in our nonlinear instability model to determine the

[1]Corresponding author.

Submitted to ASME for publication in the JOURNAL OF ENGINEERING FOR GAS TURBINES AND POWER. Manuscript received August 16, 2006; final manuscript received January 30, 2007. Review conducted by Nader Rizk.

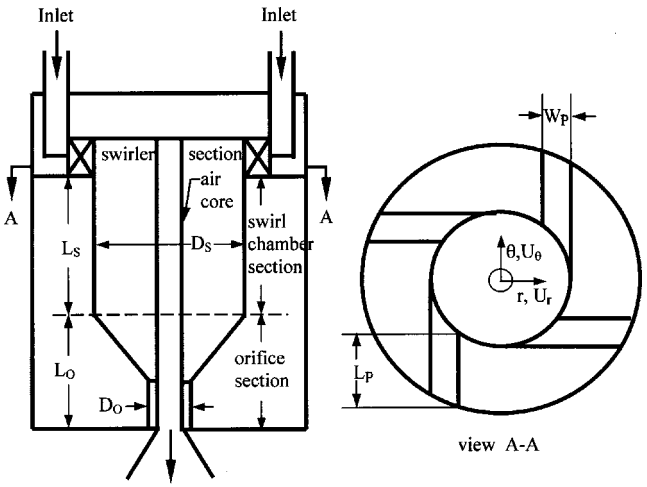

Fig. 1 A schematic of pressure swirl atomizer

breakup length. For fuel injection systems used in gas turbine combustors, the liquid fuel is atomized in an elevated pressure environment. However, most of the reported experimental work on atomizer internal flow and sheet breakup has been at atmospheric pressure. We have used the coupled model of internal flow/external sheet breakup to study the effect of elevated pressure.

We first consider the computational modeling of the internal flow field.

Internal Flow Field. A number of computational investigations of the flow field inside pressure swirl atomizers are available. Yule and Chinn [9] have performed computations for the liquid phase in the atomizer. The boundary between the liquid and the air-core is modeled with a free-surface routine, which adjusts the grid until the static pressure at the boundary is equal to atmospheric pressure. The two-phase flow in the atomizer has been modeled using the Arbitrary-Lagrangian-Eulerian (ALE) method by Xue et al. [4], Sakman et al. [5], Jeng et al. [10], and Xue et al. [11]; and the volume-of-fluid (VOF) method by Hansen et al. [12], Hansen and Madsen [13], Dash et al. [14], and Ibrahim et al. [15], among others. These studies show that the ALE and the VOF methods can be used to simulate the two phase flow in the pressure-swirl atomizer and determine the properties of the liquid sheet exiting from the atomizer. These computational studies have confirmed the significant effect of atomizer geometry on the sheet characteristics as shown earlier by the simplified inviscid flow analysis of Giffen and Muraszew [16] and experimental investigations of Rizk and Lefebvre [2,3]. The most important geometric parameter was shown to be the atomizer constant, which is defined as the ratio of inlet slot area to the product of swirl chamber diameter and the exit orifice diameter. A decrease in the atomizer constant increases the cone angle and reduces the film thickness and the discharge coefficient. The effect of other geometric parameters of the atomizer including the ratio of the exit orifice diameter to the swirl chamber diameter, the length to diameter ratio of the swirl chamber, and that of the exit orifice have been studied under constant volume flow rate condition [4] and under constant pressure drop across the atomizer [11]. Furthermore, Xue et al. [5] have documented the effects of the inlet slot angle, the swirl chamber convergence angle, and the trumpet length and angle on the liquid sheet. Gavaises et al. [17] have shown that accurate estimation of the atomizer flow exit conditions plays a dominant role in the prediction of sprays injected from pressure swirl atomizers.

Nonlinear Instability. It is well known that the growth of disturbances on liquid sheet lead to sheet instability and breakup. Linear analyses are available in literature that cover a wide range of configurations viz., viscous or inviscid annular sheets with or without swirl and with or without surrounding viscous or inviscid gas flows at equal or different velocities. A comprehensive review of linear instability theories for liquid sheets and jets is given by Lefebvre [1] and more recently by Lin [18]. A drawback of the linear theory is that the underlying assumption of small disturbance amplitude limits applicability of the linear theory to the initial short time interval. The linear theory can predict the onset of instability but is unable to accurately predict the sheet deformation to breakup [19].

Only a few nonlinear analyses of thin annular liquid sheet breakup have been reported [20–23]. Lee and Wang [20,21] developed a model for the dynamic formation of spherical shells from an annular inviscid membrane issuing from a nozzle and treated the liquid layer as a membrane moving under the influence of its own inertia, surface tension, and gaseous hydrostatic pressure difference between its two sides. They have assumed that the liquid layer has zero thickness with no structure (internal flow) but with finite inertia which is subjected to change due to stretching and relaxing of the sheet during motion. Panchagnula et al. [22] developed a nonlinear model of annular liquid sheet using approximate one dimensional equation derived by thin sheet approximations. They neglected the aerodynamic effects of the gas phase inside and outside the liquid sheet. Mehring and Sirignano [23,24] developed nonlinear models of axisymmetric thin inviscid infinite (periodically disturbed) and semi-infinite (locally forced) annular liquid sheets in a surrounding void with nonzero gas core pressure at zero gravity by employing a reduced dimension approach (long-wavelength approximation). In the present paper, a nonlinear stability analysis has been carried out for annular liquid fuel sheet subjected to unequal inner and outer gas velocities by a perturbation expansion technique with the initial amplitude of the disturbance as the perturbation parameter. The liquid sheet moves at a uniform axial velocity and is subjected to inner and outer gas streams of differing axial velocities.

Mathematical Formulation

Numerical Solution Procedure. Numerical simulations of the two-phase flow field in pressure swirl atomizer are obtained by solution of the Navier-Stokes equations coupled with the VOF equation [25] implemented in the commercially available CFD code Fluent-6.2 [26] with a surface tracking technique on a fixed Eulerian structured mesh. In the VOF model, a single set of momentum equations is shared by the fluids, and the volume fraction of each of the fluids in each computational cell is tracked throughout the domain. In this method, the volume fraction of the first fluid in the cell is denoted as $\alpha=1$ for a cell containing only the first fluid, $\alpha=0$ for a cell with only the second fluid, and $0<\alpha<1$ when a cell contains the interface between the first and second fluid. The turbulent stresses in the momentum equation are modeled by the Reynolds Stress Model (RSM) [27]. This model has been recommended for swirling flows where nonisotropic turbulent effects dominate. Earlier studies on the computational simulation of flow in a pressure-swirl atomizer (Hansen et al. [12] and Hansen and Madsen [13]) have shown that the *k*-epsilon model overpredicts viscosities in this flow and is not be able to provide accurate solutions. It was found that Reynolds Stress Model was able to capture the flow field which agreed with experimental measurements [28]. Wall functions are used at all solid walls. This model requires the resolution of five transport equations for turbulent properties. The face fluxes for the VOF model are calculated using the geometric reconstruction scheme available in FLUENT 6.2 [26]. The continuum surface force (CSF) proposed by Brackbill et al. [29] is used for the surface tension model. A segregated solver algorithm was used for all cases, where the governing equations are solved sequentially. The discretization scheme used for pressure was PRESTO (Pressure Staggering Option). The SIMPLE method for the pressure-velocity coupling and second order upwind schemes were used for the momentum equations.

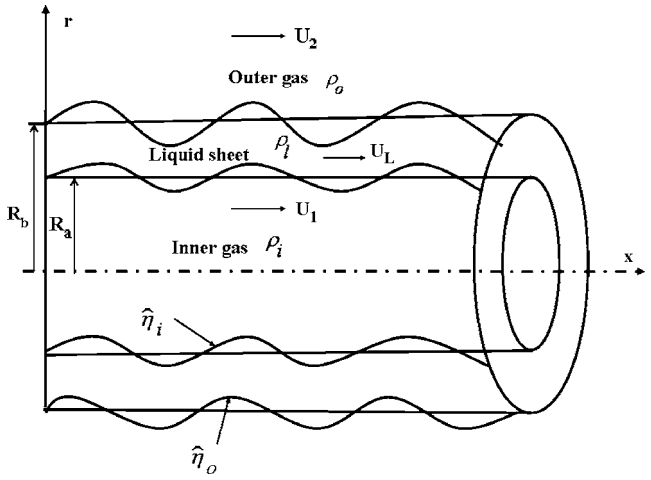

Fig. 2 A schematic of annular liquid sheet

Nonlinear Instability Analysis. A two-dimensional annular liquid sheet of constant thickness h is considered as shown in Fig. 2. The annular liquid sheet moves at a uniform axial velocity U_L and is subjected to an inner gas stream moving with a uniform velocity U_1 and an outer gas stream moving with a uniform velocity U_2. The densities of the liquid, the inner and outer gas phases are ρ_L, ρ_i, and ρ_o, respectively. To maintain an annular shape of the liquid surface, a constraint on the mean pressure of the inner and outer air streams must be imposed as $P_i - P_o = \sigma(R_a^{-1} + R_b^{-1})$. The effect of gravity is neglected because the Froude number (defined as the ratio of liquid inertia to gravity) is typically very large for practical sprays. Both phases are assumed to be inviscid and incompressible. In the present formulation, liquid and gas flows are assumed to be initially irrotational. Therefore, the entire flow field can be treated as potential flow [30]. Liao et al. [31] have shown that the disturbance growth rate increases with Reynolds number and is the same as the growth rate of an inviscid annular sheet at high Reynolds number. Hence, for the cases considered here, effect of viscosity on sheet instability can be neglected. We note that the liquid viscosity has a significant effect on the internal flow (where viscosity is taken into account in our model) but has a small effect on the breakup process (where it is neglected). When the base flow, described above, is perturbed by a small disturbance, the two liquid-gas interfaces are displaced to new locations denoted by $r_a = a + \eta_a$ and $r_b = b + \eta_b$. All physical parameters are nondimensionalized such that length, time, and density are scaled with sheet thickness h, the convection time h/U_L, and the liquid density ρ_L. The dimensionless surface deformation η_a and η_b and the velocity potential ϕ for the liquid and the gas phases must satisfy the following governing equations:

Mass conservation:

$$\nabla \phi_L^2 = 0 \quad r_a \leq r \leq r_b \tag{1}$$

$$\nabla \phi_i^2 = 0 \quad 0 \leq r \leq r_a \tag{2}$$

$$\nabla \phi_o^2 = 0 \quad r_b \leq r \tag{3}$$

The kinematic and the dynamic boundary conditions are specified at the two interfaces. The normal velocity at the interface can be related to the displacement of the interface. This is known as the kinematic condition. The force balance in the normal direction at the interface is known as the dynamic boundary condition. The kinematic conditions are:

For liquid

$$\phi_{La,r} - \eta_{a,t} + \phi_{La,x}\eta_{a,x} = 0 \quad \text{at } r_a \tag{4}$$

$$\phi_{Lb,r} - \eta_{b,t} + \phi_{Lb,x}\eta_{b,x} = 0 \quad \text{at } r_b \tag{5}$$

Inner gas: $$\phi_{i,r} - \eta_{a,t} + \phi_{i,x}\eta_{a,x} = 0 \quad \text{at } r_a \tag{6}$$

Outer gas: $$\phi_{o,r} - \eta_{b,t} + \phi_{o,x}\eta_{a,x} = 0 \quad \text{at } r_b \tag{7}$$

The dynamics boundary conditions at the two interfaces are

$$\frac{1}{2} - \frac{1}{2}g_i U_i^2 + g_i\phi_{i,t} - \phi_{L,t} + \frac{1}{2}g_i \nabla \phi_i^2 - \frac{1}{2}\nabla \phi_L^2 = \frac{-1}{\mathrm{We}_L}\left(1 + \frac{\eta_{a\theta}^2}{r^2} + \eta_{ax}^2\right)^{-(3/2)}\left\{\frac{1}{r}\left(1 + \frac{2\eta_{a\theta}^2}{r^2} + \eta_{ax}^2\right) - \frac{1 + \eta_{ax}^2}{r^2}\eta_{a\theta\theta} - \left(1 + \frac{\eta_{a\theta}^2}{r^2}\right)\eta_{axx} + \frac{2\eta_{ax}\eta_{a\theta}\eta_{ax\theta}}{r^2}\right\} + \frac{1}{\mathrm{We}_L a} \quad \text{at } r = r_a \tag{8}$$

$$\frac{1}{2} - \frac{1}{2}g_o U_o^2 + g_o\phi_{o,t} - \phi_{L,t} + \frac{1}{2}g_o \nabla \phi_o^2 - \frac{1}{2}\nabla \phi_L^2 = \frac{1}{\mathrm{We}_L}\left(1 + \frac{\eta_{b\theta}^2}{r^2} + \eta_{bx}^2\right)^{-(3/2)}\left\{\frac{1}{r}\left(1 + \frac{2\eta_{b\theta}^2}{r^2} + \eta_{bx}^2\right) - \frac{1 + \eta_{bx}^2}{r^2}\eta_{b\theta\theta} - \left(1 + \frac{\eta_{b\theta}^2}{r^2}\right)\eta_{bxx} + \frac{2\eta_{bx}\eta_{b\theta}\eta_{bx\theta}}{r^2}\right\} - \frac{1}{\mathrm{We}_L b} \quad \text{at } r = r_b \tag{9}$$

In the above equations, the dimensionless liquid Weber number (We_L), and inner gas velocity ratio (U_i), outer gas velocity ratio (U_o), inner density ratio (g_i) and outer density ratio (g_o) are defined as $\mathrm{We}_L = \rho_L U_L^2 h/\sigma$, $U_i = U_1/U_L$, $U_o = U_2/U_L$, $g_i = \rho_i/\rho_L$, and $g_o = \rho_o/\rho_L$.

In order to obtain a solution for η_a and η_b, regular perturbation theory is utilized with the initial disturbance amplitude η_o as the perturbation parameter. By means of series expansion method under the perturbation scheme, the surface deformations or the location of the two liquid gas interfaces are expanded in power series of η_o as

$$\eta_j(x,\theta,t) = \sum_{n=1}^{n=\infty} \eta_o^n \eta_{j,n}(x,\theta,t) \quad \text{where } j = a,b \tag{10}$$

The term η_o^0 is neglected from the expansion since it corresponds to the unperturbed interfaces, which are known. Assuming that $\eta_{a,n}$ and $\eta_{b,n}$ and all its derivatives are of the same order of magnitude, the forms of the kinematic boundary conditions suggest that the velocity potentials for the liquid and the gas phases can also be expanded in power series of η_o as

$$\phi_j(x,r,\theta,t) = \sum_{n=0}^{n=\infty} \eta_o^n \phi_{j,n}(x,r,\theta,t) \quad \text{where } j = L,i, \text{ and } o \tag{11}$$

where $\phi_L^0 = x$, $\phi_i^0 = U_i x$, and $\phi_o^0 = U_o x$ represent the base flow field.

Since Eqs. (1)–(3) are linear, each velocity potential ($\phi_{L,n}$, $\phi_{i,n}$, and $\phi_{o,n}$) must satisfy the governing equations independently. The corresponding boundary conditions are obtained by substituting Eqs. (10) and (11) into Eqs. (4)–(9), and equating to zero the successive coefficients of the same power of η_o. Thus the governing equations and the corresponding boundary conditions for the first and the second order are obtained and are

First order (η_o):

$$\nabla \phi_{L1}^2 = 0 \quad a \leq r \leq b \tag{12}$$

$$\nabla \phi_{i1}^2 = 0 \quad 0 \leq r \leq a \tag{13}$$

$$\nabla \phi_{o1}^2 = 0 \quad b \leq r \tag{14}$$

Interface conditions:

$$\phi_{L1,r} - \eta_{a1,t} + \eta_{a1,x} = 0 \quad \text{at } a \tag{15}$$

$$\phi_{L1,r} - \eta_{b1,t} + \eta_{b1,x} = 0 \quad \text{at } b \tag{16}$$

$$\phi_{i1,r} - \eta_{a1,t} + U_i \eta_{a1,x} = 0 \quad \text{at } a \tag{17}$$

$$\phi_{o1,r} - \eta_{b1,t} + U_o \eta_{b1,x} = 0 \quad \text{at } b \tag{18}$$

$$g_i \phi_{i1,t} - \phi_{L1,t} + g_i U_i \phi_{i1,x} - \phi_{L1,x} = \frac{1}{\mathrm{We}_L}\left(\frac{\eta_{a1} + \eta_{a1,\theta\theta}}{a^2} + \eta_{a1,xx}\right) \quad \text{at } a \tag{19}$$

$$g_o \phi_{o1,t} - \phi_{L1,t} + g_o U_o \phi_{o1,x} - \phi_{L1,x} = \frac{-1}{\mathrm{We}_L}\left(\frac{\eta_{b1} + \eta_{b1,\theta\theta}}{b^2} + \eta_{b1,xx}\right) \quad \text{at } b \tag{20}$$

Initial conditions:

$$\eta_{a1}(x,\theta,0) = \cos(kx + n\theta) \text{ and } \eta_{a1,t}(x,\theta,0) = 0 \tag{21}$$

$$\eta_{b1}(x,\theta,0) = \cos(kx + n\theta) \text{ and } \eta_{b1,t}(x,\theta,0) = 0 \tag{22}$$

Second order (η_o^2)

$$\nabla \phi_{L2}^2 = 0 \quad a \leq r \leq b \tag{23}$$

$$\nabla \phi_{i2}^2 = 0 \quad 0 \leq r \leq a \tag{24}$$

$$\nabla \phi_{o2}^2 = 0 \quad b \leq r \tag{25}$$

Interface conditions:

$$\phi_{L2,r} - \eta_{a2,t} - \eta_{a2,x} = \eta_{a1,x}\phi_{L1,x} + \frac{\eta_{a1}\eta_{a1,\theta}}{a^2} - \eta_{a1}\phi_{L1,rr} \quad \text{at } a \tag{26}$$

$$\phi_{L2,r} - \eta_{b2,t} - \eta_{b2,x} = \eta_{b1,x}\phi_{L1,x} + \frac{\eta_{b1}\eta_{b1,\theta}}{b^2} - \eta_{b1}\phi_{L1,rr} \quad \text{at } b \tag{27}$$

$$\phi_{i2,r} - \eta_{a2,t} - U_i \eta_{a2,x} = \eta_{a1,x}\phi_{i1,x} + \frac{\eta_{a1}\eta_{a1,\theta}}{a^2} - \eta_{a1}\phi_{i1,rr} \quad \text{at } a \tag{28}$$

$$\phi_{o2,r} - \eta_{a2,t} - U_o \eta_{a2,x} = \eta_{a1,x}\phi_{o1,x} + \frac{\eta_{a1}\eta_{a1,\theta}}{b^2} - \eta_{a1}\phi_{o1,rr} \quad \text{at } b \tag{29}$$

$$\begin{aligned} g_i \phi_{i2,t} - \phi_{L2,t} + g_i U_i \phi_{i2,x} - \phi_{L2,x} - \frac{1}{\mathrm{We}_L}\left(\frac{\eta_{a2} + \eta_{a2,\theta\theta}}{a^2} + \eta_{a2,xx}\right) &= (\eta_{a1,t}\phi_{L1,r} + \eta_{a1}\phi_{L1,rt}) - g_i(\eta_{a1,t}\phi_{i1,r} + \eta_{a1}\phi_{i1,rt}) \\ &+ (\eta_{a1,x}\phi_{L1,r} + \eta_{a1}\phi_{L1,rx}) - g_i U_i(\eta_{a1,x}\phi_{i1,r} + \eta_{a1}\phi_{i1,rx}) \\ &+ \frac{1}{2}(\phi_{L1,x}^2 + \phi_{L1,r}^2) - \frac{1}{2}g_i(\phi_{i1,x}^2 + \phi_{i1,r}^2) \\ &+ \frac{(2\eta_{a1}^2 + 4\eta_{a1}\eta_{a1,\theta\theta} - \eta_{a1,\theta}^2 - a^2\eta_{a1,x}^2)}{2\mathrm{We}_L a^3} \quad \text{at } a \end{aligned} \tag{30}$$

$$\begin{aligned} g_o \phi_{o2,t} - \phi_{L2,t} + g_o U_o \phi_{o2,x} - \phi_{L2,x} + \frac{1}{\mathrm{We}_L}\left(\frac{\eta_{b2} + \eta_{b2,\theta\theta}}{b^2} + \eta_{b2,xx}\right) &= (\eta_{b1,t}\phi_{L1,r} + \eta_{b1}\phi_{L1,rt}) - g_o(\eta_{b1,t}\phi_{o1,r} + \eta_{b1}\phi_{o1,rt}) \\ &+ (\eta_{b1,x}\phi_{L1,r} + \eta_{b1}\phi_{L1,rx}) - g_o U_o(\eta_{b1,x}\phi_{o1,r} + \eta_{b1}\phi_{o1,rx}) \\ &+ \frac{1}{2}(\phi_{L1,x}^2 + \phi_{L1,r}^2) - \frac{1}{2}g_o(\phi_{o1,x}^2 + \phi_{o1,r}^2) \\ &- \frac{(2\eta_{b1}^2 + 4\eta_{b1}\eta_{b1,\theta\theta} - \eta_{b1,\theta}^2 - b^2\eta_{b1,x}^2)}{2\mathrm{We}_L b^3} \quad \text{at } b \end{aligned} \tag{31}$$

Initial conditions:

$$\eta_{a2}(x,\theta,0) = 0 \text{ and } \eta_{a2,t}(x,\theta,0) = 0 \tag{32}$$

$$\eta_{b2}(x,\theta,0) = 0 \text{ and } \eta_{b2,t}(x,\theta,0) = 0 \tag{33}$$

Solution Method

The first order surface deformation at the two interfaces can be written in the following form:

$$\eta_{a1}(x,\theta,t) = A_1(t)\exp(i(kx + n\theta)) + \text{c.c.} \tag{34}$$

$$\eta_{b1}(x,\theta,t) = B_1(t)\exp(i(kx + n\theta)) + \text{c.c.} \tag{35}$$

Here c.c. indicates complex conjugate. Substituting Eqs. (34) and (35) into Eqs. (15)–(18), the forms for the liquid and gas velocity potential can be obtained. Substituting these in Eqs. (12)–(14) and solving, we get the liquid and gas velocity potential in terms of $A_1(t)$ and $B_1(t)$, its complex conjugate and modified Bessel functions of r. Then substituting the gas and the liquid velocity potential in the dynamic boundary conditions (Eqs. (19) and (20)) and solving using the method of Laplace transform we find

$$A_1(t) = \sum_{j=1}^{j=4} c_{1j} a_{1j} \exp(\omega_{1j} t) \tag{36}$$

$$B_1(t) = \sum_{j=1}^{j=4} c_{1j} b_{1j} \exp(\omega_{1j} t) \tag{37}$$

The disturbance growth rates ω_{11}, ω_{12}, ω_{13}, and ω_{14} are the roots of the dispersion equations

$$\Delta_{11}\omega_{1j}^4 + \Delta_{12}\omega_{1j}^3 + \Delta_{13}\omega_{1j}^2 + \Delta_{14}\omega_{1j} + \Delta_{15} = 0 \quad j = 1,2,3, \text{ and } 4 \tag{38}$$

The expressions for Δ_{1j} are available in Ref. 28. It has been reported [31–33] that the para-varicose disturbances dominate the breakup process only at very low liquid Weber numbers. For practical fuel atomizers sheet Weber numbers are high and parasinuous disturbances are expected to dominate the breakup process. As such, parasinuous disturbance modes are considered in this study. Note that for a planar liquid sheet the most unstable disturbances are exactly out-of-phase (symmetric or varicose) and exactly in-phase (antisymmetric or sinuous). However, this need not be the case for an annular sheet [18]. The disturbance nearly in-phase is referred to a parasinuous and nearly out-of-phase as paravaricose. The first order surface deformations at the two interfaces can be written in the following form:

$$\eta_{a1}(x,\theta,t) = (c_{11}\exp(\omega_{11}t) + c_{12}\exp(\omega_{12}t))\exp(i(kx + n\theta)) + \text{c.c.} \tag{39}$$

$$\eta_{b1}(x,\theta,t) = (R(c_{11}\exp(\omega_{11}t) + c_{12}\exp(\omega_{12}t)))\exp(i(kx + n\theta)) + \text{c.c.} \tag{40}$$

$$c_{11} = \frac{\omega_{12}}{2(\omega_{12} - \omega_{11})},\ c_{12} = \frac{-\omega_{11}}{2(\omega_{12} - \omega_{11})},$$

$$\omega_{11} = \alpha - i\beta \text{ and } \omega_{12} = -\alpha - i\beta$$

The first order liquid, inner and outer gas velocity potentials are, respectively,

$$\phi_{L1} = \left[\frac{c_{11}}{2}(f_1(r)m_5 + f_2(r)Rm_8)\exp(\omega_{11}t) + \frac{c_{12}}{2}(f_1(r)m_6 + f_2(r)Rm_9)\exp(\omega_{12}t) \right] \exp(i(kx + n\theta)) + \text{c.c.} \quad (41)$$

$$\phi_{i1} = \left[f_3(r)\left(\frac{c_{11}}{2} m_{17} \exp(\omega_{11}t) + \frac{c_{12}}{2} m_{18} \exp(\omega_{12}t) \right) \right] \times \exp(i(kx + n\theta)) + \text{c.c.} \quad (42)$$

$$\phi_{o1} = \left[f_4(kr)R\left(\frac{c_{11}}{2} m_{23} \exp(\omega_{11}t) + \frac{c_{12}}{2} m_{24} \exp(\omega_{12}t) \right) \right] \times \exp(i(kx + n\theta)) + \text{c.c.} \quad (43)$$

The second order surface deformation at the two interfaces can be written in the following form;

$$\eta_{a2}(x, \theta, t) = A_2(t)\exp(2i(kx + n\theta)) + \text{c.c.} + D_a(t) \quad (44)$$

$$\eta_{b2}(x, \theta, t) = B_2(t)\exp(2i(kx + n\theta)) + \text{c.c.} + D_b(t) \quad (45)$$

where

$$A_2(t) = c_{1a}\exp(\omega_{21}t) + c_{2a}\exp(\omega_{22}t) + c_{3a}\exp(2\omega_{11}t) + c_{4a}\exp(2\omega_{12}t) + c_{5a}\exp((\omega_{11} + \omega_{12})t) \quad (46)$$

$$B_2(t) = c_{1b}\exp(\omega_{21}t) + c_{2b}\exp(\omega_{22}t) + c_{3b}\exp(2\omega_{11}t) + c_{4b}\exp(2\omega_{12}t) + c_{5b}\exp((\omega_{11} + \omega_{12})t) \quad (47)$$

$D_a(t)$ $D_b(t)$ are required to insure a conservation of mass at $t > 0$ and are obtained as

$$D_a(t) = \frac{\left(k^2 f_3 + \frac{n^2}{a^2} f_3 - f_3'' \right)(\alpha^2 + \beta^2)}{8\alpha^2}(1 - \cosh(2\alpha t)) \quad (48)$$

$$D_b(t) = \frac{\left(k^2 f_4 + \frac{n^2}{b^2} f_4 - f_4'' \right)(\alpha^2 + \beta^2)}{8\alpha^2}(1 - \cosh(2\alpha t)) \quad (49)$$

Following a procedure similar to the one described for the first order solution, after lengthy and tedious manipulations, the second order velocity potentials can be obtained as follows:

$$\phi_{L2} = [(f_5(r)c_{1a}m_1 + f_6(r)c_{1b}m_3)\exp(\omega_{21}t) + (f_5(r)c_{2a}m_2 + f_6(r)c_{2b}m_4)\exp(\omega_{22}t) + (f_5(r)(c_{3a}m_5 - m_{11}) + f_6(r)(c_{3b}m_8 - m_{14}))\exp(2\omega_{11}t) + (f_5(r)(c_{4a}m_6 - m_{12}) + f_6(r)(c_{4b}m_9 - m_{15}))\exp(2\omega_{12}t) + (f_5(r)(c_{5a}m_7 - m_{12}) + f_6(r)(c_{5b}m_{10} - m_{16}))\exp((\omega_{11} + \omega_{12})t)]\exp(2i(kx + n\theta)) + \text{c.c.} \quad (50)$$

$$\phi_{i2} = [f_7(r)c_{1a}m_{29}\exp(\omega_{21}t) + f_7(r)c_{2a}m_{30}\exp(\omega_{22}t) + (f_7(r)(c_{3a}m_{17} - m_{20}))\exp(2\omega_{11}t) + (f_7(r) \times (c_{4a}m_{18} - m_{21}))\exp(2\omega_{12}t) + (f_7(r)(c_{5a}m_{19} - m_{22})) \times \exp((\omega_{11} + \omega_{12})t))]\exp(2i(kx + n\theta)) + \text{c.c.} + A_i(t) \quad (51)$$

$$\phi_{o2} = [f_8(r)c_{1b}m_{31}\exp(\omega_{21}t) + f_8(r)c_{2b}m_{32}\exp(\omega_{22}t) + (f_8(r)(c_{3b}m_{23} - m_{26}))\exp(2\omega_{11}t) + (f_8(r) \times (c_{4b}m_{24} - m_{27}))\exp(2\omega_{12}t) + (f_8(r)(c_{5b}m_{25} - m_{28})) \times \exp((\omega_{11} + \omega_{12})t))]\exp(2i(kx + n\theta)) + \text{c.c.} + A_o(t) \quad (52)$$

where $A_i(t)$ and $A_o(t)$ are required to satisfy the dynamic boundary conditions. After a considerable amount of manipulations, the following equation for the second-order disturbance growth rate is obtained:

$$\Delta_{21}\omega_{2j}^4 + \Delta_{22}\omega_{2j}^3 + \Delta_{23}\omega_{2j}^2 + \Delta_{24}\omega_{2j} + \Delta_{25} = 0 \quad j = 1,2,3, \text{ and } 4 \quad (53)$$

The expressions for Δ_{2j} are available in Ref. [28].

The first and the second order dispersion equations are solved using *Mathematica*™. The secant method is used which requires two initial guess values. Solutions are considered convergent when values of the left hand sides of Eqs. (38) and (53) are smaller than 10^{-6}. All constants in the above equations and solutions for η_{a1}, η_{a2}, η_{b1}, and η_{b2} are available in Ref. [28] and not repeated here for brevity. The evolution of the inner and outer gas-liquid interface can be obtained from the first and the second order solution as

$$\eta_a(x, \theta, t) = \eta_o^1\eta_{a1} + \eta_o^2\eta_{a2} \quad (54)$$

$$\eta_b(x, \theta, t) = \eta_o^1\eta_{b1} + \eta_o^2\eta_{b2} \quad (55)$$

Results and Discussion

Internal Flow Field. In the computational model the flow has been assumed to be axisymmetric based on the experimental observations of Ma [34]. Ma carried out detailed measurements of the flow field in the swirl chamber of a large scale simplex atomizer using particle image velocimetry (PIV) and laser doppler velocimetry (LDV) techniques and showed that the flow field in the swirl chamber is axisymmetric even for an atomizer with only two inlet slots. To compare the computational results with experimental measurements, the assumption of axisymmetry requires determination of an equivalent "annular" inlet slot instead of the finite number of slots present in the real atomizer. The width of the "annular" slot as well as the radial and tangential velocities at the inlet are calculated by equating the angular momentum, total mass flow rate, and the kinetic energy of the liquid at the inlet ports with those in the experiments. The boundary condition for the inlet was taken to be radial and tangential velocity components. The inlet tangential and radial velocities at the wall of the swirl chamber are obtained as

$$W_{\text{inlet}} = \frac{Q}{A_p}\frac{(D_s - D_p)}{D_s}$$

and

$$V_{\text{inlet}} = \sqrt{(Q/A_p)^2 - W_{\text{inlet}}^2}$$

thus the inlet width can be calculated. At the outlet cross section, pressure outlet boundary was prescribed. All wall boundaries are taken as no-slip. For all cases, the fluids are air and water. The geometric and flow parameters for the cases considered are shown in Table 1.

Grid Independence and Validation. In order to ensure grid independence of the results, two sets of results for the same flow conditions and geometry of case 1 are shown in Table 2 with 26,682 and 46,932 cells, respectively. The difference in results using the two grids is small and indicates that 26,682 cells or similar grid is sufficient to get accurate results. The computational

Table 1 Cases of study (orifice contraction angle is 45 deg for all cases)

Case No.	Number of ports	Inlet slot area A_P (mm^2)	Orifice D_o, L_o (mm)	Swirl chamber D_s, L_s (mm)	Mass flow rate (kg/s)
1	2	203	21.6, 36.7	76, 38	0.5
2	4	406	28.8, 40.5	76, 38	0.95
3	2	203	28.8, 40.5	76, 38	0.95
4	2	203	21.6, 36.7	76, 89	0.63

results were validated by comparison with experimental data from Ref. [35] for discharge parameters, spray cone angle, film thickness, and discharge coefficient for a large-scale atomizer.

Table 3 shows a comparison of computational predictions of film thickness, spray angle, and discharge coefficient with experimental measurements for all the cases. The discharge coefficient was calculated as $C_d = Q/(A_{\text{Orifice}}\sqrt{2\Delta P/\rho_L})$. The spray cone angle is measured by making a tangent to the outer spray interface. It is seen that the computational results agree very well with the experimental measurements.

Figure 3 shows computed velocity vectors on a planar cross section in the pressure swirl atomizer for case 1. As the computational simulation is axisymmetric, only half of the flow domain is shown. The velocity vectors have radial and axial velocity components. The swirl velocity is perpendicular to the cross section and hence the swirl velocity component is not shown in the figure. As a result of the swirling motion within the swirl chamber, the pressure decreases towards the center axis. Due to the lower pressure near the center axis, an air-core is formed along the centerline. The air enters the atomizer near the centerline and is dragged along the liquid sheet exiting from the atomizer. As a result, the air axial velocity is negative near the center and is positive close to the liquid sheet. As expected the air axial velocity decreases from the atomizer exit to the swirl chamber. In the liquid phase, the positive and negative velocities indicate the existence of a number of small-scale vortices in this region, and exhibit flow patterns with recirculation, similar to flow field characteristics reported by Ma [34]. The volume fraction contours are shown in Fig. 4(*a*) and the visualization of the two phase interface for the same case from Ma [34] is shown in Fig. 4(*b*). The air core radius is considered to be located at volume fraction of 0.5 in Fig. 4(*a*). The air core diameter is nearly constant in the swirl chamber and it increases as the flow enters the exit orifice. This behavior matches well with the results of Ma [34] shown in Fig. 4(*b*).

The effect of elevated ambient pressure on the air core is shown in Fig. 5 where the air-water interface is depicted for air pressures of 1, 5, and 10 bars. It can be seen that at higher air pressure the air core diameter in the swirl chamber decreases whereas, in the orifice, a small decrease in the air core diameter is seen. The average axial and tangential velocities are lower in the swirl chamber compared to those in the exit orifice. Even with a tenfold increase in air density, the liquid inertia force in the orifice is very large compared to air friction. Hence the effect of increase in air density on film thickness in the orifice is small.

Table 2 Results for two different grid densities for case 1

	Film thickness, h (mm)	Spray cone angle (2θ)	Discharge coefficient (C_d)
26682 cells	2.2579	86.18	0.178
46932 cells	2.2704	86.18	0.177

Nonlinear Instability. The temporal evolution of the inner and outer interfaces for axial liquid Weber number of 300 for two wavelength intervals axial distance ($4\pi/k$) at different times are shown in Fig. 6. The axial dominant wave number (k) is 0.16 and the initial disturbance amplitude of 0.1 is considered. Clark and Dombrowski [36] have measured the initial disturbance amplitude of swirl spray sheets and reported a value of approximately 10^{-4} m. Therefore, an initial dimensionless disturbance amplitude (η_o) of $\sim$0.1 is considered. The disturbance amplitude is made dimensionless by the sheet thickness h. It is found that at the initial time instant, the two interfaces are moving parallel to each other. However, at a later time $T=35$, waviness appears at the interfaces due to the nonlinear interaction between the first and second order modes. As the time increases the disturbance amplitude of the inner and outer interfaces increases. The deformation of the inner and outer interfaces leads to thinning and thickening of the liquid sheet. The time at which the thickness of the liquid sheet reaches a near zero value is taken as breakup time.

Breakup Length Calculation and Validation. The nonlinear instability model is validated with the available experimental data for large scale prototype atomizer from Ref. [35] and semiempirical correlation available in Ref. [37]. Gaster [38] has shown that the spatial and temporal instability are related to each other for large Weber numbers. Using Gaster transformation [38], the breakup length can be obtained from the breakup time. The breakup length (L_b) of an annular liquid sheet is calculated from the breakup time (t_b) and the liquid velocity (U_L) as $L_b = T_b U_L$ [39]. A comparison of experimental and prediction results of the breakup length for large scale pressure swirl injectors is shown in Table 4. The predictions and experimental results are in good agreement.

Note that the growth rate is evaluated for all combinations of axial and circumferential wave numbers to determine the combination of axial (k) and circumferential wave number (n) that has the highest growth rate. This most unstable disturbance is imposed on the sheet surface and its temporal evolution is evaluated. The combination of k and n is a function of flow and geometry parameters. As such, the most unstable wave number may be different for each case considered here and shows that the model is capable of dealing with different initial conditions.

Table 3 Comparison of computational results with experimental measurements

	Film thickness, h (mm)		Spray cone angle (2θ)		Discharge coefficient (C_d)	
Case No.	Expt	CFD	Expt	CFD	Expt	CFD
1	2.24	2.27	84.7	86.18	0.17	0.177
2	3.06	3.02	76.9	75.75	0.20	0.218
3	2.41	2.18	89.9	90.59	0.12	0.133
4	2.37	2.47	76.9	82.37	0.16	0.150

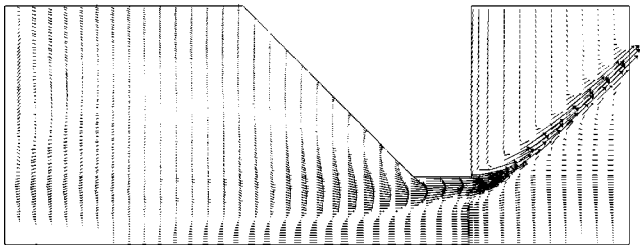

Fig. 3 Velocity vectors in the atomizer (case 1)

Kim et al. [37] have studied the effect of flow condition and geometry on flow characteristics of a swirl injector. They have carried out measurements of breakup length of sheets exiting from a pressure swirl atomizer. Kim et al. [37] have introduced a correlation for the breakup length based on their experimental data as a function of liquid Weber number (We), orifice length (L_o), orifice diameter (D_o), inlet ports are (A_p) and orifice area (A_o) as

$$L_b/D_o = 100.8\ \mathrm{We}^{-0.215}(l_o/D_o)^{0.0424}(A_p/A_o)^{0.395}$$

where

$$\mathrm{We} = \rho U_l^2 D_o/\sigma$$

It is seen from Fig. 7 that the predicted breakup length is in good agreement with the measurements of Kim et al. [37].

Figure 8 shows the temporal evolution of the dimensionless inner and outer surfaces deformation at the breakup time for equal inner and outer gas to liquid density ratios of 0.0012, 0.006, and 0.012. These density ratios correspond to ambient pressure of 1 bar, 5 bar, and 10 bar, respectively. Increasing density ratio increases the destabilizing effect of the aerodynamic forces [32]. An increase in the aerodynamic forces leads to an increase in the growth rate of disturbance and it induces a faster disintegration process. The breakup times at gas to liquid density ratios of

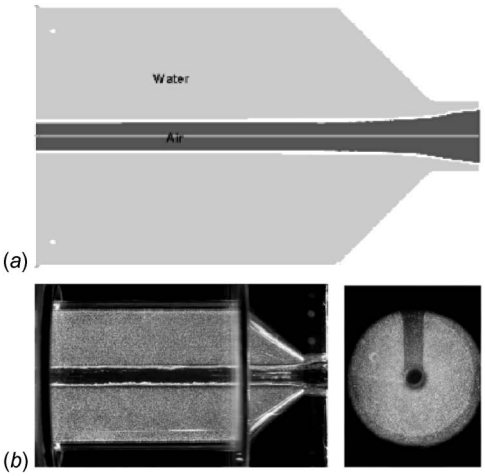

Fig. 4 Volume fraction contours (case 4) (*a*) computational prediction and (*b*) experimental observation from Ma [34]

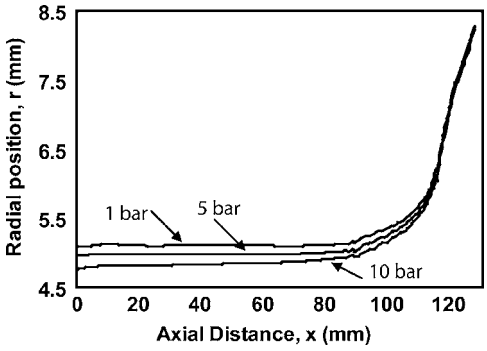

Fig. 5 Effect of air pressure on the air core diameter

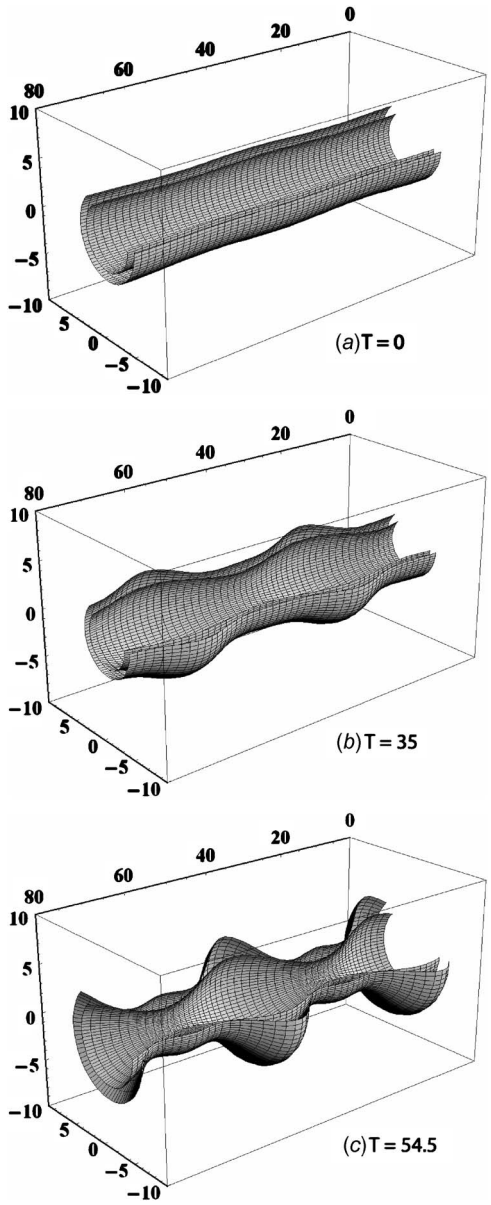

Fig. 6 Evolution of the dimensionless inner and outer surfaces deformation at the dominant wave number of k=0.16 for We_L=300, U_i=U_o=0, g_i=g_o=0.0012 (η_o=0.1) (*a*) T=0, (*b*) T=35, and (*c*) T=54.5

Table 4 Comparison of predicted with measured breakup length (large Scale nozzle [35])

Case No.	We_L at orifice exit	Breakup Length (mm)		η_o
		Experiment	Prediction	
1	421	121	113	0.11
2	614	140	127	0.1
3	741	102	104	0.18
4	630	127	90	0.1

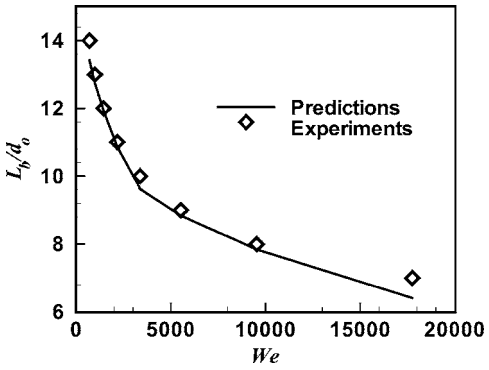

Fig. 7 Comparison of dimensionless breakup length predictions with Kim et al. [37]

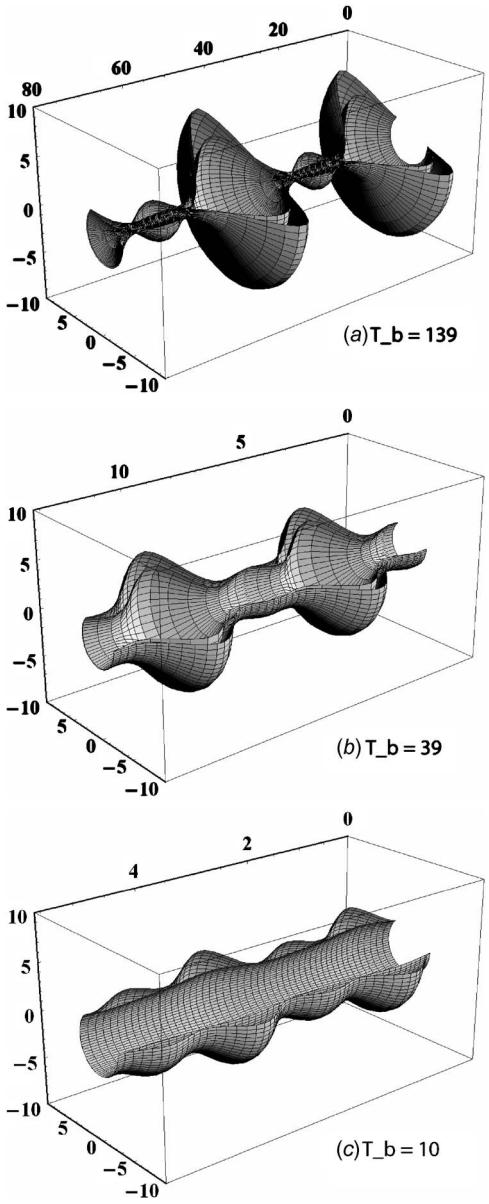

Fig. 8 Evolution of the dimensionless inner and outer surfaces deformation at different density ratios for We_L=300, U_i = U_o=0, and η_o=0.01. (*a*) g_i=g_o=0.0012 and k=0.16; (*b*) g_i=g_o =0.006 and k=0.95; and (*c*) g_i=g_o=0.012 and k=2.25.

0.0012, 0.006, and 0.012 are 139, 39, and 10. It can be seen from Fig. 8 that the significantly shorter breakup lengths are obtained due to higher liquid/air interaction with increased air-to-liquid density ratio at elevated air pressure.

Conclusions

Computational modeling of the two-phase flow in a pressure-swirl atomizer coupled with a nonlinear analysis of instability of the liquid sheet exiting from the atomizer has been carried out. The volume-of-fluid method is employed to determine the two-phase gas-liquid flow inside the atomizer. A perturbation method, with the initial amplitude of the disturbance as the perturbation parameter, is used to model the nonlinear sheet breakup and evaluate the breakup length. The models are validated using available experimental data of liquid film thickness, spray cone angle, and discharge coefficient and sheet breakup length data and correlation. The validated model is used to investigate the effect of elevated ambient pressure on the atomizer internal flow field and sheet breakup. Numerical results indicate that an increase in ambient pressure from 1 to 10 bar produces only small changes in the internal flow field. The sheet thickness and discharge coefficient increase slightly with an increase in the ambient pressure. However, the elevated pressure has significant effects on the sheet breakup process. Shorter breakup lengths are obtained due to higher liquid/air interaction with increased air-to-liquid density ratio at elevated air pressure. The coupled internal flow simulation and nonlinear sheet breakup model presented here can be used to determine breakup length for a liquid sheet emanating from a pressure-swirl atomizer.

Acknowledgment

We thankfully acknowledge the support of this work by University Research Council of University of Cincinnati and GE Transportation Systems.

Nomenclature

a = nondimensional inner sheet radius
A = area, m^2
b = nondimensional outer sheet radius
D = diameter, m
g = nondimensional gas density ratio
h = sheet thickness, mm
k = axial wave number, 1/m
L = length, m
P = Pressure, Pa
Q = liquid flow rate, m^3/s
r = radial distance, m
R_a = inner radius of liquid sheet, m
R_b = outer radius of liquid sheet, m
t = time, s
T = nondimensional time
U = mean axial velocity, m/s
U_1 = inner gas velocity, m/s
U_2 = outer gas velocity, m/s
U_L = liquid velocity, m/s
V = mean radial velocity, m/s
W = mean tangential velocity, m/s
We = weber number, $\rho U^2 h/\sigma$
x = axial distance, m

Subscripts

a = inner sheet radius
b = outer sheet radius
i = inner gas
l = liquid
L = liquid phase
o = outer gas
p = port

s = swirl chamber

Greek symbols

ϕ = velocity potential function
η = displacement disturbance, m
ρ = fluid density, kg/m^3
ω = nondimensionalized growth rate
σ = surface tension, N/m
θ = half-spray cone angle, deg

References

[1] Lefebvre, A. H., 1989, *Atomization and Spray*, Hemisphere, New York.
[2] Rizk, N. K., and Lefebvre, A. H., 1985, "Internal Flow Characteristics of Simplex Swirl Atomizers," J. Propul. Power, **1**(3), pp. 193–199.
[3] Rizk, N. K., and Lefebvre, A. H., 1986, "Influence of Liquid Properties on the Internal Flow Characteristics of Simplex Swirl Atomizers," Atomization and Spray Technology, **2**(3), pp. 219–233.
[4] Sakman, A. T., Jog, M. A., Jeng, S. M., and Benjamin, M. A., 2000, "Parametric Study of Simplex Fuel Nozzle Internal Flow and Performance," AIAA J., **38**, pp. 1214–1218.
[5] Xue, J., Jog, M. A., Jeng, S. M., Steinthorsson, E., and Benjamin, M. A., 2004, "Effect of Geometric Parameters on Simplex Atomizer Performance," AIAA J., **42**, pp. 2408–2415.
[6] Cousin, J., Ren, W. M., and Nally, S., 1999, "Recent Developments in Simulations of Internal Flows in High Pressure Swirl Injectors," Oil Gas Sci. Technol., **54**(2), pp. 227–223.
[7] Liao, Y., Sakman, A. T., Jeng, S. M., Jog, M. A., and Benjamin, M. A., 1999, "A Comprehensive Model to Predict Simplex Atomizer Performance," ASME J. Eng. Gas Turbines Power, **121**, pp. 285–294.
[8] Ibrahim, A. A., Jog, M. A., and Jeng, S. M., 2004, "Effect of Liquid Swirl Velocity Profile on Mean Droplet Diameter Predictions for Simplex Atomizers," ILASS-AMERICAS, Arlington, VA.
[9] Yule, A. J., and Chinn, J. J., 2000, "The Internal Flow and Exit Conditions of Pressure Swirl Atomizers," Atomization Sprays, **10**, pp. 121–146.
[10] Jeng, S. M., Jog, M. A., and Benjamin, M. A., 1998, "Computational and Experimental Study of Liquid Sheet Emanating From Simplex Fuel Nozzle," AIAA J., **36**, pp. 201–207.
[11] Xue, J., Jog, M. A., Jeng, S. M., Steinthorsson, E., and Benjamin, M. A., 2002, "Influence of Geometry on the Performance of Simplex Nozzles Under Constant Pressure Drop," ILASS Americas, *Proceedings of the 15th Annual Conference on Liquid Atomization and Spray Systems*, Madison, WI.
[12] Hansen, K. G., Madsen, J., Trinh, C. M., Ibsen, C. H., Solberg, T., and Hjertager, B. H., 2002, "Numerical Simulation of Internal Flow in a Large-Scale Pressure-Swirl Atomizer," ILASS-Europe, Zaragoza.
[13] Hansen, K. G., and Madsen, J., 2001, "A Computational and Experimental Study of the Internal Flow in a Scaled Pressure-Swirl Atomizer," Master's thesis, Aalborg Universitet Esbjerg, Denmark.
[14] Dash, S. K., Halder, M. R., Peric, M., and Som, S. K., 2001, "Formation of Air Core in Nozzles With Tangential Entry," J. Fluid Mech., **123**, pp. 829–835.
[15] Ibrahim, A. A., Jog, M. A., and Jeng, S. M., 2005, "Computational Simulation of Two-Phase Flow in Simplex Atomizers," ILASS-AMERICAS, Irvine, California.
[16] Giffen, E., and Muraszew, A., 1953, *The Atomization of Liquid Fuels*, Wiley, New York.
[17] Gavaises, M., and Arcoumanis, C., 2001, "Modeling of Sprays From High Pressure Swirl Atomizers," Int. J. Engine Research, **2**(2), pp. 95–117.
[18] Lin, S. P., 2003, *Breakup of Liquid Sheets and Jets*, Cambridge University Press.
[19] Sirignano, W. A., and Mehring, C., 2000, "Review of Theory of Distortion and Disintegration of Liquid Streams," Prog. Energy Combust. Sci., **26**, pp. 609–655.
[20] Lee, C. P., and Wang., T. G., 1986, "A Theoretical Model for Annular Jet Instability," Phys. Fluids, **29**, pp. 2076–2085.
[21] Lee, C. P., and Wang, T. G., 1988, "Dynamics of Thin Liquid Sheets," in *Proceedings of the 3rd International Colloquium on Drops and Bubbles*, T. G. Wang, ed., pp. 496–504.
[22] Panchagnula, M. V., Sojka, P. E., and Bajaj, A. K., 1998, "The Non-Linear Breakup of Annular Liquid Sheets," in *Proceedings of the 11th Annual Conference Liquid Atomization Spray Systems*, pp. 170–174.
[23] Mehring, C., and Sirignano, W. A., 1999, "Axisymmetric Capillary Waves on Thin Annular Liquid Sheets Part I: Temporal Stability," Phys. Fluids, **12**, pp. 1417–1439.
[24] Mehring, C., and Sirignano, W. A., 1999, "Axisymmetric Capillary Waves on Thin Annular Liquid Sheets Part II: Spatial Stability," Phys. Fluids, **12**, pp. 1440–1460.
[25] Hirt, C. W., and Nichols, B. D., 1981, "Volume of Fluid (VOF) Methods for the Dynamics of Free Boundaries," J. Comput. Phys., **39**, pp. 201–225.
[26] Fluent 6.2 User's Guide, Fluent Inc., Lebanon, NH.
[27] Launder, B. E., Reece, G. J., and Rodi, W., 1975, "Progress in the Development of a Reynold's-Stress Turbulence Closure," J. Fluid Mech., **68**(3), pp. 537–566.
[28] Ibrahim, A. A., 2006, "Comprehensive Study of Internal Flow Field and Linear and Nonlinear Instability of an Annular Liquid Sheet Emanating From an Atomizer," Ph.D. dissertation, University of Cincinnati.
[29] Brackbill, J. U., Kothe, D. B., and Zemach, C., 1992, "A Continuum Method for Modeling Surface Tension," J. Comput. Phys., **100**(2), pp. 335–354.
[30] White, F. M., 1991, *Viscous Fluid Flow*, McGraw-Hill, New York.
[31] Liao, Y., Jeng, S. M., Jog, M. A., and Benjamin, M. A., 2001, "Advanced Sub-Model for Airblast Atomizers," J. Propul. Power, **17**, pp. 411–417.
[32] Shen, J., and Li, X., 1996, "Instability of an Annular Viscous Liquid Jet," Acta Mech., **114**, pp. 167–183.
[33] Ibrahim, A. A., Jog, M. A., and Jeng, S. M., 2006, "Effect of Liquid Swirl Velocity Profile on the Instability of a Swirling Annular Liquid Sheet," Atomization Sprays, **16**(3), pp. 237–263.
[34] Ma, Z., 2002, "Investigation on the Internal Flow Characteristics of Pressure Swirl Atomizers," Ph.D. dissertation, University of Cincinnati.
[35] Benjamin, M., Mansour, A., Samant, U., Jha, S., Liao, Y., Harris, T., and Jeng, S. M., 1998, "Film Thickness, Droplet Size and Correlations for Large Pressure-Swirl Atomizers," ASME/IGTI Conference and Exhibition, Stockholm, Sweden, Paper No. 98-IG-537.
[36] Clark, C. J., and Dombrowski, N., 1972, "Aerodynamic Instability and Disintegration of Inviscid Liquid Sheets," Proc. R. Soc. London, Ser. A, **329**, pp. 467–478.
[37] Kim, D., Han, P., and Yoon, Y., 2003, "Effect of Flow Condition and Geometry on Flow Characteristics of a Swirl Injector," ILASS Americas, 16th Annual Conference on Liquid Atomization and Spray Systems, Monterey, CA.
[38] Gaster, M., 1962, "A Note on the Relation Between Temporally-Increasing and Spatially-Increasing Disturbances in Hydrodynamic Stability," J. Fluid Mech., **14**, pp. 222.
[39] Ibrahim, A. A., and Jog, M. A., 2006, "Nonlinear Breakup of a Coaxial Liquid Jet in a Swirling Gas Stream," Phys. Fluids, **18**, pp. 114101.

Benjamin D. Bellows[1]
School of Aerospace Engineering,
Georgia Institute of Technology,
Atlanta, GA 30332-0150,
and
Senior Aerothermal Engineer,
Pratt & Whitney Military Engines,
400 Main Street, M/S 184-28,
East Hartford, CT 06108
e-mail: benjamin.bellows@pw.utc.com

Mohan K. Bobba

Jerry M. Seitzman

Tim Lieuwen

School of Aerospace Engineering,
Georgia Institute of Technology,
Atlanta, GA 30332-0150

Nonlinear Flame Transfer Function Characteristics in a Swirl-Stabilized Combustor

An understanding of the amplitude dependence of the flame response to acoustic excitation is required in order to predict and/or correlate combustion instability amplitudes. This paper describes an experimental investigation of the nonlinear response of a lean, premixed flame to imposed acoustic oscillations. Detailed measurements of the amplitude dependence of the flame response were obtained at approximately 100 test points, corresponding to different flow rates and forcing frequencies. It is observed that the nonlinear flame response can exhibit a variety of behaviors, both in the shape of the response curve and the forcing amplitude at which nonlinearity is first observed. The phase between the flow oscillation and heat release is also seen to have substantial amplitude dependence. The nonlinear flame dynamics appear to be governed by different mechanisms in different frequency and flowrate regimes. These mechanisms were investigated using phase-locked, two- dimensional OH Planar laser-induced fluorescence imaging. From these images, two mechanisms, vortex rollup and unsteady flame liftoff, are identified as important in the saturation of the flame's response to large velocity oscillations. Both mechanisms appear to reduce the flame's area and thus its response at these high levels of driving.
[DOI: 10.1115/1.2720545]

Introduction

This paper describes an experimental investigation of the flame transfer function between flow disturbances and heat release oscillations in a lean, premixed combustor. This research effort is motivated by the fact that modern gas turbines, operating fuel lean to minimize exhaust emissions, are susceptible to self-excited combustion oscillations [1,2]. These instabilities generally occur when the unsteady combustion process couples with the acoustic modes of the combustion chamber. The resultant flow and structural vibrations can substantially reduce hot section part life. As such, avoiding operating regimes where high dynamics occur often requires operating at lower power outputs and/or higher pollutant emissions than the turbine is otherwise capable.

Developing rational capabilities for controlling combustion driven oscillations requires a thorough understanding of the flame's linear and nonlinear dynamics [3,4]. To illustrate, consider an acoustic disturbance with some amplitude, A. Referring to Fig. 1, note that this disturbance amplitude stays the same, decreases, or increases depending upon the relative magnitudes of the driving, $H(A)$, and damping, $D(A)$, processes; i.e., whether $H(A)=D(A)$, $H(A)<D(A)$, or $H(A)>D(A)$, respectively. Linear combustor processes generally control the balance between driving and damping processes at low amplitudes of oscillation and, thus, determine the frequency and growth rate of inherent disturbances in the combustor. Nonlinear combustor processes control the finite amplitude dynamics of the oscillations. Therefore, predicting the limit cycle amplitude of self-excited oscillations requires an understanding of the nonlinear characteristics of $H(A)$ and $D(A)$. To illustrate, Fig. 1 depicts a situation where $H(A)$ saturates and $D(A)$ remains linear, so that the two curves cross at the limit cycle amplitude, A_{LC}.

The key objective of this work is to determine the shape and parametric dependence of this driving curve, $H(A)$, upon amplitude. While studies to date suggest that the driving curve, $H(A)$ has the form shown in this figure [1,4–7], its dependence upon combustor geometry and disturbance parameters (e.g., frequency and flame shape) is poorly understood. Furthermore, the mechanism(s) responsible for these combustion process nonlinearities are largely unknown. Several theoretical studies have proposed nonlinear models based on local/global extinction of the flame [4,8], nonlinear boundary conditions [5], equivalence ratio perturbations [9], and flame front kinematics [10]. There are few experimental efforts, however, which have characterized the nonlinear flame response to flow perturbations or determined the validity/existence of these proposed nonlinear mechanisms [6,7,11–13]. These studies are summarized next.

Bellows et al. [6] and Kulsheimer and Buchner [12] attempted to quantify the nonlinear acoustic/heat release transfer function in turbulent, swirling flames by simultaneously measuring the pressure, velocity, and radical chemiluminescence over a range of disturbance amplitudes, driving frequencies and equivalence ratios. Bellows et al. [12] found that this relationship was linear for velocity amplitudes below ~20% of the mean velocity. At higher forcing levels, they found that the heat release oscillation amplitude began to saturate at $CH^{*\prime}/CH^{*}_{o}$ values of ~30–40%. Similar results were reported by Lee and Santavicca [1] and Balachandran et al. [7]. In a followup paper, Bellows and Lieuwen [14] concluded that the saturation mechanism was the presence of the so-called parametric instability, which is due to an instability of the flame front due to the oscillatory acceleration field imposed on the density jump across the flame.

While these studies confirmed the basic saturating characteristics of the flame response to perturbations, the underlying mechanism for saturation was not fully explored, primarily due to the fact that they focused on global flame characteristics, such as chemiluminescence, making it difficult to determine what the flame is actually doing. While a number of higher fidelity optical observations of the flame dynamics in unstable combustors have been reported [1,7,11,15–17], few have actually systematically measured the flame response as a function of amplitude. Baillot and co-workers [11,13] qualitatively discussed the change in

[1]Corresponding author.

Contributed by the International Gas Turbine Institute of ASME for publication in the JOURNAL OF ENGINEERING FOR GAS TURBINES AND POWER. Manuscript received November 10, 2006; final manuscript received December 22, 2006. Review conducted by Dilip R Ballal. Paper presented at the ASME Turbo Expo 2006; Land, Sea and Air (GT2006), Barcelona, Spain, May 8–11, 2006. Paper No. GT2006-91119.

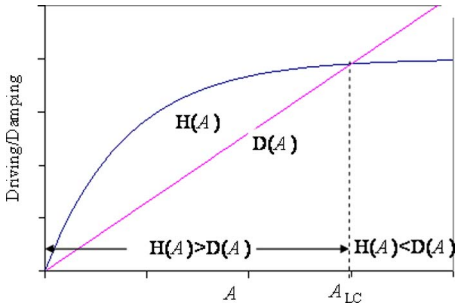

Fig. 1 Qualitative description of the dependence of acoustic driving, $H(A)$, and damping, $D(A)$, processes upon amplitude of oscillation, A

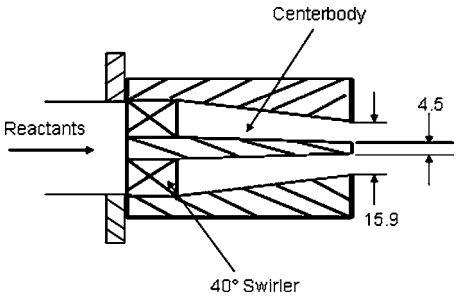

Fig. 3 Schematic of nozzle; all dimensions are in mm (not to scale)

flame shape/structure to imposed velocity oscillations for a laminar, Bunsen flame over a large range of driving frequencies and driving amplitudes. In addition, Balachandran et al. in a recent experimental work investigated the nonlinear transfer function and determined the flame response through simultaneous $OH-CH_2O$ planar laser-induced fluorescence (PLIF) imaging in a nonswirling, bluff-body burner [7]. They concluded that the rollup of the flame sheet by vortices forced by the acoustic disturbances played an important role in the saturation of the transfer function.

The objective of the present work is twofold: first, to systematically characterize the nonlinear flame response over a much larger parameter range than looked at previously, in order to elucidate the types of nonlinear flame responses and the key parametric sensitivities. Second, to perform detailed optical visualizations of the flame at a few selected points in order to better understand the flame processes controlling its nonlinear response.

Instrumentation and Experimental Facility

Experiments were performed on an atmospheric, swirl-stabilized burner, schematically shown in Fig. 2, which was operated at 10–20 KW. All tests were performed at a fixed equivalence ratio of 0.8. The flow rate regime investigated ranged from Reynolds numbers of $Re_D=21{,}000-43{,}000$ (based on premixer hydraulic diameter at exit plane) corresponding to average premixer exit plane velocities of 22–44 m/s. Reactant inlet temperatures were kept constant at room temperature.

Natural gas and air are supplied from building facilities, whose flow rates are measured with rotameters. In order to ensure that acoustic oscillations do not affect fuel/air mixing processes, the air and fuel are introduced upstream of a choke point. Thus, the equivalence ratio of the reactive mixture entering the flame is essentially constant. This was done because of the sensitivity of the flame chemiluminescence levels to both heat release rate and equivalence ratio [1].

The mixture goes through the nozzle, consisting of a 40 deg swirler and an annular passage, see Fig. 3. The flow expands into a cylindrical 70 mm i.d. and 190-mm-long quartz tube combustion chamber. Pressure oscillations are measured with Model 211B5 Kistler pressure transducers mounted downstream of the swirl vanes, located 5.85 cm and 7 cm upstream of the flame holder, respectively. Velocity oscillations are calculated using the two microphone method, outlined in, e.g., Ref. [18]. These results were checked with direct velocity measurements using a hot-wire anemometer in cold-flow conditions.

The relative magnitude of the combustion heat release oscillations are obtained by measuring the global CH^* and OH^* chemiluminescence with photomultipliers fitted with a 10 nm bandwidth filter centered at 430 nm and 310 nm, respectively. The fiber optic is installed downstream of the flame zone at an angle such that it is allowed to "view" the entire combustion zone. For the results presented in this paper, the normalized chemiluminescence measured by the photomultipliers is nearly identical. Thus CH^* chemiluminescence results will be shown for the remainder of the paper. Oscillations are driven in the combustor by two loudspeakers mounted into the 5.5-cm-diameter inlet section.

In order to observe the flame, OH planar laser-induced fluorescence (PLIF) was utilized to obtain a two-dimensional image of the flame. Figure 4 shows the layout of the laser diagnostic facility used in the present study. The laser system consists of a cluster of an Nd:YAG laser, a dye laser, and a high-resolution inductively charge coupled device (ICCD) camera. For OH PLIF, the frequency-doubled output from the dye laser was tuned near 281.4 nm to pump the R1(9) transition of the $A^1\Sigma-X^2\Pi(1,0)$

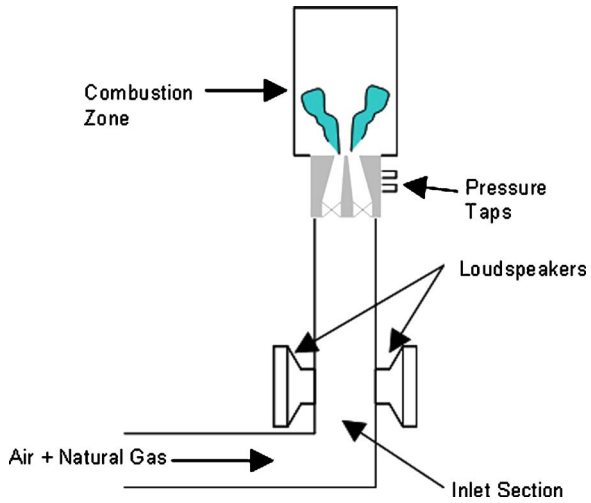

Fig. 2 Schematic of swirl-stabilized combustor

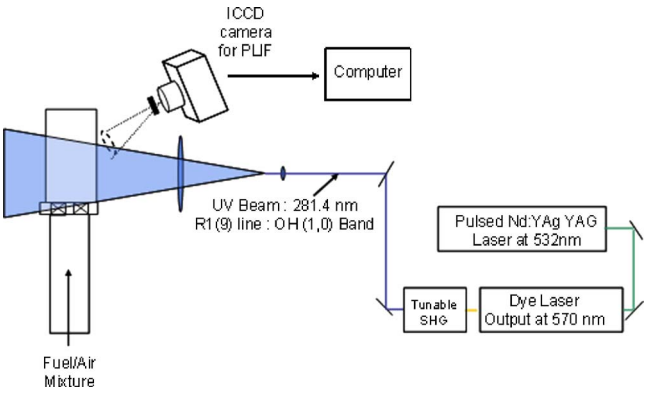

Fig. 4 Schematic of laser setup for OH PLIF imaging

band. OH fluorescence integrated over a wave number range of 300–380 nm is captured by the ICCD camera through both a WG-305 and UG-11 Schott glass filter.

The laser imaging was phase locked with the driving signal input to the loudspeakers. The frequency of image acquisition is limited by the frequency of the Nd:YAG laser which operates at 10 Hz. Therefore, since the frequencies of interest in this study are much greater than this value, successive phase-locked images were actually obtained several cycles apart from each other. Then, the flame response over a sequence of phase angles is reconstructed over different phases and different cycles. The acoustic cycle was divided into eight phases, with 200 images taken at each phase angle. The OH PLIF intensity images were corrected for background noise and also for beam profile inhomogeneities. These images were then filtered with a 3 pixel width Gaussian filter.

Results and Discussion

Parametric Characterization of Nonlinear Flame Transfer Function. Results were obtained by externally driving oscillations in the combustor with varying amplitude at a fixed frequency. Simultaneous measurements of pressure, velocity, and chemiluminescence were taken. For all cases, the combustor was quite stable in the absence of driving.

A typical transfer function between simultaneously measured CH^* chemiluminescence and velocity oscillations is shown in Fig. 5(*a*) at a Reynolds number of 21,000 and equivalence ratio of 0.8. For low forcing amplitudes, Fig. 5 shows that the CH^* chemiluminescence increases with perturbation amplitude in a linear manner. At large velocity amplitudes, the CH^* chemiluminescence saturates at values of $CH^{*\prime}/CH^*_o$ of ~0.45. These velocity and CH^* values where saturation occurs are consistent with our previous work [6]. This result indicates that "global extinction" where oscillating heat release amplitudes reach 100% of the mean, proposed theoretically by Dowling [4], is not an important mechanism at this condition. Figure 5(*b*) presents the corresponding $u'-CH^{*\prime}$ phase relationship. The phase relationship exhibits a complex amplitude dependence on the amplitude of velocity oscillations. First, the phase angle changes by nearly 50 deg over the $u'/u_0 < 0.4$ range, where the transfer function remains linear. The sharp decrease in phase angle at $u'/u_0 \sim 0.45$ occurs after the $CH^{*\prime}/CH^*_o$ value saturates.

Figure 6(*a*) presents transfer function results for driving frequencies between 130 and 150 Hz at a Reynolds number of 21,000. Figure 6 illustrates that the transfer function at 130 Hz and 140 Hz remains linear up to $CH^{*\prime}/CH^*_o$ values near 0.95 before saturating. Thus, the saturation amplitude here is substantially higher than that in Fig. 5, illustrating the substantial dependence of saturation amplitude upon flow conditions and disturbance frequency. Note that the saturation amplitude here is quite close to 100%, suggesting a "global extinction" type mechanism as proposed by Dowling [4].

Figure 6(*b*) presents the corresponding $u'-CH^{*\prime}$ phase. Similar to the comparison between the saturation amplitudes between the cases at 210 Hz and 130 Hz, the phase angle shapes for these two frequencies are also quite different. The phase angle at these frequencies exhibits significant amplitude dependence at velocity oscillation amplitudes where the gain of the transfer function remains in the linear regime. This is consistent with our previous results [6]. The phase angle is seen to remain almost constant as well, around 85–90 deg, over nearly 50% of the velocity amplitude range.

Both Figs. 5 and 6 illustrate typical shapes of transfer functions that have been observed experimentally and proposed theoretically. For low velocity amplitudes, the corresponding heat release oscillations increase linearly. At the largest velocity amplitudes, the heat release fluctuations saturate. However, more complex amplitude dependencies were observed at other conditions. Figure 7

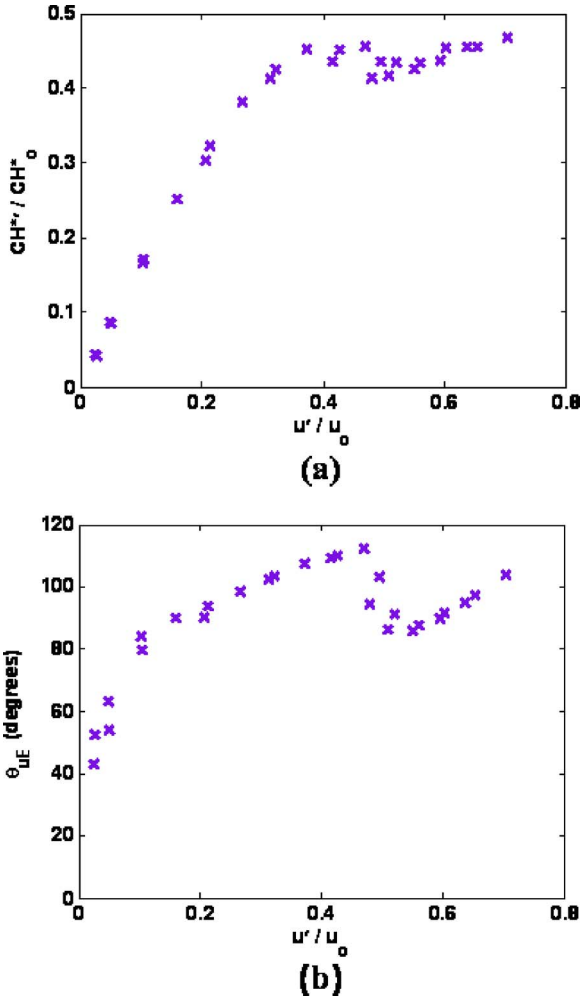

Fig. 5 Dependence of: (*a*) CH^* oscillation amplitude; and (*b*) $u'-CH^{*\prime}$ phase angle upon velocity oscillation amplitude (f_{drive} =210 Hz, ϕ=0.80 Re_D=21,000). CH^* saturation amplitude=0.45. Uncertainty in phase angle <5 deg.

shows two such cases, obtained at 340 Hz and 410 Hz, respectively. Both curves show that the CH^* chemiluminescence increases linearly with increasing velocity oscillation amplitudes at low values of driving. At 340 Hz, the CH^* oscillation amplitude begins to saturate at values around 0.65–0.7 of the mean value. However, instead of remaining nearly constant, with further increases in excitation amplitude the response increases again.

In a similar manner, for 410 Hz, Fig. 7 shows that the transfer function begins to saturate at a $CH^{*\prime}/CH^*_o$ value of 0.35. Similar to the 340 Hz case, the flame response begins to increase again before saturating again at $CH^{*\prime}/CH^*_o$, value of nearly 0.6. This trend is similar to the experimental results of Balachandran et al. for a bluff-body stabilized flame without swirl [7]. The phase (not shown) remains nearly constant over this amplitude range.

Even more complex behavior was observed at other conditions. Figure 8 presents the $u'-CH^{*\prime}$ transfer function for 160–180 Hz at a Reynolds number of 30,000 and equivalence ratio=0.8. For these three cases, after an initial linear increase in heat release oscillations, there is a sharp decrease in these values, followed by an increase. This sharp decrease in the gain of the transfer function is also manifested in the corresponding phase between the velocity and chemiluminescence oscillations. Figure 8(*b*) shows the phase angle at f_{drive}=170 Hz drops considerably (over 100 deg) between normalized velocity oscillation amplitudes of

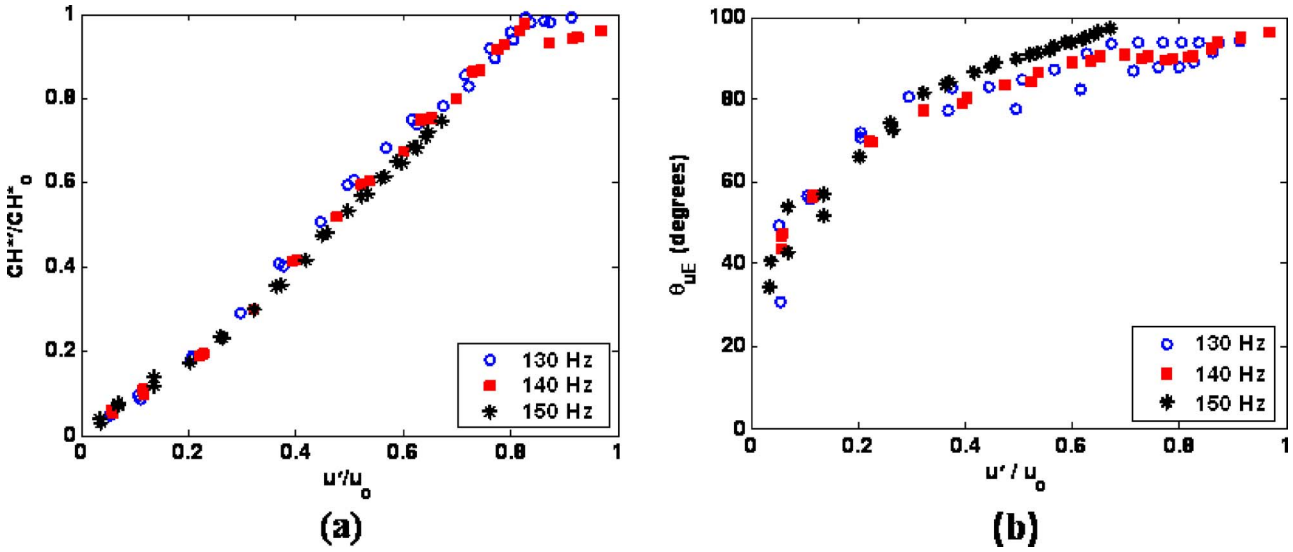

Fig. 6 Dependence of: (*a*) CH* oscillation amplitude; and (*b*) $u'-CH^{*\prime}$ phase angle upon velocity oscillation amplitude, $\phi=0.80, Re_D=21{,}000$. CH* saturation amplitude ~0.98. Uncertainty in phase angle <5 deg.

0.1 and 0.2. After this drop, the phase angle remains constant around 80 deg, at similar values as the 130–150 Hz cases shown in Fig. 6.

Analysis of the various spectra indicates that although the flame response at the driving frequency decreases with amplitude, the flame response at the first harmonic grows. Figure 9 presents the Fourier transform of the chemiluminescence and one pressure transducer for two cases: at the local maximum in the transfer function and the local minimum in the transfer function (circled in Fig. 8). Comparing the two chemiluminescence spectra, it is clear that the dominant flame response frequency shifts from the fundamental frequency to the first harmonic with an increase in driving from 10% velocity oscillation to 20% velocity oscillation. The pressure and velocity spectra, on the other hand, always show a response at the fundamental that increases with driving. Therefore, the response of the flame at the driving frequency goes to zero since the only response is at the first harmonic. Similar behavior has also been reported in bluff-body flames by Balachandran et al. [7].

One of the key conclusions we drew from this parametric study was that the flame response characteristics are more varied and

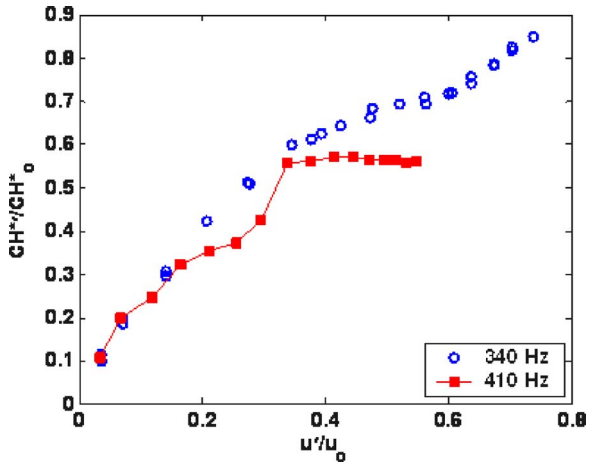

Fig. 7 Dependence of CH* oscillation amplitude upon amplitude of velocity oscillations for two driving frequencies ($Re_D=21{,}000, \phi=0.80$)

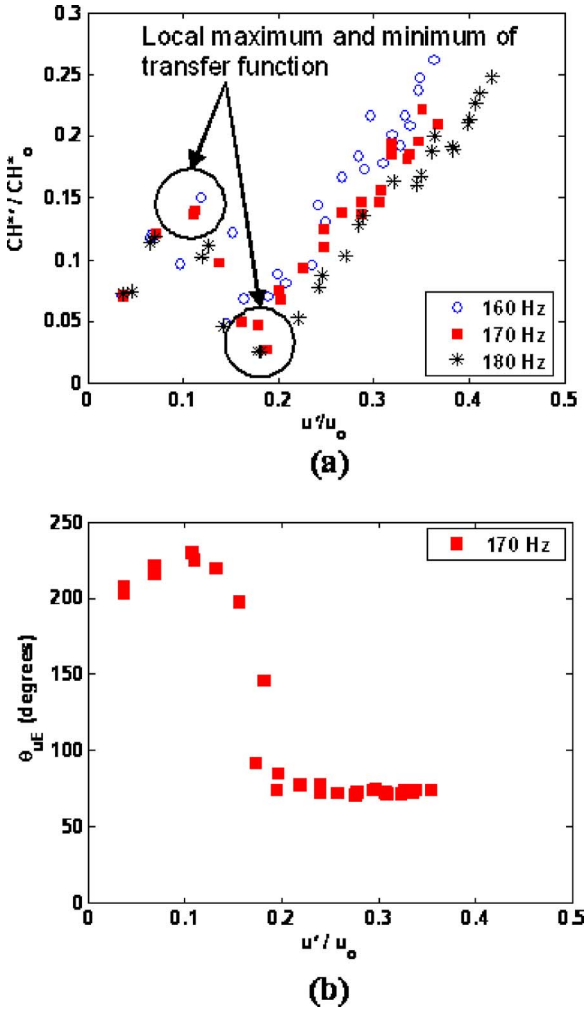

Fig. 8 (*a*) Dependence of CH* oscillation amplitude upon amplitude of velocity oscillations for $f_{drive}=160-180$ Hz; (*b*) dependence of $u'-CH^{*\prime}$ phase angle upon velocity oscillation amplitude for $f_{drive}=170$ Hz. ($Re_D=30{,}000$, $\phi=0.80$)

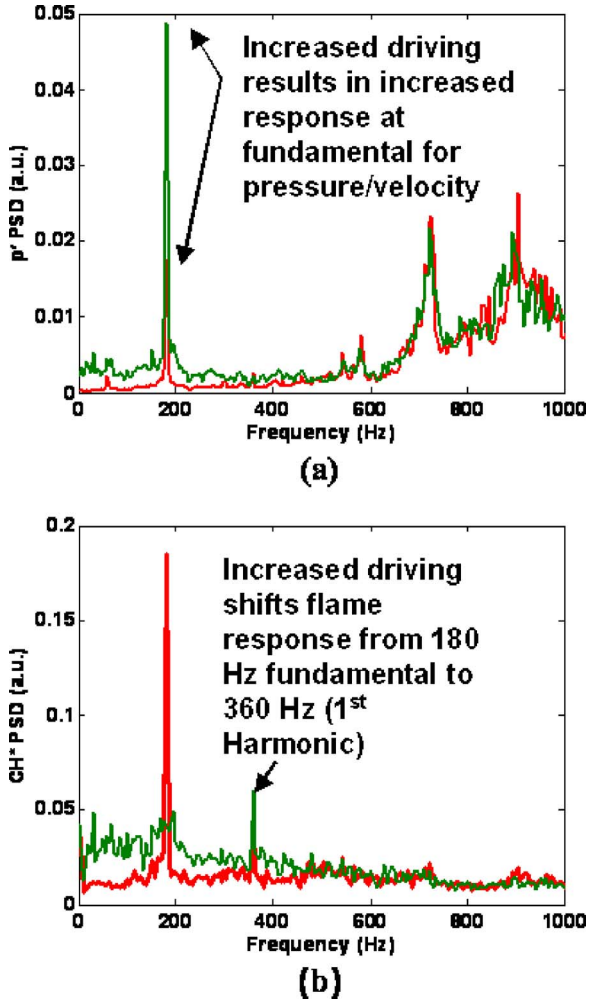

Fig. 9 Fourier transforms of: (*a*) pressure; and (*b*) CH* chemiluminescence signals at local maximum of transfer function and local minimum of transfer function for f_{drive}=180 Hz (Re_D=30,000, ϕ=0.80)

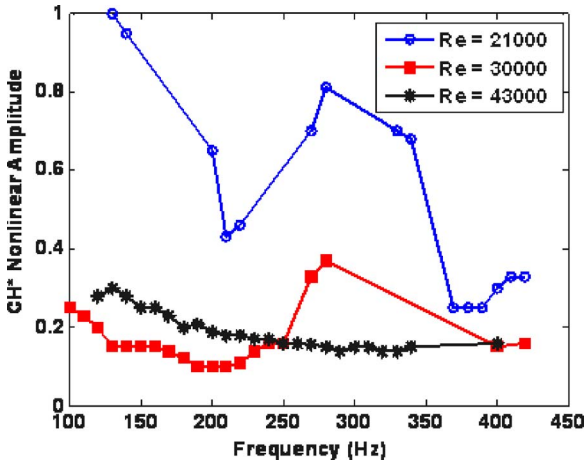

Fig. 10 Dependence of CH* nonlinear amplitude on driving frequency as a function of Reynolds number (ϕ=0.80)

complex than a simple linear response regime followed by a saturation regime. However, one of our goals for the study was to parameterize the dependence of saturation amplitude upon operating conditions, frequencies, etc. In order to compile all the results into one graph, we determined the chemiluminescence amplitude at which nonlinearity in the flame response becomes evident, see Fig. 10. This amplitude was defined as the point where the transfer function deviates from its linear value by more than 10–20%. The lower limit is set for cases such as those in Fig. 6, where saturation occurs at nearly 100% of the mean chemiluminescence value. The upper limit is set for saturation/nonlinear behaviors that occur at values much less than 100% of the mean, e.g., Figs. 7 and 8.

At the lowest flow rate, Fig. 10 indicates that the saturation amplitude varies with frequency by a factor of almost five. This frequency sensitivity is diminished at the higher flow rates. At the highest Reynolds number, the saturation amplitude is nearly constant over the frequency range investigated. Saturation at 100% chemiluminescence is only seen for the lowest flow rate. The results presented indicate that a variety of nonlinear behaviors can exist in a single combustor.

Imaging of Flame Under Large Amplitude Forcing. During this parametric study it was sometimes observed that the flame visibly changed in structure at the point where the transfer function saturates (e.g., f_{drive}=210 Hz and 410 Hz); however, this was not necessarily the case in all situations (e.g., f_{drive}=130 Hz). High-speed line of sight images of the flame confirmed this observation, as shown in Fig. 11, which shows images of the flame at two different driving amplitudes, corresponding to before and after saturation of the transfer function in Fig. 7. These sequences of images were obtained by phase locking an ICCD high-speed camera to the input driving signal. The phase angles shown are with respect to the driven velocity oscillations. The viewing area is 70 mm×70 mm. A BG-38 Schott glass filter was placed in front of the ICCD camera to eliminate wavelengths of light above ~700 nm.

Figure 11(*a*) shows the line-of-sight view of the flame at a low velocity amplitude (u'/u_0=0.2) where the transfer function remains linear in Fig. 7. At this low amplitude of oscillation, the flame has a well-defined stabilization point throughout the cycle. In contrast, Fig. 11(*b*) shows the line-of-sight view of the flame at a velocity amplitude (u'/u_0=0.6) where the flame transfer func-

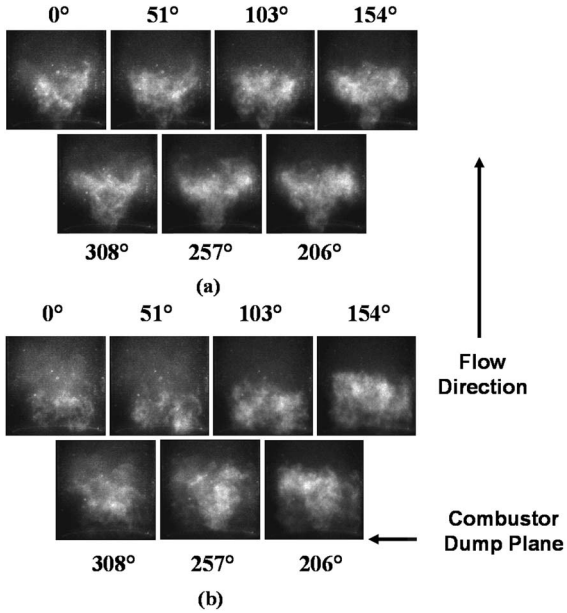

Fig. 11 Phase-locked instantaneous line-of-sight images of flame over one cycle of acoustic forcing for: (*a*) low (linear, u'/u_0=0.2); and (*b*) high (nonlinear, u'/u_0=0.6) amplitude of oscillation (f_{drive}=410 Hz, Re_D=21,000, ϕ=0.80)

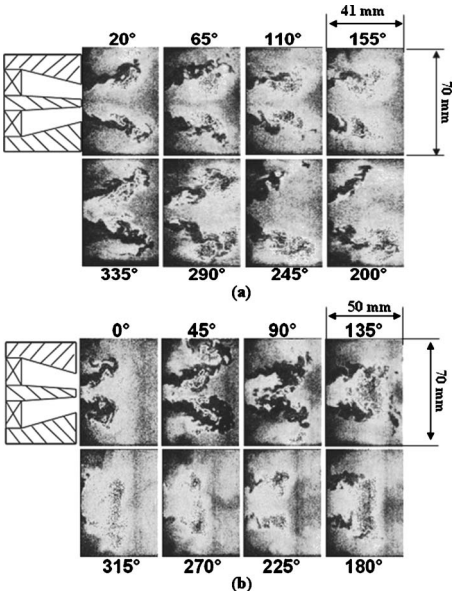

Fig. 12 Instantaneous OH PLIF images showing evolution of flame response over one cycle of acoustic forcing for: (*a*) low (linear, $u'/u_0=0.3$); and (*b*) high (nonlinear, $u'/u_0=0.9$) velocity oscillation amplitudes ($f_{drive}=130$ Hz, $Re_D=21{,}000$, $\phi=0.80$)

tion has saturated. In these images, the flame no longer extends from its stabilization point downstream of the centerbody, as shown in Fig. 11(*a*). Instead, the flame has no discernable structure. This behavior begins to occur exactly at the point of saturation (e.g., $u'/u_o=0.35$ in Fig. 7).

Since similar flame behavior seen in Fig. 11 for 410 Hz was not observed for 130 Hz, we will concentrate on these two results for the remainder of the paper. In an effort to further investigate some of the potential mechanisms controlling the nonlinear flame dynamics, we performed extensive OH-PLIF studies at these two driving frequencies.

We should emphasize two key limitations associated with interpreting these images. First, the flow is highly three dimensional, so that flame structures come in and out of the images. Second, "consecutive" images are not truly consecutive, as they were taken several cycles apart—thus, one should only attempt to infer global flow features, and not try to track the evolution of a particular flow feature from image to image.

Figure 12(*a*) presents instantaneous OH PLIF images for the 130 Hz case at a low velocity oscillation amplitude ($u'/u_0=0.3$). Here the heat release is in the linear response regime. The images obtained are phase locked to the driving signal, but the phase angles presented in these figures are with respect to the velocity oscillations calculated from the two microphone method. These figures indicate that the flame is anchored on the centerbody throughout the cycle. The oscillating velocity is evident, as the flame moves back and forth throughout the cycle; in some images, the presence of convecting flow structures are perhaps evident.

Figure 12(*b*) shows the corresponding flame response for high velocity oscillations ($u'/u_0=0.9$); at this level of driving, the instantaneous flow velocity oscillates between 2 m/s and 42 m/s throughout the cycle. Thus it oscillates between nearly reversing itself to a very high speed jet. At the velocity minimum the turbulent flame speed is on the same order as the local velocity value and the flame propagates toward the nozzle. The flame, however, does not flash back into the nozzle, but remains just outside the nozzle exit. At the point of highest flow velocity and maximum flame length, the clear rollup of the flame into the central recirculation zone is evident, see 45 deg and 90 deg.

The rapid reduction in flame area associated with this rollup,

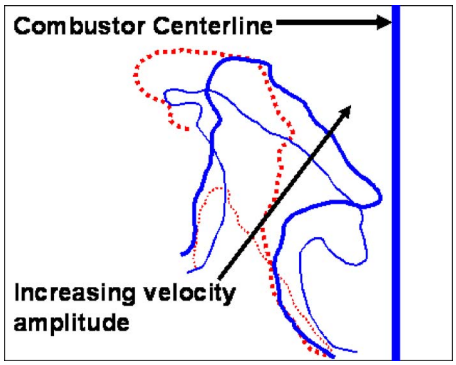

Fig. 13 Averaged flame edges at 65–110 deg phase angle at four velocity oscillation amplitudes ($f_{drive}=130$ Hz, $u'/u_0=0.3$, 0.6, 0.83, and 0.90). Dashed (- - -)/ solid (—) lines indicate peak flame response when transfer function is linear/saturated, respectively

and the subsequent flame propagation and rapid reduction in flame area, is the mechanism causing saturation of the flame response. This explains why rollup is first observed roughly at the point where the CH^* chemiluminescence saturates, at $u'/u_0\sim0.8$ in Fig. 6. This is the same observation of Balachandran et al. in a nonswirling flame [7]. Due to rollup, the flame area is very rapidly reduced, due to flame propagation normal to itself.

Also, note that the flame remains attached throughout the cycle, even at the highest amplitudes, in contrast to the 410 Hz result shown next. In addition, the flame front is substantially more corrugated at the point of highest jet velocity, 90 deg, relative to lower velocity points. These images suggest that the turbulent flame speed is modulated through the cycle.

This flame rollup can be further seen in Fig. 13 which illustrates the manner in which the flame response at the point of its maximum downstream displacement varies with disturbance amplitude. The dashed lines indicate the average flame front location (obtained by averaging all the images at this particular phase and using a gradient method to extract an edge) at excitation amplitudes where the transfer function remains linear, $u'/u_0=0.3$ and 0.6. These curves show that the downstream flame displacement increases with perturbation amplitude, but with a similar shape. In contrast, the solid lines show average flame front locations at excitation amplitudes near and beyond the point where saturation in flame response occurs, $u'/u_0=0.83$ and 0.9. Here the downstream displacement of the flame position clearly stops growing with perturbation amplitude. Instead, the reactants roll up into the central recirculation zone, causing a more rapid reduction in flame surface area relative to the lower amplitude cases due to flame propagation normal to itself.

Consider next the 410 Hz results. Recall from Fig. 7 that saturation occurred well below 100% CH^* chemiluminescence amplitude. Figure 14(*a*) shows the flame response at a low velocity amplitude ($u'/u_0=0.2$) for 410 Hz. Similar to the 130 Hz in Fig. 14(*a*) and inferred from Fig. 11, the flame is stabilized at the centerbody of the premixer. The flame increases in length and shows increased wrinkling at the peak of the cycle. Figure 14(*b*) illustrates the flame response at a high-velocity oscillation amplitude ($u'/u_0=0.6$), where the flame exhibits a very different behavior from the 130 Hz results. First, at all eight phases, the flame is clearly lifted off the centerbody and appears to be stabilized near the stagnation point in a low velocity region, as also shown in the direct flame images in Fig. 11. Only at one small part of the cycle, 45–90 deg, can the flame be seen attempting to stabilize itself on the centerbody.

The liftoff of the flame from the centerbody with increasing excitation amplitude can be seen from Fig. 15. Similar to Fig. 13, dashed lines indicate the flame front where the transfer function is

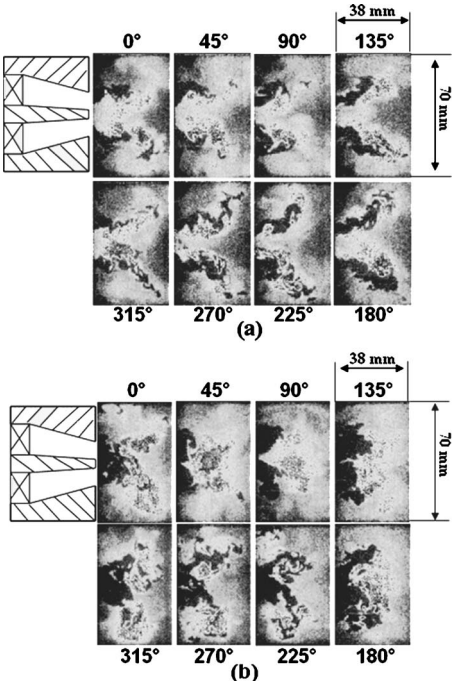

Fig. 14 Instantaneous OH PLIF images showing evolution of flame response over one cycle of acoustic forcing for: (*a*) low (linear, $u'/u_0=0.2$); and (*b*) high (nonlinear, $u'/u_0=0.6$) velocity oscillation amplitudes ($f_{drive}=410$ Hz, $Re_D=21{,}000$, $\phi=0.80$)

linear ($u'/u_0=0.2,0.3$) and the solid lines indicates peak response flame edges near and beyond the saturation point of the transfer function ($u'/u_0=0.53,0.6$). The plot clearly shows the transition of the stabilization point of the flame from the centerbody to a point downstream with increasing disturbance amplitude.

Since the flame is lifted off, the two flames that are present in the linear regime are merged together into one flame—it can be seen that the flame area is lower than it would be if the flame were attached. This unsteady liftoff, and consequent reduction in flame area, is the mechanism of nonlinearity for this case. It is first observed in the images at u'/u_0 amplitudes around 0.35; i.e., where the transfer function begins to saturate

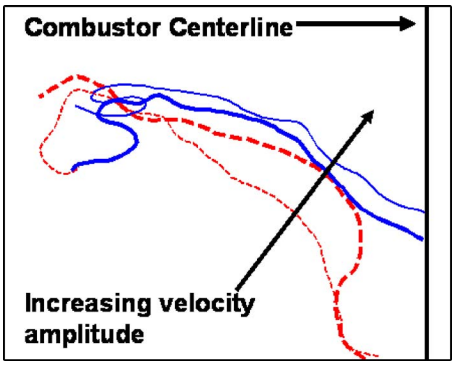

Fig. 15 Average flame edges at 180–225 deg phase angle at four velocity oscillation amplitudes ($f_{drive}=410$ Hz, $u'/u_0=0.2$, 0.3, 0.53, 0.6). Dashed (- - -)/solid (—) lines indicate peak flame response when transfer function is linear/saturated, respectively.

Conclusions

From the results presented, we can make the following conclusions. First, substantial nonlinearities in the flame response to forced velocity oscillations have been shown. The phase between the flow oscillation and heat release is also seen to have substantial amplitude dependence. Various mechanisms appear to be important in different frequency and flowrate regimes. For instance, at low flow rates, the saturation amplitude of CH^* can vary greatly with driving frequency and range from 25% to 100% of the mean value. In contrast, for higher flow rates, it is observed that the nonlinear amplitude of CH^* is roughly independent of driving frequency. In addition, the shape of the transfer function can change markedly for different driving frequencies and flow rates. Therefore, there are a variety of behaviors which are present in a single combustor. Thus, one single theory is not adequate to describe the nonlinear dynamics of a forced or unstable combustor.

OH PLIF imaging of the flame was performed at two frequencies where two mechanisms potentially controlled the saturation amplitude of the global heat release from the flame. Two phenomena, vortex rollup and flame liftoff, are found to be the key mechanisms which govern saturation of the flame transfer function from these images. The latter mechanism visibly changes the flame structure when comparing these results with line-of-sight images. Both mechanisms act to reduce the flame area.

No subharmonic flame response was observed in any of these studies, as opposed to our earlier study in another combustor. This result is not understood, as it is well known that parametric flame instabilities occur at high forcing amplitudes, resulting in a subharmonic response [13,14]. Future work will attempt to reconcile these differing observations.

Acknowledgment

This paper was prepared with the support of the US Department of Energy, Office of Fossil Energy, National Energy Technology Laboratory, under Contract NO. 02-01-SR095 (Dr. Richard Wenglarz, contract monitor). Any opinions, findings, conclusions, or recommendations included herein are those of the authors and do not necessarily reflect the views of the DOE.

References

[1] Lee, J., and Santavicca, D., 2003, "Experimental Diagnostics for the Study of Combustion Instabilities in Lean Premixed Combustors," J. Propul. Power, **19**(5), pp. 735–750.
[2] Richards, G., Straub, D., and Robey, E., 2003, "Passive Control of Combustion Dynamics in Stationary Gas Turbines," J. Propul. Power, **19**(5), pp. 795–810.
[3] Lieuwen, T., 2002, "Experimental Investigation of Limit Cycle Oscillations in an Unstable Gas Turbine Combustor," J. Propul. Power, **18**(1), pp. 61–67.
[4] Dowling, A. P., 1997, "Nonlinear Self-Excited Oscillations of a Ducted Flame," J. Fluid Mech., **346**, pp. 271–290.
[5] Dowling, A. P., 1999, "A Kinematic Model of a Ducted Flame," J. Fluid Mech., **394**, pp. 51–72.
[6] Bellows, B. D., Zhang, Q., Neumeier, Y., Lieuwen, T., and Zinn, B. T., 2003, "Forced Response Studies of a Premixed Flame to Flow Disturbances in a Gas Turbine Combustor," AIAA Paper No. #2003-0824.
[7] Balachandran, R., Ayoola, B. O., Kaminski, C. F., Dowling, A. P., and Mastorakos, E., 2005, "Experimental Investigation of the Nonlinear Response of Turbulent Premixed Flames to Imposed Inlet Velocity Oscillations," Combust. Flame, **143**, pp. 37–55.
[8] Poinsot, T., Veynante, D., Bourienne, F., Candel, S., Esposito, E., and Surget, J., 1988, "Initiation and Suppression of Combustion Instabilities," Proc. Combust. Inst., **22**, pp. 1363–1370.
[9] Peracchio, A. A., and Proscia, W. M., 1999, "Nonlinear Heat-Release/Acoustic Model for Thermoacoustic Instability in Lean Premixed Combustors," J. Eng. Gas Turbines Power, **121**, pp. 415–421.
[10] Baillot, F., Durox, D., and Prud'homme, R., 1992, "Experimental and Theoretical Study of a Premixed Vibrating Flame," Combust. Flame, **88**, pp. 149–168.
[11] Durox, D., Baillot, F., Searby, G., and Boyer, L., 1997, "On the Shape of Flames Under Strong Acoustic Forcing: A Mean Flow Controlled by an

Oscillating Flow," J. Fluid Mech., **350**, pp. 295–310.
[12] Kulsheimer, C., and Buchner, H., 2002, "Combustion Dynamics of Turbulent, Swirling Flows," Combust. Flame, **131**, pp. 70–84.
[13] Bourehla, A., and Baillot, F., 1998, "Appearance and Stability of a Laminar Conical Premixed Flame Subjected to an Acoustic Perturbation," Combust. Flame, **114**, pp. 303–318.
[14] Bellows, B. D., and Lieuwen, T., 2004, "Nonlinear Heat Release-Acoustic Interactions in a Gas Turbine Combustor," ASME Paper No. GT2004-53480.
[15] Durox, D., Schuller, T., and Candel, S., 2002, "Self-Induced Instability of a Premixed Jet Flame Impinging on a Plate," Proc. Combust. Inst., **29**, pp. 69–75.
[16] Lee, S.-Y., Seo, S., Broad, J. C., Pal, P., and Santoro, R. J., 2000, "An Experimental Estimation of Mean Reaction Rate and Flame Structure During Combustion Instability in a Lean Premixed Gas Turbine Combustor," Proc. Combust. Inst., **28**, pp. 775–782.
[17] Santhanam, V., Knopf, F. C., Acharya, S., and Gutmark, E., 2002, "Flourescence and Temperature Measurements in an Actively Forced Swirl-Stabilized Spray Combustor," J. Propul. Power, **18**, pp. 855–865.
[18] Abom, M., and Boden, H., 1988, "Error Analysis of Two-Microphone Method in Ducts With Flow," J. Acoust. Soc. Am., **83**(6), pp. 2429–2438.

Randal T. Rausch[1]
e-mail: rausch@research.ge.com

Kai F. Goebel
e-mail: goebel@email.arc.nasa.gov

Neil H. Eklund
e-mail: eklund@research.ge.com

Brent J. Brunell
e-mail: brunelbr@research.ge.com

GE Global Research,
1 Research Circle,
Niskayuna, NY 12309

Integrated in-Flight Fault Detection and Accommodation: A Model-Based Study

In-flight fault accommodation of safety-critical faults requires rapid detection and remediation. Indeed, for a class of safety-critical faults, detection within a millisecond range is imperative to allow accommodation in time to avert undesired engine behavior. We address these issues with an integrated detection and accommodation scheme. This scheme comprises model-based detection, a bank of binary classifiers, and an accommodation module. The latter biases control signals with pre-defined adjustments to regain operability while staying within established safety limits. The adjustments were developed using evolutionary algorithms to identify optimal biases off-line for multiple faults and points within the flight envelope. These biases are interpolated online for the current flight conditions. High-fidelity simulation results are presented showing accommodation applied to a high-pressure compressor fault on a commercial, high-bypass, twin-spool, turbofan engine throughout the flight envelope. [DOI: 10.1115/1.2720517]

1 Introduction

Faults affecting aircraft safety must be detected quickly to avoid undesired events such as engine surge/stall events, power loss, severe vibrations, and loss of thrust control. These events, in addition to inappropriate crew response, may lead to accidents [1]. To reduce the number of accidents, NASA established the Aviation Safety Program [2]. Within the scope of that program, this paper investigates a number of faults for which in-flight accommodation is considered.

The goal of a fault accommodation system is to regain operability and maintain commanded thrust after a fault has been detected by biasing aircraft control signals. Aircraft controllers are highly sophisticated systems with strict safety limits based on that many years of design experience. To stay within these safety confines, the control signal biases are limited to established bounds.

Figure 1 shows the top-level conceptual architecture for the detection and accommodation methods used. A model-based approach was employed to aid the diagnostics using extended Kalman filter (EKF) techniques with a component level engine model (CLM) featuring nonlinear simulation of a commercial, high-bypass, twin-spool, turbofan engine. The output of the diagnostics triggers the accommodation (actuator control adjustments). The top-level inputs to the system are the pilot input throttle resolver angle (TRA), altitude (ALT), Mach number (XM), delta from ISO standard day ambient temperature (DTAMB), as well as engine variation and health parameters (P). Data were generated for a large set of cases within the flight envelope. For all of the data sets, random variations were added to the process and measurements corresponding to engine-to-engine variation, deterioration, sensor accuracy bias, and sensor noise. The modeling and diagnosis techniques are discussed elsewhere [3] in more detail. This paper will focus primarily on the accommodation. In Sec. 2, we will first briefly introduce the model and detection schemes used, followed by a short discussion of the faults selected. Section 3 discusses fault accommodation; Sec. 4 concludes with a few final remarks.

[1]Corresponding author.

Contributed by the International Gas Turbine Institute of ASME for publication in the JOURNAL OF ENGINEERING FOR GAS TURBINES AND POWER. Manuscript received September 9, 2005; final manuscript received January 4, 2007. Review conducted by Dilip R. Ballal. Paper presented at the ASME Turbo Expo 2005: Land, Sea and Air (GT2005), June 06–09, 2005, Reno, NV. Paper No. GT2005-68300.

2 System Modeling, Detection, and Faults Selected

2.1 Model. For this study, two nonlinear models of an advanced commercial, high-bypass, twin-spool, turbofan engine were used. Both models can be run in a transient or steady state mode. The cycle workstation (CWS) is a high fidelity physics-based aircraft engine model, which acts as the real engine ("truth"). Variation, deterioration, and fault models can be injected into the CWS model. A simplified, physics-based, component level model is used as the embedded model in conjunction with the EKF to aid in fault diagnostics. The CLM takes less time to run and is less accurate than the CWS.

The idea of a model-based approach is to compare the actual plant output to the output estimated from a mathematical model that attempts to mimic the system behavior [4]. An optimal estimate of the state of the model in the presence of process noise, sensor noise, and initial condition mismatch for a nonlinear plant can be created using extended Kalman filtering techniques. The difference between the plant output and the estimated output is the residual. Residuals are used to detect changes in plant behavior: they should be near zero in fault-free case and non-zero when a fault has occurred. The detection process evaluates the residuals and monitors if and where a fault has occurred.

2.2 Source of Variation. In order to realistically represent engine behavior, sources of variation are included as simulation inputs. Specifically, we consider variability between engines, aging, and measurement processes.

2.2.1 Engine-to-Engine Variation. An engine-to-engine variation model was created for the CWS engine model. The engine-to-engine variation accounts for manufacturing and assembly variation found in new engines. These variations can be described or modeled by adding variation to the efficiency adder and flow scalar parameters on the rotating components. The model used for engine-to-engine variation adds a normally distributed random value (based on measurements of a sample of the engine population) to the nominal value of each parameter. The standard deviation of the parameter variation values ranged from 0.0% to 1.1%.

2.2.2 Deterioration. A deterioration model was created for both the CWS and CLM engine models. Some of the known deterioration mechanisms are seal and bushing leakage, clearance increases, and other main or secondary flow leaks. After evaluating analytic engine teardowns, production test data, development

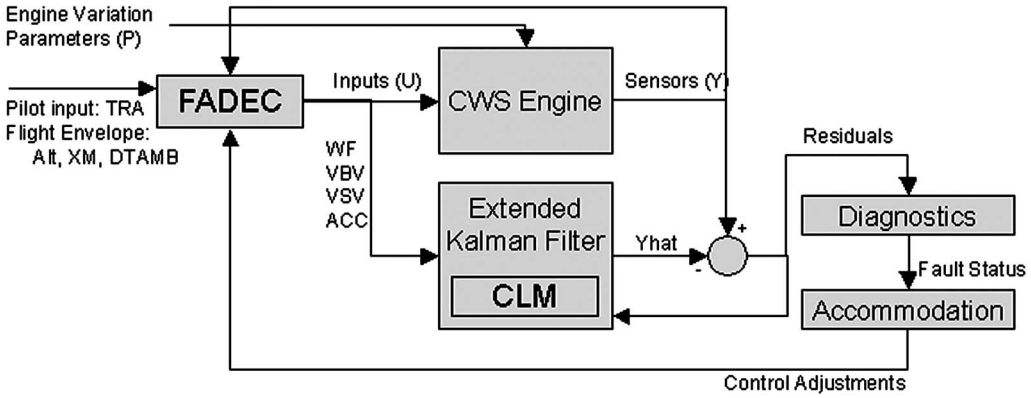

Fig. 1 High-level architecture of detection and accommodation strategy

test data, and overhaul engine findings, it was determined that the rotating component efficiencies and flow parameters, as well as leakage and clearances, are affected by deterioration. The deterioration model used in the CWS engine model is a uniform random distribution from new to fully deteriorated. The process is centered for the CLM engine model by running it only with a 50% deterioration model.

2.2.3 Sensor Accuracy. There are several factors that affect the measurement accuracy of any given sensor. Factors considered here are:

- signal conditioning—accounts for excitation, A/D conversion, filtering,
- sensor bias—accounts for sensor to sensor variation,
- profile error—accounts for radial and circumferential variation in the measured parameters,
- noise—accounts for other noise in the system.

All accuracies are two-sided (±) and modeled as normal distribution with a 2-sigma maximum variation.

2.3 Faults. One of the goals of this project is to create general diagnostic technologies for the different components of an aircraft engine system. To that end, we wanted to select actuator, engine, and sensor faults. We selected the variable stator vanes (actuator), high-pressure compressor and high-pressure turbine damage (engine), and compressor exit pressure (Ps3) sensor as the components that are the most suitable to investigate for this project based on an investigation of an engine events database of the past 20 years of DEC and FADEC controlled engines. The fault block diagram is shown in Fig. 2 and the parameters and magnitudes varied for each fault are given in Table 1.

These faults may have, by definition, safety-averse consequences, such as loss of throttle control, compressor stalls, aborted takeoffs, in-flight shutdowns, etc. It is therefore crucial to overcome these situations through proper accommodation. A prerequisite for accommodation is detection before the negative effects take place. The allowed detection time is based on criticality determined by controls designers. Detection must be completed within a time frame between 106 ms and 1.2 s, depending on the fault type (Table 2).

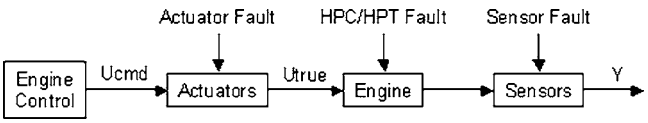

Fig. 2 Fault block diagram

2.4 Diagnostics. Specifications about the false positive and true positive rates (or false negative or true negative rates) guide classifier design. The actual specification is driven by the application and the domain wherein the classifier is executed. For example, it might be extremely undesirable to issue false positives in certain domains, while (even for the same application) it is more important to avoid false negatives in a different domain (e.g., some military versus civilian applications).

Model-based information is the foundation of many diagnostic strategies, ranging from simple thresholding to Kalman filter banks [5]. To maximize the diagnostic information, we add a classifier to the model-based detection. Specifically, we consider here (after an initial of downselect as part of the classifier design step) a support vector machine (SVM) as the classification engine [6,7].

The overall classification approach followed the scheme shown in Fig. 3. Inputs are the flight envelope (FE) data, sensor data, and Kalman filter estimates. After a preliminary variable selection, residuals are computed from which further features are calculated. After a feature selection process, the features are subjected to the classification. The classifiers were trained as binary classifiers using the fault data as one class and the normal and other fault classes as the other class. The last step is the hypothesis test that selects the final fault state.

One of the main distinctions of this study is that results are compiled for faults that can occur at any point in the flight enve-

Table 1 Fault model parameters

		Change from nominal		
Fault type	Model parameter changed	Small fault	Medium fault	Large fault
HPC fault	Efficiency	−1.5%	−3%	−5%
	flow	−1.5%	−3%	−5%
HPT fault	Efficiency	−1.5%	−3%	−5%
	flow	1.5%	3%	5%
VSV fault	Bias	0.8 deg	2.5 deg	5.0 deg
Ps3 fault	Bias	−7 PSI	−19 PSI	−30 PSI

Table 2 Allowed fault detection time

Fault	Allowed detection time
HPC	1.2 s
HPT	1.2 s
VSV	106 ms
Ps3	340 ms

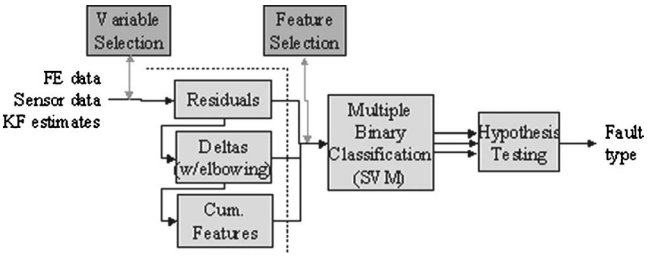

Fig. 3 Fault classification scheme

lope with any level of noise and engine deterioration. With a mandated zero false positive rate (to avoid any inappropriate accommodation), results are as listed in Table 3 that shows the confusion matrix for the output of the maximum likelihood fault selection logic.

All faults are detected at zero false positive levels upward of 90%. Only HPT and HPC faults are misclassified. If accommodation mandates that no misclassifications be made at all, then the results will deteriorate considerably because the particular combination of deterioration, flight envelope, and fault signature are completely overlapping. However, the misclassifications occur in large part only at the smallest fault level with very few misclassifications at the medium fault level and no misclassifications at the large fault level. That also implies that larger faults can be accommodated safely.

3 Fault Accommodation

The following sections detail the accommodation of a high-pressure compressor fault. The method described gives good results for HPT and VSV faults [3], however, only the HPC results are discussed in this paper.

A successful accommodation strategy will protect steady state operability, limit maximum temperature, and ensure adequate thrust. The critical measures of engine operability are the stall margins for the fan, booster, and high-pressure compressor (SMF, SMB, SMC, respectively). The controller is designed, among other things, to protect minimum stall margins required for safe operation at different points in the flight envelope. The accommodation goal is to achieve steady state stall margins in a faulted engine that are equal to or greater than the pre-fault values.

Recall that the high-pressure compressor fault (such as a blade failure) is modeled as a decrease in the efficiency and flow through the HPC. Small, medium, and large faults are modeled, respectively, to 1.5%, 3%, and 5% changes in efficiency and flow. The fault occurs as a step change over a 0.01 s interval.

Figure 4 represents a CWS simulation of a large HPC fault occurring at 0.5 s and subsequent results over the next 7 s. This response is determined by a standard controller without fault accommodation algorithms. The controller attempts to recover fan speed and thus, thrust. As a result of the fault and subsequent controller action, the booster and compressor stall margins drop below their designed (safe) values.

While Fig. 4 shows aircraft operation at a particular point in the flight envelope, one cannot necessarily extrapolate from that to

Table 3 Confusion matrix for rapid detection of selected faults (FP forced to zero) with elbow feature

	No fault est.	HPC est.	HPT est.	VSV est.	Ps3 est.
No fault	1	0	0	0	0
HPC	0.036	0.959	0.005	0	0
HPT	0.041	0.007	0.952	0	0
VSV	0.090	0	0	0.910	0
Ps3	0.049	0	0	0	0.951

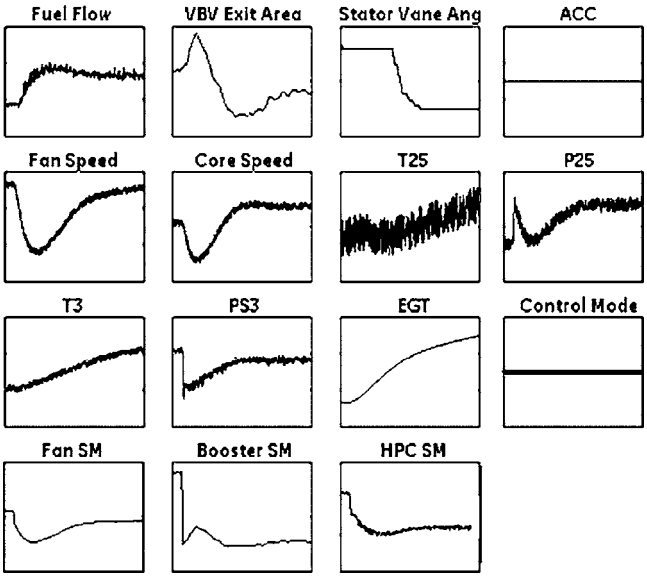

Fig. 4 Engine parameters for single HPC fault simulation

operation at other points in the flight envelope. Figure 5 encompasses an aggregation of many flight envelope points that were chosen to cover the aircraft flight envelope. The histogram shows the frequency of occurrence of a particular percentage change in each parameter. The frequency is calculated using this following equation for 458 flight envelope points

$$\frac{\boldsymbol{Y}_{t_{\text{final}}} - \boldsymbol{Y}_{t_0}}{\boldsymbol{Y}_{t_0}} \tag{1}$$

As expected, the high-pressure compressor fault causes a drop in the compressor stall margin and a significant drop in the booster stall margin. These values must be restored for safe operation of the aircraft.

3.1 Solution Description. The nonlinearity of the FADEC and the engine requires a nontraditional optimization technique to find optimal, or even feasible, accommodation strategies. Genetic algorithms (GAs) are well suited for this task. Genetic algorithms are a general-purpose optimization method based on the theory of natural selection. GAs make no assumptions about the search space, so they can be applied to almost all optimization problems [8]. However, GAs exchange applicability for speed—although they can be used on a wide variety of problems, they are typically slower to converge to a solution than algorithms designed for a specific problem. The GA Optimization Toolbox (GAOT) [9] was used to implement the GA.

This work assumes that the stall margin measures, i.e., SMF, SMB, and SMC, are acceptable measures of operability. This implies these faults are not concerned with lean blow out and that the calculated variables are an accurate representation of the actual margin between the current operating point and the stall line. Finally, it is assumed for steady state evaluation that the rate at which the actuators move to their accommodated values does not matter.

The optimization system takes the outputs of the engine simulation (SMF, SMB, SMC, FN) as inputs. The GA then generates control adjustments, which the FADEC translates to inputs for the engine simulation. Figure 6 shows the optimization architecture.

3.2 GA Parameters. Run time is a critical factor in this genetic algorithm design, as the CWS engine simulation runs more slowly than real time. In order to maximize the number of runs while still converging on a good solution, the optimization is designed to take approximately 6 h. The simulations start with a

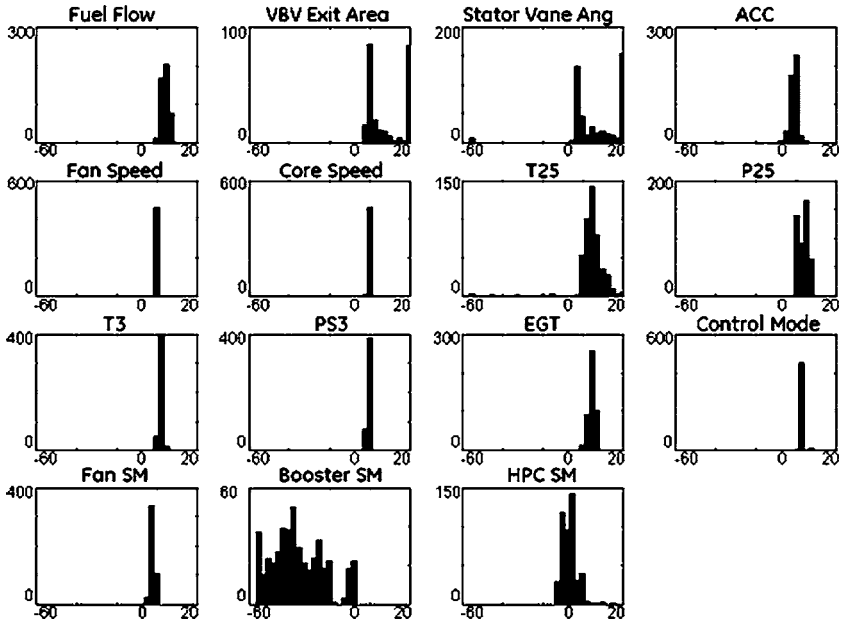

Fig. 5 Histogram representing HPC fault trends

random initial population of 30 members and finish after 30 generations. A crossover rate of 60% and a mutation rate of 5% were chosen.

3.2.1 Solution Representation. Most of the variables that represent a solution are bounded and continuous. These continuous gene values and their bounds are listed in Table 4. Two of the variables correspond to discrete switches, namely:

- auxiliary compressor bleed switch
- cowl anti-ice bleed switch

For these switches, a floating-point chromosome representation was used for which the values were rounded off. Each individual in the population is represented with a chromosome containing floating-point representations of the values in Table 4.

3.2.2 Fitness Function. In every generation, each member of the population is evaluated (each combination of control adjustments is simulated) to determine how good the solution is, and the fitness is appended to the chromosome. The goodness, or fitness, of a solution is based upon the operability and performance measures, namely:

- fan stall margin (SMF)
- booster stall margin (SMB)
- compressor stall margin (SMC)
- exhaust gas temperature (EGT)
- net thrust (FN)

As previously defined, an optimal fault accommodation strategy obtains thrust and stall margin levels similar to those prior to the fault's occurrence. A strategy is penalized for exceeding maximum temperatures. To quantify a strategy, J is maximized, where

$$j = \sum \begin{bmatrix} \text{Weight}_{\text{SMF}} \dfrac{\Delta \text{SMF}}{\text{SMF}_{t_0}} \\ \text{Weight}_{\text{SMB}} \dfrac{\Delta \text{SMB}}{\text{SMB}_{t_0}} \\ \text{Weight}_{\text{SMC}} \dfrac{\Delta \text{SMC}}{\text{SMC}_{t_0}} \\ \text{Weight}_{\text{FN}} \dfrac{\Delta \text{FN}}{\text{FN}_{t_0}} \end{bmatrix} - (\max\{0, \text{EGT}_{t_{\text{final}}} - \text{Limit}_{\text{EGT}}\})^{\exp} \quad \Delta x = |x_{t_0} - x_{t_{\text{final}}}| \tag{2}$$

and

$$\text{SMF\_WEIGHT} = 1,$$

$$\text{SMB\_WEIGHT} = 2,$$

$$\text{SMC\_WEIGHT} = 2,$$

$$\text{FN\_WEIGHT} = 3,$$

$$\text{EXPONENT} = 2.$$

3.3 Test Points. Table 5 lists a sample of the flight envelope points for which the GA was run.

3.4 Accommodation Results. At each point, a nominal, healthy engine was simulated. At 0.5 s, a fault was inserted, and 2 s later, the adjustment parameters were changed to the accommodated variables determined by the genetic algorithm. The runs

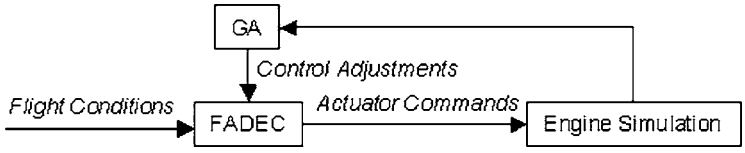

Fig. 6 Optimization architecture

Table 4 Continuous solution variables and bounds

Solution variable (gene)	Minimum value	Maximum value
VBV adjustment adder	−100	100
VSV adjustment adder	−50	50
Max core speed adder	0	1060
Horsepower extraction	0	Original value
ACC multiplier	0	100
ACC adder	0	1
Throttle	97% of original value	103% of original value
Aux bleed switch	0	24
Cowl anti-ice switch	0	1

continued for 20 s to allow transients to settle and achieve the steady state accommodated measures for operability and performance. The temporal responses for a number of test points are shown in Figs. 7–12, illustrating fan stall margin, booster stall margin, compressor stall margin, and net thrust. The six points shown are dispersed throughout the flight envelope and have different fault severity and throttle settings. In all cases, the stall margins and thrust are restored to their pre-fault values.

Table 5 Flight envelope test points

Run	HPC fault level	TRA	ALT	XM
1	Small	Low	Very low	Low
2	Large	High	Med	High
3	Small	Med	Low	High
4	Large	Med	Very low	Low
5	Small	Low	High	High
6	Large	Low	Med	Low
7	Small	Med	Med	Low
8	Large	Med	High	High
9	Large	Med	Low	Med
10	Medium	High	Low	Med
11	Medium	Med	High	Med
12	Medium	Med	Med	Very high
13	Small	Med	Low	Med
14	Medium	Very low	Low	Med
15	Medium	Med	Very low	Med
16	Medium	Med	Low	Very low
17	Medium	Med	Low	Med

3.5 Solution Analysis. Acceptable accommodation solutions have been found at all flight envelope points tested. This is cautiously taken as an indication that certain hardware faults can be accommodated with control adjustments. Some parameters, such as the max core speed adder, are not necessary for accommodation of all points. This is evident in the seemingly random solution provided for these variables from the GA. With the exception of fault level, no statistically significant correlation is found between the flight envelope points and the optimal control adjustments. There are several implications.

This makes a priori scheduling the fault accommodation very difficult. The current optimization strategy is much too slow to run in real-time on the FADEC, so the accommodation strategy must be pre-determined. This can be accomplished by solving the problem for corner and center points with the minimum number of adjustments possible. These points can be included in a standard schedule where in-between points are calculated using a weighted average of adjustments corresponding to the N closest design points. The weights are proportional to the inverse distances to the design points [3].

The plurality of optimal solutions suggests that effects of a multivariate nature are not fully taken into account, which leads to apparent lack of solution smoothness. Specifically, the GA generally finds the optimal solution for accommodation, which does not necessarily correspond to the best strategy consistent with scheduling. Including a reward in the fitness function for solution similarity to the accommodation strategy of a nearby point in the flight envelope can take care of this issue. Other penalties can be employed, such as "low accommodation effort" [3].

The genetic algorithm approach to the problem of finding control adjustments to accommodate faults is successful where hand tuning and derivative approaches have been unable to find suitable results. However, the runtime of the genetic algorithm is orders of magnitude larger than real-time. Faster solving methods exist, but none has yet been successfully employed in real-time to accommodate all flight envelope points. The dual approach of offline GA accommodation and online interpolation between design points has been shown to be successful.

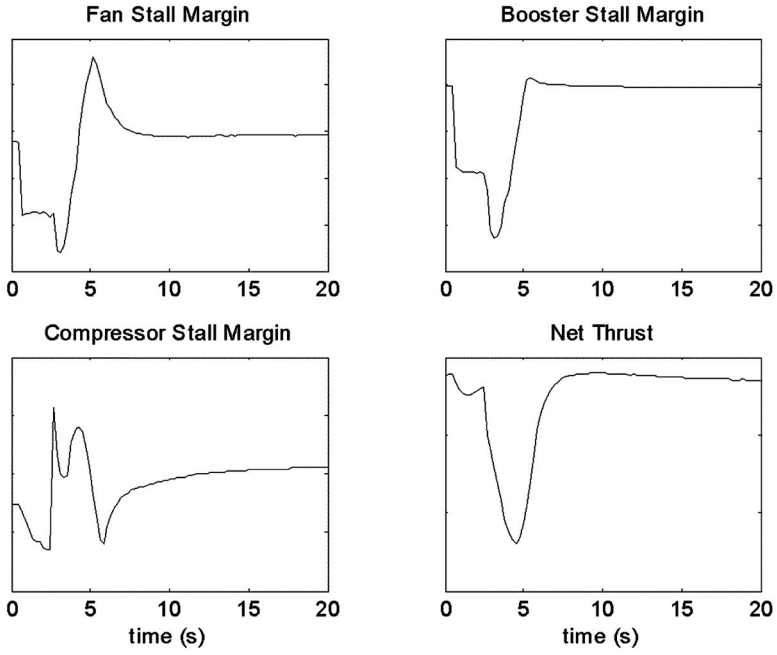

Fig. 7 Med. fault (med TRA, high Alt, med Mach)

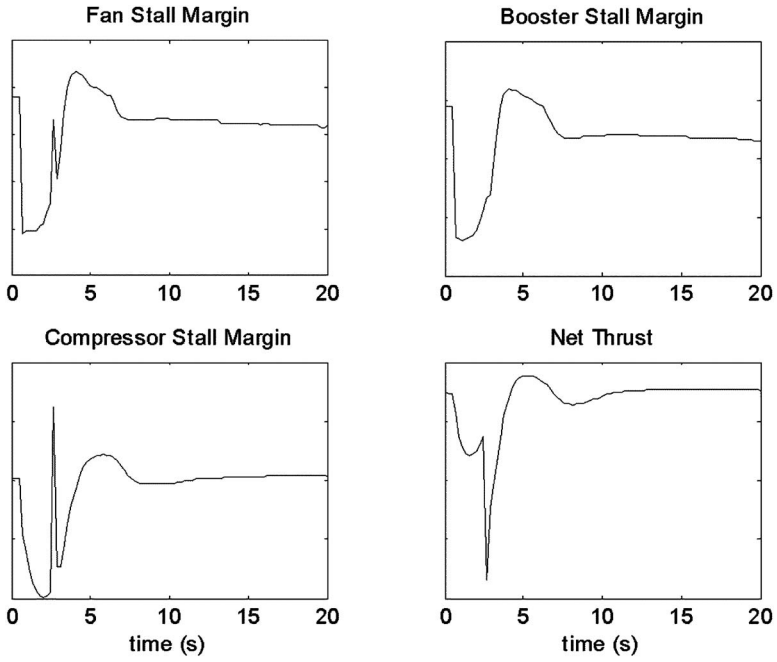

Fig. 8 Med. fault (very low TRA, low Alt, med Mach)

In some cases, the accommodation strategy causes a slight increase in thrust. While this was a permissible change in the experiment (and was bounded to small changes), in practice, this may be just as undesired as loss of thrust. Weighting the importance of thrust change in the fitness function should remedy this problem. Additionally, running the GA for a larger number of generations may be necessary for solution convergence.

Some strategies caused an initial loss of stall margin before converging on the steady state values. While this would be unacceptable in flight, the transient is ignored in the steady state evaluation. Appropriately scheduling the speed at which the actuators slew to the accommodated positions should remedy this problem.

3.6 Future Work. This method of discovering accommodation strategies should be very successful in the transient realm. The stall margin numbers are generally used to protect an engine from stall during transient operation. This same technique can easily be used to construct a transient strategy. Steady state accommodation is a necessary first step, but a complete fault accommodation strategy also schedules accommodation transiently. In fact, there are many more handles to adjust, for example, the acceleration and deceleration schedules as well as the actuator gains. The large number of possible accommodation parameters needs to be balanced with the need for solution smoothness, as discussed earlier. This paper explored a strategy that relied on first

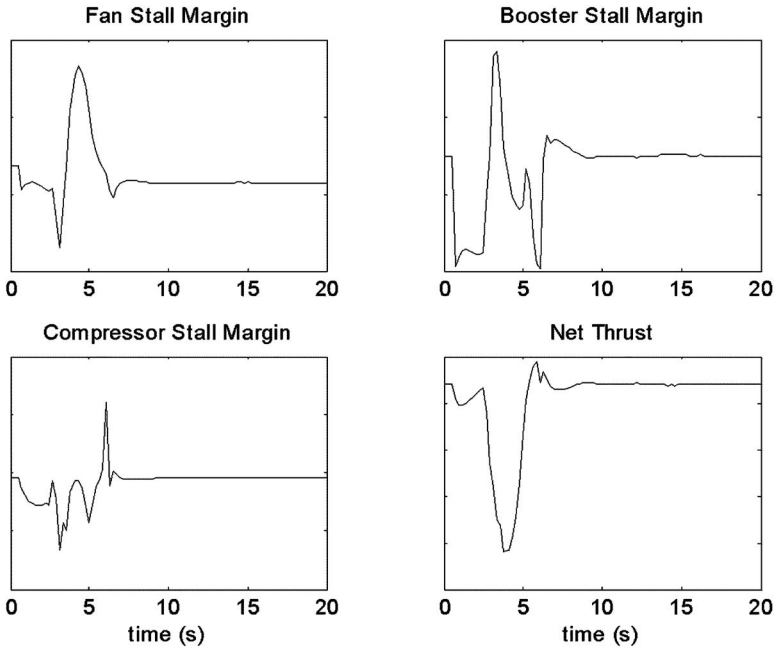

Fig. 9 Med. fault (med TRA, med Alt, very high Mach)

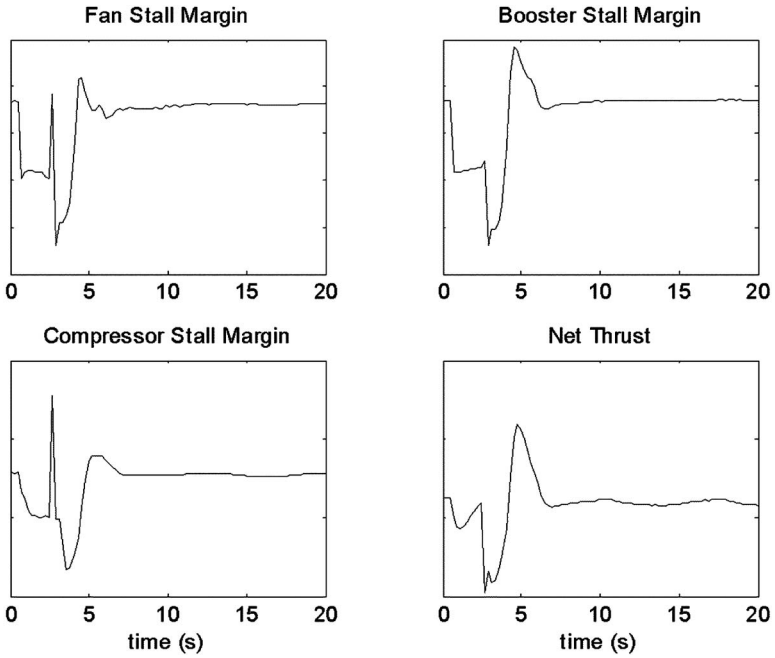

Fig. 10 Small fault (med TRA, low Alt, med Mach)

principle understanding of experts to reduce the parameters to a "good" set. A formal method should be explored that guides the user in making these choices.

Other extensions include the investigation of complete systems comprising engines and subsystems. Here, the possible interactions will pose considerable challenges due to the expected increase in complexity. An integrated approach might be explored that ensures the overall stability of the system.

Lastly, the accommodation should be examined as part of a comprehensive health management strategy that includes the secondary considerations beyond the immediate operability concerns. While the accommodation strategies presented here do potentially avert undesired system behavior, they do not address the root cause. Dealing with the required maintenance should be considered as part of the overall decision making process, taking into account impact on logistics, parts availability, flight schedule adjustments, shop loading, long-term prognostics, etc.

4 Conclusions

A method for integrated fault detection and accommodation in turbofan engines via control adjustments was presented. For detection, a scheme was employed that focused on rapid detection of relatively small aircraft engine faults. A bank of binary classifiers established the presence of the faults as determined by a quasi-maximum likelihood hypothesis test within a millisecond range,

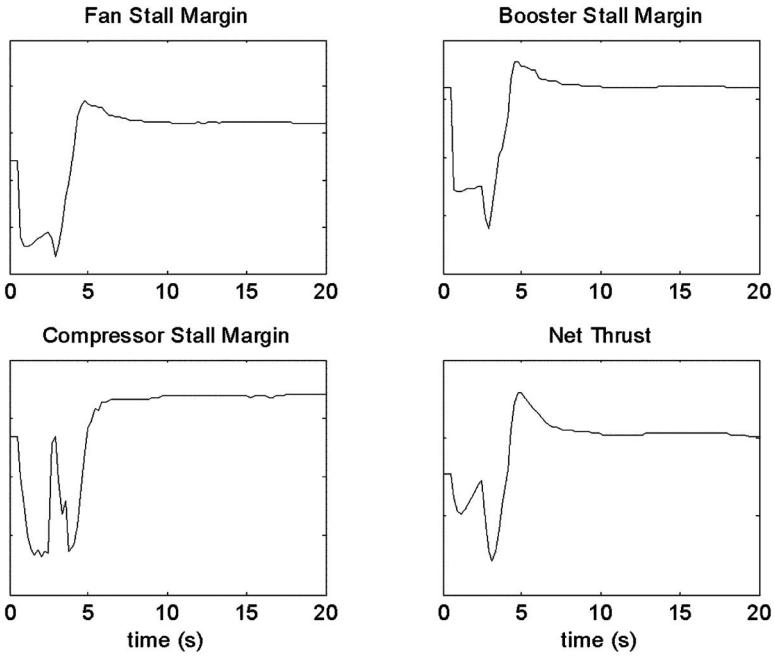

Fig. 11 Med. fault (med TRA, low Alt, very low Mach)

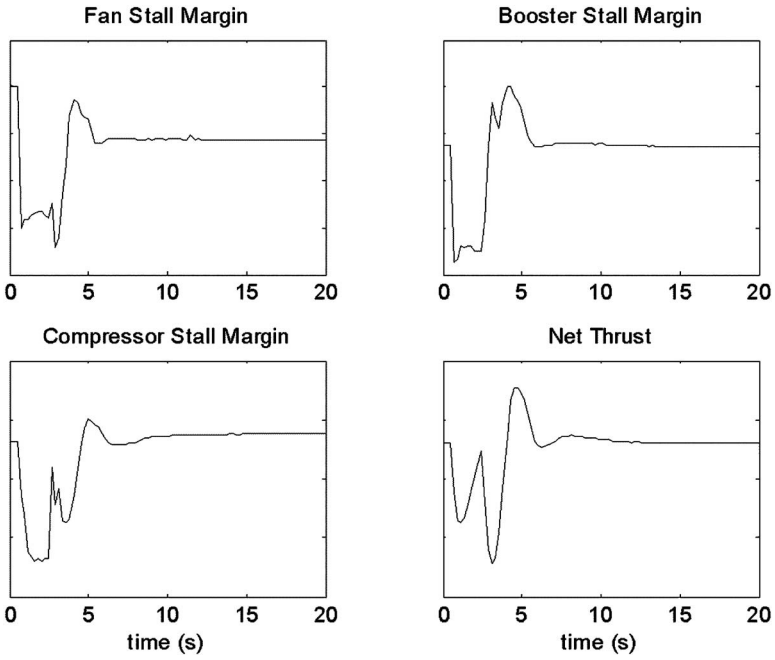

Fig. 12 Large fault (med TRA, low Alt, med Mach)

while at the same time avoiding false positives. Next, a genetic algorithm was used to identify the control adjustments necessary to maintain operability and performance. Solutions for this highly nonlinear problem were found for all fault levels and operating points tested. A dual method to schedule design adjustments across the flight envelope and interpolate between them for unscheduled operating points proved to be successful. We showed performance results for a high-pressure compressor fault at various levels of severity (small medium, high) and at different points in the flight envelope.

Acknowledgment

This work was supported by NASA Grant No. NAS3-01135 Task # 3. The authors greatly acknowledge the support of Don Simon and Tak Kobayashi (both with NASA).

Nomenclature

ACC = active clearance control
ALT = altitude
CLM = component level model (software) of high-bypass, two-rotor, turbofan
CWS = cycle workStation model (software) of high-bypass, two-rotor, turbofan
DEC = digital engine control
DTAMB = delta from ISO standard day temperature
EGT = exhaust gas temperature
EKF = extended Kalman filter
FADEC = full authority digital electronic control
FE = flight envelope
FP = false positives
FN = net thrust
GA = genetic algorithm
GAOT = genetic algorithm optimization toolbox
HPC = high-pressure compressor
HPT = high-pressure turbine
PS3 = HPC exit static pressure
SMB = booster stall margin
SMC = core stall margin
SMF = fan stall margin
SVM = support vector machine
TRA = throttle resolver angle
VBV = variable bleed valve
VSV = variable stator vane
WF = fuel flow
XM = Mach number

References

[1] AIA/AECMA, 1998, Project Report on PSM+ICR, http://www1.faa.gov/certification/aircraft/engine_psm+icr.doc.
[2] Belcastro, C. M., 2001, "Application of Failure Detection, Identification, and Accommodation Methods for Improved Aircraft Safety," *Proceedings, American Control Conference*, Arlington, VA, June 25–27. Vol. 4, pp. 2623–2624.
[3] Rausch, R., Viassolo, D., Kumar, A., Goebel, K., Eklund, N., Brunell, B., and Bonanni, P., 2004, "Towards In-Flight Detection and Accommodation of Faults in Aircraft Engines," *Proceedings, American Institute of Aeronautics and Astronautics, 1st Intelligent Systems Technical Conference*, Chicago, IL, Sep. 20–22.
[4] Gertler, J. J., 1998, "Survey of Model-Based Failure Detection and Isolation in Complex Plants," IEEE Control Syst. Mag., **8**, pp. 3–11.
[5] Kobayashi, T., and Simon, D. L., 2003, "Application of a Bank of Kalman Filters for Aircraft Engine Fault Diagnostics," ASME Paper No. GT2003-38550.
[6] Vapnik, V. N., 1995, *The Nature of Statistical Learning Theory*, Springer-Verlag, New York.
[7] Cawley, G. C., 2000, Support Vector Machine Toolbox v0.50 beta, http://theoval.sys.uea.ac.uk/~gcc/svm/toolbox, University of East Anglia, School of Information Systems, Norwich, Norfolk, UK NR4 7TJ.
[8] Goldberg, D., 2002, *The Design of Innovation: Lessons From and For Competent Genetic Algorithms*, Kluwer Academic Publishers, Norwell, MA.
[9] Houck, C., Joines, J., and Kay, M., 1995, "A Genetic Algorithm for Function Optimization: A Matlab Implementation," NCSU-IE TR 95-09.

C. Romessis
Research Associate
e-mail: cristo@mail.ntua.gr

Ph. Kamboukos
Research Assistant
e-mail: phkambou@central.ntua.gr

K. Mathioudakis
Professor
e-mail: kmathiou@central.ntua.gr

Laboratory of Thermal Turbomachines,
National Technical University of Athens,
P.O. Box 64069,
Athens 15710, Greece

The Use of Probabilistic Reasoning to Improve Least Squares Based Gas Path Diagnostics

A method is proposed to support least square type of methods for deriving health parameters from a small number of independent gas path measurements. The method derives statistical information using sets of solutions derived from a number of data records, to produce sets of candidate solutions with a lesser number of parameters. These sets can then be processed to derive an accurate component fault diagnosis. It could thus be classified as a new type of "concentrator" approach, which is shown to be more effective than previously existing schemes. The method's effectiveness is demonstrated by application to a number of typical jet engine component faults. [DOI: 10.1115/1.2436548]

Introduction

Fault detection and isolation are of great importance for gas turbines today, since they are related with issues such as safety, aircraft availability, and fleet management. In recent years, a lot of effort has been made in the field of engine diagnostics and a significant number of methods have been proposed covering a wide range of approaches for better and more reliable diagnosis.

Undoubtedly, the most popular approach is the gas path analysis (GPA). Engine diagnostics based on the GPA has been initiated with linear GPA. The fundamentals of linear gas path analysis have been posed by Urban [1]. Least squares techniques coupled with gas path analysis have been presented by Doel [2,3]. These methods interrelate through a linear system of equation, measurable quantities of thermodynamic nature along the engine (temperatures, pressures, etc.) with flow capacity and efficiency factors of engine components, representing their state of health. Linear GPA is the diagnostic approach mostly used in engines in service today applied under different formulation by the major engine manufacturers (Urban and Volponi [4], Doel [3,5], Barwell [6]).

Nonlinear GPA approaches have been developed later and constitute a more sophisticated approach, since the functional interrelation among the variables is more accurate. The first studies on nonlinear GPA for health parameter estimations were introduced by the group of the authors, through the adaptive modeling technique [7,8], which was also applied on different engine types by Tsalavoutas et al. [9] and Lambiris et al. [10]. Nonlinear GPA studies have been performed by different authors (e.g., Lee and Singh [11], Gronstedt [12], Chen and Zhu [13], Biagioni and Cinotti [14]).

The application, however, of GPA methods for the estimation of the health parameters of the engine in practical cases encounters a number of difficulties. The most important obstacle is the lack of measurements which lead to undetermined systems of equations, since the estimation of more health parameters from fewer measurements is required. In order to overcome this problem, many approaches have been proposed among which Kalman filtering (Provost [15], Volponi [16], Dewallef et al. [17]) and optimization techniques (Kamboukos et al. [18], Zedda and Singh [19], Gulati et al. [20], and Sampath et al. [21]). The basic idea of all these methods is that when individual component faults exist, they can be detected by some first decision criteria. This allows a reduction of the number of unknown health parameters which can then be evaluated more accurately, provided of course that the faulty component has been identified correctly during the first decision step.

Another problem is the inaccuracy of measurements due to the presence of noise. The effect of noise can be reduced if a series of measurements is available instead of a single measurement set. The reduction of noise can then be achieved in many ways varying from a single averaging of the available series of measurements [22] to the application of more sophisticated methods such as Kalman filtering techniques [17].

The work of the present paper uses the optimization algorithm proposed by Kamboukos et al. [18] that comprises a least squares based nonlinear gas path method for the diagnosis of component faults, coupled with a procedure of statistical processing of the diagnostic results. The proposed procedure aims to the estimation of the probability density functions (PDFs) of the health parameters which are then used for deciding which the faulty component is.

The Problem of Gas Path Fault Diagnosis

A formal description of the terms involved in the diagnostic problem can be given if the engine is considered as a system whose operating point is defined by means of a set of variables, denoted as $\mathbf{u}$. The health condition of its components is represented through the values of appropriate *health parameters*, contained in a vector $\mathbf{f}$. The engine is monitored through measured variables (speeds, pressures, temperatures, etc.), contained in a vector $\mathbf{Y}$.

The operating engine establishes a relationship between the health parameters and the measured quantities, which can be expressed through a functional relation

$$\mathbf{Y} = Y(\mathbf{u},\mathbf{f}) \tag{1}$$

The purpose of a diagnostic method is to determine the values of component health parameters of an engine (vector $\mathbf{f}$), when a set of measured quantities (vector $\mathbf{Y}$) is available for given operating conditions (vector $\mathbf{u}$). In cases usually encountered in practice, the available measurements are less than the health parameters, leading to an underdetermined system of equations, not allowing a unique determination of $\mathbf{f}$.

Least squares based methods are used for at least 2 decades by engine manufacturers to determine the health of gas turbines components, namely to estimate the vector $\mathbf{f}$ of the health parameters.

Contributed by the International Gas Turbine Institute of ASME for publication in the JOURNAL OF ENGINEERING FOR GAS TURBINES AND POWER. Manuscript received June 15, 2006; final manuscript received July 28, 2006. Review conducted by Lee Langston. Paper presented at the ASME Turbo Expo 2006: Land, Sea and Air, Barcelona, Spain, May 8–11, 2006, Paper No. GT2006-90619.

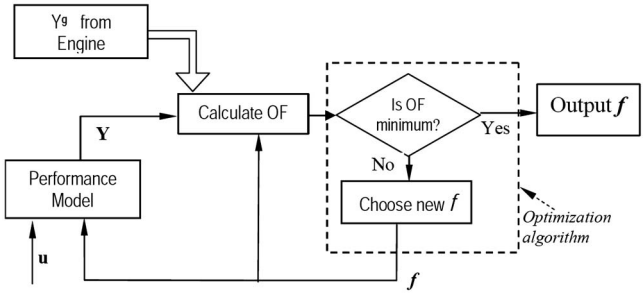

Fig. 1 Schematic representation of diagnostic procedure

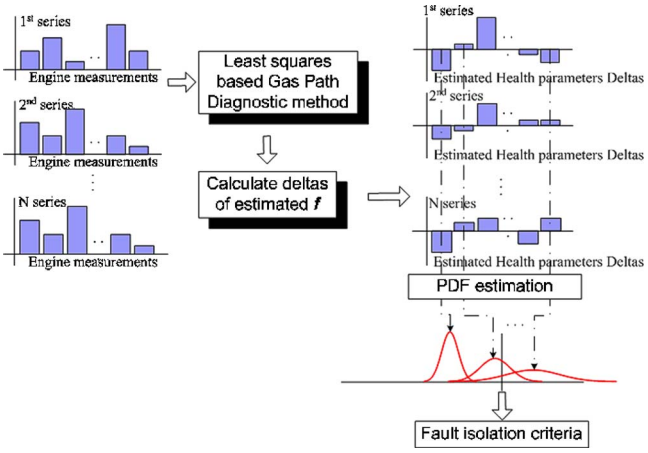

Fig. 2 Flowchart of the overall procedure of the proposed diagnostic method

Least Squares Based Gas Path Diagnostic Method

The least squares based method applied in the present paper has been proposed by Kamboukos et al. [18] and practically turns into an optimization problem by the minimization of an appropriate function.

When a set of measurement data from an engine is available, a set of values for the health parameters can be derived by solving an optimization problem, namely the minimization of a function OF. The solution is obtained with the interaction of a nonlinear engine performance model and an optimization algorithm, as shown in Fig. 1.

Mathioudakis et al. [23] have shown that an appropriate function for minimization is the following

$$\mathrm{OF} = \sum_{i=1}^{M} \left(\frac{Y_i - Y_i^g}{Y_i^g \boldsymbol{\sigma}_{Y_i}} \right)^2 + C_A \cdot \sum_{j=1}^{N} \left| \frac{f_j - f_j^r}{f_j^r \boldsymbol{\sigma}_{f_j}} \right| + C_S \cdot \sum_{j=1}^{N} \left(\frac{f_j - f_j^r}{f_j^r \boldsymbol{\sigma}_{f_j}} \right)^2 \tag{2}$$

The first term expresses the fact that the health parameters under estimation **f** must be such that the vector of measured quantities **Y** is reproduced as accurately as possible. The second and third terms ensure that the values of health parameters cannot be significantly different from their reference; a fact resulting from experience. It is the addition of these terms that allows the derivation of a solution for **f**, even when a smaller number of measurements is available. All deltas are weighted by the inverse of the standard deviation of the corresponding quantity. Weight factors C_A, C_S are also included, for the possibility to change the relative importance of the two groups of terms. The reference values **f** of the health parameters can be chosen to represent a "best" guess of the values to be determined.

The nature of this formulation of the diagnostic problem is that it can effectively estimate the values of the health parameters based on a limited set of measurements. However, since measurement data are noisy, the estimations based on a single data set differ from the actual values due to noise propagation. In order to overcome this problem and improve the effectiveness of the diagnosis, more than one measurement data set is needed. Using a series of data sets, the diagnosis is achieved through a two-stage procedure. In the first stage, the least square based method provides us with estimations of the health parameters, with some level of uncertainty due to the presence of noise. In the second stage of the diagnostic procedure, this uncertainty is reduced through statistical processing of the series of the health parameters estimation.

Improvement of Diagnosis Using Statistical Processing of Estimated Health Parameters

The first stage of data processing for locating the faulty component is the most crucial in the procedure described above. It is mainly for this stage that the method proposed here is suited. The method is based on statistical processing of the values of health factors determined by objective function minimization and is schematically shown in Fig. 2.

Given a sequence of N sets of measurements, acquired from the engine, a method using a minimization approach provides a series of N sets of estimated values of the health parameters. They can be expressed in terms of percentage deviations from their nominal value, at the same operating conditions. For a health parameter with value f at a specific operating point and nominal value (value during a fault free operation of the engine at the same operating conditions) f_0, its percentage deviation is called *delta of the health parameter* and is defined

$$\Delta f = \frac{f - f_0}{f_0} \times 100 \tag{3}$$

The expression of the health parameters in terms of deltas provides us with data that have a weak dependence on operating conditions, as commented on by Mathioudakis et al. [23].

Given the value of a health parameter at a specific operating point, its delta value can be obtained through the use of a performance model adapted on the specific engine.

From the estimated deltas, the PDFs of the deltas of the health parameters can then be estimated. By application of proper fault isolation criteria on the estimated PDFs, the parameters of the components that are faulty can finally be detected.

Estimation of the Probability Density Functions (PDFs). In statistics, a way of estimating the probability density function of a random variable is the Parzen window approximation [24]. Based on this approximation, given some data about a sample of a population, it is possible to extrapolate the data to the entire population.

If $\Delta f_1, \Delta f_2, \ldots, \Delta f_N$, is a sample of a random variable, like the estimated deltas of a health parameter f for instance, the Parzen window approximation of its PDF is

$$\mathrm{PDF}(\Delta f) = \frac{1}{N} \cdot \sum_{j=1}^{N} w(\Delta f - \Delta f_i) \tag{4}$$

where w is some probability density function (Fig. 3).

Quite often w is taken to be a Gaussian function with zero mean and variance $\boldsymbol{\sigma}^2$. With this assumption, Eq. (4) turns into

$$\mathrm{PDF}(\Delta f) = \frac{1}{N} \cdot \sum_{j=1}^{N} \frac{1}{\boldsymbol{\sigma}\sqrt{2\pi}} \cdot \exp\left[-\frac{(\Delta f - \Delta f_i)^2}{2\boldsymbol{\sigma}^2} \right] \tag{5}$$

In the present work, variance $\boldsymbol{\sigma}^2$ has been considered the sample variance s^2, defined

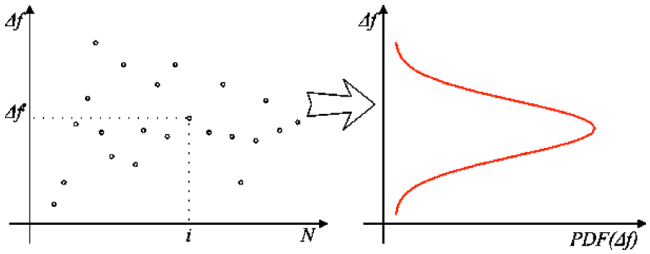

Fig. 3 Estimation of PDF of variable Δ*f* from a sample of values

$$\sigma^2 = s^2 = \frac{\sum_{j=1}^{N} \Delta f_j^2}{N-1} \tag{6}$$

Fault Isolation Criteria. The idea that is put forward here is that when the values of health parameters are evaluated from a number of measurement sets, faulty components will result in values consistently different from zero. We should expect that corresponding health parameters should exhibit large deviations with correspondingly "narrow" PDFs. Based on this, we introduce a parameter which we call the diagnostic index. The diagnostic index DI_i of a health parameter f_i is given by the product of the maximum value of the estimated PDF of Δf_i and the absolute value of the delta of the parameter for which the maximum value of the estimated PDF is obtained (most probable value), as shown in Fig. 4. It is therefore

$$DI_i = \mathrm{PDF}(\Delta f_i^{\max}) \cdot |\Delta f_i^{\max}| \tag{7}$$

where, for every $\Delta f_i \neq \Delta f_i^{\max}$, it is $\mathrm{PDF}(\Delta f_i) < \mathrm{PDF}(\Delta f_i^{\max})$

Health parameters with large most probable values of delta or high probability density for that value (indicating small uncertainty on derived estimations) will present large values of diagnostic index. On the other hand, parameters with small most probable deviations from reference value or small probability density—indicative of large uncertainty on the derived estimations—will have a high valued diagnostic index. It is thus expected that health parameters which deviate due to the presence of a component fault will have a high value of diagnostic index. Based on this, we identify as faulty the component comprising the health parameter with the highest value of diagnostic index (Fig. 5).

Method Implementation on a Turbofan Engine

In order to evaluate the effectiveness of the proposed method, application to a turbofan test case is presented. Apart from its illustrative nature, the test case also represents a situation of practical interest in today's jet engines applications. The type of engine for this application is described in Appendix A. It is selected as it has been used in applications of different diagnostic methods

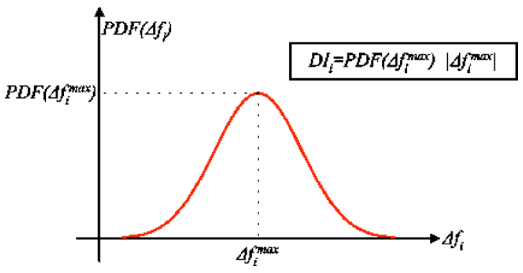

Fig. 4 Calculation of DI_i from the estimated PDF(Δf_i)

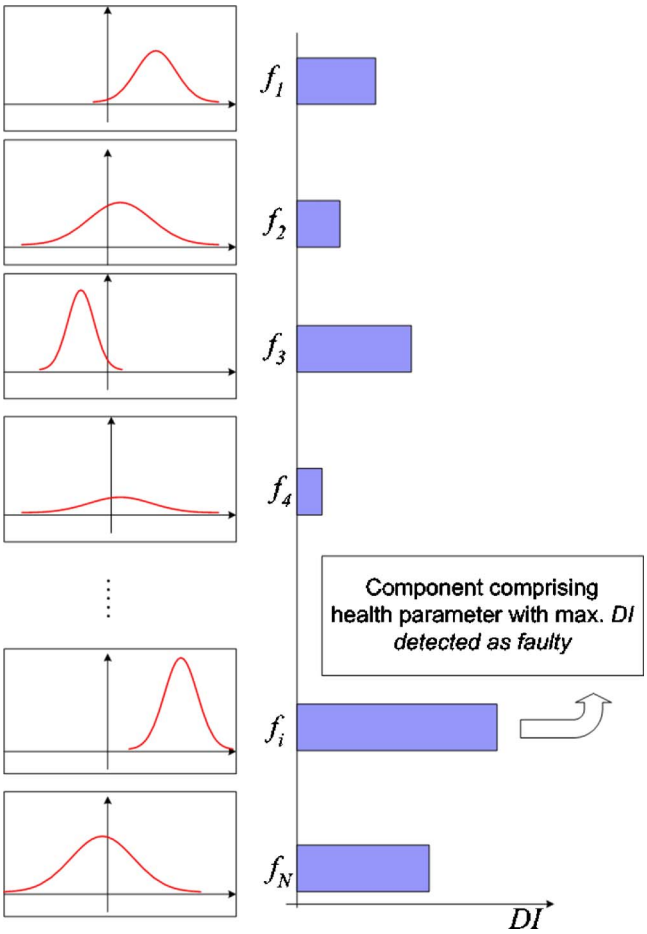

Fig. 5 Faulty component detection from estimation of PDFs

by the authors and other researchers and can be considered to constitute a benchmark case (Dewallef et al. [17], Kamboukos [18], Romessis [22]).

The proposed diagnostic method has been applied for the diagnosis of the 15 benchmark fault cases, described in Appendix B. From the series of 50 measurement sets, for each fault case, the diagnostic index of the health parameters is shown in Table 1. The highlighted values of the diagnostic indices indicate the highest values on each fault case.

From these values and according to the diagnostic criterion set in the previous paragraph, the components found to be faulty are shown in Table 2, where the actually deviated health parameters and suffered components are also presented.

From Table 2 we can conclude that in 13 out of the 15 fault cases the faulty component of the engine was detected correctly. The remaining two fault cases, where the method failed to detect correctly the component fault, were a high-pressure compressor (HPC) fault represented by a reduction of both efficiency and flow capacity (fault case **c**) and a low-pressure turbine (LPT) fault also represented by a reduction of both efficiency and flow capacity (fault case **j**). These are fault cases where observability problems occur, as has been discussed by Kamboukos et al. [18]. In a few words, this problem indicates that the available measurement set is not adequate to distinguish these fault cases among several others, with which they share a similar "signature of fault" (values of the measurement set due to the presence of fault). One way to overcome this problem is the exploitation of information from a number of different operating points by constructing a multipoint diagnostic approach, as described in detail by Kamboukos et al. [25]. This approach is practically the least squares based diagnostic method described in the present paper with the difference that

Table 1 Diagnostic indices of the health parameters for the data of the 15 benchmark fault cases

Fault cases	SW12	SE12	SW2	SE2	SW26	SE26	SW41	SE41	SW49	SE49	ASIMP
a	**0.233**	0.86	0.032	0.064	0.107	0.015	0.000	0.021	0.011	0.008	0.003
b	0.018	**0.321**	0.033	0.004	0.029	0.000	0.000	0.000	0.022	0.08	0.004
c	0.004	0.003	0.048	**0.240**	0.016	0.090	0.000	0.000	0.025	0.004	0.003
d	0.004	0.002	0.055	0.106	0.196	**0.392**	0.008	0.013	0.016	0.004	0.029
e	0.035	0.094	0.056	0	**0.231**	0	0	0	0.032	0.038	0.082
f	0.052	0.016	0.061	0	0	0	**0.390**	0	0.07	0.39	0.017
g	0.153	0.017	0.03	0.036	0.069	0.020	**0.553**	0.196	0.215	0.281	0.139
h	0.066	0.076	0.092	0.012	0.040	0.013	0	**0.227**	0.139	0.123	0.156
i	0.07	0.01	0.012	0.047	0.04	0	0.014	0.033	0	**0.529**	0
j	0.005	0.024	0.078	0.046	0.021	0.013	0.007	**0.094**	0.025	0.023	0.030
k	0.053	0.043	0.055	0.023	0.055	0.012	0.015	0.017	**0.124**	0.008	0.053
l	0.075	0.02	0.011	0.003	0	0	0.008	0	**0.198**	0.057	0
m	0	0.004	0.09	0.023	0.006	0	0	0	0	0	**0.188**
n	0.003	0.004	0.026	0.040	0.04	0.014	0	0	0.007	0.005	**0.314**
o	0.090	0.117	0.052	0.003	0.019	0	0.006	0	0.023	0.043	**0.334**

is applied in several operating points at the same time combining information that allows the increase of the number of measurements, thus forming a well determined diagnostic system for the estimation of the health parameters.

Table 2 Diagnostic performance on the set of 15 benchmark fault cases

Fault case	Actually deviated parameters	Affected component	Estimated affected component
a	SW12, SE12, SW2, SE2	LPC	LPC
b	SE12	LPC	LPC
c	SW26, SE26	HPC	LPC
d	SE26	HPC	HPC
e	SW26	HPC	HPC
f	SW41	HPT	HPT
g	SW41, SE41	HPT	HPT
h	SE41	HPT	HPT
i	SE49	LPT	LPT
j	SW49, SE49	LPT	HPT
k	SW49	LPT	LPT
l	SW49	LPT	LPT
m	A8IMP	Nozzle	Nozzle
n	A8IMP	Nozzle	Nozzle
o	A8IMP	Nozzle	Nozzle

In order to evaluate the improvement that the multipoint approach can achieve, the diagnostic procedure proposed in the present paper, using the multipoint approach instead of the least squares based method, has been applied to the 15 benchmark fault cases. The diagnostic indices of the health parameters for each fault case are shown in Table 3.

From this table it becomes clear that the multipoint approach handles efficiently the observability problems on fault cases **c** and **j**, since these faults are detected correctly, improving the effectiveness of the diagnostic procedure.

A further approach, regarding the uncertainty of the health parameters estimation this time, can be achieved if a second pass of the diagnostic procedure follows. The basic idea is described in Fig. 6.

First, from a given series of measurements data application of the diagnostic procedure provides an estimation of the faulty component of the engine. In a second pass, the diagnostic procedure is applied once again for the same measurement data, with the difference that the unknown health parameters are now limited to those describing the health condition of the component found to be faulty in the first pass. The remaining health parameters are given their nominal values since they describe the condition of components found to be healthy.

This reduction of the number of the unknowns leads to a well

Table 3 Diagnostic indices of the health parameters for the 15 benchmark fault cases using the multipoint approach

Fault cases	SW12	SE12	SW2	SE2	SW26	SE26	SW41	SE41	SW49	SE49	A8IMP
a	**0.272**	0.194	0.152	0.008	0.000	0.024	0.035	0.000	0.057	0.006	0.080
b	0.135	**0.612**	0.005	0.008	0.010	0.003	0.028	0.000	0.049	0.020	0.113
c	0.001	0.022	0.002	0.126	**0.358**	0.324	0.000	0.034	0.007	0.052	0.000
d	0.077	0	0.005	0.052	0	**0.508**	0.037	0.005	0.059	0.025	0.047
e	0.044	0	0.012	0.054	**0.200**	0.020	0.024	0.009	0.010	0.048	0.030
f	0.069	0.007	0	0.061	0.002	0.018	**0.616**	0.006	0.080	0.040	0.052
g	0.006	0.007	0.004	0.093	0.042	0.046	0.380	**0.427**	0	0.027	0.008
h	0.047	0.003	0	0.058	0.013	0.049	0.029	**0.538**	0.043	0.018	0.067
i	0	0.007	0.017	0.124	0.057	0.043	0	0.013	0.009	**0.488**	0
j	0.018	0.006	0	0.098	0.010	0.038	0.018	0.026	0.095	**0.242**	0.009
k	0.056	0	0.020	0.076	0.004	0.050	0.029	0.027	**0.096**	0.050	0.048
l	0.007	0.005	0.019	0.055	0.011	0.006	0	0.009	0.075	**0.185**	0.009
m	**0.090**	0	0.003	0.052	0.001	0.007	0.029	0.006	0.037	0.026	**0.067**
n	0.026	0	0.004	0.061	0.003	0.021	0.009	0.008	0.008	0.009	**0.206**
o	0.040	0	0	0.090	0.015	0.050	0.011	0.036	0.002	0.056	**0.0326**

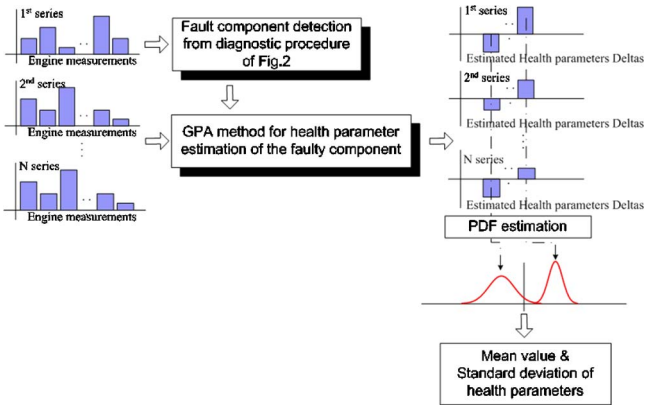

Fig. 6 Flowchart of the two-pass procedure for the improvement of the health parameter estimation

determined diagnostic system allowing an estimation of the health parameters with less uncertainty, expressed as smaller standard deviations of the estimated PDFs.

Table 4 shows the mean values and the standard deviations of the estimated PDFs of the health parameters of the components found to be faulty for the 15 benchmark fault cases on the two passes of the diagnostic procedure.

Table 4 Mean values and deviations of the estimated PDFs on the two-passes of the diagnostic procedure for the 15 benchmark fault cases using the multipoint approach

		First		Second	
Fault case	Detected health parameters	(Mean val.)	σ	(Mean val.)	σ
a	SW12	−1.10	1.32	−1.03	0.38
	SE12	−0.55	1.17	−0.57	0.67
	SW2	−0.65	1.43	−0.73	0.55
	SE2	0.20	1.67	−0.56	1.02
b	SW12	−0.80	1.67	0.03	0.37
	SE12	−1.10	0.65	−1.27	0.74
	SW2	0.10	1.67	−0.08	0.33
	SE2	0.20	1.67	0.03	0.84
c	SW26	−1.70	1.42	−1.28	0.23
	SE26	−1.05	1.20	−0.89	0.12
d	SW26	0.00	1.67	0.16	0.74
	SE26	−1.20	0.85	−1.10	0.28
e	SW26	−1.25	1.67	−1.02	0.66
	SE26	−0.20	1.67	−0.05	0.20
f	SW41	1.30	0.80	0.95	0.21
	SE41	0.00	1.67	0.01	0.07
g	SW41	−1.00	1.05	−1.03	0.24
	SE41	−0.80	0.72	−1.12	0.09
h	SW41	0.25	1.67	−0.03	0.27
	SE41	−0.90	0.60	−1.12	0.09
i	SW49	−0.20	1.67	−0.04	0.25
	SE49	−1.05	0.90	−1.07	0.13
j	SW49	−0.70	1.67	−0.91	0.22
	SE49	−0.65	1.10	−0.51	0.07
k	SW49	−0.06	1.67	−1.01	0.20
	SE49	−0.35	1.67	−0.02	0.13
l	SW49	0.50	1.67	0.95	0.26
	SE49	−0.60	1.40	−0.66	0.15
m	SW12	−0.70	1.67	−0.51	0.21
	SE12	0.00	1.67	0.00	0.01
	SW2	0.00	1.67	0.00	0.01
	SE2	0.00	1.67	0.00	0.01
n	A8IMP	−1.50	1.28	−1.00	0.18
o	A8IMP	1.35	1.20	2.00	0.18

From this table we can see that in cases where the faulty component was detected correctly from the first pass, the second pass led to an estimation of the health parameters with significantly smaller ranges of deviations. In cases where the first pass fails to detect correctly the faulty component, of course the second pass could not lead to a correct diagnosis.

Discussion

The proposed method focuses on the improvement of a standalone diagnostic method by statistical processing of extracted diagnostic conclusions on a series of input information. It should therefore be considered as a frame in which several methods can be embedded improving their effectiveness.

The considered statistical processing targets the reproduction of the probability density functions, from which the required statistical parameters are calculated, rather than the direct calculation of sample statistical parameters like other methods perform. This is very important since the sample statistical parameters may lead to incorrect diagnostic conclusions if the available measurement set is poor or not representative of the population it represents. For instance, Kamboukos et al. [18] proposed the use of a diagnostic index, similar to the one proposed in the present paper which is, however, calculated directly from the sample statistical parameters that are the sample mean values of the estimated health parameters and the sample standard deviations of the estimations (sample diagnostic index). Table 5 shows the diagnostic indices, as defined by Kamboukos et al. [18], for the 15 benchmark fault cases examined and the estimations of the health parameters with the multipoint approach.

A comparison of this table with Table 3, where the diagnostic indices are calculated through Eq. (7), shows that the diagnostic index proposed in the present paper leads to better results. In one case (fault case **k**), by use of the sample diagnostic index, the actually deviated health parameter SW49 is not detected correctly, since it does not have the maximum value of diagnostic index, while this is achieved with the diagnostic index proposed in the present paper. In many other cases, although both ways of defining the diagnostic index lead to the correct detection of the actually deviated health parameters, the proposed way provides the actual deviated parameters with significantly higher values of diagnostic index than the other parameters (as for instance, fault case **c**).

Concluding Remarks

The method of statistical processing of the diagnostic conclusions provided by a least-square based gas path diagnostic method, in order to improve diagnosis, has been presented.

The statistical processing consists of an estimation of the probability density function of the estimated deviations of the health parameters of the engine. Based on these density functions, a parameter indicative of the health condition of the components of the engine, introduced in the present paper, can be calculated.

Application on a turbofan test case has also been presented. The examined fault cases indicate that the proposed method is reliable and can be used for the improvement of diagnosis of component faults that the existing method leads to.

Acknowledgment

The work for this paper has been carried out in the frame of TATEM program and financial support of the EU is gratefully acknowledged.

Nomenclature

A8IMP = exhaust area
C_A = weighted factor (Eq. (A1))
C_s = weighted factor (Eq. (A1))
DI_i = diagnostic index of health parameter f_i (Eq. (7))

Table 5 Diagnostic indices of the health parameters for the 15 benchmark fault cases using the multipoint approach

Fault cases	SW12	SE12	SW2	SE2	SW26	SE26	SW41	SE41	SW49	SW49	A8IMP
a	**1.193**	0.922	0.745	0.107	0.014	0.305	0.452	0.041	0.374	0.159	0.445
b	0.521	**2.179**	0.128	0.098	0.123	0.075	0.357	0.027	0.336	0.258	0.468
c	0.032	0.296	0.055	0.407	0.917	**1.954**	0.057	0.439	0.095	0.457	0.004
d	0.358	0.009	0.134	0.294	0.039	**1.895**	0.472	0.144	0.385	0.318	0.321
e	0.314	0.050	0.158	0.381	**0.520**	0.252	0.313	0.228	0.132	0.426	0.274
f	0.403	0.178	0.026	0.319	0.051	0.228	**1.955**	0.157	0.385	0.345	0.365
g	0.107	0.171	0.097	0.461	0.285	0.412	1.247	**1.767**	0.000	0.349	0.104
h	0.351	0.067	0.032	0.432	0.165	0.429	0.378	**2.183**	0.255	0.224	0.382
i	0.005	0.169	0.214	0.405	0.317	0.373	0.035	0.336	0.113	**1.652**	0.027
j	0.155	0.412	0.024	0.433	0.131	0.327	0.231	0.333	0.466	**1.055**	0.120
k	0.330	0.017	0.255	0.432	0.092	0.436	0.357	0.340	0.411	**1.055**	0.314
l	0.088	0.122	0.241	0.271	0.146	0.141	0.002	0.233	0.474	**0.811**	0.108
m	**0.448**	0.001	0.068	0.248	0.035	0.156	0.370	0.144	0.248	0.334	0.371
n	0.235	0.080	0.094	0.295	0.84	0.263	0.232	0.191	0.107	0.221	**1.050**
o	0.269	0.016	0.027	0.478	0.195	0.432	0.291	0.455	0.051	0.486	**1.770**

EPM = engine performance model
$\mathbf{f}$ = vector of the health parameters of the engine
f_0 = nominal value of a health parameter
$\mathbf{f}^r$ = reference values of vector $\mathbf{f}$
HPC = high-pressure compressor
HPT = high-pressure turbine
LPC = low-pressure compressor
LPT = low-pressure turbine
η_i = efficiency of component with entrance at station i
NOZZLE = nozzle
OF = function for minimization (Eq. (A1))
P_{amb} = ambient pressure
PDF = probability density function
P_i = total pressure at station i of the engine
SE_i = efficiency factor at station i of the engine (Eq. (A2))
SW_i = flow factor at station i of the engine (Eq. (A1))
s^2 = sample standard deviation (Eq. (6))
T_i = total temperature at station i of the engine
$\mathbf{u}$ = vector of measurements defining operating point
w = probability density function (Eq.(4))
W_i = gas mass flow rate at station i
WFE = fuel flow rate
XNHP = high-pressure shaft rpm
XNLP = low-pressure shaft rpm
$\mathbf{Y}$ = vector of measured quantities on an engine
Y_i^g = measured value of Y_i
Δf = delta of health parameter f
$\boldsymbol{\sigma}$ = standard deviation
$\boldsymbol{\sigma}_{f_i}$ = standard deviation of health parameter f_i

Subscripts

1,2,..8 = station along the engine gas path, Fig. 7
ref = reference values (value in "healthy" engine)

Appendix A: Engine Layout and Representation

The layout of the considered turbofan engine, used as a test case, and the considered set of measurements for monitoring the condition of the engine is shown in Fig. 7. The choice of this type of engine and instrumentation is discussed in Mathioudakis et al. [23].

The operating point of the engine is defined by measurement of the quantities: P_{amb}, $P1$, $T1$, and WFE, forming vector $\mathbf{u}$, while rotating speeds of the two spools (XNLP and XNHP) and pressures and temperatures at several stations form vector $\mathbf{Y}$.

Component faults are simulated by deviations of several *health parameters* from their nominal values. In the current work, flow and efficiency factors of each module of the engine at Stations 12, 2, 26, 41, 49, and 8, forming vector $\mathbf{f}$ are used as health parameters (see also Stamatis et al. [26]). For a component with entrance at station i of the engine we have

$$\text{flow factor: } SW_i = (W_i \cdot \sqrt{T_i}/P_i)/(W_i \cdot \sqrt{T_i}/P_i)_{\text{ref}} \qquad \text{(A1)}$$

$$\text{efficiency factor: } SE_i = \eta_i/(\eta_i)_{\text{ref}} \qquad \text{(A2)}$$

The quantitative interrelation among the health parameters and the measurements is expressed through an engine performance model (EPM) produced by Stamatis et al. [7] and adapted to individual engines to reproduce accurately their performance.

Appendix B: Benchmark Fault Cases

A set of fault scenarios has been examined, covering different possible faults in all individual components on the engine. This set of cases has been defined by Curnock [27] and the fault cases have been used for evaluation by several researchers and diagnostic methods (Dewallef et al. [17], Kamboukos [18], Romessis [22], and Mathioudakis et al. [23]).

For each examined fault case data from a sequence of 50 operating points are used. They are typical readings taken every 5 min over the cruise sections of a flight.

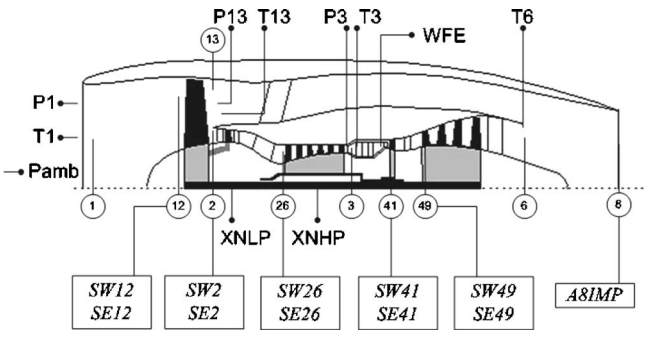

Fig. 7 Layout and station numbering and measurements of the considered turbofan engine.

Table 6 Health parameters deviations for the considered fault cases

Fault case	Actual deviations of health parameters
a	ΔSW2=−0.7%, ΔSE2=−0.4%, ΔSW12=−1%, ΔSE12=−0.5%
b	ΔSE12=−1%
c	ΔSW26=−1%, ΔSE26=−0.7%
d	ΔSE26=−1%
e	ΔSW26=−1%
f	ΔSW41=+1%
g	ΔSW41=−1%, ΔSE41=−1%
h	ΔSE41=−1%
i	ΔSE49=−1%
j	ΔSW49=−1%, ΔSE49=−0.4%
k	ΔSW49=−1%
l	ΔSW49=+1%, ΔSE49=−0.6%
m	ΔA8IMP=+1%
n	ΔA8IMP=−1%
o	ΔA8IMP=+2%

The considered component fault cases are representative of those usually encountered in practice and can be expressed as percentage deviations of the health parameters from their nominal value (Table 6).

References

[1] Urban, L. A., 1972, "Gas Path Analysis Applied to Turbine Engine Conditioning Monitoring," Paper No. AIAA/SAE 72-1082.

[2] Doel, D., 1993, "An Assessment of Weighted-Least-Squares Based Gas Path Analysis," ASME Paper No. 93-GT-119.

[3] Doel, D., 1994, "TEMPER-A Gas Path Analysis Tool for Commercial Jet Engines," ASME J. Eng. Gas Turbines Power, **116**, pp. 82–89.

[4] Urban, L. A., and Volponi, A. J., 1992, "Mathematical Methods of Relative Engine Performance Diagnostics," SAE Trans., 101, Journal of Aerospace, Paper 922048.

[5] Doel, D., 2002, "Interpretation of Weighted Least Squares Gas Path Analysis Results," ASME Paper No. GT-2002-30025.

[6] Barwell, M. J., 1987, "COMPASS-Ground Based Engine Monitoring Program for General Applications," SAE Technical Paper 871734.

[7] Stamatis, A., Mathioudakis, K., and Papailiou, K. D., 1990, "Adaptive Simulation of Gas Turbine Performance," ASME J. Eng. Gas Turbines Power **112**, pp. 168–175.

[8] Stamatis, A., Mathioudakis, K., Smith, M., and Papailiou, K. D., 1990, "Gas Turbine Component Fault Identification by Means of Adaptive Performance Modeling," ASME Paper No. 90-GT-376.

[9] Tsalavoutas, A., Pothos, S., Mathioudakis, K., and Stamatis, A., 1999, "Monitoring of the Performance of a Twin Spool Ship Propulsion Turbine by Means of Adaptive Modeling," RTO Symposium on Gas Turbine Operation and Technology for Land, Sea and Air Propulsion and Power Systems, Ottawa, Canada, October 18–21, Paper No. RTO-MP-34.

[10] Lambiris, B., Mathioudakis, K., Stamatis, A., and Papailiou, K. D., 1994, "Adaptive Modeling of Jet Engine Performance With Application to Condition Monitoring," J. Propul. Power, **10**(6), pp. 890–896.

[11] Lee, Y., and Singh, R., 1996, "Health Monitoring of Turbine Engine Gas Path Components and Measurement Instruments," ASME Paper No. 96-GT-242.

[12] Groenstedt, T. V., 2001, "A Multi Point Gas Path Analysis Tool for Gas Turbine Engines With a Moderate Level of Instrumentation," *Proceedings of 15th ISABE*, Bangalore, India, Sept. 3–7, Paper No. ISABE-2001-1139.

[13] Chen, D. G., and Zhu, Z. L., 2001, "Model Identification-Based Fault Analysis Method Applied to Jet Engines," *Proceedings of 15th ISABE*, Paper No. ISABE-2001-1111.

[14] Biagioni, L., and Cinotti, R., 2001, "Turboshaft Engine Condition Monitoring by Bayesian Identification," *Proceedings of 15th ISABE*, Paper No. ISABE-2001-1034.

[15] Provost, M. J., 1994, "The Use of Optimal Estimation Techniques in the Analysis of Gas Turbines," Ph.D. thesis, Cranfield University, UK.

[16] Volponi, A., 1994, "Sensor Error Compensation in Engine Performance Diagnostics," ASME Paper No. 94-GT-58.

[17] Dewallef, P., Léonard, O., and Mathioudakis, K., 2004, "On-Line Aircraft Engine Diagnostic Using a Soft-Constrained Kalman Filter," ASME Paper No. GT2004-53539.

[18] Mathioudakis, K., Kamboukos, Ph., and Stamatis, A., 2004, "Gas Turbine Component Fault Detection From a Limited Number of Measurements," Proc. Inst. Mech. Eng., Part A, **218**, pp. 609–618.

[19] Zedda, M., and Singh, R., 1999, "Gas Turbine Engine and Sensor Diagnostics," *Proceedings of 14th ISABE*, Paper No. ISABE 99-7238.

[20] Gulati, A., Taylor, D., and Singh, R., 2001, "Multiple Operating Point Analysis Using Genetic Algorithm Optimization for Gas Turbine Diagnostics," *Proceedings of 15th ISABE*, Paper No. ISABE 2001-1139.

[21] Sampath, S., Gulati, A., and Singh, R., 2002, "Fault Diagnostics Using Genetic Algorithms for Advanced Cycle Gas Turbine," ASME Paper No. GT-2002-30021.

[22] Romessis, C., and Mathioudakis, K., 2004, "Bayesian Network Approach for Gas Path Fault Diagnosis," ASME Paper No. GT2004-53801.

[23] Mathioudakis, K., Kamboukos, Ph., and Stamatis, A., 2002, "Turbofan Performance Deterioration Tracking Using Non-linear Models and Optimazation Techniques," ASME J. Turbomach. **124**, pp. 580–587.

[24] Parzen, E., 1962, "On Estimation of a Probability Density Function and Mode," Ann. Math. Stat. **33**, pp. 1065–1076.

[25] Kamboukos, P., and Mathioudakis, K., 2006, "Multipoint Non-linear Method for Enhanced Component and Sensor Malfunction Diagnosis," ASME Paper No. GT-2006-90451.

[26] Stamatis, A., Mathioudakis, K., Ruiz, J., and Curnock, B., 2001, "Real Time Engine Model Implementation for Adaptive Control & Performance Monitoring of Large Civil Turbofans," ASME Paper No. 2001-GT-0362.

[27] Curnock, B., 2001, "OBIDICOTE Programme Work Package 4: Steady-State Test Cases for Engine Deterioration," Rolls Royce Report, Document Number DNS78608.

Igor Loboda
School of Mechanical and Electrical Engineering,
National Polytechnic Institute,
Santa Ana Street,
1000, Mexico City,
Federal District,
Post Office 04430, Mexico
e-mail: loboda@calmecac.esimecu.ipn.mx

Sergiy Yepifanov
National Aerospace University,
Chkalov Street, 17,
Kharkov,
Post Office 61070, Ukraine
e-mail: aedlab@ic.kharkov.ua

Yakov Feldshteyn
Compressor Controls Corporation,
4725 121 Street,
Des Moines, IA 50323
e-mail: yfeldshteyn@cccglobal.com

A Generalized Fault Classification for Gas Turbine Diagnostics at Steady States and Transients

Gas turbine diagnostic techniques are often based on the recognition methods using the deviations between actual and expected thermodynamic performances. The problem is that the deviations generally depend on current operational conditions. However, our studies show that such a dependency can be low. In this paper, we propose a generalized fault classification that is independent of the operational conditions. To prove this idea, the probabilities of true diagnosis were computed and compared for two cases: the proposed classification and the conventional one based on a fixed operating point. The probabilities were calculated through a stochastic modeling of the diagnostic process. In this process, a thermodynamic model generates deviations that are induced by the faults, and an artificial neural network recognizes these faults. The proposed classification principle has been implemented for both steady state and transient operation of the analyzed gas turbine. The results show that the adoption of the generalized classification hardly affects diagnosis trustworthiness and the classification can be proposed for practical realization. [DOI: 10.1115/1.2719261]

Introduction

Gas turbine performance deterioration has a significant impact on the engine lifetime and the owner's revenue. In general, this results in the engine operation at a higher inlet temperature for a specified load. That is why a poorly maintained gas turbine uses up its lifetime more rapidly. In order to improve engine reliability and reduce operational costs, advanced condition monitoring systems have been developed. In these systems, fault localization algorithms based on the gas path analysis may be considered as important and sophisticated. They provide an insight into gas turbine components' performances, which can significantly reduce total repair period and costs.

A lot of gas path faults, such as fouling, tip rubs, seal wear, foreign object damage, and erosion, are well known. Their detailed description can be found, for example, in the study conducted by Mejer-Homji et al. [1]. The authors have provided a thorough discussion of the gas turbine performance degradation related to the above-mentioned faults.

These faults affect gas path monitored variables (pressures, temperatures, rotation speeds, fuel consumption, and some others); therefore, actual fault types and engine component degradation can be potentially detected while analyzing gas path measurement data. In practice, it is difficult to pinpoint the exact problem just through monitored variables analysis. Firstly, the effects of gas turbine operational conditions are much greater and obscure fault influences. By operational conditions we mean all variables that completely define gas turbine behavior at steady states or transients. These variables can be divided into control variables and ambient conditions. Possible control variables are fuel consumption, rotor speeds, and some others. A control system maintains them at preset level or changes them according to a given program. Ambient conditions include ambient air temperature, pressure, and humidity. Secondly, due to the thermodynamic relations every fault influences all gas path variables and sometimes the impacts of different faults are similar. Furthermore, measurement and registration errors additionally mask fault displays.

To overcome the described difficulties, two general approaches are followed in gas turbine diagnostics. The first approach [2–5] is based on the identification techniques of a nonlinear thermodynamic gas path model. As the components suffer damage, their performances change accordingly. The thermodynamic model, in addition to the monitored variables and operational conditions, employs special internal parameters called "correction factors." These factors are able to shift component performance maps and to simulate component degradation by direct use of the model. For an inverse identification procedure, the goal is to find the correction factors that minimize difference between the model-generated and measured quantities. Besides the model's higher accuracy, the simplification of the diagnostic process is achieved because the determined factors contain information on the current technical state of every component. For the sake of further accuracy enhancement, an identification procedure can involve gas path data from different operating points to compute a single estimation of the correction factors. Therefore, variable operational conditions are not an obstacle here. However, this advanced diagnostic approach has some difficulties. The thermodynamic model is an integral part of diagnostic process, and, in addition to measurement errors, the inherent inaccuracy of the model also affects the analysis. The model's ability to describe a normal engine's technical condition can be considerably enhanced using available data for healthy engines but the real fault information is usually limited. That is why inaccuracy of the thermodynamic model is related first and foremost to a lack of accuracy in the fault simulation.

The presented paper follows the second approach because it has a theoretical possibility to exclude complex thermodynamic models (and the related inaccuracy) from the diagnostic process and to increase engine diagnosis reliability. This approach [6–10] involves common methods of the pattern recognition theory to classify actual engine technical condition. The necessary fault classes are constructed on real fault displays in the space of deviations of monitored variables, and a diagnostic decision about the state is made in the same space. The direct use of real fault data does not mean giving up mathematical models altogether. A simplified

Contributed by the International Gas Turbine Institute of ASME for publication in the JOURNAL OF ENGINEERING FOR GAS TURBINES AND POWER. Manuscript received June 29, 2006; final manuscript received January 24, 2007. Review conducted by Dave Doel. Paper presented at the ASME Turbo Expo 2006: Land, Sea and Air (GT2006), May 8–11, 2006, Barcelona, Spain. Paper No. GT2006-90723.

data-driven model will be necessary, for example, to describe a healthy engine's behavior. Some features of the considered approach are noted below.

In practice, available actual information rarely suffices to form a representative classification, especially in the beginning of an engine life cycle. This occurs because of the rare and occasional fault appearance, variations in fault displays for different engines, different maintenance conditions, and very high costs of real fault simulation on a test bed. These difficulties explain the lack of quantitative information needed to form real classes. That is why mathematical models are also involved [6,10–12]. Another peculiarity of current studies of the second approach is the strong interest in the practical results of the gas turbine diagnosis during transient operation [7,10,12] that promises to increase diagnosis accuracy. The growing application of such innovative recognition tools as artificial neural networks [6,10,13] is also worthy of notice.

With respect to the limitation of the reviewed studies, we can point out the following. Firstly, there is no clear answer as to how to take into account the changes in operational conditions while describing the fault recognition process. Some works apply the reduction of monitored variables to a common fixed operating point and standard day conditions, but the reduction formulas are not exact enough [14]. Moreover, it is not clear how to apply the reduction for transient operation. In the other works, deviations of the monitored variables from their normal values are computed to avoid an effect of operational conditions. However, the deviations still usually contain an influence of these conditions, which stands in the way of a correct recognition. Secondly, the majority of the works lack numerical estimation of the final trustworthiness of diagnosis so they cannot ensure effectiveness of the proposed techniques.

Over the recent years, while following the mentioned approach to fault recognition, we have examined gas turbine diagnostic techniques by means of fault simulation on the basis of the thermodynamic model, statistical testing of fault localization process, and the analysis of the obtained diagnosis trustworthiness indices [8,9,15]. The model allows us to estimate the diagnosis trustworthiness because the faults are known beforehand. On the basis of the obtained trustworthiness indices, various gas turbine diagnostics problems can be effectively investigated that is hardly possible under field conditions. The thermodynamic model serves two functions in these investigations: to determine variables of a monitored healthy gas turbine and to compute the same variables for different implanted faults. To take full advantage of this approach in the real diagnostic systems, the thermodynamic model, complex and sometimes not accurate enough, can be replaced with a simplified mathematical model of the healthy engine state (for example, polynomial model [15]) and real fault description.

To continue with such investigations, the presented paper discusses a problem of gas turbine diagnosis by neural networks under both steady state and transient conditions. The described approach, algorithms adjustment, and the peculiarities of operation can present practical interest for specialists in gas turbine diagnostics. However, the paper is chiefly concerned with the formation of the generalized fault classification that would not be sensitive to the changes in operational conditions.

The study was conducted for a two-shaft aero-derived gas turbine driving a pipeline gas compressor. The gas turbine was presented in the simulation by static and dynamic models.

Technical Approach to Diagnosis at Steady States

Static Model. Nowadays computer models are indispensable for the research and development of gas turbine diagnostics techniques replacing expensive real engine tests. Since the studies of Saravanamuttoo et al. [in particular, 2], application of the nonlinear one-dimensional thermodynamic models, such as the models used in the present paper and other studies [4–6], has become standard practice.

Structurally, a nonlinear model of steady states (static model) presents an $(m\times 1)$ vector of gas path monitored variables $\mathbf{Y}$ as a function of a vector of operational conditions (control variables and ambient conditions) $\mathbf{U}$ as well as a vector of correction factors $\boldsymbol{\Theta}$, which helps to describe component faults. This function can thus be written as $\mathbf{Y}=F(\mathbf{U},\boldsymbol{\Theta})$. It is determined as a solution of algebraic equation system reflecting mass, heat, and energy balance for all components under stationary conditions.

In order to extract useful diagnostic information from the raw measured data, it is a common preliminary operation [see, for example, [16]] to calculate deviations of monitored variables.

Deviations. The expression

$$\delta Y_i^* = \frac{Y_i^* - Y_{0i}}{Y_{0i}}, \quad i = 1,m \tag{1}$$

introduces relative deviations δY_i^* of actual measured values Y_i^* from their normal values Y_{0i}.

Taking into account that the given expression has a difference type, assume that model and measurement systematic errors are eliminated, vector $\boldsymbol{\delta}\mathbf{Y}^*$ only includes random errors, and these errors have the limited Gaussian distribution. Their maximal amplitudes given by the vector $\mathbf{a_Y}$ are employed to obtain normalized deviations Z_i^* according to the following operation

$$Z_i^* = \frac{\delta Y_i^*}{a_{Yi}} \tag{2}$$

that simplifies fault class description and, as shown in [7], enhances diagnosis trustworthiness. Appendix A includes estimations of the maximal amplitudes, which were obtained on real data as described in [15]. It is clear that errors in all elements of $\mathbf{Z}^*$ have the equal scatter $(-1,1)$ because of the normalization.

Employing the static model, the normalized deviations induced by the faults can be written as

$$Z_i = \frac{Y_i(\mathbf{U},\boldsymbol{\Theta}_0+\Delta\boldsymbol{\Theta}) - Y_i(\mathbf{U},\boldsymbol{\Theta}_0)}{Y_i(\mathbf{U},\boldsymbol{\Theta}_0)a_{Yi}} \tag{3}$$

where $\boldsymbol{\Theta}_0$ is a normal value of the correction factor vector and $\Delta\boldsymbol{\Theta}$ is the fault-associated change.

The model-based vector $\mathbf{Z}$ only gives a systematic part of the deviations. To simulate the deviation vector $\mathbf{Z}^*$ associated with real measurement, a vector $\boldsymbol{\varepsilon}$ of random errors, normally distributed in the interval $(-1,1)$, should be added, so

$$\mathbf{Z}^* = \mathbf{Z} + \boldsymbol{\varepsilon} \tag{4}$$

The deviation vector $\mathbf{Z}^*$ is considered as a pattern to be recognized. The next subsection describes how to present a fault classification by a set of such patterns.

Fault Classification. Engine faults vary considerably. Hence, for the purposes of engine diagnostics this variety has to be broken down into a limited number of classes. In the pattern recognition theory, it is often supposed that an object state D can belong only to one of q preset classes

$$D_1, D_2, \ldots, D_q \tag{5}$$

We accept this hypothesis for a gas turbine fault classification.

There are many types of fault classifications. In this study, it is assumed that every class corresponds to one engine component and is described by the correction factors of this component. Such class description is a common practice in gas turbine diagnostics [1–3,10]. Two types of classes are considered: a single fault class and a multiple one. The single fault class is formed by changing one correction factor. The multiple fault class has two independently changed factors for the same component.

First of all, to form any class from the patterns $\mathbf{Z}^*$, a nonlinear dependency $\mathbf{Y}=F(\boldsymbol{\Theta})$ is determined by the piecewise-linear inter-

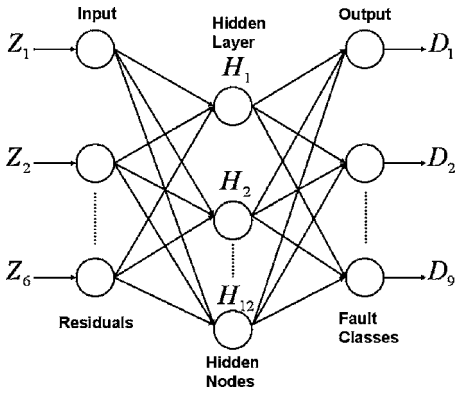

Fig. 1 Neural network structure

polation between the points computed by a static model for different values of every correction factor. Then the deviation vectors (3) corresponding to random changes of one or two correction factors are generated using the above dependency. A uniform distribution of correction factor values inside of interval $(0,-0.05)$ is employed to describe random fault severity of the engine fleet. The limit "0" gives the possibility to simulate incipient faults. The limit "−0.05" approximately corresponds to significant changes of the component performances, at which the gas turbine loses its capacity for operation due to failures or economical reasons. Finally, the random errors $\boldsymbol{\varepsilon}$ are added according to Eq. (4).

Hence, every class is given by a representative sample of the deviation vectors $\mathbf{Z}^*$ and the whole classification is a composition of these samples called a reference set $\mathbf{Zr}^*$. A plot of class representation by the reference set may be found in [8]. The fault classes are assumed to be equally probable and every class is presented by the same pattern quantity N as others. So, a total reference set volume Nr is equal to qN. Pattern generation involves a simplified model $\mathbf{Y}=F(\boldsymbol{\Theta})$ instead of the thermodynamic model because a pattern quantity Nr and corresponding number of model calls may go as high as 10,000 and more.

Diagnostic Algorithms, Neural Networks. A nomenclature of possible diagnoses

$$d_1, d_2, \ldots, d_q \tag{6}$$

corresponds to the accepted classification $D_1, D_2, \ldots, D_q$.

To make a diagnosis d, a method-dependent criterion

$$R_j = R(\mathbf{Z}^*, D_j) \tag{7}$$

is introduced as a measure of membership of a current pattern $\mathbf{Z}^*$ to class D_j. After calculating all values R_j, $j=1,q$, a decision rule

$$d = d_l \quad \text{if } R_l = \max(R_1, R_2, \ldots, R_q) \tag{8}$$

is applied. In the presented study, artificial neural networks are a recognition tool and their output functions give necessary criterion values R_j, $j=1,q$.

Neural networks present a fast growing computing technique in many fields of applications, such as pattern recognition, identification, control systems, and condition monitoring [17,18]. During network supervised learning on the known pairs of input and output (target) vectors, weights between the neurons change in a manner that ensures decreasing a mean difference (error) e between the target and the network output. In addition to the input and output layers of neurons, a network may incorporate one or more hidden layers of nodes when high network flexibility is necessary. Multiple layer perceptrons have been successfully applyied [19] to solve difficult pattern recognition problems since a back-propagation algorithm had been proposed for the training. We have chosen this network type for the fault diagnosis at both steady states and transients.

To apply a back-propagation algorithm, a layer transfer function should be differentiable. Usually it is of the sigmoid type. In the hidden layer, a tan-sigmoid function is employed. A log-sigmoid function is assigned for the output layer.

The measurement system and fault classification structures partly determine the composition of the used networks. The input layer includes m elements according to the size of the pattern vector $\mathbf{Z}^*$ to be recognized. The output layer complies with the classification structure and has q elements. The network complexity and the resolution capability are in close relation with the hidden layer quantity and node numbers. A network of one hidden layer is accepted following preliminary calculations. The number of its nodes will be chosen below.

The reference set $\mathbf{Zr}^*$ includes all data necessary to train networks. Every pattern is employed as an input vector during the learning. The element with the known fault class number in the corresponding target vector is marked as "1" and the others are zeros. The increase of the reference set volume Nr influences positively the network resolution capability; however, it puts additional strain on the computer resources. That is why the number Nr is a compromise between diagnosis accuracy requirements and an execution time.

Though the trained network is ready for practical use in a gas turbine diagnosis, an additional stage of network verification and diagnosis trustworthiness estimation is very important. It is included in the developed procedure as well.

Network Verification, Trustworthiness Indices. There is a common statistical rule that a function determined on one portion of the random data should be tested on another. Consequently, to verify a network trained on a reference set, we need one more set. The necessary set $\mathbf{Zt}^*$, called a testing set, of a volume Nt is created in the same way as the set $\mathbf{Zr}^*$. The only exception is that different series of the random numbers are involved in the calculations of the fault severity and errors in the deviations.

During the learning, network quality for a reference set is controlled by the behavior of the mean error function plotted versus learning period. The residual error obtained on a testing set would be used as a network quality criterion. However, an end user of the developed diagnostic algorithms needs to know the properties of the final diagnostic trustworthiness that, as the experience shows, are not in one-to-one correspondence with the mean error e. For this reason, for the verification of the network on its testing set, probabilities of the diagnoses $d_l, l=1,q$, are calculated when the actual class is D_j. These probabilities $Pd_{lj}=P(d_l/D_j)$ compose a square matrix Pd of diagnosis probabilities. The diagonal elements Pd_{ll} form a probability vector $\mathbf{P}$ of true diagnosis that represents an index of classes' distinguishability. Mean number of

Table 1 Diagnosis errors for single faults

	$\mathbf{P}''_e$									
Classification	ΔA_c	$\Delta\eta_c$	ΔA_{hpt}	$\Delta\eta_{hpt}$	ΔA_{pt}	$\Delta\eta_{pt}$	$\Delta\sigma_{cc}$	$\Delta\eta_{cc}$	$\Delta\sigma_{\text{in}}$	$\bar{P}''_e$
Conv.	0.166	0.266	0.132	0.265	0.146	0.172	0.154	0.174	0.168	0.1827
Gen.	0.156	0.275	0.131	0.269	0.148	0.190	0.161	0.184	0.180	0.1883

these elements—scalar $\bar{P}$—characterizes total engine diagnosability. No diagonal elements help to identify the causes of bad class distinguishability. These elements make up probabilities of false diagnosis

$$Pe_j = 1 - P_j \quad \text{and} \quad \bar{P}e = 1 - \bar{P} \tag{9}$$

The above indices are also calculated for a reference set because the difference between the indices obtained on the reference set and the testing set permits us to control the over-teaching effect.

Thus, the described approach to gas turbine diagnosis under stationary conditions includes the fault classification stages, formation of network-based diagnostic algorithm, and estimation of diagnosis trustworthiness indices. This approach has been implemented in the steady state diagnostic procedure.

The next section specifies conditions for this procedure, describes optimal network configuration choice and parameters, and gives the resulting trustworthiness of gas turbine diagnosis.

Diagnosis Under Steady State Conditions

For the nonlinear gas turbine simulation, a steady state operation was determined by fixed gas generator and power turbine speeds under standard ambient conditions. To study different steady state modes, 11 full and part-load modes were set by gas generator speeds: 10,700, 10,600, …, 9700 rpm.

Monitored variables' structure that is presented in Appendix A corresponds to a typical gas turbine measurement system and includes six gas path variables. The single type fault classification consists of nine classes, which are simulated by nine correction factors of the thermodynamic model (see Appendix B). The multiple type classification includes four items corresponding to four main components: an axial air compressor, a combustion chamber, a gas generator turbine, and a power turbine. The multiple fault classes are simulated by eight correction factors.

According to the structures of monitored variables and fault classes, the chosen network for the diagnosis at the steady states (Fig. 1) has six nodes on the input layer and nine nodes (single type classification) or four nodes (multiple type classification) for the output layer. As for the hidden layer, the number of 12 nodes was estimated as optimal [9].

The precision analysis of the statistically calculated probabilities shows that influences of the reference and testing set volumes are practically equal. The analysis also demonstrates that 1000 patterns for every class are sufficient to ensure the necessary precision.

The parameters determined above present the most common conditions of the calculations. Every deviation from these conditions will be noted additionally.

As for the training process, there are many variations of the basic back-propagation algorithm. To choose the most suitable variation for gas turbine fault recognition, 12 variations were included in the procedure one after another and compared by the execution time [9]. Two of the algorithms with the shortest times, resilient back-propagation ("rp"-algorithm) and scaled conjugate gradient algorithm ("scg"-algorithm), were chosen for next calculations. These calculations helped to verify more carefully both training algorithms. Since in some cases the "scg"-algorithm could not find the absolute minimum of the error function e, it was decided that only the resilient back-propagation algorithm be adopted for the future.

Thus, the applied network and the whole procedure have been adjusted for the gas turbine diagnosis at the steady states. The next section discusses the effects of the changes in the operational conditions and a classification that is independent of such changes.

Table 2 Diagnosis errors for multiple faults

	$\mathbf{P}''_e$				
Classification	$\Delta A_c, \Delta \eta_c$	$\Delta A_{hpt}, \Delta \eta_{hpt}$	$\Delta A_{pt}, \Delta \eta_{pt}$	$\Delta \sigma_{cc}, \Delta \eta_{cc}$	$\bar{P}''_e$
Conv.	0.100	0.205	0.073	0.133	0.1276
Gen.	0.105	0.213	0.076	0.138	0.1331

Steady State Conditions: Generalized Classification

To diagnose the considered gas turbine at different operating modes, it has been found out that class presentation in the diagnostic space $\mathbf{Z}$ is not strongly dependent on a mode change. Therefore we intended to draw up the classification that would be independent from operational conditions. To verify the idea of such classification, it has been created by incorporating patterns from all 11 steady states into every class of the reference and testing sets. In this case, a region occupied by a class is more diffused and induces greater class intersection, which leads to losses in the diagnosis trustworthiness. But how significant are these losses?

The diagnostic procedure, modified to work with a new classification, helped to quantify a possible negative effect of the proposed classification generalization. Trustworthiness indices were computed for the old and new classifications. To ensure firm conclusions, the classification comparison was drawn for both single and multiple class types. Tables 1 and 2 contain the results. In these and other tables below, the row "Conv." means the probabilities for the conventional classification averaged over all steady states. The row "Gen." contains the probabilities for the generalized classification created for, and applied at, the same steady states. It can be noted that differences of the probabilities $\mathbf{P}''_e$ between the considered classifications are small for the both class types. The mean probability $\bar{P}''_e$ also rises just a little, by 0.0055–0.0056, in the row "Gen." So the trustworthiness losses resulting from the classification generalization are insignificant.

For additional verification of the generalized classification, previous analysis was also carried out for real operational conditions. Two sets of 25 operating points were made up from a 6 month database of gas turbine performance registration at different operational field conditions. The points of each set correspond to the maximally different conditions. Their changes contain the ranges of $(9430, 10640)$ rpm for the gas generator speed, $(4740, 6000)$ rpm for the power turbine speed, $(-25, 25)\,^{\circ}\mathrm{C}$ for the ambient air temperature, and $(96, 100)$ kPa for the ambient air pressure.

Table 3 Mean probabilities of false diagnosis under real operational conditions

	Set 1 (points 1–25)		Set 2 (points 26–50)	
Classification	Single faults	Multiple faults	Single faults	Multiple faults
Conv.	0.1836	0.1297	0.1834	0.1304
Gen.	0.1836	0.1310	0.1856	0.1275
Gen.*	0.1854	0.1285	0.1848	0.1293

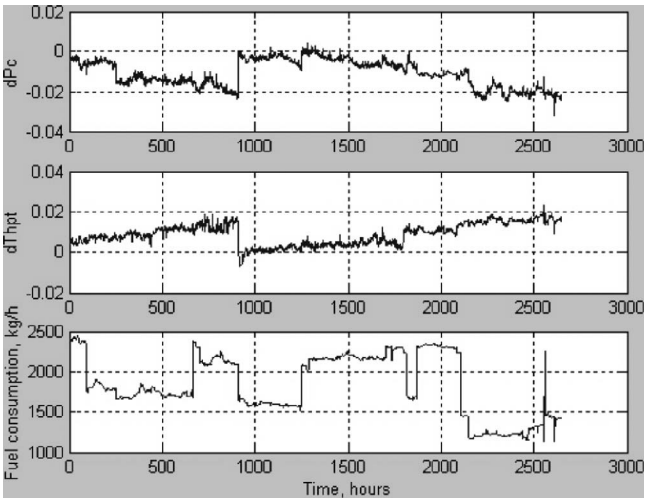

Fig. 2 Time plots of the fuel consumption and the deviations of the compressor discharge pressure (CDP) dPc and the gas generator turbine exhaust gas temperature (EGT) dThpt. (The deviations are calculated according to expression (1).)

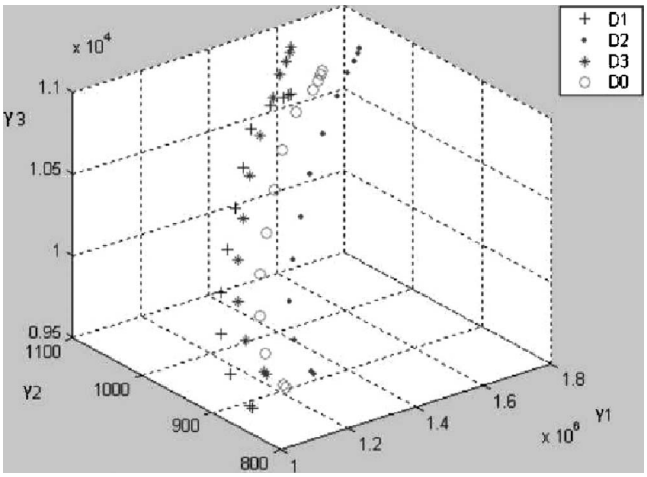

Fig. 3 Transient trajectories of simulated faults in the space of monitored variables. (Normal behavior D0 and faults D1, D2, and D3 are simulated at transient 1 of Table 8. The faults correspond to maximal change of the first three correction factors listed in Table 7. The coordinates Y1, Y2, and Y3 are compressor discharge pressure, gas generator turbine exhaust gas temperature, and gas generator rotation speed.)

Table 3 presents the results of the comparison of both classifications under these conditions. The rows "Conv." and "Gen." retain the same sense as in the previous tables. A new row "Gen.*" corresponds to the experiment in which the generalized classification is created at the points of one set but is applied to the other set, which is indicated in the head of a column. Comparing the rows "Gen." and "Gen.*" with the row "Conv.," we can see that the differences are small for all considered cases and have different signs. These differences can be considered as random calculation errors. Consequently, the proposed classification does not cause additional trustworthiness losses. This still holds true when the classification is used at the operating points different from the points of classification formation. So, the generalized classification can be applied not only to the operating points used for its creation but also to any other points.

To further substantiate the idea of the generalized classification, consider a real fault (compressor fouling) at different operating points. The above-mentioned database gives the necessary information. Figure 2 shows time plots of the deviations of two monitored variables (CDP and EGT) and a control variable of fuel consumption. A gradual change of the deviations illustrates the fouling effect; jumps in point 920 are results of a compressor wash. Comparing the plots, we can see that different operational conditions that are indicated by considerable changes of the fuel consumption do not induce visible shifts of the deviations. The analyzed real gas turbine fault is then independent of operational conditions. This is an additional argument for usefulness of the generalized classification.

The two following sections describe diagnosing and forming the generalized fault classification for the case of transients.

Diagnosis Under Transient Conditions

The approach to the diagnosis at transients generally follows the approach to the diagnosis at steady states. The differences are given below.

Features of the Approach. In the case of a transient simulation, a time variable t is added to the argument set of the function $\mathbf{Y}$ and the vector $\mathbf{U}$ is given as a time function, i.e., a dynamic model has a structure $\mathbf{Y}=F(\mathbf{U}(t),\boldsymbol{\Theta},t)$. Mathematically, the dynamic model is a differential equation system including time derivatives and, for each time step, the solution represents a quasi-steady state operating point.

On basis of the computed variables $\mathbf{Y}$, a generalized deviation vector $\mathbf{W}^*$ is determined as follows. Transients for normal and faulted engine states, which present trajectories in the space of monitored variables as shown in Fig. 3, are divided into T time-points (measurement sections). The deviation vector $\mathbf{Z}$ is calculated at the next step for every pair of similar points of "faulted" and "normal" trajectories in the same way as in the case of stationary operation. As can be seen in Fig. 4, the deviations of every fault, which are marked by the same symbol, form a compact group that will contribute to a better fault recognition. To determine $\mathbf{Z}^*$, errors are added then to every $\mathbf{Z}$ according to Eq. (4). Finally, the generalized $(mT\times 1)$ vector $\mathbf{W}^*$ is composed from all successive vectors $\mathbf{Z}^*$ of the same pair of trajectories.

As the deviation vector $\mathbf{Z}^*$ for steady states, the generalized vector $\mathbf{W}^*$ is a pattern to be recognized at transients. A reference set $\mathbf{Wr}^*$ and a testing set $\mathbf{Wt}^*$ are created from the patterns $\mathbf{W}^*$ in the same way as in the case of stationary operation. A graphical presentation of the sets $\mathbf{Wr}^*$ and $\mathbf{Wt}^*$ is similar to the plot of a

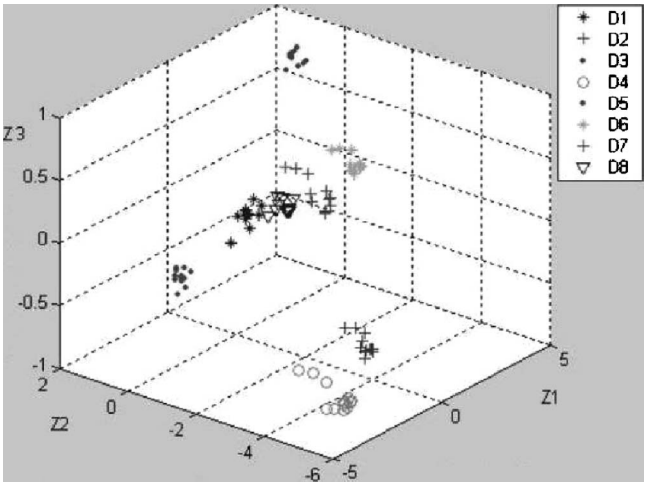

Fig. 4 Fault presentation by the deviations for transient operation. (The monitored variables and the transient are the same as in Fig. 3. Faults D1–D8 correspond to maximal change of the corrections factors listed in Table 7. No measurement errors are applied.)

Table 4 Mean probabilities of false diagnosis for different network configurations. (Scalars $\bar{P}'_e$ and $\bar{P}''_e$ mean probabilities obtained on reference and testing sets correspondingly. For every combination of given pattern and node numbers, the lowest probability $\bar{P}''_e$ is marked in bold.)

		Nodes					
		12		25		50	
N	Epochs	$\bar{P}'_e$	$\bar{P}''_e$	$\bar{P}'_e$	$\bar{P}''_e$	$\bar{P}'_e$	$\bar{P}''_e$
500	50	⋯	⋯	⋯	⋯	0.0630	0.1352
	100	0.0725	0.1385	0.0525	0.1365	0.0422	**0.1330**
	200	0.0598	0.1380	0.0395	0.1380	0.0265	0.1395
	300	0.0538	0.1380	0.0338	0.1405	0.0230	0.1375
	400	0.0508	0.1360	0.0318	0.1357	0.0223	0.1380
	500	0.0485	**0.1348**	0.0305	**0.1348**	0.0215	0.1372
1000	50	⋯	⋯	⋯	⋯	0.0819	**0.1161**
	100	0.0954	0.1185	0.0844	0.1154	0.0598	0.1126
	200	0.0816	0.1180	0.0706	**0.1140**	0.0469	0.1151
	300	0.0745	**0.1175**	0.0629	0.1159	0.0414	0.1179
	400	0.0720	0.1179	0.0594	0.1178	0.0389	0.1189
	500	0.0695	0.1195	0.0305	0.1348	0.0373	0.1202
2000	50	⋯	⋯	⋯	⋯	0.0941	0.1139
	100	0.1066	0.1213	0.0887	**0.1154**	0.0813	**0.1131**
	200	0.0927	0.1151	0.0771	0.1162	0.0672	0.1138
	300	0.0876	0.1137	0.0689	0.1156	0.0596	0.1164
	400	0.0844	**0.1136**	0.0661	0.1170	0.0562	0.1174
	500	0.0813	0.1136	0.0642	0.1181	0.0543	0.1180

reference set at steady states, which can be found in [8].

Taking into account the described features, a transient diagnostic procedure was developed. The conditions of its operation, adjustment of network parameters, and the first results are given in the next section.

Adjustment of the Network Used. For a gas turbine dynamic modeling, a fuel consumption variable has been chosen as a control variable. Seven gas path variables presented in the table in Appendix C were used to describe the faults. Different transients were simulated as specified in Appendix C. Every transient is determined by the time profile of fuel consumption (transient profile) under constant ambient conditions. The dynamic operation analyzed in this section corresponds to the first transient in the table in Appendix C.

Due to total computational complexity of the transient diagnostic procedure, only the single type fault classification was implemented. It incorporates eight classes simulated by eight correction factors listed in Appendix B.

According to the mentioned numbers, the network for the diagnosis at transients has 98 nodes on the input layer and 8 nodes on the output layer. The other network parameters have been estimated in a series of 48 calculations. Quantity of nodes in the hidden layer, pattern number to describe one class, and time steps (epochs) of the learning period were varied independently in order to define conditions for the highest diagnosis trustworthiness. The results found in Table 4 led us to draw the following conclusions:

- An increase of the pattern number N visibly reduces the error probabilities, particularly when N changes from 500 to 1000.
- An increase of node number causes growth of the overteaching because of reduction in $\bar{P}'_e$.
- An influence of epochs is not too high and the random nature of the fault simulation affects systematic tendencies here.

Taking into account these conclusions, as well as the results of extra calculations, the parameters 1000 patterns, 25 nodes, and 200 epochs have been chosen as basic. According to the table, error probability under these conditions works out at 0.114 (probability of true diagnosis 0.886). An estimated standard deviation $\sigma=0.0031$ of this probability characterizes a computational inaccuracy of this basic calculation.

In summary, the procedure for gas turbine diagnosis under transient conditions has been adjusted. It is estimated that the level of diagnosis errors can be reduced down to 11% compared with 18% obtained under stationary conditions for the single fault classes. In the next section, the effect of variable operational conditions is studied and the possibility of using the generalized fault classification for diagnosis at transients is discussed.

Transient Conditions: Generalized Classification

If different stationary modes do not influence significantly fault class description, why can this not be true under transient conditions? To answer this question, fault displays have been investigated at 16 transients under different operational conditions. The table in Appendix C specifies differences between the transients, which include independent variation of three factors: transient profile, atmospheric temperature T_H, and transient type (acceleration or deceleration).

Figure 5 helps to visualize the faults for these transients. Every fault has its own mark, which is the same for all transients. One can see that points are grouped by a mark. Compare Fig. 5 with Fig. 4, which shows the faults for the first transient only. It may be concluded that although fault regions became more diffuse, most of the faults are still easy to distinguish. So, the influence of transient change on fault description is not significant.

In order to prove this conclusion and possibily to form the generalized classification, quantitative analysis was performed for the described transients. The effect of transient peculiarity on diagnosis trustworthiness was initially checked up on in the conventional classification at every transient. The resulting error probabilities for all 16 transients are presented in Table 5. They show that the trustworthiness of the diagnosis is not greatly affected by the transient peculiarity and the variation of any of the mentioned factors.

The generalized classification was then created for all transients in the same way as previously described for steady states. Its probabilities are found in the last row. Comparing them with the probabilities of the conventional classification averaged over all

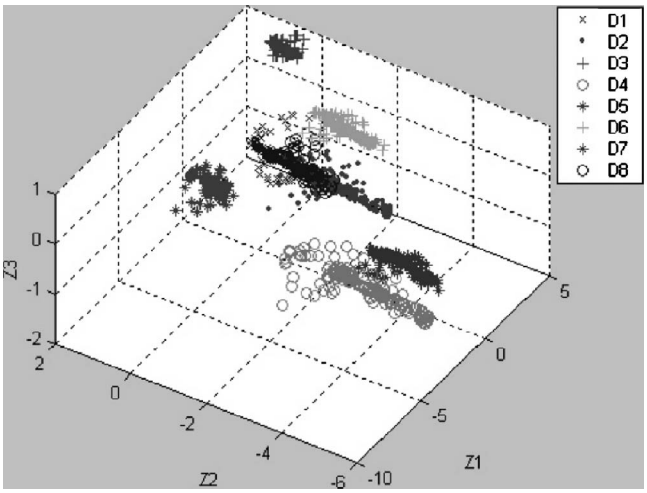

Fig. 5 Fault presentation by the deviations for different transients. (The faults are simulated at the 16 transients of Table 8. Fault severity corresponds to maximal change of the corrections factors listed in Table 7. No measurement errors are applied.)

transients (row "Conv."), it can be stated that the differences are higher than in the case of steady states. However, they are not too high: $\Delta\bar{P}''_e=0.0360$. Given the above, the diagnosis based on the generalized classification does not lead to substantial trustworthiness losses.

In addition to the fault classes presented in Table 5, which are common for steady states and transients, some specific faults may take place in dynamic operation. For example, the authors of studies [10,12] consider bearing faults under transient conditions. In order to examine the applicability of the proposed classification principle to such specific faults, we introduced into the classification two additional classes of bearing faults of gas generator and power turbine rotors. These classes were determined by the same mode as basic classes. The maximal fault severity was given by a fourfold increase of the mechanical losses from their nominal values. The previous calculations with the generalized and conventional classifications have been repeated at transients 1–4 for a new class structure (ten items) and an old one (eight items). The mean additional trustworthiness losses induced by the generalized classification were found to be comparable: $\Delta\bar{P}''_e=0.0192$ (new structure) and $\Delta\bar{P}''_e=0.0139$ (old structure). The individual losses 0.0320 and 0.0077 for new classes are not greater than for the basic ones (differences between the rows "Gen." and "Conv." of Table 5). Consequently, the faults specific for transient operation such as the bearing faults do not cause any difficulties for implementing the generalized classification.

Besides the changes in operational conditions considered in this section, a different inlet air pressure and humidity can also affect the results. However, such influence is not expected to be high. Furthermore, changes of real operational conditions are often more limited than the simulated changes. That is why the trustworthiness losses of 3.6% can be further reduced. The generalized classification thus seems to be acceptable for the gas turbine diagnostics under dynamic conditions.

Conclusions

By way of summing up, we would like to emphasize the following:

On the basis of common approach to gas turbine diagnosis involving artificial neural networks, diagnostic procedures have been developed to be used at steady states and transients. The diagnosis trustworthiness was estimated through stochastic simulation of the procedures' operation.

Experiments in the simulation of the diagnosis process under different conditions helped us to estimate the best conditions and accumulate the experience of diagnostic algorithm adjustment, which may prove useful in the practical implementation of algorithms. During the experimentation, the lowest probabilities of

Table 5 Probabilities of false diagnosis at different transients

	$\mathbf{P}''_e$								
Transients	ΔA_c	$\Delta\eta_c$	ΔA_{hpt}	$\Delta\eta_{hpt}$	ΔA_{pt}	$\Delta\sigma_{cc}$	$\Delta\eta_{cc}$	$\Delta\sigma_{in}$	$\bar{P}''_e$
				Acceleration, T_H=288.15					
1	0.077	0.208	0.076	0.227	0.098	0.089	0.101	0.098	0.1218
2	0.098	0.218	0.077	0.218	0.094	0.108	0.092	0.127	0.1290
3	0.152	0.231	0.079	0.252	0.103	0.118	0.103	0.201	0.1549
4	0.075	0.162	0.069	0.169	0.095	0.089	0.096	0.089	0.1055
				Acceleration, T_H=243.15					
5	0.088	0.181	0.078	0.191	0.100	0.105	0.094	0.096	0.1166
6	0.099	0.179	0.084	0.195	0.087	0.104	0.086	0.113	0.1184
7	0.154	0.224	0.082	0.230	0.117	0.117	0.098	0.189	0.1514
8	0.087	0.165	0.071	0.165	0.084	0.109	0.075	0.079	0.1044
				Deceleration, T_H=288.15					
9	0.097	0.198	0.070	0.165	0.099	0.108	0.091	0.088	0.1145
10	0.105	0.189	0.088	0.175	0.106	0.108	0.077	0.084	0.1165
11	0.166	0.232	0.093	0.256	0.094	0.133	0.105	0.190	0.1586
10	0.089	0.174	0.071	0.180	0.079	0.114	0.087	0.083	0.1096
				Deceleration, T_H=243.15					
13	0.099	0.138	0.078	0.146	0.099	0.104	0.085	0.084	0.1041
14	0.090	0.145	0.084	0.162	0.102	0.120	0.076	0.099	0.1098
15	0.165	0.248	0.092	0.235	0.111	0.129	0.107	0.174	0.1576
16	0.094	0.149	0.065	0.165	0.078	0.108	0.072	0.109	0.1050
	Averaged probabilities obtained on the conventional and generalized classifications								
Conv.	0.108	0.190	0.079	0.196	0.097	0.110	0.090	0.119	0.1236
Gen.	0.159	0.262	0.094	0.240	0.112	0.148	0.093	0.169	0.1596

Table 6 Accuracy and structure of monitored variables (+ =monitored variable, −=idle variable)

No.	Variable	$\mathbf{a}_Y$	Steady state condition	Transient condition
1	Compressor discharge total pressure	0.015	+	+
2	Gas generator turbine total pressure	0.015	+	+
3	Compressor total temperature	0.025	+	+
4	Gas generator turbine exhaust gas total temperature	0.015	+	+
5	Power turbine total temperature	0.020	+	+
6	Fuel consumption	0.020	+	−
7	Gas generator rotation speed	0.005	−	+
8	Power turbine rotation speed	0.005	−	+
	Total quantity m of monitored variables		6	7

false diagnosis were found. This permitted us to determine reachable trustworthiness levels for gas turbine diagnosis at steady states and transients.

The main accomplishment of the presented research is the realization and examination of the idea that fault classification can be independent from the actual operating mode. A generalized classification has been proposed. It combines faults descriptions obtained under different operational conditions and allows diagnosis under any conditions. The proposed classification principle was verified separately for steady states and transients. In both cases, the results have shown that the generalized classification practically does not reduce the trustworthiness level. On the other hand, the suggested classification drastically simplifies the gas turbine diagnosis because it is formed once and used later without changes. Therefore, the diagnostic technique based on the generalized fault classification can be successfully implemented in gas turbine health monitoring systems.

Acknowledgment

Support for this work was provided by the National Polytechnic Institute of Mexico (Project No. 20050709).

Table 7 Structure of varied correction factors for simulating the fault classes (+=utilized factors, −=idle factors)

No.	Correction factor	Steady state condition: Single classes	Steady state condition: Multiple classes	Transient condition, single classes
1	ΔA_c—compressor flow factor	+	+	+
2	$\Delta\eta_c$—compressor efficiency factor	+	+	+
3	ΔA_{hpt}—high pressure turbine flow factor	+	+	+
4	$\Delta\eta_{hpt}$—high pressure turbine efficiency factor	+	+	+
5	ΔA_{pt}—power turbine flow factor	+	+	+
6	$\Delta\eta_{pt}$—power turbine efficiency factor	+	+	−
7	$\Delta\sigma_{cc}$—combustion chamber total pressure recovery factor	+	+	+
8	$\Delta\eta_{cc}$—combustion efficiency factor	+	+	+
9	$\Delta\sigma_{in}$—inlet device total pressure recovery factor	+	−	+
	Total quantity of factors	9	8	8

Nomenclature

$\mathbf{a_Y}$ = vector of maximal amplitudes of random errors in the deviations $\boldsymbol{\delta Y}^*$
D = fault class
d = diagnosis
e = mean error function
m = number of monitored gas path variables
N = number of patterns to describe one class
$\mathbf{P}$ = vector of true diagnosis probabilities
$\bar{P}$ = mean probability of true diagnoses
Pd = matrix of diagnosis probabilities
$\mathbf{Pe}$ = probability vector of false diagnosis
$\bar{P}e$ = mean probability of false diagnoses
q = number of fault classes
"rp" = resilient back-propagation learning algorithm
"scg" = scaled conjugate gradient learning algorithm
t = time variable
T = number of measurement sections for one transient
$\mathbf{U}$ = vector of operational conditions
$\mathbf{W}$ = vector of normalized deviations of monitored variables at transients
$\mathbf{Wr}^*$ = reference set for transients
$\mathbf{Wt}^*$ = testing set for transients
$\mathbf{Y}$ = vector of gas path monitored variables
$\mathbf{Z}$ = vector of normalized deviations of monitored variables at steady states
$\mathbf{Zr}^*$ = reference set for steady states
$\mathbf{Zt}^*$ = testing set for steady states
Δ = absolute change of any variable
ΔA = flow correction factor
$\Delta\eta$ = efficiency correction factor
$\Delta\sigma$ = total pressure recovery correction factor
$\boldsymbol{\delta Y}$ = vector of relative deviations of monitored variables
$\boldsymbol{\varepsilon}$ = vector of normalized random errors
σ = standard deviation
$\boldsymbol{\Theta}$ = vector of correction factors

Subscripts and Superscripts

* = measured value
c = compressor
cc = combustion chamber
hpt = high pressure turbine
in = inlet device
pt = power turbine
i = index of gas path variable Y
j = index of class D
l = index of diagnosis d
$r(\,')$ = reference set
$t(\,'')$ = testing set

Appendix A

See Table 6.

Appendix B

See Table 7.

Appendix C

A simulated gas turbine transient is a dynamic process of the fixed period of 2.8 seconds. It is determined by a transient profile, fixed atmospheric temperature, and standard atmospheric pressure. The transient profile is given by a section of fuel consumption constant value Gf_1, a section of a lineal consumption change from Gf_1 to Gf_2 during a time t, and a section of constant value Gf_2.

Table 8 Simulated transients

Transient no.	t (s)	Gf_2/Gf_1	Transient profile	T_H (K)	Transient type
1	1.5	2.0	1	288.15	Acceleration
2	2.2	2.0	2	288.15	Acceleration
3	0.1	1.2	3	288.15	Acceleration
4	0.6	2.0	4	288.15	Acceleration
5	1.5	2.0	1	243.15	Acceleration
6	2.2	2.0	2	243.15	Acceleration
7	0.1	1.2	3	243.15	Acceleration
8	0.6	2.0	4	243.15	Acceleration
9	1.5	1/2.0	1	288.15	Deceleration
10	2.2	1/2.0	2	288.15	Deceleration
11	0.1	1/1.2	3	288.15	Deceleration
12	0.6	1/2.0	4	288.15	Deceleration
13	1.5	1/2.0	1	243.15	Deceleration
14	2.2	1/2.0	2	243.15	Deceleration
15	0.1	1/1.2	3	243.15	Deceleration
16	0.6	1/2.0	4	243.15	Deceleration

The totality of simulated transients includes 16 items and is presented in Table 8. As can be seen, these transients are determined by an independent variation of the transient profile (four profiles), atmospheric temperature T_H (two values), and transient type (two types). The profiles of deceleration are similar to the acceleration profiles; the only difference is the opposite direction of a fuel consumption change.

References

[1] Cyrus, B. M., Mustapha, A. C., and Hatim, M. M., 2001, "Gas Turbine Performance Deterioration," *Proceedings of the Thirtieth Turbomachinery Symposium*, Turbomachinery Laboratory, Sep. 17–20, Houston, Texas A&M University, TX, pp. 139–175.

[2] Saravanamuttoo, H. I. H., and MacIsaac, B. D., 1983, "Thermodynamic Models for Pipeline Gas Turbine Diagnostics," ASME J. Eng. Power, **105**(10), pp. 875–884.

[3] Benvenuti, E., 2001, "Innovative Gas Turbine Performance Diagnostics and Hot Part Life Assessment Techniques," *Proceedings of the Thirtieth Turbomachinery Symposium*, Turbomachinery Laboratory, Sep. 17–20, Houston, Texas A&M University, TX, pp. 23–31.

[4] Kamboukos, Ph., and Mathioudakis, K., 2003, "Comparison of Linear and Non-Linear Gas Turbine Performance Diagnostics," IGTI/ASME Turbo Expo, Atlanta, GA, June 16–19.

[5] Yepifanov, S., and Loboda, I., 2003, "Gas Path Model Identification as an Instrument of Gas Turbine Diagnosing," IGTI/ASME Turbo Expo, Atlanta, GA, June 16–19.

[6] Roemer, M. J., and Kacprzynski, G. J., 2000, "Advanced Diagnostics and Prognostics for Gas Turbine Engine Risk Assessment," IGTI/ASME Turbo Expo, Munich, Germany, May 8–11.

[7] Turney, P., and Halasz, M., 1993, "Contextual Normalization Applied to Aircraft Gas Turbine Engine Diagnostics," J. Appl. Intell., Springer, Vol. 3.

[8] Loboda, I., 2003, "Trustworthiness Problem of Gas Turbine Parametric Diagnosing," 5th IFAC Symposium on Fault Detection, Supervision and Safety of Technical Processes, Washington, DC, June 9–11.

[9] Loboda, I., Nakano Miyatake, M., Goryachiy, A. et al., 2005, "Gas Turbine Fault Recognition by Artificial Neural Networks," The Fourth International Congress of Electromechanical Engineering and Systems, National Polytechnic Institute, Mexico City, Mexico, Nov. 14–18.

[10] Ogaji, S. O. T., Li, Y. G., Sampath, S., and Singh, R., 2003, "Gas Path Fault Diagnosis of a Turbofan Engine From Transient Data Using Artificial Neural Networks," IGTI/ASME Turbo Expo, Atlanta, GA, June 16–19.

[11] MacIsaac, B. D., and Muir, D. F., 1991, "Lessons Learned in Gas Turbine Performance Analysis," Canadian Gas Association Symposium on Industrial Application of Gas Turbines, Banff, Alberta, Canada, October 16–17.

[12] Sampath, S., Li, Y. G., Ogaji, S. O. T. Singh, R., 2003, "Fault Diagnosis of a Two Spool Turbofan Engine Using Transient Data: A Genetic Algorithm Approach," IGTI/ASME Turbo Expo, Atlanta, GA, June 16–19.

[13] Greitzer, F. L., Kangas, L. J., Terrones, K. M., Maynard, M. A., Wilson, B. W., Rawlovski, R. A., Sisk, D. R., and Brown, N. B., 1999, "Gas Turbine Engine Health Monitoring and Prognostics," International Society of Logistics (SOLE) 1999 Symposium, Las Vegas, NV, Aug. 30–Sep. 2.

[14] Yepifanov, S., Kuznetsov, B., and Bogaenko, I., 1998, *Design of Gas Turbine Engine Control and Diagnosing Systems*, Technica, Kiev, Ukraine.

[15] Loboda, I., Yepifanov, S., and Feldshteyn, Y., 2004, "Deviation Problem in Gas Turbine Health Monitoring," IASTED International Conference on Power and Energy Systems, Clearwater Beach, FL, Nov. 28–Dec. 1.

[16] Basseville, M., 2003, "Model-Based Statistical Signal Processing and Decision Theoretic Approaches to Monitoring," Fifth IFAC Symposium on Fault Detection, Supervision and Safety of Technical Process, Washington, DC, June 9–11, pp. 1–12.

[17] Rao, B. K. N., 1996, *Handbook of Condition Monitoring*, Elsevier Advanced Technology, Oxford.

[18] Duda, R. O., Hart, P. E., and Stork, D. G., 2001, *Pattern Classification*, Wiley-Interscience, New York.

[19] Haykin, S., 1994, *Neural Networks*, Macmillan College Publishing, New York.

Integration of On-Line and Off-Line Diagnostic Algorithms for Aircraft Engine Health Management

Takahisa Kobayashi
ASRC Aerospace Corporation,
21000 Brookpark Road,
Cleveland, OH 44135

Donald L. Simon
U.S. Army Research Laboratory,
Glenn Research Center,
21000 Brookpark Road,
Cleveland, OH 44135

This paper investigates the integration of on-line and off-line diagnostic algorithms for aircraft gas turbine engines. The on-line diagnostic algorithm is designed for in-flight fault detection. It continuously monitors engine outputs for anomalous signatures induced by faults. The off-line diagnostic algorithm is designed to track engine health degradation over the lifetime of an engine. It estimates engine health degradation periodically over the course of the engine's life. The estimate generated by the off-line algorithm is used to "update" the on-line algorithm. Through this integration, the on-line algorithm becomes aware of engine health degradation, and its effectiveness to detect faults can be maintained while the engine continues to degrade. The benefit of this integration is investigated in a simulation environment using a nonlinear engine model.
[DOI: 10.1115/1.2747640]

Keywords: in-flight fault detection, trend monitoring, on-board engine model, Kalman filter

Introduction

Early detection of faults is an important aspect in the health management of aircraft gas turbine engines. Undetected faults can lead the aircraft engine into an undesirable operating condition where the compressor stall margin is reduced or turbine temperature is higher than the expected value. Under such a condition, safety and efficiency of engine operation may be compromised. Thus, it is critical to detect faults as early as possible and take the necessary corrective actions to avoid undesirable engine operation.

To achieve a real-time fault detection capability, on-line diagnostic algorithms have been developed by several researchers [1–4]. An on-line diagnostic algorithm is designed to run on an on-board engine computer in real time. It processes measured engine outputs to detect and, if possible, isolate a fault. Fault detection is pursued based on the fact that the measured engine outputs deviate from their reference condition values when an aircraft engine experiences a fault. An on-line diagnostic algorithm, however, encounters a challenge in achieving reliable performance. This challenge arises from the fact that the measured engine outputs are influenced not only by faults but also by engine health degradation. Engine health degradation is a normal aging process that all aircraft engines will experience due to usage and therefore is not considered as a fault, whereas a fault is an abnormal, unexpected event. Given the measured engine outputs, it is difficult to discern whether the engine output deviations are due to a fault or health degradation. Unless this issue is addressed, the on-line diagnostic algorithm will lose its effectiveness to detect faults as the engine degrades over its lifetime.

One approach to address the above issue is to integrate the on-line diagnostic algorithm with an off-line trend monitoring algorithm. The task of an off-line trend monitoring algorithm is to track the engine health condition over the lifetime of an engine. It estimates the engine health condition based on steady-state engine output data recorded during flight [5–7]. Since health degradation is a gradual process, the off-line algorithm needs to update its estimate at a relatively low frequency, such as once per a few flights or days. This periodically updated knowledge of engine health condition can be used to adjust the on-line diagnostic algorithm. Through this integration, the on-line diagnostic algorithm becomes aware of health degradation, and its effectiveness to detect faults can be maintained while the engine continues to degrade.

In this paper, an on-line fault detection algorithm and an off-line trend monitoring algorithm are integrated, and the benefit of this integration is investigated in a simulation environment. The on-line fault detection algorithm is based on the hybrid Kalman filter [8,9], and the off-line trend monitoring algorithm is based on the extended Kalman filter [10]. In the following sections, the details of each algorithm are described, followed by the application of the design methodology to a large commercial aircraft engine model. Then, the effectiveness of the integrated diagnostic approach is evaluated using simulated examples of health degradation and faults.

Problem Background: Influence of Faults and Health Degradation

Although aircraft gas turbine engines are highly reliable, they may encounter numerous types of faults during flight. Sensor faults are most likely to occur [1], but rotating components and actuators may also experience faults. When an aircraft engine experiences a fault, the measured engine outputs deviate from their reference condition values. Therefore, fault detection can be accomplished by monitoring for shifts in measured engine outputs induced by faults. This is, however, a challenging problem since shifts in measured engine outputs are induced not only by faults but also by engine health degradation. Engine health degradation is the result of usage and manifests itself as degraded performance of engine components such as compressors and turbines. As it worsens gradually over time, the deviation of the measured engine outputs from their reference condition values increases.

Contributed by the International Gas Turbine Institute of ASME for publication in the JOURNAL OF ENGINEERING FOR GAS TURBINES AND POWER. Manuscript received April 26, 2007; final manuscript received May 1, 2007. Review conducted by Dilip R Ballal. Paper presented at the ASME Turbo Expo 2007: Land, Sea and Air (GT2007), May 14–17, 2007, Montreal, Quebec, Canada. Paper No. GT2007-27518.

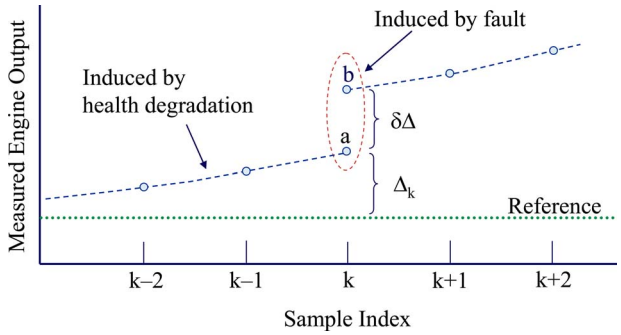

Fig. 1 Influence of health degradation and faults

Figure 1 shows the influence of health degradation and faults on a measured engine output. The horizontal axis indicates the sample index with a relatively long time interval (e.g., a few flights or a few days). The vertical axis indicates the measured engine output at a specific flight condition. The reference is an expected value of that engine output, and it is derived at a specific health baseline (e.g., nominal health condition). The gradual deviation of the engine output from the reference indicates the influence of health degradation. The discrete jump from point "a" to point "b" at the kth sample indicates fault occurrence. At the sample point k, the engine output shift Δ_k from the reference is induced by health degradation while a fault induces additional shift $\delta\Delta$. Thus, the total shift $(\Delta_k + \delta\Delta)$ is observed through a sensor. An on-line diagnostic algorithm, in general, has to process this total shift in order to detect the fault. If the algorithm does not have the capability to handle the health degradation-induced shifts in the sensor measurements, it may either miss the fault or generate a false alarm. Missed detection may occur when the fault is masked by health degradation. A false alarm may be generated when health degradation is misdiagnosed as a fault. Either way, the on-line algorithm will eventually lose its diagnostic effectiveness.

To address the problem described above, the integration of an on-line fault detection algorithm and an off-line trend monitoring algorithm was proposed in Refs. [8,9]. The integration architecture of the two diagnostic algorithms is shown in Fig. 2. The on-line algorithm processes measured engine outputs in real time to detect faults during flight. Such an algorithm is generally developed at a specific health baseline, and its reference for measured engine outputs is fixed. Therefore, the measurements processed in real time contain health degradation-induced shifts, which gradually increase over the lifetime of an engine. To account for the influence of health degradation, the health baseline of the on-line algorithm must be updated periodically so that the algorithm can operate in the vicinity of the degraded engine's health condition. Through the health baseline update, the reference for measured engine outputs is shifted to the vicinity of the degraded engine's outputs (for instance, the reference is shifted to the vicinity of point "a" in Fig. 1). Consequently, the health degradation induced-shifts that the on-line algorithm encounters are significantly reduced as compared to the fixed reference case.

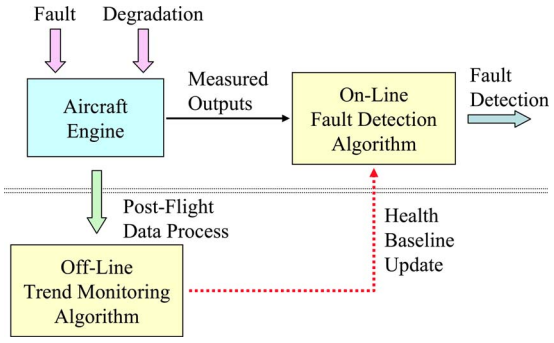

Fig. 2 Architecture of integrated diagnostic approach

The health baseline which is needed to update the on-line algorithm is provided by the off-line trend monitoring algorithm as shown in Fig. 2. The off-line algorithm processes data post-flight to estimate the health condition of the degraded engine. This data may contain engine outputs recorded at a single or multiple operating conditions. Since health degradation is a gradual process, the frequency at which the off-line algorithm operates is much lower than that of the on-line algorithm.

The algorithms used in this paper for on-line and off-line diagnostics are based on model-based estimation techniques. The on-line algorithm for fault detection is based on the hybrid Kalman filter (HKF) technique. The HKF is a uniquely structured Kalman filter which lends itself to the health baseline update. The off-line algorithm for trend monitoring is based on a derivative of the extended Kalman filter (EKF) technique. A description of each algorithm is given in the following sections.

Integration of On-Line and Off-Line Diagnostic Algorithms

The on-line and off-line diagnostic algorithms discussed in this section are based on a well-known estimation technique: the Kalman filter. Both algorithms update their estimations as new measurement data become available. The major factor that differentiates these algorithms is the frequency at which the measurement data is sampled. Because of this difference, the aircraft engine is described in a different form for each algorithm. In this section, the description of the aircraft engine is given first. Then, the descriptions of on-line and off-line diagnostic algorithms are given.

Aircraft Engine Description. An aircraft engine under consideration for on-line diagnostics is described by nonlinear equations of the following form:

$$\dot{x} = \bar{f}(x, h_k, u_{\text{cmd}}, e)$$

$$y = \bar{g}(x, h_k, u_{\text{cmd}}, e) + v \tag{1}$$

The vectors x, u_{cmd}, and e contain state variables, control command inputs, and environmental parameters, respectively. Health degradation of the engine is represented by the vector h which contains health parameters. Health parameters are efficiencies and flow capacities of the engine components such as compressors and turbines. As they deviate from the nominal (healthy) baseline, the performance delivered by each component degrades. Since health degradation progresses gradually over time, the health parameter vector is treated as a constant at the time scale where on-line diagnostics is performed. The subscript k of the health parameter vector indicates the sample index at the time scale where off-line diagnostics is performed. For given inputs, the nonlinear functions $\bar{f}$ and $\bar{g}$ generate the state derivative vector $\dot{x}$ and the sensor output vector y, respectively. The sensor outputs are corrupted by the white noise vector v.

While the aircraft engine is described in the form of Eq. (1) for on-line diagnostics, it is described in the following form for off-line diagnostics:

$$Y_k = \bar{g}_{\text{SS}}(h_k, U_k, E_k) + V_k \tag{2}$$

The vectors Y, U, and E contain steady-state values of sensor outputs, control command inputs, and environmental parameters, respectively. The subscript k indicates the sample index. The nonlinear function $\bar{g}_{\text{SS}}$ is equivalent to $\bar{g}$ in Eq. (1) at steady state. The vector V represents "steady-state" white noise, and its magnitude is much smaller than that of actual noise v contained in the raw measurements. The steady-state noise represents small biases that

exist at the time of data sampling.

In the off-line trend monitoring problem, the health parameter vector is treated as time variant; the health condition can change over the time interval between the sample points. Because of the gradual nature of health degradation, the time interval can be rather long. Depending on how the off-line trend monitoring is performed, the time interval can be a few flights or a few days.

On-Line Algorithm: Hybrid Kalman Filter. The objective of on-line fault detection is to detect faults as early as possible from the observed engine outputs. To achieve this objective, the sensor outputs in Eq. (1) are continuously processed in real time so that any shift induced by faults can be detected. The on-line diagnostic algorithm, which pursues the above objective, is based on the hybrid Kalman filter (HKF) technique [8,9]. The HKF is a uniquely structured Kalman filter which utilizes a nonlinear onboard engine model (OBEM) of the following form:

$$\dot{x}_{\mathrm{OBEM}} = f(x_{\mathrm{OBEM}}, h_{\mathrm{OBEM}}, u_{\mathrm{cmd}}, z)$$

$$y_{\mathrm{OBEM}} = g(x_{\mathrm{OBEM}}, h_{\mathrm{OBEM}}, u_{\mathrm{cmd}}, z) \tag{3}$$

This form is similar to the assumed form of the aircraft engine in Eq. (1). The vector x_{OBEM} contains the state variables of the OBEM while the vector z contains the measured parameters which define the flight condition. The vector h_{OBEM} represents the health baseline of the OBEM. By utilizing the state and output vectors of the OBEM, the following HKF equation is obtained:

$$\dot{\hat{x}} = A(\hat{x} - x_{\mathrm{OBEM}}) + K(y - \hat{y})$$

$$\hat{y} = C(\hat{x} - x_{\mathrm{OBEM}}) + y_{\mathrm{OBEM}} \tag{4}$$

The vectors $\hat{x}$ and $\hat{y}$ represent the estimate of x and y of the plant in Eq. (1), respectively. The state-space matrices A and C are derived through the linearization of the nonlinear plant model (in the present case, OBEM). The matrix K represents the Kalman gain. Similar to the general linear Kalman filter approach, the matrices A, C, and K are derived at multiple operating conditions to cover a wide operating range of the aircraft engine. Once derived, these matrices are saved in table lookup form for real-time execution of Eq. (4).

The Kalman filter, in general, is able to accurately estimate the sensor outputs as long as the plant operates under the conditions expected by the Kalman filter. When the plant experiences unexpected events such as faults, the estimation performance of the Kalman filter becomes poor, causing an increase in the residuals, $(y-\hat{y})$. Therefore, fault detection can be achieved by detecting such an increase in the residuals. To detect fault-induced shifts in the residuals, weighted sum of squared residuals (WSSR) signals are constructed as follows:

$$\mathrm{WSSR}_{\mathrm{HKF}} = (y-\hat{y})^T \Sigma^{-1} (y-\hat{y})$$

$$\mathrm{WSSR}_{\mathrm{OBEM}} = (y-y_{\mathrm{OBEM}})^T \Sigma^{-1} (y-y_{\mathrm{OBEM}}) \tag{5}$$

where

$$\Sigma = \mathrm{diag}[\sigma^2]$$

The vector σ represents the standard deviation of the sensor measurements. The square matrix Σ normalizes the residual vectors $(y-\hat{y})$ and $(y-y_{\mathrm{OBEM}})$. The fault indicator signals, $\mathrm{WSSR}_{\mathrm{HKF}}$ and $\mathrm{WSSR}_{\mathrm{OBEM}}$, indicate the existence of faults; they will increase when the engine experiences faults. To detect faults, these signals are compared against pre-established thresholds. Fault detection is declared when at least one of the two fault indicator signals exceeds a threshold. As demonstrated in Ref. [9], the utilization of the two fault indicator signals improves the fault detection capability since these signals have different sensitivities to different types of faults.

The HKF designed at any particular health condition eventually loses its estimation accuracy as the engine degrades over its lifetime, and thus the fault indicator signals will increase. This is due to the fact that the discrepancy between the design health condition of the HKF and the actual health condition of the engine increases over time. In the HKF approach, the design health condition is defined by the vector h_{OBEM} at which the OBEM operates and also by the health condition at which the matrices A, C, and K are derived.

In Refs. [8,9], it is shown that the HKF is able to maintain its estimation performance as long as the health baseline of the OBEM remains in the vicinity of the engine's health condition. Thus, the HKF-based on-line fault detection algorithm is able to maintain its effectiveness by periodically updating the health baseline of the OBEM to a new condition as follows:

$$h_{\mathrm{OBEM}} = \hat{h}_k \tag{6}$$

The vector $\hat{h}_k$ represents the estimate of the health parameter vector h_k in Eq. (1). This estimate is provided by the off-line trend monitoring algorithm, which will be discussed in the following section. The update process for the HKF is relatively simple; it is completed by feeding the estimated health degradation values into the OBEM. The matrices A, C, and K do not need to be redesigned as the health baseline of the OBEM is updated. This relatively simple update process is a major benefit of the HKF approach.

Off-Line Algorithm: Extended Kalman Filter. The objective of off-line trend monitoring is to track the health condition of an engine over its lifetime. This objective is accomplished by accurately estimating the health parameter vector h_k in Eq. (2) from the steady-state sensor outputs Y_k. The off-line diagnostic algorithm used in this study is based on a derivative of the extended Kalman filter (EKF) technique [10]. The EKF is similar to the general linear Kalman filter except that a nonlinear plant model is successively relinearized so that the validity of a linear plant representation is maintained as the plant moves from one operating condition to another. Therefore, a nonlinear plant model functions as part of the algorithm in the EKF approach. The nonlinear aircraft engine model used in the current study is given in the following form:

$$\hat{Y}_k = g_{\mathrm{SS}}(\hat{h}_k, U_k, Z_k) \tag{7}$$

This form is similar to the assumed form of the aircraft engine in Eq. (2). The vector U is the same vector that appears in Eq. (2). The vector Z contains the steady-state values of measured parameters that indicate the flight condition. The subscript k indicates the sample index. The vector $\hat{h}$ represents the estimate of the health parameter vector h, and this vector must be derived by the off-line trend monitoring algorithm.

The above nonlinear plant model can be presented in the following alternative form:

$$\hat{Y}_k = G_{k|k-1}(\hat{h}_k - \hat{h}_{k-1}) + \hat{Y}_{k|k-1} \tag{8}$$

where

$$\hat{Y}_{k|k-1} = g_{\mathrm{SS}}(\hat{h}_{k-1}, U_k, Z_k) \tag{9}$$

$$G_{k|k-1} = \frac{\partial}{d\hat{h}} g_{\mathrm{SS}}(\hat{h}_{k-1}, U_k, Z_k) \tag{10}$$

The vector $\hat{h}_{k-1}$ represents the health parameter vector estimated at the previous sample point, $k-1$. The matrix $G_{k|k-1}$ represents the influence coefficient matrix derived from the nonlinear function, $g_{\mathrm{SS}}(\hat{h}_{k-1}, U_k, Z_k)$. Given the vectors $\hat{h}_{k-1}$, U_k, Z_k, and Y_k, the health parameter vector at the sampling point k is estimated as follows [6]:

$$\hat{h}_k = \hat{h}_{k-1} + L(Y_k - \hat{Y}_{k|k-1}) \tag{11}$$

where

$$L = P_0 G_{k|k-1}^T (G_{k|k-1} P_0 G_{k|k-1}^T + R)^{-1} \tag{12}$$

The matrices P_0 and R represent the error covariance and measurement covariance, respectively. In the general Kalman filter approach (both linear and extended), the error covariance matrix is updated as the new measurement data become available [10]. This matrix, however, may diverge unless the number of available measurements is greater than or equal to the number of health parameters to be estimated. In general, the number of sensors installed on an aircraft engine is less than the number of health parameters. To avoid the divergence, the error covariance matrix is kept constant. Otherwise, the matrix update must be done with a special treatment, such as the soft-constraint approach demonstrated in Ref. [11].

Equations (9)–(12) represent the EKF algorithm. The algorithm updates its estimate as new data Y_k, U_k, Z_k become available. To check the validity of the estimated health condition, the following weighted sum of squared residuals is computed:

$$\mathrm{WSSR}_{\mathrm{EKF}} = (Y_k - \hat{Y}_k)^T \Sigma^{-1} (Y_k - \hat{Y}_k) \tag{13}$$

This signal is compared against a predetermined threshold. If the signal exceeds the threshold, it is considered that the estimated health condition is inaccurate, and thus further investigation is needed to determine a cause of inaccuracy.

After validation, the estimated health condition $\hat{h}_k$ is used to update the health baseline of the OBEM as described by Eq. (6). Through this update, the effectiveness of the on-line fault detection algorithm is maintained in the presence of health degradation. The estimated health condition also gives valuable information for engine health management. The snapshot estimation at a sample point can be used to consider whether a maintenance action is necessary or not. Thus, condition-based maintenance is possible instead of time-based maintenance. Engine health management can be further improved by interpreting the history of the estimated health condition. The estimated health condition from the past to the present reveals the degradation profile under which a specific engine operated. From this information, the health condition at a future point can be anticipated, and necessary actions may be taken to improve the safety or efficiency of the engine operation.

Application of the Integrated Methodology to an Aircraft Engine Model

The algorithms described in the previous sections require a nonlinear plant model. More specifically, the on-line algorithm requires a nonlinear model that can be executed in real time. In this section, a description of the aircraft engine model is given. For the results presented in this paper, the same model used by the diagnostic algorithms is also used to represent a real engine. The health degradation profile that the real engine may undergo is also discussed.

Engine Model. The engine model used in this paper is a nonlinear simulation of an advanced high-bypass turbofan engine, a typical power plant for a large commercial aircraft. This engine model has been constructed as a component level model (CLM), which consists of the major components of an aircraft engine. The CLM represents highly complex engine physics while being designed to run in real time. Engine performance deviations from the nominal health baseline are modeled by adjustments to efficiency and flow capacity scalars of the following five components: fan (FAN), booster (BST), high-pressure compressor (HPC), high-pressure turbine (HPT), and low-pressure turbine (LPT). There are a total of 10 adjustments that are called health parameters. The engine state variables, health parameters, actuator variables, and environmental parameters are shown in Table 1.

Table 1 Engine model variables

State variables	XNL, XNH, TMHS23, TMHS3 TMHSBL, TMHSBC, TMHS41 TMHS42, TMHS5
Health parameters	FAN efficiency, FAN flow capacity BST efficiency, BST flow capacity HPC efficiency, HPC flow capacity HPT efficiency, HPT flow capacity LPT efficiency, LPT flow capacity
Actuators	WF36, VBV, VSV
Environmental parameters	Altitude, Mach number Ambient temperature

There are a total of 11 measured parameters (y and z) that are available to the digital control unit of this engine. Table 2 shows seven sensors (y) along with their standard deviations given in percent of steady-state values at the ground maximum power condition. The control actions and diagnostics are based on those sensed variables. Table 3 shows four additional measured parameters (z) along with their standard deviations given in their actual engineering units. These four parameters indicate the ambient and engine inlet conditions. The measurements of the inlet condition, T2 and P2, are used for parameter corrections [12].

The nonlinear engine model is used in the subsequent sections to represent a real engine in Eq. (1) and the engine models in Eqs. (3) and (7) for on-line and off-line diagnostics. The engine model representing a real engine operates at given health conditions, and its flight condition is specified by the three environmental parameters listed in Table 1. This engine model operates in closed loop with a control system described in Ref. [9]. In the current control architecture, the power lever angle (PLA) is converted to desired corrected fan speed (an indicator of thrust). The control system adjusts three actuation variables to cause the corrected measured fan speed to match the desired value. The closed-loop system runs in a simulation environment at the frequency of 50 Hz.

The two engine models used for on-line and off-line diagnostics are identical except that they operate at different time scales. These two engine models operate at estimated health conditions, and their flight condition is specified by three measured parameters: T_{amb}, P_{amb}, and T2. From these three measurements, the engine models calculate the altitude, Mach number, and the temperature deviation from the standard day condition. The two engine models receive the three control commands (Table 1) gener-

Table 2 Standard deviations of controls and diagnostics sensors (σ in percent of steady-state values at ground maximum power condition)

Sensors (y)	σ (%)
XN12	0.25
XN25	0.25
P25	0.50
T25	0.75
PS3	0.50
T3	0.75
T49	0.75

Table 3 Standard deviations of ambient and engine inlet sensors (σ in actual units)

Sensors (z)	σ
T_{amb}	5.0°F
P_{amb}	0.1 psi
T2	5.0°F
P2	0.1 psi

ated by the control system.

In the current study, the same engine model is used to represent a real engine and the engine model for diagnostics. This, however, does not represent a realistic application environment; there will typically be a mismatch between the real engine and the engine model due to unmodeled and incorrectly modeled physical phenomena. To represent such a mismatch, a turbine clearance model (TCM) is added only to the engine model representing a real engine. The TCM captures the turbine clearance behavior with high fidelity, and its addition results in output mismatch between the real engine and the engine model at steady-state conditions and during transients.

Health Degradation Profile. Each aircraft engine degrades differently depending on the environmental conditions the engine is exposed to. For instance, a high concentration of sand or salt can accelerate fan or compressor degradation while tropical heat can accelerate turbine degradation. Thus, there is no such thing as a typical degradation profile that engines will undergo [13,14]. To capture this randomness, health degradation profiles considered in this paper are generated as follows:

$$h_k^i = h_{k-1}^i + \left(\frac{\eta^i}{q}\right)\varepsilon_k^i \quad \text{if } k > 0$$

$$h_k^i = \delta_k^i \quad \text{if } k = 0 \tag{14}$$

where

$$k = 0,1, \ldots ,q$$

$$i = 1,2, \ldots ,p$$

The integers q and p indicate the number of sample points and the number of health parameters, respectively. Equation (14) gives the value of the ith health parameter at the kth sample point. The scalar η^i specifies the maximum amount that the ith health parameter can deviate over q sample points. The random number ε is uniformly distributed over the range between 0 and 1. At the initial point $k=0$, each health parameter is specified by δ, a random number uniformly distributed over the range of ±0.5%. The initial health condition represents engine-to-engine variations due to manufacturing tolerance.

With the above equation, each health parameter undergoes a unique degradation profile. The degradation profile depends on the scalar η specified for each health parameter and the random number ε.

Performance Evaluation

In this section, the performance of the off-line trend monitoring algorithm is investigated first, using a specific degradation profile. The off-line algorithm estimates the engine health condition at each sample point. The estimated health condition is then used to update the on-line fault detection algorithm. After the health baseline update, the on-line algorithm's capability to detect sensor faults is evaluated. The engine to be diagnosed by both algorithms contains the TCM in order to represent model-plant mismatch that exists in the real environment.

Off-Line Trend Monitoring. The off-line trend monitoring algorithm in Eqs. (9)–(12) receives the steady-state vectors Y_k, U_k, and Z_k and estimates the engine health condition at each sample point. The time interval between the sample points is rather long as discussed earlier. The steady-state data used in this section are generated from the engine model in Eq. (1) through the following steps. First, a degradation profile that the engine model will undergo over its lifetime (q sample points) is generated using Eq. (14). The degradation profile specifies a unique health condition at each sample point. Then, at each sample point, the engine model is run at a steady-state cruise condition. The operating condition of the engine is specified by the health condition, PLA, and environmental parameters in Table 1. From the steady-state simulation run, one-second time histories of y, u_{cmd}, and z are collected. Then, the noise-corrupted time histories are averaged to obtain the steady-state vectors Y_k, U_k, and Z_k.

In the real environment, the steady-state flight condition of the engine can vary from flight to flight even at cruise. To capture this variation, PLA, altitude, Mach number, and ambient temperature are randomly varied from sample point to sample point. The PLA is varied over the range between 62 and 66 deg (intermediate power at cruise). Altitude is varied over the range between 33,000 and 37,000 ft (10,058–11,278 m). Mach number is varied over the range between Mach 0.83 and 0.85. The ambient temperature is varied within ±30°F from the standard day condition.

During a preliminary evaluation study, it was found that the off-line trend monitoring algorithm had difficulty in estimating FAN flow and LPT flow. When the actual FAN flow and LPT flow deviated toward a certain direction from their initial condition values, the estimated FAN flow and LPT flow did not follow the actual values. Instead, these estimated values deviated toward the direction opposite of the actual FAN flow and LPT flow. In the current estimation problem where the number of unknown parameters (health parameters) is greater than the number of known parameters (sensor outputs), a unique solution does not exist. The trend monitoring algorithm estimates the health parameters in such a way that the difference between the engine and model outputs is minimized in a least squares sense, while simultaneously minimizing the difference in the estimated health conditions at the current and previous sample points.[1] This approach may produce health parameter estimates that are inaccurate. To work around this problem, the following constraint is imposed: the estimated health parameters are constrained to change in the specific direction expected from the heuristic knowledge regarding health degradation. All estimated health parameters are not allowed to increase from the estimation values at the previous sample point, except for HPT flow and LPT flow which are not allowed to decrease. If an estimated health parameter changes in the direction opposite of that expected, then the estimation value at the previous sample point is used as the current estimation value.

Figure 3 shows the actual and estimated health conditions over 300 sample points of engine life. The estimated health parameters were generated under the constraint previously discussed, except for the first five sample points. During the first five sample points, the health condition of the engine is maintained at the initial health condition representing engine-to-engine variation due to manufacturing tolerance. The estimated health parameters which are initialized at the nominal health condition are allowed to change in any direction; constraints are not imposed on the estimated values during this period. The first five samples are simply used to let the estimated health parameters settle to any values in the presence of initial model-plant mismatch, which not only includes health condition mismatch but also the mismatch due to the TCM.

As can be seen in Fig. 3, the algorithm is able to follow the degradation profile quite well for three components: BST, HPC, and HPT. There are estimation errors, but the errors remain almost constant across the sample points. Thus, the deviation from the initial condition can be accurately tracked for these three components. The algorithm displays some difficulty in estimating the health parameters of FAN and LPT components; the estimation errors increase with time. The cause of this divergence is not clear. It may be due to the underdetermined nature of the current problem, or the location of the sensors may not be suited for estimating these health parameters. When this study was repeated using

[1]The algorithm given by Eqs. (11) and (12) is equivalent to the maximum a posteriori estimator [15,16] and the minimum variance estimator [15,17].

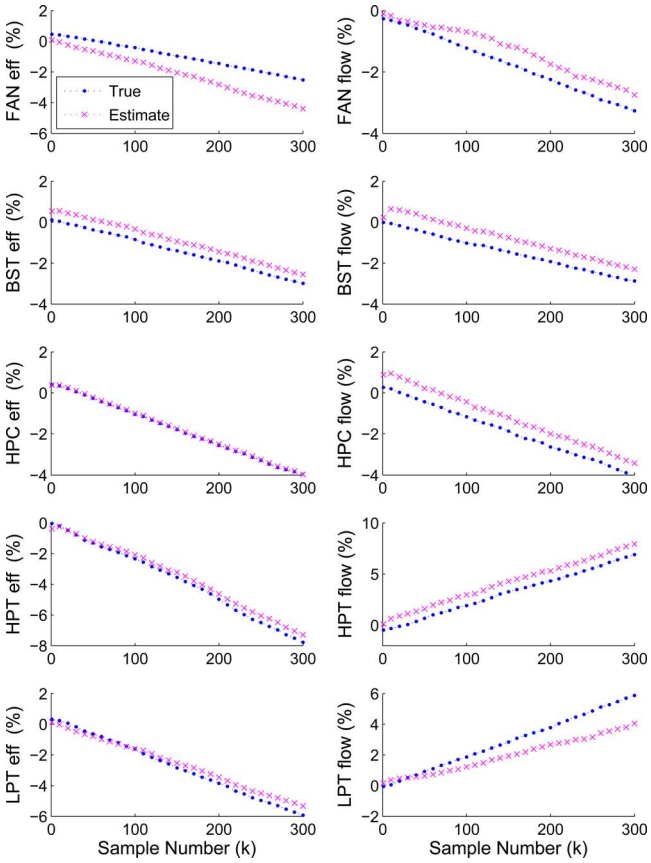

Fig. 3 Actual and estimated health degradation over the engine's lifetime

different patterns of health degradation profile, a similar tendency was observed. A total of five patterns of degradation profile, generated from Eq. (14), was investigated.

Health Baseline Update of On-Line Fault Detection Algorithm. The on-line fault detection algorithm in Eqs. (3) and (4) receives the vectors y, u_{cmd}, and z and generates the sensor output estimates and the on-board model outputs at each sample point with the time increment of 0.02 s (50 Hz). Based on the residual vectors $(y-\hat{y})$ and $(y-y_{OBEM})$, the two fault indicator signals in Eq. (5) are computed, and they are compared against pre-established thresholds. If at least one of the two fault indicator signals exceeds the threshold for 25 consecutive time steps, fault detection is declared as demonstrated in [9].

Before evaluating the fault detection capability of the on-line algorithm, the benefit through the integration of the on-line and off-line algorithms is investigated. As discussed earlier, the on-line fault detection algorithm will eventually lose its effectiveness as the engine degrades over time. This happens because the fault indicator signal values increase with the increase in discrepancy between the engine and the OBEM. To maintain diagnostic effectiveness, the health baseline of the OBEM must be updated periodically. This update is completed by feeding the estimated health condition values from the off-line trend monitoring algorithm to the OBEM. The importance of this health baseline update is illustrated in Fig. 4 where, over its lifetime of 300 sample points, the aircraft engine is subject to the specific health degradation profile shown in Fig. 3. At each sample point, the engine and the on-line diagnostic algorithm are run at the following cruise condition: 35,000 ft (10,668 m) altitude, Mach 0.84, 65 deg PLA. Figure 4 shows the steady-state values of the fault indicator signals for the following two cases: (1) the health baseline of the OBEM maintained at the nominal condition and (2) the health baseline of the

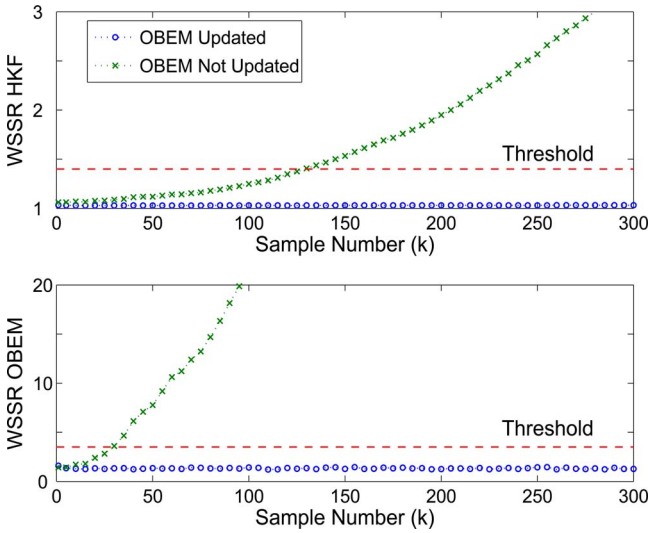

Fig. 4 Influence of engine health degradation on steady-state values of $WSSR_{HKF}$ and $WSSR_{OBEM}$

OBEM updated to the estimated health parameters shown in Fig. 3. The dashed lines indicate fault detection thresholds. The threshold values were determined using health condition mismatches between the engine and the OBEM as done in Refs. [8,9].

As can be seen in the figure, if the health baseline of the OBEM is not updated from the nominal condition, $WSSR_{HKF}$ exceeds the threshold around the 130th sample point while $WSSR_{OBEM}$ exceeds the threshold around the 30th sample point. This means that the fault detection algorithm will start misdiagnosing health degradation as a fault around the 30th sample point. To avoid generating false alarms, the thresholds must be set at much higher values. However, doing so will compromise the fault detection capability and will increase the missed detection rate when the engine is at or near the nominal health condition.

When the health baseline of the OBEM is updated periodically, the fault indicator signals remain fairly constant over the lifetime of the degrading engine. In Fig. 4, the OBEM is subject to the estimated health condition shown in Fig. 3, therefore, the estimation error in some of the health parameters increases over time. This increase in the estimation error seems to have a very minor influence on the fault indicator signals. The reason for this may be attributed to the nature of the off-line trend monitoring algorithm. The off-line trend monitoring algorithm estimates the health parameters in such a way that the difference between the engine and model outputs is minimized in a least squares sense [15–17]. Thus, the estimated health parameters are not necessarily accurate, but they are ones that minimize the difference between the engine and model outputs. When these estimated health parameters are fed into the OBEM, the outputs of the OBEM match well with the engine outputs. Consequently, the fault indicator signals remain small.

Updating the health baseline of the OBEM has the effect of shifting the engine output reference to a new value. As illustrated in Fig. 1, the original reference at which the algorithm is designed becomes obsolete as the engine continues to degrade. By shifting the reference to a new value, such as point "a" in the figure, the on-line algorithm can detect the fault-induced shift, $\delta\Delta$, more reliably.

On-Line Fault Detection: Sensor Bias Case. The on-line algorithm's capability to detect sensor bias faults is evaluated in this section. For this evaluation, the closed-loop engine is trimmed at a specific cruise condition of 35,000 ft (10,668 m) altitude, Mach 0.84, and 65 deg PLA, in the presence of health degradation and a bias in a single sensor. Then, the engine and the on-line algorithm

Table 4 Minimum sensor bias detected at cruise with 65 deg PLA

	$k=100$ (σ)	$k=200$ (σ)	$k=300$ (σ)
XN12	2.6/−4.5	2.9/−4.5	2.9/−4.4
XN25	3.2/−3.8	3.4/−3.7	3.3/−3.6
P25	1.3/−1.3	1.3/−1.3	1.3/−1.3
T25	2.1/−2.2	2.0/−2.1	2.0/−2.1
PS3	1.7/−1.6	1.7/−1.7	1.7/−1.7
T3	2.6/−2.6	2.6/−2.6	2.6/−2.6
T49	2.9/−3.5	2.9/−3.5	2.9/−3.5
T_{amb}	0.3/−0.3	0.3/−0.3	0.3/−0.3
P_{amb}	0.5/−0.5	0.5/−0.5	0.5/−0.5
T2	0.4/−0.4	0.4/−0.4	0.4/−0.4
P2	···/···	···/···	···/···

are run for 100 s at steady state. The smallest magnitude bias that is detected for each sensor is shown in Table 4. In this study, the aircraft engine and the OBEM are subject to, respectively, the actual and estimated health conditions in Fig. 3 at three sample points: $k=100$, 200, and 300.

From Table 4, it can be observed that the on-line algorithm performs consistently in the presence of health degradation; the detected bias magnitudes are almost the same at three health conditions, except for slight variations in the XN12 and XN25 sensors. For some of the sensors, detected bias magnitudes are not symmetric between the positive and negative directions. As discussed in Ref. [8], health condition mismatch between the engine and the OBEM has an effect of counteracting a sensor bias to some extent. As a result, depending on the bias direction, it takes smaller or larger magnitude for the fault indicator signals to exceed the fault detection thresholds. This lack of symmetry, however, is not as prominent as the result in Ref. [8].

As mentioned earlier, three sensor measurements, T_{amb}, P_{amb}, and T2 are used to define the flight condition for the OBEM. A bias in these sensors, therefore, causes the OBEM to operate at a flight condition different from the true condition. The table shows that biases of small magnitude are detected for these three sensors. The on-line algorithm is not able to detect a bias in the P2 sensor. This sensor is currently used for the correction of pressure measurements. Since both measured and estimated pressure values are corrected by the P2 value, a bias in this sensor does not increase the residuals. The reader should be reminded that the fault detection algorithm will not identify the biased sensor; it only indicates that a fault exists. After the detection of a fault, the identity or severity of the detected fault must be classified through the fault isolation process [18].

Discussion

The study in this paper reveals the benefit of integrating the on-line and off-line diagnostic algorithms. Through this integration, the on-line fault detection algorithm is able to maintain its diagnostic effectiveness as the aircraft engine degrades over its lifetime. The integration of the two algorithms, however, is not a trivial step. In this section, the practical aspects of the integrated approach are discussed.

One issue that influences the practicality of the integrated approach is the complexity involved in the update process of the on-line algorithm. If the update process involves a redesign of the entire on-line algorithm, such as the case for the piecewise linear Kalman filter approach [18], the redesign process may have to take place on a ground-based computer with human intervention. Furthermore, after the redesign process, the on-line algorithm must be uploaded to an on-board engine computer. Such complexity makes that approach impractical. It is desirable to keep the update process as simple as possible. In the case of the HKF, the algorithm is updated through a relatively simple process: by feeding the estimated health condition values to the OBEM. Thus, the HKF is well suited for the integrated approach.

Another issue that influences the practicality of the integrated approach is the location of the off-line trend monitoring algorithm. In general, a trend monitoring algorithm resides on a ground-based computer. In that case, the data for post-flight analysis and the off-line diagnostic results must be transmitted between the ground-based and on-board computers. There would be a number of communication and certification issues that would have to be addressed to achieve this integration.

The difficulties associated with off-board to on-board data transmission can be avoided if the off-line trend monitoring algorithm is capable of running on an on-board engine computer. Such a capability heavily depends on the off-line algorithm's robustness. As discussed earlier, trend monitoring is generally an underdetermined problem, and therefore an infinite number of solutions exist. Under this circumstance, the off-line algorithm must generate a solution (estimated health condition) "close enough" to the true solution; otherwise the algorithm may become unstable. In this paper, a simple constraint was imposed on the EKF: the estimated health parameters were constrained to change in the expected direction. The constraint was based on heuristic knowledge regarding health degradation, and it improved the stability of the EKF. Such an additional step is necessary for obtaining a reasonable solution in the underdetermined problem.

Another way of improving the stability of the EKF is to utilize steady-state measurement data obtained at multiple operating conditions. At distinctly different operating conditions, the same health condition can induce different signatures in the measured engine outputs. The utilization of multipoint data augments the number of known parameters (sensor outputs) in the problem, and therefore can improve the stability and also estimation accuracy [19,20]. Through this extra step, the robustness of the off-line algorithm may be improved, making the algorithm capable of running on an on-board engine computer.

Conclusion

A challenge in developing an on-line fault detection algorithm is making it adaptive to engine health degradation. If the algorithm has no adaptation capability, it will eventually lose its diagnostic effectiveness. To address this problem, the integration of on-line and off-line diagnostic algorithms was investigated. The off-line trend monitoring algorithm periodically estimates engine health condition over the course of engine's life. Based on the estimated health condition, the on-line fault detection algorithm is updated. Through this integration, the on-line fault detection algorithm maintains its effectiveness while the engine continues to degrade over time.

The integrated approach was investigated in a simulation environment using a nonlinear engine model. The evaluation result showed that this integration is essential to maintain on-line fault detection capability in the presence of health degradation. Practical issues of the integrated approach were also discussed. The communication between the on-line and off-line algorithm can be made less complex if the off-line algorithm is operated on an on-board engine computer. To make this possible, further research is needed in the area of off-line trend monitoring.

Acknowledgment

This research was funded by the NASA Aviation Safety Program as a task under the Integrated Vehicle Health Management Project.

Nomenclature

BST = booster
EKF = extended Kalman filter
HKF = hybrid Kalman filter

HPC = high pressure compressor
HPT = high pressure turbine
LPT = low pressure turbine
OBEM = on-board engine model
P2 = engine inlet pressure
P25 = HPC inlet pressure
P_{amb} = ambient pressure
PLA = power lever angle
PS3 = combustor inlet static pressure
T2 = engine inlet temperature
T25 = HPC inlet temperature
T3 = combustor inlet temperature
T49 = LPT inlet temperature
T_{amb} = ambient temperature
TCM = turbine clearance model
TMHS23 = BST metal temperature
TMHS3 = HPC metal temperature
TMHS41 = HPT nozzle metal temperature
TMHS42 = HPT metal temperature
TMHS5 = LPT metal temperature
TMSHBC = combustor case metal temperature
TMHSBL = combustor liner metal temperature
VBV = variable bleed valve
VSV = variable stator vane
WF36 = fuel flow
WSSR = weighted sum of squared residuals
XN12 = fan speed, measured
XN25 = core speed, measured
XNH = core speed, actual
XNL = fan speed, actual
e = environmental parameter vector
h = health parameter vector
u_{cmd} = control command vector
v = sensor noise vector
x = state variable vector
y = sensor output vector (controls/diagnostics)
z = sensor output vector (ambient/engine inlet)

References

[1] Merrill, W. C., DeLaat, J. C., and Bruton, W. M., 1988, "Advanced Detection, Isolation, and Accommodation of Sensor Failures—Real-Time Evaluation," J. Guid. Control Dyn., **11**, pp. 517–526.

[2] Luppold, R. H., Roman, J. R., Gallops, G. W., and Kerr, L. J., 1989, "Estimating In-Flight Engine Performance Variations Using Kalman Filter Concepts," AIAA Paper No. AIAA-89-2584.

[3] Kerr, J. L., Nemec, T. S., and Gallops, G. W., 1992, "Real-Time Estimation of Gas Turbine Engine Damage Using a Control-Based Kalman Filter Algorithm," ASME J. Eng. Gas Turbines Power, **114**, pp. 187–195.

[4] Brotherton, T., Volponi, A., Luppold, R., and Simon, D. L., 2003, "eSTORM: Enhanced Self Tuning On-board Real-time Engine Model," *Proceedings of 2003 IEEE Aerospace Conference*.

[5] Doel, D. L., 1994, "TEMPER—A Gas Path Analysis Tool for Commercial Jet Engines," ASME J. Eng. Gas Turbines Power, **116**, pp. 82–89.

[6] Volponi, A. J., 1994, "Sensor Error Compensation in Engine Performance Diagnostics," ASME Paper No. 94-GT-58.

[7] Mathioudakis, K., Kamboukos, Ph., and Stamatis, A., 2002, "Turbofan Performance Deterioration Tracking Using Non-Linear Models and Optimization Techniques," ASME Paper No. GT-2002-30026.

[8] Kobayashi, T., and Simon, D. L., 2006, "Hybrid Kalman Filter Approach for Aircraft Engine In-Flight Diagnostics: Sensor Fault Detection Case," ASME Paper No. GT2006-90870.

[9] Kobayashi, T., and Simon, D. L., 2006, "Hybrid Kalman Filter: A New Approach for Aircraft Engine In-Flight Diagnostics," NASA TM-2006-214491.

[10] Gelb, A., Kasper, J. F., Nash, R. A., Jr., Proce, , C. F., and Sutherland, A. A., Jr., 1974, *Applied Optimal Estimation*, The MIT Press, Cambridge, MA.

[11] Dewallef, P., Leonard, O., and Mathioudakis, K., 2004, "On-Line Aircraft Engine Diagnostics Using a Soft-Constrained Kalman Filter," ASME Paper No. GT2004-53539.

[12] Volponi, A. J., 1999, "Gas Turbine Parameter Corrections," ASME J. Eng. Gas Turbines Power, **121**, pp. 613–621.

[13] Wulf, R. H., 1979, "CF6 Jet Engine Performance Deterioration," AIAA Paper No. 79-1233.

[14] Sasahara, O., 1985, "JT9D Engine/Module Performance Deterioration Results from Back to Back Testing," Paper No. ISABE 85-7061.

[15] Crassidis, J. L., and Junkins, J. L., 2004, *Optimal Estimation of Dynamic Systems*, CRC Press, Florida, pp. 63–96.

[16] Volponi, A. J., 2003, "Foundation of Gas Path Analysis I," *Von Kalman Institute Lecture Series: Gas Turbine Condition Monitoring and Fault Diagnosis*.

[17] Roth, B. A., Doel, D. L., and Cissell, J. J., 2005, "Probabilistic Matching of Turbofan Engine Performance Models to Test Data," ASME Paper No. GT2005-68201.

[18] Kobayashi, T., and Simon, D. L., 2005, "Evaluation of an Enhanced Bank of Kalman Filters for In-Flight Aircraft Engine Sensor Fault Diagnostics," ASME J. Eng. Gas Turbines Power, **127**, pp. 497–504.

[19] Stamatis, A., Mathioudakis, K., Berios, G., and Papailiou, K., 1991, "Jet Engine Fault Detection With Discrete Operating Points Gas Path Analysis," J. Propul. Power, **7**, pp. 1043–1048.

[20] Kobayashi, T., and Simon, D. L., 2005, "Hybrid Neural-Network Genetic-Algorithm Technique for Aircraft Engine Performance Diagnostics," J. Propul. Power, **21**, pp. 751–758.

Maria Cristina Cameretti
Fabrizio Reale
Raffaele Tuccillo

Dipartimento di Ingegneria Meccanica per l'Energetica (D.I.M.E.), Università di Napoli Federico II, Italy

Cycle Optimization and Combustion Analysis in a Low-NO_x Micro-Gas Turbine

The authors discuss in this paper the potential of a method for NO_x *suppression from power plants based on microgas turbines. The method is based on the mild combustion concept but needs to be adapted to the actual operating parameters of the microturbine, thus resulting in an effective employment of the flue gas recirculation for diluting the oxygen in the inlet air. The results are first presented on a thermodynamic basis, and some cases are then analyzed with a computational fluid dynamics simulation. Both approaches suggest good perspectives for the nitric oxide control but also highlight some disadvantages in terms of increase in carbon species.* [DOI: 10.1115/1.2718232]

Introduction

The microgas turbine (MGT) employment in a wide range of power or combined generation applications solicits the academic and industrial researchers to define an optimal operating range in terms of both energetic and environmental performance. Previous authors' works [1–6] have underlined the effectiveness of the "partly recuperated cycle" concept as a tool for adapting the MGT operation to variable thermal and electrical demands. The same papers have also evidenced that the part-load operation may be characterized by an increasing NO_x production, due to the need of sustaining the flame with a considerable amount of fuel addressed to the stoichiometric pilot line.

An efficient and up-to-date way to overcome the NO_x increase at part-load operation can be found in the "mild-combustion" emerging technology [7–10]. Really, the mild or "flameless" combustion regime produces an effective control of the thermal mechanism of the nitric monoxide formation because of the simultaneous occurrence of a temperature peak cutoff and of an oxygen defect in the oxidizing species. In order for such a regime to take place, both a high reactant temperature and the oxidant dilution with inert species are needed. The first requirement is easily met in a recuperated microturbine, while the compliance with the second one implies a flue gas recirculation whose amount must be optimized in order to avoid an excessive penalty in the cycle efficiency and specific power.

The present work is addressed to the cycle optimization for a 100 kW MGT operating with a variably "recuperated and recirculated" cycle. The combined activation of the recuperator by-pass option and of the variable exhaust gas recirculation (EGR) establishes a set of independent variables that must meet a given level of thermal and mechanical output, and it also allows the combustion to take place within the mild regime. The simultaneous goal of acceptable performance and reduced emission is controlled by an integrated methodology based on the component matching analysis and the computational fluid dynamics (CFD) simulation of the combustion process. The latter refers to a lean-premixed combustor [1,4,11,12] whose adaptation to the mild regime is checked under a wide variety of conditions originated by the choices for both the recuperator by-pass and the exhaust recirculation ratios. The numerical simulation pays therefore a particular attention to the identification of the reactant self-ignition as a consequence of the oxidant dilution with exhaust gases and of the inlet temperature as well.

The variations in combustor boundary conditions could also be induced by the possibility of operating the MGT with variable shaft speed, thus producing significant changes in air mass flow rate and pressure ratio [2–6]. The proven existence of multiple degrees of freedom suggested the authors disregard this further option and proceed, in this paper, with the search of the optimal solution, in terms of energy and emission indices, within the space of the two independent variables listed before.

Micro-Gas Turbine Base Features and the Modified Layout

The main specifications and the base plant layout of the MGT considered in this paper are given in Table 1 and Fig. 1, respectively. The recent technical literature [1,2,11–17] agrees with assigning a key role to the gas-to-air recuperator for both the energetic performance and the off-design behavior of the system.

A recuperator by-pass system (Fig. 1) enhances the plant flexibility, since a wider range of thermal-to-mechanical load ratios can be covered. The possibility of splitting the exhaust mass flow, either to the recuperator or directly to the heat recovery boiler inlet, takes place according to the by-pass ratio

$$X_b = 1 - \frac{\dot{m}_{g,R}}{\dot{m}_g} \tag{1}$$

where $X_b=0$ corresponds to a fully recuperated cycle and $X_b>0$ increases the amount of recoverable thermal output.

The MGT off-design conditions are therefore induced by either a variation in the fuel mass flow rate $\dot{m}_f$ or by a change in the by-pass valve parameter X_b. The simultaneous control of both parameters allows the system to meet variable thermal and mechanical requirements [2,3]. All the computations discussed in the next sections refer to natural gas supply with the properties given in Table 2.

The previous authors' works [1–5] have demonstrated that the full-load operation without the by-pass option activation is characterized by an acceptably reduced level of NO_x emission because of the efficient combustor operation under lean-premixed conditions. Conversely, both the part-load operation and the partial by-pass of the internal recuperator produce a temperature drop at the combustor inlet. In such cases, the ignition of the lean fuel-air mixture must be aided by an increased fuel supply to the pilot line. The resulting stoichiometric flame extends the region with considerable temperature peaks within the burner, and therefore, the thermal NO mechanism is dramatically enhanced.

Contributed by the International Gas Turbine Institute of ASME for publication in the JOURNAL OF ENGINEERING FOR GAS TURBINES AND POWER. Manuscript received May 16, 2006; final manuscript received December 3, 2006. Review conducted by Dilip R. Ballal. Paper presented at the ASME Turbo Expo 2006: Land, Sea and Air (GT2006), May 8–11, 2006 Barcelona, Spain. Paper No. GT2006-90240.

Table 1 Base features of the MGT

	Micro-GT Specifications
Mech. arrangement	Single shaft
Pressure ratio	3.9
Turbine inlet temp.	1223 K
Combustor inlet temp.	905 K
Overall fuel/air eqv. ratio	0.142
Rated mech. output/speed	110 kW/64,000 rpm
Compressor	1 Radial flow compressor
Turbines	1 Radial flow turbine

In order to overcome the problem outlined above, a classical way to be followed consists of the oxidant dilution with inert species. Conceptually, this could be obtained by a partial recirculation of the exhaust gases: in this sense, some proposals exist in the technical literature with reference to twin-spool gas turbines [8] that allow an exhaust bleeding after the high-pressure turbine to dilute the air at the low-pressure compressor discharge.

In practice, the simple mechanical arrangement of the micro-gas turbine implies that the recirculated exhausts must be necessarily addressed to the compressor inlet. In such a case the potential benefits in terms of pollutant control could be negatively balanced by a significant performance decrease of the microturbine. Really, the temperature increase after the mixing with the exhaust gases would affect the compressor flow capacity and the compression work as well.

Based on the above considerations, the changes in the plant layout that are proposed in this paper (Fig. 2) include a cooling heat exchanger after the air mixing with the exhaust fraction recirculated according to the X_{EGR} parameter.

As it is self-evident, the role of the cooler is establishing the adequate temperature level at compressor inlet. On the other hand, the cooling intensity must be controlled in order to find the best compromise between two conflicting needs:

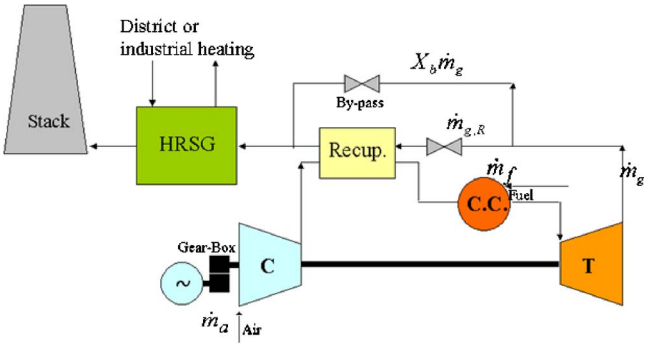

Fig. 1 Schematics of micro-gas turbine integrated with devices for recuperated cycle and heat recovery

Table 2 Natural gas features

Fuel composition	(%, molar)
CH_4	92.00
C_2H_6	3.70
C_3H_8	1.00
C_4H_{10}	0.25
N_2	2.90
CO_2	0.15
Molecular mass, g/mol	17.34
LHV, kJ/kg	47182
h_{0f}, kJ/kg	–4266.9
f_{st}	0.0620
T_{0f}, K	2220

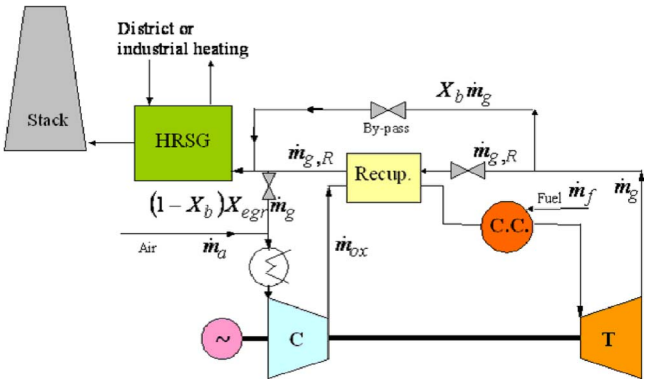

Fig. 2 Modified plant layout with the exhaust recirculation option

- As stated, the compressor inlet temperature should be lowered for avoiding an excess in performance decay.
- The combustor inlet temperature, as resulting from the compression and internal heat recovery processes, should be sufficiently high in order to ensure an efficient self-ignition of the reacting mixture with poor oxygen contents.

The latter statement explains the sense of the rather unusual cycle optimization, which is discussed in this paper: the extended objective is represented by the best performance level that complies, for each MGT load condition, with a safe combustor operation in terms of both combustion sustenance and pollutant control. The independent variables of such a process are of course the recuperator by-pass fraction X_b and the recirculation fraction X_{EGR}, together with the temperature level at compressor inlet.

Some preliminary considerations can be derived from the mass balance of the plant in Fig. 2

$$\text{EGR mass flow rate:} \quad \dot{m}_{EGR} = (1 - X_b)X_{EGR}\dot{m}_g \tag{2}$$

$$\text{Oxidant mass flow rate:} \quad \dot{m}_{ox} = \dot{m}_a + \dot{m}_{EGR} \tag{3}$$

$$\text{Mass flow rate to HRSG:} \quad \dot{m}_{g,HR} = X_b(1 - X_{EGR})\dot{m}_g \tag{4}$$

The EGR activation reduces, therefore, both the amount of inlet air and the exhaust flow to the heat recovery device, so that the pollutant control seems to involve a disadvantage in terms of energy saving. Thus the combined use of both parameters, say the X_{EGR} and the X_b ratios, may simultaneously pursue the environmental and the energetic objectives. Of course, a full recuperator by-pass (i.e., $X_b=1$) would prevent any EGR option; on the other hand, this possibility is however unrealistic because an excess in gas temperature at the HRSG inlet would occur.

Even if the proposal originates from the need of reducing the NO_x emission at part load, the benefits expected from the present proposal may be exploited also at full-load conditions. The following section will demonstrate that the exhaust recirculation may lead to a nearly zero or "one-digit-parts-per-million" emission. Furthermore, the semi-closed cycle associated with the plant arrangement in Fig. 2 results in an effective alternative to a water or steam injection system, thus avoiding a demineralized water consumption.

Although a preliminary thermodynamic analysis is helpful to derive a provisional prediction of the potential of the above proposal, a component matching approach is more appropriate to describe the changes within the microturbine operating region. The cycle analysis must be then completed with some case of CFD simulation in order to check the actual effectiveness of the optimal operating points detected.

Table 3 Results from the thermodynamic analysis at different EGR levels

ISO conditions full load T_{IT}=1223 K			
X_{EGR}	0.0	0.35	0.65
$\dot{m}_a$, kg/s	0.808	0.511	0.275
$\dot{m}_{ox}$, kg/s	0.808	0.791	0.799
$[N_2]$, % molar	78.98	78.35	76.82
$[O_2]$, % molar	20.98	19.16	14.76
$[CO_2]$, % molar	0.01	0.852	2.872
$[H_2O]$, % molar	0.01	1.636	5.546
$\dot{m}_f$, g/s	6.948	6.940	7.540
Comb. inl. temp., K	905.9	898.6	872.5
Turb. out. temp., K	951.8	953.9	958.8
Rec. out. temp., K	530.8	569.7	599.4
Air-exh. mix. temp., K	—	389.0	493.2
Compr. inl. temp., K	288.1	308.1	308.1
Mech. output, kW	109.7	98.6	102.0
Thermal efficiency	0.334	0.301	0.287
Thermal output, kW	108.7	91.8	60.5
$EICO_2$, g/kWh	621.6	709.3	805.1
[NO], ppm dry	36.06	30.81	4.02

Methods for Power Plant Simulation

Preliminary Thermodynamic Estimate. In order to proceed with a first trial estimation of the potential of the recuperated and recirculated cycle, which results from the plant layout in Fig. 2 a thermodynamic analysis was carried out, according to the specifications recalled below [3]

- The thermochemical equilibrium of the species involved in the several processes is calculated by accessing the JANAF tables [15].
- The recuperator efficiency and the related pressure losses are computed as a function of the actual gas flow rate through this device [18,19], and therefore, both parameters are affected by the power output, and by the by-pass and EGR ratios as well.
- A thermokinetic model describes the mechanism of thermal NO formation [3,20]. The related equations are solved are solved in the combustor residence time domain, and the model is sensitive to a number of conditions, such as
  - The local temperatures and species concentrations
  - The time and mass flow rate splitting in the combustor regions (i.e., primary, secondary and dilution zones)
  - The fuel subdivision between the lean-premixed and the pilot line

In this preliminary application, the thermodynamic model was employed for testing the response of the system in Fig. 2 to different values of the X_{EGR} ratio. The performance and emission prediction are summarized in Table 3.

The results in this table refer to full-load conditions, fully recuperated cycles, at the maximum level allowed for the turbine inlet temperature. The activation of the exhaust recirculation reduces the mass flow rate of external air $\dot{m}_a$, so that the oxidant mass flow consists of an increased amount of inert species. Although no component matching is estimated at this step, the oxidant mass flow rate $\dot{m}_{ox}$ is scaled according to the modified conditions at the compressor inlet: really, the inlet temperature is higher than the ambient one, despite of the high effectiveness assumed for the intercooler, and a pressure drop is also considered throughout this component.

The differences in combustor inlet temperature with respect to the reference conditions (i.e., with X_{EGR}=0) are due to variations in the recuperator efficiency, but the levels are however high enough to ensure a correct self-ignition of the reactants.

The data in Table 3 result from the thermodynamic analysis of

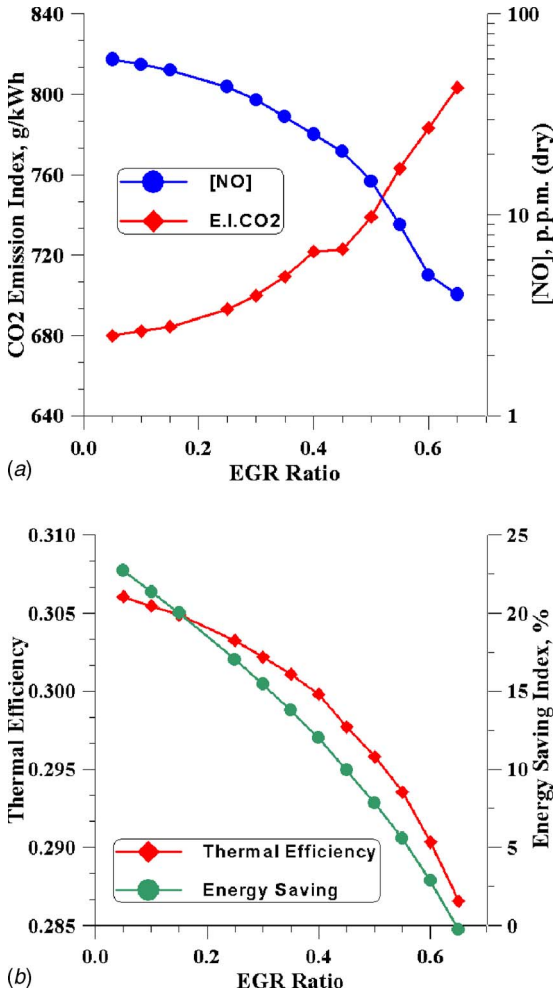

Fig. 3 Emission and performance parameter trend with the EGR ratio

the MGT performance as a function of the EGR ratio: the curves in Fig. 3 display the behavior of some emission and energy indices with this parameter: as expected, the EGR practice demonstrates a good effectiveness for the thermal NO control, whose amount can be substantially reduced for X_{EGR} levels close to 0.6–0.65. The method is, on the contrary, unfavourable in terms of CO_2 control due to the combined effect of its contents increase in the exhaust and of the thermal efficiency decay. It should be also pointed out that the EGR option involves both additional pressure losses through the intercooler and a temperature increase at compressor inlet: this explains the discontinuity observed in Table 3 for the X_{EGR}=0 case. The related performance parameters must be intended as those obtainable when the original layout in Fig. 1 is maintained.

Both Table 3 and Fig. 3 also remind us that the EGR activation results in a decrease of the recoverable thermal output and, therefore, in an unacceptable drop of the energy saving index (defined by the comparison between the primary energy supplies needed for separated and combined production of thermal and mechanical energy) when the maximum in NO reduction is achieved. More favorable results can be obtained if considering the recuperator by-pass option for increasing the thermal output availability. As examples, the curves in Fig. 4(*a*) show that, for a given level of the EGR ratio, increasing the recuperator by-pass may lead to a good compensation of the thermal efficiency decrease.

The more comprehensive diagram in Fig. 4(*b*) provides a better overview of the results that are expected from the simultaneous employment of the EGR and the recuperator by-pass valves. Both

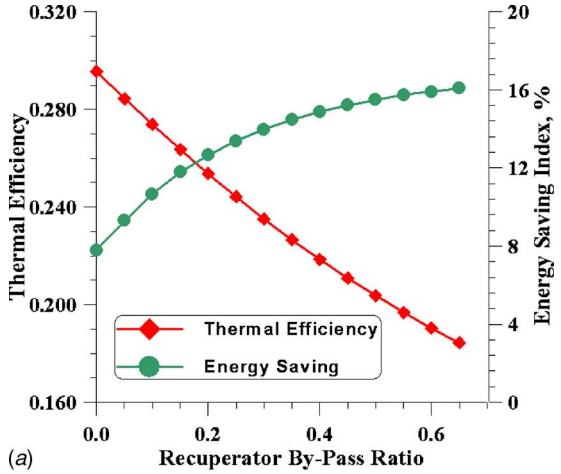

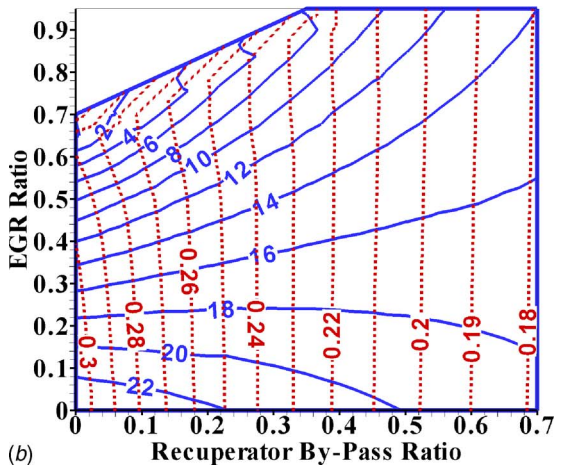

Fig. 4 Combined effect of the by-pass and EGR ratio on the MGT performance parameters

the X_b and the X_{EGR} ratio are not explored in the full theoretical range (0–1) since, as stated, limitation on the HRSG temperatures are imposed and an EGR excess would produce the steam saturation within the exhaust-air mixture, resulting in liquid water contents in the oxidant flow at the compressor inlet. Higher values of the EGR ratio are only allowed for increasing values of the recuperator by-pass ratio, since the actual mass flow rate of recirculated gases is however limited according to Eq. (2).

Finally, the diagrams in the space of the independent variables, X_b and X_{EGR}, clearly show the effect of the exhaust recirculation which mainly consists of a reduction in the combustion temperature peaks that slows down the mechanism of thermal NO formation (Fig. 5). As expected, an increase in the recuperator by-pass ratio requires a higher amount of flue gas recirculation in order to achieve a relevant reduction in nitric oxides. These results, obtained on a thermodynamic and thermokinetic basis, must be intended as a qualitative outline of the potential of the method proposed in this paper. A CFD-based analysis of the combustion process under the new conditions induced by the EGR activation is therefore needed for obtaining a more definite answer about the actual possibilities of the combustor operation with a low oxygen contents.

Off-Design Matching Analysis. Although the component matching analysis should be applied to the whole MGT operating range, a single example is presented in Fig. 6 and discussed in the following. The results refer to a constant-speed, variable-load operation in the two-dimensional space of independent variables, say

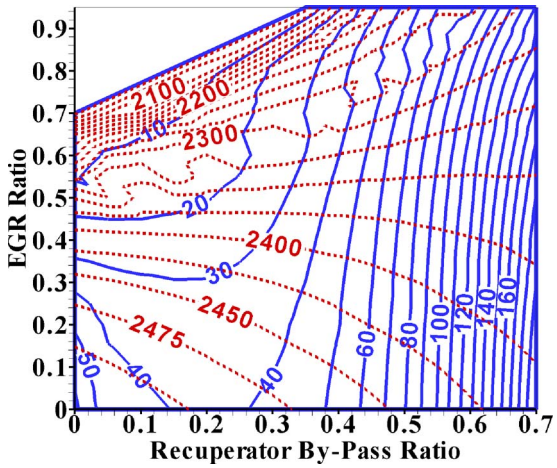

Fig. 5 Combined effect of the by-pass and EGR ratio on the thermal NO formation

the mechanical output and the EGR ratio. As known, this method allows evaluation of the actual power plant performance by including the limits in turbine and compressor flow capacities [3].

Therefore, each operating point in Fig. 6 is calculated by considering the changes in oxidant and gas flow rates through the rotating and stationary components with the corresponding pressure ratios or drops. Figure 6(*a*) displays the thermodynamic con-

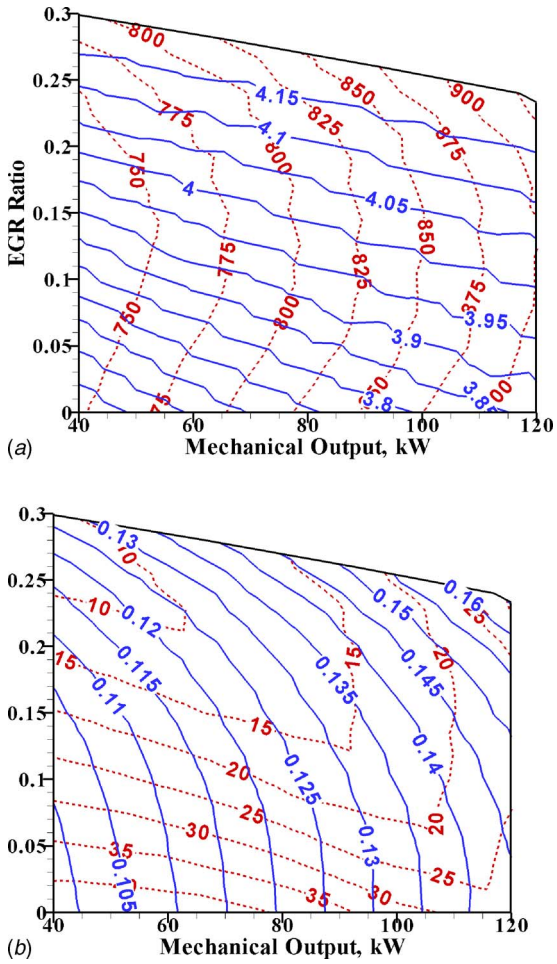

Fig. 6 Effect of variable-load, variable EGR ratio on the conditions for the thermal NO formation

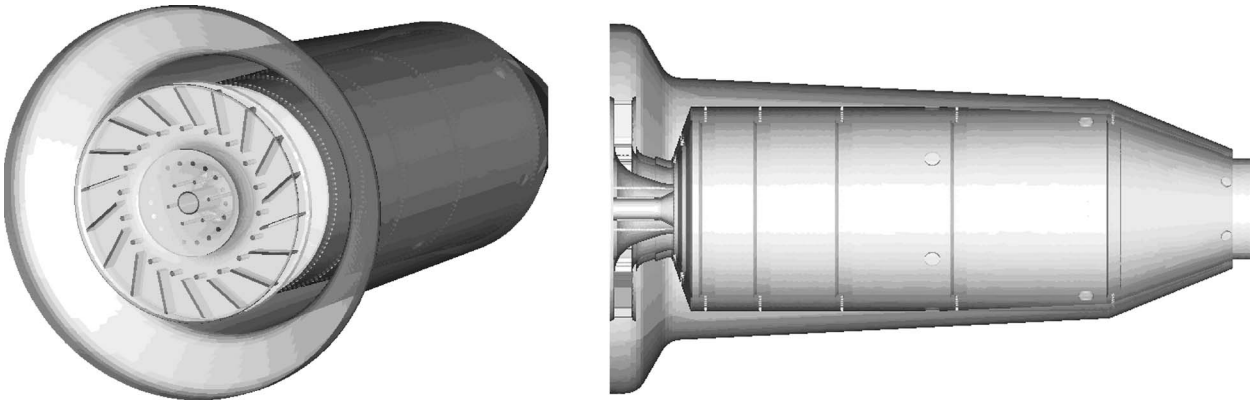

Fig. 7 Lean premixed combustor

ditions at the combustor inlet to be employed as boundary data for the CFD simulation. The information is of particular interest at part load, since the changes in inlet pressure and temperature play an important role in the combustion development. Figure 6(*a*) highlights that the EGR activation induces choking phenomena that result in a pressure increase with the X_{EGR} parameter.

Further interesting indications are provided by Fig. 6(*b*), which summarizes the overall reactant composition at the combustor inlet, together with the expected emission of thermal NO. Displaying the fuel/oxygen equivalence ratio seems to be appropriate for estimating the global effect of the variations in both fuel and air mass flows and of the exhaust recirculation as well. It is worth noting that, in terms of NO reduction, the same equivalence ratio is nearly ineffective at full-load operation while at part-load conditions, it leads to a better pollutant control. Such consideration contributes to the identification of the cycle optimization criteria of the modified plant in Fig. 2, also at off-design conditions.

CFD Validation of the EGR Potential

The Lean-Premixed Combustor. This chamber, of the tubular type, was expressly conceived by the Ansaldo Research Center [11,12] for the MGT application, and it consists of a burner, whose primary zone is supplied by a circular bladed swirler, and an external liner, which addresses the airflow to both the cooling slices and the dilution holes [4,5,11,12].

The radial fuel injection takes place immediately downstream of the blade channel through 18 injectors with 4 holes each. A complete fuel and air mixing is therefore attained prior to the primary region inlet, with an equivalence ratio of 0.55 at base rating. The mixture ignition is aided by a pilot stoichiometric flame. The rate of fuel supplied to the pilot line, through six single hole injectors, is of nearly 10% at the baseline operation but it should increase both at part load and at reduced inlet air temperatures.

A comprehensive three dimensional (3D) sketch of the combustion chamber is given in Fig. 7, together with a complete outline of a meridional section. Because of the complexity of the combustor geometry, an accurate CFD simulation requires a well-refined computational mesh. The need of examining a large number of operating conditions, in accordance with the purpose of this work, suggested the authors to employ a simplified two-dimensional (2D) domain as displayed in Fig. 8. The fully 3D computations were only employed for providing some boundary conditions to the 2D computations as detailed later on.

The two-dimensional domain was derived from the 3D one, but with a number of fundamental approximations, as follows:

- The air inlets to the external liner and to the lean-premixed line are kept separated, while in the 3D simulation the airflow split between the two regions is automatically estimated.

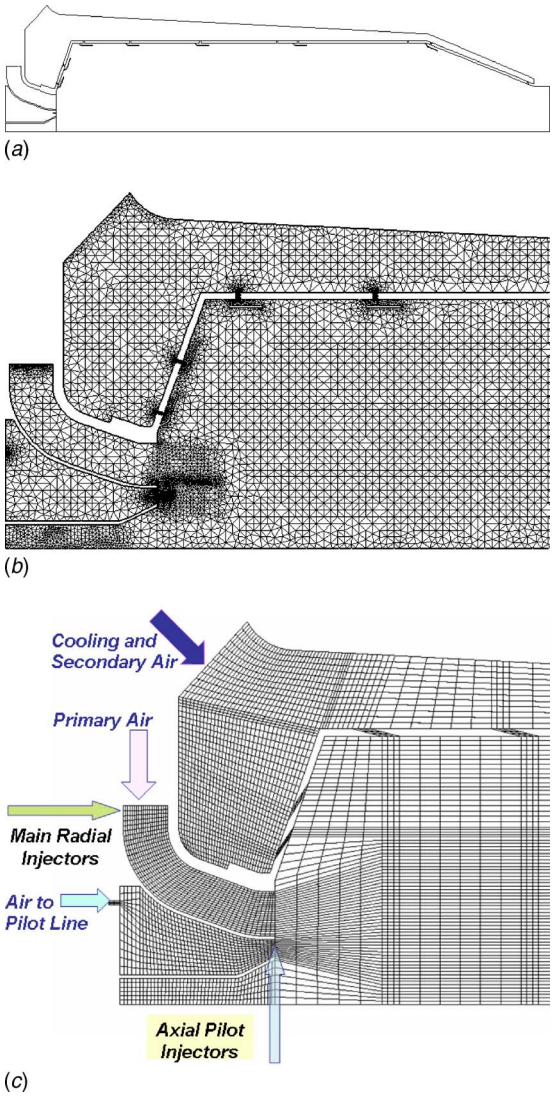

Fig. 8 2D computational domain and details of the unstructured and of the block-structured mesh

Table 4 Input data and average properties at combustor exit from KIVA computations (number in brackets refer to FLUENT results)

		Inlet data		Outlet		
Operating condition	X_{EGR}	Over. eqv. ratio	$[O_2]$ (%, mass)	$\bar{T}_{ex}$ (K)	[NO] (ppm)	[CO] (ppm)
X_b=0 Full load	0.0	0.149	23.27	1252 (1245)	26.1 (31.8)	2.19 (64.8)
	0.35	0.166	21.33	1252	20.2	2.93
	0.65	0.214	16.61	1244	7.03	4.51
	Mild regime	0.301	11.67	1239 (1225)	0.06 (2.83)	19.6 (115.8)
X_b=0.0 60% load	0.0	0.130	23.27	1080	45.4	0.672
	0.65	0.187	16.30	1074	1.74	1.09
X_b=0.25 Full load	0.0	0.169	23.27	1274	106.5	10.7
	0.80	0.251	16.43	1276	7.84	39.3

- The flow through the swirling vanes is not estimated, so that the inlet swirl angle is assigned according to the 3D results.
- A simplified geometry is also assumed for the cooling and diluting holes which are replaced by slices of equivalent flow areas.

The type of boundary conditions that are to be assigned result from the above items and are summarized as follows:

- The inlet boundaries in the 2D domain are of the velocity inflow type, and the inlet velocities are assigned in accordance with the flow rate splitting between the primary air and the secondary and dilution airflows through the liner, as estimated by the 3D flow solver.
- The swirled intake into the premixed line is given in terms of the average flow angle resulting from the 3D flow through the inlet bladed channel (Fig. 7).
- The inlet turbulent kinetic energy and the dissipation rate may be derived from the more detailed viscous flow computation in the 3D domain.
- The set of boundary condition is completed by the values of the recuperator exit temperature and pressures. Both values result from the thermodynamic simulation of the whole MGT system, together with the oxidant composition.

Preliminary 2D computations were carried out with both the FLUENT® and the KIVA3V [21] flow solvers, the first one adopting unstructured meshes, the second one operating with block-structured grids. In both cases, the grid independency was reached after a mesh refinement up to nearly 30,000 nodes. The same Fig. 8 reports details of the two meshes, with 49,000 and 32,000 nodes, respectively, with enhanced resolutions of the fuel injection regions and of the burner primary zone.

CFD Analysis of the Combustion Chamber. The fully developed combustion analysis under a variety of load and EGR conditions was carried out with the KIVA3V solver which incorporates a reliable model for the identification of the mixture self-ignition [1,3–5]. The FLUENT was only employed for a preliminary validation of the results expected in terms of temperature and pollutant distribution throughout the combustor.

Both solvers assume the finite-rate–eddy-dissipation model[22] with a kinetic scheme based on a global two-step methane oxidation mechanism [23,24]. The model also allows estimation of the residual CO contents at combustor outlet. The simultaneous solution of the Zel'dovich kinetic equations leads to the thermal NO calculation [20].

As stated, the self-ignition conditions are identified by means of two empirical correlations for the delay time of a methane/air mixture, the first one proposed by Spadaccini and TeVelde [25] and holding in a temperature range above 1300 K, the second one by Li and Williams [26] and Roy et al. [27] for the temperature range lower than 1300 K. In previous works [1,4,5], the time-delay concept was transformed into a spatial shift of the self-ignition region by the authors, thus leading to a model that is sensitive to the local temperatures and to the fuel and oxygen concentration as well. The model is therefore suitable for a satisfactory prediction of the effect of changes in the oxidant composition related to the EGR activation.

Table 4 summarizes the computational cases that were examined, first by referring to the full-load, fully recuperated cycles, and then by analyzing both a part-load condition and an example with the activation of the recuperator by-pass.

All the outlet data in this table are the mass averaged values through the combustor exit open surface and, in particular, the $\bar{T}_{ex}$ values are the average levels of the firing temperature, therefore close to those expected for the T_{IT}. As a general comment, all the results confirm the qualitative thermodynamic predictions in terms of the thermal NO decrease related with the employment of the EGR option. Regarding to the full-load operation, it is confirmed that a 0.35 value of the X_{EGR} ratio is almost unsuccessful while the limiting value of 0.65 produces successful results in terms of nitric oxide reduction. Conversely, a slight increase in CO production is observed, due to the progressive oxygen lack with the X_{EGR} levels. However, the combustion regime is fairly distant from a true mild regime, which is also included, as a theoretical example, in Table 4. Really, the typical oxygen contents inducing a mild regime (i.e., with a molar fraction lower than 10%) are never achieved with the EGR activation because of the poor fuel-air equivalence ratio required for the MGT to reach the maximum T_{IT} level. Therefore, this example only recalls that a true mild combustion could take place in the combustor examined and would lead to practically zero NO emission, with a non-negligible carbon monoxide increase. More severe results are exhibited by the FLUENT computations, which indicate in Table 4 a relevant CO production both at the baseline condition and, increasingly, at the mild regime. These calculations confirm that the changes in the oxidant composition lead to a smoother temperature profile, the latter displayed along a straight line starting from the lean-premixed channel (Fig. 9). Consequently, the thermal NO mechanism undergoes a significant slowing with substantial benefits in terms of control of this polluting species.

The numerical agreement between the results from the two different solvers is only qualitative, mainly due to the adoption of an effective self-ignition model only within the KIVA code. Neglecting the ignition delay of the fuel-air mixture leads, in the FLUENT results, to a temperature peak not only along a line starting from the pilot diffusive channel, but also along the premixed line (Fig. 10). Figure 10 shows that the more realistic estimation of the ignition start in the KIVA solver produces a fairly flatter temperature profile starting from the lean-premixing duct.

For the above reasons, the considerations in the following refer

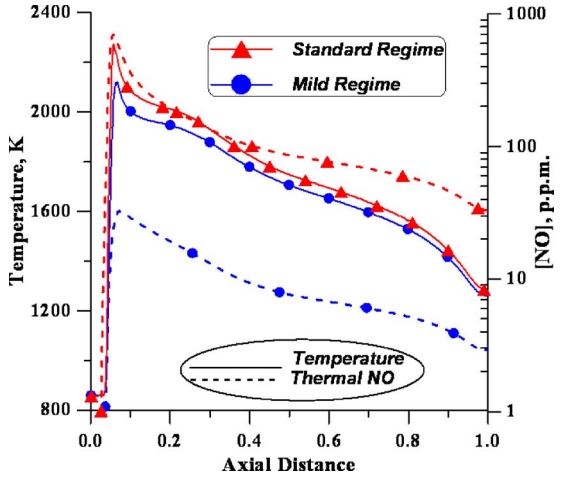

Fig. 9 Temperature and NO distributions from FLUENT calculations

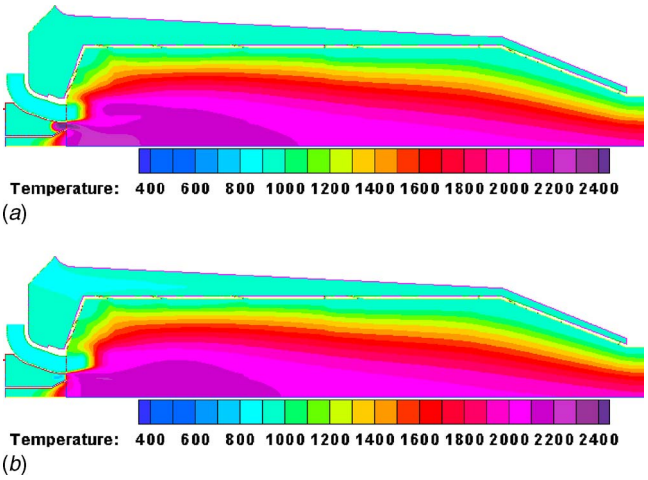

Fig. 11 Temperature distributions for different combustion regimes

only to the KIVA computations. First, the temperature distributions throughout the combustion chamber (Fig. 11) put into evidence that the EGR solution is able to reduce both the temperature peaks in the primary region and the extent of the region, above 2000 K, with high formation rates of thermal NO. The mild regime would lead to a complete removal of such regions together with the local peaks. Nevertheless, the thermal NO contours in Fig. 12 confirm that the combustor operation with the oxidant originating from an X_{EGR} value of 0.65 would be effective enough to control the mechanism of formation.

A more impressive overview of the effect both of the increasing EGR ratio and of the theoretically achievable mild regime is given in Fig. 13. An exhaust recirculation set at the 65% level already cuts off the peaks in the pilot diffusive region, while a lower level (e.g., of 35%) is unable to substantially modify the temperature profile. Of course, the true mild combustion would produce a completely smooth temperature pattern and this would result in a practically negligible NO production. However, the X_{EGR}=0.65 choice induces a decrease in the formation rate of nearly an order of magnitude, as demonstrated by Fig. 13(*b*). Figures 13(*c*) and 13(*d*) highlight the strict dependence of the CO formation on the oxygen concentration in the reactants so confirming that conflicting effects arise from the method discussed in this work. Further refinements are therefore needed to optimize the simultaneous control of both nitric and carbon monoxides.

For the sake of completeness, Fig. 14 displays the same curves as in Fig. 13(*a*) and 13(*b*) along the premixed line. In this case, the temperature profile with increasing EGR levels are fairly overlapped, but a reduction in the NO formation, however, occurs because of the decrease in the oxygen contents, which plays a fundamental role in the related mechanism [20]. Even along the premixed path, a mild regime would be characterized by a very flat temperature pattern that agrees with the enhanced uniformity already observed in Fig. 11.

The results related to the part-load operation in Figs. 15 and 16, confirm the considerations made in the previous sections:

- Operating the micro-gas turbines at constant speed, decreased fuel flow rate, reduces the overall fuel-air equivalence ratio and the combustor inlet temperature. The latter effect results from the decreased heat recovery through the recuperator.
- For both reasons, the lean mixture ignition must be aided by a stronger diffusive flame which, at 60% load, requires the 50% of the fuel to be supplied to the pilot injectors.
- Consequently, an enlargement is observed in the high temperature region with relevant NO formation rates.

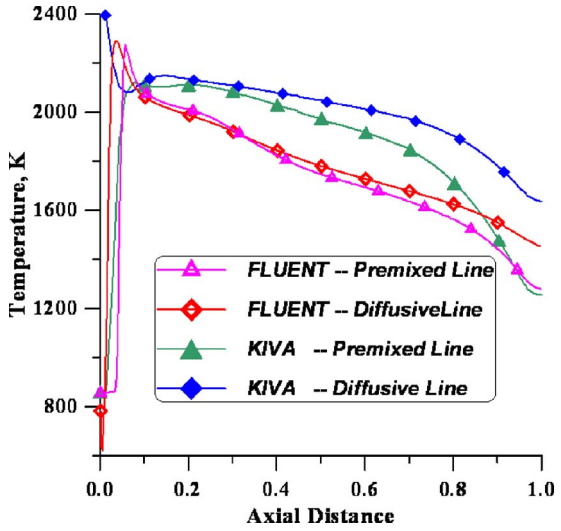

Fig. 10 A comparison of FLUENT and KIVA results

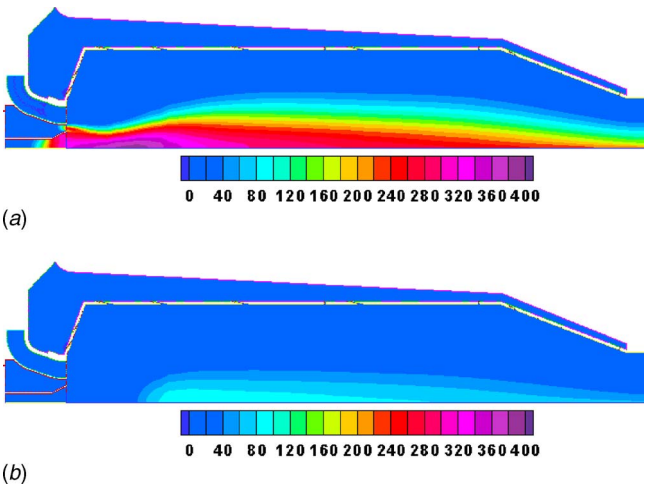

Fig. 12 Thermal NO distributions (ppm) for different combustion regimes

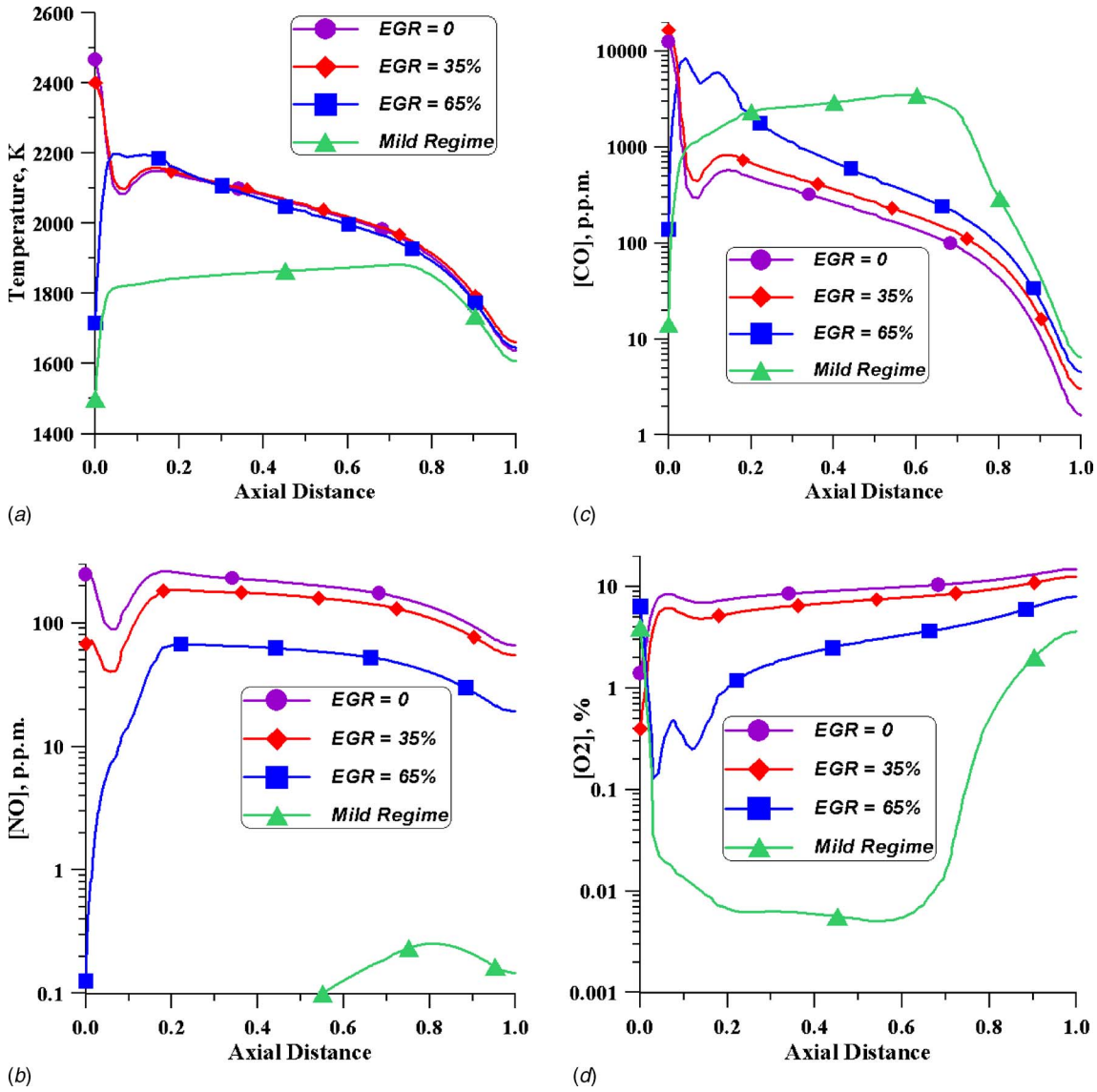

Fig. 13 Axial distributions for different combustion regimes

The oxygen reduction with the exhaust recirculation results in a drastic cutoff of the temperature peaks, which can be better appreciated in Fig. 16. The temperature profiles for standard and low-oxygen combustion strongly differ within the primary region, and they practically overlap along the secondary and the dilution zones. In this way, the reduction in the thermal NO formation is ensured, as confirmed by the related curves in the same Fig. 16. It is also of interest that the results in Table 4 confirm the indications provided by the matching analysis: the same fuel/oxygen equivalence ratio as at full-load conditions induces, at part-load, a more effective NO control. The last case listed in Table 4 refers to a full-load partly recuperated cycle condition. This situation involves a decrease in the air temperature at the combustor inlet, but it also implies a greater fuel mass addition for reaching the same T_{IT} level as in the fully recuperated conditions. The combustor operates therefore with an increased overall fuel-air equivalence ratio, and the local value of this parameter is above the stoichiometric threshold along the pilot diffusive line.

Consequently, enlarged high-temperature regions are created and the local oxygen defect delays the carbon monoxide conversion. The synthetic results in Table 4 confirm that both the NO and the CO production are increased even with the standard (i.e., with $X_{EGR}=0$). Furthermore, the thermokinetic model underpredicts the NO formation in this case, as demonstrated by the comparison of results in Tables 3 and 4. A strong reduction in such species is therefore needed, and this objective can be pursued, as suggested in Fig. 5, by a relevant amount of the EGR fraction. The related results, with $X_{EGR}=0.80$, evidence a reasonable effectiveness in the nitric oxide control. Figure 17 compares the standard and the low-oxygen combustion results, and the effect of the flue gas recirculation clearly results in a delay of the kinetic mechanism, so leading to a considerable decrease in NO contents. The results in Table 4 remind us, on the other hand, that the simple application of the EGR option to this operating condition involves unacceptable carbon monoxide levels. More refined strategies of pollutant control must be therefore set up whenever the NO reduction is balanced by such an increase in CO production.

Conclusion

Although the mild combustion regime can be only approximated by the micro-gas turbine, the adoption of the exhaust gas recirculation produces attractive effects in terms of nitric oxide control in a wide operating range. The simultaneous choice of the EGR fraction and of the recuperator by-pass ratio also allows to

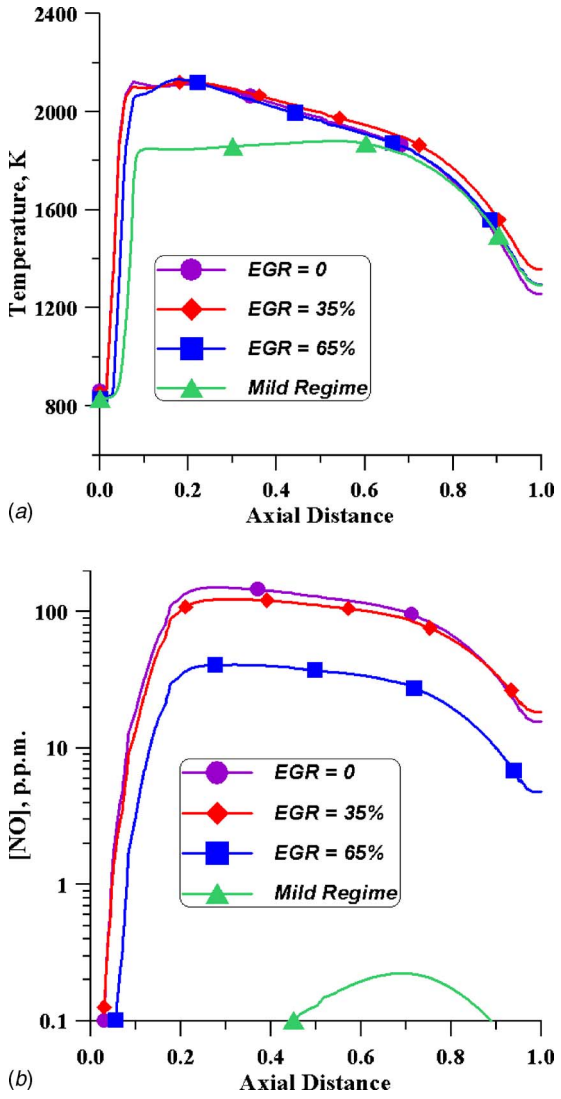

Fig. 14 Axial distributions for different combustion regimes

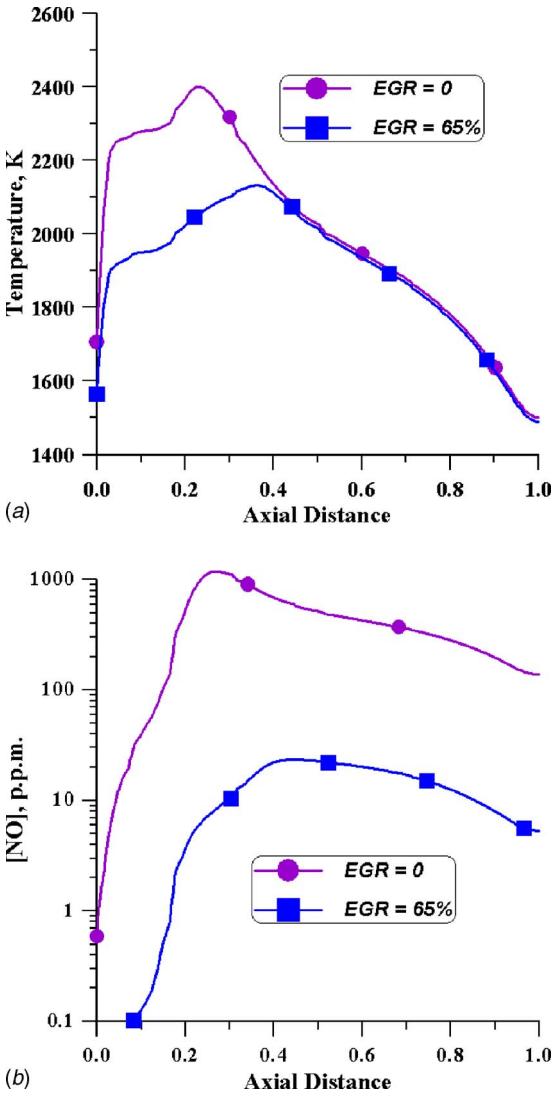

Fig. 16 Axial distributions at part-load conditions

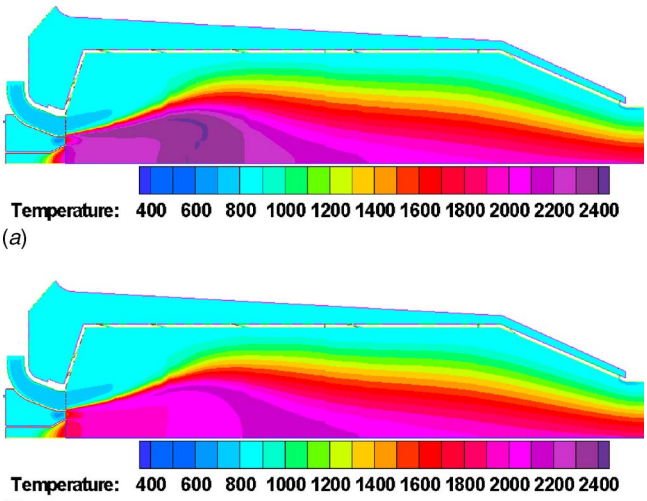

Fig. 15 Temperature distributions at part-load conditions

prevent an excess in energetic performance decay, while achieving a satisfactory control of the thermal NO formation so contributing to the total NO_x reduction.

The CFD-based analysis offers good perspectives with regard to the lean-premixed combustor operation with a low-oxygen oxidant, but it also highlights the typical problems related to the increase in carbon monoxide. Two typical ways must therefore be followed to reduce this undesired effect:

- Considering the variable speed operation for the microturbine, allowed by the emerging technology of the variable-frequency electrical generators, as a tool for a better control of the fuel-to-air ratio at both part-load and partly recuperated cycle conditions.
- Improving the combustor fluid dynamics in order to enhance the full oxidation of the unburned and partly oxidized species.

Both strategies are included in the integrated methodology proposed in the most recent authors' papers [1–6] and will be therefore the subject of their future activities for improving the potential of the method outlined in this work.

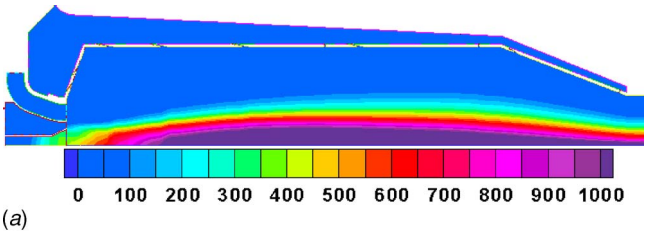

(*a*)

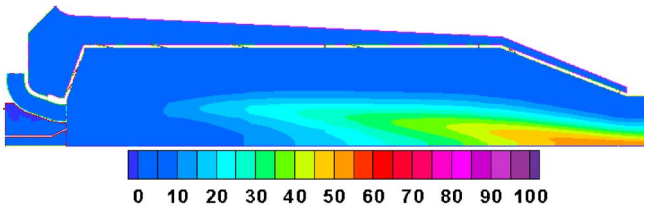

(*b*)

Fig. 17 Thermal NO distributions (ppm) at partly recuperated conditions

Acknowledgment

The Ansaldo Ricerche S.p.A. is acknowledged for suggesting provisional data of the MGT cycle parameters and combustor configuration. The reference CFD calculations are licensed by Fluent Inc.

Nomenclature

EGR = exhaust gas recirculation
f = fuel-to-air ratio
h_{0f} = enthalpy of formation
LHV = lower heating value
$\dot{m}$ = mass flow rate
MGT = microgas turbine
ppm = parts per million
T, T_{IT} = temperature turbine inlet temperature
X_b = recuperator by-pass ratio
X_{EGR} = EGR ratio

Subscripts

a = air
cc = combustion chamber inlet
ex = combustion chamber outlet
f = fuel
g = exhaust gas
ox = oxidant
R = recuperator
st = stoichiometric

References

[1] Cameretti, M. C., and Tuccillo, R., 2004, "Comparing Different Solutions for the Micro-GasTurbine Combustor," ASME Paper No. GT 2004-GT-53286.
[2] Bozza, F., and Tuccillo, R., 2004, "Transient Operation Analysis of a Cogenerating Micro-Gas Turbine," ASME Paper No. ESDA-2004-58079.
[3] Bozza, F., Cameretti, M. C., and Tuccillo, R., 2005, "Adapting the Micro-Gas Turbine Operation to Variable Thermal and Electrical Requirements," ASME J. Eng. Gas Turbines Power, **127**, pp. 514–524.
[4] Cameretti, M. C., and Tuccillo, R., 2005, "A CFD Based Off-Design Study of Micro-Gas Turbines Combustors," ASME Paper No. GT-2005-68924.
[5] Tuccillo, R., and Cameretti, M. C., 2005, "Combustion and Combustors for MGT Applications," VKI/LS on "Micro Gas Turbines," RTO-MP-AVT-131.
[6] Tuccillo, R., 2005, "Performance and Transient Behaviour of MTG Based Energy Systems," VKI/LS on "Micro Gas Turbines," RTO-MP-AVT-131.
[7] Levy, Y., Sherbaum, V., and Erenburg, V., 2005 "Fundamentals of Low-NO_x Gas Turbine Adiabatic Combustor," ASME Paper No. GT2005-68321.
[8] Camporeale, S., Casalini, F., and Saponaro, A., 2003, "Mild Combustion in a Novel Ccgt Cycle With Partial Flue Gas Recirculation," ASME Paper No. GT2003-38743.
[9] Vaz1, C. D., Borges, A. R. J., Van Buijtenen, J., Spliethoff1, H., 2004, "On the Stability Range of a Cylindrical Combustor for Operation in the Flox Regime," ASME Paper No. GT2004-53790.
[10] Kalb, R. J., and Sattelmayer, T., 2004, "Lean Blowout Limit and NO_x-Production of a Premixed Sub-ppm NO_x Burner With Periodic Flue Gas Recirculation," ASME Paper No. GT2004-53410.
[11] Croce, G., Mori, G., and Parente, J., 2003, "Assessment of Traditional and Flamelets Models for Micro Turbine Combustion Chamber Optimisation," ASME Paper No. GT-2003-38385
[12] Parente, J., Mori, G., Anisimov, V., and Croce, G., 2004, "Micro Gas Turbine Combustion Chamber Design, and CFD Analysis," ASME Paper No. GT2004-54247.
[13] Bozza, F., Cameretti, M. C., and Tuccillo, R., 2004, "The Employment of Hydrogenated Fuels From Natural Gas Reforming: Gas Turbine and Combustion Analysis," ASME J. Eng. Gas Turbines Power, **126**, pp. 489–497.
[14] Ibrahim, O., Zimmermann, P., Hirsch, C., Sattelmayer, T., Gerhard, B., and Steinbach, C., 2004, "Microturbine Operating With Variable Heat Output," ASME Paper No. GT-2004–53011.
[15] Mc Bride, B. J., and Gordon, S., 1994, "Computer Program for Calculation of Complex Equilibrium Composition and Applications," NASA RP 1311, Parts I and II.
[16] Traverso, A., Calzolari, F., and Massardo, A. F., 2003, "Transient Analysis and Control System for Advanced Cycles Based on Micro Gas Turbine Technology," ASME Paper No. GT-2003-38269.
[17] Takase, K., Furukawa, H., and Nakano, K., 2002, "A Preliminary Study of an Inter-Cooled and Recuperative Microgasturbine Below 300 kW," ASME Paper No. GT-2002-30403.
[18] Lagerström, G., and Xie, M., 2002, "High Performance & Cost Effective Recuperator for Micro-Gas Turbines," ASME Paper No. GT-2002-30402.
[19] Proeschel, R. A., 2002, "Proe 90™ Recuperator for Micro-Turbine Applications," ASME Paper No. GT-2002-30406.
[20] Zel'dovich, Y. B., Sadovnikov, P. Y., and Frank-Kamenetskik, D. A., 1947, *Oxidation of Nitrogen in Combustion*, Academy of Science of SR, Institute of Chemical Physics, Moscow-Leningrad.
[21] Amsden, A. A., 1997, "KIVA-III v: Block Structured KIVA Program Engine With Vertical or Canted Valves," LA—Los Angeles 13313—MS, Los Alamos.
[22] Magnussen, B. F., and Hjertager, B. H., 1977, "On Mathematical Modeling of Turbulent Combustion With Special Emphasis on Soot Formation," 16th Symposium on Combustion, The Combustion Institute, Pittsburgh.
[23] Nicol, G. D., Malte, P. C., Hamer, A. J, Roby, R. J., and Steele, R. C., 1998, "A Five-Step Global Methane Oxidation—NO Formation Mechanism for Lean Premixed Gas Turbine Combustione," ASME Paper No. 98-GT-185.
[24] Miller, J. A., and Bowman, C. T., 1989, "Mechanism and Modeling of Nitrogen Chemistry in Combustion," Prog. Energy Combust. Sci., **15**, pp. 287–338.
[25] Spadaccini, L. J., and TeVelde, L. J., 1982, "Autoignition Characteristics of Aircraft Type Fuels," Combust. Flame, **46**, 283–300.
[26] Li, S. C., and Williams, F. A., 2000, "Reaction Mechanism for Methane Ignition," ASME Paper No. 2000-GT-145.
[27] Roy, C. J., Moran, A. J., and Thomas, G. O., 2001, "Autoignition Characteristics of Gaseous Fuels at Representative Gas Turbine Conditions," ASME Paper No. 2001-GT-0051.

Combined First and Second-Law Analysis of Gas Turbine Cogeneration System With Inlet Air Cooling and Evaporative Aftercooling of the Compressor Discharge

A. Khaliq[1]
Department of Mechanical Engineering,
Faculty of Engineering and Technology,
Jamia Millia Islamia,
New Delhi–110 025, India
e-mail: abd_khaliq2001@yahoo.co.in

K. Choudhary
Mechanical and Automation Engineering Department,
Amity School of Engineering and Technology,
GGSIPU, New Delhi–110 061, India
e-mail: keshavendra_c@yahoo.com

A conceptual gas turbine based cogeneration cycle with compressor inlet air cooling and evaporative aftercooling of the compressor discharge is proposed to increase the cycle performance significantly and render it practically insensitive to seasonal temperature fluctuations. Combined first and second-law approach is applied for a cogeneration system having intercooled reheat regeneration in a gas turbine as well as inlet air cooling and evaporative aftercooling of the compressor discharge. Computational analysis is performed to investigate the effects of the overall pressure ratio r_p, turbine inlet temperature (TIT), and ambient relative humidity φ on the exergy destruction in each component, first-law efficiency, power-to-heat ratio, and second-law efficiency of the cycle. Thermodynamic analysis indicates that exergy destruction in various components of the cogeneration cycle is significantly affected by overall pressure ratio and turbine inlet temperature, and not at all affected by the ambient relative humidity. It also indicates that the maximum exergy is destroyed during the combustion process, which represents over 60% of the total exergy destruction in the overall system. The first-law efficiency, power-to-heat ratio, and second-law efficiency of the cycle significantly vary with the change in the overall pressure ratio and turbine inlet temperature, but the change in relative humidity shows small variations in these parameters. Results clearly show that performance evaluation based on first-law analysis alone is not adequate, and hence, more meaningful evaluation must include second-law analysis. Decision makers should find the methodology contained in this paper useful in the comparison and selection of advanced combined heat and power systems. [DOI: 10.1115/1.2747257]

Keywords: first-law, second-law, exergy destruction, gas turbine cycle, inlet cooling, evaporative after cooling, reheat, regenerative heat exchanger, cogeneration

1 Introduction

During the last few decades, there have been many attempts, by introducing more complex arrangements, to improve the performance of thermal power systems. Among these, reheat, intercooling, regeneration, and steam injection in a gas turbine cycle has been commercialized and has played an important role in the electricity generation industry because their performance greatly improved the output power in comparison to those systems using conventional gas turbine cycles. More recently, inlet air cooling and evaporative aftercooling of the compressor discharge have been used in gas turbines to further increase its power output and thermal efficiency. Inlet air cooling reduces the work of air compressors as compressor work is a function of the temperature of inlet air. As compressor work decreases, cycle efficiency increases. Evaporative aftercooling is injecting water at the inlet of a regenerative heat exchanger. The injected water is converted into steam and absorbed in the air stream. The energy gained by the injected water reduces the temperature of the air mixture, which increases the removed heat, the capacity of the regenerative heat exchanger, and cycle thermal efficiency.

In an attempt to obtain enhanced power output and thermal efficiency, De Lucia et al. [1] studied gas turbines with inlet air cooling and reported that evaporative cooling could enhance the power produced by 2–4% per year, depending on the weather. Bartolini and Salvi [2] reported an 8% increase in power and 4% increase in thermal efficiency of steam injected gas turbines when cooling the inlet air using an absorption chiller. Najjar and Zaamout [3] reported on increasing the efficiency of the gas turbine regenerative cycle by about 13% using evaporative aftercooling. Bassily [4] carried out the first law of thermodynamics or energy balance analysis of gas turbine cycles and reported that introducing indirect inlet air cooling, evaporative aftercooling of the compressor discharge along with regeneration, intercooling, and reheat increase the performance significantly. The first law of thermodynamics or energy balance method is the most commonly used; however, this is concerned only with the conversion of energy, and therefore, it cannot show how or where irreversibilities in a system or process occur. Thus, while producing the final design result, energy balance analysis is incapable on its own of locating sources of losses. Second-law analysis gives much more meaningful evaluation by indicating the association of irrevers-

[1]Corresponding author.

Submitted to ASME for publication in the JOURNAL OF ENGINEERING FOR GAS TURBINES AND POWER. Manuscript received May 16, 2006; final manuscript received May 1, 2007. Review conducted by Antonio Peretto.

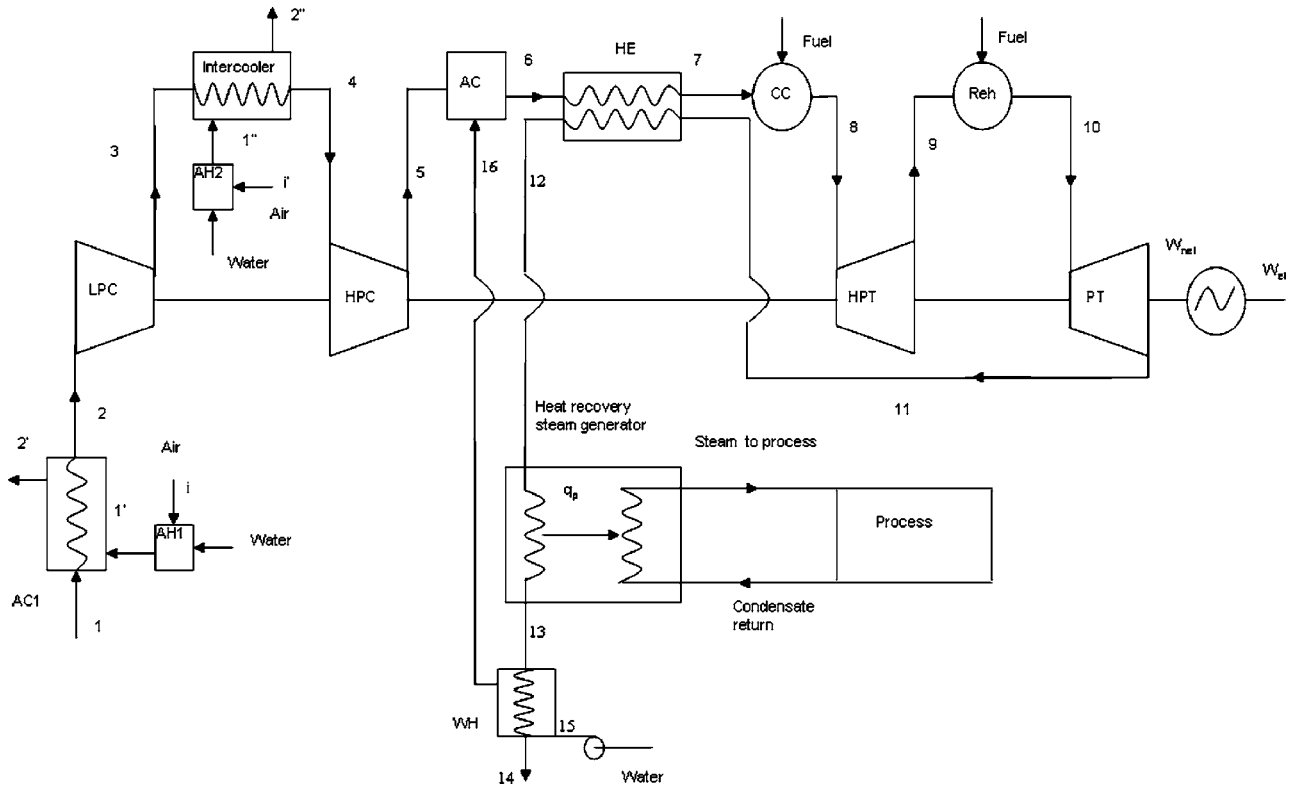

Fig. 1 Schematic diagram of the gas turbine cogeneration system with inlet air cooling and evaporative aftercooling of the compressor discharge

ibilities or exergy destruction with combustion and heat transfer processes and allows a thermodynamic evaluation of energy conservation option in power cycles, and thereby provides an indicator that points the direction in which engineers should concentrate their efforts to improve the performance of thermal power systems. Recently, Khaliq and Choudhary [5] carried out the combined first- and second-law analysis of a gas turbine cycle subjected to inlet air cooling and evaporative aftercooling of the compressor discharge. Their analysis indicates that the exergy destruction in various components of the gas turbine cycle is significantly affected by compressor pressure ratio and turbine inlet temperature, and not at all affected by ambient relative humidity.

This general theme of renewed analysis of gas turbines using the second-law approach has been applied to all of the conventional thermal power cycles; the cogeneration cycle has received its fair share of attention, due to its energy efficiency enhancement and thus reduces net energy consumption in almost all those situations where both heat and power are required, such as the sugar industry, pulp and paper industry, petroleum refining industry, textile mills, etc. Huang et al. [6] applied the exergy methodology for the thermodynamic analysis of a cogeneration system with steam injection and multiple effect evaporation. Tuma et al. [7] have derived the equations for calculation of the overall energetic and exergetic efficiency of a gas-steam cycle cogeneration system. A comparison between energy and exergy efficiency has been performed. Recently, Khaliq and Kaushik [8] conducted a study for the performance evaluation of a gas turbine cogeneration system with reheat and defined the energetic and exergetic efficiencies. They observed the effect of process steam pressure, pinch point temperature, and reheat on energetic and exergetic performance. Their results led to the conclusion that inclusion of reheat in cogeneration system provides significant improvement in electrical power output, process heat production, energetic efficiency, and exergetic efficiency. More recently, Khaliq and Khan [9] analyzed the performance of an intercooled reheat regenerative gas turbine based cogeneration system. Their results indicate that the first-law efficiency is approximately independent of pressure losses, but the second-law efficiency and the power-to-heat ratio reflects the fact that the higher pressure drops degrade the thermodynamic performance significantly.

As is seen in most of the studies in the above-cited literature, there is no study that was conducted to observe the effect of inlet air cooling, evaporative aftercooling, reheat, intercooling, and regeneration on the performance of gas turbine based cogeneration systems, by means of combined first- and second-law analysis. The exergy balances for the cycle and its components are presented and are compared to energy balances. The loss mechanisms in the combustion and heat transfer processes in various heat exchangers are identified, quantified, and broken down into their sources by component and by thermodynamic processes. The effects of compressor pressure ratio, turbine inlet temperature (TIT), and ambient relative humidity φ have been observed on the thermodynamic performance parameters of the cycle viz.: first-law efficiency, second-law efficiency, power-to-heat ratio, and the magnitude of exergy destruction in each component of the cycle. Emphasis is placed throughout on realistic component modeling based on current technological constraints.

2 System Description

Figure 1 shows the schematic diagram of a gas turbine cogeneration system with inlet air cooling and evaporative aftercooling of the compressor discharge. Ambient air is cooled and humidified in the air humidifier (AH1) before it counterpasses the inlet air to the low-pressure compressor (LPC) in the air cooler (AC1), cooling the inlet air. Air at 2 is cooled to a temperature that is close to the wet bulb temperature at 1. Compressed air from the low-pressure compressor at 3 is cooled to 4 in an indirect intercooler using ambient humidified air that is humidified in the air humidifier (AH2) and has a lower temperature than ambient temperature.

This cooled air enters the high-pressure compressor (HPC) and is compressed from state 4 to state 5. The outlet air of HPC at 5 is cooled in the aftercooler (AC) using water injection. The injected water is warmed using the exhaust of the heat recovery steam generator (HRSG) in the water heater (WH). The humid cooled air at 6 enters the regenerative heat exchanger (HE), where it exchanges heat with power turbine (PT) exhaust at 11, gets heated at 7 and supplied to the combustion chamber (CC) (where fuel is burned), producing hot gases at 8. The hot gas is then expanded to 9 in the high-pressure turbine (HPT) to a lower pressure and temperature before it is recombusted in the reheater (reh), after which the reheat gas expands through a power turbine to drive a load. Part of the heat of hot exhaust gas is used in the HE, and part of this heat is utilized in the HRSG to generate steam, and hence to produce the process heat.

3 Thermodynamic Analysis

Energy technologies are normally examined using energy analysis. A better understanding is attained when a more complete thermodynamic view is taken, which uses the second law of thermodynamics in conjunction with energy analysis, via the exergy method [10]. An exergy analysis is the combination of the first and second laws of thermodynamics, in which the efficiencies of processes and devices are evaluated and the locations and cause/sources of major inefficiencies are identified.

If the system operates in a steady-state, steady flow condition and all the nonreacting gases are arbitrarily assigned as zero thermomechanical enthalpy, entropy, and exergy at the condition of ambient pressure and temperature regardless of their chemical composition, then the entropy of mixing different gaseous components can be neglected, and the general exergy-balance equation is given by [11]

$$\dot{E}_W = \sum_{i=1}^{n} (\dot{E}_Q)_i + \sum_{\text{in}} \dot{m}e - \sum_{\text{out}} \dot{m}e - \dot{E}_D \tag{1}$$

For single stream flow,

$$\dot{E}_W = \dot{E}_Q + \dot{m}e_{\text{in}} - \dot{m}e_{\text{out}} - \dot{m}e_D \tag{2}$$

Specific exergy e is given by [12]

$$e = (c_{p_a} + \omega c_{p_v})T_a\left(\frac{T}{T_a} - 1 - \ln\frac{T}{T_a}\right) + (1+\tilde{\omega})R_a T_a \ln\frac{p}{p_a} + R_a T_a\left[(1+\tilde{\omega})\ln\left(\frac{1+\tilde{\omega}_a}{1+\tilde{\omega}}\right) + \tilde{\omega}\ln\left(\frac{\tilde{\omega}}{\omega_a}\right)\right] \tag{3}$$

where

$$\tilde{\omega} = 1.608\omega \tag{4}$$

The mass, energy, and exergy balances of the component of the plant are given below.

3.1 Air Humidifier. Applying the mass balance equation yields

$$\omega_{a_o} = \omega_{a_i} + m_w \tag{5}$$

Temperature and humidity ratio at the exit of a air humidifier can be calculated by energy balance given as

$$h_{a_i} + (\omega_{a_o} - \omega_{a_i})h_w = h_{a_o} \tag{6}$$

The enthalpy h is calculated by

$$h = 1.005t + \omega(2500 + 1.872t) \tag{7}$$

The exergy balance for the air humidifier gives exergy destruction $e_{D,\text{AH}}$

$$e_{D,\text{AH}} = e_{a_i} + m_w e_w - e_{a_o} \tag{8}$$

where e_w is given by [12]

$$e_w = h_f - h_g(T_a) - T_a s_f + T_a s_g(T_a) + [p - p_{\text{sat}}]v_f - R_v T_a \ln\varphi_a \tag{9}$$

The dry airflow rate through the air humidifier is assumed to be 1 kg/s.

3.2 Air Compressors. For a given compressor isentropic efficiency η_C and pressure ratio r_C, other state variables for the incoming and outgoing streams can be calculated. The inlet and outlet humidity ratios will be the same. The energy balance yields the compressor work W_C, and the exergy balance for the compressor gives the exergy destruction $e_{D,C}$

$$\omega_{a_i} = \omega_{a_o} \tag{10}$$

$$W_C = h_{a_o} - h_{a_i} \tag{11}$$

$$e_{D,C} = W_C + (e_{a_i} - e_{a_o}) \tag{12}$$

The temperature at the compressor outlet can be calculated from the following equation [13]:

$$\frac{T_{a_o}}{T_{a_i}} = (r_C)^{(\gamma_C - 1/\gamma_C\eta_C)} \tag{13}$$

where γ_C is the specific heat ratio across the compressor and is given by

$$\gamma_C = \frac{c_{p_c}}{c_{v_c}} \tag{14}$$

where c_{p_c} and c_{v_c} can be determined from the following relations:

$$c_{p_c} = c_{p_{\text{air}}} + \omega_{a_i} c_{p_{\text{H}_2\text{O}}} \tag{15}$$

$$c_{v_c} = c_{v_{\text{air}}} + \omega_{a_i} c_{v_{\text{H}_2\text{O}}} \tag{16}$$

$c_{p_{\text{air}}}$ and $c_{v_{\text{air}}}$ are evaluated at the average temperature across the compressor from the following relations [14]:

$$c_{p_{\text{air}}} = \frac{8.314}{28.97}(3.653 - 1.337\times10^{-3}T_{av} + 3.294\times10^{-6}T_{av}^2 - 1.913\times10^{-9}T_{av}^3 + 2.763\times10^{-13}T_{av}^4) \tag{17}$$

$$c_{v_{\text{air}}} = c_{p_{\text{air}}} - 0.287 \tag{18}$$

$c_{p_{\text{H}_2\text{O}}}$ and $c_{v_{\text{H}_2\text{O}}}$ are evaluated at the average temperature across the compressor from the following relations [14]:

$$c_{p_{\text{H}_2\text{O}}} = \frac{8.314}{18.02}(4.07 - 1.108\times10^{-3}T_{av} + 4.152\times10^{-6}T_{av}^2 - 2.964\times10^{-9}T_{av}^3 + 8.07\times10^{-13}T_{av}^4) \tag{19}$$

$$c_{v_{\text{H}_2\text{O}}} = c_{p_{\text{H}_2\text{O}}} - 0.4614 \tag{20}$$

3.3 Gas Turbines. For the expansion ratio, r_e temperature at the exit of the turbine isentropic process can be calculated by

$$T_{g_{os}} = T_{g_i}(r_e)^{(\gamma_g - 1)/\gamma_g} \tag{21}$$

The actual temperature T_{g_o} at the exit of the turbine can be calculated by

$$\eta_T = \frac{T_{g_i} - T_{g_o}}{T_{g_i} - T_{g_{os}}} \tag{22}$$

The inlet and outlet humidity ratios will be the same,

$$\omega_{g_i} = \omega_{g_o} \tag{23}$$

The energy balance yields the turbine work W_T and the exergy balance for the turbine gives the exergy destruction $e_{D,T}$ as

$$W_T = h_{g_i} - h_{g_o} \tag{24}$$

$$e_{D,T} = (e_{g_i} - e_{g_o}) - W_T \tag{25}$$

3.4 Heat Exchanger. Temperature of air (T_{a_o}) at the exit of a heat exchanger can be calculated by

$$\epsilon_{\text{HE}} = \frac{T_{a_o} - T_{a_i}}{T_{g_i} - T_{a_i}} \tag{26}$$

Assume that the air- and gas-side pressure drop, both are 2%, so that

$$p_{a_o} = 0.98 p_{a_i} \tag{27}$$

$$p_{g_o} = 0.98 p_{g_i} \tag{28}$$

The inlet and outlet humidity ratios will be the same for both air and gas so that

$$\omega_{a_i} = \omega_{a_o} \tag{29}$$

$$\omega_{g_i} = \omega_{g_o} \tag{30}$$

Applying the energy balance equation on the heat exchanger yields

$$h_{a_o} - h_{a_i} = h_{g_o} - h_{g_i} \tag{31}$$

The exergy balance of the heat exchanger yields exergy destruction

$$e_{D,\text{HE}} = (e_{a_i} - e_{a_o}) + (e_{g_i} - e_{g_o}) \tag{32}$$

3.5 Combustor. Mass of fuel supplied can be calculated by energy balance

$$H_f = \eta_{\text{CC}} m_{f_{\text{CC}}} \Delta H_r = h_{g_o} - h_{g_i} \tag{33}$$

The exergy balance of the combustion chamber yields exergy destruction.

$$e_{D,\text{CC}} = m_{f_{\text{CC}}} e_{f_{\text{CC}}} + e_{a_i} - e_{g_o} \tag{34}$$

$$e_{f_{\text{CC}}} = \Delta g_r + R_f T_a \ln \frac{p_f}{p_a} \tag{35}$$

$$\Delta g_r = \Delta H_r - T_{av}(s_P - s_R) \tag{36}$$

where $(s_P - s_R)$ is the entropy change during the combustion process and is given as [12]

$$s_P - s_R = x_a \left[c_{p_a} \ln \frac{T_{g_o}}{T_{a_i}} - R_a \ln \frac{p_{g_o}}{p_{a_i}} \right] + x_v \left[c_{p_v} \ln \frac{T_{g_o}}{T_{a_i}} - R_v \ln \frac{p_{g_o}}{p_{a_i}} \right] \tag{37}$$

where

$$x_a = \frac{1}{1 + \tilde{\omega}} \tag{38}$$

and

$$x_v = \frac{\tilde{\omega}}{1 + \tilde{\omega}} \tag{39}$$

Neglecting the effect of water vapor present in fuel, the inlet and outlet humidity ratios will be the same,

$$\omega_{a_i} = \omega_{g_o} \tag{40}$$

3.6 Heat Recovery Steam Generator. The amount of process heat produced is given by

$$q_p = h_{g_i} - h_{g_o} \tag{41}$$

The temperature of gas at the exit of HRSG can be calculated by [15]

$$T_{g_o} = (T_P + pp) - \frac{[T_{g_i} - (T_P + pp)](h_f - h_c)}{(h_g - h_f)} \tag{42}$$

assuming saturated feed water enters HRSG and saturated steam leaves the same at 1 MPa.

The inlet and outlet humidity ratios will be the same so that

$$\omega_{g_i} = \omega_{g_o} \tag{43}$$

Mass of water can be calculated by the energy balance equation as

$$h_{g_i} - h_{g_o} = m_w (h_{w_o} - h_{w_i}) \tag{44}$$

Exergy destroyed in HRSG can be calculated by

$$e_{D,\text{HRSG}} = (e_{g_i} - e_{g_o}) - m_w (e_{w_o} - e_{w_i}) \tag{45}$$

4 Performance Parameter

The relevant parameters required for the combined first- and second-law analysis of gas turbine cogeneration system with inlet air cooling and evaporative aftercooling of the compressor discharge may be considered as follows.

4.1 First-Law Efficiency (η_{I}). The ratio of all the useful energy extracted from the system (electricity and process heat) to the energy of fuel input is known as the first-law efficiency. By definition,

$$\eta_{\text{I}} = \frac{W_{el} + q_p}{H_f} \tag{46}$$

where W_{el} is the electrical power output and is given by

$$W_{el} = \eta_{\text{gen}} W_{\text{net}} \tag{47}$$

where

$$W_{\text{net}} = W_{\text{HPT}} + W_{\text{PT}} - W_{\text{LPC}} - W_{\text{HPC}} \tag{48}$$

4.2 Power-to-Heat Ratio (R_{PH}). The cost effectiveness of any cogeneration system is directly related to the amount of power it can produce for a given amount of process heat added. Hence, another parameter used to assess the thermodynamic performance of a cogeneration system is R_{PH} which is defined as

$$R_{\text{PH}} = \frac{W_{el}}{q_p} \tag{49}$$

In both the first-law efficiency and power-to-heat ratio, power and heat are treated as equal. This reflects the first law of thermodynamics, which is concerned with quantity, not energy quality. Thus η_{I} and R_{PH} are also known as first-law efficiencies.

4.3 Second-Law Efficiency (η_{II}). Since exergy is more valuable than energy according to the second law of thermodynamics, it is useful to consider both output and input in terms of exergy [16]. The amount of exergy supplied in the product to the amount of exergy associated with the fuel is a more accurate measure of the thermodynamic performance of a system which is defined as

$$\eta_{\text{II}} = \frac{W_{el} + e_P}{e_f} \tag{50}$$

where

$$e_f = e_{f_{\text{CC}}} + e_{f_{\text{reh}}} \tag{51}$$

5 Results and Discussion

In this paper, the effects of pressure ratio across the compressor r_P, turbine inlet temperature (TIT), and the ambient relative hu-

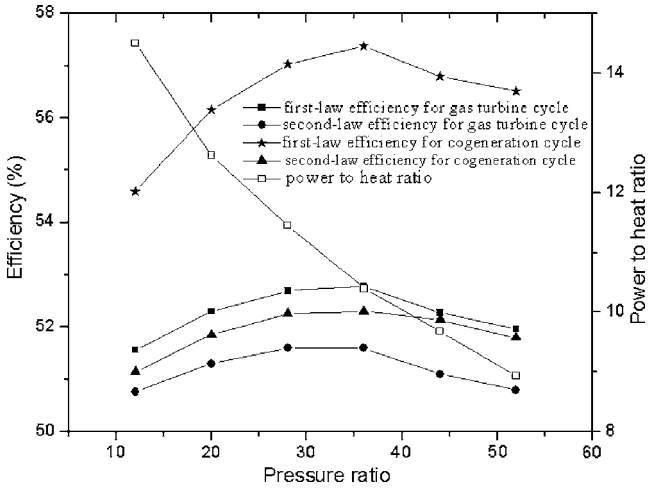

Fig. 2 Effect of variation of pressure ratio on η_I, η_{II}, and R_{PH}

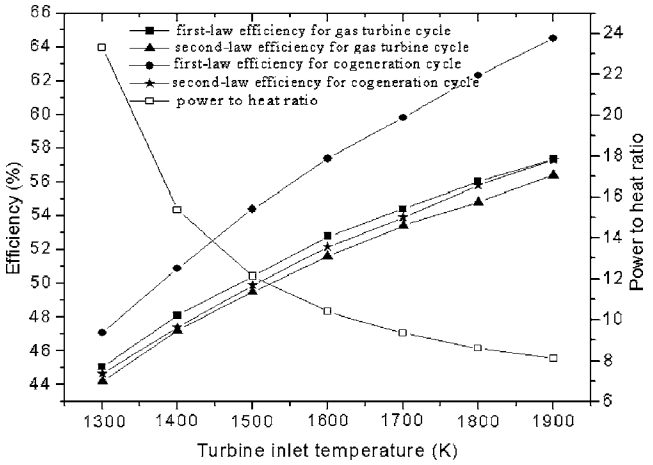

Fig. 3 Effect of variation of turbine inlet temperature on η_I, η_{II}, and R_{PH}

midity φ on the first-law efficiency and power-to-heat ratio R_{PH} is obtained by the energy-balance approach or the first-law analysis of the cycle. However, the exergy destruction or thermodynamic losses in each component and the second-law efficiency of the cycle has also been investigated under the exergy-balance approach or the second-law analysis of the cycle. To examine the effect of these operating variables on the performance parameters of the system, operating under different conditions, the following common characteristics were chosen: The relative humidity at the air humidifiers' outlet and the evaporative cooler is 100%; the pressure drop for air in the humidifiers is negligible; the pressure drop for air in the air intercooler is 1%; the pressure drop for air in the air cooler (AC1) is 1%; the pressure drop for gas in the water heater (WH) is 1%; the pressure drop for air in the air evaporative cooler (AC) is 2%; the pressure drop for air in the regenerative heat exchanger (HE) is 2%; the pressure drop for gas in the regenerative heat exchanger is 2%; the pressure drop in the combustion chamber and reheater is 4%; the effectiveness of the air cooler (AC1) is 85%; the effectiveness of the air intercooler is 90%; the effectiveness of the regenerative heat exchanger is 85%; the compressor isentropic efficiency η_C is 87%; the turbine isentropic efficiency η_T is 89%; efficiency of the combustion chamber and reheater (η_{CC} and η_{reh}) is 95%; generator efficiency (η_{gen}) is 97%; pinch point (pp) is 25°C; the temperature of condensate return is 100°C; process heat pressure is 1 MPa; the fuel is methane gas, which has a lower heating value of 50,016 kJ/kg; and the ambient pressure and temperature are, respectively, 1 bar and 298 K [4,5,8,17].

Figure 2 shows the variation of power-to-heat ratio R_{PH}, first-law efficiency, and second-law efficiency for the advanced cogeneration cycle with a compressor pressure ratio for TIT=1600 K and φ=60%. As the pressure ratio r_p increases the compressor work increases, raising the temperature at the compressor outlet. Increase in pressure ratio also increases the turbine work and the net work output of the cycle. Therefore, as r_p increases the air temperature at the inlet of HE decreases, that reduces the capacity of HE. Hence, the gas temperature at the exit of HE increases. As a result, the energy available to generate the process heat increases. Hence as r_p increases the power-to-heat ratio decreases, because at much higher pressure ratio the process heat increases significantly. As the pressure ratio increases, the air temperature at the inlet of the combustion chamber decreases due to decrease in capacity of the HE, which results in increasing the heat added to the cycle. The ratio of net work output to the heat added represents the first-law efficiency of the cycle. Hence, as r_p increases, the first-law efficiency of the cycle increases to its maximum value at r_p=36. Further increase in r_p reduces the first-law efficiency significantly because, at much higher pressure ratios, the heat added to the cycle increases as shown in Fig. 2. It also shows the variation of second-law efficiency, which is a more accurate measure of thermodynamic performance. Since the quality of fuel (i.e., exergy associated with the heat addition) is more than the heating value or energy of fuel because the exergy of fuel would increase while bringing it from the ambient pressure to combustion pressure at ambient temperature. Hence, exergy associated with the heat addition will be equal to exergy associated with the heating value of fuel plus exergy increase, i.e., mechanical exergy due to increase of pressure of fuel from the ambient to combustion state. Therefore, the second-law efficiency of the cycle is slightly lower than the first-law efficiency. The difference between the second-law efficiency for cogeneration and the gas turbine cycle is less as compared to the difference between the first-law efficiency of both the cycles because the exergy associated with process heat will be less than the energy of process heat as shown in Fig. 2.

Figure 3 shows the variation of the first-law efficiency, the second-law efficiency, and the power-to-heat ratio with the change in turbine inlet temperature for r_p=36 and φ=60%. For a given pressure ratio and ambient relative humidity, the first-law and second-law efficiencies increase with the higher TIT significantly because in a given cycle, due to evaporative aftercooling as the warm water coming out from water heater evaporates after coming in contact with air, the air temperature inlet to the heat exchanger decreases. This will enhance the heat transfer rate by absorbing greater heat from turbine exhaust in the heat exchanger, and hence the temperature of air inlet to the combustion chamber would increase, which in turn would increase the mean temperature of heat addition that leads to reduction of the magnitude of heat addition in the cycle. Therefore, cycle efficiency increases with an increase in TIT. But the power-to-heat ratio decreases appreciably because the increase in generation of process heat is greater than the electric power output at higher TIT as shown in Fig. 3.

Figure 4 shows the variation of the first-law efficiency, the second-law efficiency, and the power-to-heat ratio with the change in ambient relative humidity for TIT=1600 K and r_p=36. The increase in ambient relative humidity results in increasing the compressor inlet air temperature, which increases the mean temperature of heat addition slightly but increases the mass of fuel per kilogram of dry air significantly, which results in a larger amount of heat addition to the cycle. Therefore, the first-law efficiency of the cycle decreases initially with the increase in relative humidity. For further increase in relative humidity (40–80 %), there is sharp increase in the work output for a given heat input. Hence, the

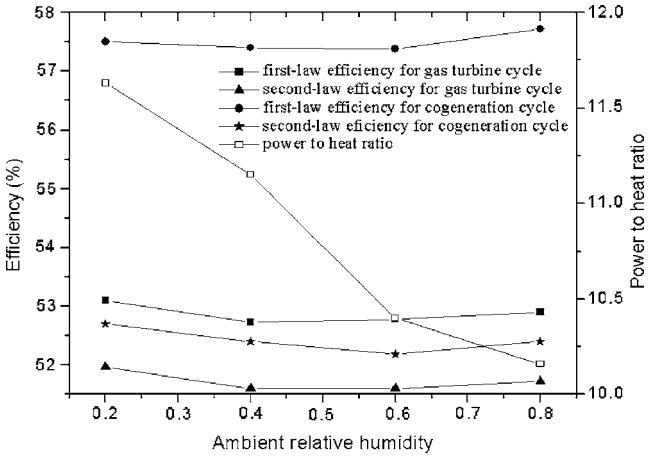

Fig. 4 Effect of variation of ambient relative humidity on η_I, η_{II} and R_{PH}

first-law efficiency starts increasing at higher ambient relative humidity as shown in Fig. 4. As the ambient relative humidity φ increases, the wet bulb temperature increases, which results in an increase of the inlet temperature to the compressor and HE due to reduction in the effect of evaporative cooling and also the mass flow increases; hence, the compressor work and heat produced in HRSG increase. Enthalpy change per kilogram of dry air across the turbine increases due to increase in specific humidity of the working fluid, which results in the increase of turbine work. The net effect is to decrease the R_{PH} as shown in Fig. 4. The second-law efficiency of the cycle also decreases initially with increase in ambient relative humidity. Further increase in ambient relative humidity results in increasing the second-law efficiency. This is because at higher ambient relative humidity the work output of the cycle is much higher, which gives 100% contribution to exergy. Hence, the second-law efficiency of the cycle is higher at higher relative humidity as shown in Fig. 4.

Table 1 shows the variation of the magnitude of exergy destruction in each component of the plant with the change in overall pressure ratio for TIT=1600 K and φ=60%. It is found that the exergy destruction in the combustion process dominates the exergy destruction picture, as expected; it represents over 60% of the total exergy destruction in the overall system. The exergy destruction in the regenerative heat exchanger comes next. As the pressure ratio increases, the exergy destruction in the combustion chamber and reheater increases significantly. This is because the increase in pressure ratio implies higher combustion pressure, which leads to larger destruction as it is seen from Eqs. (34) and (35). As the pressure ratio increases the temperature at the inlet of the intercooler increases. Thus, the temperature gradient for heat transfer in it increases with higher pressure ratio. This explains more exergy destruction in the intercooler for higher pressure ratio. On the other hand, the exergy destruction in the regenerative heat exchanger decreases as the pressure ratio increases. This is because the higher pressure ratio results in the lower power turbine exit temperature as well as higher temperature at the inlet of the HRSG as explained earlier. As a result, the exergy destruction in the HRSG increases with higher pressure ratio. As the pressure ratio increases, the exergy destruction in WH decreases because the gas temperature at the exit of the HRSG decreases for a given pinch point temperature. At a given TIT, as the pressure ratio increases the exergy destruction in the compressor and turbine increases. The exergy destructions in air humidifiers and air cooler are constant because at all pressure ratios it has been used for the same working condition. The exergy destruction in the evaporative aftercooler increases as pressure ratio increases.

Table 2 shows the variation of the magnitude of exergy destruction in each component of the plant with the change in turbine inlet temperature for r_p=36 and φ=60%. As the TIT increases, the exergy destruction in the regenerative heat exchanger increases because the temperature gradient for heat transfer in it increases with higher TIT. The exergy destruction in the combustion chamber and reheater also increases because the logarithmic mean combustion temperature for the whole cycle increases. The exergy destruction in the HRSG increases because the temperature difference between the two heat exchanging fluids (flue gas and water/steam) increases, and for the given pressure ratio of the cycle, more steam is generated by the HRSG with the higher TIT, which produces larger process heat. With increase in TIT the exergy destruction in WH decreases as the gas temperature at the exit of the HRSG decreases for a given pinch point temperature. The exergy destructions in air humidifiers, air cooler, evaporative

Table 1 Effect of variation of pressure ratio on exergy destruction in different components of the cycle for TIT=1600 K, φ=60%, p_{atm}=1 bar, T_{atm}=298 K

r_p	$e_{D,AH1}$ (kJ/kg da)	$e_{D,AC1}$ (kJ/kg da)	$e_{D,LPC}$ (kJ/kg da)	$e_{D,AH2}$ (kJ/kg da)	$e_{D,I}$ (kJ/kg da)	$e_{D,HPC}$ (kJ/kg da)	$e_{D,AC}$ (kJ/kg da)	$e_{D,WH}$ (kJ/kg da)	$e_{D,HE}$ (kJ/kg da)	$e_{D,CC}$ (kJ/kg da)	$e_{D,HPT}$ (kJ/kg da)	$e_{D,reh}$ (kJ/kg da)	$e_{D,PT}$ (kJ/kg da)	$e_{D,HRSG}$ (kJ/kg da)
12	0.1114	1.771	12.82	0.1114	5.24	10.7	12.35	6.38	66.08	164.06	22.74	118.44	21.94	10.01
20	0.1114	1.771	14.5	0.1114	7.22	12.26	16.52	5.92	56.07	192.96	26.85	149.21	25.99	12.94
28	0.1114	1.771	13.7	0.1114	8.83	13.14	19.51	5.69	49.61	209.98	30.62	168.99	29.73	14.04
36	0.1114	1.771	15.3	0.1114	9.95	13.82	22.2	4.93	43.34	224.45	33.43	183.7	32.58	16.27
44	0.1114	1.771	15.8	0.1114	11.00	14.41	24.1	3.85	38.9	239.1	35.85	193.8	35.08	21.25
52	0.1114	1.771	16.4	0.1114	11.83	14.82	25.74	2.34	34.2	247.23	41.1	200.8	36.95	20.26

Table 2 Effect of variation of turbine inlet temperature on exergy destruction in different components of the cycle for r_p=36, φ=60%, p_{atm}=1 bar, T_{atm}=298 K

TIT (K)	$e_{D,AH1}$ (kJ/kg da)	$e_{D,AC1}$ (kJ/kg da)	$e_{D,LPC}$ (kJ/kg da)	$e_{D,AH2}$ (kJ/kg da)	$e_{D,I}$ (kJ/kg da)	$e_{D,HPC}$ (kJ/kg da)	$e_{D,AC}$ (kJ/kg da)	$e_{D,WH}$ (kJ/kg da)	$e_{D,HE}$ (kJ/kg da)	$e_{D,CC}$ (kJ/kg da)	$e_{D,HPT}$ (kJ/kg da)	$e_{D,reh}$ (kJ/kg da)	$e_{D,PT}$ (kJ/kg da)	$e_{D,HRSG}$ (kJ/kg da)
1300	0.1114	1.771	15.3	0.1114	9.95	13.82	22.2	6.14	29.17	205.7	33.45	173.3	32.69	6.09
1400	0.1114	1.771	15.3	0.1114	9.95	13.82	22.2	5.75	34.46	215.5	33.55	176.74	32.7	9.37
1500	0.1114	1.771	15.3	0.1114	9.95	13.82	22.2	5.3	39.88	220.03	33.47	180.2	32.63	12.74
1600	0.1114	1.771	15.3	0.1114	9.95	13.82	22.2	4.93	45.34	224.45	33.43	183.7	32.58	16.27
1700	0.1114	1.771	15.3	0.1114	9.95	13.82	22.2	4.57	50.83	234.00	33.43	187.4	32.6	19.9
1800	0.1114	1.771	15.3	0.1114	9.95	13.82	22.2	4.15	56.3	238.4	33.46	188.0	32.4	23.6
1900	0.1114	1.771	15.3	0.1114	9.95	13.82	22.2	3.75	61.83	242.6	33.26	189.14	32.4	27.4

Table 3 Effect of variation of ambient relative humidity on exergy destruction in different components of the cycle for r_p=36, TIT=1600 K, p_{atm}=1 bar, T_{atm}=298 K

φ (%)	$e_{D,AH1}$ (kJ/kg da)	$e_{D,AC1}$ (kJ/kg da)	$e_{D,LPC}$ (kJ/kg da)	$e_{D,AH2}$ (kJ/kg da)	$e_{D,I}$ (kJ/kg da)	$e_{D,HPC}$ (kJ/kg da)	$e_{D,AC}$ (kJ/kg da)	$e_{D,WH}$ (kJ/kg da)	$e_{D,HE}$ (kJ/kg da)	$e_{D,CC}$ (kJ/kg da)	$e_{D,HPT}$ (kJ/kg da)	$e_{D,reh}$ (kJ/kg da)	$e_{D,PT}$ (kJ/kg da)	$e_{D,HRSG}$ (kJ/kg da)
0.2	0.58	1.8	14.8	0.58	8.79	13.3	22.2	12.3	47.47	219.5	33.21	177.99	32.35	12.35
0.4	0.29	1.78	15.1	0.29	9.96	13.55	22.6	5.02	45.52	224.5	33.34	178.3	32.51	15.15
0.6	0.1114	1.771	15.3	0.1114	9.95	13.82	22.2	4.93	45.34	224.5	33.43	183.7	32.58	16.27
0.8	0.021	1.77	12.43	0.021	9.9	14.14	21.6	4.92	45.43	229.4	33.57	184.1	32.81	17.05

cooler, intercooler, compressors, and turbines are also shown in Table 2 and are constant. Again, the combustion chamber and reheater are found to be a major source of irreversibility.

Table 3 shows the variation of the magnitude of exergy destruction in each component of the plant with the change in ambient relative humidity φ for TIT=1600 K and r_p=36. It is shown that the exergy destructions in all components of the plant are more or less independent of change in ambient relative humidity.

6 Conclusion

It is observed that the exergy destruction in each component of the cycle is significantly affected by the overall pressure ratio and turbine inlet temperature and not at all affected by the ambient relative humidity. The maximum exergy is destroyed during the combustion process, which represents over 60% of the total exergy destruction in the overall system. The next-largest exergy destruction occurs in the regenerator, turbine, compressor, evaporative aftercooler, intercooler, and then in the inlet air cooler. The first-law efficiency, power-to-heat ratio, and second-law efficiency of the cycle are significantly influenced by the overall pressure ratio and TIT, and small variations were observed in these parameters with the change in ambient relative humidity.

It may further be reported as the following:

1. The exergy destruction in the combustion chamber and reheater increases significantly, while in the heat recovery steam generator (HRSG), it increases slightly with the increase in pressure ratio. But the exergy destruction in the regenerative heat exchanger decreases as pressure ratio increases.
2. The exergy destruction in the regenerative heat exchanger, combustion chamber, reheater, and HRSG increases with the increase in TIT but the exergy destructions in the air humidifier, air cooler, air evaporative cooler, intercooler, compressors, and turbines seem to be constant for all TITs.
3. The exergy destructions in all components except the HRSG, water heater, and air humidifier are seen to be approximately independent of change in ambient relative humidity for a given pressure ratio and TIT.
4. The second-law efficiency increases sharply up to the pressure ratio (r_p=36), and a further increase in pressure ratio causes reduction in the second-law efficiency. Therefore, the optimum pressure ratio for a given cogeneration system corresponds to the maximum second-law efficiency found to be 36.
5. The second-law efficiency of the cogeneration system decreases initially with the increase in ambient relative humidity for the value φ=20–60% and further increase in ambient relative humidity causes increase in the second-law efficiency. Therefore, the ambient relative humidity corresponds to the minimum second-law efficiency found to be 60%.

Consequently, the values of second-law analysis can be used to identify the less efficient components of the system and also to modify them. Moreover, the suitability of the selected components can be judged by this analysis.

7 Recommendations for Future Work

Combined first- and second-law analysis can also be applied to all the energy conversion processes with thermal phenomena and all systems operating with thermal phenomena. Further work in this direction can be undertaken as follows:

1. Combined first- and second-law analysis of an indirect-fired gas turbine cogeneration system can be carried out because it has been recognized as a promising concept for energy conservation by permitting the use of coal or other low-cost fuel; significant savings of gas and oil could be realized once this technology is fully developed.
2. The worldwide demand for combined cycle power plants has increased over the last decade, especially the IGCC plant in which coal is gasified completely and the synthetic gas produced is used as fuel for the gas turbine in an integrated gasification combined cycle (IGCC). Therefore, the combined first- and second-law analysis for IGCC plants with inlet air cooling and evaporative aftercooling of the compressor discharge can be carried out to observe the complete thermodynamic view of IGCC plants.

Nomenclature

$\dot{E}$ = exergy rate (kJ/s)
H_f = heat supplied by fuel (kJ/kg (da))
ΔH_r = heat of reaction of fuel (kJ/kg of fuel)
pp = pinch point temperature
R = gas constant (kJ/kg K)
T = absolute temperature (K)
T_P = process heat temperature (°C)
W = work (kJ/kg (da))
c_p = specific heat at constant pressure (kJ/kg K)
c_v = specific heat at constant pressure (kJ/kg K)
e = specific exergy (kJ/kg (da))
e_P = specific exergy associated with process heat (kJ/kg (da))
Δg_r = Gibbs function of fuel (kJ/kg)
h = enthalpy (kJ/kg (da))
h_c = enthalpy of condensate return (kJ/kg)
h_f = enthalpy of saturated water at process steam pressure (kJ/kg)
h_g = enthalpy of saturated vapor at process steam pressure (kJ/kg)
m = mass (kg)
p = pressure (bar)
q_P = process heat (kJ/kg (da))
r_e = expansion ratio
r_p = pressure ratio
s = entropy (kJ/kg K)
t = temperature (°C)
v = specific volume (m^3/kg)

Greek Symbols

ω = humidity ratio (kilogram of water vapor per kilogram of dry air)

φ = relative humidity (%)
ϵ = effectiveness (%)
η = efficiency (%)
γ = specific heat ratio

Subscripts

AC = air evaporative cooler
AC1 = air cooler 1
AH1 = air humidifier 1
AH2 = air humidifier 2
C = compressor
CC = combustion chamber
D = destruction
HE = heat exchanger
HPC = high-pressure compressor
HPT = high-pressure turbine
I = intercooler
LPC = low-pressure compressor
P = product
PT = power turbine
Q = heat
R = reactant
W = work
WH = water heater
a = ambient air
av = average
f = fuel
g = gas
gen = generator
i = inlet
l = liquid
o = outlet
reh = reheater
sat = saturated
v = water vapor
w = water
1,2,3,…,16 = state points in the cycle

References

[1] De Lucia, M., Lanfranchi, C., and Boggio, V., 1995, "Benefits of Compressor Inlet Air Cooling for Gas Turbine Cogeneration Plants," *Proc. International Gas Turbine and Aeroengine Congress and Exposition*, Houston, June 5–8, ASME, New York, 9 pp.

[2] Bartolini, C. M., and Salvi, D., 1997, "Performance Assessment of Steam Injection Gas Turbine With Inlet Air Cooling," *Proc. International Gas Turbine and Aeroengine Congress and Exposition*, Orlando, FL, June 2–5, ASME, New York.

[3] Najjar, Y. S., and Zaamout, M. S., 1996, "Enhancing Gas-Turbine Engine Performance by means of Evaporative Regenerative Cycle," J. Inst. Energy, **69**, pp. 2–8.

[4] Bassily, A. M., 2001, "Performance Improvements of the Intercooled Reheat Regenerative Gas Turbine Cycles Using Indirect Evaporative Cooling of the Inlet Air and Evaporative Cooling of the Compressor Discharge," Proc. Inst. Mech. Eng., Part A, **215**, pp. 545–557.

[5] Khaliq, A., and Choudhary, K., 2006, "Thermodynamic Performance Assessment of an Indirect Intercooled Reheat Regenerative Gas Turbine Cycle With Inlet Air Cooling and Evaporative Aftercooling of the Compressor Discharge," Int. J. Energy Res., **30**, pp. 1295–1312.

[6] Huang, Y. C., Hung, C. I., and Chen, C. K., 2000, "Exergy Analysis for a Combined System of Steam Injected Gas Turbine Cogeneration and Multiple-Effect Evaporation," Proc. Inst. Mech. Eng., Part A, **214**, pp. 61–73.

[7] Tuma, M., Oman, J., and Sekavenik, M., 1999, "Efficiency of a Combined Gas-Steam Process," Energy Convers. Manage., **40**, pp. 1163–1175.

[8] Khaliq, A., and Kaushik, S. C., 2004, "Thermodynamic Performance Evaluation of Combustion Gas Turbine Cogeneration System With Reheat," Appl. Therm. Eng., **24**, pp. 1785–1795.

[9] Khaliq, A., and Khan, T. A., 2007, "Energetic and Exergetic Analysis of an Indirect Fired Air-Turbine Combined Heat and Power System," Int. J. Exergy, **4**, No. (1), pp. 38–53.

[10] Rosen, M. A., 1999, "Second Law Analysis: Approach and Implications," Int. J. Energy Res., **23**, No. (5), pp. 415–429.

[11] Moran, M. J., and Sciubba, E., 1994, "Exergy Analysis: Principles and Practice," ASME J. Eng. Gas Turbines Power, **116**, pp. 285–290.

[12] Bejan, A., 1997, *Advanced Engineering Thermodynamics*, Wiley, New York.

[13] Cohen, H., Rogers, G. F. C., and Soravanamutto, H. I. H., 1987, *Gas Turbine Theory*, Longman, London.

[14] Moran, M., and Shapiro, H., 2004, *Fundamentals of Engineering Thermodynamics*, Wiley, New York.

[15] Huang, F. F., and Wang, Ling, 1987, "Thermodynamic Study of an Indirect Fired Air Turbine Cogeneration System With Reheat," ASME J. Eng. Gas Turbines Power, **109**, pp. 16–21.

[16] Bejan, A., 2002, "Fundamentals of Exergy Analysis, Entropy Generation Minimization, and the Generation of Flow Architecture," Int. J. Energy Res., **26**, pp. 545–565.

[17] Radcenco, V., Vergas, J. V. C., and Bejan, A., 1998, "Thermodynamic Optimization of a Gas Turbine Power Plant With Pressure Drop Irreversibilities," ASME J. Energy Resour. Technol., **120**, No. (3), pp. 233–240.

Mario L. Ferrari
Thermochemical Power Group (TPG)-DiMSET,
Università di Genova,
Genova, Italy
e-mail: mario.ferrari@unige.it

Eric Liese
e-mail: eric.liese@netl.doe.gov

David Tucker
e-mail: david.tucker@netl.doe.gov

Larry Lawson
e-mail: larry.lawson@netl.doe.gov

National Energy Technology Laboratory,
U.S. Department of Energy,
Morgantown, WV

Alberto Traverso
e-mail: alberto.traverso@unige.it

Aristide F. Massardo
e-mail: massardo@unige.it

Thermochemical Power Group (TPG)-DiMSET,
Università di Genova,
Genova, Italy

Transient Modeling of the NETL Hybrid Fuel Cell/Gas Turbine Facility and Experimental Validation

This paper describes the experimental validation of two different transient models of the hybrid fuel cell/gas turbine facility of the U.S. DOE-NETL at Morgantown. The first part of this work is devoted to the description of the facility, designed to experimentally investigate these plants with real components, except the fuel cell. The behavior of the SOFC is obtained with apt volumes (for the stack and the off-gas burner) and using a combustor to generate similar thermal effects. The second part of this paper shows the facility real-time transient model developed at the U.S. DOE-NETL and the detailed transient modeling activity using the TRANSEO program developed at TPG. The results obtained with both models are successfully compared with the experimental data of two different load step decreases. The more detailed model agrees more closely with the experimental data, which, of course, is more time consuming than the real-time model (the detailed model operates with a calculation over calculated time ratio around 6). Finally, the TPG model has been used to discuss the importance of performance map precision for both compressor and turbine. This is an important analysis to better understand the steady-state difference between the two models. [DOI: 10.1115/1.2747265]

Introduction

Hybrid systems based on the coupling of high temperature fuel cells with micro gas turbines are considered promising energy systems for the future, especially for stationary applications. Common high temperature fuel cell technologies are two: MCFC [1–3] and SOFC [4–6]. This paper deals with SOFC hybrid systems. The SOFC hybrid technology can reach a very high efficiency level, even in small size plants, given a high average operative temperature (around 1000°C) inside the stack. Furthermore, hybrid systems will have ultra low emissions [7–9] and exhausted gases at a high temperature condition, useful for co-generative applications [10]. Another important feature regards noise pollution. Since the fuel cell itself does not have moving parts, the noise level is very low, coming only from the micro turbine usually equipped with a noise reduction case, already available for commercial machines [11].

Even though these systems have already been studied in previous works [10,12] both at on-design and off-design conditions, a transient analysis is mandatory before a wide commercialization. A transient simulation is useful [13] for choosing the control strategy to avoid malfunctions or damages during rapid load variations [12], such as:

- an excessive temperature or temperature gradient in the fuel cell;
- too high a pressure difference between the cathodic and the anodic sides;
- too low a steam-to-carbon-ratio value in the reformer;
- too high a microturbine rotational speed;
- an operating condition too close to the compressor surge line (surge margin);
- excessive thermal stress in the heat exchanger and the cell.

To support the first transient theoretical analysis [13–15] of the SOFC/mGT systems, the Office of Research and Development at the National Energy Technology Laboratory (NETL) commissioned the Hybrid Performance Project (Hyper) facility to examine, from the experimental point of view, issues related to component integration and control system development. This is a physical simulator of a Direct Fired Fuel Cell Gas Turbine Hybrid System (Fig. 1) with turbomachinery, a recuperator, and two vessels used to generate the volume capacity effect of the stack and the postcombustor. This facility has been designed to simulate a 300 kW fuel cell with a turbine load up to about 100 kW. The thermal effect of the SOFC is simulated with a natural gas-fed combustor, controlled by a real-time fuel cell model [13]. This facility, available for public research collaborations with universities and industries, is very useful for the transient validation of the models used for the cathodic side (compressor, recuperator, volumes, pipes, and turbine) simulation. This paper shows the comparison of two MATLAB®-Simulink® transient models with experimental data of the Hyper facility. While the first model has been implemented at the NETL obtaining real-time performance [16], the second one has been implemented using the TRANSEO tool [17,18].

Facility Layout

The Hyper facility (Figs. 2 and 3) is a recuperated micro gas turbine connected to two vessels to simulate the volume capacitance of the stack and the postcombustor. As already reported in [19], the main flow coming from the two recuperators (E 300 and E 305) downstream of the compressor (C 100) goes through the

Submitted to ASME for publication in the JOURNAL OF ENGINEERING FOR GAS TURBINES AND POWER. Manuscript received December 14, 2006; final manuscript received March 28, 2007. Review conducted by Dilip R Ballal.

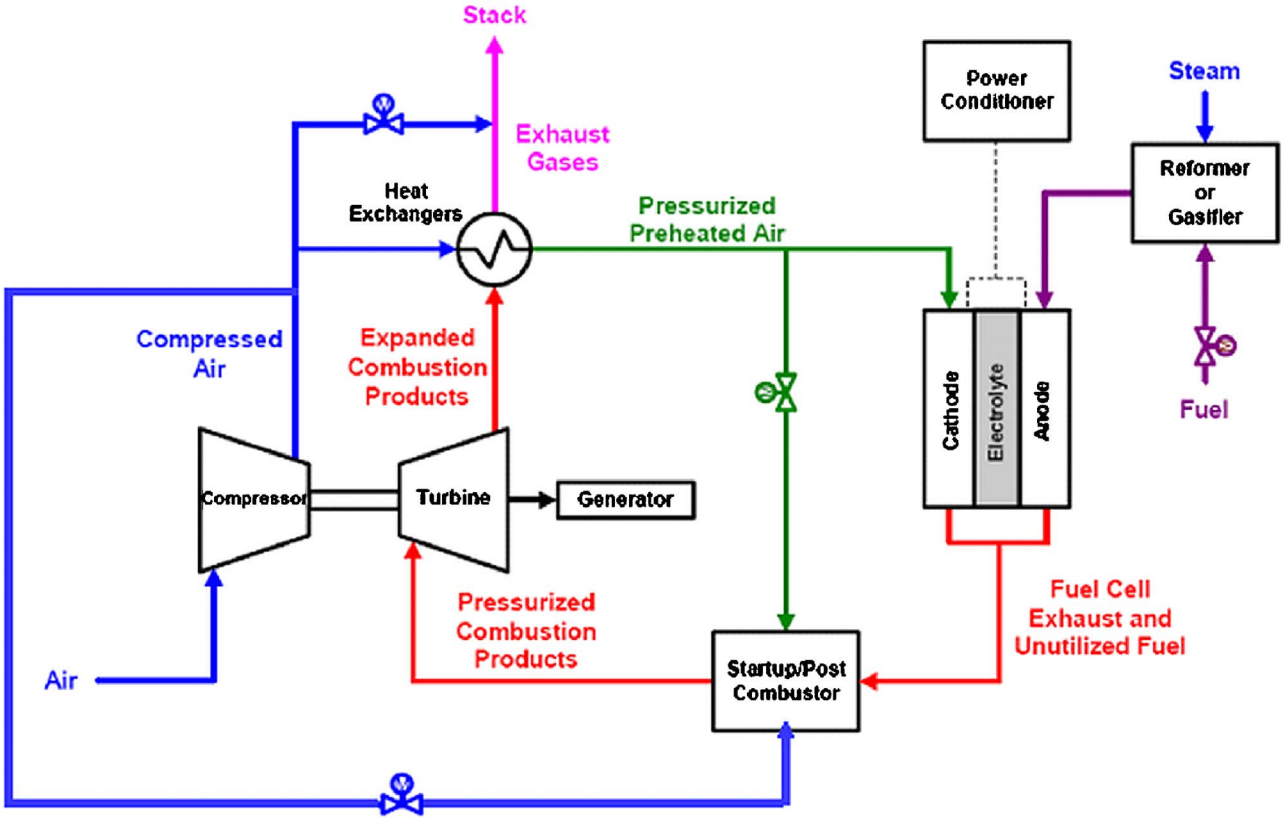

Fig. 1 Layout of a representative direct fuel cell/gas turbine hybrid system [20]

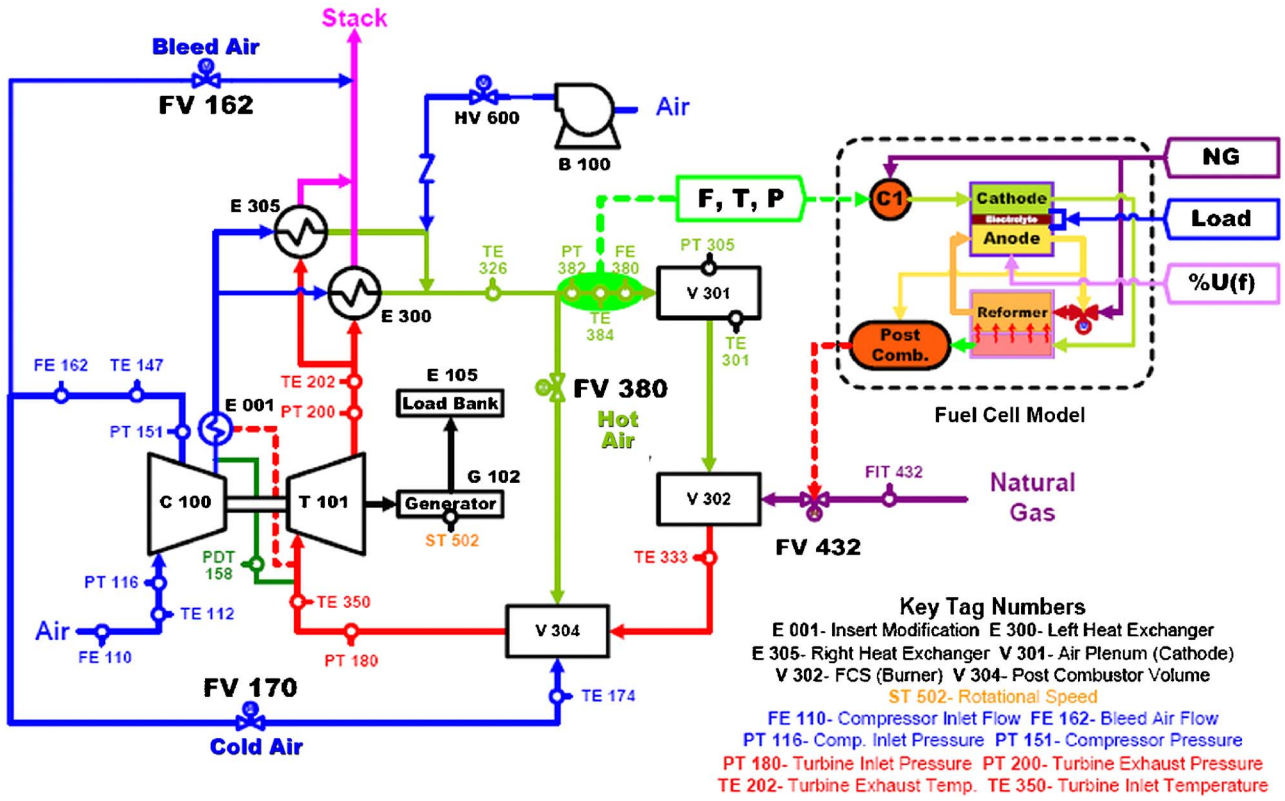

Fig. 2 Flow diagram of the Hyper facility at NETL [20]

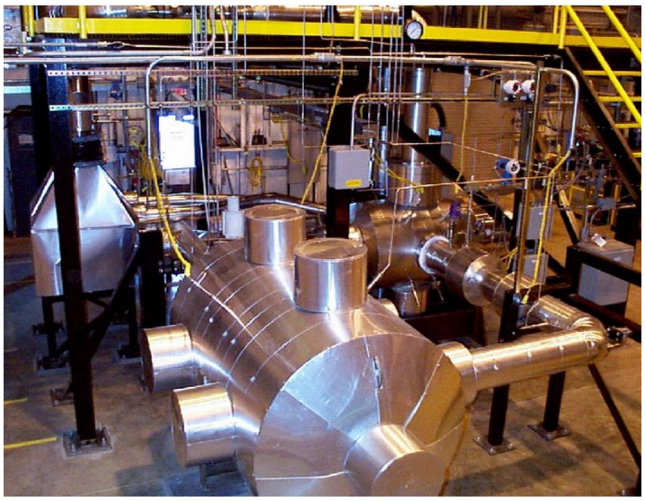

Fig. 3 Picture of the Hyper facility [16]

"Air Plenum" of 2 m^3 (V 301), necessary to simulate the stack cathode empty volume behavior. After this component the flow is fed to the combustor, called "Fuel Cell Simulator" (V 302), used to generate the same thermal effect of the cell and to sustain the machine. The combustor exhaust gases go through the "Post Combustor Volume" of 0.6 m^3 (V 304), necessary to simulate the volume capacitance of this component, and enters the turbine (T 101). The expanded gases are used in the hot side of the recuperators and driven to the outlet stack. Furthermore, Fig. 2 shows that the facility has been designed to work in parallel with a real-time SOFC model, equipped with reformer and postcombustor, used to calculate the fuel mass flow rate necessary to simulate with the combustor the real stack thermal behavior. However, in this paper the SOFC model is not used, but a PI controller regulates the fuel valve (FV 432) with the objective to maintain constant the machine rotational speed, because the aim of this work is not the analysis of the hybrid system problems, but the experimental validation of the transient models of the Hyper facility.

The facility is also equipped with three air bypass valves, FV 162, FV 170, and FV 380 (see Fig. 2). These valves provide flexibility for the start-up and for the operative conditions. The bleed valve (FV 162) is used to avoid surge conditions directly discharging to the outlet stack a part of the compressor flow. There is a cold air bypass valve (FV 170) downstream of the compressor, upstream of the heat exchangers, and a hot bypass valve (FV 380) downstream of the heat exchangers. These are used to divert flow around the fuel cell simulator volumes (V-301 and V-302).

Microturbine. The microturbine is a 120 kW Auxiliary Power Unit (APU) designed for aircraft, consisting of a single shaft direct coupled turbine (T 101), a radial compressor (C 100) and a gear driven electrical generator working at 400 Hz and loaded by an insulated resistor bank (E 105). The compressor is designed to work at a pressure ratio of about 4 delivering approximately 2 kg/s of air.

Turbine Insert Modification. The fuel system and the combustor of the original APU have been substituted with an insert modification (E 001) necessary to extract compressor air from the compressor discharge, without reducing the air flow required to cool the turbine scroll, and to route the hot gases from the fuel cell simulator to the turbine. The compressor air is driven around the turbine scroll and concentrically around the insert. It picks up heat from the turbine inlet gases, driven in the internal pipe of the modification, increasing its temperature of about 20 K at design point.

Heat Exchangers. The two counter flow heat exchangers (E 300 and E 305) are Solar Turbine Primary Surface Recuperators (PSR33) used in parallel to preheat the air going into the fuel cell pressure vessel (V 301). While the maximum operating temperature on the exhaust side is limited by restrictions on the turbine exhaust gas temperature to 910 K, the maximum operating temperature on the pressure side is limited to 780 K. The combined volume of the pressure sides and exhaust sides of the recuperators is 0.11 m^3 and 0.26 m^3, respectively.

Pressure Vessels. A first pressure vessel (V 301) is used to physically simulate the volume of the cathode and the air manifold of a 300 kW size SOFC. This is a stainless steel (AISI 304) vessel of 2 m^3 with the associated piping, designed to work at operative conditions up to 760 K. A second vessel of 0.6 m^3 (V 304) is used to emulate the behavior of the postcombustor downstream of the fuel cell. It has been built in Inconel (800HT) to support temperatures up to 1200 K at the operative conditions of 4 bar.

The Combustor. The combustor is a natural gas diffusion flame burner (V 302) used to simulate the thermal characteristics of the exhaust gases exiting the postcombustor of an SOFC system. It can be controlled to maintain constant the machine rotational speed, as performed in this work, or directly controlled by the real-time fuel cell model, as explained in other papers [19,20]. The volume of this combustor is 0.022 m^3.

Instrumentation. The test rig is equipped with sensors to acquire all the significant properties. Rotational speed is measured by an optical sensor (ST 502) which picks up laser light reflected from a rotating target on the end of the generator shaft. Pressures and temperatures are measured with apt sensors located upstream and downstream of the plant components: compressor inlet (PT 116, TE 112), compressor outlet (PT 151, TE 147), recuperator outlet (PT 382, TE 326), turbine inlet (PT 180, TE 350), turbine outlet (PT 200, TE 202), fuel cell vessel (PT 305, TE 301). There are other differential pressure sensors to measure with good accuracy the pressure losses of the most significant components [20]. The air mass flow rates are measured with annubar flow meters at the compressor inlet (FE 110), at the fuel cell vessel inlet (FE 380), and in the cold bypass line (FE 162). Another mass flow meter is used for the natural gas (FIT 432). Further details about the instrumentation performance of this test rig are reported in previous works [19,20].

Models

Both models of the Hyper facility have been developed in the MATLAB®-Simulink® environment to perform plant transient simulations. The first model has been developed by the NETL staff with the objective to reach real-time performance with sufficient fidelity of process evaluation [16]. The second one has been implemented using the TRANSEO tool [17], a software developed at TPG. Both models use the same blocks for the fuel valve and the controller, developed by Woodward Governor and the NETL staff [16].

The NETL Model. This model has been expressly developed to study the transient behavior of the Hyper facility with a simplified approach. All the components have been modeled with a lumped volume approach using global balance equations and empirical equations for losses [16] and for the recuperator effectiveness [21]. The rate of recuperator heat transfer is calculated through a ProTrax® equation (Eq. (1)) [16], chosen for its proven reliability and applicability.

$$q = \frac{e^x}{\left(\frac{e^x}{F_{\text{hot}} \cdot c_{p\_\text{hot}}} - \frac{1}{F_{\text{cold}} \cdot c_{p\_\text{cold}}}\right)} (T_{\text{hot},i} - T_{\text{cold},i}) \tag{1}$$

With x calculated through Eq. (2):

$$x = \mathrm{Nu} \cdot k_{\mathrm{bulk}} \cdot \frac{A_{\mathrm{HX}}}{\mathrm{gap}} \cdot \left(\frac{1}{F_{\mathrm{hot}} \cdot c_{p\_\mathrm{hot}}} - \frac{1}{F_{\mathrm{cold}} \cdot c_{p\_\mathrm{cold}}} \right) \quad (2)$$

A_{HX} has been derived from information provided by Solar Turbines and [21].

The general approach is based on flow calculating modules connected with pressure calculating modules, as completely explained in [16]. This structure assures correct pressure-flow solutions and keeps the model consistent.

Performance maps for the compressor and turbine were obtained from the manufacturer and used in the form of look up tables according to the Beta Line method as shown in Walsh and Fletcher [22]. Since the maps did not match experimental data exactly, the maps were scaled at zero load conditions to match experimental data. Presently, a simple scaling factor is applied to the rotational speed.

The TPG Model. The TPG model has been implemented using the TRANSEO tool, developed at the University of Genoa in previous works [17,18]. It is a Matlab®-based tool, organized in a library of components available through Simulink®, with about 30 modules and using mixtures of 27 different gases plus the water vapor. It has been developed for the off-design, transient and dynamic analyses of advanced energy systems based on microturbine technology. TRANSEO uses a standard interface between two subsequent components that is necessary to ensure the high flexibility in defining the cycle layout.

In this model the same lumped volume approach of the NETL model has been used for the compressor, the turbine, the combustor, and the volumes. Compressor and turbine are based on the interpolation of performance maps [23] obtained from the manufacturer and scaled on the basis of experimental tests. The recuperators have been modeled with a quasi 2D approach [17,24]. In the TPG model two "pipe" components have been introduced for the connecting pipes between the fuel cell volume and the combustor and to simulate the effects downstream of the postcombustor vessel. They introduce significant thermal losses typical of these zones (Eqs. (3)–(5)),

$$\frac{dT_{\mathrm{metal}}}{dt} = \frac{q_{\mathrm{metal}} - q_{\mathrm{loss}}}{M_{\mathrm{metal}} \cdot c_{\mathrm{metal}}} \quad (3)$$

$$q_{\mathrm{metal}} = A_{\mathrm{int}} \cdot h_{\mathrm{int}} \cdot (T_{\mathrm{av}} - T_{\mathrm{metal}}) \quad (4)$$

$$q_{\mathrm{loss}} = A_{\mathrm{ext}} \cdot h_{\mathrm{ext}} \cdot (T_{\mathrm{metal}} - T_{\mathrm{ext}}) \quad (5)$$

In order to model the compressor and turbine performance accurately, data from the experiments have been used to generate the turbomachinery maps. This is a reason that allows the TPG model to be more accurate than the NETL model (which scales maps provided by the manufacturer) in the range where data were acquired for the maps. The advantage for the NETL method is that a complete map is available prior to experimental testing.

In the TPG model, the coefficient values for the pressure losses and the heath exchanges have been assumed at on design conditions in accordance with the phenomenon analyzed. At off-design and transient conditions nothing has been manually tuned because these coefficients follow standard correlations [23].

Results

A comparison with the experimental data acquired with the Hyper facility is presented for both the NETL and TPG models. Starting from stationary conditions, two different power demand variations have been considered:

- 15 kW load step decrease
- 30 kW load step decrease

Both the tests reported in this work to validate the theoretical models have been carried out without bleed and hot bypass, maintaining the fractional opening of the cold bypass valve opened at 40%. Table 1 shows some data used for the transient calculations and the nominal percentage of compressor air considered for the leakage between the compressor and the turbine [16]. The system has been operated as a conventional constant speed machine, with extensive piping between compressor and turbine. The starting conditions considered in the following results are indicative for a 300 kW fuel cell hybrid system with 60 kW and 45 kW loads. For the transient behavior, it is important to point out that with the 2 m^3 plenum the energy stored in the cathode volume is an order of magnitude greater than that stored in the rotational equipment. This is a significant aspect for the shaft oscillation behavior.

Table 1 Data used in the simulations

Nominal rotational speed	40,500	rpm
Shaft mechanical inertia	0.027	kg m^2
Plenum mass: fuel cell	1310	kg
Plenum mass: postcombustor	1800	kg
Plenum volume: fuel-cell	2	m^3
Plenum volume: postcombustor	0.6	m^3
Recuperator nominal mass flow rate	1.0	kg/s
Cold bypass nominal mass flow rate	0.54	kg/s
Compressor/turbine leakage	10.5%	···

15 kW Load Step Decrease. The results reported here show the transient effects due to a 15 kW step decrease (from 60 to 45 kW) of the electrical power demand, performed at time zero of the graphics. In this test, the Atlas PI controller and the simulated controller implemented in both models have used a proportional gain of 0.001 and an integral one of 0.00075. The first important validation regards the rotational speed of the machine. Figure 4 shows that the calculated results of both models are in good agreement with the experimental data. It should be noticed that the TPG model developed with the TRANSEO tool generates closer dynamic and steady-state results probably because of its more detailed heat transfer approach, and because the compressor and turbine maps were generated from the experimental data for the range of conditions studied in this paper. Figure 5 shows that the fuel mass flow rate has similar results to the turbine speed as would be expected. Looking at the air flow rate, Fig. 6, the TPG model predicts the magnitude closer. Because the NETL fuel flow magnitude prediction matches very closely and the air flow rate is high by approximately 7%, it is likely that something has produced an error in the overall energy balance in the NETL model, such as the efficiency of the compressor or turbine, or heat loss to the cathode pressure vessel (V 301), or postcombustor vessel (V 304). One difficulty in the NETL model comes from attempting to match numerous conditions using only a simple scaling procedure of the original turbomachinery maps. As it will be shown later, not only this is a cause for potential error in the steady-state magnitude prediction already shown, but there is also some effect on the dynamic behavior. Both Figs. 5 and 6 show that the NETL model

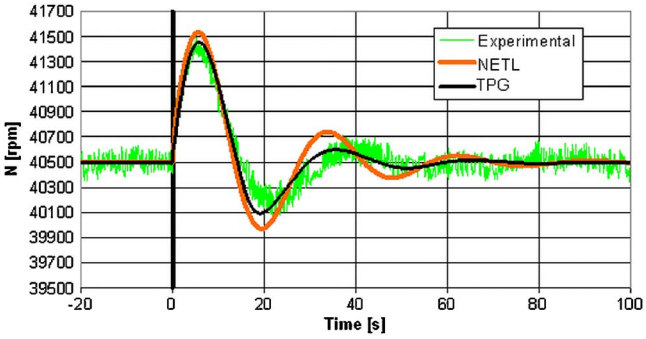

Fig. 4 15 kW load step decrease; rotational speed comparison

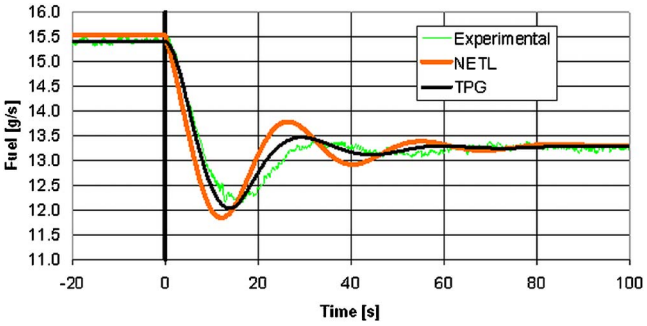

Fig. 5 15 kW load step decrease; fuel mass flow rate comparison

predicts an apparently more oscillating behavior of the system than the experimental data and the TPG model; this may be due to a less detailed representation of thermal capacitances.

Another important comparison regards temperatures. The fuel cell plenum inlet temperature is shown in Fig. 7. It is significant for the hybrid system emulation, because it is used as an input for the fuel cell real-time model (see Fig. 2). Furthermore, this property has to be checked over time because a too high fuel cell inlet temperature or temperature gradient can damage the cell stack or reduce its life. A good transient model has to well predict this temperature trend over time. Also for this property (TE 326), characterized by a high time scale response because of the high thermal capacity, the calculated transient behavior of both models is in good agreement with the experimental data.

Figure 8 shows TE 307, the combustor inlet temperature. The only difference between TE 307 and TE 326 (Fig. 7) is the heat loss of the pressure vessel used to simulate the cathode volume (V 301). As well described in the previous paragraph, in the TPG model development the attention has also been focused on the

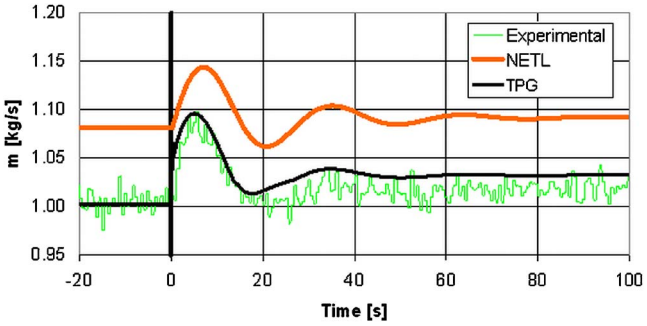

Fig. 6 15 kW load step decrease; fuel cell plenum mass flow rate comparison

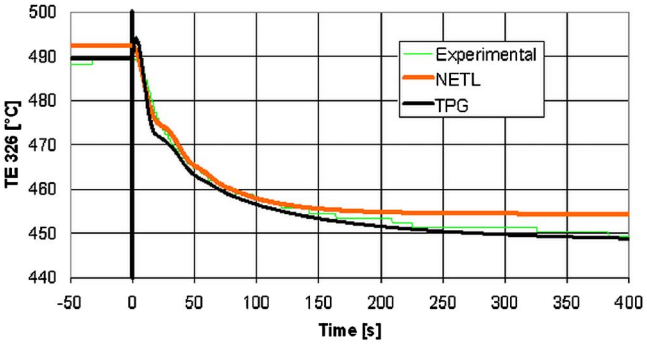

Fig. 7 15 kW load step decrease; fuel cell inlet temperature comparison

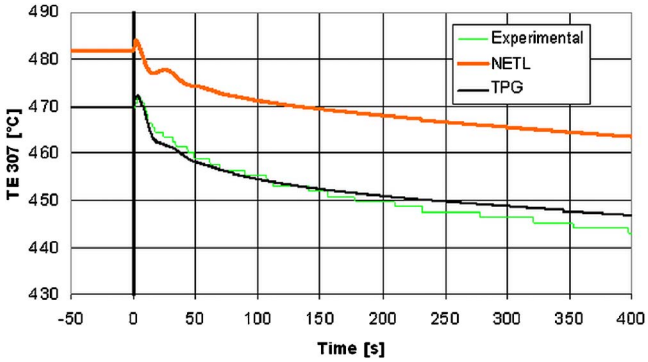

Fig. 8 15 kW load step decrease; combustor inlet temperature comparison

simulation of the heat losses in vessels and in pipes, using average heat coefficient values. Only after several simulations, it was possible to calculate the combustor inlet temperature (TE 307) with higher accuracy than the NETL model results. The heat loss simulation has not been introduced in the NETL model because its main objective is the real-time performance, while the TPG model operates with a calculation over calculated time ratio around 6.

30 kW Load Step Decrease. The 30 kW step decrease (from 45 to 15 kW) of the electrical power demand has been carried out with doubled gain values in the fuel valve PI; the proportional gain has been set to 0.002 and an integral one to 0.0015. This reason can explain the transient behavior of the system that, even if the power step is doubled, the oscillation magnitude in the rotational speed and in other properties is similar to the one presented for the 15 kW step. Furthermore, the 15 kW and 30 kW decrease tests have been carried out on different days and, for this reason, the steady-state conditions of this second test does not exactly match the final state of the previous one. Figure 9 shows that, also in this case, both model results and the experimental data are in good agreement with the experiments for the rotational speed of the machine. The fuel mass flow rate (Fig. 10) and the air mass flow rate at fuel cell plenum inlet (Fig. 11) show the reduced error obtained with the TPG model, as in the 15 kW step case. However, also the faster NETL model can show the transient behavior with enough accuracy predicting the oscillations of the system.

Another important validation regards fuel cell plenum inlet temperature (Fig. 12). Also in this case it is possible to see the performance improvement obtained with the TPG model increasing the calculation accuracy. However, the transient trend and the time scale characterization have been predicted with enough accuracy by both models.

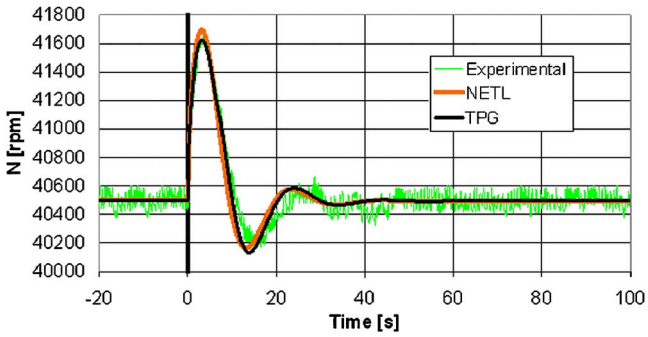

Fig. 9 30 kW load step decrease; rotational speed comparison

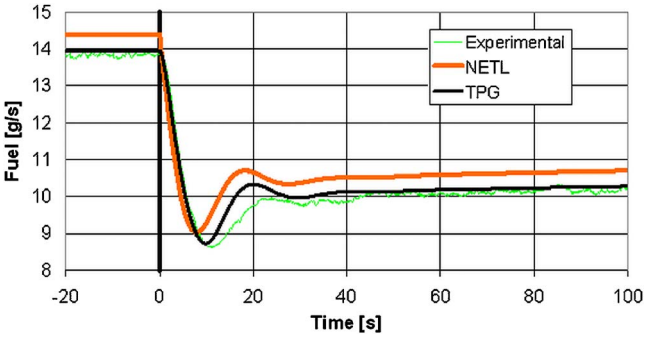

Fig. 10 30 kW load step decrease; fuel mass flow rate comparison

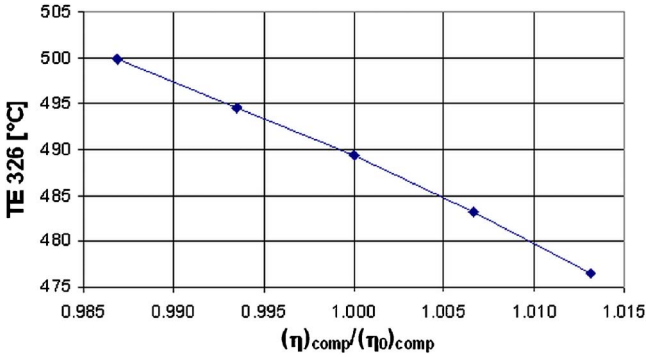

Fig. 13 Fuel cell inlet temperature; compressor efficiency variation

Importance of Performance Map Precision

This section shows the importance of performance map precision for both compressor and turbine and explains some of the discrepancy between TPG and NETL models. For this reason, some simulations have been carried out with the TPG model studying the effects of a compressor or a turbine efficiency variation typical of manufacturer map tolerance. However, a similar discussion, not reported here for brevity, can be performed for the mass flow rate maps. The attention has been focused on the fuel cell inlet temperature because its importance from the cell safety point of view. However, the simulations have shown that the performance map precision affects all the temperatures of the facility. Figures 13 and 14 show the values of the fuel cell inlet temperature, obtained at steady-state conditions, versus the normalized values of compressor or turbine efficiency. In all these results the electrical power demand has been maintained at 60 kW and the valves have been set as in the results reported in the previous paragraph. While Fig. 13 reports the effect (TE 326) of compressor efficiency tolerance, Fig. 14 shows the variation of the same temperature coming from a turbine efficiency small variation. These figures point out that the temperature result can be significantly different for a slight difference in turbomachinery efficiency. In both cases, the machine efficiency increase changes the power balance between compressor and turbine and, to maintain constant the rotational speed, generates a fuel mass flow rate reduction. As a consequence, the TIT decrease generates a TOT reduction and, because the cycle is recuperated, a fuel cell inlet temperature decrease. This influence of performance map variation justifies the importance of obtaining, if possible, accurate map data for use in the simulation models as done with the TPG model.

To conclude this analysis, the TPG model has been used to resimulate the 15 kW load step decrease with a 1% turbine efficiency increase. Figure 15 shows a slight increase in the amplitude of the rotational speed transient behavior, and Fig. 16 shows a 10°C TE 326 decrease during the whole time dependent phenomenon. However, since the frequency is not much affected, a model based on manufacturer maps, as the NETL one, is enough to calculate the property transient trends preventing risky situations for the system.

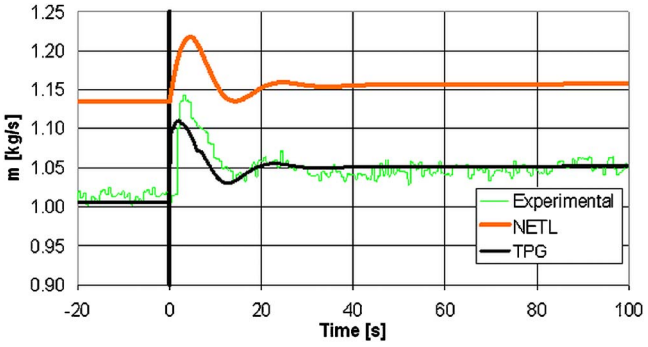

Fig. 11 30 kW load step decrease; fuel cell plenum mass flow rate comparison

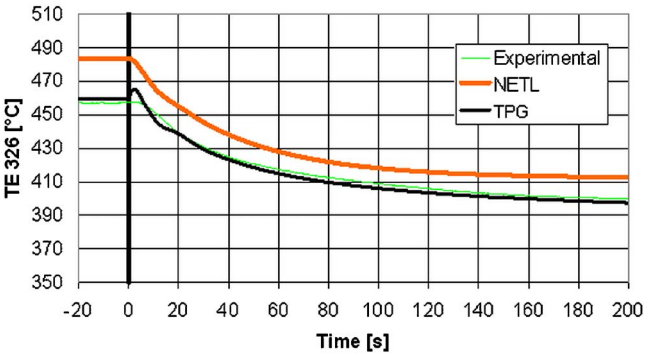

Fig. 12 30 kW load step decrease; fuel cell inlet temperature comparison

Conclusions

This work regards the experimental validation of simulation tools for hybrid system applications. The activity has been carried out with the U.S. DOE-NETL Hyper facility at Morgantown (WV). The main activities presented here are:

- a brief description of the facility for the emulation of hybrid systems with a recuperated micro gas turbine coupled with two vessels for the fuel cell and postcombustor volume capacitance physical simulation;

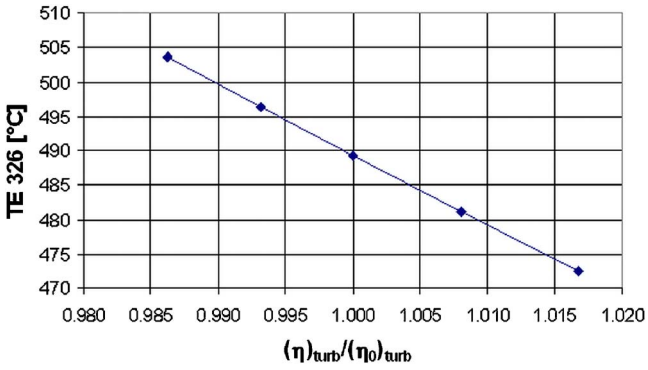

Fig. 14 Fuel cell inlet temperature; turbine efficiency variation

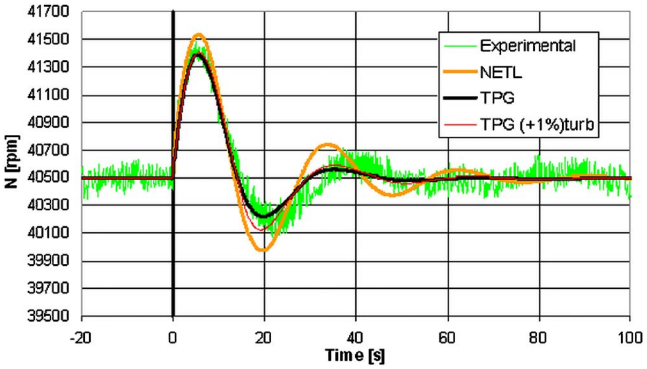

Fig. 15 Rotational speed comparison; case with the turbine efficiency increased

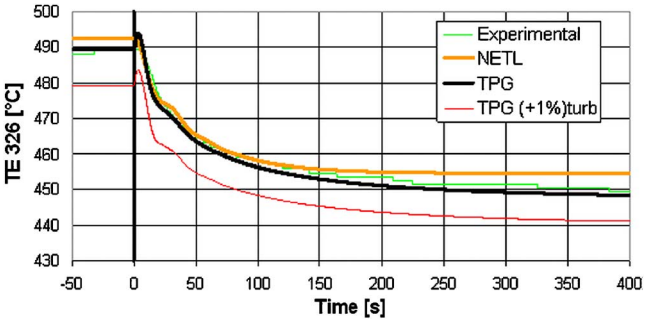

Fig. 16 Fuel cell inlet temperature comparison; case with the turbine efficiency increased

- the presentation of the main characteristics of both NETL and TPG models of the Hyper experimental facility;
- the model validation successfully comparing the results with the experimental data. For this reason two load step decreases have been considered showing the main differences in the performance of the models. The results have shown the NETL model to characterize the frequency of the oscillations and time scales of the transients fairly well, despite having some difficulties with the steady-state and amplitude predictions. The TPG model has performed better primarily because it has used the experimental data to generate the turbomachinery maps for the range of conditions considered, and because it considers a more detailed heat transfer approach, including heat losses in the cathode plenum (V 301) as well. Unfortunately, the heat loss characteristics of the postcombustor plenum are more difficult to obtain experimentally and therefore to compare with.

In conclusion, while the NETL model is essential to get real-time predictions of qualitative transient response over a broad range of off-design operating conditions, the more precise and more time consuming TPG model would be better when higher fidelity results are needed. However, both models calculate with good accuracy the transient trends of phenomena preventing risky situations for the plant components.

It is important to underline that both validated models are currently used inside further works to study the coupling between various SOFC stacks and microturbines and to develop complete control system strategy for these hybrid plants [14,25].

Acknowledgment

The authors would like to thank David Ruehl, the Hyper facility operator, for his support in the experiments and tireless maintenance of the facility. Furthermore, the Italian authors gratefully acknowledge FP-VI European Integrated Project FELICITAS (TIP4-CT-2005-516270) [26] coordinated by the Fraunhofer Institute, Germany.

Nomenclature

APU = Auxiliary power unit
DOE = Department of energy
MCFC = Molten carbonate fuel cell
mGT = micro gas turbine
NETL = National Energy Technology Laboratory
NG = natural gas
PI = proportional integral controller
SOFC = solid oxide fuel cell
TPG = Thermochemical Power Group

Variables

A = thermal exchange area, m^2
c = specific heat, J/kg K
c_p = constant pressure specific heat, J/kg K
F = mass flow rate, kg/s
gap = distance between heat exchanger plates, m
h = exchange coefficient, W/m^2 K
k_{bulk} = bulk thermal conductivity, W/mK
M = mass, kg
N = microturbine rotational speed, rpm
Nu = Nusselt number
P = pressure, Pa
q = heat flux, W
T = temperature, K
TIT = turbine inlet temperature, K
TOT = turbine outlet temperature, K
x = dimensionless parameter of Eq. (1)

Subscripts

0 = on design
av = flow average
comp = compressor
ext = external
HX = heat exchanger
i = counter increment
int = internal
turb = turbine

References

[1] Roberts, R. A., Brouwer, J., Liese, E., and Gemmen, R., 2005, "Development of Controls for Dynamic Operation of Carbonate Fuel Cell-Gas Turbine Hybrid Systems," ASME Paper No. 2005-GT-68774.
[2] Bedont, P., Grillo, O., and Massardo, A. F., 2002, "Off-Design Performance Analysis of a Hybrid System Based on an Existing MCFC Stack," ASME Paper No. 2002-GT-30115.
[3] Campanari, S., and Macchi, E., 2001 "Comparative Analysis of Hybrid Cycles Based on Molten Carbonate and Solid Oxide Fuel Cells," ASME Paper No. 2001-GT-383, ASME Turbo Expo, New Orleans.
[4] Ghezel-Ayagh, H., Daly, J. M., and Wang, H. Z., 2003, "Advances in Direct Fuel Cell/Gas Turbine Power Plants," ASME Paper No. 2003-GT-38941.
[5] Magistri, L., Bozzolo, M., Tarnowski, O., Agnew, G., and Massardo, A. F., 2003, "Design and Off-Design Analysis of a MW Hybrid System Based on Rolls-Royce Integrated Planar SOFC," ASME Paper No. 2003-GT-38220.
[6] Agnew, G. D., Bozzolo, M., Moritz, R. R., and Berenyi, S., 2005, "The Design and Integration of the Rolls-Royce Fuel Cell Systems 1 MW SOFC," ASME Paper No. 2005-GT-69122.
[7] Hirscenhofer, J. H., Stauffer, D. B., Engleman, R. R., and Klett, M. G., 1998, "Fuel Cell Handbook," DOE Report No. DOE/FETC-99/1076, U.S. Department of Energy, Morgantown, WV.
[8] Singhal, S. C., 2000, "Advances in Solid Oxide Fuel Cell Technology," Solid State Ionics, **135**, p. 305.
[9] Veyo, S. E., Shockling, L. A., Dederer, J. T., Gillet, J. E., and Lundberg, W. L., 2002, "Tubular Solid Oxide Fuel Cell/Gas Turbine Hybrid Cycle Power Systems: Status," ASME J. Eng. Gas Turbines Power, **124**, pp. 845–849.
[10] Magistri, L., 2003, "Hybrid System for Distributed Generation," Ph.D. thesis, TPG-DiMSET, University of Genoa.
[11] Tison, R., 2000, *Microturbines in the New Millennium*, Energy Publications, Southwestern Energy, pp. 17–20.
[12] Costamagna, P., Magistri, L., and Massardo, A. F., 2001, "Design and Part-Load Performance of a Hybrid System Based on a Solid Oxide Fuel Cell Reactor and a Micro Gas Turbine," J. Power Sources, **96**, pp. 352–368.

[13] Gemmen, R. S., Liese, E., Rivera, J. G., and Brouwer, J., 2000, "Development of Dynamic Modelling Tools for Solid Oxide and Molten Carbonate Hybrid Fuel Cell Gas Turbine Systems" ASME Paper No. 2000-GT-0554.
[14] Ferrari, M. L., Magistri, L., Traverso, A., and Massardo, A. F., 2005, "Control System for Solid Oxide Fuel Cell Hybrid Systems," ASME Paper No. 2005-GT-68102.
[15] Siller, C., Thorud, B., and Bolland, O., 2005, "Safe Dynamic Operation of a Simple SOFC/GT Hybrid Cycle," ASME Paper No. 2005-GT-68481.
[16] Shelton, M., Celik, I., Liese, E., Tucker, D., and Lawson, L., 2005, "A Transient Model of a Hybrid Fuel Cell/Gas Turbine Test Facility Using Simulink," ASME Paper No. 2005-GT-68467.
[17] Traverso, A., 2005, "TRANSEO Code for the Dynamic Simulation of Micro Gas Turbine Cycles." ASME Paper No. 2005-GT-68101.
[18] Traverso, A., Calzolari, F., and Massardo, A. F., 2003, "Transient Behavior of and Control System for Micro Gas Turbine Advanced Cycles," ASME J. Eng. Gas Turbines Power, **127**, pp. 340–347.
[19] Tucker, D., Liese, E., VanOsdol, J. G., Lawson, L. O., and Gemmen, R. S., 2003, "Fuel Cell Gas Turbine Hybrid Simulation Facility Design," ASME International Mechanical Engineering Congress and Exposition, New Orleans, LA.
[20] Tucker, D., Lawson, L., VanOsdol, J., Kislear, J., and Akinbobuyi, A., 2006, "Examination of Ambient Pressure Effects on Hybrid Solid Oxide Fuel Cell Turbine System Operation Using Hardware Simulation," ASME Paper No. 2006-GT-91291.
[21] McDonald, C. F., 2000, "Low Cost Recuperator Concept for Microturbine Applications," ASME Paper No. 2000-GT-167.
[22] Walsh, P. P., and Fletcher, P., 1998, *Gas Turbine Performance*, Blackwell Science/ASME.
[23] Traverso, A., 2004, "TRANSEO: a New Simulation Tool for Transient Analysis of Innovative Energy Systems," Ph.D. thesis, TPG-DiMSET, University of Genoa.
[24] Traverso, A., Massardo, A. F., and Scarpellini, R., 2006, "Externally Fired Micro-Gas Turbine: Modelling and Experimental Performance," *Applied Thermal Engineering*, Elsevier Science, Vol. 26, pp. 1935–1941.
[25] Ferrari, M. L., 2006, "Transient Analysis of Solid Oxide Fuel Cell Hybrid Plants and Control System Development," Ph.D. thesis, TPG-DiMSET, University of Genoa.
[26] FELICITAS European Project No. TIP4-CT-2005-516270, First Year Report, May 2006.

Rotordynamic Performance of Flexure Pivot Hydrostatic Gas Bearings for Oil-Free Turbomachinery

Xuehua Zhu
SKF China Ltd.,
Shanghai, China
e-mail: Susan.Zhu@skf.com

Luis San Andrés
Mast-Childs Professor
Fellow ASME
Texas A&M University,
College Station, TX 77843-3123
e-mail: Lsanandres@mengr.tamu.edu

Micro-turbomachinery demands gas bearings to ensure compactness, light weight, and extreme temperature operation. Gas bearings with large stiffness and damping, and preferably of low cost, will enable successful commercial applications. Presently, tests conducted on a small rotor supported on flexure pivot hydrostatic pad gas bearings (FPTPBs) demonstrate stable rotordynamic responses up to 100,000 rpm *(limit of the drive motor). Test rotor responses show the feed pressure raises the system critical speed (increase in bearing direct stiffness) while the viscous damping ratio decreases. Predictions correlate favorably with experimentally identified (synchronous) direct stiffness bearing force coefficients. Identified experimental gas bearing synchronous damping coefficients are 50% or less of the predicted magnitudes, though remaining relatively constant as the rotor speed increases. Tests without feed pressure show the rotor becomes unstable at* ~81 krpm *with a whirl frequency ratio of 20%. FPTPBs are mechanically complex and more expensive than cylindrical plain bearings. However, their enhanced stability characteristics and predictable rotordynamic performance makes them desirable for the envisioned oil-free applications in high speed micro-turbomachinery.*
[DOI: 10.1115/1.2720518]

Keywords: gas bearings, rotordynamics, oil-free turbomachinery

Introduction

Gas film bearings offer low friction and small power dissipation, enabling their successful application in air-cycle machines, high-precision instruments, auxiliary power units, and high-speed micro-turbomachinery [1,2]. In addition, gas bearings do not require costly, complex sealing and lubricant circulation systems, allowing for compact rotor-bearing systems with fewer parts. Furthermore, oil-free bearing turbomachinery eliminate process fluid contamination and are environmental friendly.

However, gas film bearings have low load capacity because of the inherently low viscosity of the gas, and thus require a minute film thickness to accomplish their intended function. Gas bearing fabrication and installation tends to be expensive and time consuming. In addition, rigid surface geometry gas bearings offer little damping and may not limit effectively rotor motions while traversing critical speeds. Hydrodynamic gas bearings are prone to show self-excited subsynchronous instabilities, limiting their application to rotor speeds not exceeding, approximately, twice the first natural frequency of the rotor-bearing system [3].

Two kinds of (self-excited) instabilities are apparent in hybrid (hydrodynamic/hydrostatic actions) gas bearings [4]. The pneumatic hammer is due to gas trapped within local volumes and whose pressure is out of phase with the rotor dynamic motion [5]. Improper restrictor design with large discharge volume leads easily to this dangerous instability, which can occur even without rotor spinning. Hydrodynamic instability is due to the sudden loss of effective damping at whirl frequencies typically 50% of rotor speed, and coinciding with a system natural frequency. San Andrés and Childs [6] demonstrate that hybrid bearings with angled injection improve rotordynamic performance with virtual elimination of cross-coupled stiffness coefficients and null or negative whirl frequency ratios.

Czolczynsk [7] provides a comprehensive review of gas bearing applications and the numerical analysis for prediction of frequency-dependent force coefficients. San Andrés and Wilde [8] advance the accurate and numerically stable finite element analysis of gas bearings into very high-speed numbers.

References [9–11] detail the research at the authors' institution on inexpensive gas bearings for oil-free turbomachinery. Wilde and San Andrés [10,11] report on the dynamic forced performance of a high-speed rotor supported on (rigid) multiple lobed hybrid gas bearings. In general, as the supply pressure into the bearings rises, the test bearings show an increase in direct stiffness, albeit the damping ratio of the rotor-bearing system decreases considerably. Sufficiently large external pressurization enables safe rotor operation at speeds well above the system's first natural frequency. Nonetheless, severe hydrodynamic instability eventually becomes apparent, thus limiting the reliability of the tested bearing configurations.

Tilting pad gas bearings eliminate the well-known hydrodynamic instability by not generating cross-coupled stiffness coefficients. However, this type of bearing is mechanically complex since each pad has several degrees of freedom, including pitch, yaw, and roll. The multiplicity of parameters governing the performance of tilting pad gas bearings demands complex analytical methods for prediction of force coefficients and rotor-bearing system stability. Lund [12,13] introduced a perturbation solution of the Reynolds equation to obtain frequency dependent, linearized dynamic force coefficients of a tilting pad bearing, and investigated the influence of pad flexibility on the dynamic force coefficients.

Conventional tilting pad oil-lubricated bearings support high performance turbomachinery operating well above critical speeds. However, the bearings' time-accumulated drawbacks, namely, pad

Contributed by the International Gas Turbine Institute of ASME for publication in the JOURNAL OF ENGINEERING FOR GAS TURBINES AND POWER. Manuscript received April 14, 2006; final manuscript received January 2, 2007. Review conducted by Claus Myllerup. Paper presented at the ASME Turbo Expo 2004: Land, Sea and Air (GT2004), June 14–17, 2004, Vienna, Austria. Paper No. GT2004-52321.

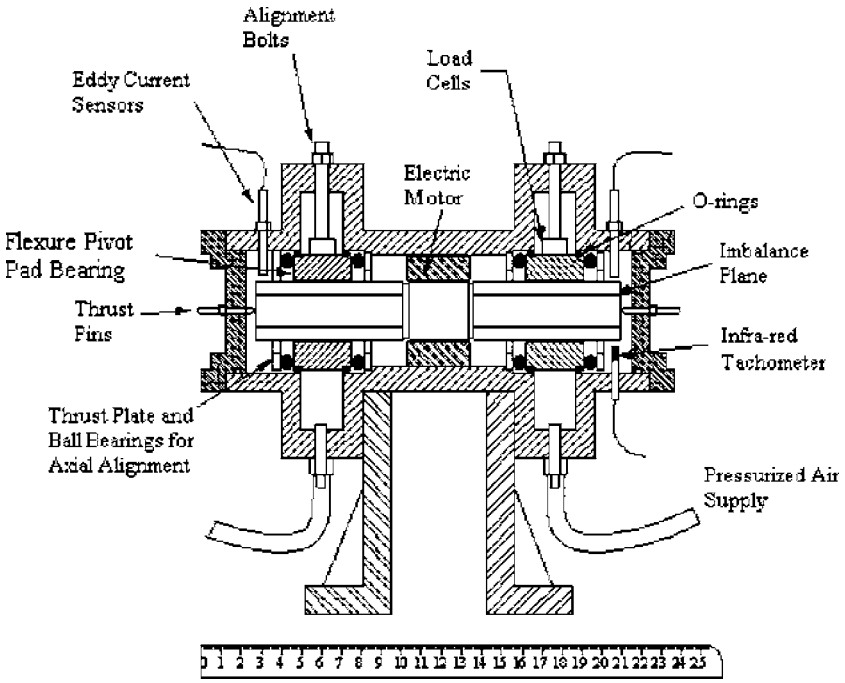

Fig. 1 Schematic cross sectional view of test rig (unit: cm)

wear and flutter and loss of nominal clearance, result in poor performance in the long run. The flexure pivot tilting pad bearing (FPTPB) offers a marked improvement over the conventional design since its wire electro discharge machining (EDM) construction renders an integral pads-bearing that eliminates pivot wear and stack-up of tolerances on assembly [14]. Each pad connects to the bearing shell through a thin flexural web that provides a low rotational stiffness, thus ensuring small cross-coupled stiffness coefficients and delaying or avoiding altogether subsynchronous rotordynamic instabilities [15]. The rotational structural stiffness of the pad web determines the amount of cross-coupled stiffness coefficients. A thick web renders a nearly rigid pad bearing with its inherent instability limit. Low rotational web stiffnesses (thin webs) make an ideal tilting pad bearing; however, concentrated web stresses and fatigue may be of concern [16]. Nonetheless, proper engineering design can lead to a substantial margin of the endurance limit for the web structural material.

Armentrout et al. [16] show that large pad clearances aid to improve the stability of oil-lubricated FPTPBs. Chen et al. [14] also demonstrate that offset pivot designs provide higher stiffnesses, reduce the bearing sensitivity to clearance changes, and offer a higher logarithmic decrement (more damping). Successful applications [17,18] demonstrate oil lubricated FPTPBs have a larger load capacity and lower lubricant temperature rise than do conventional tilting pad bearings. Applications of FPTPBs with compressible fluids, namely, air, are of current interest and hereby advanced.

This paper advances the technology of gas film bearings, FPTPB type, for applications to oil-free turbomachinery by demonstrating their rotordynamic performance, reliability, and durability. The objective is to investigate experimentally the dynamic forced performance of a rotor supported on gas FPTPBs supplied with pressurized air, i.e., a hybrid bearing configuration. Rotordynamic displacements and bearing transmitted forces are measured during coast-down tests to baseline and calibrated imbalance masses. Run-up tests are conducted to high speeds in search of regions of rotordynamic unstable response. The bearings synchronous stiffness and damping coefficients are estimated from the measured responses. Predicted stiffness coefficients are in close agreement with the identified bearing parameters.

Experimental Facility

Figure 1 depicts the test rig of symmetric construction and with a steel main body integrating a brushless electric motor armature. The controller provides 0.9 kW of continuous power, and the motor can reach a speed of 100,000 rpm. The motor drives a rotor supported on two identical flexure pivot pad gas bearings. This rotor consists of a steel shaft, 15 mm diameter and 190 mm in length, onto which two cylindrical sleeves are press-fit. The rotor has a machined diameter of 28.48 ± 0.001 mm. A coating of Teflon® (solid lubricant with low friction) enlarged the rotor diameter to 28.52 ± 0.003 mm at the bearing locations. The coating is applied as a spray at room temperature [19]. Eight holes, each 1 mm in diameter, are spaced equally at each rotor end face. Imbalance masses can be placed in these holes for imbalance response measurements. Thrust pins in both casing covers prevent axial rotor movements.

Figure 2 depicts the design drawing and a photograph of the test FPTPBs. Each bearing has four arched pads, each with 60% pivot offset. The nominal bearing bore diameter is 28.56 ± 0.003 mm with a 40% machined preload. Pressurized air flows into the bearing middle plane through eight identical orifices, 0.38 mm in diameter. Four radial holes are machined directly through the flexural webs and serve to pressurize directly each pad. The other four holes (not radial due to construction difficulties) discharge in the regions between adjacent pads. The bearings are installed in the (static) load on pad configuration. Table 1 lists the main dimensions of the test rotor and the hybrid FPTPBs. The radial clearance of the bearing pads is just ~ 0.020 mm.

Three piezoelectric load cells are attached to the bearing outer diameter, and this is installed into the test rig using three alignment bolts 120 deg apart. A cover plate pushes each bearing into the test rig, and O-rings on each bearing side seal the bearing chamber preventing air leakage. The airflow into each bearing is controlled by on/off valves connected to the main pressure source (shop line). The gas piping system includes a pressure regulator, dryer/filter, pressure gauges, and flowmeters. On each casing end, two orthogonally positioned eddy-current displacement transducers are installed to measure rotor motions, as shown in Fig. 1. An

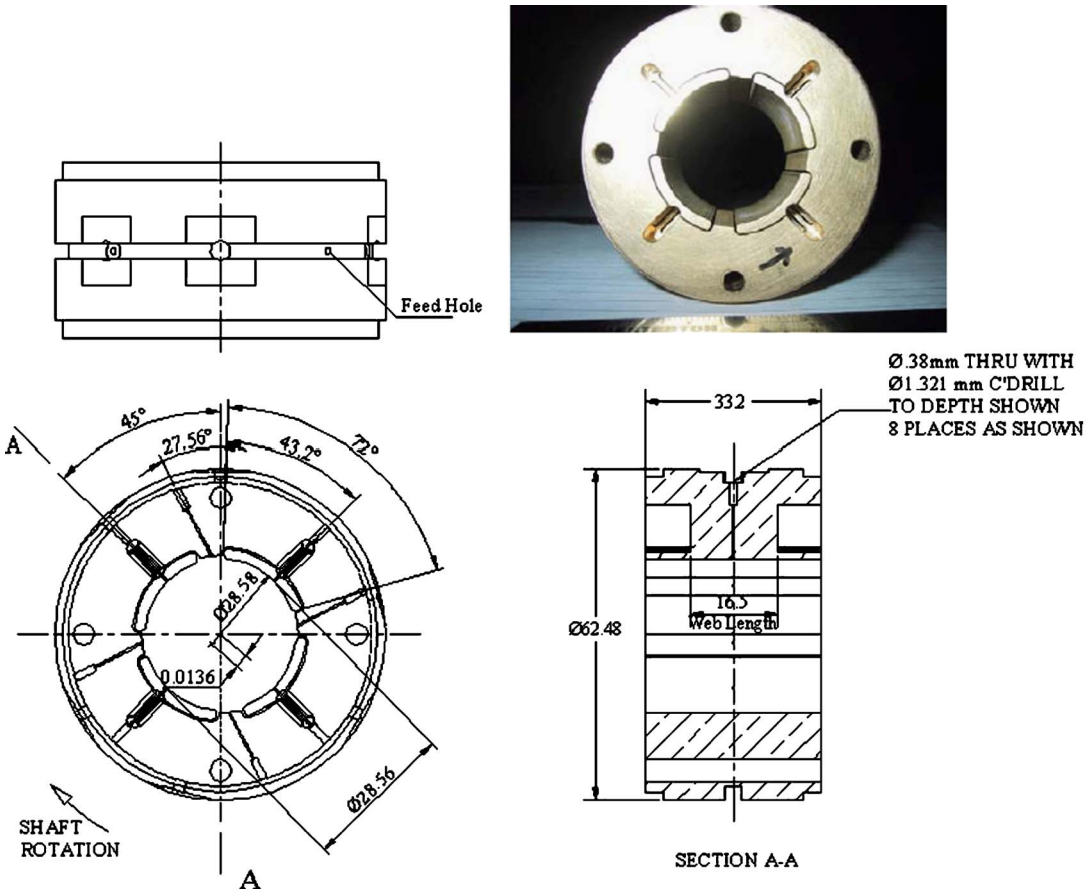

Fig. 2 Flexure pivot hydrostatic pad gas bearing. Photograph of bearing and details of bearing geometry.

infrared tachometer installed inside one of the bearing chambers records the rotor speed and offers a key phasor signal for rotor vibration data. Refer to [9,10] for an extensive description of the test rig features.

Experimental Response of the Rotor Supported on FPTPBS

Coast-down speed tests record the rotor dynamic motions and transmitted bearing loads for various imbalance conditions and three feed absolute pressures, 2.39, 3.77, and 5.15 bar (20, 40, and 60 psig). The imbalance measurements consist of a baseline (remnant imbalance) response and calibrated mass imbalance responses. Pressurized air enters into each bearing pad through the small feed orifices in the webs. The holes in between adjacent pads are obstructed. Table 2 summarizes the imbalance configurations for tests exciting the rotor cylindrical and conical modes of motion. Identical masses (m_i) are located at the rotor ends, at the same angular location and displaced 180 deg to excite cylindrical and conical modes.

Table 1 Main parameters of test rig and flexure pivot bearings

Parameter	Value
Rotor mass M	0.827 kg
Final rotor diameter with coating d	28.52±0.003 mm
Bearing bore diameter D	28.56±0.003 mm
Bearing diametrical clearance $2C$	40±4.5 μm
Bearing axial length L	33.2 mm
Pads number and arc length	4 (72 deg)
Pad pivot offset	60%
Pad preload r	40%
Pad mass moment of inertia	0.253 gram mm^2
Web rotational stiffness	20 Nm/rad
Number of feed orifices	8
Feed orifice diameter	0.38 mm

Coastdown Imbalance Response. Figures 3 and 4 depict the peak-peak amplitudes of rotor motion and bearing transmitted load for a supply pressure equal to 3.77 bar (absolute). The graphs show the responses at the left bearing (vertical plane) for the remnant imbalance and two calibrated imbalances, U_1 and U_2, respectively. Note that the added imbalance mass increases the critical speed from 13,500 rpm (baseline) to 14,100 rpm. The conical mode imbalance distribution (U_2), determines larger amplitudes of motion in displacement and transmitted force than the cylindrical mode excitation (U_1). The rotor displacements while crossing the critical speed are at least 40 μm in magnitude, i.e., as large as the bearing nominal diametrical clearance of 40 μm, thus

Table 2 Mass imbalances for cylindrical and conical mode motions

Imbalance name	Mass m_i (g)	Displacement u (μm)	Location
U_1	0.050	1.45	In phase 0 deg
U_2	0.050	1.45	Out of phase 180 deg

Note: Uncertainty in mass is 0.008 gram and displacement (u)±0.02 μm

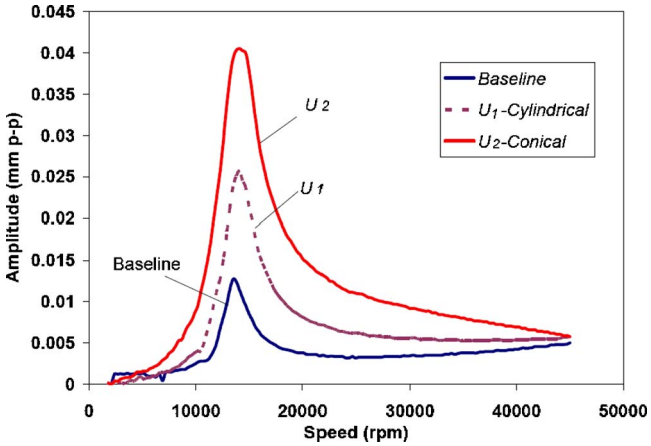

Fig. 3 Synchronous peak-peak rotor amplitudes versus rotor speed for remnant imbalance and two imbalance conditions exciting combined cylindrical/conical modes. Imbalances U_1 =1.45 μm, U_2=1.45 μm. Supply pressure 3.77 bar (absolute).

demonstrating the tilting ability of the test bearings. The waterfall plot in Fig. 5 shows the frequency content of the rotor vibration as the rotor speed increases to 50 krpm and evidences no rubbing or apparent instability, as expected. The displacement response is mostly synchronous, albeit small amplitude motions at twice rotor speed are evident. The test measurements demonstrate the enhancing stability characteristic of the FPTPB. The largest transmitted force is ~11 N, more than twice the magnitude recorded from the baseline response, and 2.75 times half the rotor weight. Rotor motion amplitudes and transmitted bearing forces at the other bearing (right) and at the horizontal plane are similar in magnitude, and not reproduced for brevity. The rotor responses did not show conditions of subsynchronous activity in any of the experiments to speeds as high as 99 krpm. Recall that earlier tests with rigid surface hybrid bearings (see [9–11]) revealed severe hydrodynamic instabilities.

Figure 6 depicts the synchronous peak-peak amplitudes of rotor motion versus speed for three increasing feed pressures into the gas bearings. The supply pressures are 2.39, 3.77, and 5.15 bar (absolute), and determine critical speeds at 11,400, 13,500, and 15,300 rpm, respectively. Note that the rotor motion amplitude increases with feed pressure while traversing a critical speed.

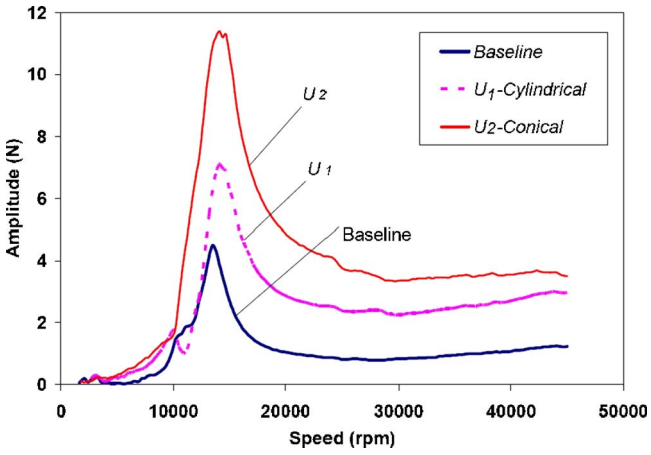

Fig. 4 Transmitted amplitudes of bearing load versus rotor speed for remnant imbalance and two mass imbalances exciting combined cylindrical/conical modes. Left bearing vertical force sensor. Imbalances U_1=1.45 μm, U_2=1.45 μm. Supply pressure 3.77 bar (absolute).

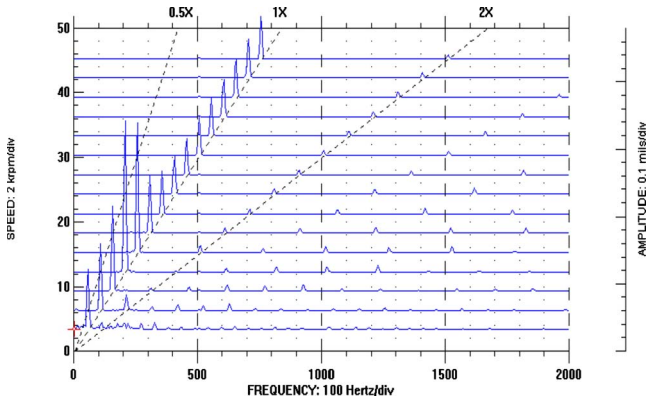

Fig. 5 Waterfall plot of rotor amplitudes with conical imbalance excitation U_2. At left bearing vertical plane (LV). Test at 3.77 bar (absolute) supply pressure.

Thus, as previously shown in [9,11], hydrostatic pressurization increases the gas bearing direct stiffness but lowers the system damping ratio. Figure 7 displays the transmitted (left vertical) bearing loads versus rotor speed for increasing feed pressures. Note the rapid increase in transmitted load as the feed pressure increases. The largest magnitude of about 6 N is nearly 50%

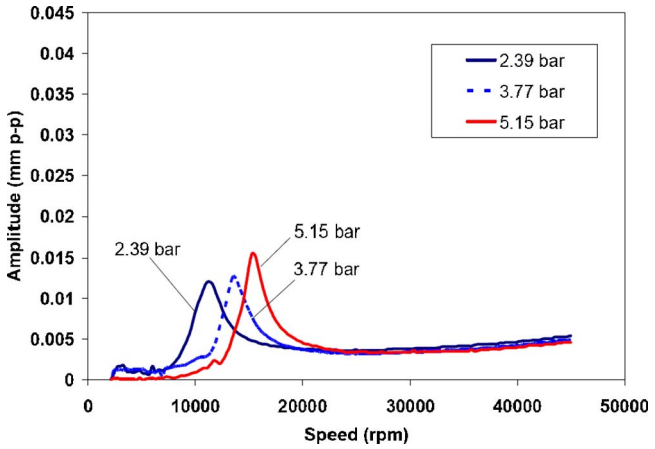

Fig. 6 Baseline synchronous rotor peak-peak amplitudes versus rotor speed for three supply pressures (absolute)

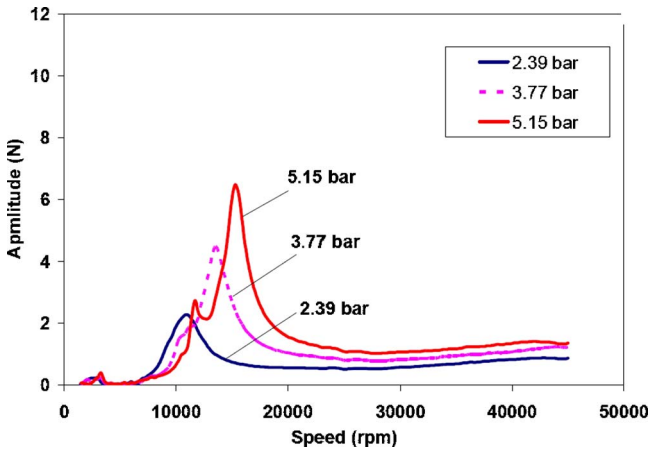

Fig. 7 Baseline transmitted bearing force amplitudes versus rotor speed for three supply pressures. Left bearing vertical load sensor.

Table 3 Estimated gas bearing damping ratio and equivalent stiffness extracted from rotor imbalance responses. Left bearing — horizontal plane.

Imbalance condition	Supply absolute pressure (bar)	Critical speed (rpm)	Damping ratio ζ	K_{eq} (MN/m)
Remnant	2.39	10,800	0.111	0.529
	3.77	13,190	0.080	0.789
	5.15	15,000	0.080	1.020
U_1	2.39	11,700	0.090	0.621
	3.77	14,100	0.053	0.902
	5.15	15,600	0.048	1.100
U_2	2.39	11,990	0.113	0.652
	3.77	14,400	0.083	0.940
	5.15	16,500	0.082	1.230

higher than half the rotor weight (4.05 N). The bearing transmitted loads are obviously almost negligible in the high-speed range, i.e. 20,000 rpm to 45,000 rpm.

Estimation of Damping Ratios and Equivalent Stiffness. The Q-factor method is used in lightly damped systems to estimate the viscous damping ratio ($\zeta < 0.1$) of the rotor on its bearings. The equivalent bearing stiffness (K_{eq}) is easily determined from the critical speed (ω_c) and the rotor mass shared by each bearing, i.e., $K_{eq} = \frac{1}{2} M \omega_c^2$. Table 3 presents the critical speeds, estimated damping ratio, and equivalent stiffness for the left bearing (horizontal direction) as determined from the rotor imbalance responses for the baseline condition and calibrated imbalance responses. Damping ratios shown decrease as the supply pressure increases. An average damping ratio of 10% appears adequate for most test conditions.

Equivalent gas bearing stiffnesses (K_{eq}) at the critical speed increase from ~0.6 MN/m to 1.2 MN/m as the supply pressure increases from two to five times the ambient value condition. Table 3 also shows that the supply pressure increases the rotor-gas bearing system critical speed from 11 krpm to nearly 16 krpm. The drop in damping ratio is solely due to the increase in stiffness rather than a decrease in the physical damping magnitude. Wilde and San Andrés [10] report similar experimental performance characteristics for other simpler gas bearings.

Determination of Threshold Speed of Instability. The rotor mounted on the flexure pivot hydrostatic pad gas bearings shows dynamically stable responses to rotor speeds as high as 99,000 rpm, thus evidencing the test bearings provide little or negligible cross-coupled stiffness coefficients. Experiments under pure hydrodynamic operation (no external feed pressure) were conducted at rotor speeds well above the rigid mode critical speeds (~11 krpm to 16 krpm). The supply pressure lines are closed after the rotor passes through the critical speed and reaches the lowest test speed of 20 krpm. The rotor runs up in speed to a top speed of 90,000 krpm. During this operating condition, the bearings are self-acting, i.e., working as hydrodynamic bearings. Figure 8 depicts a waterfall of the rotor displacements, amplitudes and frequency content, as the speed increases to 90 krpm. A subsynchronous instability, of hydrodynamic type, appears at a speed of 81,180 rpm (1,353 Hz) with a whirl frequency equal to 271 Hz (16,260 rpm). The whirl frequency ratio is 0.20. Most importantly, however, the whirl frequency corresponds closely with the lowest critical speed (natural frequency) of the rotor on its bearings. The Appendix shows a more conservative prediction of instability with a whirl frequency ratio equal to 0.30 under pure hydrodynamic operation. Recall that the bearing is not an ideal tilting pad bearing due to its integral construction, i.e., pads attached to a flexural structural element. Opening the air supply line and pressurizing the gas bearings immediately stabilized the rotor.

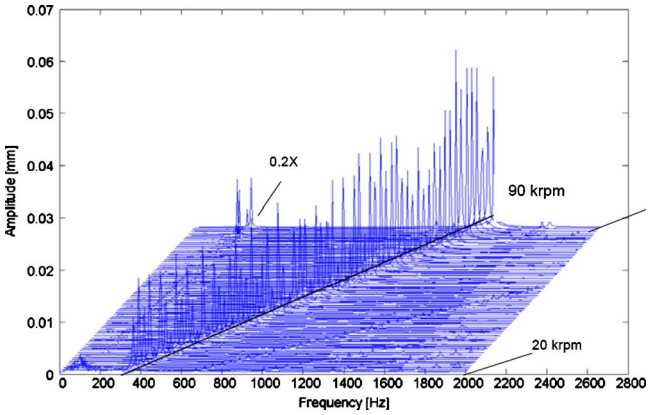

Fig. 8 Waterfall plot of rotor amplitudes at right bearing vertical plane (RV). Speed run up test without external pressurization. Speed range 20 krpm to 90 krpm.

A series of experiments were conducted with the feed orifices into the pads plugged (no hydrostatic pad pressurization) and the orifices in between adjacent pads open. At the beginning, the rotor would not lift with the four orifices in-between pads supplied with external pressure. Apparently the discharge plenum has a large volume and the orifice pressures acting on the rotor surface could not lift the rotor. The two top in-between pad orifices were then obstructed to provide a hydrostatic push upwards, thus ensuring rotor lift-off and avoidance of rotor rubbing at start up. The lift-off supply pressure is 5.15 bar (absolute). However, when the rotor speed approaches the lowest motor speed (10,400 rpm) severe subsynchronous amplitude motions became apparent. The subsynchronous instability gradually vanishes as the air supply pressure is reduced and eventually removed. This event shows that pneumatic hammer is the cause for the instability since the discharge curtain volume (between orifice end and rotor) is quite large.

Experimental Estimation of Bearing Dynamic Force Coefficients. Imbalance responses, referring to the configurations shown in Table 2, facilitate the identification of bearing force coefficients over a speed range. Since the test gas bearings offer little cross-coupling stiffness, the method simplifies to an estimation of the transfer function, load over displacement, and from which the bearing stiffness and damping can be obtained. Let (F_X, F_Y) be the synchronous components of the transmitted forces, and (X, Y) be the complex amplitudes of motion. The force coefficients, direct damping and stiffness, can then be obtained from the fundamental relationships

$$K_{XX} + i\omega C_{XX} = \frac{F_X}{X} \quad K_{YY} + i\omega C_{YY} = \frac{F_Y}{Y} \tag{1}$$

where ω is a frequency synchronous with rotor speed. Note that in the identification procedure, a vector addition renders the vertical (X) and horizontal (Y) transmitted loads from the measured forces at the three angular locations, 120 deg apart.

Figure 9 shows the identified synchronous speed direct stiffness (K_{XX}) and damping (C_{XX}) coefficients for the three test supply pressures. In general, the direct stiffness (K_{XX}, K_{YY}) increase both with pressure supply and rotor speed. The estimated coefficients correlate well with the equivalent stiffness determined from the rotor amplitude at the critical speed, as shown in Table 3. On the other hand, the direct damping coefficients show an erratic behavior with rotor speed, though decreasing in magnitude as the feed pressure increases. Note that the physical magnitude of the damping coefficients is rather small. In the speed range from 20 krpm to 30 krpm, the identification of damping coefficients is not reliable since the shaft amplitudes of motion are quite small. Recall that damping is best extracted from large amplitude motions while

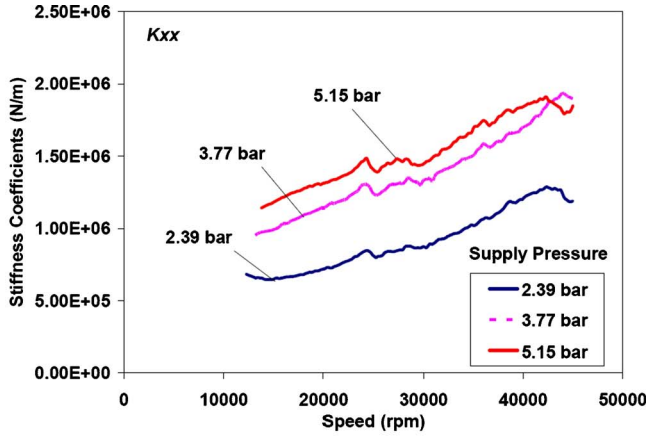

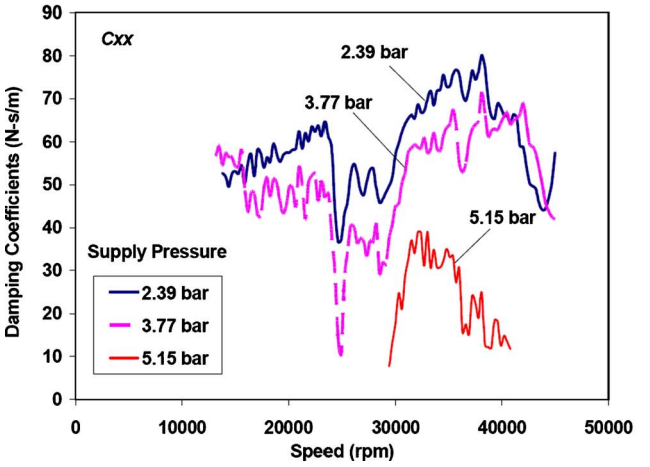

Fig. 9 Estimated experimental gas bearing direct stiffness and damping coefficients (K_{XX}, C_{XX}) versus rotor speed for three supply pressures. Synchronous speed force coefficients, *X*-vertical.

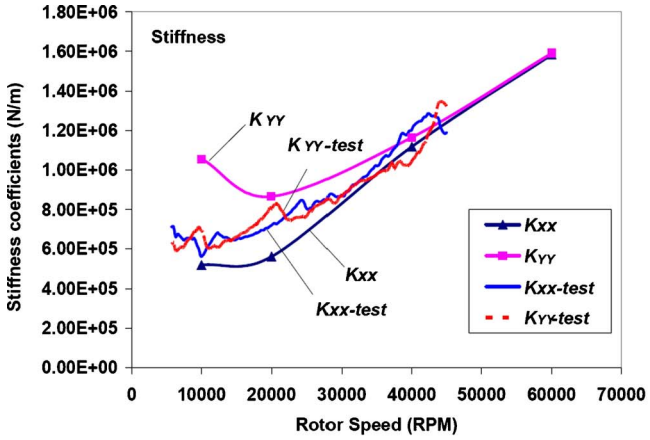

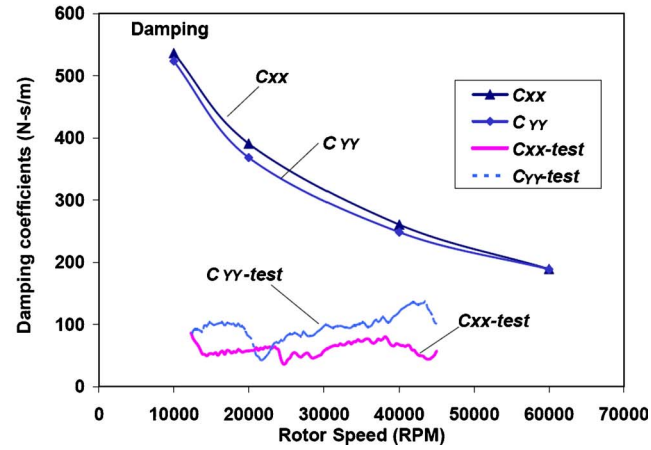

Fig. 10 Comparison of predicted and experimentally identified (2.39 bar supply pressure) synchronous direct stiffness and damping force coefficients for gas bearing. Predictions do not include external pressurization.

crossing a critical speed.

The prediction of bearing synchronous force coefficients is based on finding the gas flow and film pressure in the bearings. A computational finite difference analysis solves Reynolds equation for gas films, i.e.

$$\frac{1}{R^2}\frac{\partial}{\partial\theta}\left(\frac{Ph^3}{12\mu}\frac{\partial P}{\partial\theta}\right)+\frac{\partial}{\partial z}\left(\frac{Ph^3}{12\mu}\frac{\partial P}{\partial z}\right)=\frac{\Omega}{2}\frac{\partial}{\partial\theta}(Ph)+\frac{\partial}{\partial t}(Ph) \quad (2)$$

Small-amplitude rotor motions about an equilibrium position lead to a nonlinear partial differential equation for the static pressure field, and a set of first-order linear partial differential equations for perturbed pressures. The first-order pressure fields determine the rotordynamic force coefficients, stiffness, and damping, as functions of the excitation frequency and other operating conditions. The Appendix presents the prediction of the FPTPB static eccentricity, power loss, and force coefficients with synchronous and non-synchronous analysis [20]. The computational analysis used to obtain the predictions does not include hydrostatic pressurization.

Figure 10 shows a comparison between the predicted synchronous direct force coefficients and the experimentally derived direct stiffness and damping coefficients. The test coefficients are determined from the imbalance response measurements and the lowest feed pressure of 2.39 bar (absolute). The predicted direct stiffnesses (K_{XX}, K_{YY}) match well the experimentally identified coefficients, in particular at high rotor speeds where hydrodynamic effects dominate the fluid flow in the bearing. Test direct damping coefficients are substantially smaller than the predicted coefficients. These results are demonstrative of the limited damping characteristics of gas bearings. The predicted damping coefficients, larger than those experimentally derived, evidence a limitation of the lubrication model implemented. Perhaps the operating gas viscosity is less and the actual bearing clearance larger than the values used in the simulations.

Finally, Ref. [21] includes comparisons of the test force coefficients to predictions from an updated computational analysis that accounts for the effect of hydrostatic pressurization through the feed holes into the bearing pads. The latest predictions are in better agreement with the experimental results than the ones hereby presented.

Conclusions

Comprehensive experiments conducted on a test rotor supported on hybrid flexure pivot tilting pad bearings (FPTPBs) demonstrate their excellent stability characteristics and ability to carry dynamic loads. Imbalance responses tests were conducted for feed pressures up to five times ambient and for rotor speeds as high as 100,000 rpm. The rotordynamic performance of the FPTPBs is superior to that of pressurized three-lobe cylindrical bearings tested earlier [10,11], and which showed severe subsynchronous instabilities, in particular at low feed pressures.

The imbalance response measurements demonstrate that hydrostatic pressurization increases the gas bearings direct stiffness coefficients, raising the first rigid mode rotor-bearing system critical speeds. The viscous damping ratios determined from the rotor peak response at its critical speed decrease as the feed pressure increases. Predictions for direct stiffness correlate well with ex-

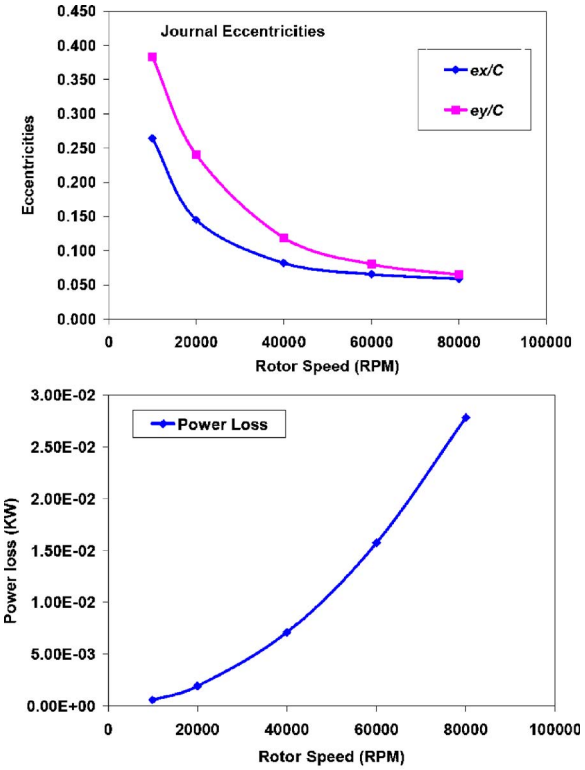

Fig. 11 Predicted journal eccentricities (e/C) and power loss versus rotor speed for tilting pad gas bearing without external pressurization

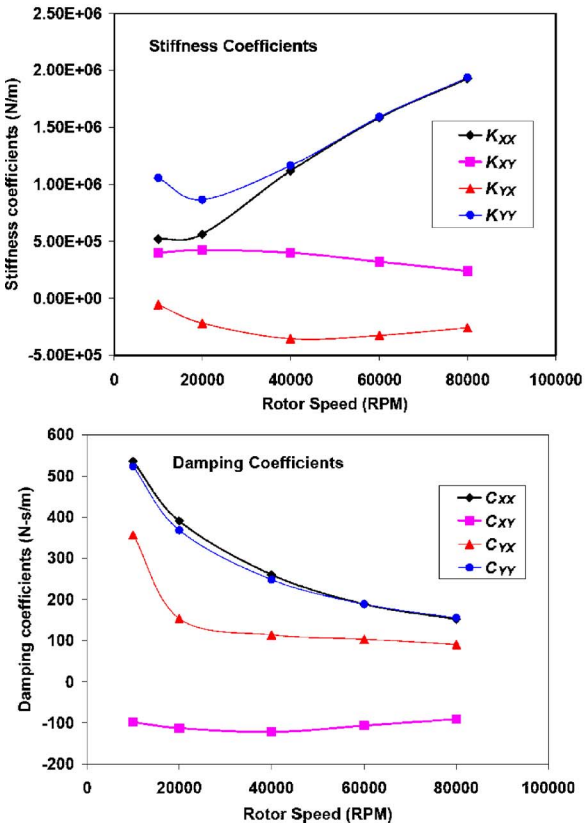

Fig. 12 Predicted synchronous stiffness and damping force coefficients versus rotor speed for tilting pad gas bearing without external pressurization

perimentally identified synchronous force coefficients. Test damping coefficients are about 50% or less of the predicted magnitudes. Measurements without external feed pressure show the onset of a subsynchronous instability at about 81 krpm with a whirl frequency ratio equal to 0.2. The instability caused large (harmful) amplitude motions with the rotor rubbing on its bearings.

The experiments and analysis advance the application of gas bearings for oil-free turbomachinery applications. FPTPBs are more mechanically complex and costlier than cylindrical plain bearings. However, their enhanced stability characteristics and predictable rotordynamic performance makes them desirable for high-speed micro-turbomachinery.

Acknowledgment

The support of the Turbomachinery Research Consortium is acknowledged. Thanks to former student Deborah Osborne-Wilde for designing the test bearings and to KMC, Inc., for manufacturing the bearings to the desired specifications.

Nomenclature

C = bearing radial clearance (m)
C_{ij} = bearing damping coefficients; $i,j=X,Y$ (N-s/m)
d = nominal rotor diameter with coating (m)
D = bearing bore diameter (m)
e_X, e_Y = journal eccentricity displacements (m)
F_X, F_Y = transmitted (synchronous) bearing forces (N)
h = film thickness (m)
K_{ij} = bearing stiffness coefficients; $i,j=X,Y$ (N/m)
K_{eq} = bearing equivalent stiffness coefficient (N/m)
$K_{\delta\delta}$ = pad moment stiffness coefficients (N/m)
L = bearing axial length (mm)
m_i = calibrated imbalance mass (g)
M = rotor mass (kg)
P = film pressure (bar)
r = bearing preload
R = rotor radius (m)
R' = radial location of imbalance mass (m)
u = imbalance displacement (m), $u=m_iR'/(m_i+0.5M)$
U_1, U_2 = calibrated imbalance displacements (m)
X,Y,Z = inertial coordinate system
ω_c = rotor critical speed (rad/s)
Ω = rotor speed (rad/s)
ω = excitation frequency (rad/s)
ζ = damping ratio at critical speed
θ = circumferential coordinate (rad)
μ = gas viscosity (Pa s)

Appendix: Prediction of Gas Bearing Static and Dynamic Performance Characteristics

A computational program analysis calculates the static and dynamic forced response of flexibly mounted, multiple pad (hydrodynamic) gas bearings and seals [20]. The flexural web in the FPTPB provides nearly rigid radial and transverse stiffness. The moment stiffness $K_{\delta\delta}$=20 Nm/rad is known from the bearing provider. The static load on each bearing equals 4.05 N and the rotor speed varies from 10 krpm to 80 krpm. Force coefficients are calculated for a range of operating speeds and synchronous whirl frequencies or for a number of whirl frequencies keeping the rotor speed constant.

Figure 11 shows the journal eccentricity components and drag power versus rotor speed for the applied (static) load of 4.05 N. The journal eccentricity component (Y), transverse to the load direction (X), is slightly larger than the (X) component, thus denoting a degree of cross-coupling in the FPTPB. Note that the

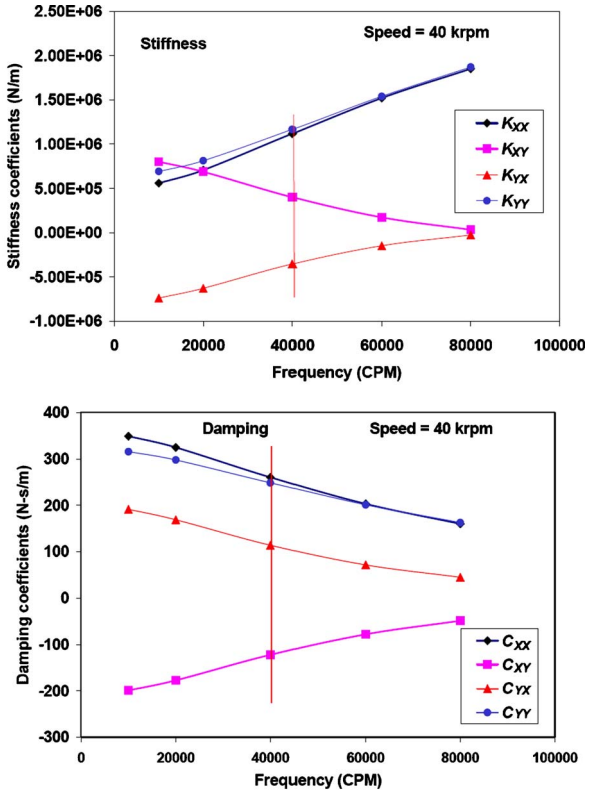

Fig. 13 Effect of excitation frequency on predicted gas bearing force coefficients. Rotor speed=40 krpm. No external pressurization.

rotor approaches the centered condition, null eccentricity, as the journal speed increases. The bearing drag power is very small, i.e., a few watts, and is proportional to the rotor speed to the power 2.

Figure 12 displays the bearing synchronous stiffness and damping force coefficients versus rotor speed. These force coefficients are evaluated at a frequency coinciding with the rotor angular speed in cycles/s, and thus are appropriate to conduct imbalance response predictions of the rotor-gas bearing system. The cross-coupled stiffness coefficients are in general small, while the direct stiffness coefficients increase with rotor speed. The direct damping coefficients, on the other hand, decrease rapidly as the rotor speed increases, denoting a reduction in the ability of the gas bearing to attenuate high frequency vibrations.

Figure 13 depicts the effect of excitation frequency on the force coefficients for operation at a rotor speed of 40 krpm. In the graphs, the vertical lines mark the excitation frequency coinciding with rotor speed. Note that the direct stiffness coefficients increase rapidly with frequency showing the typical gas bearing hardening effect. On the other hand, the direct damping coefficients reduce dramatically as the excitation frequency raises. Cross-coupled stiffness coefficients show a similar behavior. It is well known that at high excitation frequencies, gas bearings become quite stiff (hardening effect), with little or no viscous damping force coefficients.

The predictions show the FPTPB has a whirl frequency ratio of about 0.30 for operation above 30 krpm. However, since the gas bearing direct stiffness increase with speed, the rotor-bearings system natural frequency also raises thus delaying the onset of a hydrodynamic instability.

References

[1] Denhard, W. G., and Pan, C. H. T., 1968, "Application of Gas-Lubricated Bearings to Instruments," ASME J. Lubr. Technol., **90**, pp. 731–739.

[2] Wong, R. Y., Stewart, W. L., and Rohlok, H. E., 1968, "Pivot-Pad Journal Gas Bearing Performance in Exploratory Operation of Brayton Cycle Turbocompressor," ASME J. Lubr. Technol., **90**, pp. 687–700.

[3] Fuller, D. D., 1969, "A Review of the State-of-the-Art for Design of Self-Acting Gas-Lubricated Bearing," ASME J. Lubr. Technol., **91**, pp. 1–16.

[4] Lund, J. W., 1967, "A Theoretical Analysis of Whirl Instability and Pneumatic Hammer for a Rigid Rotor in Pressurized Gas Journal Bearings," ASME J. Lubr. Technol., **89**, pp. 154–163.

[5] Stowell, T. B., 1971, "Pneumatic Hammer in a Gas Lubricated Externally Pressurized Annual Thrust Bearing," ASME J. Lubr. Technol., **93**, pp. 498–503.

[6] San Andrés, L., and Childs, D., 1997, "Angled Injection-Hydrostatic Bearings Analysis and Comparison to Test Results," ASME J. Tribol., **119**, pp. 179–187.

[7] Czolczynski, K., 1999, *Rotordynamics of Gas-Lubricated Journal Bearing System*, Springer-Verlag, Berlin, Chap. 4.

[8] San Andrés, L., and Wilde, D., 2001, "Finite Element Analysis of Gas Bearings for Oil-Free Turbomachinery," Revue Européenne des Eléments Finis, **10**(6/7), pp. 769–790.

[9] Zhu, X., and San Andrés, L., 2005, "Experimental Response of a Rotor Supported on Rayleigh Step Gas Bearings," ASME Paper No. GT 2005–68296.

[10] Wilde, D. A., and San Andrés, L., 2006, "Experimental Response of Simple Gas Hybrid Bearings for Oil-Free Turbomachinery," ASME J. Eng. Gas Turbines Power, **128**, pp. 626–633.

[11] Wilde, D. A., and San Andrés, L., 2006, "Comparison of Rotordynamic Analysis Predictions With the Test Response of Simple Gas Hybrid Bearings for Oil Free Turbomachinery," ASME J. Eng. Gas Turbines Power, **128**, pp. 634–643.

[12] Lund, J. W., 1968, "Calculation of Stiffness and Damping Properties of Gas Bearings," ASME J. Lubr. Technol., **90**, pp. 793–803.

[13] Lund, J. W., and Pederson, L. B., 1987, "The Influence of Pad Flexibility on the Dynamic Coefficients of a Tilting Pad Journal Bearing," ASME J. Tribol., **109**, pp. 65–70.

[14] Chen, W. J., Zeidan, F. Y., and Jain, D., 1994, "Design, Analysis and Testing of High Performance Bearing in a High Speed Integrally Geared Compressor," *Proc. 23rd Turbomachinery Symposium*, Texas A&M University, Turbomachinery Laboratory, College Station, TX, pp. 31–42.

[15] Zeidan, F. Y., 1992, "Developments in Fluid Film Bearing Technology," Turbomach. Int., **33**, pp. 24–31.

[16] Armentrout, R. W., and Paquette, D. J., 1993, "Rotordynamic Characteristics of Flexure-Pivot Tilting-Pad Journal Bearings," STLE Tribol. Trans., **36**, pp. 443–451.

[17] Kepple, W. E., Read, D. W., and Zeidan, F. Y., 1998, "Experience in the Use of Flexure Pivot Tilt Pad Bearings in Boiler Feedwater Pumps," *Proc. 5th International Pump Users Symposium*, Texas A&M University, Turbomachinery Laboratory, College Station, TX, pp. 77–83.

[18] Kardine, A. W., Agahi, R., Ershaghi, B., and Zeidan, F. Y., 1996, "Application of High Speed and High Efficiency Hydrogen Turboexpanders in Refinery Service," *Proc. 25th Turbomachinery Symposium*, Texas A&M University, Turbomachinery Laboratory, College Station, TX, pp. 95–101.

[19] Wilde, D., and San Andrés, L., 2004, "Experimental Lift Off Characteristics and the Effect of a Low Friction Coating on the Startup Response of Simple Gas Hybrid Bearings for Oil-Free Turbomachinery," ASME Paper No. GT 2004-54183.

[20] Delgado, A., San Andrés, L., and Justak, J., 2004, "Analysis of Performance and Rotordynamic Force Coefficients of Brush Seals With Reverse Rotation Ability," ASME Paper No. GT 2004-53614.

[21] San Andrés, L., 2006, "Hybrid Flexure Pivot-Tilting Pad Gas Bearings: Analysis and Experimental Validation," ASME J. Tribol., **128**, pp. 551–558.

The Lomakin Effect in Annular Gas Seals Under Choked Flow Conditions

Mihai Arghir
Cyril Defaye
Jean Frêne

LMS (UMR 6610 CNRS),
Université de Poitiers,
France

The paper deals with the static stability of annular gas seals under choked flow conditions. For a centered straight annular seal, choking can occur only in the exit section because the gas is constantly accelerated by friction forces. From the mathematical standpoint, the flow choking corresponds to a singularity that was never dealt with numerically. The present work introduces an original numerical treatment of this singularity that is validated by comparisons to the analytical solution for planar channel flow. An interesting observation stemming from these results is that the usual hypothesis of considering the flow as being isothermal is not correct anymore for a gas accelerated by a pressure gradient; the characteristics of the flow are the same but the quantitative results are different. The analysis of eccentric annular seals then shows that choked flow conditions produce a change in the static stiffness. For a subsonic exit section, the Lomakin effect is represented by a centering radial force opposed to the rotor displacement. For a choked exit section, the radial force stemming from an eccentricity perturbation has the same direction as the rotor displacement. The annular seal becomes then statically unstable. From the physical standpoint, this behavior is explained by the modification of the Lomakin effect, which changes sign. The pressure and Mach number variations along the seal depict the influence of high compressible flow regimes on the Lomakin effect. This characteristic has never been depicted before.
[DOI: 10.1115/1.2434344]

Introduction: Compressible Channel Flow

Annular gas seals usually work under weak or mild subsonic flow conditions, but for certain ratios between the exit and the inlet pressures, the regime can become transonic. Figure 1 depicts the Mach number inside a straight stator-grooved annular seal. This result was obtained by numerically integrating the complete Navier-Stokes equations. The flow is accelerated from an incompressible Mach number in the feeding chamber and in the inlet section toward $M=1$ in the exit section. For a simple annular seal (without grooves) the flow shows the same characteristics. These can be explained by the influence of the friction forces as it follows [1]. It is common knowledge that the nonviscous subsonic flow in a nozzle is accelerated by the decrease of the normal section. After reaching the sonic conditions ($M=1$), its acceleration is still possible by an appropriate increase of the normal section. The pressure driven flow in a parallel channel with closely spaced walls has a similar behavior. Because of the small channel height compared to its length, the wall friction forces cannot be neglected anymore as in the case of the nozzle. Moreover, these viscous forces have a tremendous importance. Under the influence of friction, the subsonic flow in the constant height channel is accelerated in exactly the same manner as in the converging part of the nozzle. The difference from the case of the nozzle is that once the sonic regime is attained it cannot be exceeded in the parallel channel. Indeed, in the case of nonviscous flow, for accelerating the flow beyond $M=1$ the nozzle must switch its shape from convergent to divergent after the sonic section. This corresponds to a change of the dS/dx sign from negative to positive. Unlike the section of the nozzle, the viscous forces (wall friction) in the parallel channel cannot be forced to change their sign. If the walls of the channel are parallel, there is no mean to accelerate the flow beyond $M=1$. It means that sonic conditions can occur only at the exit section of the parallel channel.

This remark holds for a subsonic flow. If the flow at the inlet section of the parallel channel is supersonic, then viscous forces will decelerate the flow. Sonic conditions can occur at the exit section, but again, due to the fact that viscous forces that are of constant sign are responsible for decelerating the supersonic flow, the regime can never become subsonic. From the standpoint of compressibility effects, a parallel channel can be regarded as a converging nozzle, either accelerating a subsonic flow or decelerating a supersonic one but never going beyond $M=1$ in the exit section (Table 1).

A centered annular seal is normally considered as a parallel channel with a length much larger than its height. All the abovementioned remarks made for the compressible channel flow hold also for the centered annular seal. The pressure-driven flow is subsonic in the inlet section and is next accelerated under the influence of the viscous forces toward the exit section. For certain ratios between the exit and the inlet pressure, the flow regime in the exit section can reach $M=1$. As for the nozzle, the flow is then choked. This means that lowering the exit pressure and keeping the inlet pressure constant will not lead to an increase of the mass flow rate. The physical explanation borrowed from the compressible nozzle flow is that once the sonic conditions are attained in the exit section, the information of a decreasing exit pressure cannot be transmitted in the upstream part of the seal. Of course, increasing the inlet pressure and keeping the exit pressure constant will equally lead to sonic conditions in the exit section but to a larger mass flow rate because different flow conditions are forced in the upstream part of the channel.

This peculiar behavior of annular seal flow has never been described theoretically because of the numerical difficulties that will be explained in the following. Published experimental results of the dynamic characteristics of annular seals [2,3] have only

Contributed by the International Gas Turbine Institute of ASME for publication in the JOURNAL OF ENGINEERING FOR GAS TURBINES AND POWER. Manuscript received May 29, 2006; final manuscript received August 30, 2006. Review conducted by J. Jeffrey Moore. Paper presented at the ASME Turbo Expo 2006: Land, Sea and Air, May 8–11, 2006, Barcelona, Spain. Paper Number GT2006-91151.

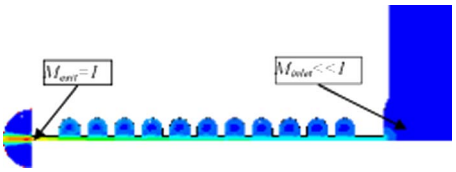

Fig. 1 Mach number in a straight stator-grooved annular seal

pointed out the existence of choked flow conditions. In the mean time, due to the lack of a theoretical model, the stability of annular seals under choked flow conditions was never tackled. It is common knowledge that for incompressible or mildly compressible annular seals the Lomakin effect is responsible for the static stability of the seal; the radial force arising with increasing eccentricity is negative and cancels the displacement perturbation. The goal of the present work is to show that for a choked annular seal the Lomakin effect can be different and the seal can become statically unstable.

In the following, the main idea enabling the numerical solution of choked annular seals will be described and validated. In the second part, the direct stiffness and the Lomakin effect of annular seals will be discussed together with the conditions of static stability.

Numerical Treatment of the Choked Flow

The flow in annular seals is dominated by inertia forces so the mathematical model is represented by the system of the bulk-flow equations [4]

$$\frac{\partial(\rho H)}{\partial t}+\frac{\partial(\rho HW)}{\partial z}+\frac{\partial(\rho HU)}{R\partial\theta}=0 \tag{1}$$

$$\frac{\partial(\rho HW)}{\partial t}+\frac{\partial(\rho HWW)}{\partial z}+\frac{\partial(\rho HUW)}{R\partial\theta}=-H\frac{\partial P}{\partial z}+\tau_{Sz}+\tau_{Rz} \tag{2}$$

$$\frac{\partial(\rho HU)}{\partial t}+\frac{\partial(\rho HWU)}{\partial z}+\frac{\partial(\rho HUU)}{R\partial\theta}=-H\frac{\partial P}{R\partial\theta}+\tau_{S\theta}+\tau_{R\theta} \tag{3}$$

$$c_p\frac{\partial(\rho HT)}{\partial t}+c_p\frac{\partial(\rho HWT)}{\partial z}+c_p\frac{\partial(\rho HUT)}{R\partial\theta}=(\dot{q}_S-\dot{q}_R)+H\left(\frac{\partial P}{\partial t}+W\frac{\partial P}{\partial z}+U\frac{\partial P}{R\partial\theta}\right)+[R\omega\tau^H_{R\theta}-W(\tau_{Sz}+\tau_{Rz})-U(\tau_{S\theta}+\tau_{R\theta})] \tag{4}$$

These equations are generally integrated using a finite volume discretization and a segregated approach borrowed from computational fluid dynamics [5]; for strong compressible flow, the numerical approach is based on a density upwind procedure and was previously described in Ref. [6].

Table 1 Effects of compressibility for non—viscous and viscous flows

	Non-viscous nozzle flow	Viscous flow in a parallel channel
Accelerating flow	Decreasing flow section, U_m, $M<1$, $M=1$	Friction force, U_m, $M<1$, $M=1$
Decelerating flow	Decreasing flow section, U_m, $M>1$, $M=1$	Friction force, U_m, $M>1$, $M=1$

A peculiar problem arises for imposing the exit boundary conditions for choked flow. If the flow in the exit section is subsonic $M_{\text{exit}}<1$ then the corresponding pressure has its downstream imposed value, $P_{\text{exit}}=P_{\text{downstream}}$. (It is supposed that there is no pressure recovery effect in the exit section.) If the flow in the exit section is choked, $M_{\text{exit}}=1$, then the corresponding pressure is no longer linked to the imposed downstream pressure. The exit pressure must be then extrapolated from pressure values in the vicinity of the exit section and inside the seal

$$P_{\text{exit}}=\begin{cases}P_{\text{downstream}}, & M_{\text{exit}}<1\\ \text{EXTRAPOL}(P_{\text{int}}), & M_{\text{exit}}=1(\text{or } M_{\text{exit}}\geqslant 1)\end{cases} \tag{5}$$

The value EXTRAPOL(P_{int}) is larger than $P_{\text{downstream}}$. From the mathematical standpoint, this *discontinuity* in the exit pressure values corresponds to a singularity enlightened by the simplified one-dimensional bulk-flow equation in a parallel channel for adiabatic flow ([1], pp. 136–137),

$$\frac{1-M^2}{\kappa M^4\left(1+\frac{\kappa-1}{2}M^2\right)}\frac{dM^2}{dx}=\frac{4f}{D_h} \tag{6}$$

It is clear from Eq. (6) that if $M=1$ then $dM/dx\rightarrow\pm\infty$ in order to have a finite friction coefficient f. This peculiar behavior of the bulk-flow equations in the exit section made impossible a numerical solution for exactly choked flow conditions. This difficulty is now overridden by using artificial continuous pressure boundary conditions in the exit section

$$P_{\text{exit}}=\begin{cases}P_{\text{exit }0}=P_{\text{downstream}}, & M_{\text{exit}}<M_0=0.95\\ P_{\text{exit }0}+\dfrac{P_{\text{exit }1}-P_{\text{exit }0}}{1-M_0}(M_{\text{exit}}-M_0), & M_0<M_{\text{exit}}<1\\ P_{\text{exit }1}=\text{EXTRAPOL}(P_{\text{int}}), & M_{\text{exit}}=1\ (\text{or } M_{\text{exit}}\geqslant 1)\end{cases} \tag{7}$$

Validation of the Numerical Approach

This new numerical approach was validated by comparisons to analytical results of the isothermal flow in a parallel channel with closely spaced walls ([7], pp. 404–407)

$$\frac{1}{2}(1-\bar{P}^2)+(M^*_{\text{inlet}})^2\,ln\,\bar{P}=\chi M^*_{\text{inlet}}\bar{x}$$

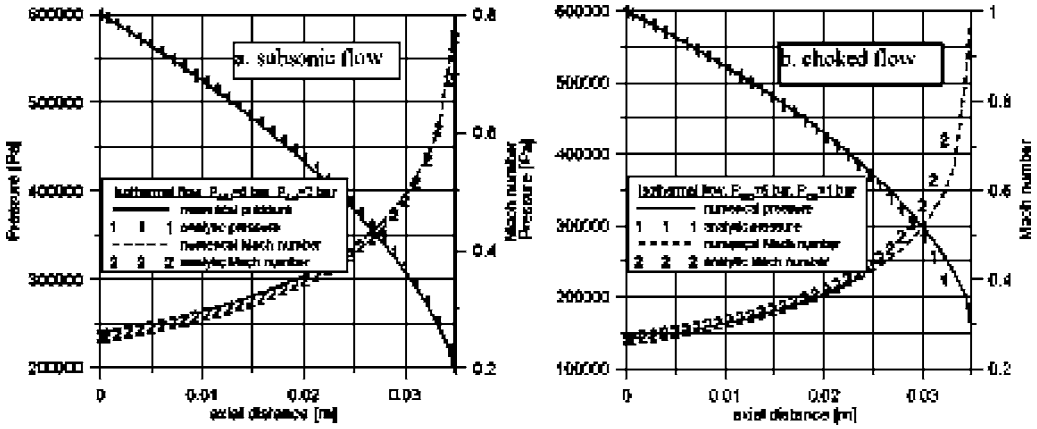

Fig. 2 Pressure and Mach number variations in a parallel channel

$$\bar{P} = \frac{P}{P_{\text{inlet}}} \quad \bar{x} = \frac{x}{L} \quad \chi = \frac{12\mu L}{C^2\sqrt{P_{\text{inlet}}\rho_{\text{inlet}}}} \tag{8}$$

Equation (8) is similar to (7) but for isothermal flow conditions. Indeed, the isothermal inlet Mach number can be expressed in function of the mass flow rate in the channel

$$M^*_{\text{inlet}} = \frac{\dot{m}}{C\sqrt{P_{\text{inlet}}\rho_{\text{inlet}}}}, \quad \dot{m} = \rho VC \tag{9}$$

For a given pressure ratio between the exit and the inlet section $\bar{P}_{\text{exit}} = P_{\text{exit}}/P_{\text{inlet}}$ and for $\bar{x}=1$, Eq. (8) can be regarded as a second-order algebraic equation for M^*_{inlet} and the mass flow rate $\dot{m}$. This second-order algebraic equation has real solutions only for $\bar{P}_{\text{exit}} > M^*_{\text{inlet}}$; for values $\bar{P}_{\text{exit}} < M^*_{\text{inlet}}$, the pressure derivative at the exit section has a singular behavior indicating the presence of a choked flow.[1].

Figures 2(*a*) and 2(*b*) depict the variation of the pressure and of the Mach number along a parallel channel ($\mu = 1.8 \times 10^{-5}$ Pa s, $L=35$ mm, $C=50$ μm, $T_{\text{inlet}}=25\,^{\circ}$C) for the same inlet pressure and two different downstream pressures. On Figure 2(*a*) the flow in the exit section is subsonic and the imposed downstream pressure of 2 bar is equal to the calculated exit pressure. The numerical results are identical to the analytical ones. The results depicted on Fig. 2(*b*) show a choked flow for an imposed downstream pressure of 1 bar. In this case, the calculated exit pressure is estimated by extrapolating inner values and is larger than the imposed downstream pressure. Because of the regularization of the pressure described by Eq. (7), the numeric solution cannot accurately match the analytical results in the vicinity of the exit section. Moreover, due to the singular behavior underlined by Eq. (6), the analytic solution cannot be calculated in the close vicinity of the sonic exit.

Figures 3 and 4 show the typical behavior of a choked flow in a parallel channel. It is to be underlined that the classical treatment of gas lubrication problems is to consider that the flow is isothermal. Figure 3 depicts the mass flow rate calculated for isothermal and nonisothermal (adiabatic walls) conditions as well as the analytic solution obtained for isothermal flow. The effect of flow choking (constant mass flow rate when lowering the downstream pressure) is clearly depicted by the two numeric results and by the analytic solution. In spite of this expected result, there is a very good agreement between the isothermal numerically calculated results and the analytic values. Results depicted on Fig. 3 prove the correct use of the pressure regularization relation (7). Moreover, a somewhat unexpected result is the difference between the isothermal and the nonisothermal numerical solutions. It is common practice in gas lubrication to consider the flow as being isothermal. This is not correct for pressure-driven conditions where the flow acceleration is accompanied by an important decrease of the temperature. Qualitatively, the isothermal and the nonisothermal results show the same behavior, but the quantitative results can be different.

Figure 4 depicts the exit pressure and Mach number when lowering the downstream pressure for a constant inlet pressure of 6 bar. One can see that as long as the flow is subsonic, the exit pressure is equal to the downstream value. The flow becomes

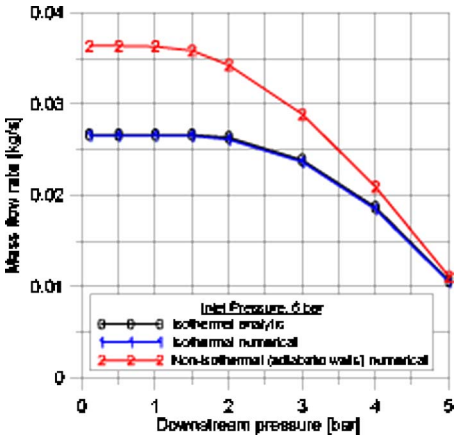

Fig. 3 Mass flow rate in a parallel channel

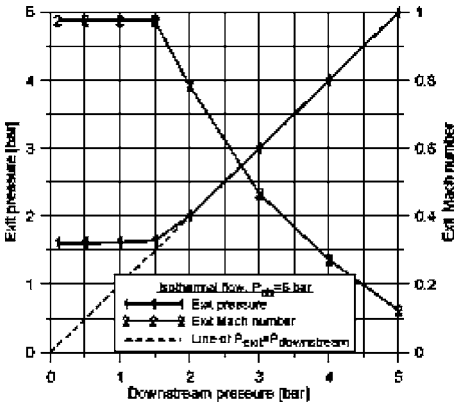

Fig. 4 Exit pressure and Mach number in a parallel channel

[1]By deriving Eq. (8), one obtains $d\bar{P}/d\bar{x} = (\chi M^*_{\text{inlet}}\bar{P})/[(M^*_{\text{inlet}})^2 - \bar{P}^2]$.

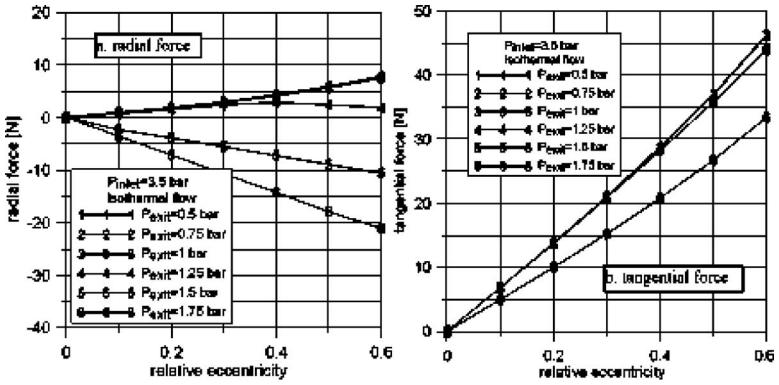

Fig. 5 Forces in an annular seal

choked for a value of the downstream pressure of 1.75–2 bars. For lower downstream pressures, the exit pressure has a constant value and $M_{exit}=1$, showing the usual behavior of a choked flow.

Static Analysis of an Annular Seal: Lomakin Effect

Figures 5(*a*) and 5(*b*) depict the radial and tangential forces in an annular seal with increasing eccentricity. The geometric data and working conditions of the seal are $L=35$ mm, $R=38.25$ mm $C=200$ μm, $\omega=2576$ rad/s, $\xi_{inlet}=0.1$ and $\xi_{exit}=1$ (no exit pressure recovery). The feeding temperature was $T_{inlet}=25\,^{\circ}$C, and the corresponding properties of the air were $\rho=1.225$ kg/m^3 and $\mu=1.8\times10^{-5}$ Pa s. The upstream pressure was held constant $P_{upstream}=3.5$ bar, whereas the downstream pressure was varied between 0.5 bar and 1.75 bar (pressure ratios between 0.143 and 0.5). For large downstream pressures, the exit flow is subsonic, whereas for the lower ones, the exit section is choked. For a subsonic exit flow, when $P_{exit}\geqslant 1.5$ bar the values of the radial force with increasing eccentricity are negative. This is the well-known centering Lomakin effect of annular seals. The physics of this effect as it is encountered in an incompressible or mildly compressible annular seal are depicted in Fig. 6. The Lomakin effect is responsible for the static stability. As any hydrostatic system, an annular seal is statically stable if its natural tendency is to cancel any eccentricity perturbation. It then means that the radial force arising from an increasing eccentricity must be of opposite sign (negative). For a choked flow ($P_{exit}<1.5$ bar), the values of the radial force depicted in Fig. 5(*a*) have positive values, which show a tendency to increase the eccentricity perturbation. The annular seal is then *statically unstable*. In order to explain this peculiar behavior of the radial force, one must analyze the pressure variation along the lines of minimum and maximum film thickness of the annular seal. Figure 7(*a*) depicts these two pressure variations compared to the pressure along the centered annular seal for the case of subsonic flow exit ($P_{exit}=P_{downstream}=1.75$ bar). The flow is accelerated from almost zero velocity in the upstream chamber to a low compressible velocity in the inlet section. This acceleration is governed by inertia effects, producing a pressure drop that can be described by the Bernoulli equation, $P_{upstream}=P_{inlet}+(1+\xi_{inlet})\rho W_{inlet}^2/2$. (Generally, the flow in the inlet section of the seal is incompressible, and the original Bernoulli equation can be used.)

The pressure variation is not different from the one depicted in Fig. 6. Compared to the case of the centered annual seal, the inlet pressure drop is smaller in the minimum film thickness section and higher in the vicinity of the maximum one. The fact that close to the minimum film thickness the pressure drop is smallest shows that the axial velocity also has the lowest value. Similarly, the axial velocity is largest in the vicinity of the maximum film thickness.

Figure 7(*b*) depicts how the compressible flow is then accelerated toward the exit section due to the friction forces in the annular seal. For a high downstream pressure, the flow is subsonic in the exit section and the pressure along the minimum film thickness line is always larger than the one along the maximum film thickness ($P_{(-1-)}$ and $P_{(-2-)}$ in Fig. 7(*a*)). This behavior explains the classical centering Lomakin effect and the static stability of the annular seal that can be roughly described as

$$P_{(-1-)}-P_{(-2-)}=\underbrace{(P_{(-1-)}-P_{(-0-)})}_{>0}-\underbrace{(P_{(-0-)}-P_{(-2-)})}_{>0} \tag{10}$$

Figures 8(*a*) and 8(*b*) depict the pressure and the Mach number variations along the seal when the downstream pressure is low and

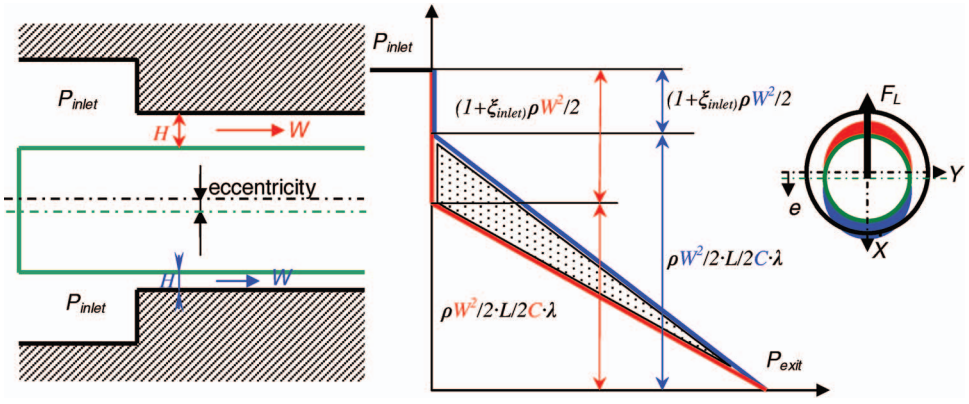

Fig. 6 Centering Lomakin effect for an incompressible flow regime

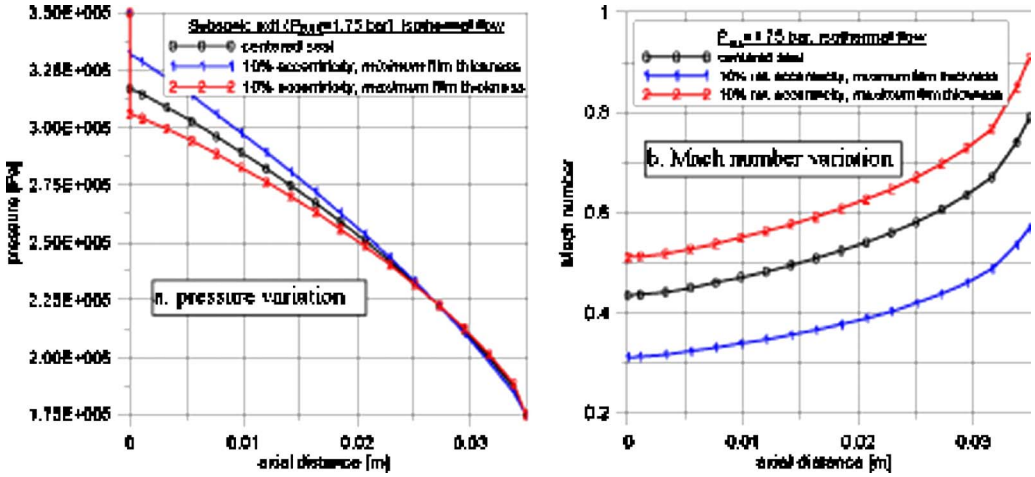

Fig. 7 Pressure and Mach number variation for a subsonic exit

the exit section is choked. Figures 9(*a*) and 9(*b*) depict the contours of the Mach number inside the unwrapped seal for the same cases; it can be seen that the exit Mach number is sonic ($M_{\text{exit}}=1$) in the minimum film thickness as well as in the maximum film thickness section. Figures 8(*b*) and 9 show that the inlet flow is accelerated at different rates toward the same Mach number in the exit section. The acceleration of the flow is higher along the line of minimum film thickness than along the line of maximum film thickness. This leads to a negative contribution of $P_{(-1-)}$-$P_{(-0-)}$, and for high compressible regimes, even $P_{(-0-)}$-$P_{(-2-)}$ can become negative. In this case, the resulting force will have the same sign as the eccentricity and the Lomakin effect is negative. The annular seal can be statically unstable if the exit flow is choked.

Figure 5(*a*) depicts that for high eccentricities and for $P_{\text{exit}}=1.25$ bar the slope of the radial force becomes negative. This means that the static stiffness has negative values and the effect of the choked exit section is not dominant anymore. Indeed, Fig. 10 shows that for high eccentricities the exit section is not completely choked and subsonic flow conditions appear in the vicinity of the minimum film thickness section.

These conclusions were obtained for isothermal flow. It was shown that an accelerating high compressible flow cannot be considered as being isothermal because it naturally lowers its temperature. The results obtained for nonisothermal compressible flow with adiabatic walls are not presented for brevity, but they show the same negative Lomakin effect and static instability of choked annular seals.

Summary and Conclusions

The paper presents the numerical treatment of choked flow in parallel channels and annular seals. Up to now this problem was unsolved due to the singularity accompanying these flow conditions in the exit section. The numerical analysis then showed that under exit choked flow conditions annular seals can be statically unstable. This means that the radial force arising in a choked annular seal tends to increase an eccentricity perturbation. This is opposite to the classical Lomakin centering effect but is not surprising. Indeed, the Lomakin effect was enlightened for incompressible annular seals, and it was shown in this paper that the effect prevails under weak or mild compressible flow conditions leading to a subsonic exit section. It is only under choked flow conditions in the exit section (sonic flow) that the annular seal can become statically unstable. Nevertheless, Fig. 5(*a*) shows that the absolute values of the negative static stiffness are lower than the values of the static stiffness obtained when the seal is statically stable.

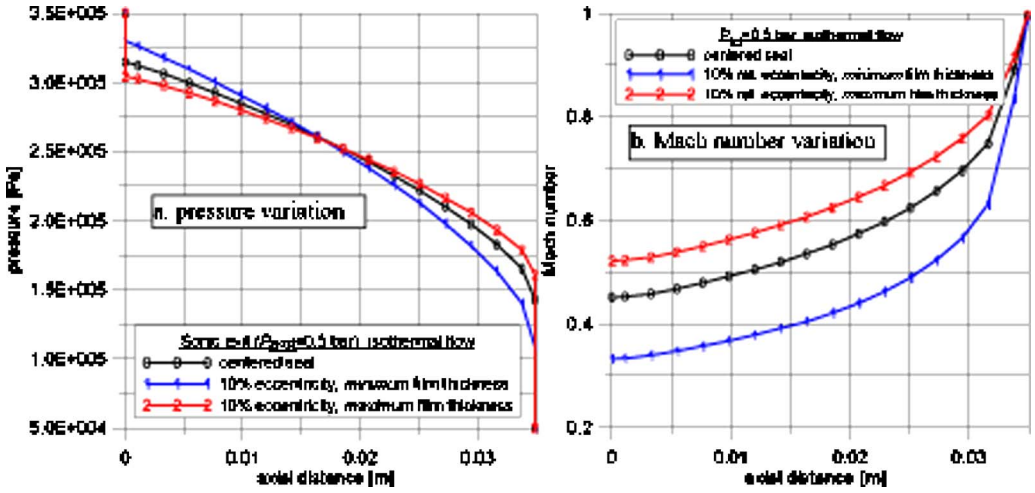

Fig. 8 Pressure and Mach number variation for a sonic exit

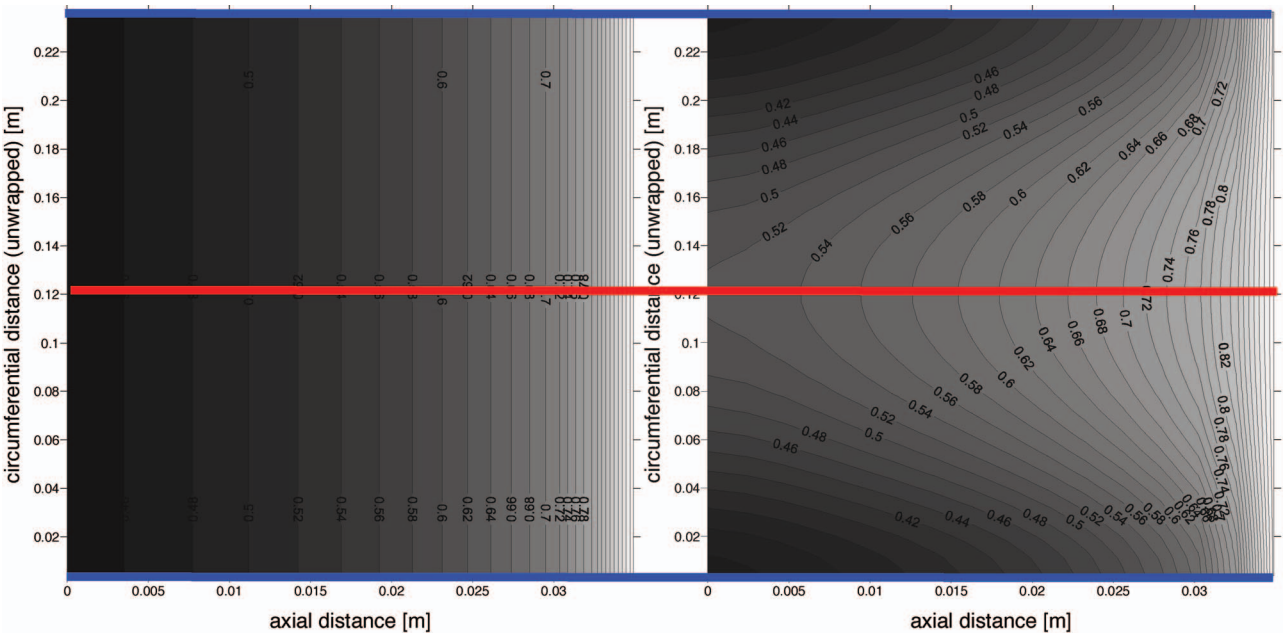

Fig. 9 Mach number variation in the unwrapped annular seal for a choked exit section (blue line: minimum film section; red line: maximum film section)

Nomenclature

C = clearance (m)
c_p = specific heat (J/kg/K)
D_h = hydraulic diameter (m)
$e_{X,Y}$ = static eccentricity (m)
f = friction coefficient
H = film thickness (m)
M = adiabatic Mach number, $M=V/\sqrt{\kappa P/\rho}$
M^* = isothermal Mach number, $M^*=V/\sqrt{P/\rho}$
$\dot{m}$ = mass flow rate (Kg/m/s)
L = characteristic length (m)
P = pressure (Pa)
$\dot{q}$ = wall heat flux, $\dot{q}_i=(k\partial T/\partial y)_i$, $i=R,S$
R = rotor (journal) radius (m)
T = temperature (K)
U = circumferential velocity (m/s)
V = resultant velocity (m/s)
W = axial velocity (m/s)
$x=R\theta$ = circumferential direction
z = axial direction
ε = relative eccentricity, $\varepsilon_{X,Y}=e_{X,Y}/H$
κ = ratio of specific heats (1.4 for air)

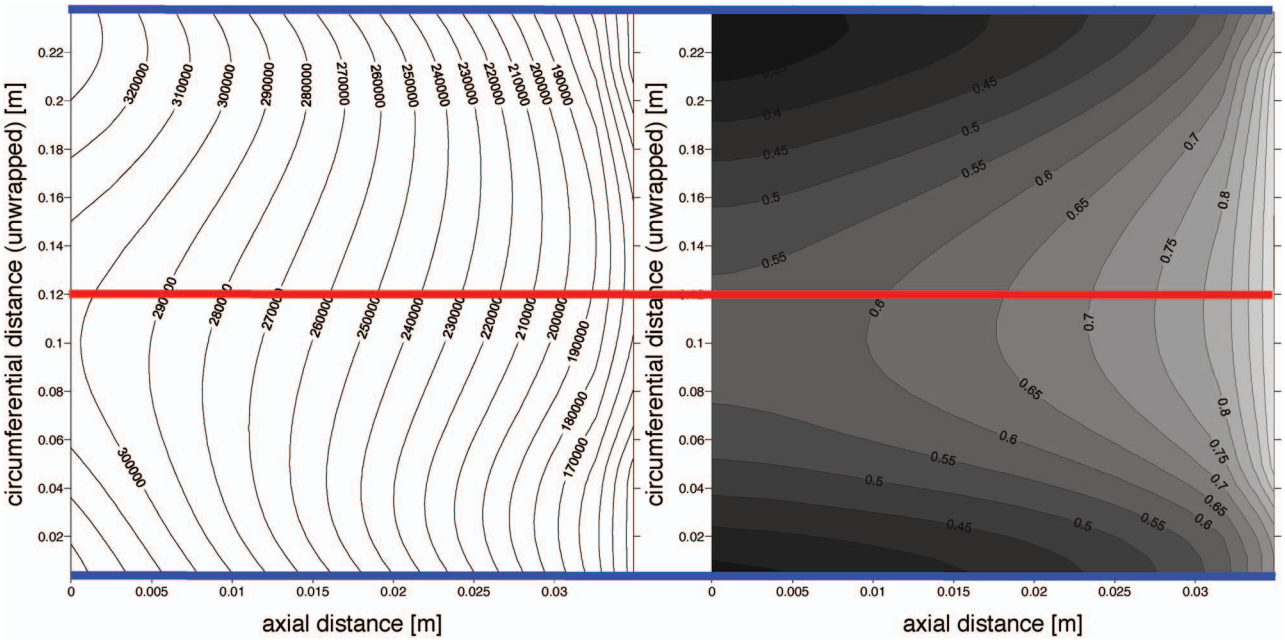

Fig. 10 Pressure and Mach number variation in the unwrapped annular seal for P_{exit}=1.25 bar and ε_X=0.6 (blue line: minimum film section; red line: maximum film section)

ξ = concentrated inertia coefficient
θ = angular coordinate (rad)
μ = dynamic viscosity (Pa s)
ρ = density (kg/m^3)
τ = shear stress (N/m^2)
ω = rotation speed (rad/s)
λ = linear pressure drop

Subscript

R, S = rotor, stator

References

[1] Carafoli, E., and Constantinescu, V. N., 1984, *Dinamica Fluidelor Compresibile*, Editura Academiei, Bucharest, Romania.

[2] Alexander, C. R., Childs, D. W., and Yang, Z., 1995, "Theory Versus Experiment for the Rotordynamic Characteristics of a Smooth Annular Gas Seal at Eccentric Positions," ASME J. Tribol., **117**, pp. 148–152.

[3] Ransom, D. L., and San Andrés, L., 1999, "Identification of Force Coefficients From a Gas Annular Seal—Effect of Transition Flow Regime to Turbulence," Tribol. Int., **42**(3), pp. 487–494.

[4] Yang, Z., San Andrés, L., and Childs, D. W., 1993, "Thermal Effects in Cryogenic Liquid Annular Seals—Part I: Theory and Approximate Solution," ASME J. Tribol., **115**, pp. 267–276.

[5] Ferziger, J. H., and Peric, M., 1996, *Computational Methods for Fluid Dynamics*, Springer-Verlag, Berlin.

[6] Arghir, M., and Frêne, J., 2001, "Numerical Solution of Lubrication's Compressible Bulk Flow Equations: Applications to Annular Gas Seals Analysis," ASME Paper No. 2001-GT-117.

[7] Constantinescu, V. N., 1995, *Laminar Viscous Flow*, Springer-Verlag, Berlin.

A Virtual Tool for Prediction of Turbocharger Nonlinear Dynamic Response: Validation Against Test Data

Luis San Andrés
e-mail: lsanandres@mengr.tamu.edu

Juan Carlos Rivadeneira

Mechanical Engineering Department,
Texas A&M University,
College Station, TX 77843

Kostandin Gjika

Christopher Groves

Honeywell Turbo Technologies,
88155 Thaon les,
Vosges, France

Gerry LaRue
Honeywell Turbo Technologies,
Torrance, CA 90505

Advances on the modeling of nonlinear rotor-bearing models for prediction of the dynamic shaft response of automotive turbochargers (TCs) supported on floating ring bearings (FRBs) are presented. Comprehensive test data for a TC unit operating at a top speed of 65 krpm *serves to validate the model predictions. The static forced performance of the support FRBs considers lubricant thermal effects, thermal expansion of the shaft and bearings, and entrance pressure losses due to centrifugal flow effects. The bearing analysis also yields linearized rotordynamic force coefficients for the inner and outer lubricant films. These coefficients are used with the rotor model to predict the synchronous response to imbalance and the system natural frequencies and stability. A method renders an accurate estimation of the test rotor imbalance by using the actual vibration measurements and influence coefficients derived from predictions using linearized bearing force coefficients. Predicted ring rotational speeds, operating radial clearances, and lubricant viscosities for the inner and outer films are the main input to the nonlinear time transient analysis. The nonlinear response model predicts the total shaft motion, with fast Fourier transforms showing the synchronous response, and amplitudes and whirl frequencies of subsynchronous motions. The predicted synchronous amplitudes are in good agreement with the measurements, in particular at high shaft speeds. The nonlinear analysis predicts multiple frequency subsynchronous motions for speeds ranging from* 10 krpm to 55 krpm *(maximum speed* 70 krpm*), with amplitudes and frequencies that correlate well with the test data. The comparisons validate the comprehensive rotor-bearings model whose ultimate aim is to save TC design time and accelerate product development.* [DOI: 10.1115/1.2436573]

Introduction

In a turbocharger (TC), hot exhaust gases from the internal combustion (IC) engine spin a turbine wheel connected through a shaft to a compressor wheel, thus providing additional air for the combustion process. TCs are common in diesel engines for automobiles, trucks and marine applications. Diesel engines have lower power-to-weight ratio compared to gasoline engines; thus, turbocharging becomes the most suitable way to improve their performance [1].

Figure 1 shows an assembly cut of a typical TC unit. Due to low production costs and ease of machining, TC assemblies are commonly supported on engine-oil lubricated floating ring bearings (FRBs) or semi-floating ring bearings (SFRBs), which are prone to show one or more subsynchronous motions of large amplitude over a wide operating speed range [2–8].

A typical FRB comprises of a cylindrical sleeve between the rotor and the bearing housing, thus creating two lubricant films. In operation, the inner and outer film clearances along with the lubricant viscosity within each film largely determine the FRB forced performance. Viscous shear in the inner oil film causes the rotation of the floating ring while shear in the outer oil film retards its motion. The floating ring spins at a fraction of the rotor velocity, thus showing reduced overall power losses when compared to a plain journal bearing [1,3].

The shaft subsynchronous whirl motions, caused by the shearing of the inner and outer oil films within each bearing, generally reach a limit cycle which enables the continuous operation of the TC [8]. Linear stability analyses [4–7] show that the threshold speed of instability of rotors mounted in FRBs is sensitive to small changes in the outer film clearance. The speed range of stable operation increases when the outer film clearance is reduced, albeit at the expense of larger drag power losses. In a SFRB configuration the floating ring is locked by a pin that allows it to precess but not to rotate, i.e. the outer film acts as a squeeze film damper.

The adoption of an isothermal flow model to predict the rotational speed in a FRB yields poor results with respect to test data. Isothermal bearing flow predictions agree with test data only at low shaft speeds, where thermal effects are not of great importance [8]. As the shaft speed increases, predicted ring speeds are much higher than measured ones due to significant variations in FRB film clearances and effective oil viscosities.

Turbocharger rotordynamic design followed, until recently, costly test stand iteration due to the lack of accurate and efficient predictive nonlinear tools. Current research aims to develop test validated rotordynamic models coupled to realistic bearing force models [9–14]. The software tool emulates a virtual laboratory, effectively aiding to design better TC products with increased reliability in a shorter cycle time.

San Andrés and Kerth [9] present a comprehensive thin film flow model for prediction of FRB forced response, including a lumped-parameter thermal energy balance determining the effective lubricant viscosity and thermal growth of the rotor, bearing, and floating ring. The predictions for ring speed show a reasonable correlation to test data obtained for a TC operating with a thin lubricant and for various feed pressures and inlet tempera-

Contributed by the International Gas Turbine Institute of ASME for publication in the JOURNAL OF ENGINEERING FOR GAS TURBINES AND POWER. Manuscript received July 19, 2006; final manuscript received July 20, 2006. Review conducted by Dilip R. Ballal. Paper presented at the ASME Turbo Expo 2006: Land, Sea and Air, (GT2006), Barcelona, Spain, May 8–11, 2006. Paper No. GT2006-90873.

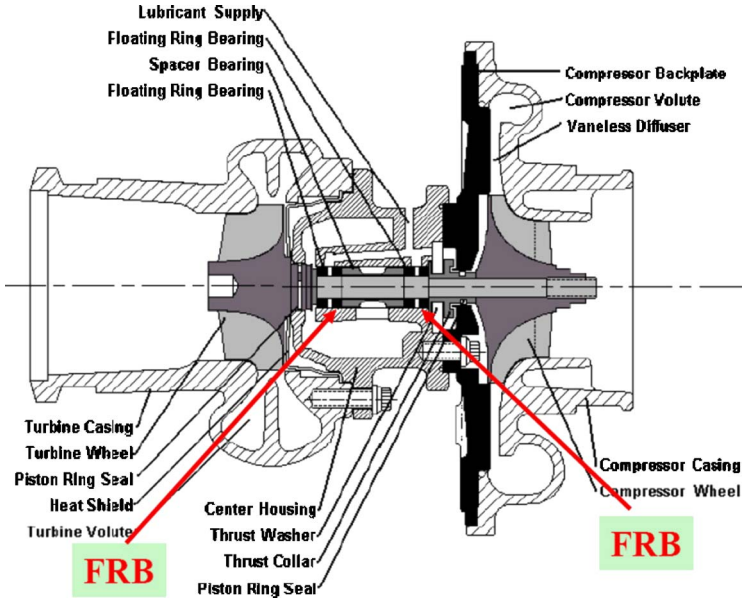

Fig. 1 Schematic view of an automotive turbocharger supported on floating ring bearings

tures. In Ref. [10], a nonlinear rotordynamics program integrates the FRB model and predicts well the frequency content of the measured response, although the corresponding amplitudes of rotor motion are too large. The nonlinear model and test data demonstrate the persistence of two subsynchronous whirl frequencies at approximately 50% of the ring speed and 50% of the ring and shaft speeds.

Kerth [11] reports shaft motions measured in a TC supported on FRBs and shows detailed comparisons to predictions from the bearing and rotordynamic models, respectively [9,10]. San Andrés et al. [12] present predictions for a TC rotor supported on SFRBs and comparisons to shaft motion test data collected at the compressor end to speeds as high as 240 krpm. The experimental and predicted results show that the synchronous (1*X*) motions are but a small fraction of the total shaft motion, with large subsynchronous motions being persistent throughout the entire operating speed range. Predictions of synchronous amplitudes, derived from the linear and nonlinear rotor-bearing models, are slightly smaller relative to the test amplitudes, the discrepancy being attributed to the uncertainty in the actual imbalance mass distribution and its location. The nonlinear predictions for subsynchronous whirl frequencies agree well with measurements, evidencing that the (linearly unstable) shaft motions correspond to excitations of the rotor conical mode and its harmonics. In Ref. [13], more successful correlations of nonlinear rotordynamics predictions to test data for a different unit TC supported on FRBs further validate the models and open the path for the implementation of the software as a virtual design tool by a major TC manufacturer.

This paper presents further progress on the validation, against test data, of the linear and nonlinear rotor-bearing models in Refs. [9,10]. Significant improvements in predicting TC shaft motions are due to the proper prediction of the operating (inner and outer) film clearances, estimation of the test rotor imbalance distribution, and characterization of the side loads induced by lubricant feed pressure. The benchmarking lends credence to the validity of the integrated computational model.

TC Rotor Model and Free–Free Modes

Figure 2 depicts a photograph of the TC rotor supported on FRBs, and Fig. 3 shows the rotordynamic structural model comprising of 42 finite elements for the rotor, and two elements for each floating ring bearing. Equivalent imbalance masses are noted at the center of gravity (CG) of the compressor and turbine wheels.

Figure 4 presents the measured and predicted first two free–free mode shapes for the TC rotor. The measurements were obtained with the rotor at ambient conditions. The predicted and measured first and second natural frequencies equal 688 Hz and 640 Hz, and 2190 Hz and 2016 Hz, respectively. The good correlation between test and predicted mode shapes is essential to validate the rotor structural model.

The FRBs are modeled with an updated version of the flow model advanced in Ref. [9] and that includes centrifugal pressure losses into the inner films. The program predicts the FRB static performance parameters based on the equilibrium state for specified load and shaft speed ranges. The program also calculates FRB rotordynamic force coefficients for the inner and outer films, needed for linear stability analysis (eigenvalues) and prediction of the synchronous (1*X*) response to imbalance.

Speeds for Floating Ring Bearings

References [9,11] detail the test rig and experimental procedure, including the measurement of floating ring rotational speed using a fiber optic sensor. Shaft speed run up and coast down tests were performed to a top speed of 65 krpm. The lubricant used is commercial ISO VG 10 oil. The test matrix included three lubricant feed pressures equal to 158 kPa, 206 kPa, and 272 kPa and vari-

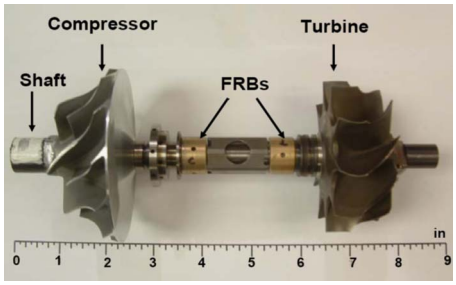

Fig. 2 Automotive turbocharger: rotor assembly and floating ring bearings (FRBs)

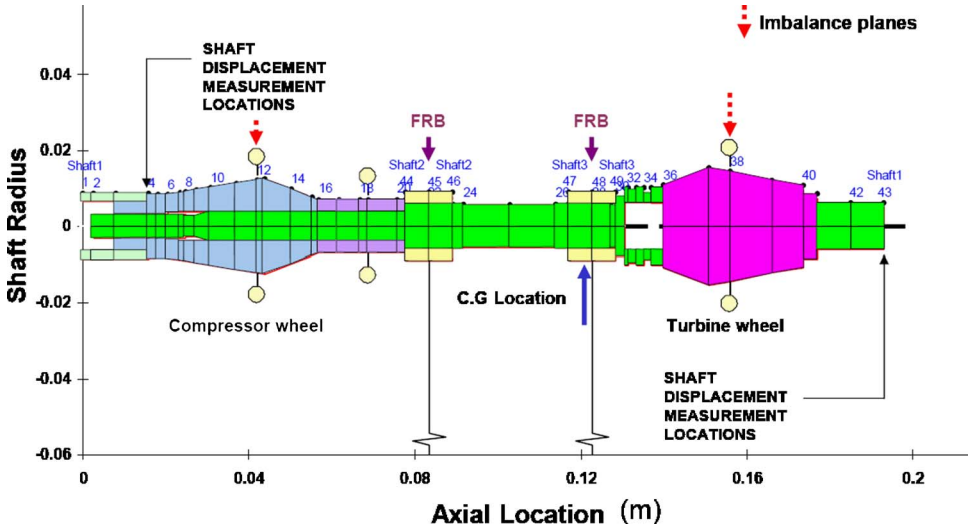

Fig. 3 Structural FE model of turbocharger rotor and floating ring bearings. Locations of shaft motion measurements and mass imbalance planes noted. (Dimensions in m).

ous inlet temperatures, 32–46°C. Pairs of orthogonally positioned eddy current sensors recorded shaft motions at the compressor and turbine ends for TC operation under cold conditions, i.e., turbine driven by shop compressed air.

Figure 5 depicts the measured and predicted ring speed ratios (ratio of ring to shaft rotational speed) for the turbine (top) and compressor (bottom) FRBs for lubricant feed pressures ranging from 158 kPa to 272 kPa (23–39 psig) and a nominal inlet temperature of 38°C. In the analysis, the shaft and casing are at the same temperature as the lubricant feed, as is appropriate for cold air operating conditions. The highest ring speed ratios, for both compressor and turbine FRBs, are measured and predicted at the lowest shaft speeds, decreasing in magnitude as the shaft speed increases. Note that, at the compressor side FRB, the ring speed ratio drops suddenly from ~40% to~30% shaft speed at 30 krpm. The turbine floating ring shows a steadier decline in its rotational speed. The experimental results show scattered points at high shaft speeds, not indicative of faulty data acquisition (DAQ) but most likely evidencing that the floating rings actually stopped spinning at the highest shaft speeds. A discussion on this issue follows later. The predicted ring speeds show little dependence on the lubricant supply pressure or inlet temperature, as is also evident in the test data. Note that the predicted ring speeds correlate poorly with the measurements at low shaft speeds.

Lubricant Exit Temperature and Viscosity

Reference [11] details the measurements of inlet lubricant flow and feed pressure. The lubricant flow splits into the two floating ring bearings and the thrust bearing. The predictions below are based on the global thermal energy balance from all components. Figure 6 shows predicted and measured lubricant exit tempera-

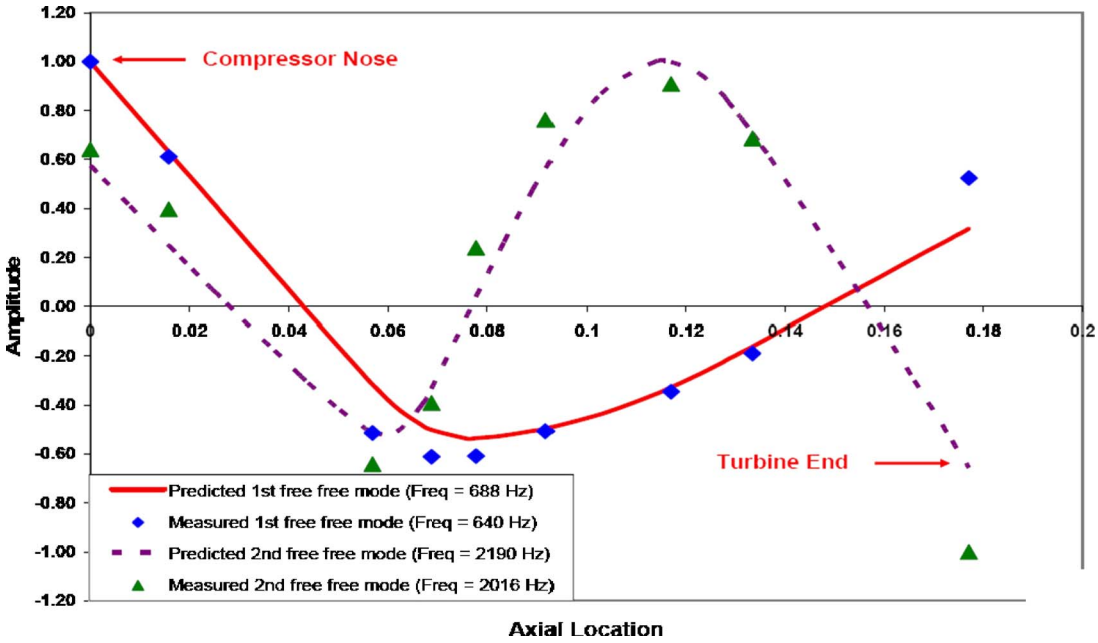

Fig. 4 Free–free mode shapes for turbocharger rotor—predictions and measurements at room temperature. (Dimensions in m).

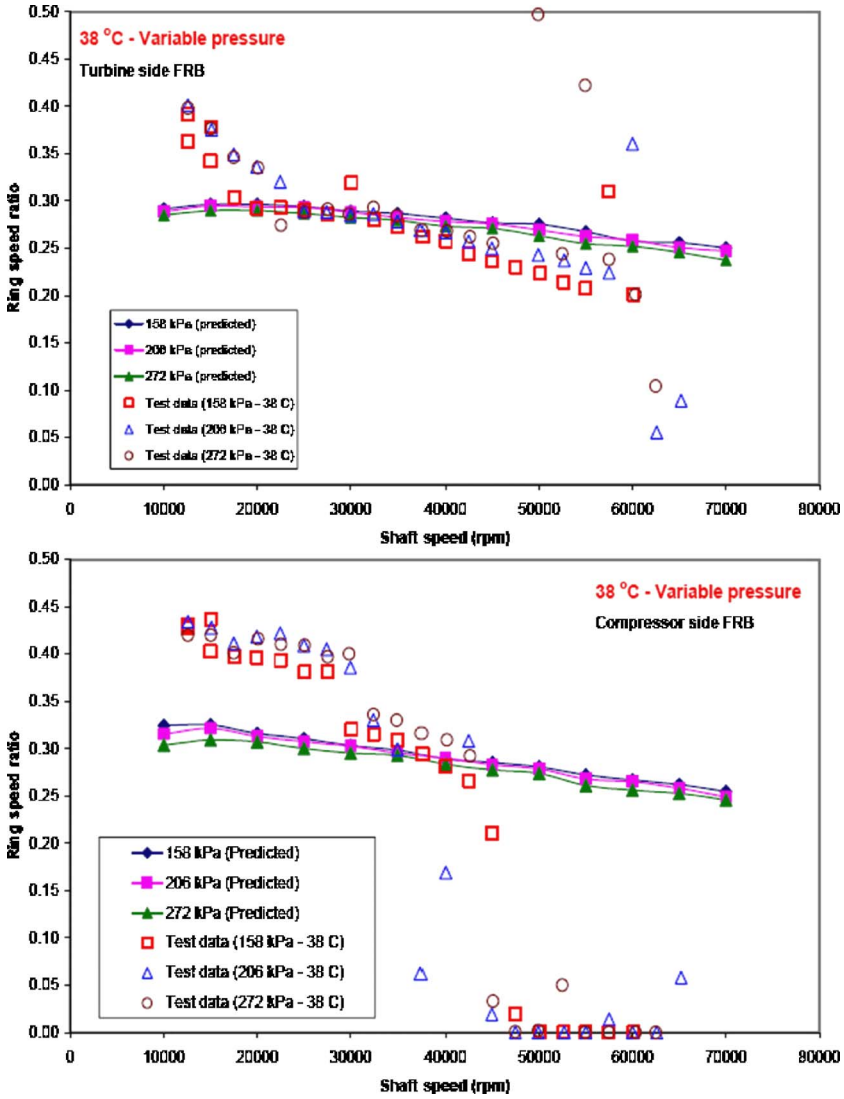

Fig. 5 Floating ring speed ratios at turbine and compressor side bearings—predictions and measurements for 38°C oil inlet temperature and increasing feed pressures

tures for tests with 206 kPa oil feed pressure and 38°C inlet temperature. The measured temperature is that of the lubricant flowing out of the TC, i.e., representative of the thermal mixing of the inner and outer film flows. The predictions, agreeing well with the test data, show a rapid increase in exit temperature as shaft speed increases (~5°C raise at the top speed of 65 krpm). The actual temperature at the discharge of the inner film is difficult to measure; however, the predictions show a larger temperature rise than that of the lubricant flow exiting the TC, and which affects the effective viscosity of the inner fluid film.

Figure 7 depicts effective lubricant viscosities for the inner and outer films of each FRB versus shaft speed. As the drag (shear) power increases with speed, the lubricant heats while flowing through the films and the oil viscosity, a function of temperature, decreases. Both compressor and turbine side FRBs show similar effective viscosities for the shaft speed range considered. In the analysis, thermal expansion of the journal, ring, and bearing housing are accounted for to predict accurate inner and outer film clearances at each operating point. The change in operating clearances is due to the heating of the lubricant flowing through the inner and outer films.

Discussion on Measured Shaft Motions

Figure 8 depicts waterfall graphs of TC shaft motion amplitudes recorded at the turbine and compressor ends. The horizontal axis shows the frequency content of the motion while the in-plane axis depicts the shaft speed. The test data correspond to a lubricant feed pressure of 206 kPa and inlet temperature of 38°C. The horizontal (X) and vertical (Y) shaft motions are similar in magnitude; thus for brevity only the motion amplitudes along the vertical direction are displayed.

The test data amplitudes are shown in dimensionless form relative to the limit of maximum physical motion at the turbine end. The waterfalls for shaft speeds ranging from 12.5 krpm to 65 krpm show multiple subsynchronous vibration components. The subsynchronous frequencies track the synchronous motions at a fraction of the shaft speed, characteristic of oil whirl in plain cylindrical bearings. Post-processing of the collected fast Fourier transform (FFT) data evidences that the largest subsynchronous amplitudes concentrate at whirl frequencies between 50% and 60% of shaft speed, thus denoting a characteristic instability of the inner film in the FRBs. Other subsynchronous

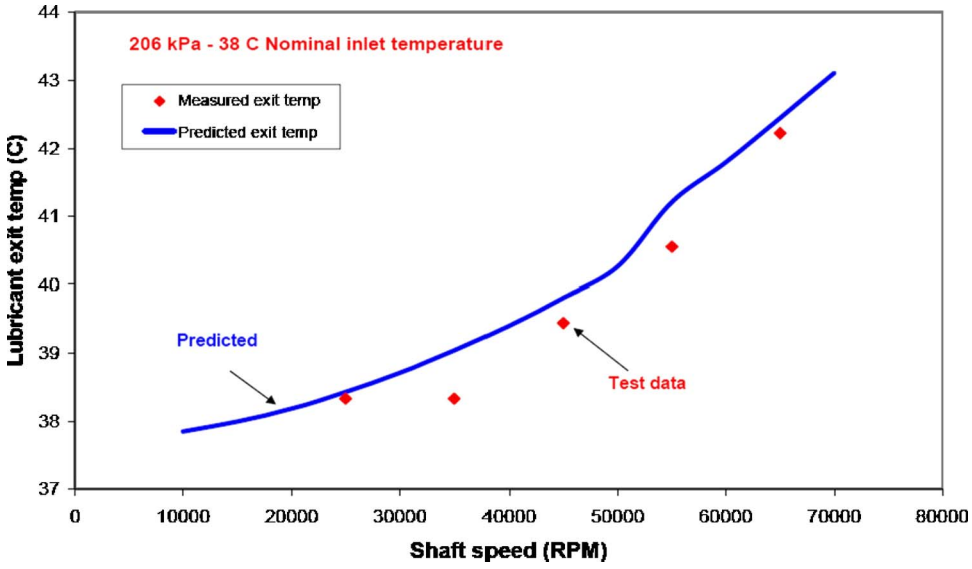

Fig. 6 Predictions and measurements of lubricant exit temperature: 38°C lubricant inlet temperature and 206 kPa feed pressure

motions of lesser amplitude appear at ~20% of shaft speed. The lower subsynchronous frequency is characteristic of the outer film instability. The synchronous (1*X*) motions are dominant in amplitude throughout the operating speed range when compared to the subsynchronous motions, except at the top speed (65 krpm) where the largest amplitude with a whirl frequency at 50% of shaft speed suddenly appears. These large motions prevented operation at higher shaft speeds. Most importantly, however, is the realization that at the top shaft speed the FRBs stopped spinning and locked, thus generating the large amplitude instability, best known as oil whip.

Comparisons of synchronous (1*X*) and subsynchronous motions for various operating conditions show that the shaft motions do not depend greatly on the lubricant supply pressure or inlet temperature. Similar conclusions were derived for tests in a TC unit supported on semi-floating ring bearings (see Ref. [12] for details).

Predictions of TC Rotor Stability and Synchronous Shaft Motions

The rotordynamic eigenvalue analysis relies on the specification of the stiffness and damping force coefficients for the inner

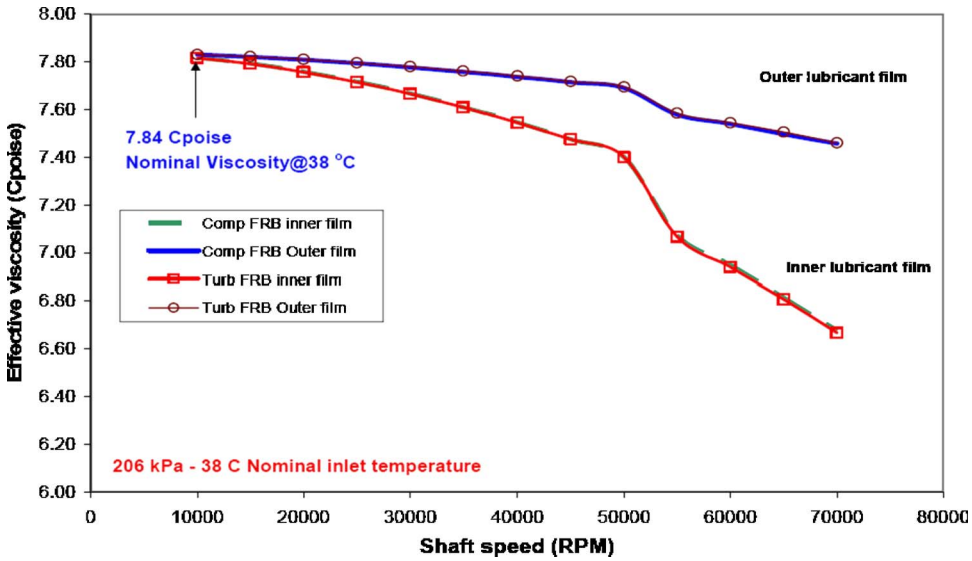

Fig. 7 Predicted effective lubricant viscosity for inner and outer films of FRBs: 38°C lubricant inlet temperature, 206 kPa supply pressure

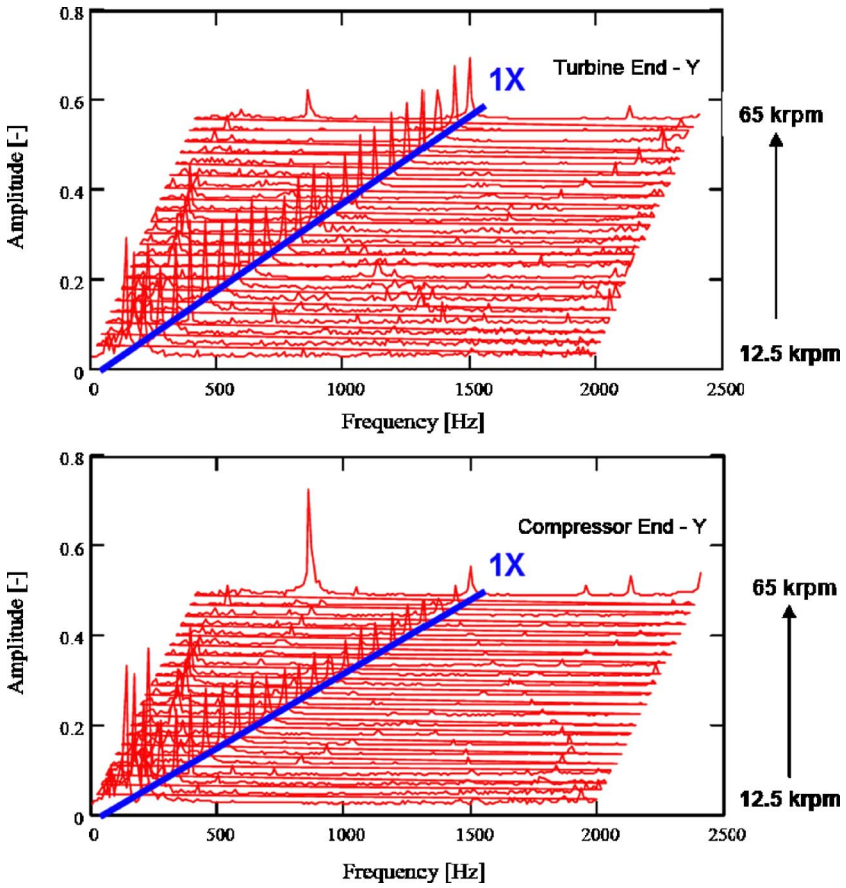

Fig. 8 Waterfall of measured shaft motions at compressor and turbine ends of TC rotor: tests at 38°C lubricant inlet temperature and 206 kPa supply pressure

and outer films at the turbine and compressor FRBs. Figure 9 depicts the predicted damped natural frequencies and mode shapes for operation with lubricant at feed pressure of 206 kPa and inlet temperature of 38°C.

The first three predicted critical speeds are at 4 krpm, 20 krpm, and 67.5 krpm, respectively. The lowest forward mode (60–90 Hz) is rigid body conical; the second mode (330 Hz) is

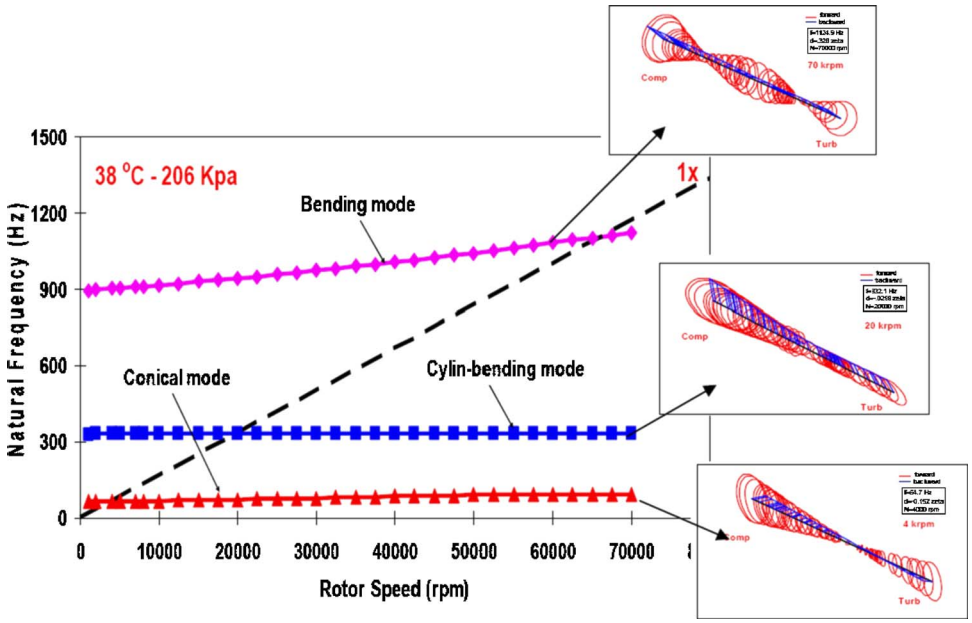

Fig. 9 Predicted damped natural frequencies and associated mode shapes: 38°C lubricant inlet temperature, 206 kPa supply pressure

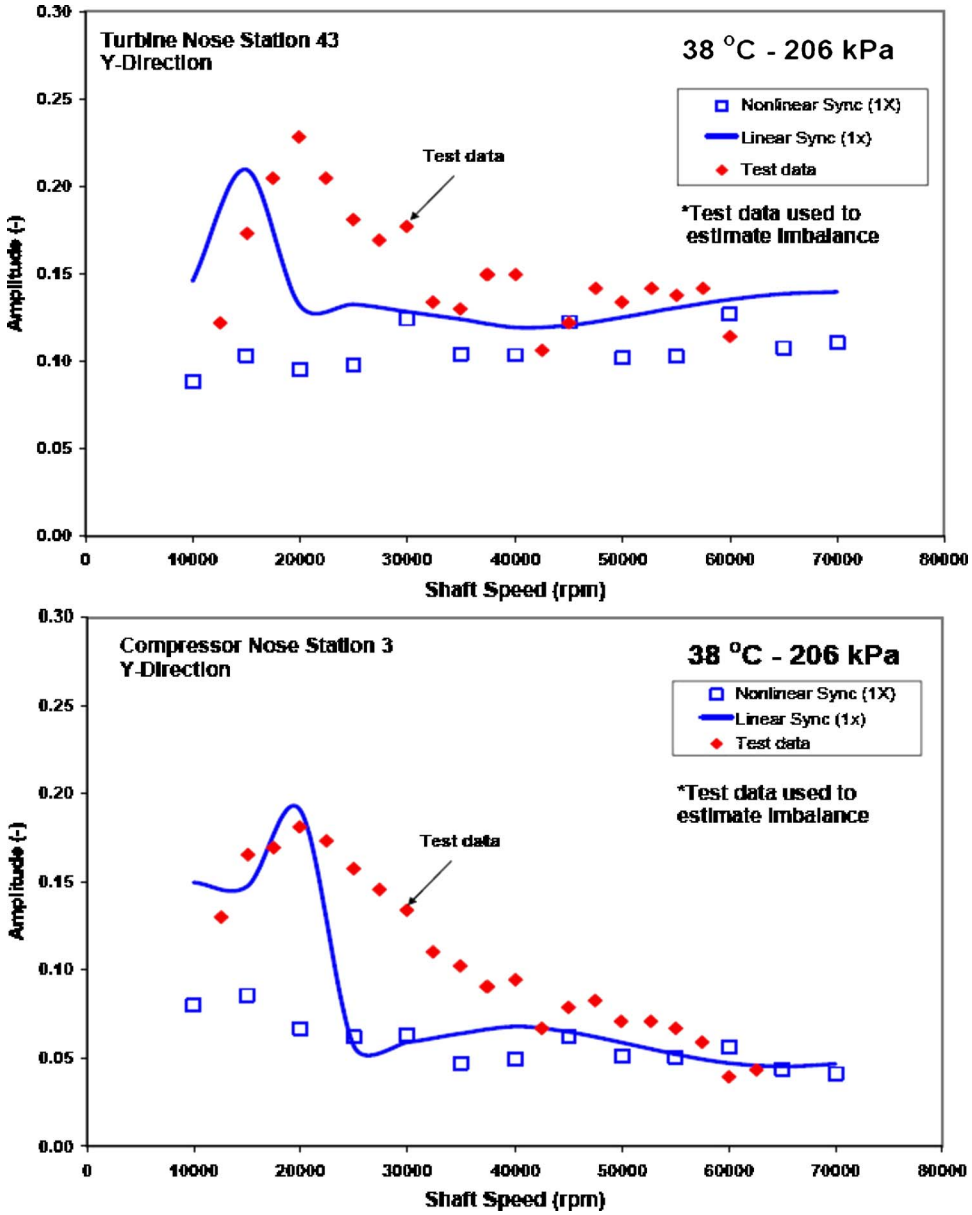

Fig. 10 Measured and predicted synchronous (1*X*) motions at the turbine and compressor ends of TC rotor: lubricant at 38°C and 206 kPa supply conditions

known as cylindrical bending; and the third is the first elastic rotor mode. The analysis predicts the rotor conical mode to be unstable (damping ratio <0) from startup, becoming stable as shaft speed increases). This mode shows a significant dependence on the lubricant feed pressure, becoming stable at lower shaft speeds (30 krpm$\rightarrow$0 krpm) as the feed pressure increases. The rotor cylindrical-bending mode is always unstable, irrespective of the lubricant feed pressure condition.

As in the experiments, shaft motion predictions—linear and nonlinear—were obtained at the compressor and turbine ends of the TC rotor. The synchronous (1*X*) response relies on the specification of the actual imbalance distribution on the rotor. The TC rotor assembly imbalance condition, when evaluated independently after the tests were completed, resulted in very poor predictions (see Ref. [11]). The two-plane imbalance was identified at a low shaft speed, not representative of the actual test conditions. Rivadeneira [14] details an ingenious method to *estimate* the TC rotor imbalance condition, as derived from the measured amplitudes at one of the high shaft speeds, and using the linear rotordynamics model to generate influence coefficients. The method is akin to a two-plane balance correction method applied to a computational model.

Figure 10 shows the amplitudes of TC synchronous motion at the turbine and compressor ends versus shaft speed. In the graphs, diamond markers represent the experimental results, square markers correspond to results from the nonlinear rotordynamics analysis, and the solid line depicts results from the linear analysis. A complete description of the predictions obtained from the nonlinear analysis follows later.

Predictions from the linear analysis show good agreement with the test data, in particular at shaft speeds below 20 krpm and greater than 40 krpm. The predicted (cylindrical-bending) critical speed agrees reasonably well with the measurements. The test data show a steady reduction of the 1*X* amplitudes as shaft speed increases. On the other hand, the *linear analysis* predictions show a sudden drop of synchronous amplitudes for shaft speeds ranging

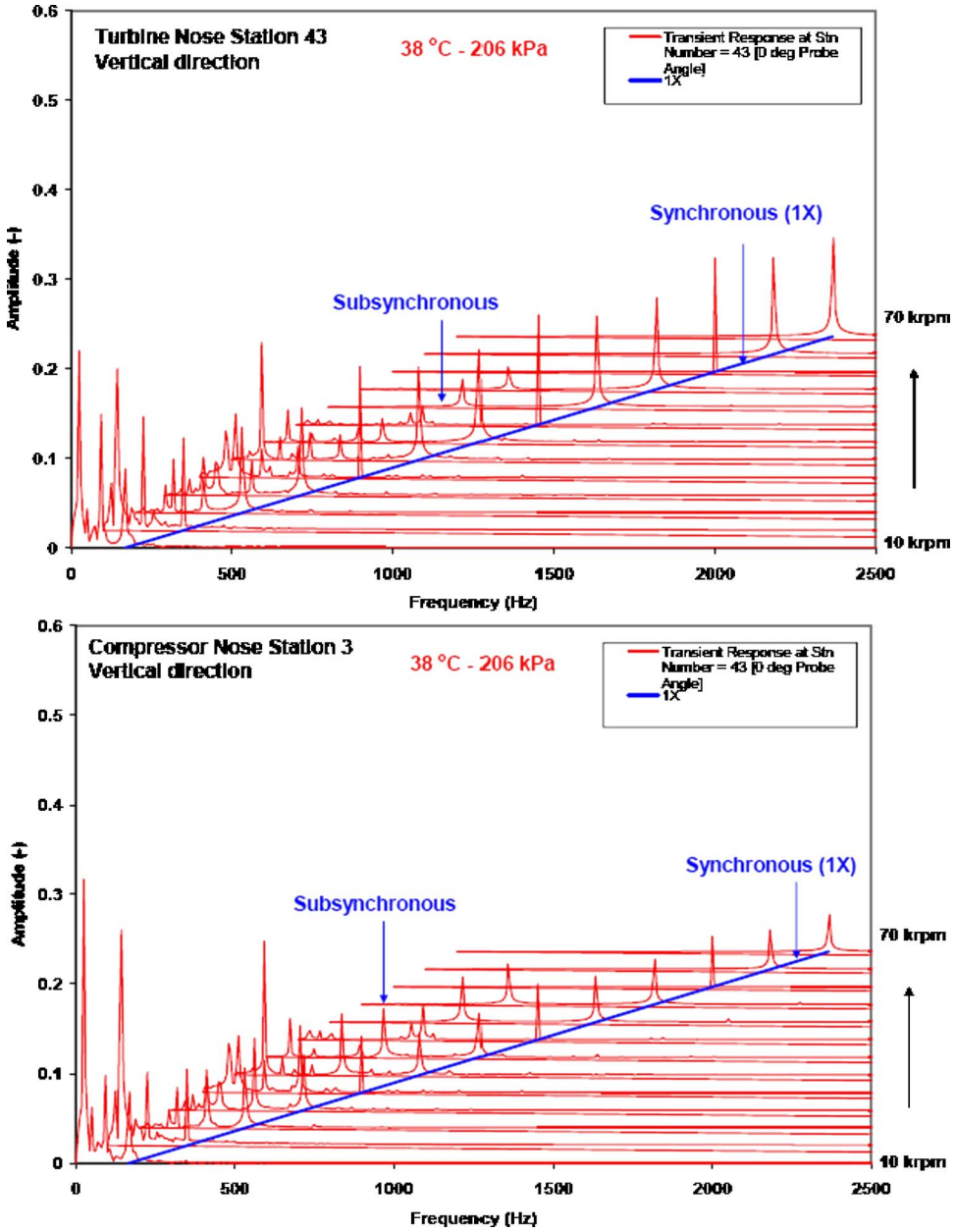

Fig. 11 Waterfall of predicted vertical shaft motions at the turbine and compressor ends of TC rotor. Lubricant at 38°C and 206 kPa supply conditions

from 20 krpm to 30 krpm, underpredicting the measurements.

Note that at the critical speed the linear analysis predictions are larger than the amplitudes predicted by the nonlinear analysis, thus evidencing less damping. The amplitudes of synchronous motion predicted by the nonlinear model do not evidence the critical speed because at low shaft speeds the total motion includes a rather large amplitude subsynchronous component that obscures the synchronous response (see Fig. 11).

Nonlinear Predictions of Shaft Motion and Comparison to Test Data

Linear rotordynamic analyses are restricted to predicting the synchronous (1*X*) response to imbalance, and not the amplitudes and multiple (subsynchronous) frequency components of shaft motion. In the transient response analysis, the equations of motion of the TC rotor system are numerically integrated with the nonlinear FRB reaction forces being calculated at each time step. The nonlinear analysis was conducted for shaft speeds ranging from 10 krpm (167 Hz) to 70 krpm (1167 Hz) and lasting a sufficiently "long time" to warrant the prediction of a quasi-steady-state motion condition. The results that follow were obtained using a total integration time of 1 s and 12,800 time steps, resulting in a time step equal to 78 μs. The maximum frequency span equals 6400 Hz with a minimum frequency step of 12.5 Hz. From the full set of transient results, only the quasi-steady-state portion is analyzed (last 1024 points=0.080 s). Below, shaft motion amplitudes along the vertical (*Y*) direction are presented relative to the physical limit of conical motion at the turbine side of the TC rotor.

Figure 11 shows the waterfall of predicted shaft amplitudes of motion as shaft speed increases. The horizontal and vertical axes display the frequencies and amplitudes of shaft motion, respectively. The nonlinear analysis predicts subsynchronous motions for shaft speeds ranging from 10 krpm to 55 krpm. The test data

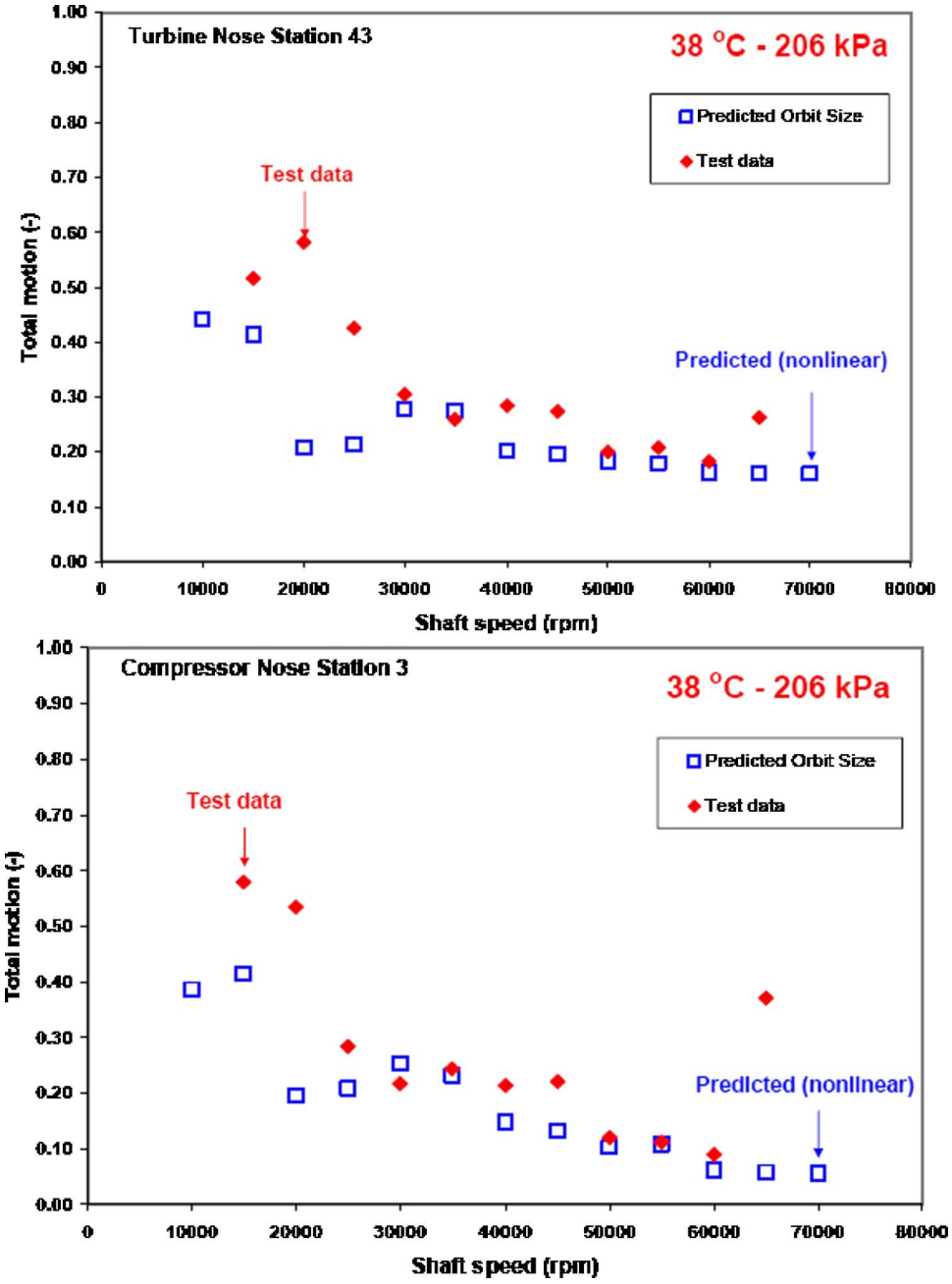

Fig. 12 Predicted and measured total shaft motion at the turbine and compressor ends of TC rotor: lubricant at 38°C and 206 kPa supply conditions

on the other hand, shows subsynchronous vibrations along the entire operating speed range (12.5–65 krpm). The waterfalls of shaft motion for the tests and predictions make evident a complex rotor response, rich in subsynchronous activity. There are large differences in vibration signature between the compressor and turbine shaft ends since the TC assembly center of mass is very close to the turbine end FRB, thus determining dissimilar static loads on the compressor and turbine side bearings.

In a post-processing analysis, total shaft motion (pk–pk) amplitudes are determined from the limit cycle orbits. Figure 12 depicts the predicted and measured total shaft motion at the turbine and compressor ends. The largest total motion amplitudes are notorious at the lowest shaft speeds (<20 krpm). At higher speeds, the amplitudes of total motion decrease rapidly with increasing shaft speed, in particular at the compressor end. The slightly smaller test data that predicted total motion at speeds below 20 krpm may be attributed to the poorly predicted synchronous (1*X*) amplitudes. Note that for shaft speeds above 55 krpm, the predicted response is purely synchronous (see Fig. 11). On the other hand, the test data show large total motion amplitudes (see Fig. 8). There is excellent correlation of subsynchronous predictions to test data for shaft speeds ranging from 25 krpm to 60 krpm. Note that in spite of the large synchronous (1*X*) and subsynchronous amplitudes in the test data and predictions, the amplitudes of total shaft motion are well below the physical limit.

The test data and predictions are filtered to capture the amplitude and frequency of the peak responses. The threshold amplitude for the analysis is 3% of the physical limit. Figures 13 and 14 display the measured and predicted amplitudes of subsynchronous motions versus shaft speed and whirl frequency ratio (WFR), respectively. WFR denotes the ratio of subsynchronous whirl fre-

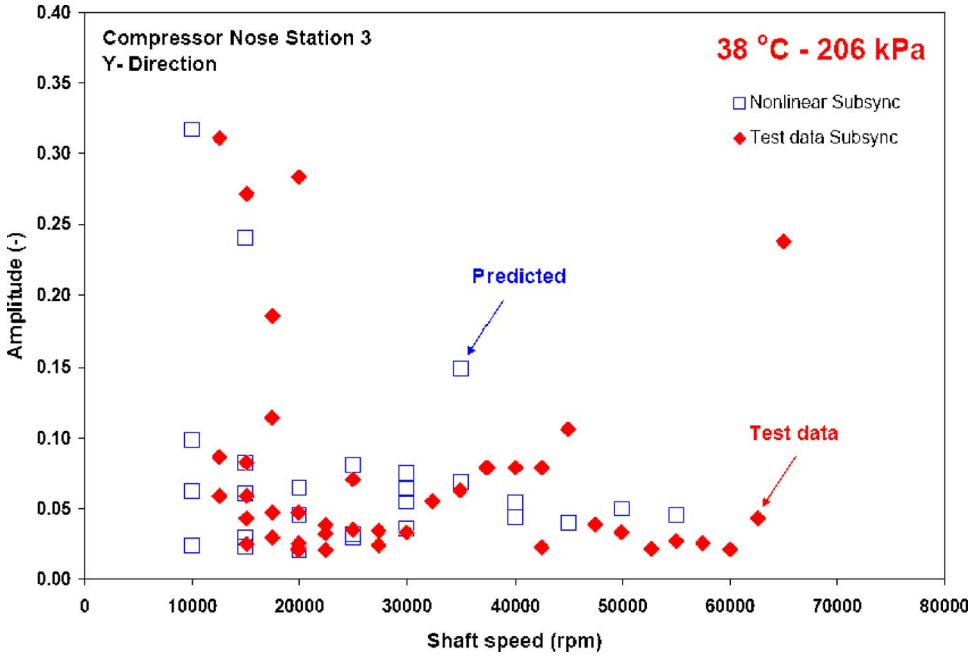

Fig. 13 Amplitude of subsynchronous motions (*Y* direction) versus shaft speed at the compressor end of TC rotor: lubricant at 38°C and 206 kPa supply conditions

quency to shaft synchronous speed frequency. For brevity, the results are shown only for the compressor end of the TC rotor. In the graphs, diamond and square markers denote the test data and nonlinear predictions, respectively. The test data and predictions show the largest amplitudes of subsynchronous motions occurring at low shaft speeds (<20 krpm) for both compressor and turbine ends of the rotor. Note that the test data show more subsynchronous activity than the predictions. At shaft speeds >20 krpm, the measured and predicted amplitudes of subsynchronous motion reach amplitudes equivalent to 10% of the physical limit. Predicted amplitudes are slightly lower than the measurements at shaft speeds above 35 krpm. In general, the predictions and test data show similar trends as shaft speed increases. The measurements indicate that most subsynchronous activity (largest amplitudes) occurs in the range of 90–150 Hz, closely corresponding with the conical mode of vibration. On the other hand, the predictions show the largest amplitudes at a low WFR, roughly at 50% of the floating ring rotational speed.

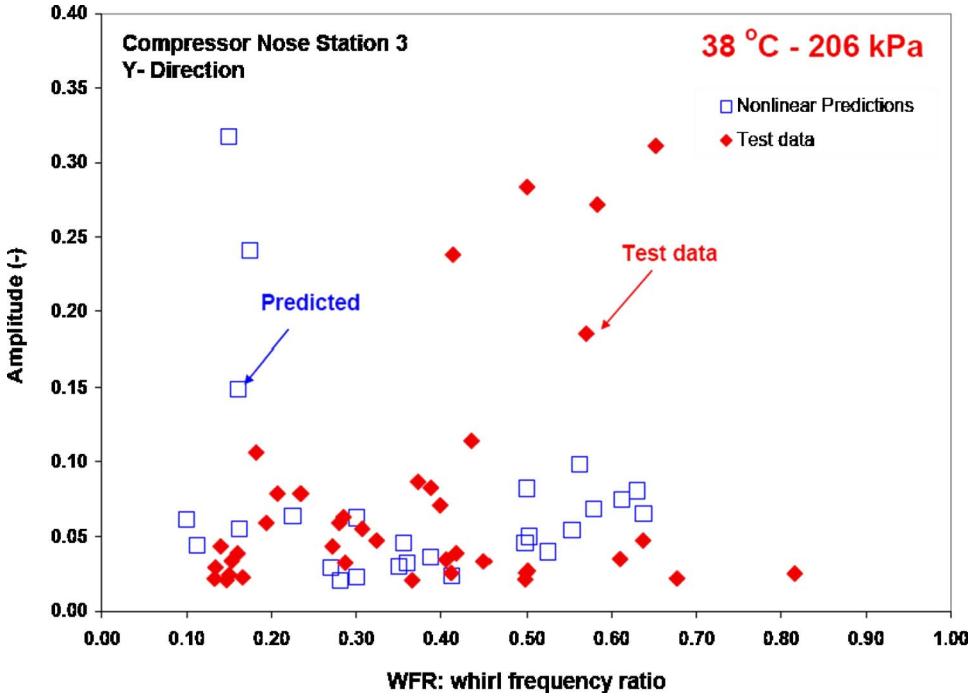

Fig. 14 Amplitude of subsynchronous motions (*Y* direction) versus whirl frequency ratio at the compressor end of TC rotor: lubricant at 38°C and 206 kPa supply conditions

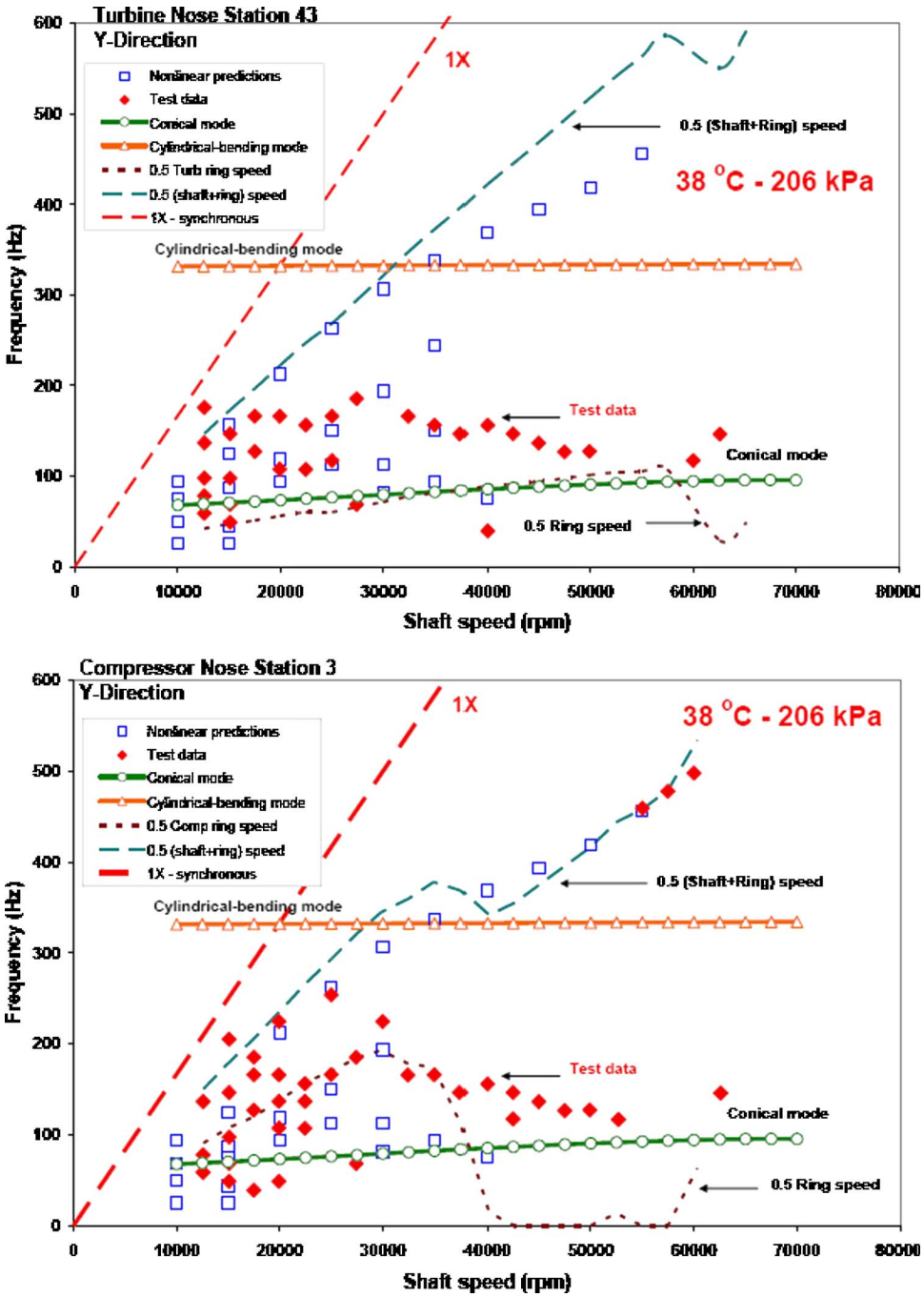

Fig. 15 Predicted and measured subsynchronous whirl frequencies versus shaft speed (turbine and compressor rotor ends): lubricant at 38°C and 206 kPa supply conditions

Figure 15 depicts the filtered subsynchronous frequencies of motion versus shaft speed. The top and bottom graphs correspond to motions at the turbine and compressor ends of the TC rotor, respectively. Diamond and square markers denote the experimental data and nonlinear predictions, respectively. The graphs also include the predicted damped natural frequencies from the linear analysis and the measured ring speeds. At low shaft speeds, below 30 krpm, the measured subsynchronous frequencies at the compressor end of the TC rotor are related to the line that tracks 50% of the ring rotational speed, thus evidencing the instability of the outer film in the FRB. The nonlinear analysis predicts subsynchronous motions with whirl frequency at 50% of the ring plus shaft speeds. This motion is evident in the test data only at the compressor end of the rotor and for shaft speeds below 25 krpm and above 55 krpm. In general, the tests shows the excitation of two subsynchronous whirl frequencies; the first one with frequencies ranging from 60 Hz to 200 Hz and the second one with frequencies ranging from 130 Hz to 500 Hz.

Closure

The paper presents progress on the validation, against test data, of linear and nonlinear rotordynamic models built to predict the dynamic shaft response of TC rotors supported on FRBs. The ultimate goal is to develop a virtual tool for optimizing turbocharger designs and minimize product development.

The present results show significant improvements in predicting TC shaft motions, in particular with the implementation of a two-

plane balance method with model derived influence coefficients that renders accurate estimation of the tested rotor imbalance. The linear model yields accurate predictions of the synchronous response to imbalance, in particular at the highest shaft speeds. As in the test data, waterfall spectra of the predicted (nonlinear) shaft motions at the compressor and turbine ends of the TC rotor show multiple frequency subsynchronous motions along the test shaft speed range. The predicted amplitudes and frequencies of subsynchronous motions are in good agreement with the measurements within specific ranges of operating shaft speed.

Further nonlinear predictions using the measured (actual) rotational speeds for the FRBs lead to a much improved correlation with the test data (see Ref. [14]). The simulations demonstrate that the floating rings stopped spinning at high shaft speeds and became locked. Hence then the onset of the large amplitude instability at 50% of shaft speed eached the top shaft speed (see Fig. 8). These results will be presented in a future publication.

Acknowledgment

The continued support of Honeywell Turbo Technologies is gratefully acknowledged.

References

[1] Shaw, C., and Nussdorfer, T., 1947, "An Analysis of the Full-Floating Journal Bearing," NACA Report No. 866, pp. 95–107.
[2] Born, H., 1987, "Analytical and Experimental Investigation of the Stability of the Rotor-Bearing System of a New Small Turbocharger," ASME Paper No. 87-GT-110.
[3] Orcutt, F., and Ng, C., 1968, "Steady-State and Dynamic Properties of the Floating-Ring Journal Bearing," ASME J. Lubr. Technol. **90**, pp. 243–253.
[4] Tanaka, M., 1996, "A Theoretical Analysis of Stability Characteristics of High Speed Floating Bush Bearings," *Proceedings of the 6th International Conference on Vibrations in Rotating Machinery, IMechE Conference Transaction 1996–6*, Oxford, UK, September, Paper C500/087/96, pp. 133–142.
[5] Tatara, A., 1970, "An Experimental Study on the Stabilizing Effect of Floating Bush Journal Bearings," Bull. JSME **13**, pp. 859–863.
[6] Tanaka, M., and Hori, Y., 1972, "Stability Characteristics of Floating Bush Bearings," ASME J. Lubr. Technol. **94**, pp. 248–259.
[7] Li, C., 1982, "Dynamics of Rotor Bearing Systems Supported by Floating Ring Bearings," ASME J. Lubr. Technol. **104**, pp. 469–477.
[8] Trippett, R., and Li, D., 1983, "High-Speed Floating-Ring Bearing Test and Analysis," ASLE Trans. **27**(1), pp. 73–81.
[9] San Andrés, L., and Kerth, J., 2004, "Thermal Effects on the Performance of Floating Ring Bearings for Turbochargers," Proc. Inst. Mech. Eng., Part J: J. Eng. Tribol. **218**, pp. 1–14.
[10] Holt, C., San Andrés, L., Sahay, S., Tang, P., LaRue, G., and Gjika, K., 2005, "Test Response and Nonlinear Analysis of a Turbocharger Supported on Floating Ring Bearings," ASME J. Vibr. Acoust. **127**(2), pp. 107–212.
[11] Kerth, J., 2003, "Prediction and Measurement of the Rotordynamic Response of an Automotive Turbocharger with Floating Ring Bearings," M.S. thesis, Texas A&M University, College Station, TX.
[12] San Andrés, L., Rivadeneira, J., Chinta, M., LaRue, G., and Gjika, K., 2005, "Nonlinear Rotordynamics of Automotive Turbochargers—Predictions and Comparisons to Test Data," ASME J. Eng. Gas Turbines Power, **129**, pp. 488–493.
[13] San Andrés, L., Rivadeneira, J. C., Gjika, K., Chinta, M., and LaRue, G., 2005, "Advances in Nonlinear Rotordynamics of Passenger Vehicle Turbochargers: A Virtual Laboratory Anchored to Test Data," *Proceedings of the 3rd World Tribology Conference*, Washington DC, September, Paper WTC 2005–64155.
[14] Rivadeneira, J., 2006, "Predictions versus Measurements of Turbocharger Nonlinear Dynamic Response," M.S. thesis, Texas A&M University, College Station, TX.

A New Bump-Type Foil Bearing Structure Analytical Model

Sébastien Le Lez

Mihaï Arghir

Jean Frene

Laboratoire de Mécanique des Solides,
Université de Poitiers,
Téléport 2-SP2MI,
Boulevard Marie et Pierre Curie,
BP 30179,
86962 Futuroscope Chasseneuil Cedex, France

A gas bearing of bump foil type comprises an underlying structure made of one or several strips of corrugated sheet metal covered by a top foil surface. The fluid film pressure needs to be coupled with the behavior of the structure for obtaining the whole bearing characteristics. Unlike in classical elasto-aerodynamic models, a foil bearing (FB) structure has a very particular behavior due to friction interfaces, bump interactions, and nonisotropic stiffness. Some authors have studied this complex behavior with the help of three-dimensional finite element simulations. These simulations evidenced a lack of reliable analytical models that can be easily implemented in a FB prediction code. The models found in the literature tend to overestimate the foil flexibility because most of them do not consider the interactions between bumps that are highly important. The present work then develops a model that describes the FB structure as a multidegree of freedom system of interacting bumps. Each bump includes three degrees of freedom linked with elementary springs. The stiffnesses of these springs are analytically expressed so that the model can be adjusted for any dimensions and material properties. Once the stiffness matrix of the whole FB structure is obtained, the entire static system is solved taking friction into account. Despite its relative simplicity, comparisons with finite elements simulations for various static load distributions and friction coefficients show a good correlation. This analytical model has been integrated into a foil bearing prediction code. The load capacity of a first generation foil bearing was then calculated using this structure model as well as other simplified theoretical approaches. Significant differences were observed, revealing the paramount influence of the structure on the static and dynamic characteristics of the foil bearing. Some experimental investigations of the static stiffness of the structure were also realized for complete foil bearings. The structure reaction force was calculated for a shaft displacement with zero rotation speed, using either the multidegree of freedom model or the usual stiffness formulas. The comparisons between theoretical and experimental results also tend to confirm the importance of taking into account the bump interactions in determining the response of the structure.
[DOI: 10.1115/1.2747638]

Introduction

A bump-type foil bearing is a gas bearing constituted of one or several corrugated sheets covered by one or several smooth sheets. Over the past 20 years considerable advancements have been achieved in the solution of the compressible Reynolds equation. However the lack of knowledge of the structure static and dynamic behavior constitutes the main problem in foil bearings prediction codes. Due to the strong coupling that exists between the fluid film and the structure, numerical predictions of the performance of such bearings can still be inaccurate.

Numerous authors attempted to study this structure either experimentally or theoretically. Static experimental investigations were made by Ku and Heshmat [1] on a flat bump strip. The static load deflection characteristics of a complete foil bearing constituted of a multistage bump layer were measured by Heshmat [2]. More recently Rubio and San Andres conducted the most complete analysis of a foil bearing static structural stiffness and developed an analytical model of the structural foil bearing response [3].

The first theoretical model of a single bump static stiffness was given by Wallowit and Anno [4] and used by Heshmat et al. assuming a zero friction coefficient [5]. The model is still attractive and was recently used by Peng and Khonsari [6,7]. A more elaborate structural deflection model of a complete bump strip using the shell theory and considering friction was then presented by Ku and Heshmat [8]. Carpino et al. studied the effects of membrane stresses in the prediction of foil bearing performance [9] and developed a finite element formulation for foil bearings with Peng and Talmage supported by an elastic foundation [10–12]. A second formulation for the single bump static stiffness was given by Iordanoff considering friction between the corrugated sheet and the shell housing and using different boundary conditions for the welded and nonwelded bumps [13]. Finite element structural calculations were also used by some authors either to couple the structural deflections to a gas thrust bearing prediction code [14] or to study more accurately the static behavior of the bump strip layer [15,16].

All these different approaches are of great interest for improving the understanding of the bump type foil structure behavior and for rendering more accurate foil bearing prediction codes. However, the analytical formulas found in the literature tend to overestimate the foil flexibility because most of them do not consider the interactions between bumps that are highly important. In this paper, a new static structural model considering the structure as a multidegree of freedom model is presented. Finite element simulations and experimental tests data are then used to validate this model.

Theoretical Analysis

Foil Bearing Structure Discretization. In order to simplify the presentation, a strip constituted of two bumps is first considered (Fig. 1). The height of the bump strip layer is supposed to be small compared to the radius of the bearing so that the curvature effects can be neglected. The main idea of the model is to consider the

Contributed by the International Gas Turbine Institute of ASME for publication in the JOURNAL OF ENGINEERING FOR GAS TURBINES AND POWER. Manuscript received April 26, 2007; final manuscript received April 27, 2007. Review conducted by Dilip R Ballal. Paper presented at the ASME Turbo Expo 2007: Land, Sea and Air (GT2007), Montreal, Quebec, Canada, May 14–17. Paper No. GT2007-27078.

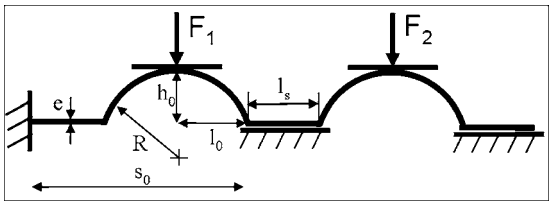

Fig. 1 Two bumps strip

continuous structure as a discrete one with a restricted number of nodes. The nodes are linked by springs whose stiffness will be analytically expressed (Fig. 2). The model depicted in Fig. 2 has 6 degrees of freedom, namely two vertical displacements (v_1, v_3) and four horizontal displacements (u_1-u_4). This is the minimum required for enlightening the coupling between two successive bumps. The elementary characteristics of the bump strip model are the stiffnesses k_i and the transmission force angle θ_d.

The elementary stiffnesses k_i can be calculated by energetic methods for imposed boundary conditions. These boundary conditions have a non-negligible impact on the static response of the structure. Two kinds of boundary conditions will be used for the extremity nodes of the arcs: free rotation or no rotation (Fig. 3). When the actual structure is subjected to a static load, neither of these conditions is fully respected. Nevertheless, it is possible to differentiate in the actual continuous structure the regions of slight and important rotations. As presented in Fig. 3, finite element simulations were used to identify these zones. It clearly appears that the last bump of the strip, i.e., the bump located at the free end, must be considered separately. For all the other ones, the elementary stiffnesses are calculated with the boundary conditions depicted in Figs. 4–7. The calculation of the stiffnesses k_1 and k_3 of the last bump uses different boundary conditions shown in Figs. 8 and 9. Their analytical expressions are then different and to distinguish them they will be noted as $k_{1\text{bis}}$ and $k_{3\text{bis}}$ in the following.

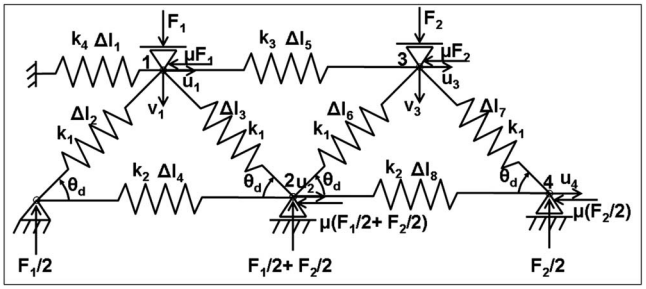

Fig. 2 The six DOF model

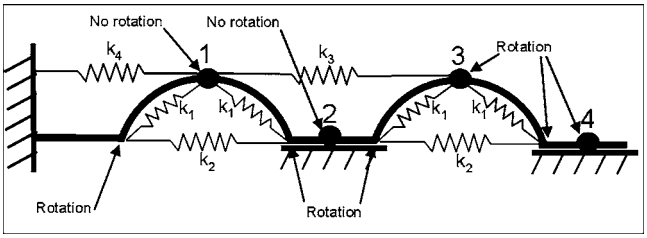

Fig. 3 Boundary conditions for calculating the elementary stiffness

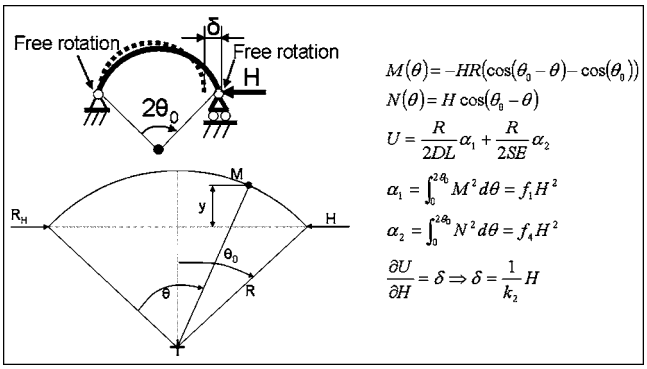

Fig. 5 Calculation of the elementary stiffness k_2

Calculation of Elementary Characteristics. The elementary stiffnesses and transmission force angles are determined by using the energetic method. First the bending moments and normal

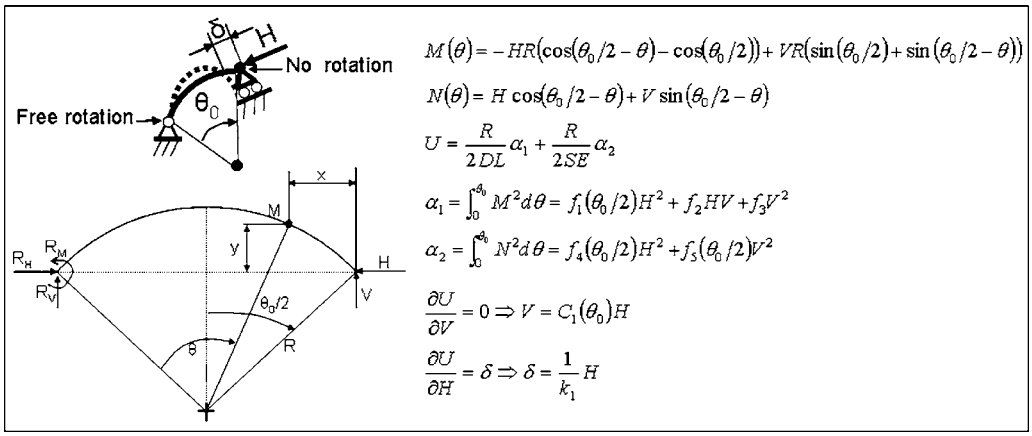

Fig. 4 Calculation of the elementary stiffness k_1

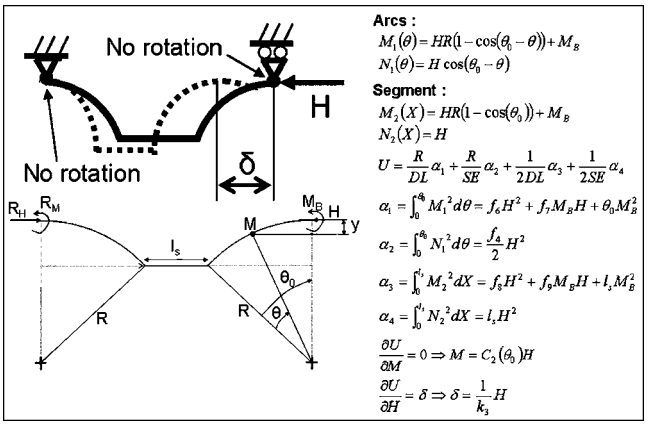

Fig. 6 Calculation of the elementary stiffness k_3

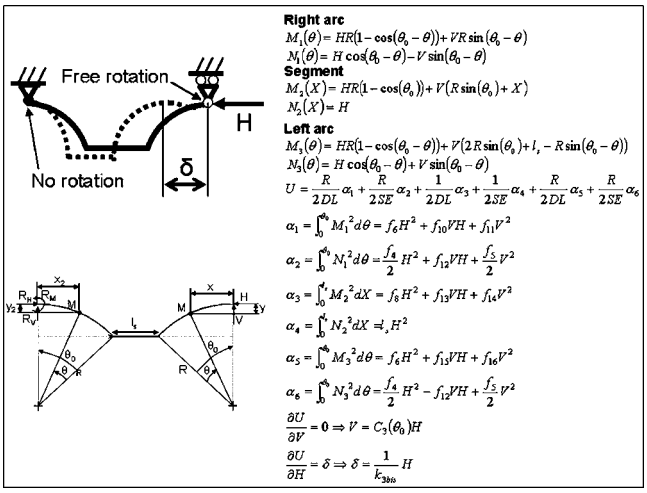

Fig. 9 Calculation of the elementary stiffness k_{3bis}

loads are calculated in all regions of the elementary structures as shown in Figs. 4–11. Then the elastic deformation energy is calculated [17,18]

$$U = \int_0^l \left(\frac{M^2}{2\mathrm{DL}} + \frac{N^2}{2\mathrm{SE}} \right) dl \tag{1}$$

Once the expression of the elastic deformation energy is obtained, Castigliano's theorem is used to calculate the expressions either of the elementary spring stiffnesses or of the transmission force angles. These calculations, which are classical strength of materials problems, are quite long and they are not fully detailed in this paper. It is worthwhile to note that this effort of analytical calculation has to be done only once for a given type of corrugated bump sheet (here with circular cylinders). Indeed the elementary characteristics obtained are valid for any dimensions (arc length, bump angle, etc.) and materials used.

The expressions of the elementary characteristics are given hereafter. For more clarity f_i and C_i stand for $f_i(\theta_0)$ and $C_i(\theta_0)$. These functions are detailed in Appendices A and B

$$k_1 = \left[\frac{R}{2\mathrm{DL}}(2f_1(\theta_0/2) + f_2 C_1) + \frac{R}{2\mathrm{SE}}(2f_4(\theta_0/2)) \right]^{-1} \tag{2}$$

$$k_{1\mathrm{bis}} = \left[\frac{Rf_1(\theta_0/2)}{\mathrm{DL}} + \frac{Rf_4(\theta_0/2)}{\mathrm{SE}} \right]^{-1} \tag{3}$$

$$k_2 = \left[\frac{Rf_1}{\mathrm{DL}} + \frac{Rf_4}{\mathrm{SE}} \right]^{-1} \tag{4}$$

$$k_3 = \left[\frac{R}{\mathrm{DL}}(2f_6 + f_7 C_2) + \frac{R}{\mathrm{SE}}(f_4) + \frac{1}{2\mathrm{DL}}(2f_8 + f_9 C_2) + \frac{l_s}{\mathrm{SE}} \right]^{-1} \tag{5}$$

$$k_{3\mathrm{bis}} = \left[\frac{1}{2\mathrm{DL}}(4Rf_6 + Rf_{10}C_3 + Rf_{15}C_3 + 2f_8 + f_{13}C_3) + \frac{1}{\mathrm{SE}}(Rf_4 + l_s) \right]^{-1} \tag{6}$$

$$k_4 = \left[\frac{R}{2\mathrm{DL}}\left(2f_6 - \frac{f_7^2}{2\theta_0}\right) + \frac{Rf_4}{2\mathrm{SE}} \right]^{-1} \tag{7}$$

$$\theta_d = \tan^{-1}\left(-\left[\frac{R}{\mathrm{DL}}\left(2f_{17} - \frac{f_{19}^2}{2\theta_0}\right) + \frac{Rf_4}{\mathrm{SE}} \right] \Big/ \left[\frac{R}{\mathrm{DL}}\left(f_{18} - \frac{f_{19}f_{20}}{2\theta_0}\right) - \frac{Rf_{12}}{\mathrm{SE}} \right] \right) \tag{8}$$

$$\theta_{\mathrm{dbis}} = \tan^{-1}\left(-\left[\frac{R^3 f_{21}}{\mathrm{DL}} + \frac{Rf_4}{\mathrm{SE}} \right] \Big/ \left[\frac{R^3 f_{22}}{\mathrm{DL}} - \frac{Rf_{12}}{\mathrm{SE}} \right] \right) \tag{9}$$

Stiffness Matrix of the Whole Structure. The global stiffness matrix of the whole structure is derived from the expression of the potential energy. To determine this potential energy, the elongation of the elementary springs needs to be expressed. For more clarity these elongations will be first expressed for the strip con-

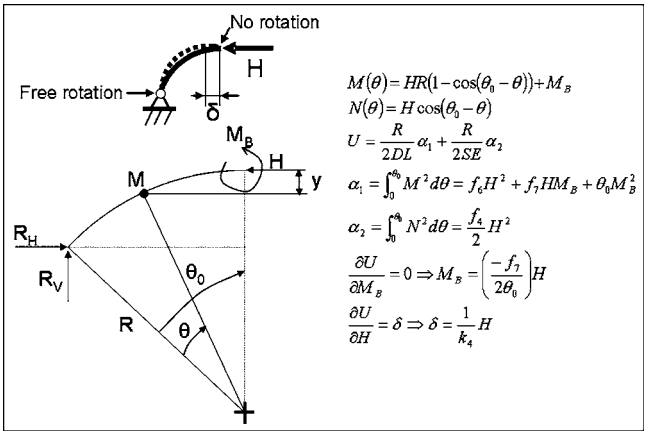

Fig. 7 Calculation of the elementary stiffness k_4

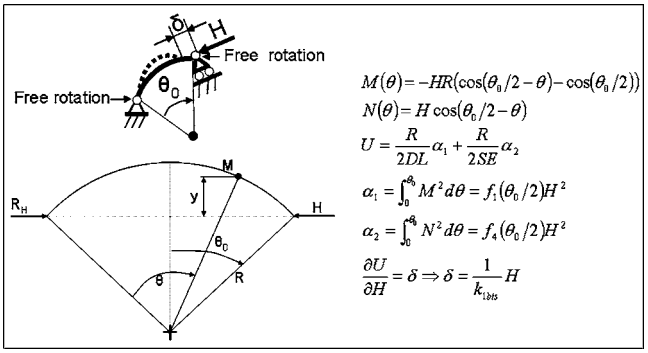

Fig. 8 Calculation of the elementary stiffness $k_{1\mathrm{bis}}$

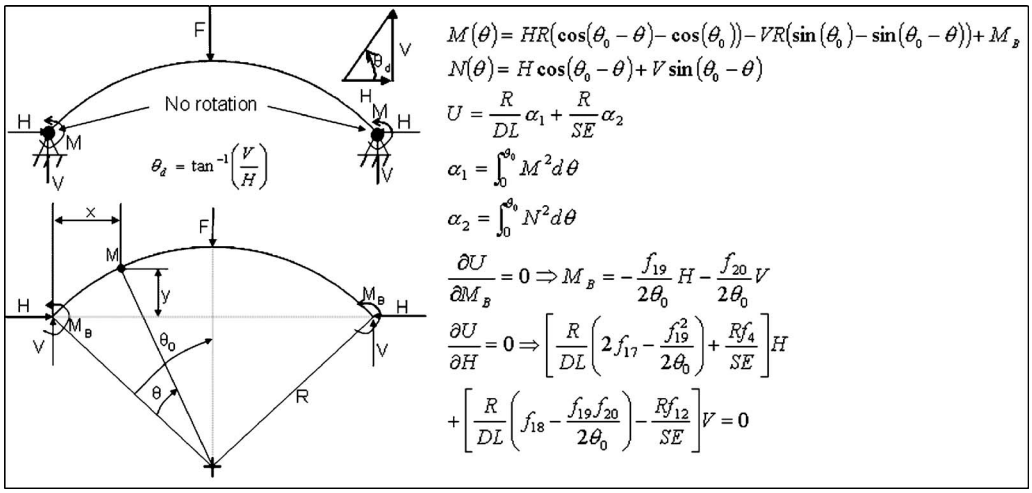

Fig. 10 Calculation of the transmission force angle θ_d

stituted of two bumps having the same elementary characteristics k_i and θ_d shown in Fig. 2. Then the results will be extended to the general case of n bumps with the last bump having different elementary characteristics k_{ibis} and θ_{dbis}.

The elongations of the eight springs are depicted in Fig. 2. The model is considered to be linear, i.e., the final configuration is close from the initial configuration. Hence the eight elongations are

$$\Delta l_1 = u_1 \quad \Delta l_5 = u_3 - u_1$$

$$\Delta l_2 = u_1 c - v_1 s \quad \Delta l_6 = u_3 c - v_3 s - u_2 c$$

$$\Delta l_3 = u_2 c - u_1 c - v_1 s \quad \Delta l_7 = u_4 c - u_3 c - v_3 s$$

$$\Delta l_4 = u_2 \quad \Delta l_8 = u_4 - u_2 \tag{10}$$

where c stands for $\cos(\theta_d)$ and s stands for $\sin(\theta_d)$. The potential energy is then calculated

$$E_{\text{pot}} = \tfrac{1}{2}\{k_1(\Delta l_2^2 + \Delta l_3^2 + \Delta l_6^2 + \Delta l_7^2) + k_2(\Delta l_4^2 + \Delta l_8^2) + k_3\Delta l_5^2 + k_4\Delta l_1^2\} \tag{11}$$

This leads to

$$\begin{aligned} E_{\text{pot}} = \tfrac{1}{2}\{&k_1(2u_1^2c^2 + 2v_1^2s^2 + 2u_2^2c^2 + 2u_3^2c^2 + 2v_3^2s^2 + u_4^2c^2 - 2u_1u_2c^2 \\ &- 2v_1u_2cs - 2u_2u_3c^2 + 2u_2v_3cs - 2u_3u_4c^2 - 2v_3u_4cs) \\ &+ k_2(2u_2^2 + u_4^2 - 2u_2u_4) + k_3(u_1^2 - 2u_1u_3 + u_3^2) + k_4u_1^2\} \end{aligned} \tag{12}$$

For a linear system, the potential energy is a quadratic form of the stiffness matrix [19]. The static behavior of the system is depicted by the equation $KX = F$. For the sample case of two identical bumps, this system can be expressed

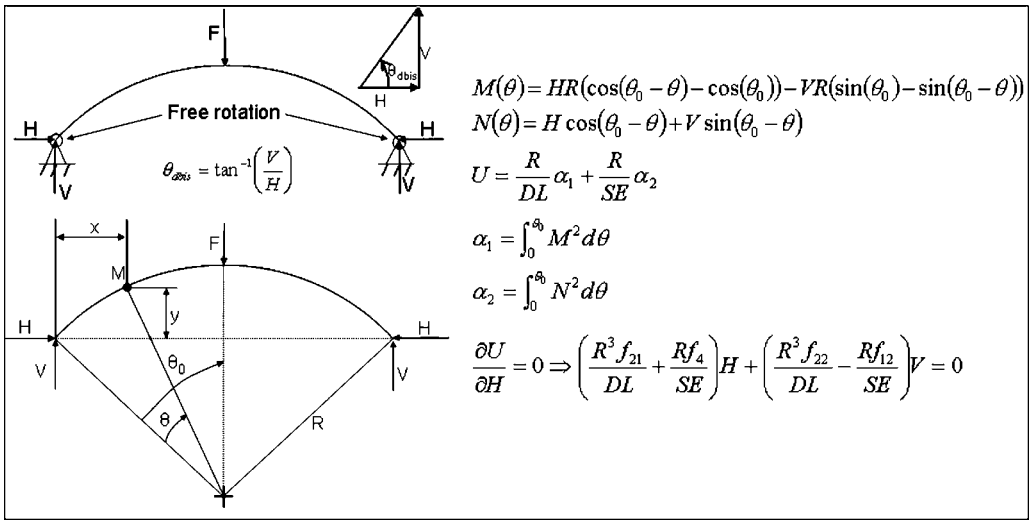

Fig. 11 Calculation of the transmission force angle θ_{dbis}

$$\begin{bmatrix} 2c^2k_1+k_3+k_4 & 0 & -c^2k_1 & -k_3 & 0 & 0 \\ 0 & 2s^2k_1 & -csk_1 & 0 & 0 & 0 \\ -c^2k_1 & -csk_1 & 2c^2k_1+2k_2 & -c^2k_1 & csk_1 & -k_2 \\ -k_3 & 0 & -c^2k_1 & 2c^2k_1+k_3 & 0 & -c^2k_1 \\ 0 & 0 & csk_1 & 0 & 2s^2k_1 & -csk_1 \\ 0 & 0 & -k_2 & -c^2k_1 & -csk_1 & c^2k_1+k_2 \end{bmatrix} \cdot \begin{bmatrix} u_1 \\ v_1 \\ u_2 \\ u_3 \\ v_3 \\ u_4 \end{bmatrix} = F \tag{13}$$

For the general case of n bumps, the vector of generalized coordinates is defined as

$$X = [u_1\ v_1\ u_2\ \cdots\ u_{2n-1}\ v_{2n-1}\ u_{2n}]^T \tag{14}$$

The global stiffness matrix can be seen as the sum of two matrices. The first one represents the stiffness of the bumps taken individually, and the second one represents the coupling between the bumps

$$K = K_{\mathrm{IND}} + K_{\mathrm{COUP}} \tag{15}$$

These matrices are given in Fig. 12 for the general case of n bumps. The last blocks of the matrices are different from the others due to the different transmission force angle θ_{dbis} and stiffnesses $k_{1\mathrm{bis}}$, $k_{3\mathrm{bis}}$ of the last bump.

Integration of Friction—Numerical Procedure. Friction is taken into account by imposing external loads opposed to the horizontal displacements u_i of the bumps. The magnitude of these loads is given by Coulomb's law. The normal loads at the bottom of the bumps are calculated by static equilibrium with the simplifying assumption of no friction, which does not affect significantly the results of the model.

At the beginning of the procedure all the horizontal displacements are supposed to be oriented from the fixed end to the free end of the strip as shown in Fig. 2. The initial external load vector can then be expressed for the general case of n bumps

$$F = [-\mu F_1\ F_1\ -\mu(F_1/2+F_2/2)\ \cdots\ -\mu F_n\ F_n\ -\mu(F_n/2)]^T \tag{16}$$

In the actual foil bearing structure, horizontal displacements of the bumps can be oriented either toward the free end, the fixed end, or they can be zero (stick condition) depending on the pressure load profile. To test the stick condition and to find the actual direction of the horizontal displacements, an algorithm constituted of five steps is used:

(1) Initial conditions: all the horizontal displacements u_i are considered to be positives (oriented towards the free end);
(2) System resolution: the matrix system $KX=F$ is solved using a rapid direct method (K is symmetric);
(3) Check of the direction of the horizontal displacements: from the fixed end, every direction of horizontal displacement of the nodes is checked. When a node is found to have changed displacement direction, the sign of the friction reaction force is modified in the load vector F, the checking

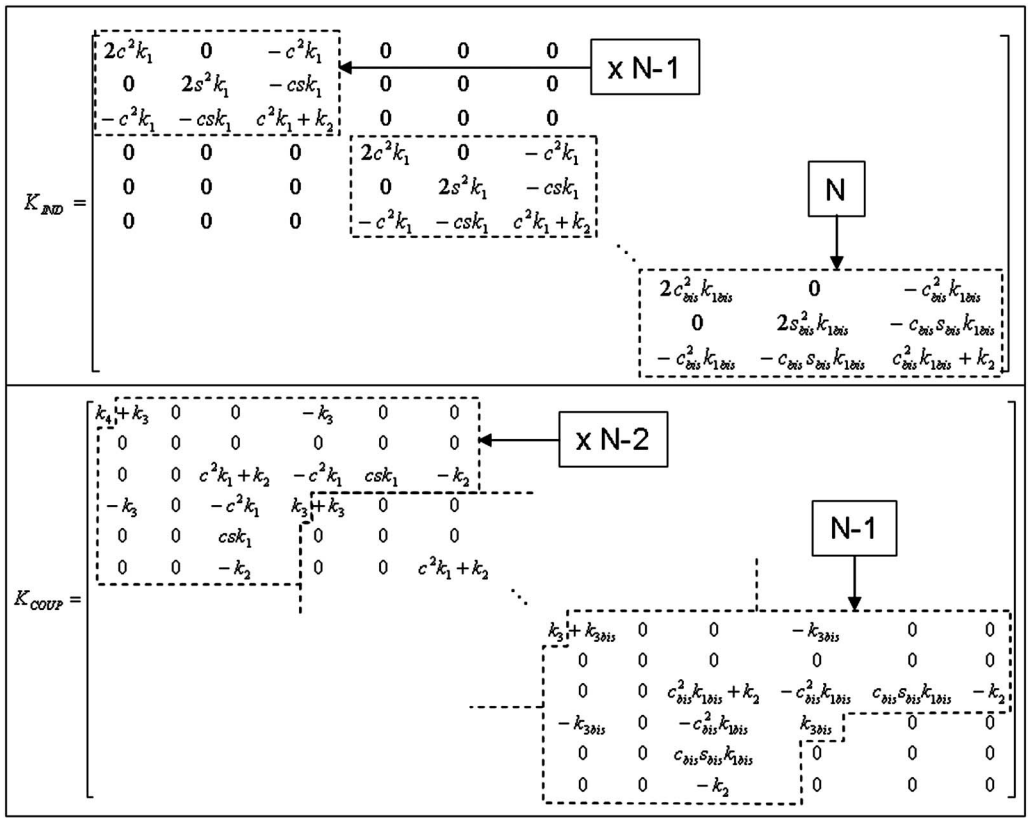

Fig. 12 Stiffness matrices

process is stopped, and the algorithm goes to Step 4. If there is no change found, this means that a convenient load vector F was imposed and the algorithm stops and exits the loop.

(4) System resolution: the matrix system $KX=F$ is solved again; and

(5) Check of stick condition: if the node whose friction force has just been modified in the Step 3 change of direction of displacement again, this means that the friction force imposed at this node is definitely greater than the springs reaction force acting at this node. In this case this node is considered to be stuck and the system loses 1 degree of freedom (modification of K and F). If this stick condition is encountered the algorithm goes to Step 1 and the process is repeated for a system with $n-1$ degrees of freedom. If not, the algorithm goes back to Step 3 and the check of the directions of displacement continues from the last modified node toward the free end.

Integration of the Model in a Foil Bearing Prediction Code. An existing gas bearing prediction code has been adapted to include the structural deformation of foil air bearings. This code allows the numerical solution of the compressible Reynolds equation in the frame of the finite volumes method of discretization. An original aspect of the numerical solution is a new upwind procedure borrowed from aerodynamics [20].

The coupling between the fluid film and the deformable structure takes place in the expression of the film thickness. Most of the results present in the literature use a bump static stiffness K_S to calculate this film thickness

$$h_i = C_0 - C_0\varepsilon\cos(\theta_i - \varphi) + \frac{P_i - P_{\text{ref}}}{K_S} \tag{17}$$

Frequently this static stiffness is determined for a single bump without taking into account the interactions between the bumps. To express this static stiffness, formulas of Heshmat [5] (Eq. (18)) and of Iordanoff [13] (Eq. (19)) are widely used

$$K_S = \frac{Et^3}{2s_0(1-\nu^2)l_0^3} \tag{18}$$

$$K_S^{\text{fw}} = \frac{Et^3\sin^3(\theta_0)}{12l_0^3 s_0 J(\mu,\theta_0)(1-\nu)^2}, \quad K_S^{\text{ff}} = \frac{Et^3\sin^3(\theta_0)}{6l_0^3 s_0 J(\mu,\alpha)(1-\nu)^2} \tag{19}$$

K_S^{fw} and K_S^{ff} are, respectively, the bump stiffness per unit area for the fixed-free end bump and for the free-free end bumps (see Ref. [13] for the definition of the I and J geometrical functions).

In contrast to these approaches, the present model doesn't enable the use of a constant stiffness. As it will be shown in the second part of the paper, some combinations of dry friction values and load distributions can lead to upward displacements near the fixed end of the structure. Consequently, the use of a constant stiffness is not really adapted to describe the behavior of such a structure.

Since the model developed in this paper directly gives the displacements of the top of the bumps, its integration in the foil bearing code is relatively simple. The average pressure on a bump is calculated for each iteration step in the resolution of the Reynolds equation. These loads are then applied to the structural model which gives in return the vertical (or radial) displacements of the top of the bumps (v_i). The deflections of the structure δ_i can then be expressed in the center of the mesh cells by linear interpolation. The expression of the film thickness follows

$$h_i = C_0 - C_0\varepsilon\cos(\theta_i - \varphi) + \delta_i \tag{20}$$

δ_i can be either positive (downward displacements) or in some cases negative (upward displacements).

Theoretical Results

Comparisons With Finite Elements Results. Finite element simulations have been performed for a structure made of ten bumps and of a deformable top foil. The finite element model is fully described in Ref. [16]. The values of the geometrical characteristics and of the elastic properties of the material are the same as in Refs. [6,21] and are given in Table 1. Four load distributions have been considered: uniform, decreasing, increasing and increasing/decreasing as shown in Fig. 13. For all cases, the total equivalent force is the same as the one generated by a uniform pressure of $2\cdot10^5$ Pa. Outputs of the finite element model are the vertical displacements of the top of the bumps.

These results are represented in Fig. 13 and are compared to the displacements obtained either with the "NDOF model" or with formulas from Refs. [5,13]. Bump number 1 is located at the fixed end of the strip, whereas bump number 10 is located at the free end. The vertical axis represents the vertical displacements of the top of the bumps. A downward displacement, i.e., following the load direction, is positive and an upward displacement is negative. The case with a uniform pressure distribution is purely theoretical and cannot occur in a real loaded foil bearing. The most representative case of pressure distribution on a single strip foil bearing is likely to be the increasing/decreasing one (Fig. 13(*d*)).

A good correlation is obtained between finite element results and the structural NDOF model for various load distributions. This tends to validate the above presented theoretical analysis. Moreover the need of considering the bump interactions in the structural response is clearly evidenced in these figures. The stiffness formulas, which seem much more adapted than the NDOF model to describe the behavior of a single bump, give results very far from the finite element simulations when a complete strip is considered. By neglecting the bumps interactions they render a much more deformable structure which will influence the whole foil bearing response as presented in the following.

It is important to note that the top foil effects are not considered in the NDOF model. Although this top foil is modeled as a deformable shell in the finite element simulation, its effect does not appear clearly in Fig. 13. Indeed the top foil mainly affects the structural deflections between the bumps which are not represented in the figures. In the following, the structural deflection between two adjacent bumps is considered to be linear. However, in a real foil bearing structure as well as in the finite element simulations, the top foil evidences a wavy shape between the bumps. This shape can affect the pressure distribution and thus the static and dynamic performances of the bearing. To obtain more accurate predictions of the entire foil bearing performances the top foil should be considered by using either an analytical model or a finite element formulation. The top foil could also be integrated directly to the NDOF model by adding some more nodes and elementary springs between the tops of the bumps.

Influence on a Foil Bearing Load Capacity. The load capacity of the air foil bearing described in Table 1 has been calculated for a rotating speed of 30,000 rpm. The fixed end of the bump foil strip was located at the opposite of the shaft radial displacement.

The load versus eccentricity curves are plotted in Fig. 14 for the three models. The load capacity of a rigid bearing of 31.8 μm clearance (infinite structural stiffness) is also represented. It can be seen that the load capacity of the foil bearing is greatly affected by the choice of the structural model. This was clearly explained by Kim and San Andres [21,22] based on the fact that the gas foil bearing combines in series the gas film and structural stiffnesses.

Table 1 Dimensions and materials of the bump type foil bearing

L (mm)	38.1
D_{FB} (mm)	19.05
C_0 (μm)	31.8
Number of strips	1
Number of bumps	26
t (μm)	102
s_0 (mm)	4.572
l_0 (mm)	1.778
l_s (mm)	1.016
h_0 (mm)	0.508
θ_0 (deg)	31.9
E (GPa)	214
ν	0.29
μ	0.1

Thus when the gas film stiffness increases, i.e., at extremely high speeds, the structural stiffness is the only commanding one in the actual operation of foil bearings

$$\frac{1}{K_{\mathrm{FB}}} = \frac{1}{K_f} + \frac{1}{K_S} \Rightarrow \underset{K_f \to \infty}{K_{\mathrm{FB}}} = K_S \tag{21}$$

For low structural stiffness values, as the ones given by the single bump formulas, the eccentricity necessary for balancing the static load is more important than the one obtained with the NDOF model. At high eccentricities, the difference between the results issued from the stiffness formulas and the NDOF model can reach 100%. It is also interesting to note that the influence of the structure becomes significant only for relative eccentricity values larger than 0.5.

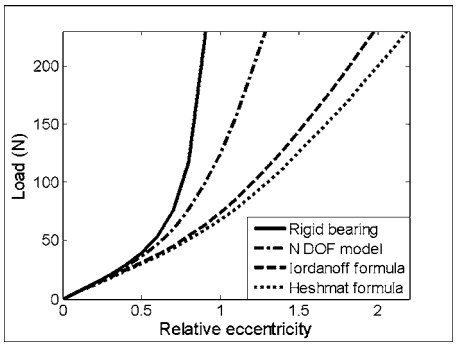

Fig. 14 The influence of the structure on the foil bearing load capacity

Experimental Validation

Experimental Procedure. Static load tests have been conducted on four foil bearings of first generation (see Ref. [23] for the definition of FB generations) (Fig. 15). The dimensions of

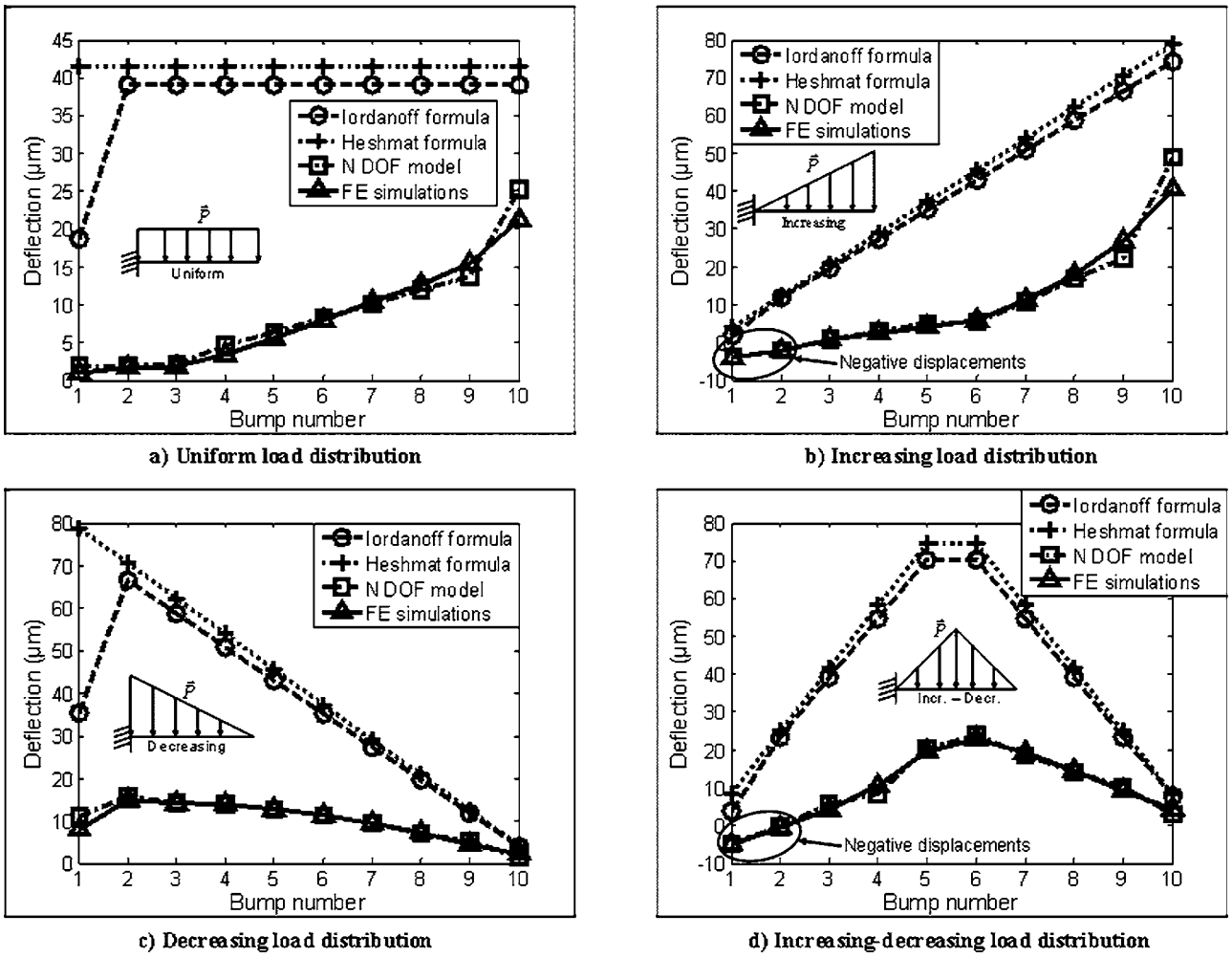

a) Uniform load distribution

b) Increasing load distribution

c) Decreasing load distribution

d) Increasing-decreasing load distribution

Fig. 13 Bumps deflection for various load distributions

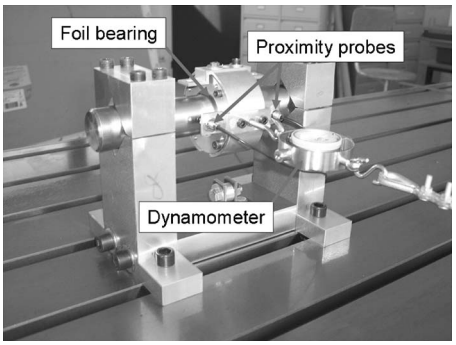

Fig. 15 Experimental static load tests

these bearings have been measured and are the same as depicted in Table 1. Proximity probes of 0.08 μm resolution were mounted on the bearing housing, facing the shaft. These two sensors were equally spaced from the midplane of the bearing and allowed to get a mean displacement value independent of the bearing misalignment. A static load was imposed on the floating bearing with a screw/nut system.

The coordinate system of the bearing and the angular location of the spot weld are shown in Fig. 16. Two spot welds location have been tested, the first one at 180 deg (upward as in Fig. 16) and the second one at 270 deg. The static loading was horizontal, i.e., at 90 deg and 270 deg, without dismounting the probes. The load versus displacement curves evidenced an interval with low or zero stiffness. This interval was considered to be approximately twice the nominal clearance of the bearing [24]. Clearance is a term which is unsuitable to describe the geometry of a foil bearing since there is often a preload between the foil structure and the shaft. However this notion of clearance is still helpful to compute the foil bearing static or dynamic response.

The maximum tested load was approximately 200 N which corresponds to a reasonable value given by the manufacturer, not to be exceeded in further experiments with a rotating shaft (specific pressure 20 psi). The load incremental variation was roughly 10 N (less for the softer region). Due to the presence of dry friction and adhesion phenomena in the foil bearing structure, loading and unloading curves were not really identical. To obtain a single curve which can be compared to numerical results, mean displacement values were calculated from the loading and unloading curves.

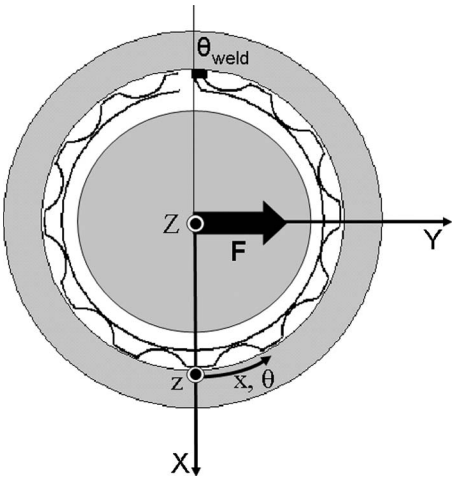

Fig. 16 Coordinate system of the foil bearing

Code Modification. The foil bearing prediction code can compute the top bumps displacement from the pressure profile of the aerodynamic film. The contact problem between a shaft at rest and the structure is more delicate to deal with. Two solutions can be envisaged: to impose a static load to the shaft or to impose a displacement to the shaft. If the stiffness of each bump is known (formulas from Refs. [5,13] for instance), the solution of the imposed load problem is conceivable. However with the NDOF structural model, the stiffness of the bumps is unknown and depends on the bumps interactions and friction direction. Therefore the determination of the load distribution on each bump is a difficult problem and the contact problem will be treated with the imposed displacement formulation.

Heshmat Formula. Using the Heshmat formula [5], each discrete cell of the mesh has the same static stiffness K_S. The relative eccentricities of the shaft ε_X and ε_Y, as well as the initial radial clearance C_0 are inputs data. For every angle θ_i (see Fig. 16), the foil deflection is given by

$$\delta(\theta_i) = C_0\varepsilon_x \cos(\theta_i) + C_0\varepsilon_y \sin(\theta_i) - C_0 \tag{22}$$

A negative deflection means that there is no contact between the foil and the shaft. In this case the actual deflection of the foil has to be zero. The actual deflection is thus defined as

$$\delta(\theta_i) = \max\{C_0(\varepsilon_x \cos(\theta_i) + \varepsilon_y \sin(\theta_i) - 1), 0\} \tag{23}$$

Calculation of the reaction forces of the structure is then immediate

$$F_X = \sum_i K_S\delta(\theta_i)\cos(\theta_i)S_i \tag{24}$$

$$F_Y = \sum_i K_S\delta(\theta_i)\sin(\theta_i)S_i \tag{25}$$

The assumption of an identical stiffness for the whole structure renders an isotropic bearing. Hence there will be no cross-coupling stiffness of the structure with this model.

Iordanoff Formula. The Iordanoff formula [13] model was studied by Rubio and San Andres [3]. The only differences between this model and the Heshmat model are that the stiffness is not the same for the first bump and the other ones and can be a function of the actual height of the bumps

$$h_0^*(\theta_i) = h_0 - \delta(\theta_i) \tag{26}$$

where $\delta(\theta_i)$ is defined in Eq. (23).

Reaction forces of the structure are then

$$F_X = \sum_i K_S(\theta_i)\delta(\theta_i)\cos(\theta_i)S_i \tag{27}$$

$$F_Y = \sum_i K_S(\theta_i)\delta(\theta_i)\sin(\theta_i)S_i \tag{28}$$

If the first bump is not in contact with the shaft there will be no cross coupling stiffness of the structure for this model too.

NDOF Model. Contrary to the two other models, the NDOF approach does not give a direct link between the foil deflection and the structure restoring force. With this model it is necessary to find the loads on each bump that will cause the foil to take the exact shape of the shaft. An iterative procedure is thus needed.

The initial deflections of the bumps due to the shaft displacement are given by

$$v(\theta_b) = \max\{C_0(\varepsilon_x \cos(\theta_b) + \varepsilon_y \sin(\theta_b) - 1), 0\} \tag{29}$$

where θ_b is the angular position of the tops of the bumps and $v(\theta_b)$ correspond to v_1 and v_3 in Fig. 2. At this stage the horizontal displacements u_i are neglected.

Then the elongations of the k_1 springs, which are the only ones that will give a vertical reaction force, are calculated. For each

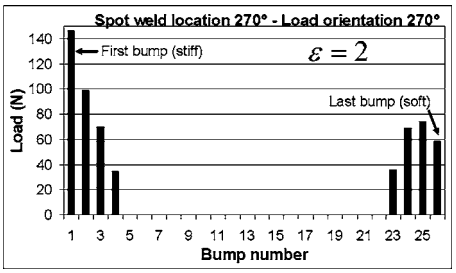

Fig. 17 Load distribution on the bumps

bump, these elongations are noted Δl_{b1} for the left spring k_1 and Δl_{b2} for the other one. Hence, the radial reaction force of a bump is

$$F_b = k_1 \sin(\theta_d)(\Delta l_{b1} + \Delta l_{b2}) \tag{30}$$

These loads can be used as inputs in the NDOF model. Once the resolution of the model is performed, the angular position of the top of the bumps has changed due to nonzero horizontal displacements u_i. The above procedure is then repeated taking into account the horizontal displacements in the calculation of the springs elongations. These successive iterations continue until the convergence of the reaction forces. As an example, the load distribution on the bumps is presented in Fig. 17 for the bearing described in Table 1.

Reaction forces of the whole bearing structure are then easily calculated

$$F_X = \sum_b F_b \cos(\theta_b) \tag{31}$$

$$F_Y = \sum_b F_b \sin(\theta_b) \tag{32}$$

Contrary to the two previous models a cross-coupling stiffness of the structure can be obtained with this model.

Comparisons Between Experimental and Theoretical Results. Experimental and theoretical results of the static loading of one foil bearing are given in Figs. 18 and 19. From a qualitative point of view these curves can be related to those obtained by Rubio and San Andres [3]. However their bearing was a second generation bearing constituted of a single top foil but with five bump strips around the bearing sleeve (each strip had five bumps making a total of 25 bumps). With several short strips, it is likely to get more sliding bumps than with a single strip of 26 bumps. Their structure was then softer than the one considered in this paper which renders a quantitative comparison not possible.

When the shaft does not move toward the welding point of the bump foil (Fig. 18) a good correlation between experiments and

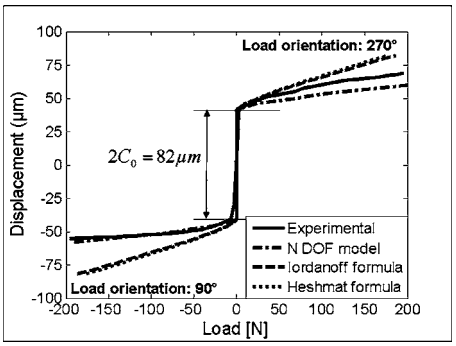

Fig. 18 Bearing structure static loading—spot weld location: 180 deg

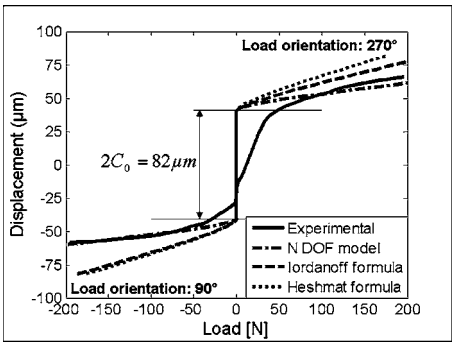

Fig. 19 Bearing structure static loading—spot weld location: 270 deg

the NDOF model is obtained. As stated before, the formulas from Refs. [5,13] seem to underestimate the structure stiffness by neglecting the bumps interactions. The same tendency is also depicted in Fig. 19 when the shaft moves toward the opposite side of the weld spot.

An interesting point is that all bearings tested were softer when the weld spot was loaded. Contrary to the results obtained with the models using formulas from Refs. [5,13], this characteristic also appears, in a less significant way, with the NDOF model. Indeed even if the first bumps of the strip are really stiff, the last ones are really soft (see Fig. 17).

Summary and Conclusions

An analytical model of the whole corrugated sheet has been presented in this paper. Unlike most of the analytical formulas found in the literature, this model takes into account the interactions between the bumps which leads to a stiffer foil bearing structure. Depending on the load distribution and on the friction coefficient, the tangential displacements can be either oriented toward the free end or toward the fixed end of the strip. In the case of stick conditions, the tangential displacements can also be zero. In the same way, the vertical (radial) displacement of the top of the bumps can be either oriented upward or downward. An upward displacement can occur in some conditions even if the bump is (lightly) loaded. The definition of a stiffness formula independent of the load distribution seems then to be inappropriate to correctly describe the static behavior of the structure.

The results of the analytical model have been compared with finite element simulations for a corrugated sheet constituted of ten bumps. Four load distributions have been evaluated analytically assuming a friction coefficient of 0.1. In all the cases the results of the NDOF model agreed well with the FE simulations. The single stiffness formulas tend to underestimate the structure rigidity by neglecting the load distribution and the interactions between the bumps. The structural effects on the foil bearing load capacity were also presented. As expected, the characteristics of the bearing are greatly affected by the structural model.

Finally an experimental procedure has been used to validate these theoretical results. The numerical code has also been modified to compute the whole bearing structure reaction force in response to a nonrotating shaft displacement and the theoretical and experimental results correlate.

Apart from taking into account the interactions between bumps the present model can be easily applied to other types of corrugated sheets by determining new analytical elementary characteristics k_i and θ_d. It is also intended that the formulation in terms of stiffness matrix should be extended to a dynamic structural model able to deal with dissipative effects.

Acknowledgment

The authors wish to thank *Turbomeca* and *Microturbo* as well as *MAIA* work group for supporting this activity.

Nomenclature

- c = cosine of the transmission force angle (=cos(θ_d))
- c_{bis} = cosine of the last bump transmission force angle (=cos(θ_{dbis}))
- C_i = functions defined in Appendix B
- C_0 = initial bearing clearance (m)
- D = flexural rigidity of a shell ($=Et^3/12(1-\nu^2)$) (N m)
- D_{FB} = foil bearing diameter (m)
- E = bump foils Young's modulus (Pa)
- E_{pot} = potential energy (N m)
- f_i = functions defined in Appendix A
- F = External load vector (N)
- F_b = load applied on the bump b (N)
- $F_{X,Y}$ = structure reaction force in direction X, Y (N)
- FB = foil bearing
- h_i = film thickness in mesh cell i (m)
- h_0 = initial bump height (m)
- h_0^* = actual bump height (m)
- k_i = elementary springs stiffness (N m^{-1})
- k_{ibis} = last bump elementary springs stiffness (N m^{-1})
- K = global stiffness matrix (N m^{-1})
- K_{COUP} = coupling stiffness matrix (N m^{-1})
- K_f = static stiffness of the gas film (N m^{-3})
- K_{FB} = static stiffness of the foil bearing (N m^{-3})
- K_{IND} = individual bumps stiffness matrix (N m^{-1})
- K_S = static structural stiffness (N m^{-3})
- l_s = length of the segment between the bumps (m)
- l_0 = bump half length (m)
- L = foil width–length of the bearing (m)
- M = bending moment (N m)
- N = normal load (N)
- P_i = pressure on mesh cell i (Pa)
- P_{ref} = reference pressure (Pa)
- R = bump radius (m)
- s = sine of the transmission force angle (=sin(θ_d))
- s_{bis} = sine of the last bump transmission force angle (=sin(θ_{dbis}))
- s_0 = bump pitch (m)
- S = section area of the foil ($=tL$) (m^2)
- S_i = area of a discrete cell (m^2)
- t = foils thickness (m)
- u_i = horizontal displacements of the structure nodes (m)
- U = elastic deformation energy (N m)
- v_i = vertical displacements of the structure nodes (m)
- X = general coordinates vector (m)
- Δl_i = elementary springs elongation (m)
- δ_i = foil deflection in mesh cell i (m)
- ε = relative eccentricity
- $\varepsilon_{X,Y}$ = relative eccentricity in direction X, Y
- φ = attitude angle (rad)
- μ = friction coefficient
- ν = bump foils Poisson's ratio
- θ_0 = half bump angle (rad)
- θ_b = angular position of the top bump b (rad)
- θ_d = transmission force angle (rad)
- θ_{dbis} = last bump transmission force angle (rad)
- θ_i = angular position of the mesh cell i (rad)

Appendix A—Functions $f_i(x)$

$$f_1(x) = 2R^2x - \frac{3R^2}{2}\sin(2x) + R^2x\cos(2x)$$

$$f_2(x) = 4R^2\frac{x}{2}\cos(x/2)\sin(x/2) - 4R^2\sin^2(x/2)$$

$$f_3(x) = 2R^2\frac{x}{2}\sin^2(x/2) - R^2\cos(x/2)\sin(x/2) + R^2\frac{x}{2}$$

$$f_4(x) = x + \frac{1}{2}\sin(2x)$$

$$f_5(x) = x - \cos(x)\sin(x)$$

$$f_6(x) = \frac{R^2}{2}\cos(x)\sin(x) + \frac{3R^2x}{2} - 2R^2\sin(x)$$

$$f_7(x) = -2R\sin(x) + 2Rx$$

$$f_8(x) = R^2(1-\cos(x))^2 l_s$$

$$f_9(x) = 2R(1-\cos(x))l_s$$

$$f_{10}(x) = R^2 + R^2\cos^2(x) - 2R^2\cos(x)$$

$$f_{11}(x) = -\frac{R^2}{2}\cos(x)\sin(x) + \frac{R^2x}{2}$$

$$f_{12}(x) = -\sin^2(x)$$

$$f_{13}(x) = R(1-\cos(x))l_s^2 + 2R^2\sin(x)(1-\cos(x))l_s$$

$$f_{14}(x) = \frac{l_s^3}{3} + R\sin(x)l_s^2 + R^2\sin^2(x)l_s$$

$$f_{15}(x) = -R^2 + 4R^2x\sin(x) + 2R^2\cos(x) + 2Rl_sx - R^2\cos^2(x) - 2Rl_s\sin(x) - 4R^2\sin^2(x)$$

$$f_{16}(x) = l_s^2x - 2Rl_s - 4R^2\sin(x) + 2Rl_s\cos(x) + 4Rl_sx\sin(x) + \frac{R^2x}{2} + \frac{7}{2}R^2\cos(x)\sin(x) + 4R^2x\sin^2(x)$$

$$f_{17}(x) = R^2\cos^2(x)x - \frac{3R^2}{2}\cos(x)\sin(x) + \frac{R^2x}{2}$$

$$f_{18}(x) = R^2 - 2R^2\sin^2(x) - 2R^2\cos(x) + R^2\cos^2(x) + 2R^2x\cos(x)\sin(x)$$

$$f_{19}(x) = 2R\sin(x) - 2Rx\cos(x)$$

$$f_{20}(x) = 2R - 2R\cos(x) - 2Rx\sin(x)$$

$$f_{21}(x) = 3x - \frac{3}{2}\sin(2x) - 2x\sin^2(x)$$

$$f_{22}(x) = -3\sin^2(x) + 4\sin^2\left(\frac{x}{2}\right) + x\sin(2x)$$

Appendix B—Functions $C_i(x)$

$$C_1(x) = \frac{-f_2(x)/\mathrm{DL}}{2f_3(x)/\mathrm{DL} + 2f_5(x/2)/\mathrm{SE}}$$

$$C_2(x) = \frac{-Rf_7(x) - f_9(x)/2}{2Rx + l_s}$$

$$C_3(x) = \frac{-\frac{1}{2\mathrm{DL}}(Rf_{10}(x) + Rf_{15}(x) + f_{13}(x)) - \frac{R}{2\mathrm{SE}}(f_{12}(x) + f_8(x))}{\frac{1}{\mathrm{DL}}(Rf_{11}(x) + Rf_{16}(x) + f_{14}(x)) + \frac{Rf_5(x)}{\mathrm{SE}}}$$

References

[1] Roger Ku, C. P., and Heshmat, H., 1993, "Compliant Foil Bearing Structural Stiffness Analysis-Part 2: Experimental Investigation," ASME J. Tribol., **115**, pp. 364–369.

[2] Heshmat, H., 1994, "Advancements in the Performance of Aerodynamic Foil Journal Bearings: High Speed and Load Capability," ASME J. Tribol., **116**, pp. 287–295.

[3] Rubio, D., and San Andrés, L., 2004, "Bump-Type Foil Bearing Structural Stiffness: Experiments and Predictions," *Proceedings ASME Turbo Expo*, Vienna, Austria, ASME Paper No. GT 2004-53611.

[4] Walowit, J. A., and Anno, J. N., 1975, *Modern Developments in Lubrication Mechanics*, Applied Science Publishers Ltd, London, UK, Chap. 7.

[5] Heshmat, H., Walowit, J. A., and Pinkus, O., 1983, "Analysis of Gas-Lubricated Foil Journal Bearings," J. Lubr. Technol., **105**, pp. 647–655.

[6] Peng, Z. C., and Khonsari, M. M., 2004, "Hydrodynamic Analysis of Compliant Foil Air Bearings with Compressible Air Flow," ASME J. Tribol., **126**, pp. 542–546.

[7] Peng, Z. C., and Khonsari, M. M., 2004, "On the Limiting Load-Carrying Capacity of Foil Bearings," ASME J. Tribol., **126**, pp. 817–818.

[8] Roger Ku, C. P., and Heshmat, H., 1992, "Compliant Foil Bearing Structural Stiffness Analysis-Part 1: Theoretical Model Including Strip and Variable Bump Foil Geometry," ASME J. Tribol., **114**, pp. 394–400.

[9] Carpino, M., Medvetz, L. A., and Peng, J. P., 1994, "Effects of Membrane Stresses in the Prediction of Foil Bearing Performance," STLE Tribol. Trans., **37**(1), pp. 43–50.

[10] Peng, J. P., and Carpino, M., 1993, "Calculation of Stiffness and Damping Coefficients for Elastically Supported Gas Foil Bearings," ASME J. Tribol., **115**, pp. 20–27.

[11] Peng, J. P., and Carpino, M., 1997, "Finite Element Approach to the Prediction of Foil Bearing Rotor Dynamic Coefficients," ASME J. Tribol., **119**, pp. 85–90.

[12] Carpino, M., and Talmage, G., 2003, "A Fully Coupled Finite Element Formulation for Elastically Supported Foil Journal Bearings," STLE Tribol. Trans., **46**(4), pp. 560–565.

[13] Iordanoff, I., 1999, "Analysis of an Aerodynamic Compliant Foil Thrust Bearing: Method for a Rapid Design," ASME J. Tribol. **121**, pp. 816–822.

[14] Heshmat, C. A., Xu, D., and Heshmat, H., 2000, "Analysis of Gas Lubricated Foil Thrust Bearings using Coupled Finite Element and Finite Difference Methods," ASME J. Tribol., **122**, pp. 199–204.

[15] Lee, D. H., Kim, Y. C., and Kim, K. W., 2005, "The Static Performance Analysis of Air Foil Journal Bearings Considering Three-Dimensional Structure of Bump Foil," *Proceedings ASME World Tribology Congress*, Washington, DC, ASME Paper No. WTC 2005-63728.

[16] Le Lez, S., Arghir, M., and Frene, J., 2007, "Static and Dynamic Characterization of a Bump-Type Foil Bearing Structure," ASME J. Tribol., **129**, pp. 75–83.

[17] Timoshenko, S., 1954, *Résistance des Matériaux II: Théorie Développée et Problèmes*, Librairie Polytechnique Ch. Béranger, Paris, France, Chap. 2.

[18] Timoshenko, S., 1940, *Theory of Plates and Shells*, McGraw-Hill, New York.

[19] Tong, K. N., 1960, *Theory of Mechanical Vibrations*, Wiley, New York, Chap. 2 & 3.

[20] Arghir, M., Le Lez, S., and Frene, J., 2006, "Finite Volume Solution of the Compressible Reynolds Equation: Linear and Non-Linear Analysis of Gas Bearing," Proc. Inst. Mech. Eng., Part J: J. Eng. Tribol., **220**, pp. 617–627.

[21] Kim, T. H., and San Andres, L., 2005, "Heavily Loaded Gas Foil Bearings: a Model Anchored to Test Data," *Proceedings ASME Turbo Expo*, Reno-Tahoe, NV, ASME Paper No. GT 2005–68486.

[22] San Andres, L., and Kim, T. H., 2005, "Gas Foil Bearings: Limits for High-Speed Operation," *Proceedins ASME World Tribology Congress*, Washington, DC, ASME Paper No. WTC 2005–63398.

[23] DellaCorte, C., and Valco, M. J., 2000, "Load Capacity Estimation of Foil Air Journal Bearings for Oil-Free Turbomachinery Applications," STLE Tribol. Trans., **43**(4), pp. 795–801.

[24] Radil, K., Howard, S., and Dykas, B., 2002, "The Role of Radial Clearance on the Performance of Foil Air Bearings," *Proceedings STLE/ASME International Joint Tribology Conference*, Cancun, Mexico, STLE/ASME Paper No. 2002-TRIB-101.

Denis Laxalde
École Centrale de Lyon,
Laboratoire de Tribologie et Dynamique des Systèmes,
36 Avenue Guy de Collongue,
69134 Ecully Cedex, France
and
Snecma-Safran Group,
77550 Moissy-Cramayel, France
e-mail: denis.laxalde@ec.lyon.fr

Jean-Pierre Lombard
Snecma-Safran Group,
77550 Moissy-Cramayel, France

Fabrice Thouverez
École Centrale de Lyon,
Laboratoire de Tribologie et Dynamique des Systèmes,
36 Avenue Guy de Collongue,
69134 Ecully Cedex, France

Dynamics of Multistage Bladed Disks Systems

This paper presents a new and original method for dynamical analysis of multistage cyclic structures such as turbomachinery compressors or turbines. Each stage is modeled cyclically by its elementary sector and the interstage coupling is achieved through a cyclic recombination of the interface degrees of freedom. This method is quite simple to set up; it allows us to handle the finite element models of each stage's sector directly and, as in classical cyclic symmetry analysis, to study the nodal diameter problems separately. The method is first validated on a simple case study which shows good agreements with a complete 360 deg reference calculation. An industrial example involving two HP compressor stages is then presented. Then the forced response application is presented in which synchronous engine order type excitations are considered.
[DOI: 10.1115/1.2747641]

1 Introduction

The mechanical design of gas turbine rotors is traditionally fulfilled through stage by stage analysis. However, in modern engines, dynamical phenomena involving multiple stages (adjoining or not) of bladed disks tend to appear and can then be of primary interest for gas turbine professionals. On the other hand, the traditional (single stage) analysis of bladed disks dynamics is usually performed using the cyclic symmetry reduction which allows us to analyze a complete rotationally periodic structure by considering only one of its elementary sectors. Examples in the literature are numerous on this subject, from the early developments of cyclic symmetry method [1,2] to specific researches on bladed disks dynamics [3,4]. Withal, in such analysis, the interstage coupling is necessarily neglected, its eventual effects cannot be accounted for, and this can lead to significant deviations from the real (multistage) system. For example, Bladh et al. [5] have show that the interstage coupling can significantly affect the dynamics of the multistage assembly and that the traditional single stage analysis can, in some cases, lead to an underestimation of vibratory levels.

Few strategies exist to answer the challenge of multistage modeling and a major issue is that, since a multistage assembly of cyclic structures is a priori no longer cyclic, the cyclic symmetry reduction cannot be used straightforward. Some [6] have used full 360 deg models to study the (free and forced) dynamics of multistage systems. However, such techniques often yield prohibitive computational costs. Component mode synthesis methods (with multilevel reductions) have also been used [7,8] but these strategies can be somewhat difficult to use in a design process.

In the present paper, we put forward a new strategy to study the dynamics of multistage assemblies using a cyclic symmetry reduction. This method handles the sector finite element modeling directly and involves a realistic interstage coupling based on a cyclic recombination of the interface on the chosen nodal diameter. Following a brief review of the cyclic symmetry method (Sec. 2), the proposed method will be detailed in Sec. 3. Then, some numerical examples and results will be presented in Sec. 4 to validate the method and highlight the importance of such multistage calculations in the design of turbomachinery components.

Contributed by the International Gas Turbine Institute of ASME for publication in the JOURNAL OF ENGINEERING FOR GAS TURBINES AND POWER. Manuscript received April 26, 2007; final manuscript received April 27, 2007. Review conducted by Dilip R Ballal. Paper presented at the ASME Turbo Expo 2007: Land, Sea and Air (GT2007), Montreal, Quebec, Canada, May 14–17, 2007. Paper No. GT2007-27083.

2 Cyclic Symmetry for Single Stages

In this section, a brief review of the classical cyclic symmetry modeling is done which mainly aims at defining some notations. A cyclic structure composed of N sectors is considered. Its displacement vector can be split as

$$\mathbf{x} = [\mathbf{x}_0,\ \mathbf{x}_1,\ \ldots,\ \mathbf{x}_{N-1}]^T \tag{1}$$

where $\mathbf{x}_j$ is the displacement vector of the jth sector.

As a consequence of the rotational periodicity, the mode shapes are such that each sector has the same deflection and a constant phase difference from the adjacent sectors. This intersector phase angle is $\beta_n = 2\pi n/N$ and the harmonic index $n = 0, 1, \ldots, N-1$ is called the nodal diameter number.

As a result, any dynamical problem on the complete cyclic structure

$$M\ddot{\mathbf{x}} + C\dot{\mathbf{x}} + K\mathbf{x} = \mathbf{f}_e \tag{2}$$

can be transformed (exactly) into reduced problems on the reference sector (corresponding to each nodal diameter number n)

$$M_n\ddot{\tilde{\mathbf{x}}}_n + C_n\dot{\tilde{\mathbf{x}}}_n + K_n\tilde{\mathbf{x}}_n = \tilde{\mathbf{f}}_{e,n} \tag{3}$$

The displacement vector in the cyclic base $\tilde{\mathbf{x}}_n$ is obtained from the reference sector's displacement vector in which the *left* intersector degrees of freedom, ${}^l\mathbf{x}_0$, have been eliminated using the relation to the *right* intersector degrees of freedom, ${}^r\mathbf{x}_0$, for each n nodal diameter

$${}^l\mathbf{x}_0 = e^{-(2i\pi n/N)r}\mathbf{x}_0 \tag{4}$$

The reduced matrices M_n, C_n, and K_n are obtained by applied this periodicity conditions on the reference sector's structural matrices.

As the structures considered have symmetric structural matrices, $\tilde{\mathbf{x}}_n$ and $\tilde{\mathbf{x}}_{N-n}$ contain the same relevant information and thus among the N possible values of the nodal diameter index n only N_s of these are to be calculated

$$N_s = \begin{cases} N/2 + 1 & \text{if } N \text{ is even} \\ (N+1)/2 & \text{if } N \text{ is odd} \end{cases} \tag{5}$$

Each reduced problem Eq. (3) is solved in cyclic coordinates $\tilde{\mathbf{x}}_n$ (for the reference sector) and the transformation in physical coordinates (complete structure) is given by

$$\mathbf{x} = \mathbf{e}_n \otimes \tilde{\mathbf{x}}_n \quad \text{with } \mathbf{e}_n = [1 \; e^{2j\pi n/N} \; e^{4j\pi n/N} \; \ldots \; e^{[2(N-1)j\pi n/N]}]^T \tag{6}$$

where $\otimes$ is the Kronecker product.

For further readings, see Refs. [1,2,9].

3 A Multistage Cyclic Symmetry Method

We suggest a new strategy to analyze the dynamics of multistage cyclic structures. This method was originally proposed by the authors in Ref. [10]. It is called *multistage cyclic symmetry* since the cyclic symmetry strategy is used to model each stage. The interstage coupling is ensured through a cyclic expansion of the interface degrees of freedom of each stage. The method will be detailed based on the example of two stages, respectively, composed of N_1 and N_2 sectors ($N_1 < N_2$). This method is applicable for any dynamical problems in free and forced responses. In this paper, we focused on linear applications for modal analysis and forced steady-state response. Extension to nonlinear steady-state response calculations can easily be considered by combining the cyclic symmetry approach with Fourier methods [11,12].

3.1 Equations of the Motion. We consider the general dynamical problem involving several coupled stages, each having a second-order equation of the motion of the form

$$M^{(s)}\ddot{\mathbf{x}}^{(s)} + C^{(s)}\dot{\mathbf{x}}^{(s)} + K^{(s)}\mathbf{x}^{(s)} = \mathbf{f}_e^{(s)} \quad (s = 1 \text{ or } 2) \tag{7}$$

in which $M^{(s)}$, $C^{(s)}$, and $K^{(s)}$ are mass, damping, and stiffness matrices; $\mathbf{x}^{(s)}$ is the displacement vector; and $\mathbf{f}_e^{(s)}$ is the external forces on the full stage s.

Since each stage is rotationally periodic, it can be represented by its elementary sector in its own cyclic base by the following uncoupled nodal diameters equations

$$M_n^{(s)}\ddot{\tilde{\mathbf{x}}}_n^{(s)} + C_n^{(s)}\dot{\tilde{\mathbf{x}}}_n^{(s)} + K_n^{(s)}\tilde{\mathbf{x}}_n^{(s)} = \tilde{\mathbf{f}}_{e,n}^{(s)}, \quad \text{for } n \in [0 \ldots N_s^{(s)} - 1] \tag{8}$$

The proposed method aims at coupling the models of each stage in their own cyclic components.

3.2 Interstage Coupling. At the interface between stages 1 and 2, the coupling is achieved by enforcing continuity of displacements (or other variables) on the interstage boundary in the common physical base

$$\Delta^b\mathbf{x} = A^b\mathbf{x}^{(1)} - {}^b\mathbf{x}^{(2)} = \mathbf{0} \tag{9}$$

where the left superscript ^{b} refers the restrictions to the interstage boundary degrees of freedom and A is a constraint matrix which makes the two interstage meshes compatible (multipoint constraints).

Equation (9) can be rewritten, using each stage's cyclic base, as

$$A\sum_{n=0}^{N_1-1} \mathbf{e}_{N_1,n} \otimes {}^b\tilde{\mathbf{x}}_{i,n}^{(1)} + \sum_{p=0}^{N_2-1} \mathbf{e}_{N_2,p} \otimes {}^b\tilde{\mathbf{x}}_{i,p}^{(2)} = 0 \tag{10}$$

Then, we can project Eq. (10) on any nodal diameter vector of the stage 2 cyclic base ($p \in [0 \ldots N_2 - 1]$) and obtain

$$(\mathbf{e}_{N_2,p}^* \otimes \mathcal{I}_{b_2})A\sum_{n=0}^{N_1-1} \mathbf{e}_{N_1,n} \otimes {}^b\tilde{\mathbf{x}}_{i,n}^{(1)} + {}^b\tilde{\mathbf{x}}_{i,p}^{(2)} = 0 \tag{11}$$

where the identity matrices $\mathcal{I}_{b_s}$ ($s = 1, 2$) ensure the compatibility of the interstage interface.

In Eq. (11), the coupling terms between nodal diameters n and p of each stage's base are

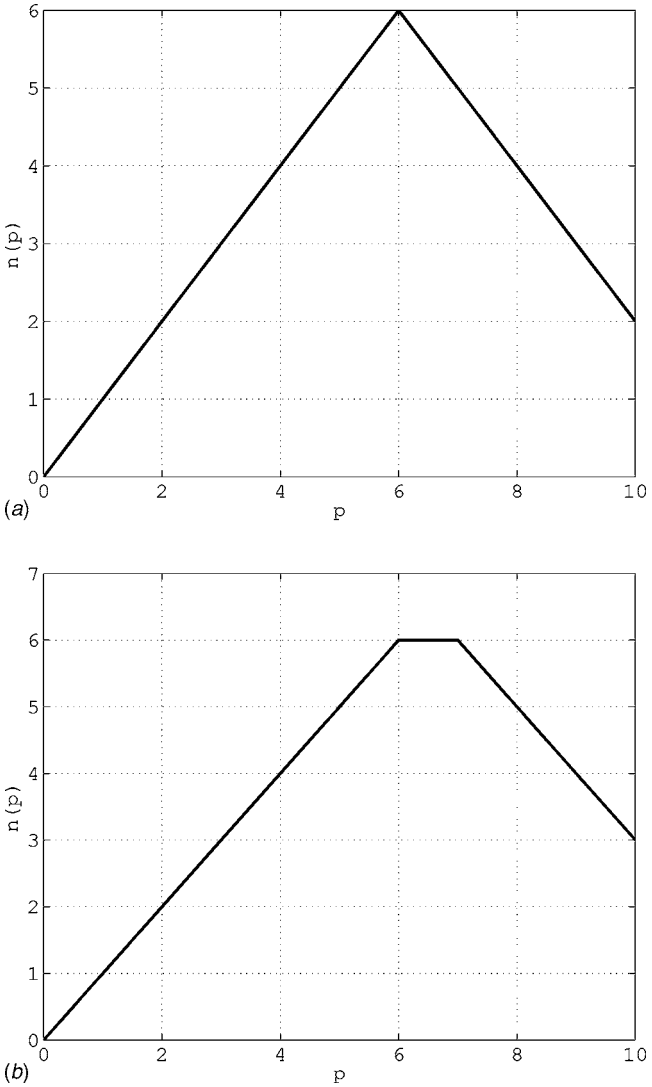

Fig. 1 "Nodal diameter equivalence" rule; (*a*) $N_1 = 12$ and $N_2 = 20$, (*b*) $N_1 = 13$ and $N_2 = 20$

$$\mathcal{C}(p,n) = (\mathbf{e}_{N_2,p}^* \otimes \mathcal{I}_{b_2})A(\mathbf{e}_{N_1,n} \otimes \mathcal{I}_{b_1}) \tag{12}$$

The cornerstone of the proposed method is to neglect the coupling between "distinct" nodal diameters of each stage's base. Here, we can define the correspondence of nodal diameter indexes between the two stage's bases (which may not be obvious since the stages have different number of sectors). For any nodal diameter index $p \in [0 \ldots N_2]$ of stage 2, we can define the corresponding "equivalent" nodal diameter index of stage 1 $n(p)$ as

$$n(p) = \begin{cases} p & \text{if } p \leqslant N_1 \\ N_1 - \begin{cases} p(\text{mod } N_1) & \text{if } N_1 \text{ is odd} \\ p(\text{mod } N_1) & \text{if } N_1 \text{ is even} \end{cases} & \text{if } p > N_1 \end{cases} \tag{13}$$

This correspond to the aliasing of the discrete Fourier transform. The "nodal diameter equivalence" is illustrated by Fig. 1, with the even (Fig. 1(*a*)) and odd (Fig. 1(*b*)) cases. Finally, the restriction of the interstage projection given by Eq. (11) to "equivalent" nodal diameters leads to

$$\left(\mathbf{e}_{N_2,p}^* \otimes \mathcal{I}_{b_2}\right)A(\mathbf{e}_{N_1,n(p)} \otimes \mathcal{I}_{b_1})^b\tilde{\mathbf{x}}_{i,n(p)}^{(1)} + {}^b\tilde{\mathbf{x}}_{i,p}^{(2)} = 0 \tag{14}$$

This assumption will next be referred as the one-to-one nodal diameter coupling assumption.

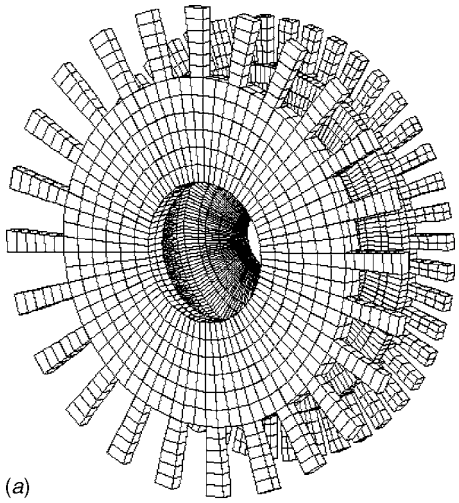

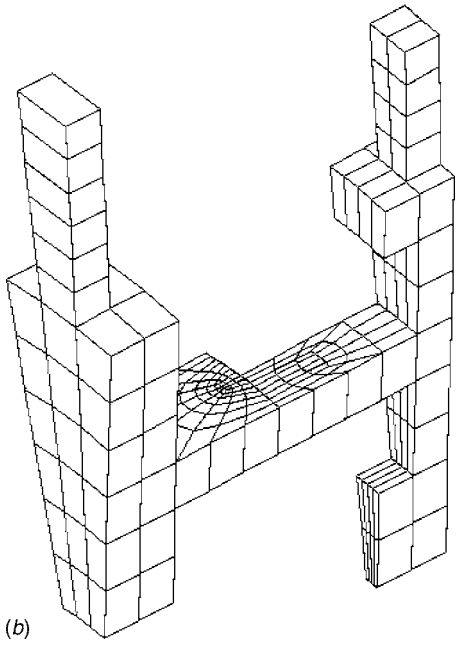

Fig. 2 Finite element model of two cyclic structures—$N_1=24$, $N_2=45$

3.3 Multistage Cyclic Symmetry Reduction. The one-to-one nodal diameter coupling assumption makes possible the multistage coupling in the cyclic bases for each nodal diameter separately. We can append two stage models in their own cyclic base and according to the previously defined nodal diameter correspondence relation (13) as

$$\begin{pmatrix} M_{n(p)}^{(1)} & 0 \\ 0 & M_p^{(2)} \end{pmatrix} \begin{bmatrix} \ddot{\tilde{\mathbf{x}}}_{n(p)}^{(1)} \\ \ddot{\tilde{\mathbf{x}}}_p^{(2)} \end{bmatrix} + \begin{pmatrix} C_{n(p)}^{(1)} & 0 \\ 0 & C_p^{(2)} \end{pmatrix} \begin{bmatrix} \dot{\tilde{\mathbf{x}}}_{n(p)}^{(1)} \\ \dot{\tilde{\mathbf{x}}}_p^{(2)} \end{bmatrix} + \begin{pmatrix} K_{n(p)}^{(1)} & 0 \\ 0 & K_p^{(2)} \end{pmatrix} \times \begin{bmatrix} \tilde{\mathbf{x}}_{n(p)}^{(1)} \\ \tilde{\mathbf{x}}_p^{(2)} \end{bmatrix} = \begin{bmatrix} \tilde{\mathbf{f}}_{e,n(p)}^{(1)} \\ \tilde{\mathbf{f}}_{e,p}^{(2)} \end{bmatrix} \tag{15}$$

Next, if each stage displacements vector is split as

$$\tilde{\mathbf{x}}_{n(p)}^{(1)} = [{}^b\tilde{\mathbf{x}}_{n(p)}^{(1)}, {}^i\tilde{\mathbf{x}}_{n(p)}^{(1)}]^T \quad \text{and} \quad \tilde{\mathbf{x}}_p^{(2)} = [{}^b\tilde{\mathbf{x}}_p^{(2)}, {}^i\tilde{\mathbf{x}}_p^{(2)}]^T$$

Eq. (14) can be used to eliminate the cyclic components of the interstage boundary of stage 2

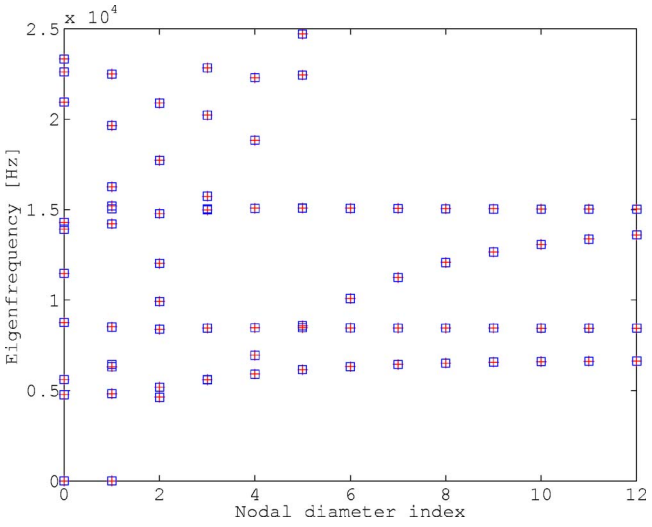

Fig. 3 Eigenfrequency correlation (□)/multistage cyclic symmetry (+)

$$\begin{bmatrix} \tilde{\mathbf{x}}_{n(p)}^{(1)} \\ \tilde{\mathbf{x}}_p^{(2)} \end{bmatrix} = \mathcal{T}_p \tilde{\mathbf{x}}_p^{(1,2)} \tag{16}$$

with

$$\mathcal{T}_p = \begin{pmatrix} \mathcal{I}_{b_1} & 0 & 0 \\ 0 & \mathcal{I}_{i_1} & 0 \\ \mathcal{B}_p & 0 & 0 \\ 0 & 0 & \mathcal{I}_{i_2} \end{pmatrix}, \quad \mathcal{B}_p = (\mathbf{e}_{N_2,p}^* \otimes \mathcal{I}_{b_2}) A (\mathbf{e}_{N_1,n(p)} \otimes \mathcal{I}_{b_1})$$

and

$$\tilde{\mathbf{x}}_p^{(1,2)} = [{}^b\tilde{\mathbf{x}}_{n(p)}^{(1)}\ {}^i\tilde{\mathbf{x}}_{n(p)}^{(2)}\ {}^i\tilde{\mathbf{x}}_p^{(2)}]^T$$

The final multistage one-to-one nodal diameter dynamical problem can be defined as

$$M_p^{(1,2)} \ddot{\tilde{\mathbf{x}}}_p^{(1,2)} + C_p^{(1,2)} \dot{\tilde{\mathbf{x}}}_p^{(1,2)} + K_p^{(1,2)} \tilde{\mathbf{x}}_p^{(1,2)} = \tilde{\mathbf{f}}_{e,p}^{(1,2)} \tag{17}$$

with

$$M_p^{(1,2)} = \mathcal{T}_p^{\mathrm{T}} \begin{pmatrix} M_{n(p)}^{(1)} & 0 \\ 0 & M_p^{(2)} \end{pmatrix} \mathcal{T}_p$$

$$C_p^{(1,2)} = \mathcal{T}_p^{\mathrm{T}} \begin{pmatrix} C_{n(p)}^{(1)} & 0 \\ 0 & C_p^{(2)} \end{pmatrix} \mathcal{T}_p$$

$$K_p^{(1,2)} = \mathcal{T}_p^{\mathrm{T}} \begin{pmatrix} K_{n(p)}^{(1)} & 0 \\ 0 & K_p^{(2)} \end{pmatrix} \mathcal{T}_p \tag{18}$$

This method allows the study of nodal diameter modes separately as for individual stages, each being modeled with its own elementary sector. The size of problem (17) is close to the sum of the two individual stages problem sizes. The accuracy of this method in modal analysis and particularly the validity of the one-to-one nodal diameter coupling will be demonstrated by numerical examples in Sec. 4.1.

3.4 Superposition. The multistage cyclic symmetry formalism allows us to isolate the nodal diameter contributions of the response. However, in some cases and particularly in forced response, the dynamics of the multistage system can feature simultaneous contributions of different nodal diameters. To handle such problems, two strategies can be used. The first is to use the "superposition principle" as in typical single stage cyclic symmetry analysis; that is to say, the external forcing distribution on each

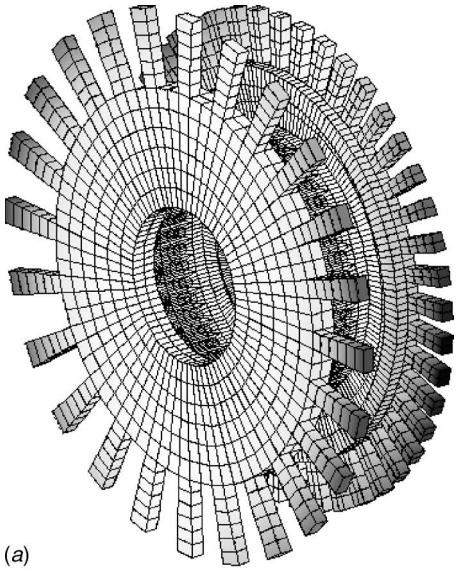

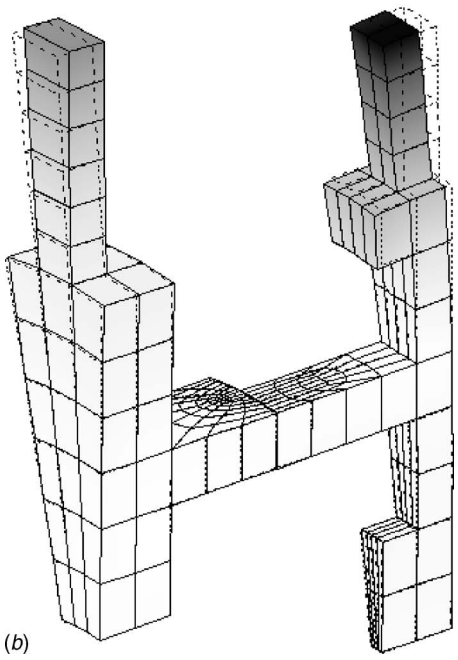

Fig. 4 One nodal diameter mode at 4824 Hz

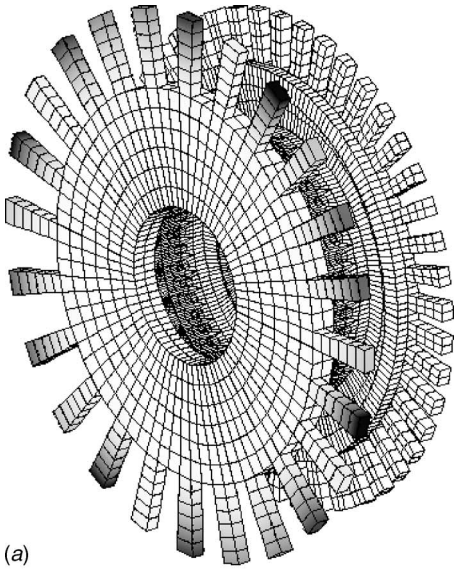

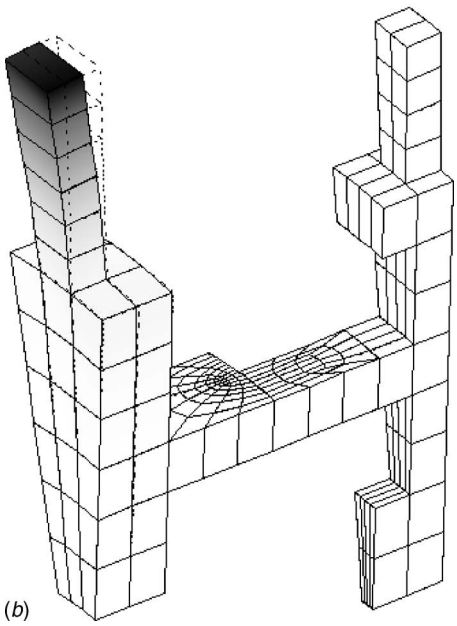

Fig. 5 Five nodal diameter mode at 6147 Hz

stage is first decomposed into elementary cyclic forces corresponding to nodal diameter contributions of each stage and then with each uncoupled, nodal diameter projected, the equation can be solved individually. The global response is then obtained by summing all contributions. The second is to consider all harmonic components of the excitation (or response) in the projection step of the multistage cyclic symmetry method. As an example, if two harmonics (or nodal diameter numbers) p and q are considered, the projection Eq. (14) becomes

$$\mathcal{B}_{p,q}\begin{bmatrix}\tilde{\mathbf{x}}^{(1)}_{i,n(p)}\\ \tilde{\mathbf{x}}^{(1)}_{i,n(q)}\end{bmatrix}+\begin{bmatrix}\tilde{\mathbf{x}}^{(2)}_{i,p}\\ \tilde{\mathbf{x}}^{(2)}_{i,q}\end{bmatrix}=0 \tag{19a}$$

with

$$\mathcal{B}_{p,q}=([\mathbf{e}_{N_2,p},\mathbf{e}_{N_2,q}]^{*}\otimes\mathcal{I}_{b_2})A([\mathbf{e}_{N_1,n(p)},\mathbf{e}_{N_1,n(q)}]\otimes\mathcal{I}_{b_1}) \tag{19b}$$

4 Numerical Results

The rest of the paper is dedicated to numerical applications. First, a validation example will be used to evaluate the performances of the proposed method in modal analysis. Then, an industrial application based on two HP compressor rotating stages will be presented in both modal and forced responses. The importance of multistage dynamic analysis will also be discussed.

4.1 Validation Example. In this part we evaluate the performance of the *multistage cyclic symmetry* method on a numerical example. We consider two stages of cyclic structures with simple geometry: the first being composed of 24 elementary sectors and the second of 45 elementary sectors. Figure 2 shows the finite elements meshes of the two elementary sectors and of the whole structure. The results on the *multistage cyclic symmetry* method are compared to a full 360 deg analysis taken as a reference.

4.1.1 Correlation on Modal Data. Figure 3 gathers the eigenfrequencies calculated by the two methods plotted versus their nodal diameter index. The correlation appears to be correct. This

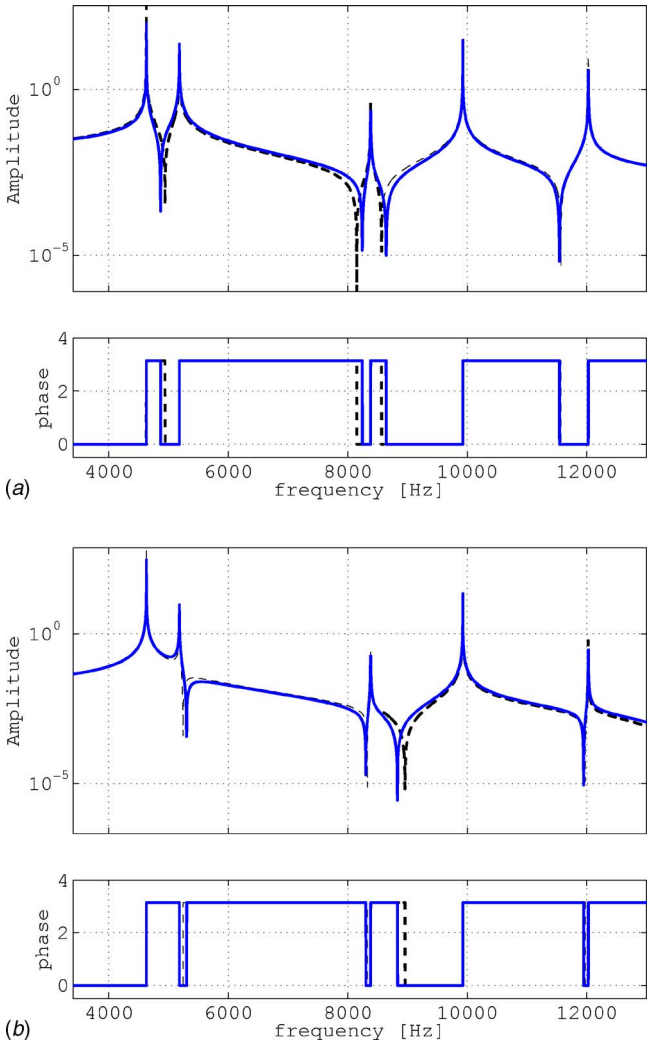

Fig. 6 FRF correlation; (---) reference, (—) multistage cyclic symmetry; (*a*) Blade 1, (*b*) Blade 2

attests to the quality of the prediction of the *multistage cyclic symmetry* method and the validity of the one-to-one nodal diameter projection assumption.

Next, we show and compare (in a qualitative way) the modal deformed shapes. Figures 4 and 5 show results from: (*a*) the reference analysis, and (*b*) the *multistage cyclic symmetry* for various nodal diameter numbers. In these examples we can distinguish some modes localized in only one stage (Fig. 5) and some others with a clear multistage behavior (Fig. 4). Here again, the correlation is correct.

4.1.2 Correlation on Frequency Responses. We now investigate the forced response of the two stages model of Fig. 2. We consider two distributions of forces on each blade of each stage with a spatial periodicity of n (n nodal diameters), such that the force of the jth blade of stage s is

$$f_j^{(s)} = F_0 \cos\frac{2n\pi}{N_s}(j-1)\cos\omega t, \quad s = 1 \text{ or } 2 \tag{20}$$

For a wave number of $n=2$, the frequency responses are displayed in Fig. 6 for the first blade of each stage. The correlation appears to be globally correct. The resonances (frequency and levels) are correctly represented by the multistage cyclic symmetry. There only appears to be small shifts on the antiresonances between the two calculations. This might be related to the one-to-one approximation of the multistage cyclic symmetry method described in

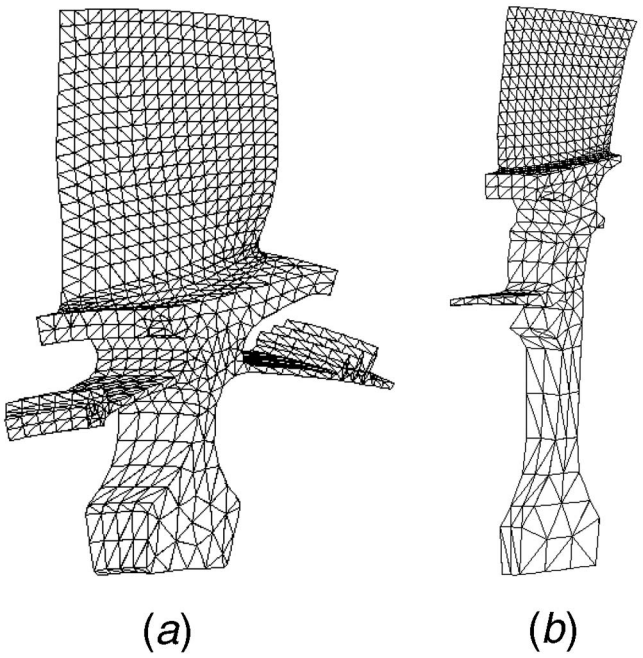

Fig. 7 Finite element models of two HP compressor blisks; (*a*) 1st stage – 36 sectors, (*b*) 2nd stage – 60 sectors

Sec. 3. This is quite similar to a truncation effect in modal analysis. However, the global dynamics remains well approximated.

4.2 Industrial Case Study. Next, an industrial application of the multistage cyclic symmetry method is presented. Figure 7 shows the finite element models (sectors) of two HP compressor blisks which have 36 and 60 sectors, respectively. The computation times of a traditional multistage analysis (with 360 deg models) are clearly prohibitive and thus useless during a realistic design process; in contrast, multistage cyclic symmetry analysis can provide satisfying results with reasonable computational times.

4.2.1 Modal Analysis. For this representative model, we found it interesting to show the influence of the interstage coupling by comparing the results of single stage analysis to the multistage case on a modal analysis. For the single stage analysis we applied a fixed boundary condition on the interstage interface. Figure 8

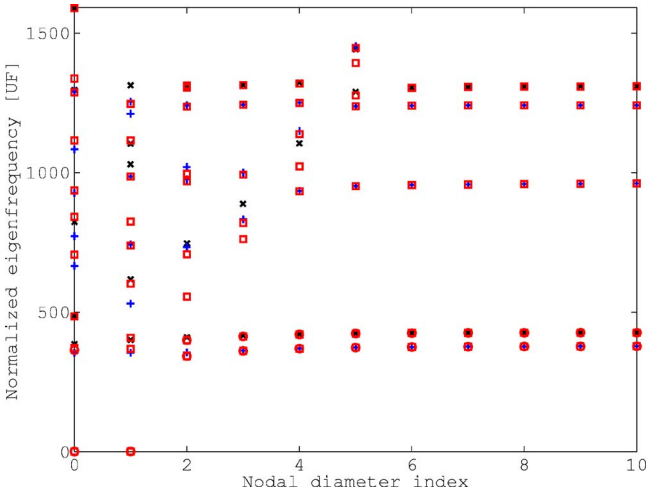

Fig. 8 Influence of interstage coupling, eigenfrequency/nodal diameter (ND) map (from 0 to 10 ND), stage 1 alone (×), stage 2 alone (+), coupled stages (□)

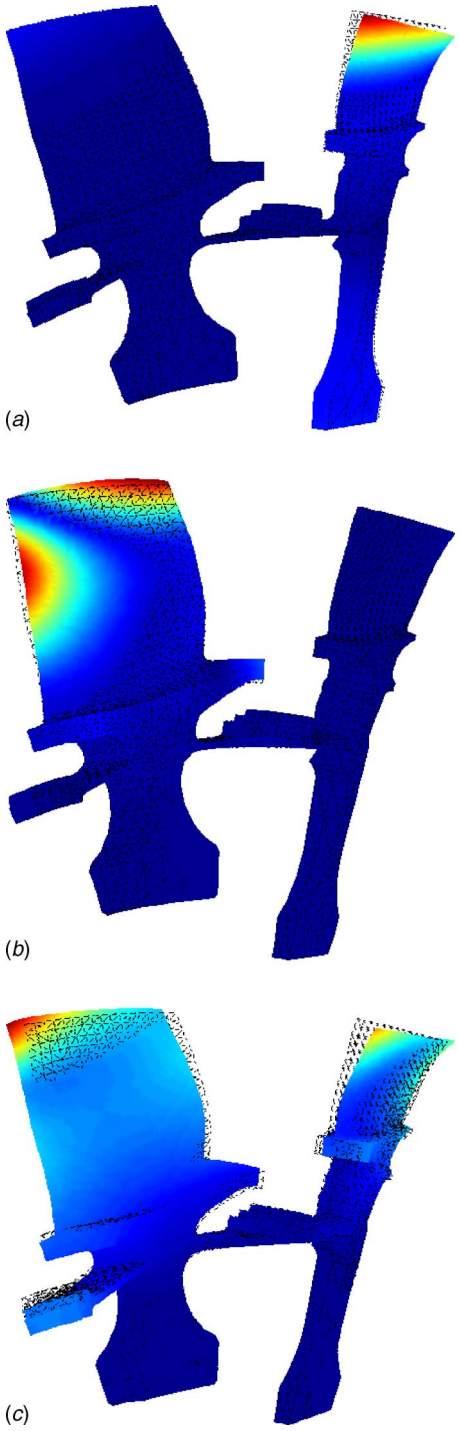

Fig. 9 Examples of modal deformed shapes; (*a*) 5th mode at 0 ND, 68 UF, (*b*) 7th mode at 9 ND, 124 UF, (*c*) 5th mode at 3 ND, 76 UF

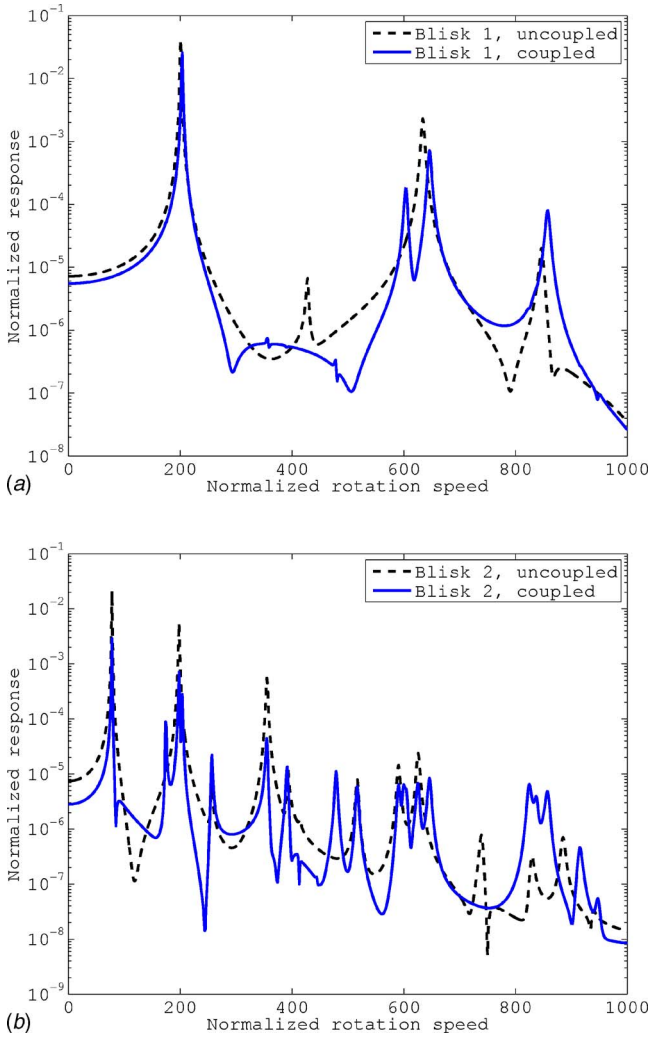

Fig. 10 Frequency responses with and without interstage coupling; (*a*) Blisk 1, (*b*) Blisk 2

gathers the (normalized) eigenfrequencies of these three calculations. The influence of the interstage coupling is noticeable and new modes appear that could not be predicted by a single stage analysis. This is particularly observable in small nodal diameter numbers. In effect, in these cases, the *blade/disk* coupling is generally more important than for higher nodal diameter numbers where the disk's participation is usually smaller. In addition, we provide some examples of modal deformed shapes from the multistage computation in Fig. 9. Some modes show a weak interstage coupling, such as the ones represented in Figs. 9(*a*) and 9(*b*), and feature nearly a single stage behavior. On the other hand, Fig. 9(*c*) displays a strongly (interstage) coupled behavior and can obviously not be represented in traditional single stage analysis. This comparison clearly shows the influence of the multistage coupling in the design of multistage blade disks systems.

4.2.2 Forced Response. The case of steady-state response to a periodic excitation is now addressed. We again consider the two HP blisks system and we apply synchronous excitations on each stage with distinct engine orders. The excitation on stage 1 (36 sectors) is of engine order 7 and the excitation on stage 2 (60 sectors) is of engine order 3. The distributions of forces are harmonic and rotating and the excitation frequencies are multiples of the rotation speed and of the engine order. Figure 10, the response curves of the two stages (Fig. 10(*a*) for stage 1 and Fig. 10(*b*) for stage 2) are plotted versus the rotation speed. We compare the response of each stage alone (with fixed interstage interface) to the two stages coupled. These response were calculated using a modal superposition and a nodal diameter superposition as explained in Sec. 3.

The first remark would be that the multistage responses have a higher frequency content than the single-stage responses and that some peaks appear due to the interstage coupling. This is a major remark for the designer. In effect, as the bladed disks are usually designed by avoiding any coincidence of the modal response to the engine excitation, the possible transfer of vibratory energy

between stages (adjacent or not) can, with the present method, be predicted. Another important point relates to the vibration levels which significantly differ between the two computations; in effect, even when the peaks location (frequency) seems to be correctly evaluated by the single stage analysis, the resonant levels are generally lower in the multistage case. Because of the interstage coupling, the vibratory energy seems to spread over the two stages and this tends to reduce the vibratory levels in individual stages.

5 Conclusions

A new strategy to study the dynamics of multistage cyclic structures, such as turbine engine bladed disks, has been proposed. It is based on a cyclic symmetry modeling of individual stages (in their respective cyclic base) and an accurate interstage coupling in the common physical base. This method appears quite simple to carry out since the sector models of each stage are handled directly and the coupling involves few additional difficulties. The results from numerical simulations show the accuracy of this method. Also, an industrial application highlight the importance of such calculations for the designer.

Acknowledgments

Thanks go to Snecma for its technical and financial support. This work takes place in the framework of the MAIA mechanical research and technology program sponsored by the CNRS, ONERA, and SAFRAN group.

References

[1] Thomas, D. L., 1979, "Dynamics of Rotationally Periodic Structures," Int. J. Numer. Methods Eng., **14**, pp. 81–102.
[2] Wildheim, J., 1981, "Excitation of Rotationally Circumferentially Periodic Structures," J. Sound Vib., **75**, pp. 397–416.
[3] Srinivasan, A. V., 1984, "Vibrations of Bladed Disks Assemblies—A Selected Survey," ASME J. Vib., Acoust., Stress, Reliab. Des., **106**, pp. 165–168.
[4] Slater, J. C., 1999, "Forced Response of Bladed Disks Assemblies—A Survey," Shock Vib. Dig., **31**, pp. 17–24.
[5] Bladh, R., Castanier, M. P., and Pierre, C., 2003, "Effects of Multistage Coupling and Disk Flexibility on Mistuned Bladed Disk Dynamics," J. Eng. Gas Turbines Power, **125**, pp. 121–130.
[6] Rzadkowski, R., and Drewczynski, M., 2006, "Forced Vibration of Several Bladed Discs on the Shaft," ASME Paper No. GT2006–90158.
[7] Bladh, R., Castanier, M. P., and Pierre, C., 2001, "Reduced Order Modeling Techniques for Dynamic Analysis of Mistuned Multi-Stage Turbomachinery Rotors," ASME Paper No. GT2001-0276.
[8] Song, S. H., Castanier, M. P., and Pierre, C., 2005, "Multi-Stage Modeling of Turbine Engine Rotor Vibration," *Proceedings of IDETC/CIE*, Long Beach, CA, September 24–28.
[9] Henry, R., 1980, "Calcul des Fréquences et Modes des Structures Répétitives Circulaires," Journal de Mécanique Appliquée, **4**, pp. 61–82.
[10] Laxalde, D., Thouverez, F., and Lombard, J.-P., 2007, "Dynamical Analysis of Multi-Stage Cyclic Structures," Mech. Res. Commun., **34**, pp. 379–384.
[11] Petrov, E., 2004, "A Method for Use of Cyclic Symmetry Properties in Analysis of Nonlinear Multiharmonic Vibrations of Bladed Disks," J. Turbomach., **126**, pp. 175–183.
[12] Laxalde, D., Thouverez, F., and Lombard, J.-P., 2007, "Vibration Control for Integrally Bladed Disks using Friction Ring Dampers," ASME Paper No. GT2007–27087.

Supersonic Virtual Valve Design for Numerical Simulation of a Large-Bore Natural Gas Engine

Gi-Heon Kim
National Renewable Energy Laboratory,
Golden, CO 80401

Allan Kirkpatrick

Charles Mitchell

Department of Mechanical Engineering,
Colorado State University,
Fort Collins, CO 80523

In many applications of supersonic injection devices, three-dimensional computation that can model a complex supersonic jet has become critical. However, in spite of its increasing necessity, it is computationally costly to capture the details of supersonic structures in intricate three-dimensional geometries with moving boundaries. In large-bore stationary natural gas fueled engine research, one of the most promising mixing enhancement technologies currently used for natural gas engines is high-pressure fuel injection. Consequently, this creates considerable interest in three-dimensional computational simulations that can examine the entire injection and mixing process in engines using high-pressure injection and can determine the impact of injector design on engine performance. However, the cost of three-dimensional engine simulations—including a moving piston and the kinetics of combustion and pollutant production—quickly becomes considerable in terms of simulation time requirements. One limiting factor is the modeling of the small length scales of the poppet valve flow. Such length scales can be three orders of magnitude smaller than cylinder length scales. The objective of this paper is to describe the development of a methodology for the design of a simple geometry supersonic virtual valve that can be substituted in three-dimensional numerical models for the complex shrouded poppet valve injection system actually installed in the engine to be simulated. Downstream flow characteristics of the jets from an actual valve and various virtual valves are compared. Relevant mixing parameters, such as local equivalent ratio and turbulence kinetic energy, are evaluated in full-scale moving piston simulations that include the effect of the jet-piston interaction. A comparison of the results has indicated that it is possible to design a simple converging-diverging fuel nozzle that will produce the same jet and, subsequently, the same large-scale and turbulent-scale mixing patterns in the engine cylinder as a real poppet valve. [DOI: 10.1115/1.2747251]

Introduction

Natural gas fueled engines have been used for many years in stationary applications, such as gas compression and electric power generation. In the United States alone, there are over 8000 large bore (bore >30 cm) slow speed (speed <500 rpm) natural gas engines in use. The most common configuration is a two-stroke cycle with direct injection of natural gas into the cylinder. With the enactment of air emission regulations, reducing exhaust emission levels from pipeline engines has become increasingly important. Poor in-cylinder mixing due to ineffective fuel delivery is believed to be problematic in these natural gas engines. In addition, poor combustion stability, including high misfire rates and variation in cycle-to-cycle peak pressure, can result from insufficient fuel-air mixing. Observed high levels of combustion variability and documented engine performance improvements due to mixing enhancements support this relationship.

One of the most promising mixing enhancement technologies currently used is high-pressure fuel injection. Natural gas is typically injected at low pressures, 1–3 bar above manifold pressure. Since natural gas pipelines operate at pressures of the order of 35 bar, it is of interest to explore the use of pipeline gas at high pressure as the source for injected fuel. Consequently, this creates considerable interest in three-dimensional computational simulations that can examine the entire injection and mixing process in engines using high-pressure injection and can determine the impact of injector design on engine performance. However, the cost of three-dimensional engine simulations—including a moving piston and the kinetics of combustion and pollutant production—quickly becomes considerable in terms of simulation time requirements. This cost is particularly high if the computational model has to capture the details of the complex supersonic flow structures in and near the intricate geometry of the injection valve. However, for an overall simulation designed to examine engine features, such as the extent of fuel-air mixing, combustion, power production, and pollutant generation, the details of these supersonic flow structures may not be critical. Indeed, it is probable that only the downstream jet characteristics are of crucial importance in these macroscopic engine performance studies.

The objective of this paper is to describe the development of a methodology for the design of a simple geometry virtual valve that can be substituted in three-dimensional numerical models for the complex shrouded poppet valve injection system actually installed in the engine. Downstream flow characteristics of the jets passing through an actual valve and various virtual valves were compared. In addition, parameters assessing the extent and effectiveness of mixing were evaluated in full-scale cylinder moving piston simulations that considered the effect of the jet-piston interaction.

As an example of computation of local fuel injection flow fields, Kim et al. [1] examined the injection of natural gas from the two typical types of poppet valves: an unshrouded low-pressure (4 bar) injection valve and a shrouded high-pressure (35 bar) injection valve. The results showed that large stagnation pressure losses occurred as the fuel passes through the poppet valve in both cases. In the low-pressure injection case, the losses were sufficient to cause the downstream fuel jet to be completely subsonic. In contrast, the supply pressure was sufficiently high in

Contributed by the Internal Combustion Engine Division of ASME for publication in the JOURNAL OF ENGINEERING FOR GAS TURBINES AND POWER. Manuscript received August 16, 2005; final manuscript received February 20, 2007. Review conducted by Margaret Wooldridge.

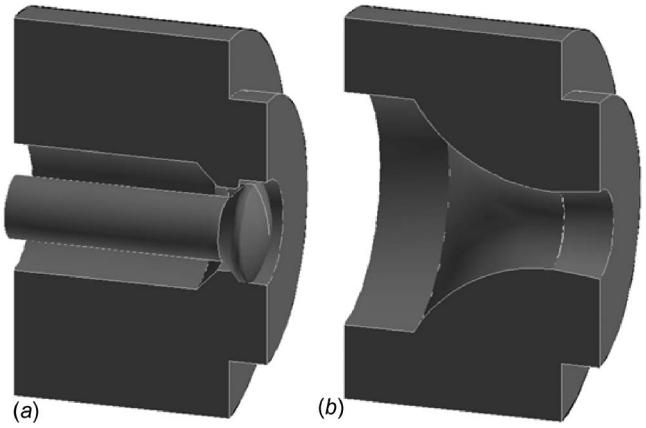

Fig. 1 Schematics of an actual valve currently in use for high-pressure natural gas injection on a large-bore engine (*a*) and schematics of a simple converging-diverging type virtual valve designed for 3D computations (*b*)

the high-pressure injection case that, in spite of large stagnation pressure losses, the jet was still supersonic downstream.

Many researchers computing overall engine performance have used a virtual nozzle as an alternative to modeling the exact geometry of the gas injector. Numerical models of engine performance incorporating subsonic natural gas injection from a simple orifice into an engine cylinder are presented by Gaillard [2], Han et al. [3], and Gundappa et al. [4]. Hill and Ouellette [5] and Mather and Reitz [6] developed the concept of a virtual nozzle sized proportionally to the diameter of the Mach disk, which appears in high-pressure jets from simple orifices, in order to model the subsonic flow downstream of the jet. However, the experimental measurements of Olsen and Wilson [7] indicate that a significant portion of the injected fuel jet penetration distance is in the supersonic flow regime. Studies of sonic and supersonic gas injection with a poppet valve are much more limited. Of particular note is the pioneering work of Boyer et al. [8] who used schlieren photography to study the injection and scavenging processes in a Cooper GMV engine.

There are a number of methods used to quantify the mixing performance of a fuel injector. In this paper, two parameters, mixture mass fraction and fuel mass fraction, are used. The mass fractions are divided into lean, flammable, and rich categories. Papageorgakis and Assanis [9] used the mixture mass fraction as a basis of comparison, while Abraham and Magi [10] used the fuel mass fraction. The nonflammable (rich or lean) mixture mass fraction is related to the emissions performance because it indicates the relative volume of the combustion chamber that may be susceptible to pollutant formation resulting from incomplete combustion. The flammable fuel mass fraction is related to the combustion efficiency because it indicates the relative mass of fuel that is combustible.

Virtual Valve Design

A converging-diverging nozzle with a conical diverging section was adopted as the simplified virtual injection valve in this study because of its geometrical simplicity. An actual poppet valve in use for 35 bar high-pressure fuel injection is presented in Fig. 1(*a*) and a converging-diverging nozzle type virtual valve in Fig. 1(*b*). Several combinations of throat area and supply pressure for this virtual valve were tested. In each case, these parameters were determined by matching the downstream jet characteristic Mach number and the fuel mass injection rate, with the values for the actual poppet valve.

Quasi-one-dimensional isentropic flow relations and ideal gas relations were used to determine the required injection pressure and the dimensions of the virtual nozzle. Figure 2 is a schematic showing the nozzle parameters: tank (supply) pressure p_0, throat radius r^*, and nozzle exit radius r_e.

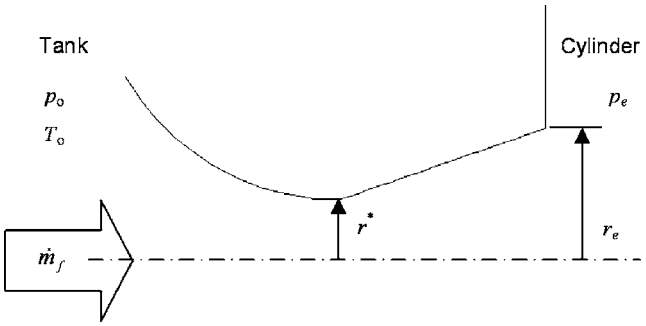

Fig. 2 Design parameters and conditions for virtual valves

The injection stagnation pressure for the virtual valve can be determined from given downstream conditions using Eq. (1), which assumes isentropic flow occurs through the virtual nozzle and a constant value for γ

$$\frac{p_0}{p_e} = \left(1 + \frac{\gamma - 1}{2} M_{ae}^2\right)^{\gamma/\gamma - 1} \tag{1}$$

Under the same assumptions, the nozzle throat area A^* and its corresponding radius can be determined from Eq. (2) for a given fuel mass flow rate $\dot{m}_f$.

$$A^* = \frac{\dot{m}_f}{p_0}\sqrt{\frac{RT_0}{\gamma}}\left(\frac{\gamma + 1}{2}\right)^{\gamma + 1/[2(\gamma - 1)]} \tag{2}$$

Similarly, the nozzle exit area and its corresponding radius were calculated using the area-Mach number relation given by

$$\left(\frac{A_e}{A^*}\right)^2 = \frac{1}{\mathrm{Ma}_e^2}\left[\frac{2}{\gamma + 1}\left(1 + \frac{\gamma - 1}{2}\mathrm{Ma}_e^2\right)\right]^{(\gamma+1)/(\gamma-1)} \tag{3}$$

where A_e is the nozzle exit area required to expand the fuel jet to the cylinder pressure at exit.

Comparison of Downstream Characteristics of Fuel Jet

Detailed axisymmetric numerical simulations for the fuel gas injections using the actual and virtual valves were carried out to compare the injection performance of the valves. Methane was injected through each valve into an open cylinder, which was kept at a constant pressure of 1 bar. The cylinder pressure varies slowly with a mean value close to 1 bar during injection in actual engines. The computational domain in this set of calculations included the valve geometries and the piston top but not the cylinder wall. The near valve region and entire domain grids used for these numerical simulations are shown at Fig. 3. Since the poppet valve operates electronically with a top hat profile, the computational simulation assumed a fully open valve. At valve opening, the valve moves very quickly to its maximum height, and it stays still for most of the valve open duration; then it closes again quickly. Since the maximum valve height is very small (only 0.635 mm, ~1/1000 of the cylinder length scale) and the valve is stationary for major duration of fuel gas injection, the valve motion was not incorporated in the simulations. Instead, an imaginary membrane was introduced inside the valve to simulate valve opening and closing. The computational domain was discretized by using a variable-size grid axisymmetric mesh in the computations. Grid adaptation was used to refine the mesh and locate the rapidly varying expansion and compression structures. Because of its grid adaptation capability, FLUENT was used as the computational fluid dynamics (CFD) solver. The computations were carried out on PCs and Linux machines.

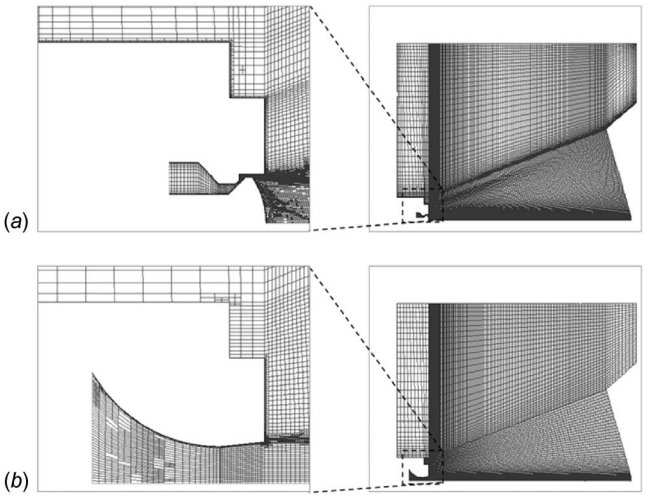

Fig. 3 Computational grids used in axisymmetric computations for an actual-valve injection (*a*) and for a virtual valve injection (*b*)

Three different virtual valves used in the computations are presented here for comparison to the conventional actual valve. Design Mach numbers at the nozzle exit, $Ma_e=1.53$ for virtual-1 and $Ma_e=1.95$ for virtual-2, were determined from the downstream Mach number profile of the jet issuing from actual poppet valve as shown in Fig. 4. The virtual-3 design is midway between the virtual-1 and virtual-2 designs and will be discussed later in connection with the flammable mixture fraction. Table 1 shows the design parameters and the resulting jet characteristics of these valves. Note that the virtual valve injection pressures are only 10–20 % of the actual poppet valve injection pressure.

Each axial momentum flow rate $\dot{p}_x$ was calculated with Eq. (4) at 18 cm downstream of the valve exit and at 11 ms after start of injection,

$$\dot{p}_x = \int_0^\infty \rho v_x^2 2\pi r dr \tag{4}$$

Because the injection jet flow approaches a local steady state within 2 ms and the fuel injection duration of these engines is ~11 ms, most the of comparisons for validation of the virtual valves were carried out at 11 ms after start of injection. Figure 5(*a*) shows the distribution of Mach number along the jet centerline axis. The axial distance was measured from the nozzle exit plane in each case. The actual valve flow profile had a largely

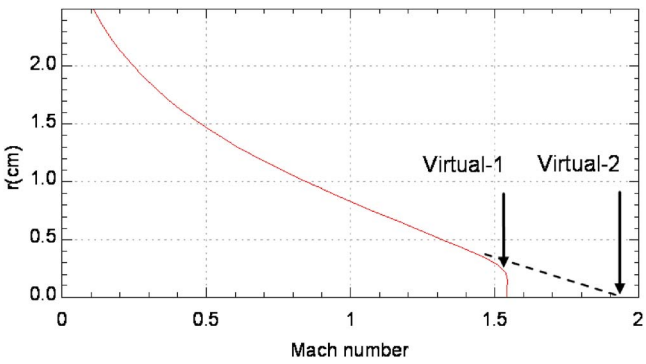

Fig. 4 Mach number profile of the jet issuing from conventional poppet valve at 18 cm downstream from shroud nozzle exit. Design exit Mach numbers of virtual-1 and virtual-2 are marked on the graph.

Table 1 Virtual valve design parameters and the characteristics of jets issued from the tested valves

	Actual	Virtual-1	Virtual-2	Virtual-3
$\dot{m}_f$ (kg/s)	0.131	0.130	0.129	0.132
$\dot{p}_x$ (N)	98.9	79.3	91.9	87.2
Ma_e		1.53	1.95	1.74
p_0 (bar)	35	3.73	7.16	5.13
r^* (mm)		8.14	5.88	6.91
r_e (mm)		8.95	7.65	8.22

annular character. The resulting repeating structures of expansion and compression were eventually damped away downstream, with some losses in stagnation pressure accompanying this process. Downstream of the oscillations, the Mach number of the fuel jet that issued from the conventional poppet valve increased slightly before it started to decrease. This is due to the initial jet profile. As discussed in Kim et al. [1], the jet emanating from this type of poppet valve exhibits an initial jet profile with an annular radial profile. The maximum speed for this type of jet occurs well off the axis. The small and gradual increase of Mach number for the real valve can thus be traced to momentum transfer to the axis from the higher velocity regions off the axis.

The main goal of the virtual valve design is to replicate the actual fuel jet after the flow structures resulting from the poppet geometry have died down. In both of the virtual valves, virtual-1 and virtual-2, the Mach number of the supersonic fuel jet oscillated just downstream of the nozzle exit, as shown in Fig. 5(*a*). These oscillations were due to the fact that neither of the nozzle designs resulted in perfect expansion through the nozzle. Because of the simple conical shape of the diverging section in our virtual valves, the injection jet is not a one-dimensional parallel flow at the nozzle exit. The one-dimensional isentropic formulas used to calculate the exit area are thus not entirely accurate and cause the nozzles based on these formulas to have a slightly overexpanded flow from the nozzle exit. The core Mach number of the fuel jets issuing from the virtual valves reached a constant value ~8 cm downstream and remained constant until the momentum of the jet's core started to diffuse outward in the radial direction. In contrast to the real shrouded valve, the virtual valve converging-diverging nozzles produced essentially one-dimensional flows at the exit. The jet was further slowed as it eventually entered the region influenced by the existence of the piston top located 30 cm downstream. Comparing the axis Mach number profiles, virtual-1 showed better agreement with the actual valve in the initial jet region, and virtual-2 followed the real profile more closely as the piston surface was approached.

Radial distributions of axial velocity and axial momentum flux at this location are compared in Figs. 5(*b*) and 5(*c*), respectively. At the axial location 18 cm from the nozzle exit, all the jets presented here had developed typical bell-shaped profiles and were still free from the effect of the piston top. As can be seen from Fig. 5, virtual-2 profiles for velocity and axial momentum flux were very similar to those of the real valve except near the axis. This dissimilarity of near axis profiles is relatively unimportant in designing a virtual nozzle, since the relative amount of mass flow is small near the axis. This is because the cross-sectional flow area is proportional to the square of the radial distance from the axis.

The axial momentum flux, shown in Fig. 5(*c*), was integrated over the jet cross section in order to get the numerical values of axial momentum flow rate presented in Table 1. The profiles of Figs. 5(*b*) and 5(*c*) strongly imply that virtual nozzles can produce satisfactory approximations of the downstream fuel jet issuing from a real poppet valve in spite of the quite different geometries and supply conditions, as well as significant differences in upstream jet structures.

Because interaction of the fuel jet with the piston top is be-

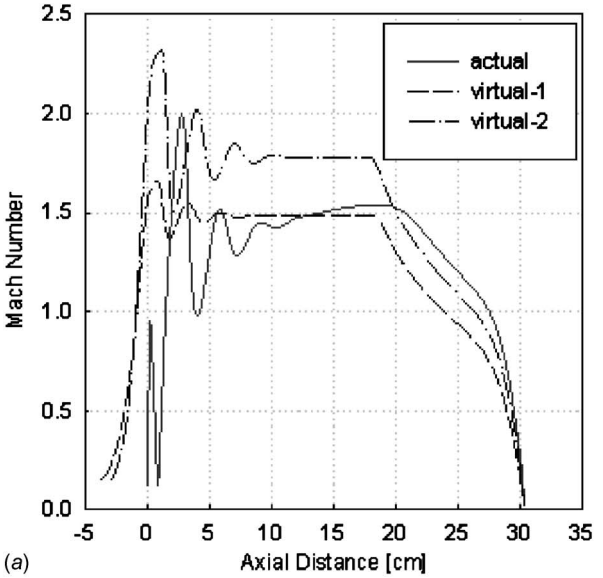

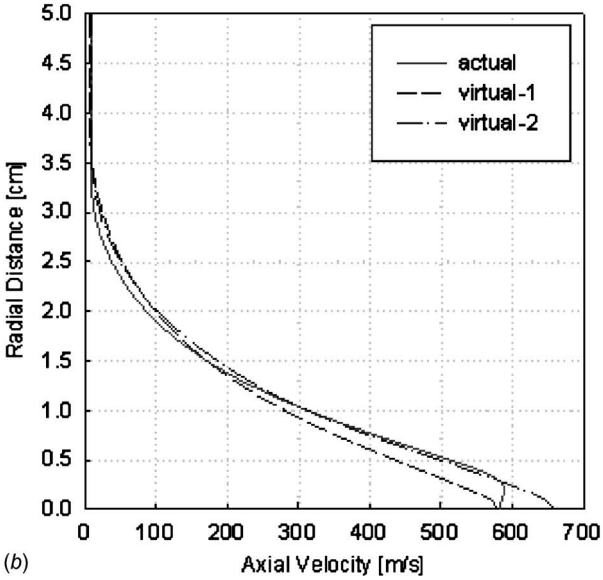

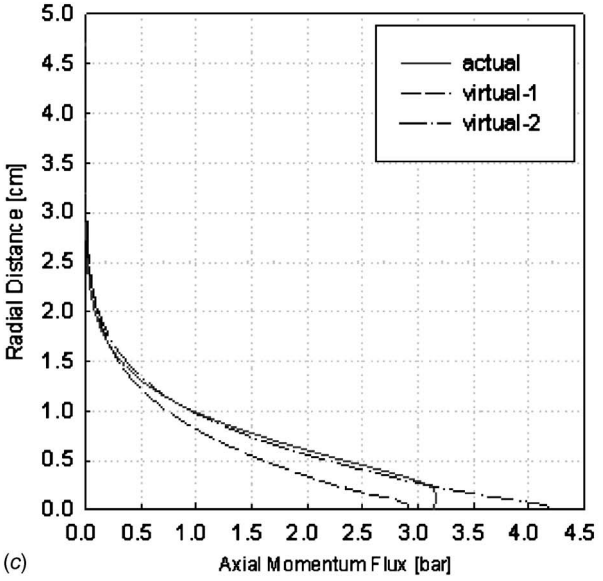

Fig. 5 Comparisons of centerline Mach number profiles among the tested valves (*a*), axial velocity (in m/s) distribution at 18 cm downstream jets (*b*), and axial momentum flux (in bar) at 18 cm downstream jets (*c*)

lieved to play a significant role in fuel-air mixing, the jet penetration rate could be of importance. Penetration depth comparisons among the actual and the virtual valves are presented by showing the velocity magnitude contours at increasing times from the start of injection in Fig. 6. The actual valve and virtual-1 valve contours show good agreement, while the jet issuing from the virtual-2 valve penetrates slightly faster than the others. The difference in penetration depths comes from the fact that the maximum velocity of virtual-2 is larger than those of the others, as shown in Fig. 5(*b*). It should be observed that since the penetration time to the piston top is of the order of 1 ms, while the total injection period is ~11 ms, small differences in penetration rate are unlikely to have any substantial impact on overall mixing behavior.

Comparison of Mixing Statistics in Full-Scale Engine Cylinder

Moving piston simulations in a 35 cm bore and stroke engine cylinder for the conventional shrouded poppet valve and for the virtual valves were carried out in order to compare the overall mixing characteristics. Figure 7 shows the grid systems designed to investigate the interaction between the fuel jets and the moving piston top in the cylinder. The computations were axisymmetric, and the effects of scavenging were not included. In this set of computations, the piston moves from bottom dead center (BDC) to top dead center (TDC). Injection started at 115 deg before TDC, and the injection duration was 20 deg of crank angle. The total amount of fuel injected into the cylinder was the same for all valves, and the overall equivalence ratio was fixed as 0.68 in each simulation. For these numerical experiments, the CFD solver STARCD was used using its moving mesh capabilities. The computations were carried out on a SUN Ultra Sparc workstation and Linux machines.

The effectiveness of fuel-air mixing was examined by calculating flammable fuel fractions and flammable mixture fractions during the injection. The flammable mixture fraction is defined as the ratio of the flammable mass of mixture to the total mass in the cylinder at any instant. Similarly, the flammable fuel fraction is defined as the ratio of the mass of flammable fuel to the total fuel mass in the cylinder. Note that the flammable mixture fraction considers those fractions of the mass where only air is present, while the flammable fuel fraction does not. The mixture and fuel fractions are computed by integrating over all of the computational cells in the cylinder volume with

$$f_m = \frac{\text{flammable mass of mixture}}{\text{total mass of mixture}} \tag{5}$$

$$f_f = \frac{\text{mass of fuel included in flammable mixture}}{\text{total mass of fuel}} \tag{6}$$

A nonflammable lean mixture in a cell is defined as one with an equivalence ratio of 0.5; a flammable mixture has an equivalence ratio between 0.5 and 2.0; and a nonflammable rich mixture has an equivalence ratio of >2.0. These definitions of nonflammable lean, nonflammable rich, and flammable mixtures are based on laminar flame propagation limits at atmospheric pressure and nominal atmospheric temperature. Since the lean limit is generally observed not to be strongly affected by temperature and pressure, and since this is the limit of consequence in lean burning engines, predictions based on these limits should still be useful.

Equivalence ratio contours during and after injection are shown in Fig. 8. The contours for each valve are presented from 72 deg before TDC to TDC in increments of 18 crank angle degrees. In the absence of scavenging flows, mixing appeared to be dominated by jet impingement on the piston and fuel flow redirection along the surface of piston top and cylinder wall. In an overall sense, fuel-air mixing occurred in a similar way in the virtual and the real valve cases. Note that in each frame, the dark region

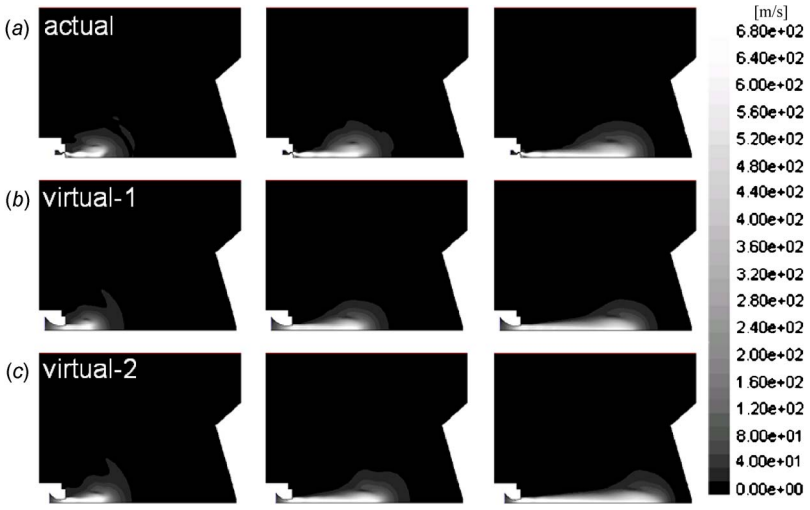

Fig. 6 Velocity magnitude contours (in m/s) at 0.3 ms, 0.6 ms, and 0.9 ms for comparison of penetration rates of actual valve (*a*) virtual-1 (*b*), and virtual-2 (*c*).

represents the chamber volume that is below the lean flammability limit. In spite of the differences of the injection geometries and the supplied pressure, the size and the strength of the induced vortex in each valve system, as well as the spatial distribution of fuel, showed good agreement.

Figure 9 shows how the flammable mixture fraction changes with time. The relative amount of flammable mixture can be interpreted as indicative of the extent of mixing. As can be seen in Fig. 9, the two virtual valves already discussed produced flammable mixture fraction curves that bracketed the results for the real valve. In response to this prediction, an additional virtual valve with design variables bracketed by the other two was developed.

This valve, denoted as virtual-3, had a throat radius of 6.91 mm and a supplied injection pressure of 5.13 bar. These values result from applying the virtual nozzle design procedure described earlier when the exit Mach number was specified as 1.74, midway between the values for virtual-1 and virtual-2. The corresponding flammable mixture fraction prediction for virtual-3 can be seen to be very close to that of the real valve at all crank angles.

Mass-averaged turbulent kinetic energy at the time of ignition, corresponding to 9 deg before TDC, was calculated using Eq. (7). Results for the four examined valves are compared in Fig. 10. The turbulent kinetic energy is of interest since minimization of the combustion duration in an engine requires a high turbulent intensity. Consistent with the flammable mass fraction predictions, the predictions of turbulent kinetic energy for virtual-3 simulate the actual valve very closely and lie between the predictions for virtual-1 and virtual-2. Figure 10 shows that the virtual-3 valve

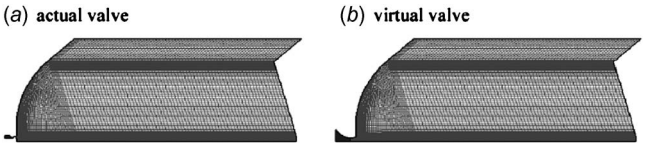

Fig. 7 Grid systems used for in-cylinder mixing simulations with moving piston top: (*a*) is for the real valve and (*b*) is for virtual nozzles

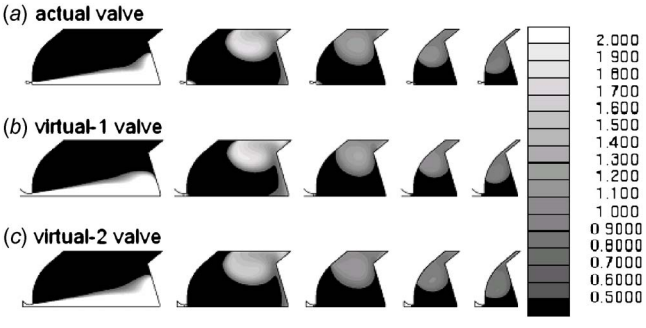

Fig. 8 Equivalence ratio contour sequences from 108 deg of crank angle before TDC to TDC in intervals of 27 deg of crank angle for actual valve injection (*a*), for virtual-1 (*b*), and for virtual-2 (*c*).

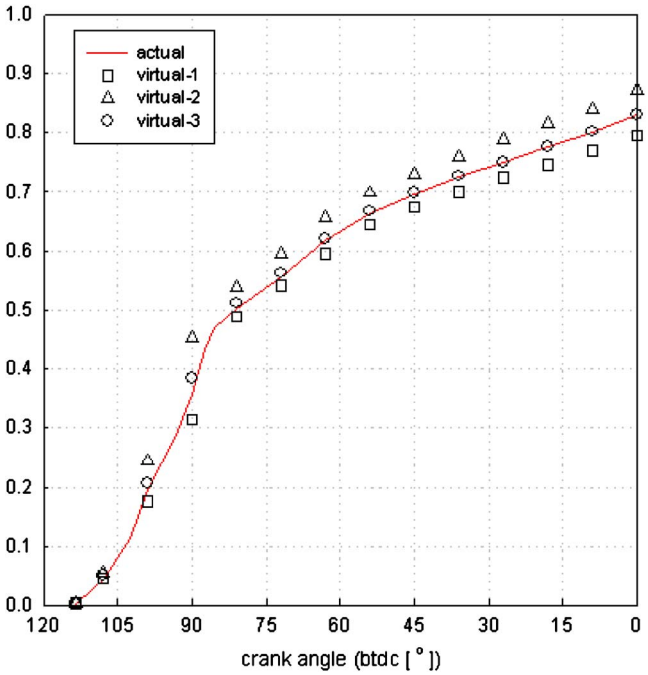

Fig. 9 Flammable mixture fraction changes with crank angle (degrees in BTDC)

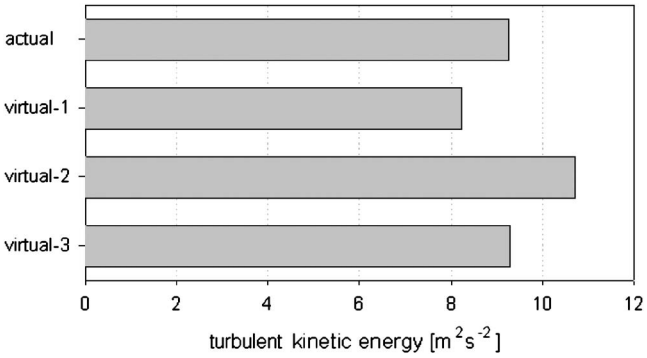

Fig. 10 Comparison of mass averaged turbulent kinetic energy at nine crank angle degrees before TDC for each tested valve

properly reproduces the turbulent kinetic energy in mean value in the cylinder as an initial condition for the combustion processes that follow,

$$\bar{k} = \frac{\int k\rho dV}{\int \rho dV} \tag{7}$$

Statistical distributions of mixture and fuel mass over the range of equivalence ratios of the mixture were investigated in order to evaluate how well virtual-3 reproduced the performance of the real valve. Distributions at 9 deg before TDC for mixture mass and fuel mass are presented in Figs. 11(*a*) and 11(*b*), respectively. These figures show the distributions of the total mixture mass (Fig. 11(*a*)) and total fuel mass (Fig. 11(*b*)) bounded with specific spans of equivalence ratio. The distributions predicted for the real valve and virtual-3 are generally identical throughout the range of observed equivalence ratios. Achieving the similarity of these distributions is important in three-dimensional engine simulations, for instance, in the case of nitrogen oxide production, where the local flame temperature is critical.

Verification of reproducibility for the spatial distributions of mixing extent and turbulence quantities over a cylinder volume are important for the combustion and pollutant production calculations that follow in engine simulations. Equivalence ratio contours in the engine cylinder at 9 deg before TDC for both the actual valve and the virtual-3 valve are compared in Fig. 12. The comparisons of the turbulent kinetic energy contours for these valves are shown in Fig. 13 at the same crank angle. The magnitudes and patterns of these distributions for both the real valve and the virtual-3 valve match each other quite closely. This implies that using the proposed virtual valve to model the actual poppet

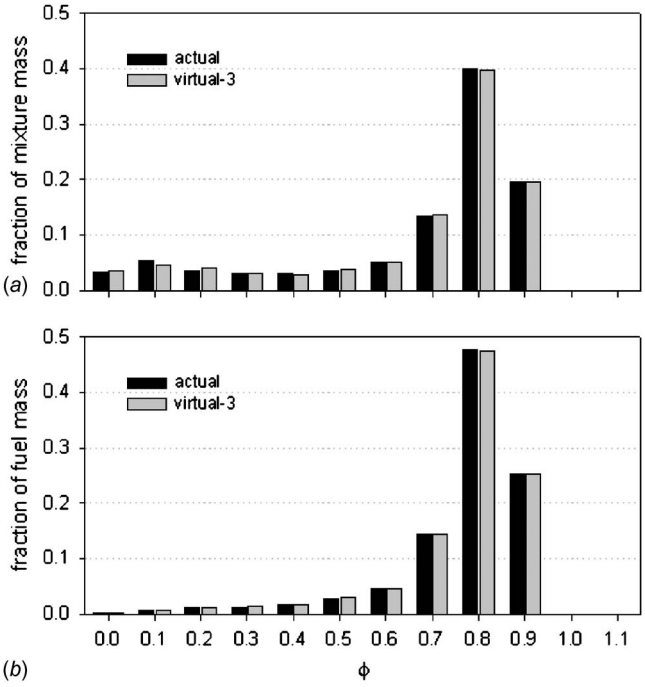

Fig. 11 Mass distribution with equivalence ratio for the mixture gas (*a*) and for the fuel gas (*b*)

valve in a three-dimensional engine CFD simulation will provide an accurate representation of engine conditions at ignition while alleviating computational difficulties significantly. Interestingly the virtual-3 valve produced nearly identical mixing and turbulence levels in the engine while requiring only 15% of the injection pressure compared to the real valve injection. This is direct evidence of the very poor efficiency of standard poppet valve designs for delivering injection momentum compared to ideal expansion nozzles. The results seem to indicate that a virtual valve can be successful in simulating not only the average mixing characteristics of a real valve but also many of the detailed mixing characteristics.

Conclusions

A virtual valve was developed that can be used in a complex three-dimensional CFD computation to simulate an actual poppet valve with supersonic gas injection. An axisymmetric two-dimensional CFD analysis was carried out with an actual poppet valve geometry and injection condition. The jet characteristics downstream were evaluated and reproduced using a virtual valve. In this study, a simple converging-diverging nozzle was chosen as the virtual valve design. Lower (for virtual-1) and upper (for

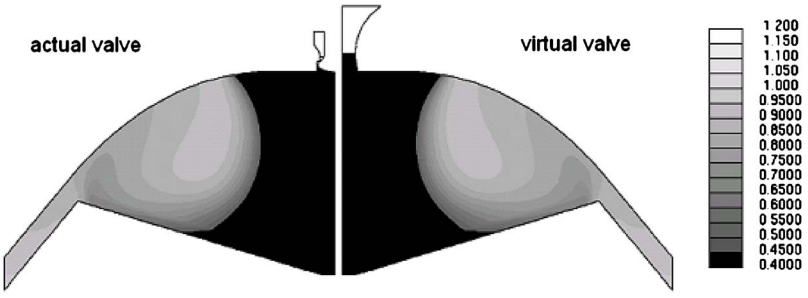

Fig. 12 Comparison of spatial distribution of fuel at nine crank angle degrees before TDC by showing the equivalence ratio contours for actual and for virtual-3 valve

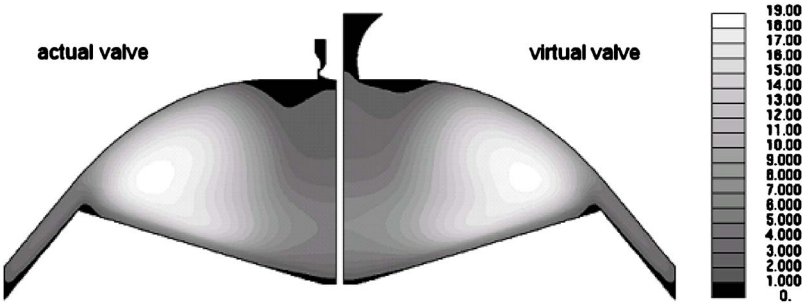

Fig. 13 Comparison of spatial distribution of turbulent kinetic energy (TKE) (in m^2/s^{-2}) at nine crank angle degrees before TDC by showing TKE contours for actual and for virtual-3 valve

virtual-2) bounds of Mach numbers downstream were selected to determine the virtual injection pressures required to simulate the real valve. A third virtual valve (virtual-3) was then designed for a Mach number midway between those of the first two and proved to provide the best simulation of the real valve. The nozzle throat area in each design was chosen to match the mass injection rate. The exit area of the nozzle was calculated using one-dimensional isentropic relationships. Fuel mixing characteristics in a full-scale engine cylinder were compared to verify the performance of the virtual nozzles through additional axisymmetric moving boundary calculations.

The results have indicated that a simple converging-diverging virtual valve, which is designed by the procedure described here, can produce a good approximation of the downstream fuel jet issuing from a real poppet valve. Finally, with the proper design a virtual valve can be used successfully in many three-dimensional numerical studies that might be practically impossible if the complex flow structures in the real valve had to be captured in computational simulations.

Nomenclature

A^* = area of nozzle throat
A_e = area of nozzle exit
Ma_e = Mach number at nozzle exit
R = gas constant
T_0 = stagnation temperature of injection gas
f_f = flammable fuel fraction
f_m = flammable mixture fraction
k = turbulent kinetic energy
$\dot{m}_f$ = mass flow rate of fuel
$\dot{p}_x$ = axial momentum flow rate
p_0 = stagnation pressure of injection gas
p_e = static pressure at nozzle exit
r^* = radius of nozzle throat
r_e = radius of nozzle exit
ϕ = equivalence ratio
γ = specific heat ratio
ρ = density of mixture

References

[1] Kim, G.-H., Kirkpatrick, A., and Mitchell, C., 2004, "Computational Modeling of Natural Gas Injection in Large Bore Engines," ASME J. Eng. Gas Turbines Power, **126**(3), pp. 656–664.
[2] Gaillard, P., 1984, "Multidimensional Numerical Study of the Mixing of an Unsteady Gaseous Fuel Jet With Air in Free and in Confined Situations," SAE Paper No. 840225.
[3] Han, Z., Tsao, K., and Abdalla, M., 1994, "Computation of the In-Cylinder Processes of a Natural Gas Engine," SAE Paper No. 940213.
[4] Gundappa, M., Denlinger, M., Dulaney, K., Campbell, L., and McCarthy, J., 2000, "Computational Fluid Dynamics Modeling of Internal Combustion Engine Performance and Emissions," *Proc Gas Machinery Conference*, GMRC, Austin, TX..
[5] Hill, P., and Ouellette, P., 1999, "Transient Turbulent Gaseous Fuel Jets for Diesel Engines," ASME J. Fluids Eng., **121**(1), pp. 93–101.
[6] Mather, D. K., and Reitz, R., 2000, "Modeling the Effects of Auxiliary Gas Injection on Diesel Engine Combustion and Emissions," SAE Paper No. 2000-01-0657.
[7] Olsen, D., and Willson, B., 2001, "Planar Laser Induced Fluorescence Imaging of Gas Injection From Fuel Valves for Large Bore Natural Gas Engines," *Proc. ASME Fall 2001 ICE Conference*, ASME, New York, pp. 17–24.
[8] Boyer, R., Craig, D., and Miller, C., 1954, "A Photographic Study of Events in a 14-In. Two-Cycle Gas Engine Cylinder," Trans. ASME, **76**, pp. 97–108.
[9] Papageorgakis, G., and Assanis, D., 1998, "Optimizing Gaseous Fuel-Air Mixing in Direct Injection Engines Using an RNG Based k-ε Model," SAE Paper No. 980135.
[10] Abraham, J., and Magi, V., 1997, "Computations of Transient Jets: RNG k-ε Model Versus Standard k-ε Model," SAE Paper No. 970885.

A Study on Fluidized Bed-Type Particulate Filter for Diesel Engines

Sung-Sub Kee
e-mail: sskee@energy.kyoto-u.ac.jp

Ali Mohammadi

Takuji Ishiyama

Takaaki Kakuta

Graduate School of Energy Science,
Kyoto University,
Yoshida Honmachi, Sakyo-ku,
Kyoto, 606-8501, Japan

A fluidized bed-type diesel particulate filter (DPF) was applied to filter particulate matter (PM) in diesel engine exhaust gas. The effects of the fluidized bed design parameters, such as gas velocity, bed particle size, and height, on PM and smoke filtration efficiencies, and pressure drop were experimentally investigated using a single-cylinder direct injection (DI) diesel engine. High PM filtration efficiency and low pressure drop were achieved with the DPF, especially at a lower gas velocity. The PM filtration efficiency was higher with a smaller bed particle size at the lower gas velocity; however, it drastically decreased with an increase in gas velocity due to excessive fluidization of the bed particles. Increase in bed height led to higher PM filtration efficiency while causing an increase in pressure drop. The theoretical work was also conducted for further investigation of the effects of the above-mentioned parameters on PM filtration. These results indicated that diffusion filtration was the dominant mechanism for PM filtration under the conditions of this study and that the decrease in PM filtration efficiency at high gas velocity was caused by a deterioration in the diffusion filtration. The bed particle diameter and the bed height should be optimized in order to obtain a high filtration efficiency without increasing the DPF size. [DOI: 10.1115/1.2747255]

Introduction

Distributed power systems, such as on-site electric generators and co-generation plants, have recently received attention. These systems allow simultaneous generation of heat and electricity without any power-line loss, and thus, they have higher energy efficiency compared to conventional centralized power plants [1]. Gas turbines, gas engines, and diesel engines have been used as prime movers in these systems. Among these engines, diesel engines have the advantage of generating electricity with high efficiency [2,3]. However, emission of nitrogen oxides (NO_x) and particulate matter (PM) is a barrier for wider application of diesel engines, especially in urban areas.

In order to reduce NO_x and PM emissions, several combustion technologies that suppress in-cylinder formation of harmful matters, such as high-pressure fuel injection, injection rate control [2], and exhaust gas recirculation (EGR) [4], have been investigated by other researchers. Combined with these technologies, the use of after-treatment devices is crucial to preserving quality of the atmosphere. For NO_x reduction, the selective catalytic reduction (SCR) system is an established technology for stationary engines. On the other hand, highly efficient low-cost PM reduction methods are not yet developed. Appropriation of recently developed diesel particulate filters (DPFs) for automobile engines [5,6] may be attractive because of their high performance. However, many stationary diesel engines use high sulfur content heavy oil, which obstructs the use of catalyst-combined DPF because the sulfur deteriorates PM filtration and filter durability [7,8]. Even though noncatalyzed DPFs, such as wall-flow monolith, ceramic foam, wire mesh, etc., were used, the accumulation of ash, which is the noncombustible residue of the heavy oil or lubrication, inside the DPF causes an increase of exhaust back pressure and results in increased fuel consumption [9]. Therefore, a different type of DPF is needed for stationary engines. As a new type, the DPF made of ceramic felt combined with metal mesh was recently proposed [8]. The test results demonstrated high filtration efficiency even for high-sulfur fuel with the injection of potassium carbonate aqueous solution. However, further research is needed to develop a DPF with high filtration efficiency, high durability, and low cost.

Fluidized beds have been widely applied to remove aerosols from product gases in coal combustion, coal gasification, biomass treatment, and many other applications [10–12]. When using the fluidized bed for the PM filtration, PM is captured by the fluidized bed particles when the exhaust gases pass through. Since the bed particles move freely, there should be a lower increase in engine back pressure due to PM accumulation, thereby enhancing the engine performance. Furthermore, relatively simple design and operation of the fluidized bed should allow low manufacturing and maintenance costs.

Water-cooled fluidized beds and electrostatic systems have already been investigated for PM filtration in diesel engines [13,14]. Improvements in the PM filtration efficiency and reduction in engine back pressure were reported in these studies. However, the effects of design parameters in the fluidized bed have not yet been investigated systematically.

This study aimed to develop a fluidized bed-type DPF dedicated to stationary diesel engines while focusing on low manufacturing and maintenance costs. The potential of the DPF to filtrate the PM from diesel engines and the effects of the fluidized bed design parameters, such as gas velocity, bed particle size, and bed height on PM filtration efficiency and filter pressure drop, were investigated. Experiments were carried out using a single-cylinder test engine. Furthermore, the theoretical work was conducted to understand measured effects of these parameters in order to develop a strategy for the optimization of the filter system.

Filtration Mechanisms and Calculation of Filtration Efficiency in Fluidized Bed

To explain the trend of measured filter efficiency, PM filtration efficiency in a fluidized bed was calculated based on the work of Clift et al. [15]. Explaining their work in brief, four mechanisms are recognized in aerosol filtration by a fluidized bed, namely, diffusion, inertial, gravity, and interception filtrations. First, the diffusion filtration is due to the contact of an aerosol particle with

Contributed by the Internal Combustion Engine Division of ASME for publication in the JOURNAL OF ENGINEERING FOR GAS TURBINES AND POWER. Manuscript received March 2, 2006; final manuscript received February 9, 2007. Review conducted by Jim Cowart.

Table 1 Filtration efficiency of each individual mechanism

Mechanism	Efficiency
Diffusion filtration	$E_D=(4.36/\varepsilon)(D/Ud_c)^{2/3}$
Inertia filtration	$E_I=[\mathrm{St}/(\mathrm{St}+0.062\varepsilon)]^3$
Gravity filtration	$E_G=0.0375(N_G)^{1/2}$
Interception filtration	$E_{DI}=6.3N_{DI}^2\varepsilon^{-2.4}$

a bed particle caused by the Brownian motion. Second, the inertial filtration occurs when an aerosol particle deviates from a curved gas stream line and collides with a bed particle due to the inertia. Third, the gravitational settling filtration is the capture of an aerosol particle that drops out of the gas stream due to the gravitational force. Finally, direct interception filtration, which is direct blocking of an aerosol particle by a bed particle, is also considered. The filtration efficiency of a single bed particle E is expressed by the ratio of the number of captured aerosol particles to the number of particles approaching a bed particle. The filtration efficiency E is determined as the sum of the filtration efficiencies ($E=E_D+E_I+E_G+E_{DI}$) for each mechanism mentioned above. The filtration efficiencies of each mechanism are shown in Table 1.

The diffusion filtration efficiency in Table 1 is valid when the Schmidt number Sc is in the range of $165<\mathrm{Sc}<70{,}600$. The Stokes number St and Reynolds number Re of bed particles should be in the range of $0.002<\mathrm{St}<0.02$, $\mathrm{Re}<130$, respectively, for the calculation of the inertial filtration. The Reynolds number of bed particles should be in the range of $0.05<\mathrm{Re}<30$ for the calculation of the gravitational settling filtration efficiency. The filtration efficiencies listed in Table 1 are applicable to the calculation of the PM filtration efficiency because Sc, St, and Re satisfy the above conditions, assuming that the PM is spherical and has a density of 1.25 g/cm^3 [16] and a diameter of 100 nm [17].

The superficial gas velocity U affects the filtration efficiency because it influences flow regime inside a bed. Gas velocity at which the pressure drop balances with the bed weight is called the minimum fluidization velocity U_{mf}. When the velocity U is below U_{mf}, the bed is stationary in a macroscopic sense and this state is called "fixed bed." When U is slightly increased above U_{mf}, then the flow of bed particles is observed to be convectional with the bubbles flowing out of the bed. This state is called "fluidized bed." Further increase in U causes severe entrainment of bed particles into the gas flow, and they begin to escape from the bed chamber.

For calculation of U_{mf}, the Galileo number Ga is defined as

$$\mathrm{Ga}=\frac{\rho_g(\rho_c-\rho_g)gd_c^3}{\mu} \tag{1}$$

After setting the void fraction at the minimum fluidization velocity ε_{mf} to 0.4, which is a typical value for spherical particles, the Reynolds number Re_{mf} is given by the following empirical equation:

$$\mathrm{Re}_{mf}=25.7(\sqrt{1+5.53\times10^{-5}\mathrm{Ga}}-1) \tag{2}$$

The U_{mf} is then derived by the following equation:

$$U_{mf}=\frac{\mathrm{Re}_{mf}\mu}{d_c\rho_g} \tag{3}$$

The overall performance of the fluidized bed is usually described by the overall penetration efficiency PE, which is the ratio of the aerosol concentration in exit gas to the concentration in gas entering the fluidized bed. And the overall filtration efficiency f of the fluidized bed is described by $f=1-\mathrm{PE}$.

For the fixed bed state, f is expressed by

$$f=1-\exp(-\kappa H) \tag{4}$$

Here, κ is a rate constant for filtration, which is related to the filtration efficiency of a single bed particle E.

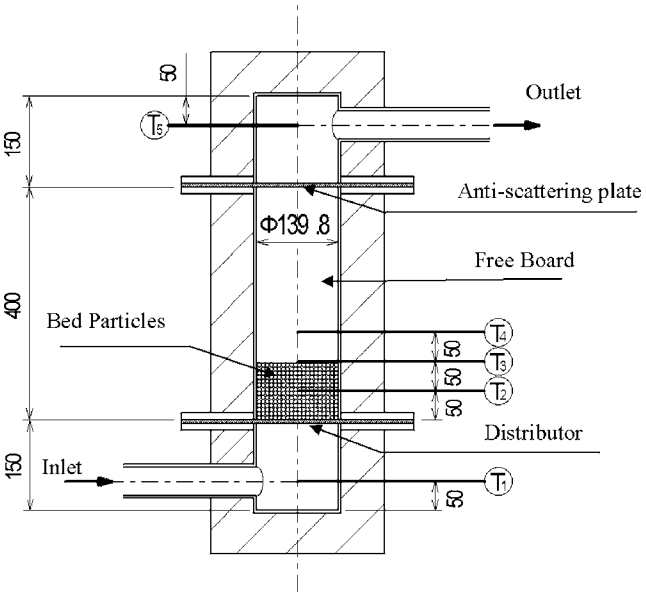

Fig. 1 Structure of a fluidized bed-type DPF

$$\kappa=\frac{3E(1-\varepsilon)}{2d_c} \tag{5}$$

In Eq. (4), $\exp(-\kappa H)$ is a probability of the aerosol particles being penetrated on passing through the fluidized bed height H.

For the fluidized bed state, the filtration efficiency f is defined by the following equation considering the penetrations through jet region PE_j and bed region PE_b.

$$f=1-(\mathrm{PE}_b\times\mathrm{PE}_j) \tag{6}$$

$$\mathrm{PE}_b=\frac{X(m_2e^{-m_1}-m_1e^{-m_2})-(1-\beta)m_1m_2(m_2e^{-m_1}-m_1e^{-m_2})}{X(m_2-m_1)}$$

$$\mathrm{PE}_j=1-\left(\frac{N_{or}}{N_{or}+0.078}\right)^3 \quad \text{when } N_{or}>0.8$$

To determine m_1 and m_2, filtration rate constant j should be determined. j is calculated by the following equation using E:

$$j=\kappa(H-H_j)=\frac{3E(1-\varepsilon_{mf})(H-H_j)}{2d_c} \tag{7}$$

The detail of above explanation can be found in Ref. [15].

Experimental Apparatus

The cross section of a fluidized bed DPF used in this study is shown in Fig. 1. The DPF, which had a cylindrical shape with an inner diameter of 139.8 mm, consisted of a distributor, a free board, an anti-scattering plate, and bed particles. The distance from the distributor to the anti-scattering plate was 400 mm. The distributor was made up of a 2 mm thick stainless steel plate with large numbers of small orifices to generate uniform gas flow and to suppress the pulsation of inlet flow. Each orifice had a diameter of 0.318 mm and a pitch of 2.4 mm with an opening area 1.38% of the total cross-sectional area. The anti-scattering plate was installed to prevent runaway of the bed particles from the fluidized bed. It had many holes of 0.2 mm dia and 0.45 mm pitch, making up a total opening area of 15.5%. The bed particles were made of alumina. The standard particles had diameters d_c ranging from 0.5 mm to 1.0 mm, whereas smaller particles with $d_c=0.3-0.5$ mm were also used to evaluate the effect of particle size. The standard bed height H at quiescent state was set to 100 mm and was increased up to 200 mm in the experiments for

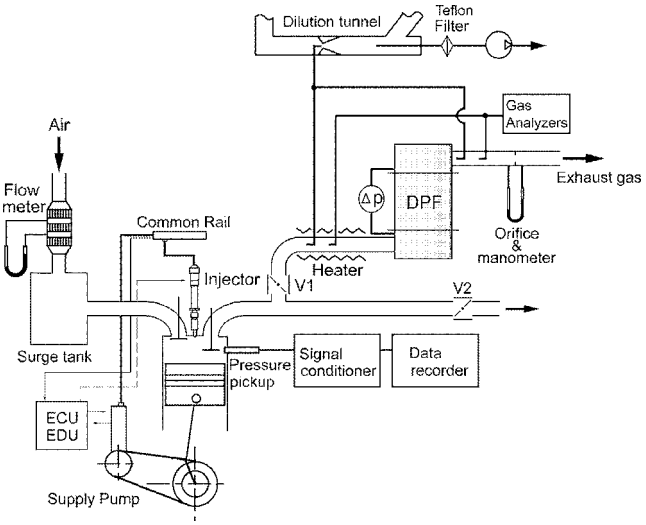

Fig. 2 Experimental setup

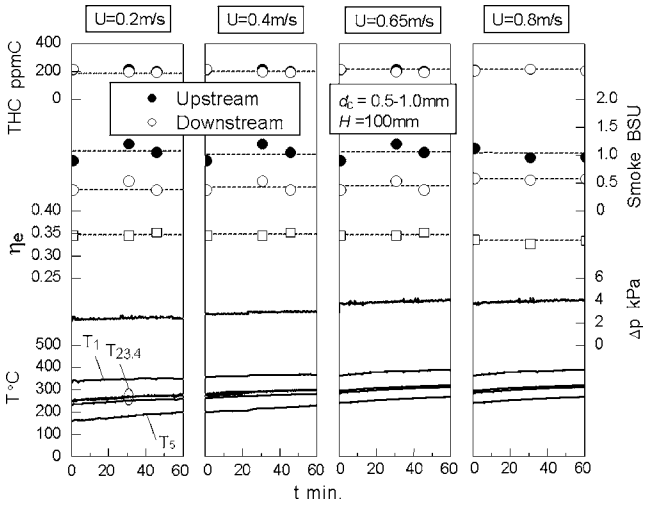

Fig. 3 Variation of exhaust emissions and bed temperature at inlet and outlet of fluidized bed-type DPF

investigating the effect of H. The superficial gas velocity in the fluidized bed, which is defined as volumetric flow rate divided by cross-sectional area of the bed, was varied in the range of $U=0.2-0.8$ m/s. The capacity of the fluidized bed was designed so that the bed particles reach the minimum fluidized bed velocity U_{mf} when approximately half of exhaust gases from the engine flow into the bed under the standard conditions of d_c and H. The DPF inlet temperature T_1, inside temperatures T_2, T_3, T_4, and outlet temperature T_5 were measured using thermocouples (K-type, o.d. 3.2 mm). The pressure difference (pressure drop) between the inlet of the distributor and the exit of the anti-scattering plate was measured using a digital differential pressure gauge (NAGANO GC62). The time histories of the temperatures and the pressure drop were recorded by a digital data recorder (YOKOGAWA MV200).

The experimental system is schematically illustrated in Fig. 2. The engine used a single-cylinder DI diesel engine (YANMAR NFD170) with a common-rail high-pressure injection system (DENSO ECD-U2). The engine specifications are given in Table 2. The fuel used was JIS No. 2 diesel fuel (LHV 43.7 MJ/kg, Cetane index 57), which was injected using an injection nozzle with six 0.18 mm holes. All measurements were conducted at thermally steady states of the engine at a fixed speed of 1800 rpm, under a break mean effective pressure (BMEP) of 0.64 MPa, an inlet cooling water temperature of 80°C, and a lubricating oil temperature of 90°C. The engine was operated using pilot injection to achieve a smoke level of 1 BSU at the inlet of the DPF. The main injection was fixed at to dead center (TDC), and the pilot injection timing was adjusted to obtain a constant smoke level with an injection pressure of 100 MPa. The flow rate of exhaust gas through the DPF was regulated by a valve V1 and measured with an orifice flow meter installed downstream of the DPF.

Smoke and total hydrocarbons (THC) emissions were measured using a Bosch smoke meter and a flame ionization detector (FID) (F-TECHO, EXL-311), respectively. The PM was collected on a Teflon filter (47 mm dia, 0.5 μm pore) at a dilution ratio from 15 to 20, and measured using a minidilution tunnel (i.d. 70 mm, throat diameter 14 mm). The PM concentration was expressed as mass per volume of exhaust gas. PM consists of a solid fraction (soot) and a soluble organic fraction (SOF). In this experiment, the PM is mainly composed of solid fraction because of the high engine load [18].

Table 2 Engine specifications

Engine type	DI diesel engine, single-cylinder Four-stroke-cycle, naturally aspirated
Bore × stroke	102 mm × 105 mm
Compression ratio	17.8:1
Swirl ratio	2.6
Combustion chamber	Toroidal type
Injection system	Common-rail

Experimental Results

Observation of Flow Condition Inside a Fluidized Bed. The effect of gas velocity on flow condition in the DPF was first investigated with standard bed particles and bed height. The gas velocity was varied in the range of $U=0.5-1.14$ m/s, thus changing the engine speed under motoring operation. The upper cover of the DPF was removed to observe the state of bed particles. When the gas velocity U was lower than 0.52 m/s, the bed particles slowly moved up and down. Increasing U up to 0.62 m/s, the bed particles showed intense movement; therefore, this velocity was considered as the minimum fluidized bed velocity U_{mf}. With an increase in the gas velocity to $U=0.72$ m/s, many bubbles were observed to flow through the bed. With further increase in gas velocity to $U=0.84$ m/s, the bed particles occasionally jumped up over the anti-scattering plate. Further increases in U caused jumping away of a large number of particles. Therefore, the gas velocity was controlled below 0.8 m/s in this study.

Effects of Gas Velocity. Next, the effects of the gas velocity on PM and smoke filtrations were investigated. The gas velocity U was varied in the range of 0.2–0.8 m/s using the standard bed particles and bed height. In each condition of U, new bed particles were used and the distributor and the anti-scattering plate were cleaned to make the same condition. Figure 3 shows temperatures in the DPF T_1-T_5, pressure drop Δp, brake thermal efficiency η_e, smoke, and THC concentrations at the downstream and upstream of the DPF against time t. The time histories of Δp and T_1-T_5 are the results during an hour from the inlet temperature T_1 reached quasi-steady state after a few hours of the exhaust gas introduction into the DPF. The smoke and THC measurements were also conducted several times after T_1 reached quasi-steady state. The range of PM concentration in the upstream of the DPF was 70–80 mg/m^3. The temperatures T_2, T_3, T_4, and T_5 increased with increasing U. Δp also increased with increasing U; however, it reaches nearly a constant value at 4 kPa for U above 0.65 m/s. η_e was hardly affected by gas velocity. As U increases, the smoke

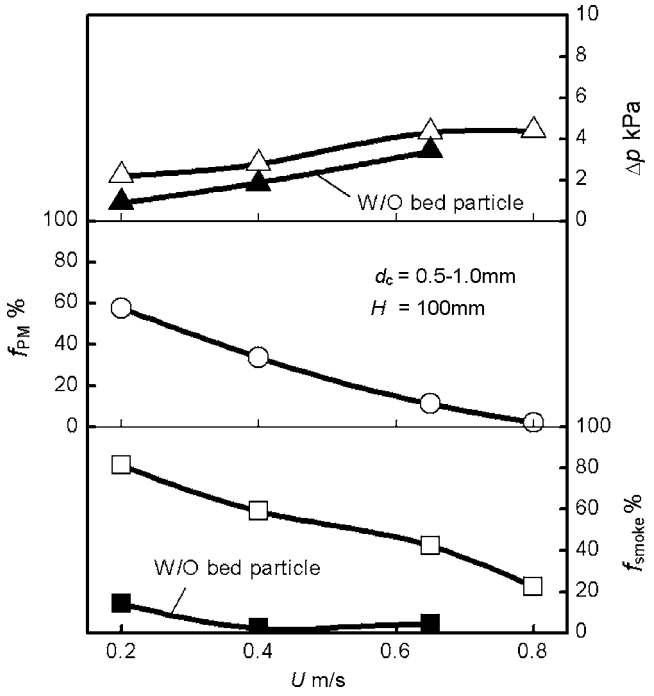

Fig. 4 Effects of gas velocity on PM and smoke filtrations and pressure drop

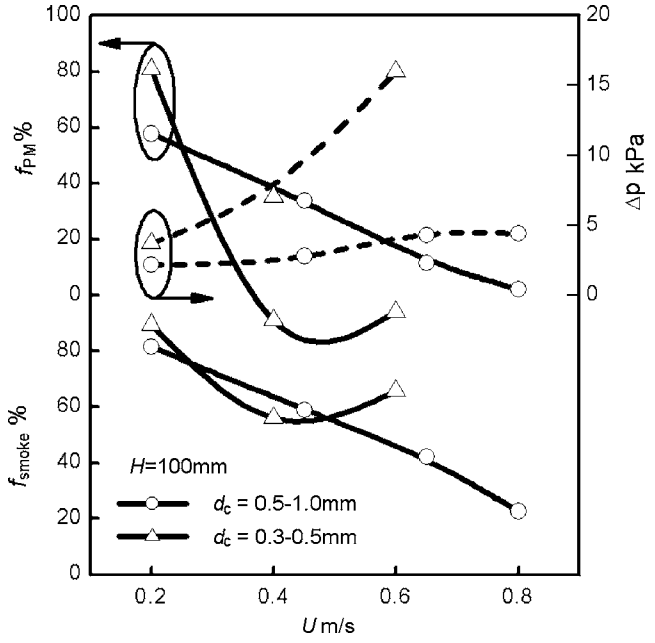

Fig. 5 Effects of bed particle diameter on PM and smoke filtrations and pressure drop

concentration downstream the DPF increased, while THC concentration scarcely changed. The PM filtration ratio f_{PM} and smoke filtration ratio f_{smoke} were calculated by the following equations.

The mean values of f_{PM}, f_{smoke}, and Δp in the condition of Fig. 3 against the gas velocity U are shown in Fig. 4. Here, the solid symbols represent Δp (solid triangles) and f_{smoke} (solid squares) in the case of no bed particles,

$$f_{PM} = \left(1 - \frac{PM_{out}}{PM_{in}}\right) \times 100 \quad (\%) \tag{8}$$

$$f_{smoke} = \left(1 - \frac{smoke_{out}}{smoke_{in}}\right) \times 100 \quad (\%) \tag{9}$$

As shown, while f_{smoke} was higher than that of f_{PM} at each gas velocity, both f_{PM} and f_{smoke} increased with decreasing gas velocity. A comparison of pressure drop between the cases with and without bed particles indicated that a large part of the pressure drop came from the distributor and the anti-scattering plate in the DPF. The pressure drop through the bed particles was not much influenced by the change in the gas velocity. There was a slight f_{smoke} increase by the distributor and the anti-scattering plate at a lower gas velocity of U=0.2 m/s; however, it was negligible for U>0.4 m/s.

Effects of Bed Particle Diameter and Bed Height. The effects of the diameter of the bed particles and the bed height on the filtration efficiency were investigated. Figure 5 compares f_{PM} and f_{smoke} and Δp between different bed particle diameters ranging from d_c=0.5–1.0 mm and d_c=0.3–0.5 mm. The use of smaller bed particles improved f_{PM} and f_{smoke} at a gas velocity of U =0.2 m/s. Increasing U to 0.4 m/s, the smaller bed particles gave a rapid decrease of f_{PM}, which shows negative values, although f_{smoke} was similar to that of the larger particles. In this case, bed particles collided with the anti-scattering plate and many pieces of broken bed particles were found on both the upper and lower surfaces of the plate after the experiments. The fragments of bed particles flowed downstream the DPF and were collected on the Teflon® filter at the time of PM measurement, thus causing negative f_{PM}. These fragments also stuck on the smoke filter paper. However, since the particle is whitish, the blackness did not increase, resulting in no considerable decrease in f_{smoke}. Figure 5 also shows that the smaller particles lead to higher Δp at each gas velocity and that its value reaches about 16 kPa at U=0.6 m/s. This higher pressure drop is probably again due to the clogging of the anti-scattering plate by broken bed particles at higher gas velocity.

The results of the effects of bed height H on the performance of the DPF are presented in Fig. 6. H was increased from

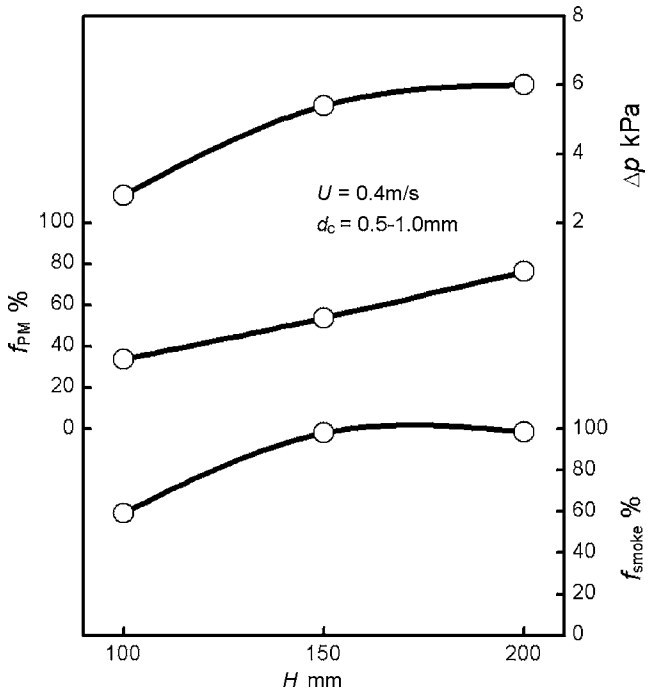

Fig. 6 Effects of bed height on PM and smoke filtrations and pressure drop

Table 3 Minimum fluidization velocity at different bed particle diameter

d_c (mm)	0.2	0.4	0.6	0.7	0.8	1.0	1.2
U_{mf} (m/s)	0.04	0.15	0.33	0.44	0.55	0.78	1.0

100 mm to 150 mm and 200 mm using standard bed particles (d_c=0.5–1.0 mm) at U=0.4 m/s. The increased bed height resulted in an increase in f_{PM} and f_{smoke} by probably promoting contact of PM particles with the bed particles, while it caused an increase in the pressure drop. The filtration efficiencies of PM and smoke were 76% and 98%, respectively, and at H=200 mm the pressure drop Δp was 6 kPa.

Theoretical Analysis. Theoretical work was conducted in order to better understand the experimental results and to find ways to improve the filtration efficiency. First, to determine flow condition in the DPF, the minimum fluidization velocity U_{mf} was calculated from Eqs. (1)–(3). The results for several bed particle diameters are shown in Table 3. In this study, the calculations were simplified by assuming that the fluidized bed consists of monodisperse particles with a harmonic mean diameter d_h [19], which was derived from measured size distribution of the bed particles used in the experiments. For the standard bed particles (d_c =0.5–1.0 mm), d_h was 0.84 mm, which gave U_{mf} close to the previously mentioned observation result (U_{mf}=0.62 m/s) as shown in Table 3.

The effects of superficial gas velocity on PM filtration efficiency were evaluated. Table 4 shows the input data for the calculation. Here, the bed temperature and the density of bed particle were assigned based on our measurements. And, a fraction of bubble phase and an average bubble size were assigned based on the literature [13]. Figure 7 shows PM filtration efficiencies f at superficial gas velocities U=0.1–1.0 m/s and bed heights H =100–200 mm. The bed particle diameter and PM diameter were set at d_h=0.84 mm and d_p=100 nm, respectively. Void fractions of ε=0.3 and ε_{mf}=0.4 [15] were applied. The solid symbols in Fig. 7 indicate the experimental data at each bed height. The dotted vertical line denotes U_{mf}. The PM filtration efficiency f was calculated using Eq. (6) in the cases where U was higher than U_{mf} (fluidized bed regime), and using Eq. (4) in the cases with U lower than U_{mf} (fixed bed regime). f decreased with increasing U regardless of H, with larger H giving higher f. In the fluidized bed condition, f was lower and the influence of H was weaker compared to the fixed bed condition. As shown in Fig. 7, these trends correlate well with the experimental results. Some discrepancies were observed between the theoretical and experimental results in cases with H=200 mm at lower U and H=100 mm at U =0.8 m/s. Further study is needed on the effects of spatially heterogeneous flow, void size and fraction, and the size distribution of bed particles to understand these anomalies.

Table 4 Input data for calculation

Bed temperature (°C)	250
Density of bed particle (g/cm^3)	3.95
Fraction of bubble phase (%)	10
Average bubble size (cm)	3

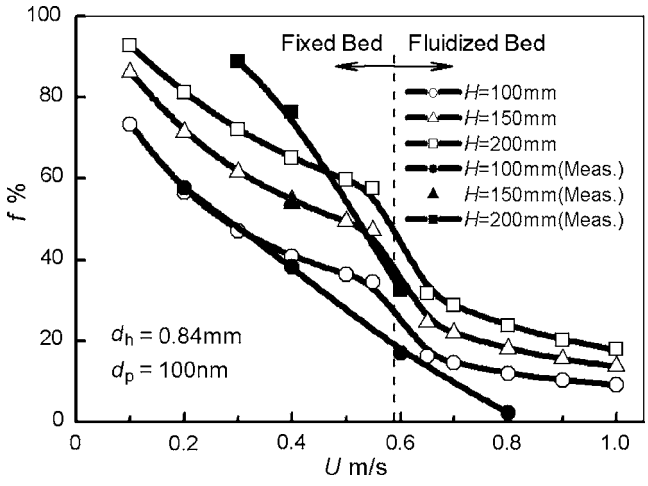

Fig. 7 Effects of gas velocity on PM filtration efficiecy against bed height

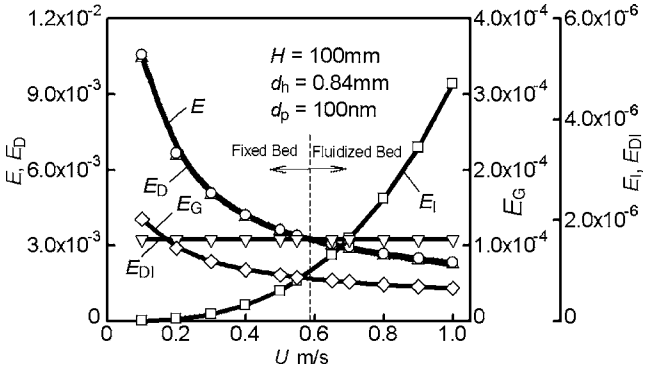

Fig. 8 Filtration efficiency of individual mechanisms against gas velocity

Next, to reveal the predominant phenomenon in PM filtration, the contribution of each filtration mechanism was analyzed. Figure 8 shows the total filtration efficiency of a single bed particle E and the individual filtration efficiencies of E_D, E_I, E_G, and E_{DI} against the superficial gas velocity U at the bed height of H =100 mm. The total filtration efficiency E decreased with increasing U. It is clear that diffusion filtration efficiency E_D had the most significant effect on E. Although the inertial filtration efficiency E_I increased with the increase in U, this increase was much smaller compared to E_D. Thus, the diffusion filtration is the dominant mechanism in the fluidized bed-type DPF. The lower PM filtration efficiency at higher gas velocity is caused by the decrease in diffusion filtration efficiency, which is inversely proportional to $U^{2/3}$ as shown in Table 1. To obtain higher E_D at a fixed U, reducing bed particle diameter d_h would be effective according to the equation given in Table 1. Therefore, the effect of bed particle size was evaluated.

PM filtration efficiencies were calculated in the diameter range of d_h=0.4–1.0 mm under conditions of the bed height of H =100 mm and PM diameter of d_p=100 nm. The calculated PM filtration efficiencies f are plotted against the superficial gas velocity U in Fig. 9. The dotted vertical lines denote U_{mf} in each d_h, respectively. When U was below U_{mf}, the smaller bed particle gave a higher f. As expected from the results above, the smaller bed particle diameter promoted diffusion filtration, leading to a significant increase in PM filtration efficiency. On the other hand, in a fluidized bed, f decreased rapidly with an increase in U. These trends correlated well with the experimental results shown in Fig. 5. Thus, the use of smaller bed particles requires low superficial velocities, which may be attained with a DPF with larger inner diameter at a fixed exhaust gas flow rate. Increase in DPF size can be avoided with the use of larger bed particles. In this case, a larger bed height is necessary to maintain the filtration efficiency.

Figure 10 shows results of a strategy to decide bed particle diameter d_h and bed height H. Here, $C_{\Delta p}$ is a pressure drop ratio, Δp divided by the reference pressure drop at d_h=0.84 mm and

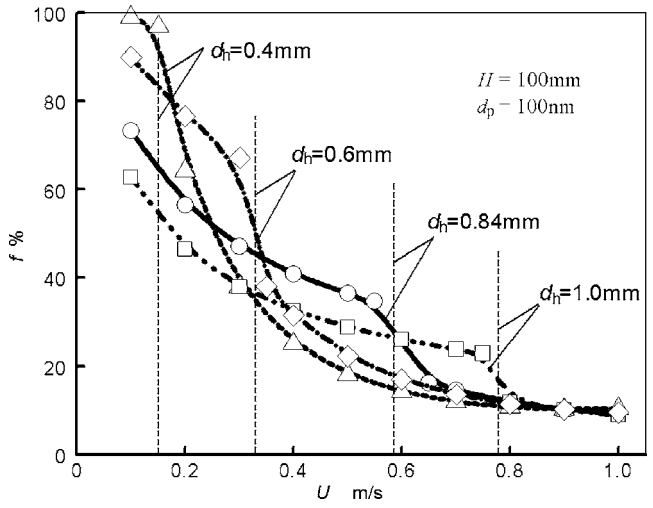

Fig. 9 Effects of bed particle diameter on PM filtration efficiency

$H=100$ mm. Δp was calculated using Ergun's equation [20]. The fixed-bed-state filtration efficiency f and $C_{\Delta p}$ were plotted against d_h changing H from 100 mm to 700 mm for a constant superficial velocity U of 0.3 m/s. Based on the target values of f and $C_{\Delta p}$ as 70% and 1.5, respectively, various combinations of d_h and H were selected as indicated by the vertical lines with arrows. The requirement for f was fulfilled in all cases by selecting larger H in accordance with the increase in d_h. $C_{\Delta p}$ was approximately constant as long as f was fixed. However, in practical use, H is restricted due to the limitation of space for the installation of the DPF. Therefore, both H and d_h must be optimized simultaneously.

Conclusions

The effects of gas velocity, bed particle size, and bed height in a fluidized bed on PM and smoke filtration efficiencies, and pressure drop were experimentally investigated using a single-cylinder DI diesel engine. The theoretical work was also conducted for further investigation on the effects of the mentioned parameters on the PM filtration efficiency. The following conclusions are derived from the results.

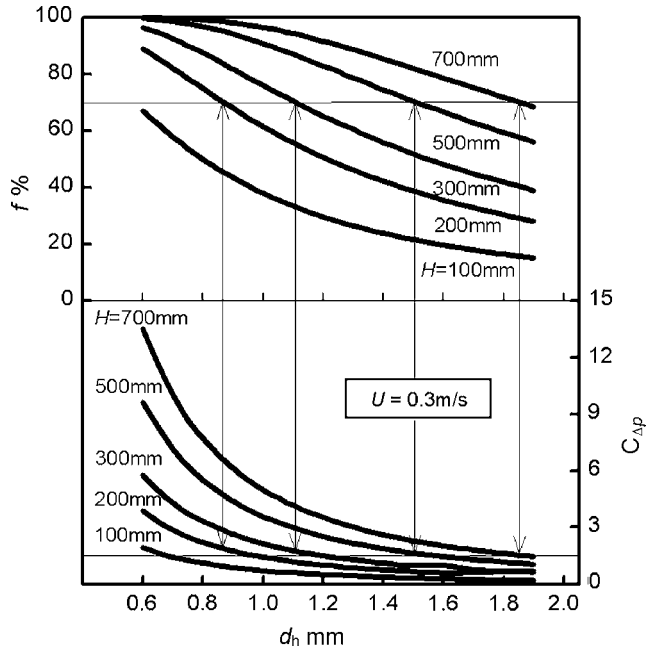

Fig. 10 PM filtration efficiency and relative pressure drop for various bed particle diameters and bed heights

Experimental Results. 1. In the fluidized bed-type DPF, PM and smoke filtration efficiencies increased with decreasing gas velocity. The smoke filtration ratio was higher than PM at any given gas velocity.

2. Smaller bed particles led to better PM and smoke filtration efficiencies at a low gas velocity; however, the PM filtration efficiency drastically decreased with an increase in gas velocity due to excessive fluidization of the bed particles.

3. Increasing the bed height gave higher PM and smoke filtration efficiencies, while causing an increase in pressure drop.

Theoretical Results. 1. In the fluidized bed-type DPF, diffusion filtration was found to be the dominant mechanism, and the decrease in the PM filtration efficiency at a high gas velocity observed in experimental results was caused by deterioration in the diffusion filtration.

2. Smaller bed particles gave a higher PM filtration efficiency under a fixed bed condition; however, a larger inner diameter of the DPF was required to maintain a fixed exhaust gas flow rate. The increase in DPF size can be avoided by employing larger bed particles and a larger bed height in order to maintain high filtration efficiency.

Acknowledgment

The authors would like to acknowledge ATI for providing the fluidized bed used in this study. Further thanks are due to Teppei Matsumoto, a graduate student of Kyoto University, for his assistance during the experiments.

Nomenclature

$C_{\Delta p}$ = pressure drop ratio
D = Brownian diffusivity, m^2/s $(=Fk_BT/3\pi\mu d_p)$
d_p = diameter of an aerosol particle, m
d_c = diameter of a bed particle, m
d_h = harmonic mean diameter of bed particle, m $(=1/(\Sigma M_i/(d_c)_i))$
d_o = distributor orifice diameter, m
E = single particle filtration efficiency
F = Stokes-Cunningham slip correction factor
f = overall filtration efficiency
f_{PM} = PM filtration ratio
f_{smoke} = smoke filtration ratio
g = gravitational acceleration, m/s^2
Ga = Galileo number
H = total bed height, m
H_j = gas jet height above distributor $(=5.2d_o(\rho_g g d_o)^{0.3}(1.3(U_{or}/gd_o)^{0.2}-1))$
j = filtration rate constant
K = interphase transfer coefficient per unit volume of bubble phase
k_B = Boltzmann's constant $(=1.380622\times10^{-23}$ J/K)
M_i = mass fraction of material
m_1, m_2 = roots of the equation below $((1-\beta)\ m^2-[X+(1-\beta)k]\ m+kX(1-\beta e^{-Y})=0)$
N_G = gravitational settling parameter $(=Fgd_p^2(\rho_p-\rho_g)/18\mu U)$
N_{DI} = interception parameter $(=d_p/d_c)$
N_{or} = $(=\mathrm{St}_{or}(N_{uc})^{1/3})$
N_{uc} = terminal velocity of a bed particle $(N_{uc}^{1/3}=(3\rho_g^2/4\rho_c g\mu)^{1/3}u_{tc})$
PE = overall penetration efficiency

PE_b = penetration of aerosol particles through bubbling part of fluidized bed
PE_j = penetration of aerosol particles through jet
Re_{mf} = Reynolds number at minimum fluidization
Sc = Schmidt number ($=\mu/\rho_p D$)
St = Stokes number ($=F\rho_p d_p U/9\mu d_c$)
St_{or} = Stokes number in distributor orifice, m^2/s
U = superficial velocity of gas through a fluidized bed, m/s
U_{mf} = minimum fluidization velocity, m/s
U_{or} = mean gas velocity through a distributor orifice, m/s
u_{tc} = terminal velocity of a bed particle, m/s
X = cross-flow factor ($=(H-H_j)K\varepsilon_B/\beta U$)
Y = ($=\alpha d_c K\varepsilon_B/\beta U$)
T = gas temperature, K

Greek Symbols

α = filter depth associated with a single layer of bed particles ($=\pi/6(1-\varepsilon_{mf})^{1/3}$)
B = fraction of fluidizing gas passing through a bed in bubble phase
ε = void fraction
ε_B = time-averaged fraction of the cross-sectional area occupied by bubble phase
ε_{mf} = void fraction at minimum fluidization
η_e = brake thermal efficiency
κ = rate constant for filtration, 1/m
μ = gas viscosity, Ns/m^2
ρ_p = density of an aerosol particle, kg/m^3
ρ_c = density of a bed particle, kg/m^3
ρ_g = density of gas, kg/m^3

References

[1] Strachan, N., and Dowlatabadi, H., 2002, "Distributed Generation and Distribution Utilities," Energy Policy, **30**, pp. 649–661.
[2] Kakuda, M., Numata, A., and Takaishi, R., 2003, "Newly Developed Diesel Engines for Generator Set," Tech. Rev.-Mitsubishi Heavy Ind., **40**, No. 4, pp. 250–253 (in Japanese).
[3] Richard, J. W., and Bryan, G. R., 1992, "New Local Power Stations: An Economic Assessment," Utilities Policy, **2**(2), pp. 108–119.
[4] Japan Petroleum Energy Center, 2003, "Low-Emission Off-Road Engine Technology Development," Petroleum Energy Center News, **7**, pp. 1–10, (in Japanese).
[5] Oyama, K., and Kakegawa, T., 2000, "Japan Clean Air Program—Step 1 Study of Diesel Vehicle and Fuel Influence on Emissions," SAE Paper No. 2000-01-1973.
[6] Hums, E., Joisten, M., Muller, R., Sigling, R., and Spielmann, H., 1996, "Innovative Lines of SCR Catalysis: NO_x Reduction for Stationary Diesel Engine Exhaust Gas and Dioxin Abatement for Waste Incineration Facilities," Catal. Today, **27**, pp. 29–34.
[7] Lanni, T., 2003, "Fine Urban and Precursor Emissions Control for Diesel Urban Transit Buses," Environ. Pollut., **123**, pp. 427–437.
[8] Setoguchi, T., Oda, Y., Sugiyama, T., Nochi, A., Kawamura, W., and Yoshida, S., 2003, "Advanced Cleanup Technology of Exhaust Gas From High Sulfur Content Oil-Fueled Diesel Engine," Mitsubishi Juko Giho, **40**, No. 6, pp. 352–355 (in Japanese).
[9] Suresh, A., Khan, A., and Johnson, J. H., 2000, "An Experimental and Modeling Study of Cordierite Traps—Pressure Drop and Permeability of Clean and Particulate Loaded Traps," SAE Paper No. 2000-01-0476.
[10] Clift, R., 1983, "Fundamental Processes in Gas Filtration," Trans. Ins. Eng.: Aust. Mech. Eng., **8**, No. 4, pp. 181–191.
[11] Congalidis, P. J., and Georgakis, C., 1981, "Multiplicity Patterns in Atmospheric Fluidized Bed Coal Combustors," Chem. Eng. Sci., **36**, No. 9, pp. 1529–1545.
[12] Matsumura, Y., and Minowa, T., 2004, "Fundamental Design of a Continuous Biomass Gasification Process Using a Supercritical Water Fluidized Bed," Int. J. Hydrogen Energy, **29**, pp. 701–707.
[13] Shi, J. P., and Harrison, R. M., 2001, "Study of a Water-Cooled Fluidized Bed Diesel Particle Agglomeration," Powder Technol., **115**, pp. 146–156.
[14] Kittelson, D. B., Reinertsen, J., and Michalski, J., 1991, "Further Studies of Electrostatic Collection and Agglomeration of Diesel Particles," SAE Paper No. 910329.
[15] Clift, R., Ghadiri, M., and Thambimuthu, K. V., 1981, "Filtration of Gases in Fluidized Beds," *Progress in Filtration and Separation*, R. J. Wakeman, ed., Elsevier, Amsterdam, Vol. 2, pp. 75–123.
[16] Qian, G. H., Burdick, I. W., Pfeffer, R., Shaw, H., and Stevens, J. G., 2004, "Soot Removal From Diesel Engine Exhaust Using a Rotating Fluidized Bed Filter," Adv. Environ. Res., **8**, pp. 387–395.
[17] Khalekl, I., 2000, "Characterization of Particle Size Distribution of a Heavy-Duty Diesel Engine During FTP Transient Cycle Using Elpi," SAE Paper No. 2000-01-2001.
[18] Hori, S., and Narusawa, K., 1998, "Fuel Composition Effects on SOF and PAH Exhaust Emissions From DI Diesel Engines," SAE Paper No. 980507.
[19] Shirai, T., 1965, "Ryuudousou," Kagakugijutsu (in Japanese).
[20] Ergun, S., 1952, "Mass-transfer Rate in Packed Columns Its Analogy to Pressure Loss," Chem. Eng. Prog., **48**, No. 5, pp. 227–236.

Study of Multimode Combustion System With Gasoline Direct Injection

Zhi Wang
Jian-Xin Wang
Shi-Jin Shuai
Yan-Jun Wang
Guo-Hong Tian
Xin-Liang An

State Key Laboratory of Automotive Safety and Energy,
Tsinghua University,
Beijing 100084, China

In this paper, a multimode combustion system was developed in a gasoline direct injection engine. A two-stage fuel-injection strategy, including flexible injection timings and flexible fuel quantity, is adopted as a main means to form desired mixture in the cylinder. The combustion system can realize five combustion modes. The homogeneous charge spark ignition (HCSI) mode was used at high load to achieve high-power output density; stratified charge spark ignition (SCSI) was adopted at intermediate load to get optimum fuel economy; stratified charge compression ignition (SCCI) was introduced at transient operation between SI and CI mode. Homogeneous charge compression ignition (HCCI) was utilized at part load to obtain ultralow emissions. Reformed charge compression ignition (RCCI) was imposed at low load to extend the HCCI operation range. In SI mode, the stratified concentration is formed by introducing a second fuel injection in the compression stroke. This kind of stratified mixture has a faster heat release than the homogeneous mixture and is primarily optimized to reduce the fuel consumption. In CI mode, the cam phase configurations are switched from positive valve overlap to negative valve overlap (NVO). The test results reveal that the CI combustion is featured with a high gradient pressure after ignition and has advantages in high thermal efficiency and low NO_x emissions over SI combustion at part load. [DOI: 10.1115/1.2718221]

Introduction

Homogeneous charge compression ignition (HCCI) has advantages in high thermal efficiency and low emissions and will possibly become a promising combustion mode for internal combustion engines. However, HCCI engine can only run well within a narrow range of speed and load. One of the key technologies for the HCCI engine is to widen the operating range over the whole map. Unfortunately, even though HCCI operation at high load may be obtained, the NO_x reduction benefit is very small compared to conventional gasoline engine with three-way catalyst. Meanwhile, the fuel-consumption advantage of gasoline HCCI over SI combustion is reduced at high load due to the reduced level of throttling. For high-load operation, the engine should be again switched to traditional SI or CI operation. Therefore, the multimode combustion is a practical operation strategy for the HCCI engine application [1].

Nowadays, the gasoline HCCI research that existed can be divided into two categories as follows according to compression ratio (CR).

Ultralean Mixture With High CR. The relative air/fuel ratio of these gasoline HCCI engine varies from 3 to 5 and the range of CR varies from 16 to 21, like conventional diesel engines. For instance, GM [2], Sandia [3], and KTH [4], investigated gasoline HCCI combustion on gasoline direct injection engines that were modified from heavy-duty diesel engines. The high-CR gasoline HCCI engine can realize ultralow NO_x emission (1 ppm) and high thermal efficiency (43%) at fixed operation points [5]. Therefore, high-CR gasoline HCCI is suitable for stationary operation.

Slight-Lean Mixture With Low CR. The relative air/fuel ratio of these gasoline HCCI engines varies from 1 to 2, and the range of CR varies from 10 to 13 like conventional gasoline engines. High-octane fuel cannot be ignited by compression under the conditions of the slight-lean mixture with low CR. The method of realizing the HCCI in such a case is to trap a certain amount of hot exhaust gas to increase the temperature in the cylinder. For instance, Volvo [6] adopted Lotus' VVT mechanism to realize negative valve overlap (NVO) for various exhaust gas recirculation (EGR) ratios. Subaru [7] realized gasoline HCCI based on three camshafts with a different NVO configuration. AVL [8,9] CSI engine realized gasoline HCCI by adopting second exhaust valve opening to rebreathe the hot EGR. Low CR gasoline HCCI engine results in an maximum fuel economy improvement compared to conventional SI operation of maximum 26%, NO_x emissions vary from 0 to 200 ppm [8].

Low CR gasoline HCCI engines can be conveniently switched to conventional SI mode at high load, which makes them more practical in the near future. In this paper, we shall concentrate on the application of low CR gasoline HCCI engines.

For gasoline fuels the homogeneous charge is normally formed by the port injection with a conventional injector. However, recent researches [1,10,11] show that gasoline-fueled HCCI engine with direct fuel multistage injection makes it possible to extend the range of HCCI operation. Both homogeneous and inhomogeneous mixtures can be achieved through direct injection (DI) strategy, which provides more flexibility to control HCCI combustion.

In SI mode, the stratified concentration can be formed by introducing a second fuel injection in the compression stroke [12]. But in HCCI mode, the cam phase has to be switched from conventional valve overlap to NVO so that a large amount of hot residual is trapped in the cylinder. The hot residual is used as a means of controlling the charge temperature necessary for HCCI combustion [13].

This paper describes a gasoline direct injection engine with a multimode combustion system. Two-stage direct injection was used to optimize combustion in SCSI mode at medium load and to control ignition timing in HCCI mode at part load. The objective of the work is to study ignition and combustion characteristics in a gasoline direct injection engine with a multimode combustion system.

Contributed by the Internal Combustion Division of ASME for publication in the JOURNAL OF ENGINEERING FOR GAS TURBINES AND POWER. Manuscript received April 1, 2006; final manuscript received October 2, 2006. Review conducted by Margaret Wooldridge. Paper presented at the 2006 Fall Conference of the ASME Internal Combustion Engine Division (ICEF2006), November 5–8, 2006, Sacramento, CA.

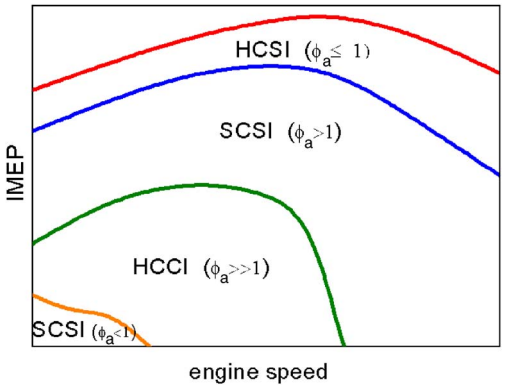

Fig. 1 Combustion modes and corresponding operation regions of gasoline engine

Multimode Combution system

Engine Operation Strategies. Figure 1 gives the operation regions of the different combustion modes in the gasoline HCCI engine. During the cold-start operation, a stratified local rich fuel/air mixture near the spark plug is formed by a late injection in the compression stroke and then ignited by the spark. It is called stratified charge spark ignition (SCSI) combustion mode. After the warmup running, the engine goes into the HCCI combustion region using internal EGR to have a high thermal efficiency and very low engine-out NO_x emission. At medium load, the engine runs on a lean SCSI combustion for fuel economy. At high load, the engine operates in the stoichiometric homogeneous charge spark ignition (HCSI) for high power output. Since the problem of emission and fuel economy at high load are already solved successfully using three-way catalyst (TWC) and wide-open throttle (WOT) strategy in conventional gasoline engines, this paper will concentrate on the SCSI, HCCI and quasi-HCCI, combustion modes.

Fuel Injection Strategies

Figure 2(*a*) shows injection strategy in SI mode. Intake top dead center (TDC) and combustion TDC are defined as 0 deg and 360 deg, respectively, in this paper. Gasoline direct injection timing can vary in a wide range, from intake to compression stroke. Two-stage injection strategy is more flexible than one injection and controls the distribution of mixture concentration in the cylinder more effectively since it can optimize two injection timings and the ratio of two injection quantities to control the mixture formation and combustion. In the multimode combustion system, homogeneous charge can be realized by the first fuel injection in intake stroke and stratification charge can be obtained by the second fuel injection in compression stroke. Therefore, a robust SCSI combustion under the medium load condition can be realized.

For transient operation of SI/HCCI switch process, injection parameters should be changed in next cycle, simultaneously, including valve lift curves, throttle opening percentage, injection strategies, as well as spark timings. Figure 2(*b*) shows injection strategy in CI mode. Gasoline direct injection timing can vary in a wide range from exhaust stroke to compression stroke. Negative valve overlap (NVO) is a practical approach to obtain internal EGR. This makes it possible to utilize thermal atmosphere for fuel evaporation and reforming. Therefore, HCCI ignition timing can be controlled and the low load range can be extended by introducing the first fuel injection in NVO period for reform. When NVO combines with multiple direct injection strategies, three CI combustion modes, such as SCCI, HCCI, and RCCI, can be achieved.

The injection in the compression process (I_S) can form stratified charge. The so-called stratified charge compression ignition (SCCI) has capabilities to suppress knocking [14], to reduce HC

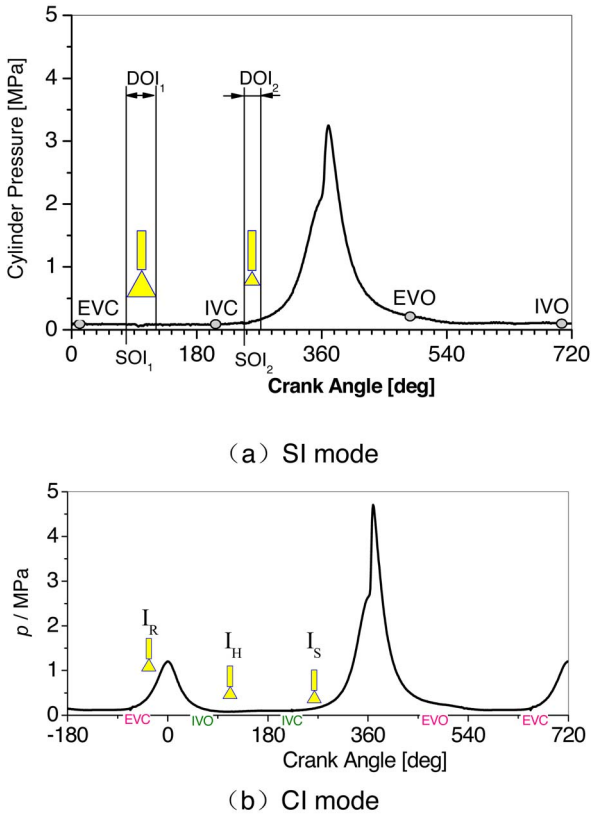

Fig. 2 Injection strategies of GDI engine at different combustion mode: (*a*) SI mode and (*b*) CI mode

emission, to extend the high load limit and is suitable for the transient operation. Early fuel injection in intake stroke (I_H) can obtain HCCI due to sufficient mixing time available to form homogeneous charge [15,16].

In the period of NVO, part of the exhaust gas is trapped in the cylinder and recompressed. In NVO period, the direct-injected fuel (I_R) will be reformed due to internal EGR atmosphere with the high temperature and pressure, and an amount of active species occurs, which improves the ignition property [11]. This combustion mode is called RCCI in this paper.

By combining above three injection strategies and adjusting fuel quantity and injection timing of each pulse, the temperature, concentration, and species of the mixture distributed in cylinder can be controlled flexible. As a result, the HCCI ignition timing and combustion rate can be controlled.

Experimental Setup

The investigation was carried out on a dual-cylinder four-stroke test engine. The engine specifications are listed in Table 1. The properties of the test fuel are listed in Table 2.

The HCCI combustion system is described in the previous literature [17]. Using NVO to trap mass of internal EGR is an effective method to realize gasoline HCCI combustion. The rapid and stable SI/HCCI mode switch demands a rapid response variable cam phaser to change the intake-exhaust cam phase significantly in one engine cycle. As a result, the SI/HCCI mode switch can be achieved in the next engine cycle.

A two-stage variable valve timing (TS-VVT) mechanism was designed and used in the experiment, as shown in Fig. 3. The TS-VVT mechanism is a practical cam unit for a two-valve engine with low cost and rapid response, since variable cam timing (VCT) equipment is not needed. Both the cam phase and the lift can be changed in one engine cycle by the TS-VVT. Meanwhile,

Table 1 Engine specifications

Type	Two-cylinder in-line, four-stroke, DI
Number of Valves	2 per cylinder
Bore	95 mm
Stroke	115 mm
Connecting rod	210 mm
Compression ratio	13
Throttle position	WOT at CI mode POT at SCCI and SCSI mode
EGR	Internal EGR at CI mode without EGR at SI mode
Intake temp.	Ambient
Fuel	Gasoline (RON93)
Injector	High-pressure swirl injector
Injection pressure	5 MPa
Head bottom	Flat
Intake port	Helical

Table 2 Properties of the test fuel

Marketing Gasoline	93#
RON	94.4
MON	83.0
Oxygen content (wt)	0.21
Density (20°C)(g/cm^3)	0.7487
C/H	6.42
Stoichiometric A/F ratio	14.6

both intake and exhaust cam profiles can be switched simultaneously due to the same main oil passage in the cylinder head with a single overhead cam shaft (SOHC). Therefore, the desired residual gas is trapped by switching cam profiles in next engine cycle. As a result, the SI mode and HCCI mode can be stably and rapidly switched.

A combustion mode switch process from SI to HCCI is shown in Fig. 4. The cylinder pressure traces, NO_x, IMEP, intake, and exhaust valve timing, as well as throttle opening are indicated at every continuous engine cycle. Before the switch, the engine was running at SI mode with POT (part open throttle) and PVO (positive valve overlap). NO_x emission is more than 2000 ppm. After the last SI cycle, the intake cam and exhaust cam profiles were switched simultaneously by the TS-VVT. As the cam profile was switched to NVO, a great amount of exhaust gas was trapped at the end of last SI cycle. The high in-cylinder temperature due to heavy hot internal EGR made the mixture successfully self-ignited in the next engine cycle (first HCCI cycle). After several cycles of stabilization, the throttle was smoothly opened to WOT. The IMEP reaches to the same level as SI mode before the switch. The peak cylinder pressure increased dramatically. The NO_x emission decreases significantly and rapidly to near zero. The whole switch process is within ten engine cycles, ~1 s in 1000 rpm engine speed. Furthermore, in the SI-HCCI transient period, the engine ran robustly without any abnormal combustion (misfire or knocking) occurrence. SI/HCCI combustion modes with different cam phases can be obtained by replacing cams on the SOHC. The cam-phase configurations in the experiments are listed in Table 3.

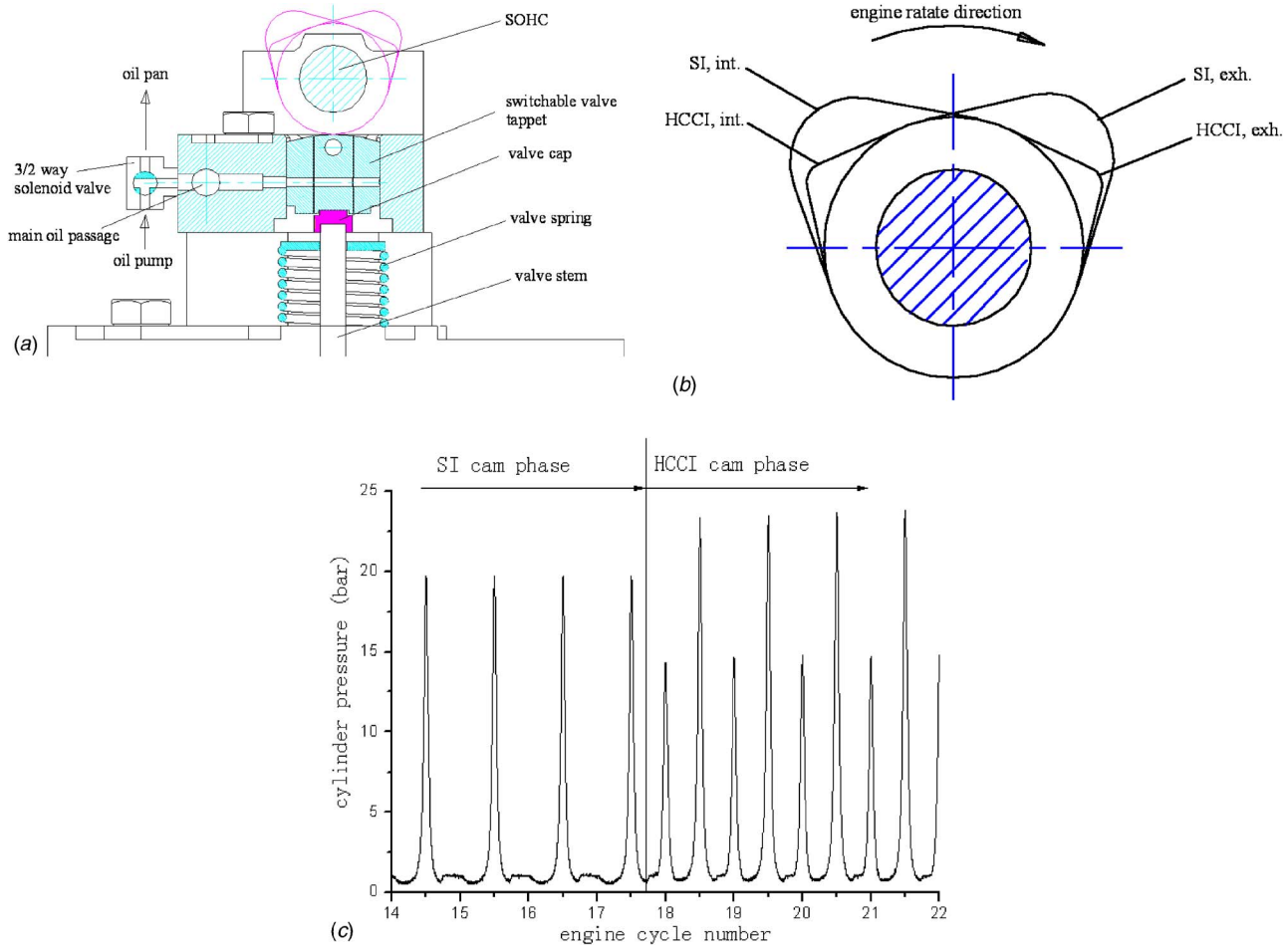

Fig. 3 Two-stage variable valve timing mechanism: (*a*) SOHC with CPS, (*b*) multiple cam profiles with synchro switch, and (*c*) measured cylinder pressure traces in continuous engine cycles at motoring case

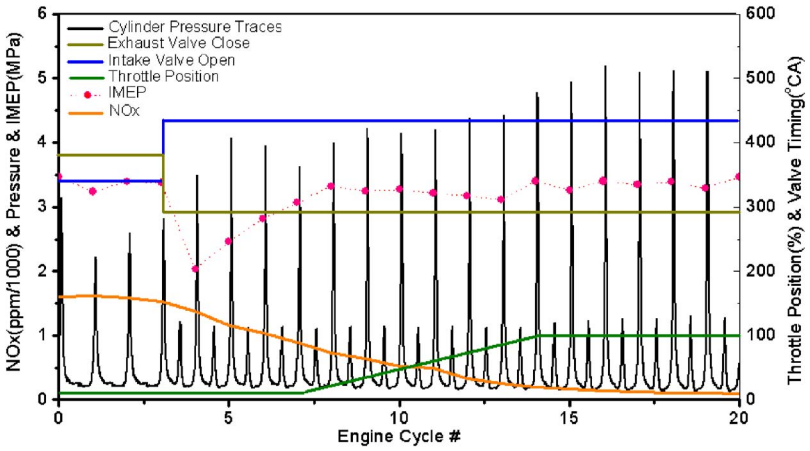

Fig. 4 Transient SI-HCCI switch process

Experimental Results and Discussion

SCSI. A different stratified charge can been formed by adjusting the ratio of the first fuel injection to the second at the same total fuel mass per cycle. The spark timing at 1400 rpm and 1800 rpm are 24°CA BTDC and 20°CA BTDC, respectively, according the engine calibration. Figure 5 shows the effects of the ratio of g_{b2}/g_{b1} on the engine's performance, fuel economy, emission, and combustion stability. As can be seen from the Fig. 5, the ratio is in the range of 1:4–1:3 and can result in a higher BMEP, a higher fuel economy (lower BSFC), and lower COV. The engine's performances will be worse when the ratio is out of the range. When the ratio is in this range, CO and HC emissions are much lower than those when the ratio is not in this range, meanwhile, NO_x will be comparably higher. The phenomenon is mainly due to the different roles of g_{b2} and g_{b1}. The first injected fuel is used to form a homogeneous charge in the combustion chamber, whereas the second is to form a rich stratified charge around the spark plug. When the ratio is in the range, the mixture around the spark plug is easy to be ignited, which can lead to a stable ignition; whereas the mixture at other places of the chamber is not too lean, which can make the flame propagate very quickly and produce less HC and CO. When the second injection fuel quantity is too little, the mixture around the spark plug is not rich enough, which will lead to a unstable initial flame kernel and a high cycle variation. HC and CO emission will increase due to the unstable combustion. When the second injection fuel quantity is too large while the first injection is too small, the mixture gradient will increase, which will lead to a large CO and HC formation in the too rich mixture due to the incomplete combustion, while the NO_x is lower due to the lower combustion temperature. The engine's performance is worse either way.

Figure 6 presents the effects of the ratio on the combustion indicator diagrams and the heat release curves at same total fuel mass per cycle. The indictor diagrams show that a higher combustion pressure and a high rate of pressure increase in the chamber when the ratio is 1:4; the heat release curves also show that the rate of heat release is higher and the combustion period is shorter when the ratio is 1:4. When the ratio is 0, which means a lean homogeneous charge in the chamber, the maximum heat release rate is retarded and the combustion speed is obviously slower. When the second fuel injection is large (the ratio of g_{b2}/g_{b1} is increasing), mixture concentration changes rapidly, which can result in a same quick increase of initial heat release as in the case of the ratio being 1:4 but a slower heat release and longer combustion due to the too lean mixture at the moment.

Table 3 Cam-phase configuration (°CA)

	SI (Cam0)	HCCI (Cam1)	HCCI (Cam2)	HCCI (Cam3)
EVO BBDC	56	44	52	45
EVC ATDC	10	−58	−66	−75
IVO BTDC	10	−64	−80	−75
IVC ABDC	50	24	40	45

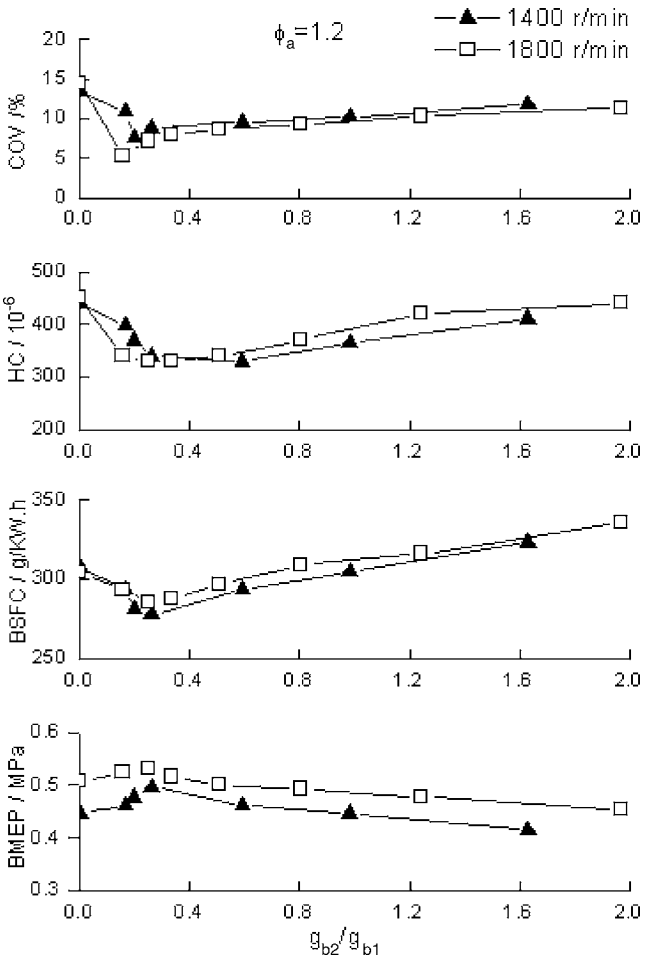

Fig. 5 Effects of g_{b2}/g_{b1} on combustion and emission performance at same total fuel mass per cycle

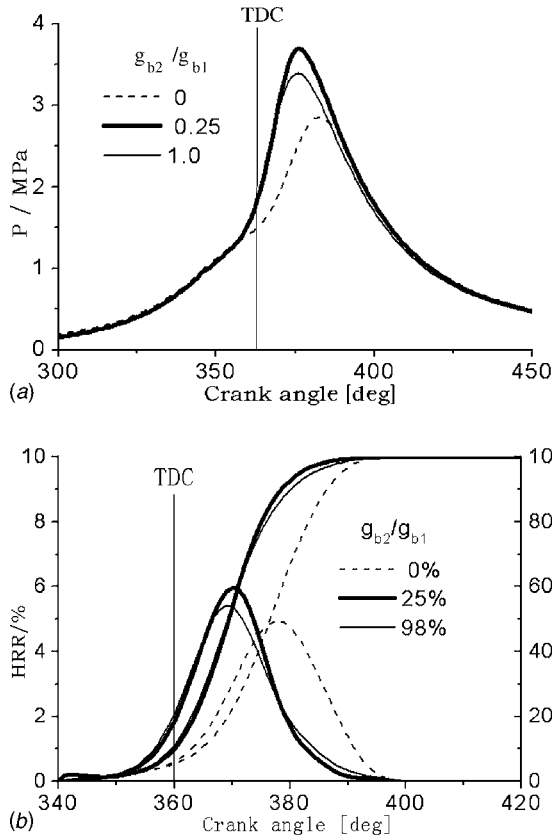

Fig. 6 Effects of g_{b2}/g_{b1} on indicated diagram and the corresponding rate of heat release at same total fuel mass per cycle

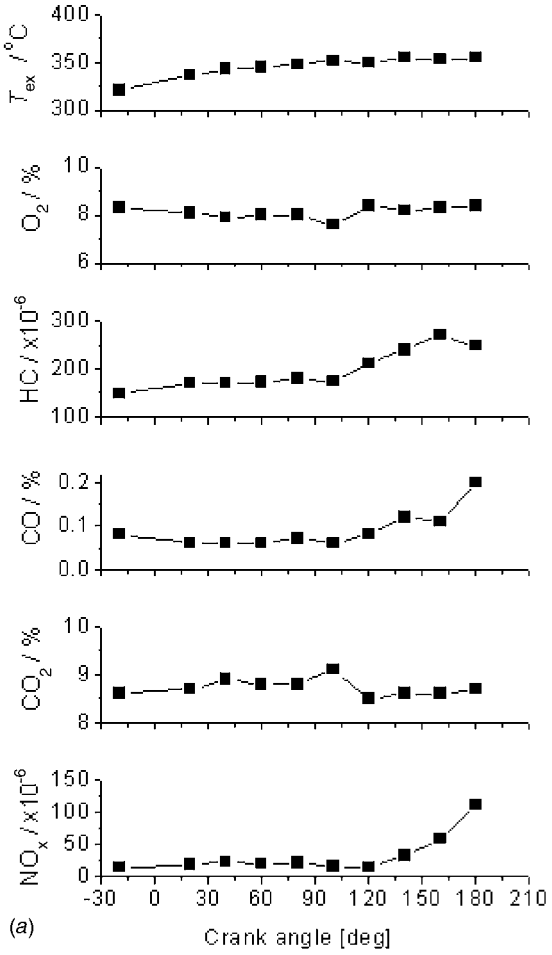

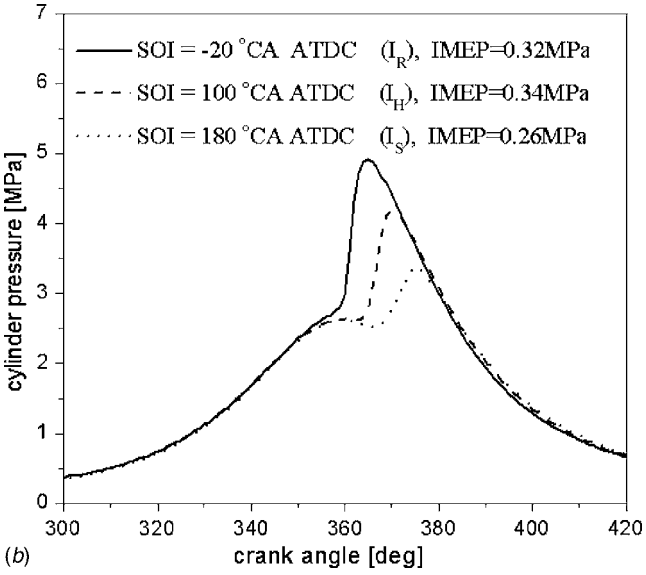

Fig. 7 Effect of injection timing on combustion and emission characteristics at CI combustion mode: (*a*) Emissions and (*b*) indicator diagram and ROHR

RCCI, HCCI, and SCCI. In order to investigate the effect of properties of mixture on CI combustion, combustion and emission data were measured with varying start of single injection (SOI) from the NVO period to compression stroke. Figure 7(*a*) shows the combustion and emission characteristics with single-stage injection from −20°CA to 180°CA ATDC. The total injected fuel mass, g_b=18 mg, cam1.

From Fig. 7(*a*), it can be seen that, with the retarding injection timing, the exhaust temperature increases gradually. When fuel injection occurs at an early paint of the intake stroke, low ambient pressure leads to long spray penetration. Meanwhile, the piston is very close to the injector. Spray will impinge directly on the bottom of the piston bowl. Oil film on the piston bowl results in slightly higher CO emission.

When fuel injection occurs at the middle of the intake stroke (SOI=100°CA), the interaction between intake air motion and spray evaporation reaches optimum utilization [18]. CO_2 emissions reach to the maximum while O_2, HC, CO, and NO_x emissions reach the minimum, simultaneously. That means the more homogeneous mixture was formed and more complete combustion was achieved.

When injection occurs at late of intake stroke, spray will impinge directly on the cylinder wall [18]. Oil film on the cylinder wall results in higher HC and CO emissions. With retarding SOI after 140°CA, it leads to uncompleted combustion gradually. CO_2 emissions decrease greatly, CO and HC emissions increase. Meanwhile, NO_x emission increases rapidly. With retarding SOI after 140°CA, SCCI combustion characteristics appeared. Concentration distributes as a rich mixture located at the exhaust side of cylinder and a lean mixture near the intake side of cylinder [18]. SCCI leads to NO_x and CO emissions increase due to the local high temperature and fuel-rich zone, while HC emissions decrease due to less wall quench. Combustion duration becomes longer and the exhaust temperature increase. With retarding SOI after 180°CA, misfire occurs and the engine cannot be run. Therefore, there is an optimal value of the first injection timing (100°CA), which results in better engine performance and more homogeneous charge.

Figure 7(*b*) shows three typical indicted diagrams and ROHR

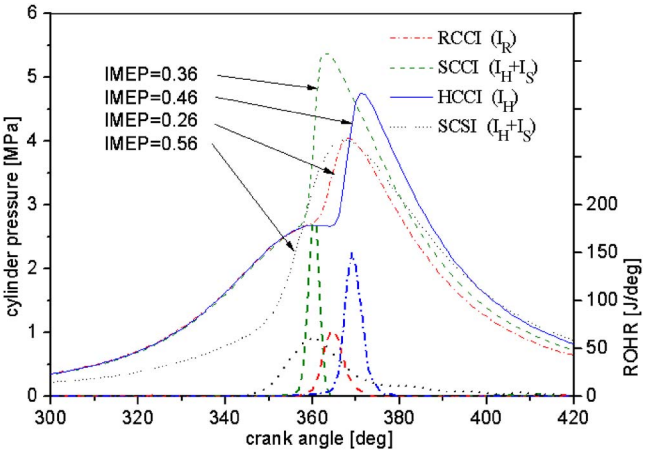

Fig. 8 Typical indicator diagrams and the corresponding ROHRs at different combustion modes

abstracted from Fig. 7(*a*). The significant effect of the start of injection timing on CI combustion can be seen. When the fuel injection occurs at −20°CA (NVO period), RCCI combustion was achieved. The ignition timing is early (355°CA, before the TDC), RCCI is likely to lead to knocking. When the fuel injection occurs at 100°CA, HCCI combustion was achieved with low NO_x emission and higher thermal efficiency. When the fuel injection occurs at 180°CA, SCCI combustion was achieved. At the low load operation case under the test conditions of single injection, SCCI combustion leads to the late ignition timing (364°CA, after the TDC), longer combustion duration, higher CO emissions and higher exhaust temperature.

Comparison of Combustion Modes

Figure 8 shows the comparison of typical indicated diagrams and ROHR at typical operation points with different combustion modes shown in Fig. 1. Table 4 shows the comparison of the corresponding injection strategies and emission data at different modes.

From Fig. 8, it reveals the CI combustion features as a high-pressure gradient after ignition. From the Table 4, it reveals that CI has advantages in high thermal efficiency and low NO_x emissions over SI combustion at part load.

In HCCI mode, the homogeneous mixture was compression ignited, simultaneously, after TDC. Since the ignition timing is after TDC, the peak of the cylinder pressure and temperature are low. Meanwhile, heat transfer is low. As a result, both low NO_x emissions and low fuel consumption were obtained.

Table 4 Injection strategies and emissions at different combustion modes

Combustion mode	RCCI	HCCI	SCCI	SCSI
Injection strategies	I_R	I_H	I_H+I_S	I_H+I_S
Throttle percentage	WOT	WOT	12.5%	12.5%
Switchable cam-phase configuration	Cam1	Cam1	Cam1	Cam0
SOI (°CA ATDC)	−45	100	100	100
g_b (mg)	13	22	18	29
g_{b1}:g_{b2}			5:1	3:1
φ_a	1.72	1.52	1.53	1.20
CO (%)	0.10	0.04	0.07	0.50
CO_2 (%)	8.4	9.4	9.3	12.4
O_2 (%)	8.7	7.3	7.5	3.7
HC (ppm)	119	246	166	320
NO_x (ppm)	8	36	342	2500
IMEP (MPa)	0.26	0.46	0.36	0.56
ISFC (g/kW h)	221	212	215	245

In RCCI mode, the homogeneous mixture was compression ignited, simultaneously, near TDC. Reformed fuel in the NVO period improves ignition property of the mixture, which leads to earlier ignition. However, heat release due partly to oxidization in NVO leads to higher temperature in the cylinder. Meanwhile, a little backflow from the cylinder to the intake port may occur when the intake valve opens [17]. The mass of fresh intake air decreases, and the pumping loss increases in spite of WTO. As a result, RCCI leads to higher fuel consumption with earlier ignition.

In SCCI mode, the two-stage injection strategy (I_H+I_S) was used to form a stratified charge before ignition. The stratified mixture was compression ignited sequentially before TDC. The mixture at periphery of the fuel-rich zone ignited first [14]. This leads to local higher temperature and corresponding higher NO_x emissions (342 ppm). Although the NO_x emissions are slightly higher at SCSI mode, the total NO_x emissions are still much less than that of SCSI combustion mode (2500 ppm). NO_x emissions in three of the CI modes decrease significantly compare to that of the conventional SI mode.

It is found that SCCI is likely to lead to late ignition of misfire at low load with single injection, as shown in Fig. 7(*b*), while SCCI leads to earlier ignition at higher load with two-stage injection as shown in Fig. 8. This can be explained by the fact of internal EGR. For the high-octane-number fuel, there must be a mass of active radicals generated before ignition under the test conditions of normal intake temperature. Partly, fuel injection in NVO can realize the fuel reformation and enhance ignition capability [10,17,18]. Therefore, SCCI cannot be run without NVO injection at low load. While at higher load, the mixture temperature in the cylinder is higher due to the higher temperature of internal EGR since the temperature near TDC exceeds the temperature of fuel auto-ignition. The local temperature and concentration are inhomogeneous in the stratified charge. The first auto-ignition spot is easy to occur at the ignitable spots where both temperature and concentration are appropriate in the inhomogeneous charge. Therefore, SCCI can enhance the ignition property at the range of HCCI high load limit. As a result, SCCI is easy to switch to SCSI mode with the same injection strategy and same throttle position. To avoid misfire at HCCI/SI transient operation during the process of cam profiles switch the SCCI mode is suitable for CI/SI operation.

In SCSI mode, SI Cam profiles (Cam0) were enabled. Cam phase was switch to conventional phase of the SI engine without NVO. From Fig. 8, it can be seen that the cylinder pressure before combustion TDC is lower than that of CI mode due to pumping loss with a part-open throttle. However, pumping loss is much lower in SCCI mode with NVO due to short intake period and less fresh air is required at low load. Two-stage injection strategy (I_H+I_S) was used to form a stratified charge before spark ignition in the SCSI mode. A stratified mixture was ignited by spark and burned due to flame propagation. The combustion duration is ~40°CA. Therefore, ISFC is higher than that in CI mode and NO_x emissions increases significantly.

HCCI Operation Range

The HCCI operation region of the three NVO phases is shown in Fig. 9. In the large NVO (Cam3), the engine can reach the lowest load with stable combustion. In the whole operation region of Cam3, COV is <1%. So the Cam3 strategy is suitable for low-speed, middle-low load operation mode. The small NVO cam phase (Cam2) traps less internal EGR. The intake fresh air leads to misfire in low-speed low-load operation region. Since the temperature of mixture at the end of compression stroke cannot reach the HCCI ignition point, the low-speed region is narrow, the engine cannot even run below 1000 rpm. On the contrary, the high-

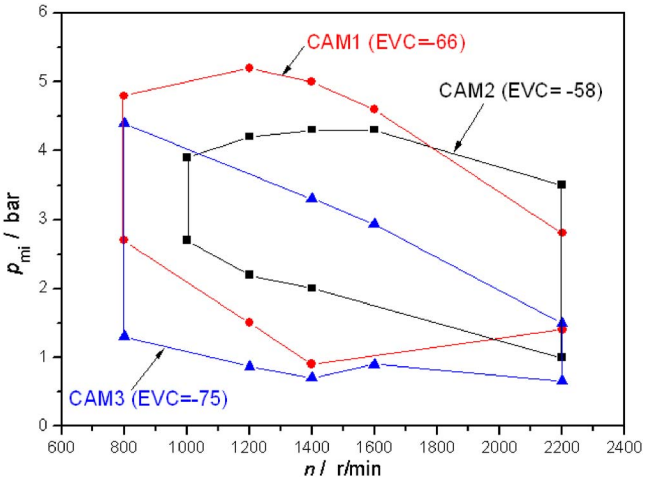

Fig. 9 HCCI operation region of three NVO phases

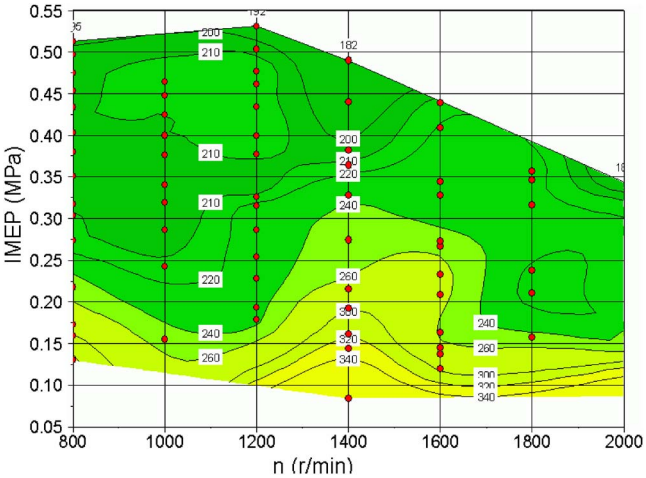

Fig. 11 Fuel consumption (ISFC, g/kW h) of gasoline DI HCCI engine

speed region is wide, and this Cam2 configuration is suitable for high-speed, high-low operation mode. The moderate NVO cam phase (Cam1) makes the engine reach the highest load (n =1200 rpm, IMEP=0.53 MPa); the operation region of this cam phase is the widest. Therefore, Cam1 is the optimized cam phase configuration.

Since NO_x emissions are very low in CI modes, only HC and CO emissions need to be after-treated, engine can run at lean burn conditions with TWC at part load. Unlike conventional PFI gasoline engine, λ should be fixed to 1 for the requirement of TWC. Meanwhile, engine load can be controlled by direct-injected fuel quantities with variable injection strategies at different operation points like diesel engines.

Two-stage direct injection (TSDI) strategy is a practical approach to control the HCCI combustion effectively in our previous study [17]. This study to the injection ratio and injection timing show that, either earlier or more preinjection in the NVO period leads to earlier ignition and more rapid combustion. Therefore, TSDIs are applied to the HCCI engine map.

Figure 10 shows the experiment results of the operation region for the GDI-HCCI engine. The engine injection strategies MAP was achieved by the optimization of injection parameters. The HCSI mode is used in the high load region near stoichiometric mixture. In the middle-high load region, the SCSI is used at λ =1.1–1.4. In the middle-low load region, the HCCI mode is used at λ=1.4–1.8. Within the HCCI mode, when ϕa is high, the main injection in the intake process, assisted with the preinjection in NVO process, can stabilize the ignition. When ϕa is low, the main injection in the intake process assisted by the injection in compression process can control the ignition and avoid knocking. In the transient process of HCCI and SCSI modes, misfiring is easy to happen due to a high level of residual gas. The SCCI mode can stabilize the combustion. Therefore, SCCI is suitable for the HCCI/SI switch.

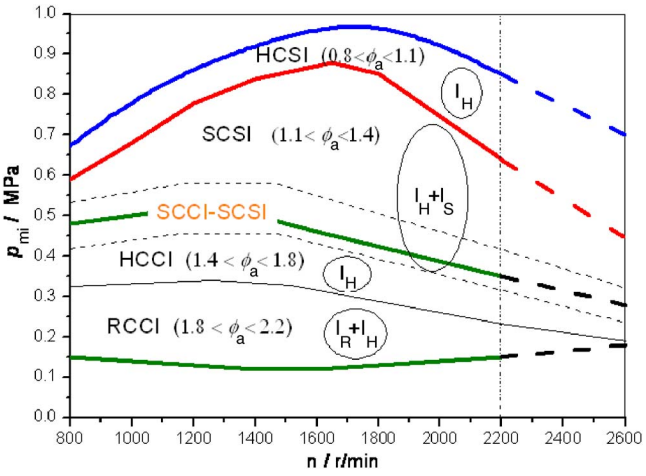

Fig. 10 Optimized injection strategies and corresponding combustion modes

HCCI Engine Map

The HCCI test engine fuel consumption MAP is shown in Fig. 11. The middle-low operation area can be covered by the HCCI combustion mode. In the wide HCCI mode region, the indicated fuel consumption is <240 g/kW h. The NO_x emission MAP of this engine is shown in Fig. 12. In the wide HCCI mode region, NO_x emission is lower than 40 ppm. HC emission is similar with the traditional gasoline engine before TWC. CO emission is lower than that of the traditional gasoline engine before TWC.

The high fuel consumption of traditional gasoline is mainly in middle-low load region. But this region can be covered with gasoline HCCI combustion. The throttle of the HCCI mode is widely opened, which causes low pump losses. The homogeneous lean burn has a high specific heat ratio κ, which leads to higher in-cylinder mean temperature and lower local temperature than that of SI engine. Thus it has high heat efficiency and low NO_x emission, and the indicated fuel consumption reaches that level of diesel engine. Therefore, a gasoline engine solves the problem of high fuel consumption in middle-low load region and reduces the NO_x emission at the same time.

Conclusions

In this paper, a multimode combustion system with direct injection was developed on a two-cylinder gasoline engine. Through the injection strategies combined with switchable cam profiles, different combustion modes (HCSI, SCSI, SCCI, HCCI, RCCI) were realized in a four-stroke gasoline direct injection engine. The effects of injection strategies and cam-phase configurations on combustion, emission, and operation range were studied. It was found that:

1. A simplified cylindrical piston combustion chamber and the helical intake port are designed to assist the stable combustion of the mixture, which reduce the difficulties of the combustion system design.

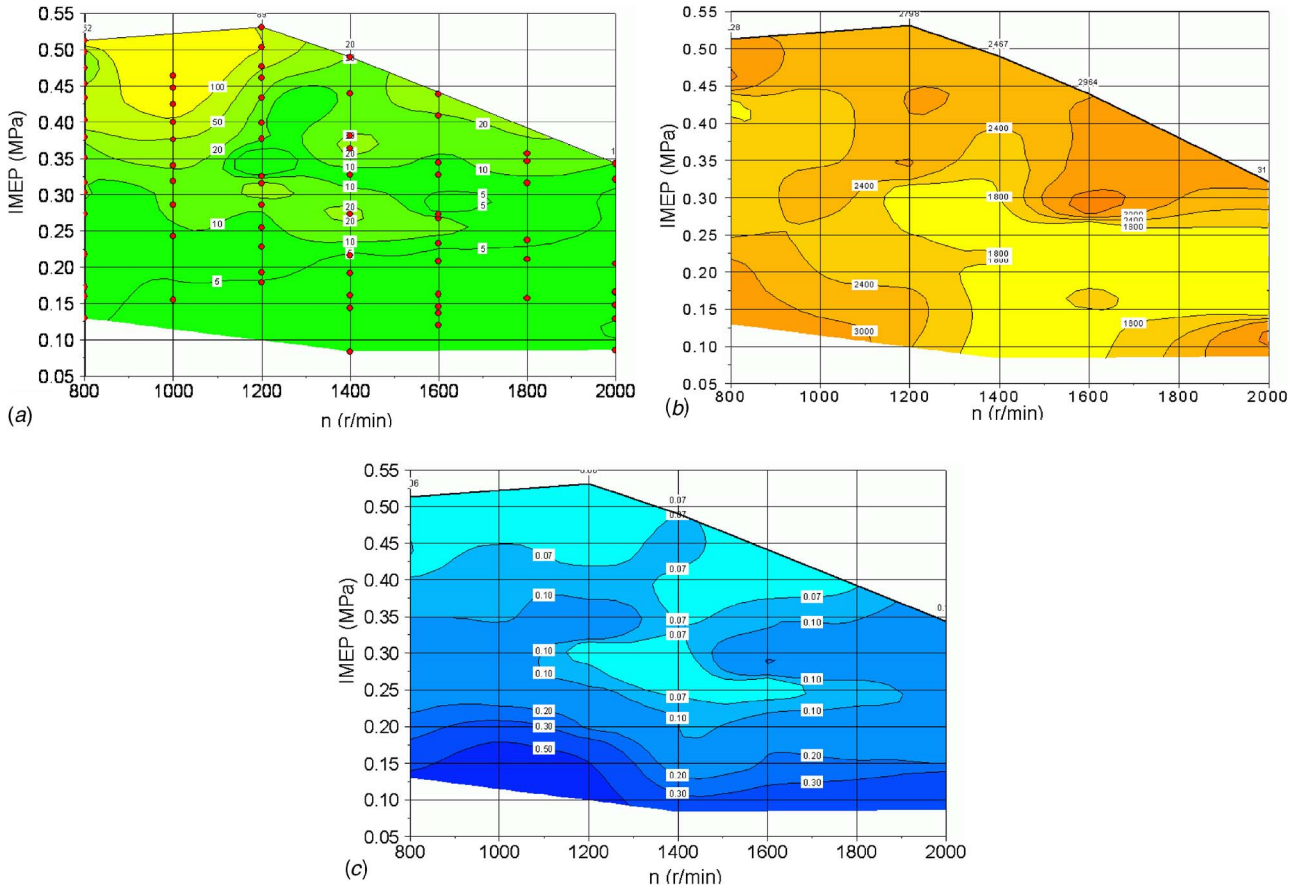

Fig. 12 Emissions of gasoline DI HCCI engine: (*a*) NO_x emission ($\times 10^{-6}$), (*b*) THC emission ($\times 10^{-6}$), and (*c*) CO Emission (%)

2. The combustion modes can be switched and controlled by fuel-injection strategies in a GDI engine with a two-stage variable valve-timing mechanism.
3. In SCSI mode, different fuel quantity ratios of the second injection to the first have significant effects on the mixture formations and engine performances. A ratio of 0.25–0.3 can form an ignitable mixture around the spark plug.
4. In SCCI mode, stratified combustion leads to local higher temperature and corresponding higher NO_x emissions. Whereas NO_x emissions are still much less than that of the SCSI combustion mode at same load. Sequential ignition slows the combustion rate at HCCI high load limit.
5. In HCCI mode, ignition timing can be controlled by introducing part fuel in the NVO period for reforming. HCCI combustion can be operated from 1 bar to 5 bar IMEP with different NVO, has the advantages of rapid response, high stability, low fuel consumption, low emission, and widely operation region. In the whole stable region, the lowest fuel consumption is 182 g/(kW h), NO_x emission is <40 ppm.
6. In RCCI mode, the low load range can be extended to idle operation by injecting total fuel mass during the NVO period.
7. The HCCI operation region of three NVO phases shows that the engine can reach the lowest load with large NVO configuration and the highest speed with small NVO. The moderate NVO cam phase makes the engine reach the highest load ($n=1200$ rpm, IMEP=0.53 MPa). The operation region of moderate NVO cam phase is the widest.
8. Since NO_x emissions are very low in CI modes, the engine can run at lean burn conditions with TWC at part load. Meanwhile, load can be controlled by direct injected fuel quantities with variable injection strategies at different operation points.

Acknowledgment

This research work is supported by the National Key Basic Research Plan ("973" Plan), "Basic research on combustion theory of new generation IC engines and alternative fuels—Controlled homogeneous compression ignition of high octane fuels," under Grant No. 2001CB209204.

Nomenclature

ATDC = after top dead center
BDC = bottom dead center
BTDC = before top dead center
CAD = crank angle degree
CI = compression ignition
COV = coefficient of variation
CR = compression ratio
DI = direct injection
DOI = duration of injection
$dp/d\phi$ = rate of pressure rise [MPa/deg]
EGR = exhaust gas recirculation
EVC = exhaust valve close
EVO = exhaust valve open
g_b = total fuel mass per cycle
g_{b1} = fuel mass of the first injection
g_{b2} = fuel mass of the second injection
GDI = gasoline direction injection
HCCI = homogeneous charge compression ignition
HCSI = homogeneous charge compression ignition

IMEP = indicated mean effective pressure
ISFC = indicated specified fuel consumption
IVC = intake valve close
IVO = intake valve open
MON = motor octane number
n = engine speed (rpm)
NO_x = nitrogen oxides
NVO = negative valve overlap
PFI = port fuel injection
p_{in} = intake pressure
POT = part open throttle
PVO = positive valve overlap
RCCI = radical charge compression igntion
ROHR = rate of heat release
RON = research octane number
SCCI = stratified charge compression ignition
SCSI = stratified charge spark ignition
SI = spark ignition
SOI = start of injection
TDC = top dead center
TSDI = two-stage direct injection
T_{in} = intake temperature
T_{ex} = exhaust temperature
TWC = three-way catalyst
VCT = variable cam timing
WOT = wide-open throttle
η_i = thermal efficiency
ϕ = fuel/air equivalence ratio
ϕ_a = air/fuel equivalence ratio

References

[1] Zhao, F., Asmus, T. W., Assains, D. N., Dec, J. E., Eng, J. A., Najt, P. M., 2003, *Homogenous Charge Compression Ignition (HCCI) Engine: Key Research and Development Issues*, Society of Automotive Engineers, Warrendale, PA.

[2] Marriott, C. D., Kong, S.-C., and Reitz, R. D., 2002, "Investigation of Hydrocarbon Emissions From a Direct Injection-Gasoline Premixed Charge Compression Ignited Engine," SAE Paper No. 2002-01-0419.

[3] Keller, J., and Singh, G., 2001, "Update on Engine Combustion Research at Sandia National Laboratories," SAE Paper No. 2001-01-2060.

[4] Sjöberg, M., Edling, L.-O., Eliassen, T., Magnusson, L., and Ångström, H.-E., "GDI HCCI: Effects of Injection Timing and Air Swirl on Fuel Stratification, Combustion and Emissions Formation," SAE Paper No. 2002-01-0106.

[5] Dec, J. E., and Sjöberg, M., 2002, "HCCI Combustion: The Sources of Emissions at Low Loads and the Effects of GDI Fuel Injection," 8th Diesel Engine Emissions Reduction Workshop, August 25–29.

[6] Koopmans, L., and Denbratt, I., 2001, "A Four Stroke Camless Engine, Operated in Homogeneous Charge Compression Ignition Mode With Commercial Gasoline," SAE Paper No. 2001-01-3610.

[7] Kaneko, M., Morikawa, K., et al., 2001, "Study on Homogeneous Charge Compression Ignition Gasoline Engine," 5th International Symposium on Diagnostics and Modeling of Combustion in Internal Combustion Engines (COMODIA 2001) July, Nagoya.

[8] Fuerhapter, A., Piock, W. F., and Fraidl, G. K., 2003, "CSI-Controlled Auto Ignition—The Best Solution for the Fuel Consumption Versus Emission Trade-Off?" SAE Paper No. 2003-01-0754.

[9] Fuerhapter, A., Unger, E., Piock, W. F., and Fraidl, G. K., 2004, "The new AVL CSI Engine–HCCI Operation on a Multicylinder Gasoline Engine," SAE Paper No. 2004-01-0551.

[10] Koopmans, L., Ogink, R., and Denbratt, L., 2003, "Direct Gasoline Injection in the Negative Valve Overlap of a Homogeneous Charge Compresson Ignition Engine," SAE Paper No. 2003-01-1854.

[11] Urushihara, T., Hiraya, K., Kakuhou, A., and Itoh, T., 2003, "Expansion of HCCI Operating Region by the Combination of Direct Fuel Injection, Negative Valve Overlap and Internal Fuel Reformation," SAE Paper No. 2003-01-0749.

[12] Kuwahara, K., Ueda, K., and Ando, H., 1998, "Mixing Control Strategy for Engine Performance Improvement in a Gasoline Direct Injection Engine," SAE Paper No. 980158.

[13] Santoso, H., Matthews, J., and Cheng, W. K., 2005, "Managing SI/HCCI Dual-Mode Engine Operation," SAE Paper No. 2005-01-0162.

[14] Wang, Z., Wang, J.-X., and Shuai, S.-J., 2005, "Effects of Spark Ignition and Stratified Charge on Gasoline HCCI Combustion With Direct Injection," SAE Paper No. 2005-01-1037.

[15] Sun, Y., Shuai, S.-J., Wang, J.-X., and Wang, Y.-J., 2003, "Numerical Simulation of Mixture Formation and Combustion of Gasoline Engines With Multi-Stage Direct Injection Compression Ignition (DICI)," SAE Paper No. 2003-01-1091.

[16] Sjöberg, M., Edling, L.-O., Eliassen, T., Magnusson, L., Angström, H. E., 2002, "GDI HCCI: Effects of Injection Timing and Air Swirl on Fuel Stratification, Combustion and Emissions Formation," SAE Paper No. 2002-01-0106.

[17] Wang, Z., Wang, J.-X., Shuai, S.-J., Tian, G.-H., and An, X.-L., "Experimental and Computational Studies on Gasoline HCCI Combustion Control Using Injection Strategies," ASME Paper No. GTP05-1167.

[18] Wang, Y.-J., Wang, J.-X., Shuai, S.-J., et al., 2005, "Study of Injection Strategies of Two-Stage Gasoline Direct Injection (TSGDI) Combustion System," SAE Paper No. 2005-01-0107.

Kris Quillen

Rudolf H. Stanglmaier

Engines and Energy Conversion Laboratory,
Colorado State University,
Ft. Collins, CO 80524

Luke Moughon

Rosalind Takata

Victor Wong

Sloan Automotive Laboratory,
Massachusetts Institute of Technology,
Cambridge, MA 02139

Ed Reinbold

Rick Donahue

Waukesha Engine Dresser,
Waukesha, WI 53188

Friction Reduction by Piston Ring Pack Modifications of a Lean-Burn Four-Stroke Natural Gas Engine: Experimental Results

A project to reduce frictional losses from natural gas engines is currently being carried out by a collaborative team from Waukesha Engine Dresser, Massachusetts Institute of Technology (MIT), and Colorado State University (CSU). This project is part of the Advanced Reciprocating Engine System (ARES) program led by the U.S. Department of Energy. Previous papers have discussed the computational tools used to evaluate piston-ring/cylinder friction and described the effects of changing various ring pack parameters on engine friction. These computational tools were used to optimize the ring pack of a Waukesha VGF 18-liter engine, and this paper presents the experimental results obtained on the engine test bed. Measured reductions in friction mean effective pressure (FMEP) were observed with a low tension oil control ring (LTOCR) and a skewed barrel top ring (SBTR). A negative twist second ring (NTSR) was used to counteract the oil consumption increase due to the LTOCR. The LTOCR and SBTR each resulted in a ~0.50% improvement in mechanical efficiency (η_{mech}). [DOI: 10.1115/1.2719262]

Introduction

Power Cylinder Friction. Mechanical friction consumes 4–15% of the total energy in a modern internal combustion engine. From these mechanical losses, power cylinder friction accounts for the largest part (40–55%) with 30–50% of that from the rings [1]. Mechanical loading, gas pressure, oil properties, oil impurities, piston motion, and other parameters affect the piston ring friction. Figure 1 illustrates a typical piston ring pack.

Many methods of reducing engine friction have been proposed and developed. Lubrication effects, mechanical design, and surface modification are some areas that can potentially reduce engine friction.

Mechanical design involves the piston and ring geometry. Tian [2] described a method for modeling the effects of the combined ring pack, which Smedley [3] applied extensively to analyze the different parameters involved in the ring design for low friction for a natural gas engine. The effects of piston design parameters and their effect on lubrication and friction have been described by Moughon [4]. These are only a few of the many papers on the subject.

Surface modifications to the piston rings and liners have been shown to have a potential for friction reduction. Etsion [5] used surface texturing of the piston rings to reduce friction. Sadeghi [6] used a similar technique to reduce friction by texturing the cylinder liner. Jocsak [7] has created a model that predicts the effects of honing groove cross-hatch angle on friction. These are only few of the many papers on the subject.

ARES Friction Reduction Group. The Advanced Reciprocating Engine Systems (ARES) program is a collaborative project funded by the U.S. Department of Energy. The overall goal of the ARES program is to develop stationary natural gas engines with 50% brake thermal efficiency. The role of the ARES friction reduction group is to provide improved engine technologies to reduce mechanical losses and help meet the ARES target. The current focus of the study is to reduce friction in the power cylinder assembly via improvements to mechanical design, lubricants, and material surface characteristics. Previously, the ring pack was analyzed numerically and the improved ring pack has now been tested on a full-scale engine. Analytical results for the lubrication studies [8] and material studies [7] have already been produced at MIT, and these results will be tested experimentally on the Waukesha VGF engine at a later time.

Ring Pack Modifications

Through computer modeling preformed at MIT, a low-friction ring pack design has been developed. According to the model results, the modified ring pack design has an overall friction reduction potential of 35% compared to the baseline (stock) configuration [9]. The ring pack modifications include a skewed barrel top ring (SBTR), a negative twist second ring (NTSR), and a low tension oil control ring (LTOCR). The LTOCR model is described by Tian in [10].

According to the model, the largest source of frictional loss is the oil control ring (~66%) [8]. The LTOCR has a reduced tension force, causing a decrease in friction. The tension has to be high for ring/liner conformability. However, decreasing the ring tension allows more oil past the oil control ring and is expected to increase the rate of oil consumption. In order to minimize the adverse effects to the LTOCR, a NTSR can be used. For a negative twist ring, the force balance is unstable near TDC combustion, which causes flutter to occur there. The flutter lets gases flow behind the ring and push oil down to the crank case, reducing the oil consumption [10,11]. A potentially adverse effect of the NTSR ring is an increase in blow-by flow. However, the model predicts that the blow-by increase is not significant for the combined low-friction configuration.

Contributed by the Internal Combustion Engine Division of ASME for publication in the JOURNAL OF ENGINEERING FOR GAS TURBINES AND POWER. Manuscript received July 13, 2006; final manuscript received January 11, 2007. Review conducted by Thomas W. Ryan III. Paper presented at the 2006 Spring Conference of the ASME Internal Combustion Engine Division (ICES2006), May 7–10, 2006, Aachen, Germany.

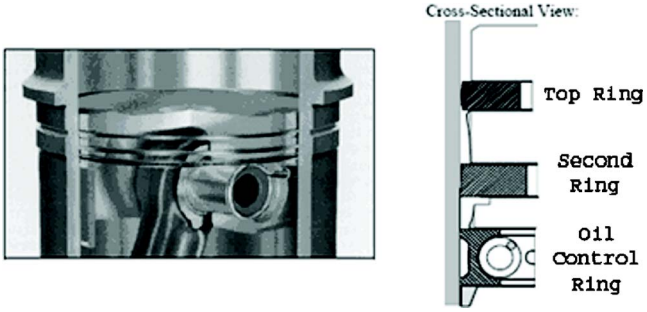

Fig. 1 Typical piston ring pack

The second largest contributor to FMEP is the top ring near top dead center (TDC) during combustion. To reduce friction on the top ring, a SBTR profile was selected. Figure 2 illustrates the basic concept of the skewed barrel design. B_1 and B_2 are the axial distances from the ring edge to the widest part of the ring profile. P_1 and P_2 are the pressures above and below the ring, respectively. The benefit comes from a force balance in the radial direction. High gas pressure acts on the back of the ring and on the front over the length B_1. Low gas pressure acts over B_2. Therefore, over the length B_1 there is a balance resulting in no net radial force. There is a net force over B_2, $B_2*(P_1-P_2)$. The value of B_1 has no effect on the radial forces; only changing B_2 changes the force balance. The way this affects friction is that if you have a smaller B_2, you will get a smaller net radial force.

In summary, the MIT model predicted that the low-friction ring pack should result in a 35% reduction in overall friction from the ring pack, with small changes in oil consumption and blow-by [9].

Friction Measurements

Experimental Approach. Several approaches have been used for measuring frictional losses in internal combustion engines, including custom-built "floating liner" engines [12–14] and engines with instrumented connecting rods [15]. The approach used in this project was selected because it could be performed in an unmodified, full-scale, multicylinder engine at full load.

In this study, FMEP was determined by calculating the net (indicated) mean effective pressure (NMEP) from pressure traces and subtracting the brake mean effective pressure (BMEP), as shown in Eq. 1. This method is simple to perform, as long as NMEP and BMEP can be measured accurately. Although the FMEP represented the mechanical efficiency of the engine as a whole, changes in FMEP were assumed to be a result of the changes in piston rings, as everything else was held constant.

$$\text{FMEP} = \text{NMEP} - \text{BMEP} \tag{1}$$

Friction was measured on a Waukesha VGF F18 in-line six cylinder power generation engine. This engine is rated at 400 bhp (298 kW) at 1800 rpm and was equipped with extensive instrumentation. Measurements were made at 1800 rpm and 70%, 80%, 90%, and 100% of full load.

Cylinder pressure measurements were made with Kistler 6067C water cooled pressure transducers (donated by the Kistler Corp.)

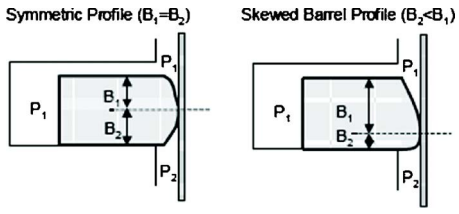

Fig. 2 Illustration of skewed barrel profile design

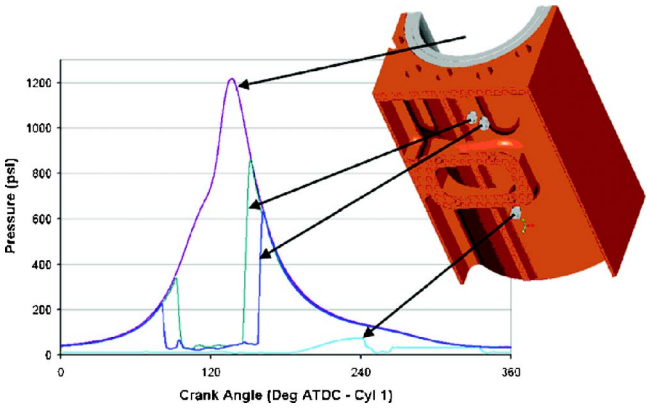

Fig. 3 Cylinder 5 pressure transducer measurements

These transducers were selected for the high level of accuracy needed in computing mean effective pressures. The pressure sensors output a charge signal that was converted to a 0 to 5 V signal using Kistler 5010B charge amplifiers. These signals were then scaled and recorded by a Hi-Techniques Win600 high-speed data acquisition (DAQ) system. The Hi-Techniques system recorded the pressure signals in all six cylinders as well as three inter-ring pressure sensors in cylinder 5 (Figs. 3 and 4). Kistler 6052A transducers were selected for installation on the liner due to their compact size. The inter-ring pressure traces were used to verify the model predictions for the land pressures around TDC and bottom dead center (BDC). Figure 3 illustrates a typical pressure trace set recorded by the four pressure transducers in cylinder 5. The Hi-Techniques system was used to record raw pressure measurements as well as calculate values such as IMEP and burn durations.

The location of the cylinder liner pressure transducers installed on cylinder 5 is shown in Fig. 4.

A BEI brand optical encoder was used to synchronize the pressure measurements to the crankshaft position. Initially, an increment of 0.25 crank angle degrees (CAD) was used. However, it was found that this did not provide sufficient resolution to accurately measure the expected friction reduction. An offset of a single encoder pulse (0.25 CAD) resulted in a change of more than 1.5 psi (10.3 kPa) in IMEP (or FMEP). This issue was alleviated by using an encoder with a 0.1 CAD resolution. A one pulse offset with the new encoder (0.1 CAD) resulted in a 0.7 psi (4.8 kPa) change in IMEP. In order to prevent potential encoder coupler flexure problems and other synchronization errors, an in-

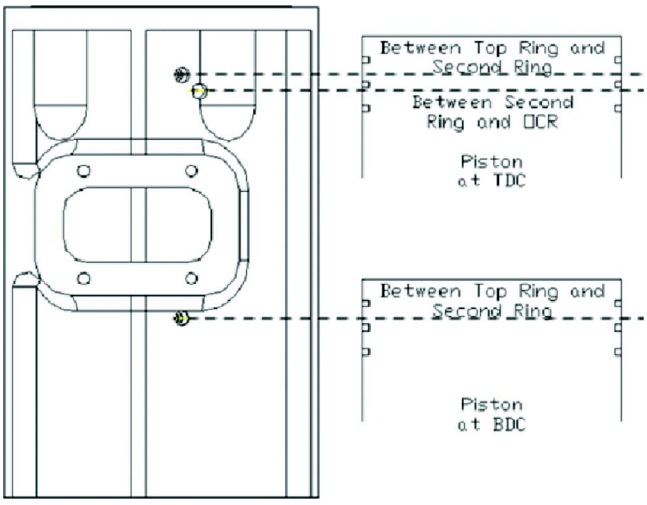

Fig. 4 Cylinder 5 pressure transducer locations

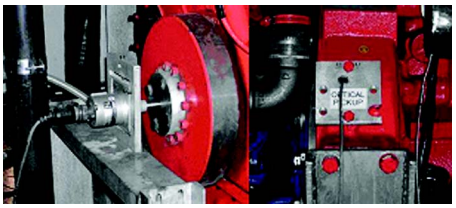

Fig. 5 Optical encoder and optical pickup

dependent optical pickup was placed on the flywheel as seen in Fig. 5. This signal was used as a consistent reference to locate the crankshaft rotational position. Use of the 0.1 CAD resolution encoder resulted in a drawback because the Hi-Techniques system could only sample 500 cycles at that resolution, which was half of the desired number of samples. This issue was resolved by collecting two consecutive data samples of 500 cycles each at each desired operating point.

The NMEP values were calculated from the raw pressure output files of the Hi-Techniques system using Eqs. (2)–(4) [16]. The independent optical signal was used as the reference to validate the location of TDC for the encoder.

$$\mathrm{NMEP} = -\frac{(2 \cdot \pi/360)\int_{-360}^{360} P\,dV}{V_d} \tag{2}$$

P, dV, and V_d represent the instantaneous pressure, rate of change of the volume, and the displacement volume, respectively. Equation (3) was used to determine the displacement volume.

$$V_d = \frac{\pi B^2}{4} L \tag{3}$$

B and L represent the cylinder bore and the stroke length, respectively. The final equation needed to determine the NMEP is Eq. (4)

$$dV = \frac{\pi B^2}{4}\left[a \sin(\theta)\left(1 + \frac{a \cos(\theta)}{\sqrt{L^2 - a^2 \sin^2(\theta)}}\right)\right] d\theta \tag{4}$$

In the equations above, a is the crank radius and θ is the angular crank position relative to TDC.

The engine was loaded using Midwest Dynamometer model 322 eddy current dynamometer (Fig. 6) and a Dyn-Loc IV Digital Dynamometer controller. The controller used a load cell as feedback in its closed-loop control mode. The speed was monitored using a magnetic pickup attached to the shaft of the dynamometer. Calibration on the load cell was performed before every day of testing. BMEP was calculated from Eq. (5).

$$\mathrm{BMEP} = \frac{4\pi\tau}{V_d} \tag{5}$$

τ is the brake torque measured by the load cell at the dynamometer.

Fig. 6 Eddy current dynamometer

Fig. 7 AVL automatic oil consumption meter

The oil consumption of the engine was measured with an AVL 403S automatic oil consumption meter, shown in Fig. 7. This instrument was selected due to its high accuracy and simplicity. The meter had a refill accuracy of ±1 g and a level measurement accuracy of ±2 μm. A constant-volume method was used.

This method involves adding a known quantity of oil and measuring the time required for the oil level to return to its original level. This was then repeated automatically. A minimum testing time of 3 h was used to allow the oil consumption measurement to equilibrate. After each test, the total consumed oil and total time were used to calculate the rate of oil consumption. Figure 8 shows a typical output of the oil consumption meter. After a few hours of measurement, the oil consumption rate was found to stabilize.

The ring blow-by was also of interest in this experiment. A J-Tech Associates VF563B in-line flow meter specifically designed for blow-by flow measurement was used, as shown in Fig. 9. Its accuracy was ±2% of full scale, which was 16 ACFM for this meter. This meter uses the principle of vortex shedding to measure the flow rate of the blow-by gases. A small strut inside the flow tube created Karman vortices, and the frequency of the vortices was measured by an ultrasonic beam.

The engine was also equipped with other instrumentation required to maintain the engine at the desired operating conditions. A National Instruments™ DAQ system was used to control and record all parameters of interest on the engine including temperatures, flow rates, pressures, emissions, speed, and load.

Engine Test Procedure. Early in the testing it was found that variations in combustion stability could affect the FMEP measurements with this technique. In essence, the day-to-day variation in natural gas composition from the pipeline was affecting the combustion stability at high load and biasing the NMEP measure-

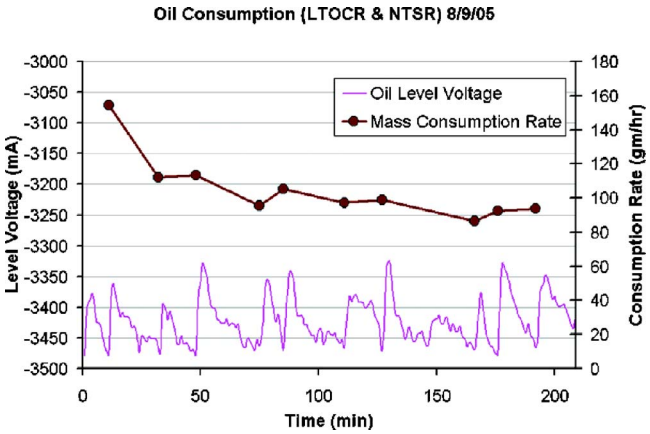

Fig. 8 Output from the oil consumption meter (LTOCR & NTSR at 1800 rpm and 400 bhp (298 kW))

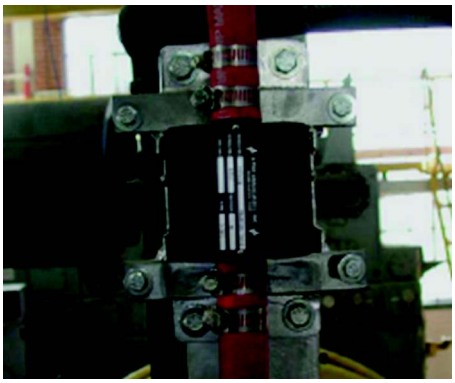

Fig. 9 Blow-by flow meter

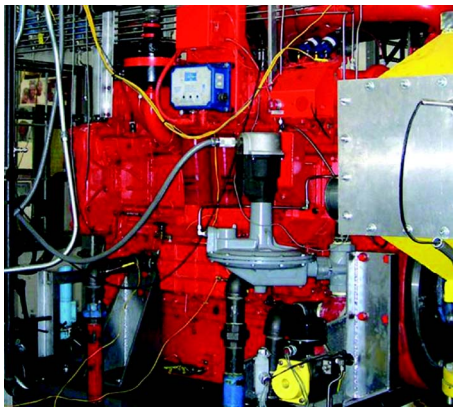

Fig. 11 Assembled test engine

ments. In order to alleviate this condition, a closed loop air-fuel ratio controller was installed, and the engine was operated at a relatively "rich" condition.

An air-fuel ratio sweep was performed to identify the best operating air-fuel ratio for these tests. This desired operating air-fuel ratio was selected at a point where the coefficients of variation (COV) of the IMEP of the cylinders were not affected by fuel composition changes. The COV of the IMEP of cylinder 6 and the engine average are plotted against exhaust O_2 level in Fig. 10. Cylinder 6 is displayed because it has a tendency to become unstable at lower exhaust O_2 levels than the other cylinders. All subsequent tests were performed at 6% O_2.

Each day of testing, the engine was brought to the desired operating conditions and allowed to stabilize. Thermal stability was achieved when the cooling water was maintained at 180°F (82.2°C) and the oil temperature was maintained at 175°F (79.4°C). After these temperatures were reached, they were maintained at that level by a closed-loop control system. After the engine stabilized, all important operating conditions, such as exhaust O_2, were verified. The DAQ logging system was also started. This recorded temperatures, pressures, flows, and load. The conditions were recorded at 1 Hz for a minimum of 5 min and averaged. The Hi-Techniques also recorded pressure traces while the DAQ system was running. Five hundred cycles of cylinder pressure were saved twice in order to obtain the desired 1000 cycles of data. The high number of cycles was desired in order to minimize the effects of cycle-to-cycle variations that naturally occur in the engine. After all of the data were collected, the values were averaged and all calculations were made, including FMEP.

It should be noted that small changes in brake thermal efficiency (BTE) due to the changes in friction could not be measured with the existing equipment. The fuel composition was measured at the beginning of each test point with a gas chromatograph (GC). This information was used to calculate the fuel's energy content (lower heating value, LHV) and molecular weight. The molecular weight was used in conjunction with the measured volumetric flow rate to calculate the fuel mass flow rate. However, measurement errors in the fuel composition and volumetric flow rate were found to be greater than the changes in BTE due to the reductions in engine friction. The BTE was also affected by changes in fuel composition. It should be noted that the FMEP measurements were designed to not be effected by fuel composition.

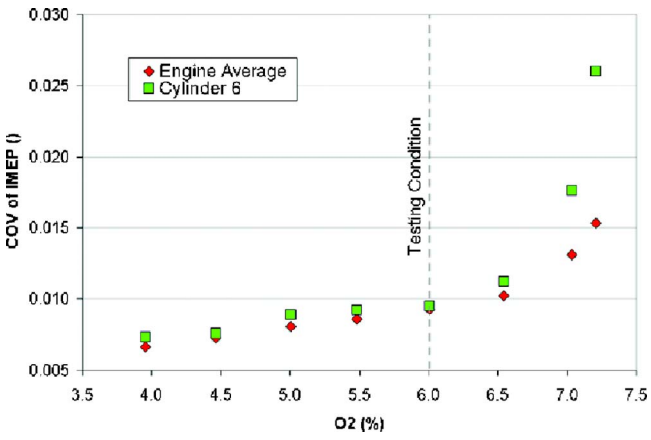

Fig. 10 COV of IMEP of cylinder 6 and the cylinder average

During oil consumption measurements, the engine operating conditions, especially temperature, were held constant. The oil consumption meter was started and allowed to run for a minimum of 3 h. During the oil consumption measurement, the data logging procedure described above was performed several times.

Due to the small expected changes in FMEP relative to the numerous random variations possible in the measurements, several tests were performed at each operating condition and then averaged. The average FMEP value at each operating condition and the 95% confidence interval were calculated. In order to verify that the engine baseline friction did not "drift" over time, repeated baseline engine builds were tested.

Piston Ring Change Procedure. An important element in the procedure for testing different rings was the process of changing them. This process usually took between 2 and 3 full days to complete. The first step was to remove all of the wires, tubing, and instrumentation that "get in the way" or connect to parts that must to be removed (Fig. 11).

All of the coolant systems were drained and sections of the exhaust and intake were removed. The valve covers, rocker arms, and push rods were then removed, followed by the fuel regulator and oil cooler. Jacket water connections were also disconnected. The head bolts were removed and the heads lifted off of the engine. The pistons were removed using the access openings in the side of the engine to remove the connecting rod cap screws. Finally, the pistons were removed from the engine from the top (Fig. 12). The disassembled engine can be seen in Fig. 13.

The rings were then changed one piston at a time, and the engine was then reassembled in the reverse order. During this process, engine parts were cleaned and examined, and gaskets and seals were replaced as needed. The need to disassemble and rebuild the engine for every configuration of the rings tested had the potential to introduce additional variability in the measurements. Although it is unreasonable to expect that the engine condition was absolutely identical after every rebuild, extreme care was taken during this procedure. In addition, in order to ensure consistency in the ring exchange procedure, a single person was

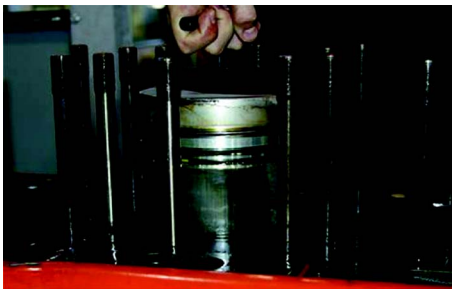

Fig. 12 Piston removal

tasked with changing the rings every time.

The rings tests were performed in the following order:

1. LTOCR and NTSR 1
2. baseline 1
3. LTOCR
4. baseline 2
5. SBTR
6. LTOCR and NTSR 2
7. baseline 3
8. low-friction configuration (LTOCR, NTSR, SBTR)

A summary of the various actions taken to improve the sensitivity of the FMEP measurements includes:

- using an encoder with a smaller increment, 0.1 CAD instead of the 0.25 CAD encoder used initially
- using an independent optical pickup on the flywheel to verify the location of TDC
- increasing the number of measurements at each operating condition
- operating the engine at lower exhaust O_2 levels in order to decrease the effects of fuel composition on combustion stability
- implementing a closed loop controller to maintain exhaust O_2 levels
- changing rings in a way that minimized variation during the engine rebuilds, and randomize the ring test order

Results and Discussion

The main goal of this study was to determine the effect of the piston ring design on FMEP. A plot summarizing the different test sets is shown in Fig. 14. Each ring configuration data set was averaged and plotted along with the 95% confidence interval (CI) as the error bars. The CI was calculated from Eq. (6) [17].

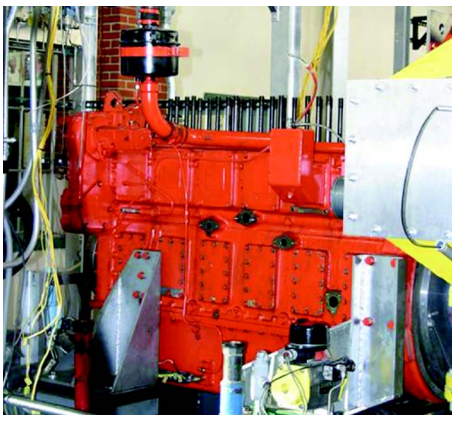

Fig. 13 Disassembled test engine

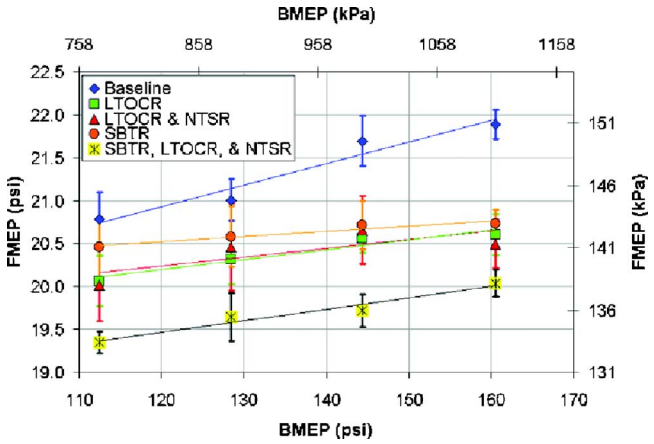

Fig. 14 FMEP versus BMEP at 1800 rpm (combined baseline results)

$$\mathrm{CI} = z_{\alpha/2}\frac{\sigma}{\sqrt{n}} \tag{6}$$

where n is the number of samples in the set, $z_{\alpha/2}$ is the value obtained from the standard normal distribution, and σ is the standard deviation of data set. For a 95% confidence, $z_{\alpha/2}$ is 1.96.

The baseline ring pack was tested three times (with different "builds") in order to verify that the baseline engine friction was not changing over time. This also allowed us to investigate whether the engine tear-down and rebuild process had a significant effect on the FMEP measurements. The three baseline engine tests are shown in Fig. 15. A slight FMEP difference can be seen between the three baseline tests. However, the friction reduction trends discussed here are still valid. The data presented in all plots other than Fig. 15 include all three baseline tests to compute the average and statistics.

The FMEP results of the various rings were compared with the baseline configuration to determine the reduction in FMEP. The friction reductions measured tend to be conservatively predicted using the MIT model (Fig. 16). The error bars on the model predictions show the bounding oil supply conditions used by the model. The error bars on the experimental differences in Fig. 16 were calculated using Eq. (7) [17].

$$\mathrm{Error} = z_{\alpha/2}\sqrt{\frac{\sigma_1^2}{n_1} + \frac{\sigma_2^2}{n_2}} \tag{7}$$

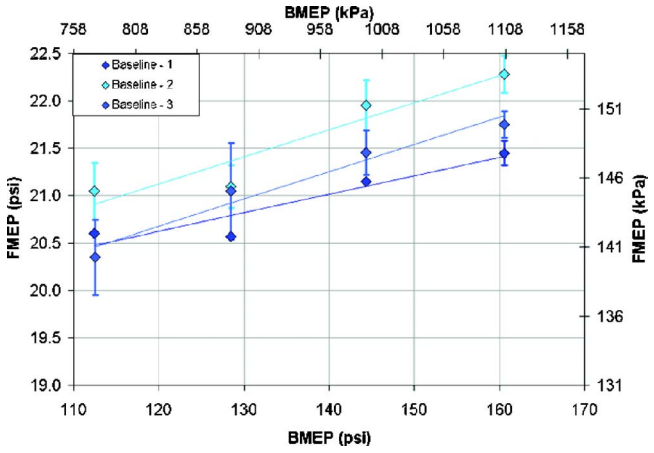

Fig. 15 FMEP vs. BMEP at 1800 rpm (separate baseline results)

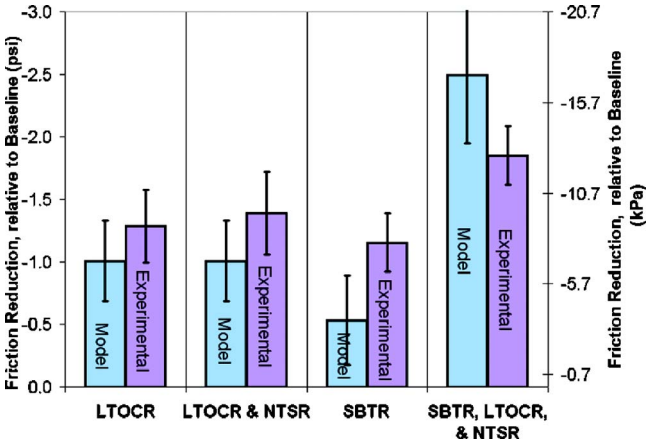

Fig. 16 Experimental and modeled FMEP results at 1800 rpm and 400 bhp (298 kW)

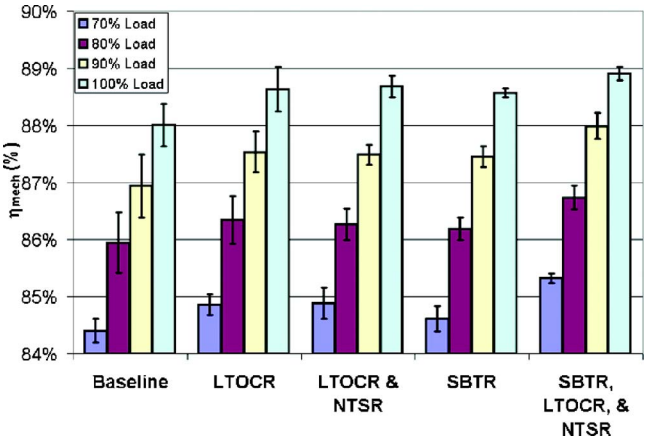

Fig. 18 η_{mech} versus BMEP at 1800 rpm

The mechanical efficiency (η_{mech}) was also calculated using Eq. (8):

$$\eta_{mech} = \frac{\text{BMEP}}{\text{NMEP}} \tag{8}$$

These mechanical efficiency results are shown in Figs. 17 and 18. The effects of the rings were not expected to be additive, since each change affects the other rings.

The measured oil consumption of the engine is shown in Fig. 19. Oil consumption measurements are notoriously variable over time, and, due to the relatively short tests times used to measure oil consumption in this study (~3 h), the measurements are thought to only be an indication of the general trend of the consumption rate. In general, the oil consumption tended to increase when the LTOCR was used and then returned to the somewhat lower value with the NTSR. The SBTR appeared to have a relatively small effect the oil consumption.

The average blow-by measurements and 95% confidence intervals are shown in Fig. 20. As shown, all ring configurations display a slightly increasing blow-by rate with increasing engine load. However, blow-by differences between all configurations are relatively small. The NTSR seemed to have a slightly higher blow-by than the others, which was expected from the ring pack design characteristics and numerical predictions. However, the change does not appear to be very significant and is not cause for concern.

Summary and Conclusions

A ring pack model developed at MIT was used to design a low-friction ring pack configuration for a Waukesha VGF 18 liter engine. The low-friction ring pack features a skewed barrel top ring, a negative twist second ring, and a low-tension oil control ring. The MIT model predicted that the low-tension oil control ring has a potential to decrease ring pack friction by 20–30%, and the skewed barrel top ring has the potential to reduce ring pack

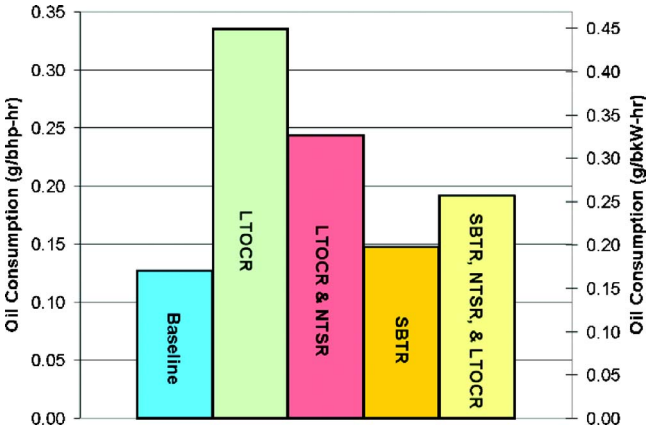

Fig. 19 Measured oil consumption at 1800 rpm and 400 bhp (298 kW)

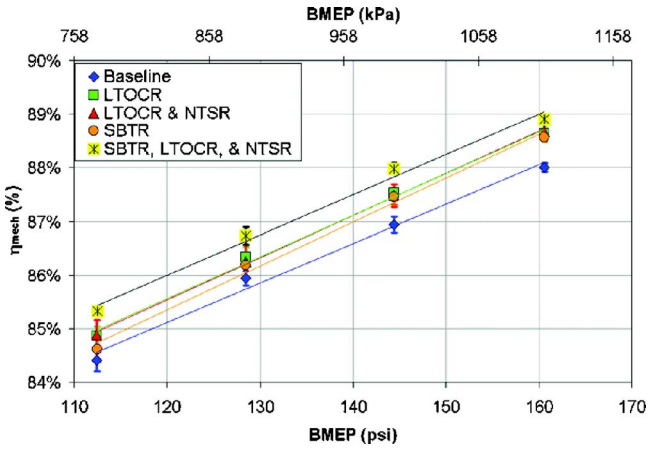

Fig. 17 η_{mech} versus BMEP at 1800 rpm

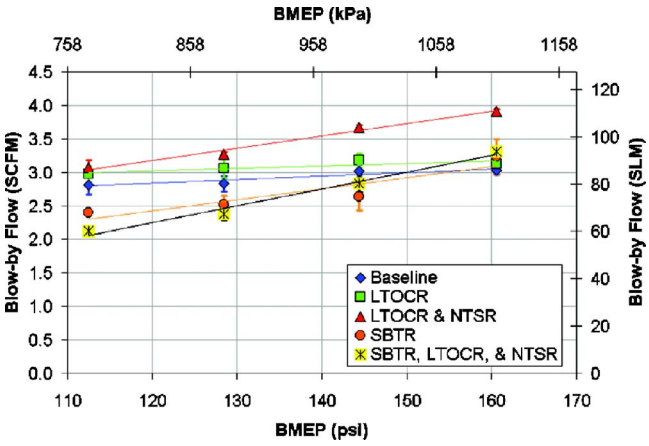

Fig. 20 Blow-by flow versus BMEP at 1800 rpm

friction by 15–25%. Use of the negative twist second ring can help offset the adverse effects of the LTOCR on the rate of oil consumption.

In order to measure the small reductions in FMEP on an unmodified full-scale engine, it was necessary to improve the instrumentation used on the engine and the methodology used for measurements. The experimental results from this study showed that the SBTR and LTOCR rings can indeed reduce FMEP, and that the NTSR can help control the oil consumption rate. The results of combining all three ring designs showed a total engine FMEP reduction of 7–10% from the baseline configuration without significantly increasing oil consumption or blow-by flow. The measured FMEP reductions displayed good agreement with the model predictions.

Acknowledgment

This project is sponsored by the United States Department of Energy, as part of the Advanced University Reciprocating Engines Program (AUREP) under DOE Cooperative Agreement No. DE-FC26-02NT41339. We thank the DOE ARES project monitors, Tom George, Rob Martinez, William Cary Smith, and in particular our technical project monitor Raj Sekar, and especially the DOE manager and sponsor, Ronald Fiskum for the encouragement and support. Prior work and the methodology used in the analyses were supported by related research in the MIT Industrial Consortium on Lubrication in I.C. Engines.

Nomenclature

a = crank radius
ARES = Advanced Reciprocating Engine System
AUREP = Advanced University Reciprocating Engines Program
B = cylinder bore
BDC = bottom dead center
BMEP = brake mean effective pressure
BTE = brake thermal efficiency
CAD = crank angle degree
CI = confidence interval
COV = coefficient of variance
DAQ = data acquisition
dV = rate of change of volume
FMEP = friction mean effective pressure
GC = gas chromatograph
IMEP = indicated mean effective pressure
L = stroke length
LTOCR = low tension oil control ring
n = no. of samples in a set
NMEP = net indicated mean effected pressure
NTSR = negative second ring with a static twist
P = instantaneous pressure
SBTR = skewed barrel top ring
TDC = top dead center
V_d = displacement volume
$z_{\alpha/2}$ = value obtained from the standard normal distribution
η_{mech} = mechanical efficiency
θ = angular crank position relative to TDC
σ = standard deviation of a data set
τ = measured torque applied to the dynamometer

References

[1] Richardson, D. E., 2002, "Review of Power Cylinder Friction for Diesel Engines," Trans. ASME: J. Eng. Gas Turbines Power, **122**, pp. 506–519.
[2] Tian, T., and Wong, V. W., 2000, "Modeling the Lubrication, Dynamics, and Effects of Piston Dynamic Tilt of Twin-Land Oil Control Rings in Internal Combustion Engines," Trans. ASME: J. Eng. Gas Turbines Power, **122**, pp. 119–129.
[3] Smedley, G., Mansouri, S. H., Tian, T., and Wong, V. W., 2004, "Friction Reduction Via Piston Ring Design for an Advanced Natural-Gas Reciprocating Engine," ASME-ICED Fall Technical Conference, ASME Paper No. ICEF2004-879.
[4] Moughon, L., and Wong, V. W., 2005, "Effects of Lubricant and Piston Design on Reciprocating Engine Friction," ASME-ICED Fall Technical Conference, ASME Paper No. ICEF2005-1343.
[5] Etsion, I., Kligerman, Y., and Shinkarenko, A., 2005, "Improving Tribological Performance on Piston Rings by Partial Surface Texturing," Trans. ASME, J. Tribol., **123**, pp. 632–638.
[6] Sadeghi, F., Bolander, N. W., and Gerber, G. R., 2005, "Piston Ring Friction Reduction Through Surface Modification," ASME-ICED Fall Technical Conference, ASME Paper No. ICEF2005-1346.
[7] Jocsak, J., Li, Y., Tian, T., and Wong, V. W., 2005, "Analyzing the Effects of Three-Dimensional Cylinder Liner Surface Texture on Ring-Pack Performance With a Focus on Honing Groove Cross-Hatch Angle," ASME-ICED Fall Technical Conference, ASME Paper No. ICEF2005-1333.
[8] Takata, R., and Wong, V., 2006, "Effects of Lubricant Viscosity on Ring/Liner Friction in Advanced Reciprocating Engine Systems," *Proceedings of the ICEF2006, ASME-ICED 2006*, ICEF2006-1526.
[9] Wong, V. W., Tian, T., Smedley, G., and Jocsak, J., 2004, "Low-Engine-Friction Technology for Advanced Natural-Gas Reciprocating Engines," Annual Technical Progress Report, June 1–30, DoE Cooperative Agreement No. DE-FC26-02NT41339.
[10] Tian, T., 2002, "Dynamic Behaviors of Piston Rings and their Practical Impact. Part 1: Ring Flutter and Ring Collapse and their Effects on Gas Flow and Oil Transport," Proc. Inst. Mech. Eng., IMechE Conf., **216**, pp. 209–227.
[11] Tian, T., 2002, "Dynamic Behaviors of Piston Rings and their Practical Impact. Part 2: Oil Transport, Friction and Wear of Ring/Liner Interface and the Effects of Piston and Ring Dynamics," Proc. Inst. Mech. Eng., IMechE Conf., **216**, pp. 229–247.
[12] Takiguchi, M., Machida, K., and Furuhama, S., 1988, "Piston Friction Forces of a Small High Speed Gasoline Engine," ASME J. Tribol., **110**, pp. 112–118.
[13] Yoshida, H., Kazunori, K., and Sagawa, J., 1990, "Effects of Surface Treatments on Piston Ring Friction Force and Wear" SAE Trans., **99**, pp. 1236–1245.
[14] Hamatake, T., Kitahara, T., Wakuri, Y., and Soejima, M., 1993, "Friction Characteristics of Piston Rings in a Reciprocating Engine," Lubr. Sci., **6**(1), pp. 21–40.
[15] Kim, M., Kiehne, T., and Matthews, R. D., 2005, "Friction Force Measurements Using the Instantaneous IMEP Method and Comparison With RING-PAK Simulations," ASME-ICED Fall Technical Conference, ASME Paper No. ICEF2005-1300.
[16] Heywood, J. B., 1988, *Internal Combustion Engine Fundamentals* McGraw-Hill Inc., New York.
[17] Devore, J. L., 2000, *Probability and Statistics for Engineering and The Sciences*, 5th ed., Duxbury Thomson Learning, Pacific Grove, CA.

Numerical and Experimental Analysis of the Intake Flow in a High Performance Four-Stroke Motorcycle Engine: Influence of the Two-Equation Turbulence Models

Angelo Algieri
e-mail: a.algieri@unical.it

Sergio Bova
e-mail: s.bova@unical.it

Carmine De Bartolo
e-mail: c.debartolo@unical.it

Alessandra Nigro
e-mail: anigro@unical.it

Mechanics Department,
University of Calabria,
87030 Arcavacata di Rende (CS), Italy

An experimental and numerical analysis of the intake system of a production high performance four-stroke motorcycle engine was carried out. The aim of the work was to characterize the fluid dynamic behavior of the engine during the intake phase and to evaluate the capability of the most commonly used two-equation turbulence models to reproduce the in-cylinder flow field for a very complex engine head. Pressure and mass flow rates were measured on a steady-flow rig. Furthermore, velocity measurements were obtained within the combustion chamber using laser Doppler anemometry (LDA). The experimental data were compared to the numerical results using four two-equation turbulence models (standard k-ε, realizable k-ε, Wilcox k-ω, and SST k-ω models). All the investigated turbulence models well predicted the global performances of the intake system and the mean flow structure inside the cylinder. Some differences between measurements and computations were found close to the cylinder head while an improving agreement was evident moving away from the engine head. Furthermore, the Wilcox k-ω model permitted the flow field inside the combustion chamber of the engine to be reproduced and the overall angular momentum of the flux with respect to the cylinder axis to be quantified more properly. [DOI: 10.1115/1.2719265]

Keywords: internal combustion engine, laser Doppler anemometry, computational fluid dynamics

Introduction

A fluid dynamic analysis in an internal combustion engine (ICE) is a very complex task due to the variety of phenomena that take place in the combustion chamber. This is especially true for production motorcycle engines owing to their high crankshaft rotational speed and their complex geometry. In these engines the search for high performances makes necessary a profound understanding of the intake process.

Several studies on this topic exist in the literature. Most of them are focused on global experimental and numerical investigations [1–4]. Few studies, instead, present simultaneously experimental and numerical investigation for the in-cylinder flow [5,6]. This depends on the possibility of having both a system that permits velocity measurements to be acquired and enough computational resources to analyze the flow in the whole intake system accurately.

In the last few years, a host of experimental investigations have been carried out adopting dimensionless discharge and flow coefficients with the aim to provide global information on engine head breathability [7–9], while laser Doppler anemometry (LDA) [10,11], particle image velocimetry (PIV) [12,13], and hot wire anemometry (HWA) [14,15] techniques have been used to define the flow field inside the cylinder of internal combustion engines. In particular, steady flow testing is a widely adopted procedure in the ICE research community to study the fundamentals of the intake process and to evaluate the flow capacity and the in-cylinder flow field of the actual engines, owing to its relative simplicity and the proper simulation of the real intake phase [16–20].

On the other hand, the study of the ICE by means of numerical analysis is a widespread technique due to the relevant increase in the computational power and the availability of commercial codes able to analyze flow field in complex geometries. Theoretically, all the turbulent flows can be simulated by solving the Navier-Stokes equations exactly. However, the direct numerical simulation (DNS) technique can be used only for low Reynolds number, owing to the high computational efforts to resolve the whole spectrum of turbulent scales. An alternative approach to the DNS technique is large eddy simulations (LES). In this case, large eddies are directly solved while eddies smaller than mesh sizes are modeled. Since phenomena taking place in ICE depend on these main flow structure, LES is particularly appealing for ICE applications owing to the moderate Reynolds numbers that characterize the in-cylinder flow [21,22]. Nevertheless, to capture large and intermediate scale flow structures inside the combustion chamber, a sub-millimeter mesh spacing, using a second order or higher numerical method, is required [21,23]. This corresponds to 100^3 cells at least inside the cylinder. The model turns out to be inapplicable when the analysis has to be extended to the whole intake system. For these reasons three-dimensional models for flow in ICE are based on Reynolds-averaged Navier-Stokes equations (RANS) [24–27]. In this framework all the turbulence scales are modeled, with considerable reduction in the computational effort

Submitted to ASME for publication in the JOURNAL OF ENGINEERING FOR GAS TURBINES AND POWER. Manuscript received August 21, 2006; final manuscript received January 24, 2007. Review conducted by Christopher J. Rutland.

but also in the numerical accuracy. The shortcomings of RANS models for ICE applications have been broadly discussed in the literature [28–30]. Specifically, Hanjalic [28] showed that in a reciprocating engine the second moment closure models (Reynolds stress model) with appropriate modifications have the potential to solve complex flow field better than the models based on the Boussinesq approximation. Although, for steady flow analysis Bianchi and Fontanesi [1] and Auriemma et al. [31] highlighted that the two-equation turbulence models well reproduce the in-cylinder flow with a good agreement between experimental and numerical results. These single point closure models are widely used for industrial applications with large and complex computational domain due to the high robustness and to the lower computational cost. In these cases the reluctance of users to adopt models with more differential equations (i.e., seven for the Reynolds stress model) and their numerical stiffness long remains the major deterrent [28].

The present work aims to analyze the flow field inside the intake system of a high performance production motorcycle engine and to evaluate the capability of two-equation turbulence models to reproduce properly the flow field in a very complex computational domain.

To this purpose four two-equation turbulence models were considered while pressure and mass flow rates measurements were taken on a steady-flow rig. Furthermore, LDA data were acquired inside the combustion chamber and a comparison between experimental and numerical results was proposed.

Experimental Apparatus

The experimental investigation focused on the head of a high performance four-stroke internal combustion engine. The head is part of an L-twin cylinder motorcycle engine, characterized by two valves and two spark-plugs per cylinder. Figure 1 shows the engine head while Table 1 lists its main characteristics.

The experimental analysis was carried out by means of a steady-flow rig, enabling air to be forced through the intake system of the engine head by means of a blower, while the valve lift is fixed to a selected value. The flow rig can deliver flow rates in the range 40–600 m^3/h for ambient-cylinder pressure drops up to about 10 kPa at low flow rates and 5 kPa at the highest flow rates.

In addition to global mass flow rate, the facility also enables local velocity measurements with LDA. To this purpose, optical access to the cylinder was obtained through a window perpendicular to the cylinder axis. The LDA system is a one-color system (i.e., capable of measuring one component of the velocity) in a backscattering configuration, with a Bragg cell frequency shifter.

The system uses an Argon-Ion Laser as light source (2 W on the green line, at $\lambda = 514.5$ nm) and optical fibers for both transmitting and collecting optics. The main geometrical data of the optical system are

- *beam spacing* 38 mm
- *focal length* 400 mm
- *probe volume width* 0.194 mm
- *probe volume length* 4.09 mm
- *number of fringes* 35 mm
- *fringe spacing* 5.42 μm

If a frequency shifter module is used, the number of fringes depends on other parameters, such as record length, center frequency, and band width used by the signal processor. In the case of the reported measurements, the resulting number of fringes was 48.

The movement of the LDA probe is obtained by using a micrometer *x-y* traversing system. The probe can also be rotated around its axis and moved vertically (*z* axis). A dedicated signal processor, which performs fast Fourier transform processing of the original signal in order to extract the Doppler frequency, is used for the analysis of the Doppler signal and ensures rejection of the signal produced by different particles that may be present within the measuring volume at the same time. The processor is linked to a computer in order to store and analyze the data.

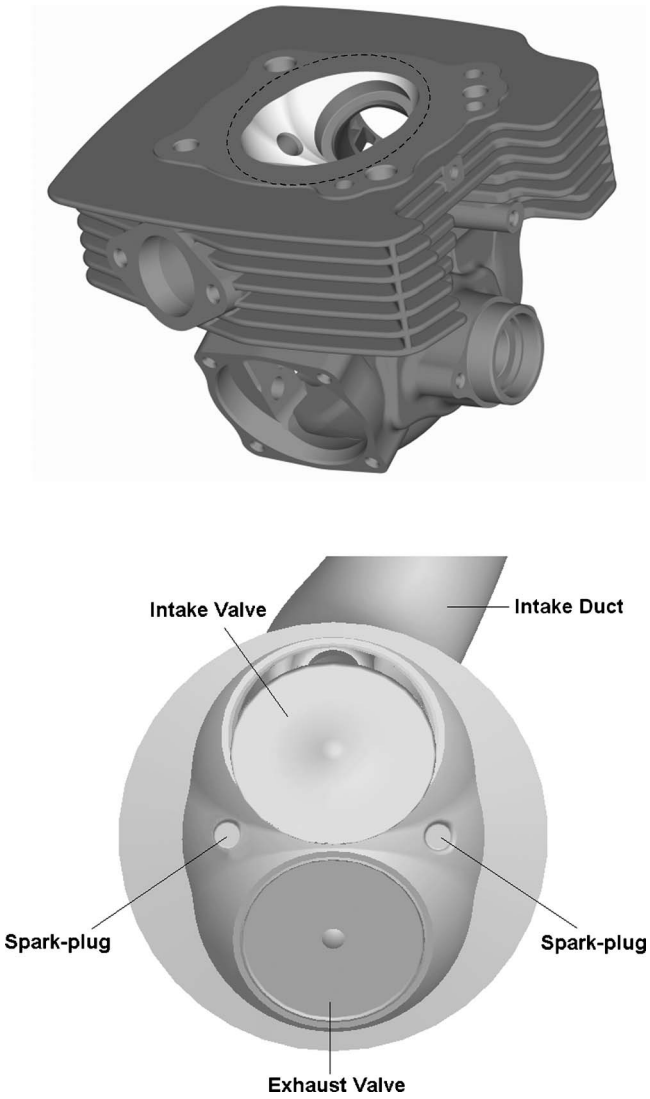

Fig. 1 Motorcycle engine

For the seeding system a fluidized bedlike scheme was employed. A fraction of the inlet air is first dried and then passed through a horizontal porous diaphragm on the top of which a layer of silica "micro-balloons" is deposited. The air stream then carries the particles and is subsequently mixed with the main intake air at the engine inlet. Figure 2 shows a scheme and a picture of the experimental setup; more details have been given in [32–34].

Table 1 Characteristics of the engine

Stroke/bore	L/B	0.761
Intake valve diameter/bore	D_v/B	0.479
Throttle diameter/bore	D_t/B	0.479
Compression ratio	r_c	10
Engine power	69.2 kW @ 8000 rpm	
Engine torque	94.2 Nm @ 6000 rpm	
Cooling system	Air cooled	

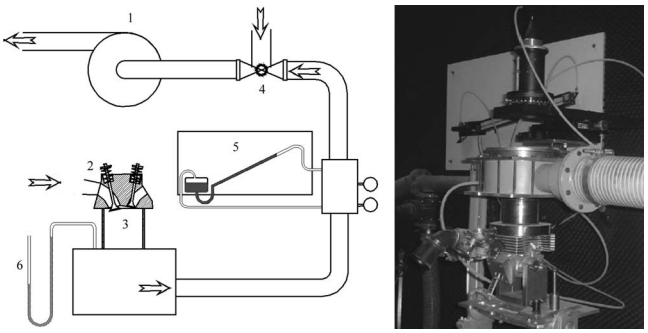

Fig. 2 Experimental setup

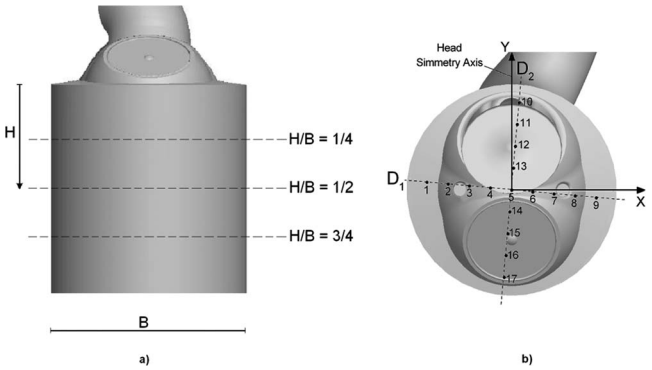

Fig. 3 LDA analysis: measurement locations

Experimental Investigation

A twofold approach was adopted to analyze experimentally the fluid dynamic behavior of the high performance four-stroke motorcycle engine during the intake phase. The engine head was examined in terms of global performances and in terms of local velocity measurements. In particular, the flow coefficient was used to define the head breathability, while the laser Doppler anemometry (LDA) technique was employed to determine the flow field inside the combustion chamber.

Flow Coefficient. The usual flow coefficient was used as global performance indicator [16,35]. It is defined as a ratio of the actual (measured) mass flow rate to reference mass flow rate:

$$C_f = \frac{\dot{m}_{meas}}{\dot{m}_r} \tag{1}$$

If p_0 and T_0 are the ambient pressure and temperature and p_C is the cylinder pressure, and the flow is subsonic, the reference mass flow rate is given by:

$$\dot{m}_r = A_{ref} \frac{p_0}{\sqrt{R \cdot T_0}} \left(\frac{p_C}{p_0}\right)^{1/\gamma} \left\{ \frac{2 \cdot \gamma}{\gamma - 1} \left[1 - \left(\frac{p_C}{p_0}\right)^{(\gamma-1)/\gamma} \right] \right\}^{1/2} \tag{2}$$

If, instead, the flow is choked, the mass flow is formalized as follows:

$$\dot{m}_r = A_{ref} \cdot \frac{p_0}{\sqrt{R \cdot T_0}} \cdot \gamma^{1/2} \left(\frac{2}{\gamma + 1}\right)^{(\gamma+1)/2 \cdot (\gamma-1)} \tag{3}$$

The reference area is the valve outer seat area:

$$A_{ref} = \frac{\pi D_v^2}{4} \tag{4}$$

where D_v is the intake valve diameter.

The ambient-cylinder pressure drop was set at $\Delta p = 7.3$ kPa. This value makes sure that the intake flow is fully turbulent and that the dimensionless flow coefficients are independent of the pressure drop for all the analyzed configurations. In fact, to this purpose the "port Reynolds number"[1] should always exceed 60,000 at low valve lifts and 90,000 at high valve lifts [16] and this requirement is fully respected in this work.

The overall uncertainty of flow coefficients was always lower than 3%, and it decreased with valve lift. In particular, for $L_v/D_v > 0.074$ the uncertainty dropped to a value that was lower than 2%.

LDA Measurements. The local characterization of the flow inside the combustion chamber was achieved by the laser Doppler anemometry (LDA) technique. The measurements were carried out fixing the valve lift ($L_v/D_v = 0.178$) and the ambient-cylinder pressure drop ($\Delta p = 7.3$ kPa). The wide-open throttle (WOT) configuration was considered. Data were collected on three measuring planes perpendicular to the cylinder axis at different distances from the engine head. Figure 3(*a*) shows the measuring planes and the relative distance from the head ($H/B = 1/4$, $H/B = 1/2$ and $H/B = 3/4$).[2]

Seventeen measuring points, distributed on two equally spaced diameters (D_1 and D_2), were defined on each measuring plane (Fig. 3(*b*)). In particular, the D_2 diameter is rotated by 5 deg clockwise with respect to the engine head symmetry axis (y axis).

At each measuring point two velocity components (along the x and y directions) were recorded. To verify the previous measurements a third component was acquired and it was compared to the value calculated from the x and y components, recording a good agreement. Three thousand samples were collected for each velocity component. The typical data rate was 0.1–0.3 kHz with 70–95% of the data valid. The relative uncertainty on the LDA measurements, which is mainly due to the setup of the electronic system, was lower than 2.2%.

Model Flow Description

Fluent is the flow solver used in the study [37]. The parallel version of the commercial code allows one to compute big meshes on several processors. The code uses structured, unstructured, and hybrid meshes.

Numerical Method. The discretization of the governing equations is based on a cell-centered finite volume method. The compressible RANS equations were solved with a steady segregated implicit solver. A second-order accuracy scheme in space for the diffusive and convective terms of the governing equations was used to reduce the numerical diffusion. Grid independence was ensured by refining the grid till no appreciable changes in the numerical solution were noticed. The convergence was checked by examining the decay in the residuals and by monitoring the variations in the mass flow rate between the inlet and the outlet sections of the computational domain as a function of the iterations. Residuals were defined as the sum of the absolute imbalance of the discrete conservation equation (d.c.e.) for a general variable, ϕ, throughout the computational cells.

The iterative calculations process was stopped when the residual values became constant for several iterations (say, 100 or more). Besides, a very low percentage variation between inlet and outlet mass flow rates was imposed.

Turbulence Modeling. To investigate the single-points closure influence on the prediction of the flow field in the intake system,

[1]The port Reynolds number is defined as the Reynolds number calculated at the intake port. More details are given in [16,36].

[2]B is the cylinder bore.

the RANS simulations were carried out by using four two-equation turbulence models.

First, the k-ε model was adopted [38]. This is the most widely used and validated turbulence model in the literature, although it does not perform properly in mixing layers and jets [39]. Second, the "realizable" version of the standard k-ε model was considered to account for the influence of these flows on the annular jet expansion in the cylinder [40]. Following Shi et al., the realizable version permits the deficiencies of the traditional k-ε model (turbulent normal stress less than zero and violation of the Schwarz inequality) to be overcome. This is obtained by adopting a new eddy-viscosity formula and a new equation for the dissipation term, ε. Furthermore, two versions of the k-ω model (namely Wilcox and SST models) were selected in order to predict free shear flows more accurately with the same accuracy in the boundary layer analysis of the k-ε models [39]. In particular, the Wilcox 1998 model represents an improvement on the original k-ω model [41] (high sensitivity to freestream boundary conditions for ω and poor predictions of some free shear flows). The SST k-ω model, instead, modifies the turbulent viscosity definition to account for the transport of the principal turbulent shear stress [42]. In addition, a blending function is adopted to ensure that the model equations behave like the Wilcox model in the near-wall area and like the k-ε standard model in the far-field zones.

Near Wall Treatment. A blended law of wall was used for the k-ε turbulence models. Specifically, the model allows one to handle fine and coarse mesh regions in the same domain by blending the laws of the wall for the laminar and turbulent layer [43]. This is very important in ICE, since the complex in-cylinder flow often does not satisfy the near-wall dimensioning of the high Reynolds approach ($y^+=40\div50$) [44]. In this way, it was possible to solve the near-wall flow for intermediate mesh zones that are too fine for the near-wall cell centroid to lie in the log-layer turbulent region but also too coarse to properly resolve the viscous sublayer.

Many near-wall first cells in the combustion chamber are in the viscous sublayer, with the possibility that $y^+=0$, owing to the flow separation. This problem was overcome by using k-ω approaches. These models, in fact, do not require special near-wall treatment and their implementation in the code is sufficiently robust so that it was possible to use them on coarse mesh zones (near-wall first cell in the log layer) [37].

Computational Domain. The computational domain coincides with the geometry of the intake system investigated at the steady flow rig. It consists of an upper volume representing the intake plenum, the intake bell mouth, the throttle plate, the intake duct, and the engine cylinder with the intake valve.

The complex geometry of the motorcycle engine did not allow the computational domain to be simplified, in order to reduce the computational effort. The mesh generator Gambit was used to create the computational grid [45].

A hybrid mesh was used for the discretization of the domain. It consists of tetrahedral and wedge cells. The tetrahedral cells were adopted for the discretization of the engine head and of the duct that contains the throttle plate. The wedge cells were used for the discretization of the remaining geometry. The total number of grid cells was about 2,500,000, with about 800,000 for the valve and the head region.

Several simulations were performed to obtain a mesh-independent solution and to define the optimum grid refinement.

Boundary Conditions. Computations were carried out for a fixed valve lift reproducing the test rig experiments ($L_v/D_v=0.178$). As for the total pressure and temperature values at the inlet section, the ambient experimental ones were used. Conversely, at the exit section, the pressure value, which resulted in a mass flow rate equal to the experimental one, was selected by means of an iterative procedure, in order to compare the numerical data with LDA velocity measurements. Furthermore, the values of the whole turbulence quantities were set to zero, as the intake air comes from the rest and no turbulence generator exists before the trumpet. Besides, the velocity components on the wall were set to zero (nonslip condition).

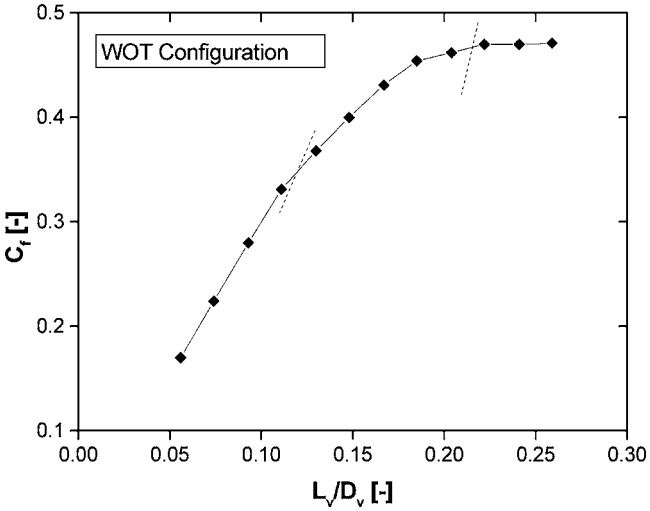

Fig. 4 Effect of the valve lift on head breathability. WOT configuration.

Results

Experimental Analysis. Figure 4 shows the fluid dynamic efficiency of the engine head in terms of flow coefficient as a function of the dimensionless valve-lift (L_v/D_v). The figure refers to the wide-open throttle (WOT) configuration. A progressive increase in the flow coefficient is observed when the valve-lift increases. This is due to an upsurge in the mass flow rate entering the combustion chamber until $L_v/D_v \leq 0.222$. A plateau is reached for $L_v/D_v > 0.222$ and there are negligible effects on the head breathability owing to the dimensions of the intake port and of the valve stem that define the minimum flow area at high valve lifts.

Figure 4 also depicts the presence of three different regions characterized by decreasing slopes in the flow coefficient curve that corresponds to different flow regimes, in line with the results found in the literature [35,46]. In particular, for low valve lift, the flow remains attached to the valve head and seat due to the high viscous phenomena. While raising the curtain area, a flow separation occurs, first of all, at the valve head and, successively, at the valve seat.

To examine the fluid dynamic behavior of the engine head in more detail and to characterize the flow field inside the combustion chamber, the laser Doppler anemometry (LDA) technique was used. Measurements were carried out by fixing the valve lift ratio at $L_v/D_v=0.178$ in the WOT configuration and by considering three measuring planes perpendicular to the cylinder axis, as illustrated in Fig. 3.

The local analysis (Fig. 5) depicts a similar flow field on the three measuring planes, with the presence of two contrarotating vortices, whose position tends to remain stable. The comparison of the LDA data highlighted that, in this engine, the global flow structure is conserved when one moves away from the engine head. On each plane, the center of the combustion chamber is characterized by the largest velocity values, while the lowest velocities are localized near to the cylinder wall (points 10 and 17) and near to the rotational axes of the two vortices (points 2-3 and 7-8).

Some differences in the flow orientation are present at points 4 and 6. Here, on the $H/B=1/4$ plane, the velocity vectors move

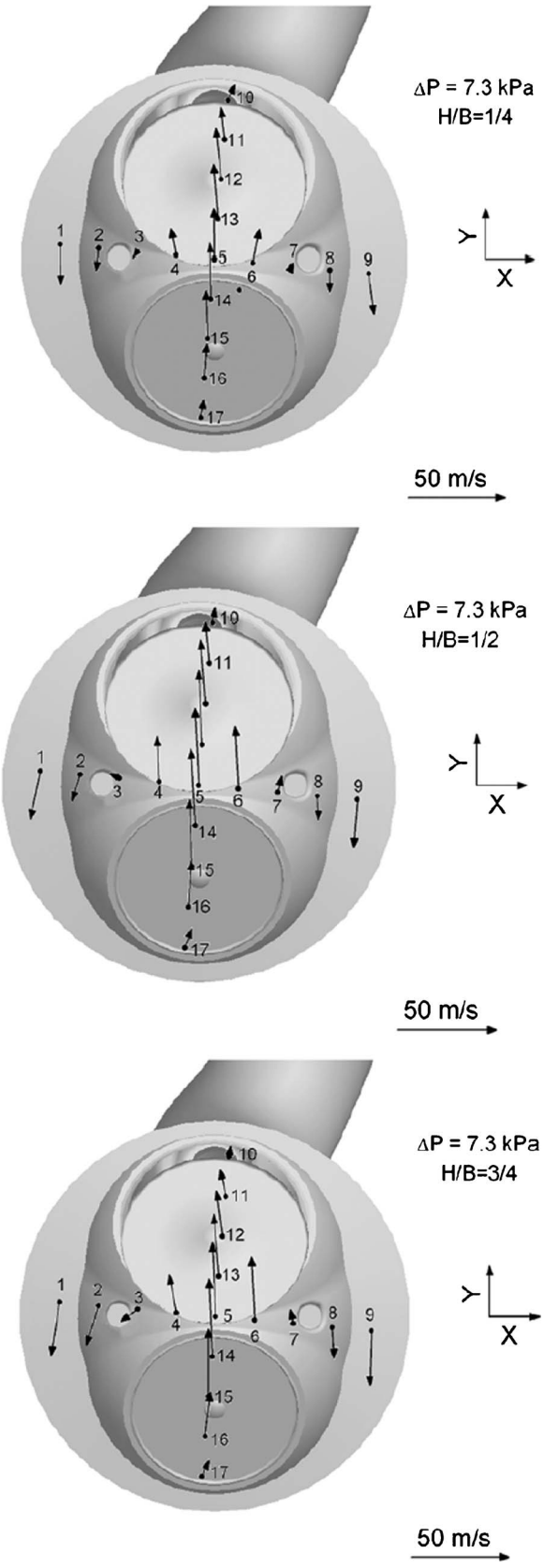

Fig. 5 Velocity measurements on the three measuring planes

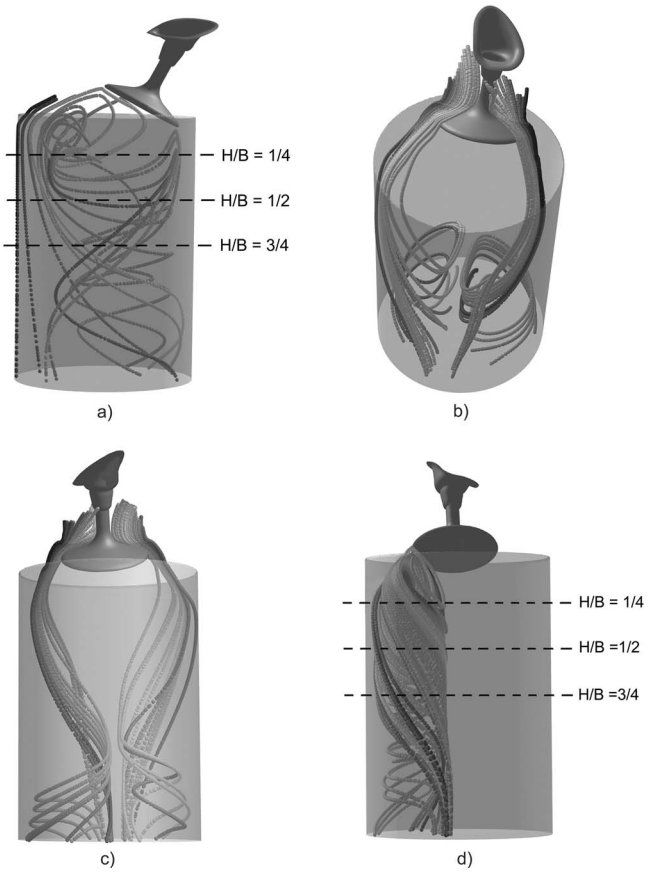

Fig. 6 Three-dimensional in-cylinder flow

away from the y direction because of the greatest interaction with the flow entering the combustion chamber, while there are negligible differences in the vectors' directions along diameter D_2. Moreover, the flow field comparison shows that the velocity values increase with the distance from the engine head as the flow becomes more organized, while the flow symmetry tends to reduce slightly moving away from the head.

Numerical Analysis. The experimental mass flow rate through the intake system was imposed to evaluate the influence of the different two-equations turbulence models on the numerical solution of the RANS equations.

The three-dimensional flow structure inside the combustion chamber is shown in Fig. 6 in terms of path lines. The high speed flow around the intake valve forms an expanding annular jet that hits the cylinder walls and flows along it toward the exit. Furthermore, the interaction between the inflow and the cylinder walls creates a wide recirculating region behind the intake valve (Fig. 6(a)) and two helicoidal contrarotating vortices (Figs. 6(b) and 6(c)). Near to the intake valve the rotation axes of the two vortices are almost perpendicular to the cylinder axis, while moving away from the engine head the flow structures rotate and their axis becomes parallel to the cylinder axis (Fig. 6(d)).

To compare the four models, Fig. 7 depicts the flow field in a vertical plane that contains the axis of the combustion chamber and the D_2 diameter. The vortices below the intake valve are always centered under the exhaust valve and their position depends on the adopted turbulence model. In particular, the k-ε model predicts the lowest distance from the wall and the largest vortex intensity.

Figure 8 shows the velocity vectors in a vertical plane containing the axis of the combustion chamber and the D_1 diameter. In this plane the symmetrical flow consists of two wider contrarotating vortices in the bulk flow region and of two smaller corner vortices close to the engine head. Also in this case, the maximum vortex intensity refers to the k-ε model, for which the dimensions of the corner vortices are smaller than the others.

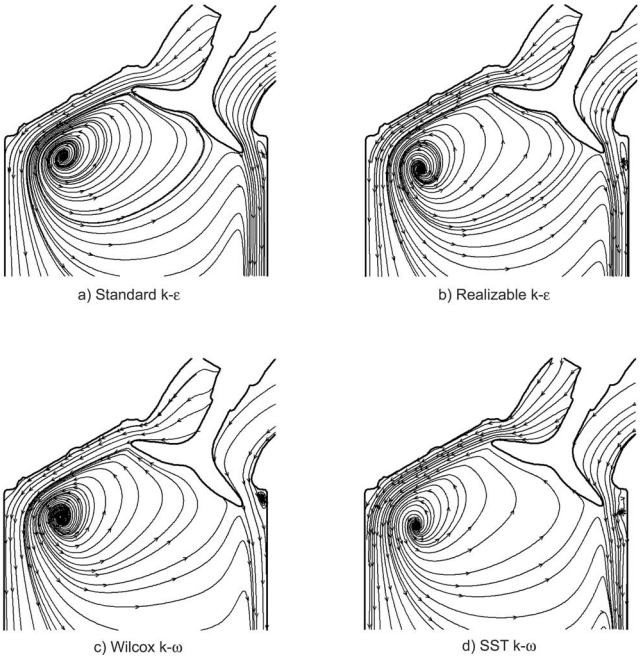

Fig. 7 Numerical in-cylinder flow field: vertical plane with D_2 diameter

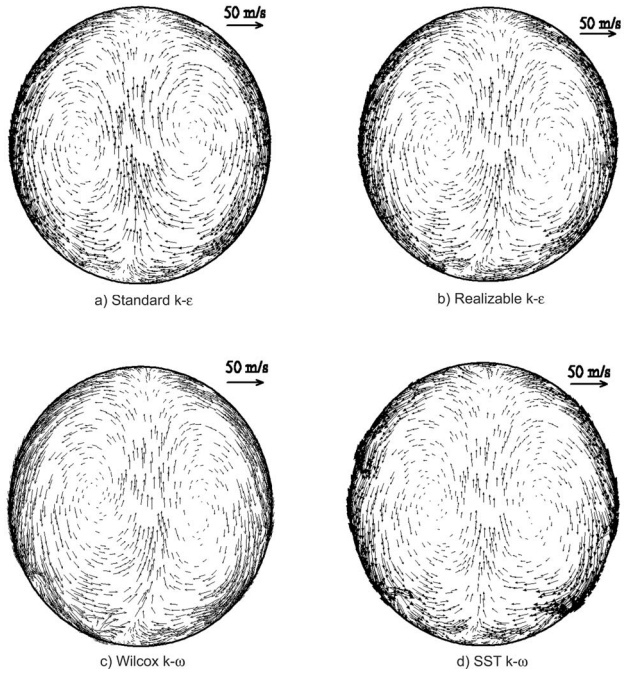

Fig. 9 Numerical in-cylinder flow field: horizontal plane $H/B = 1/4$

Figures 9–11 illustrate the vector velocity distribution on the three planes orthogonal to the cylinder axis. The velocity distribution confirms the complex structure and the presence of two large contra-rotating vortices. The two structures are centered near the D_1 diameter, but the position depends on the turbulence model. Furthermore, the figures indicate that, with exception of the k-ε model, the vortex intensity increases moving away from the engine head owing to the different inclination of the vortices on the three measuring planes (Fig. 6(*d*)).

Numerical to Experimental Comparison. The comparison between experimental and numerical results was carried out in two steps: the assessment of the turbulence models in the prediction of the outlet experimental pressure and the assessment of the

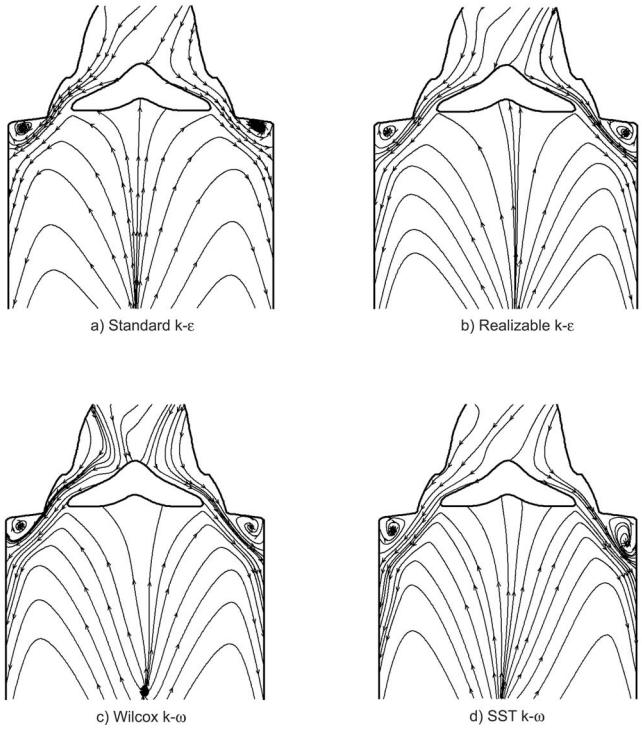

Fig. 8 Numerical in-cylinder flow field: vertical plane with D_1 diameter

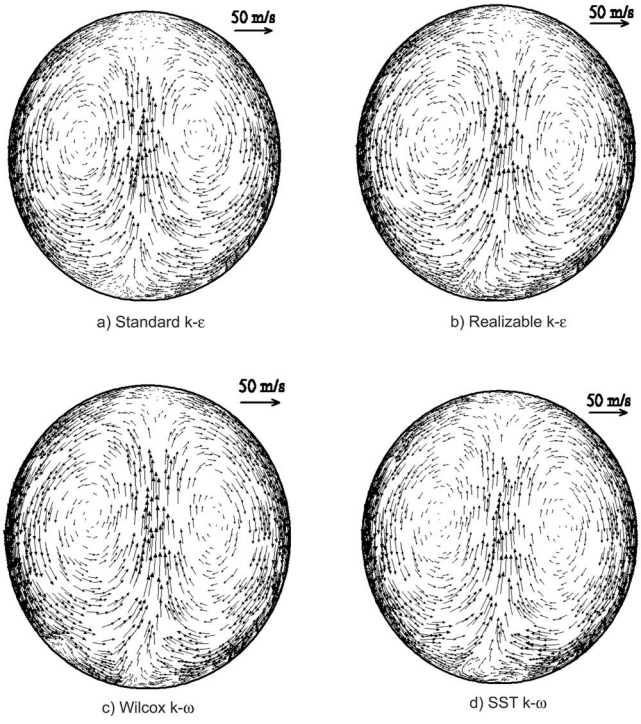

Fig. 10 Numerical in-cylinder flow field: horizontal plane $H/B = 1/2$

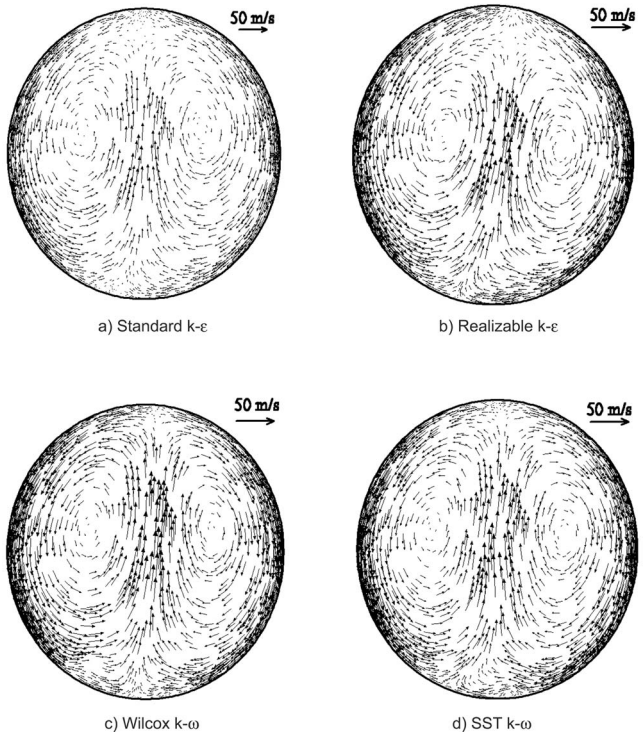

Fig. 11 Numerical in-cylinder flow field: horizontal plane *H/B*=3/4

turbulence models in the prediction of the in-cylinder flow.

Figure 12 shows a comparison of numerical and experimental static pressure values at the exit section of the cylinder, while Fig. 13 depicts the percentage errors for the four turbulence models.

The figures indicate clearly that all the turbulence models reproduce well the experimental pressure value at the exit section. In fact, the percentage difference between experimental and numerical values are always lower than 2.5%. In particular, the k-ω Wilcox turbulence model determines a noticeable error reduction in the estimate of static pressure (percentage error = 0.09%). Furthermore, the analysis shows that the SST k-ω results are very similar to the high Reynolds (standard and realizable k-ε) data: this means that the significant improvement in the error reduction does not depend on the near-wall treatment, adopted for the k-ω models, but on the characteristics of the Wilcox k-ω model in the

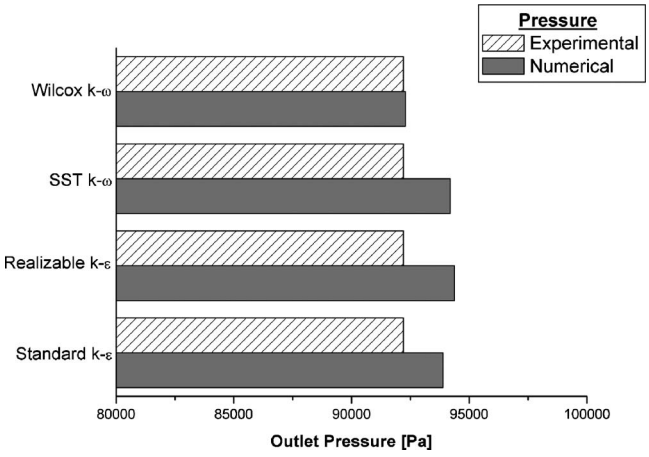

Fig. 12 Numerical and experimental static pressure at the outlet section

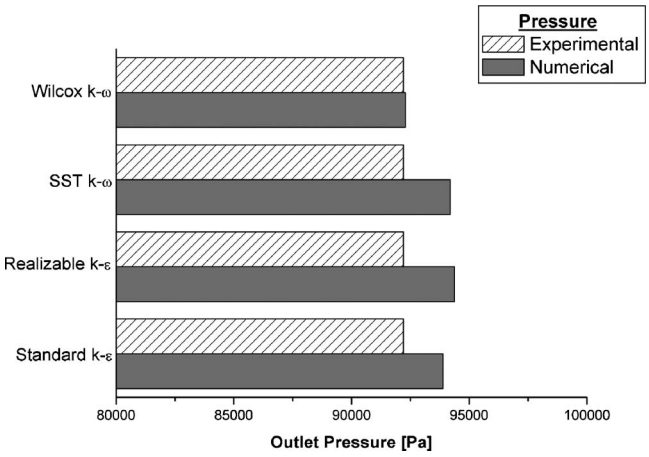

Fig. 13 Percentage error in the static pressure at the outlet section

far-field zones of the flow. In fact, the model is calibrated to provide spreading rates that are consistent with measurements for far-wakes, mixing layers, and plane, round, and radial jets [39]. This characteristic makes the Wilcox k-ω results closer to the experimental one than the k-ε family models and it reproduces the in-cylinder flow field more accurately.

Figures 14 and 15 compare LDA measurements and CFD data on the three measuring planes for the k-ε and k-ω turbulence models, respectively. Specifically, the plots refer to the projection of the mean velocity on the x-y planes. Figures indicate an overall good agreement between experimental and numerical results. The plots highlight, also, that the largest differences are localized close to the intake valve, plane $H/B=1/4$ along the D_2 direction (Figs. 14(b) and 15(b)). Here the Boussinesq eddy-viscosity approximation may fail due to the presence of nonequilibrium and three-dimensional effects below the intake valve. As a consequence, the strong curvature of the streamlines and the recirculating regions (Fig. 6(a)), localized near to the cylinder walls and valves, could not account for single-points closures correctly. As observed in Fig. 6(a), moving away from the engine head these phenomena reduce, the flow field becomes more organized, and the numerical data become significantly closer to the experimental ones (plane $H/B=1/2$ and $H/B=3/4$).

For a more detailed comparison, the k-ε turbulence models will be first considered (Fig. 14). On the $H/B=1/2$ plane along the D_1 direction, Fig. 14(c) depicts a good agreement between numerical and experimental results close to the wall $|x| \geq 10$ mm while the differences increase as the distance from the cylinder axis diminishes (-10 mm$\leq x \leq 10$ mm). On the same plane, on the contrary, a slight misalignment of the standard k-ε results with respect to LDA data was registered in this region. Some differences were registered along the D_2 direction (Fig. 14(d)). In particular, the gap between numerical and experimental results raises as the distance from the cylinder axis diminishes. Besides, near to the cylinder wall the standard k-ε data are lower than the experimental ones, $y>40$ mm. Moving away from the engine head ($H/B=3/4$), the agreement between realizable k-ε data and experimental measurements improves (Figs. 14(e) and 14(f)). As in the previous case, the largest differences can be observed along the D_2 direction. Moreover, larger differences between experimental and numerical data were found when the standard k-ε model was used.

In particular, the standard k-ε results on the $H/B=3/4$ plane (Fig. 14(e)) were very similar to the corresponding ones computed on the plane closer to the engine head ($H/B=1/2$, Fig. 14(c)) and a developed in-cylinder air motion was predicted.

As for the k-ω models (Fig. 15), the comparison between LDA

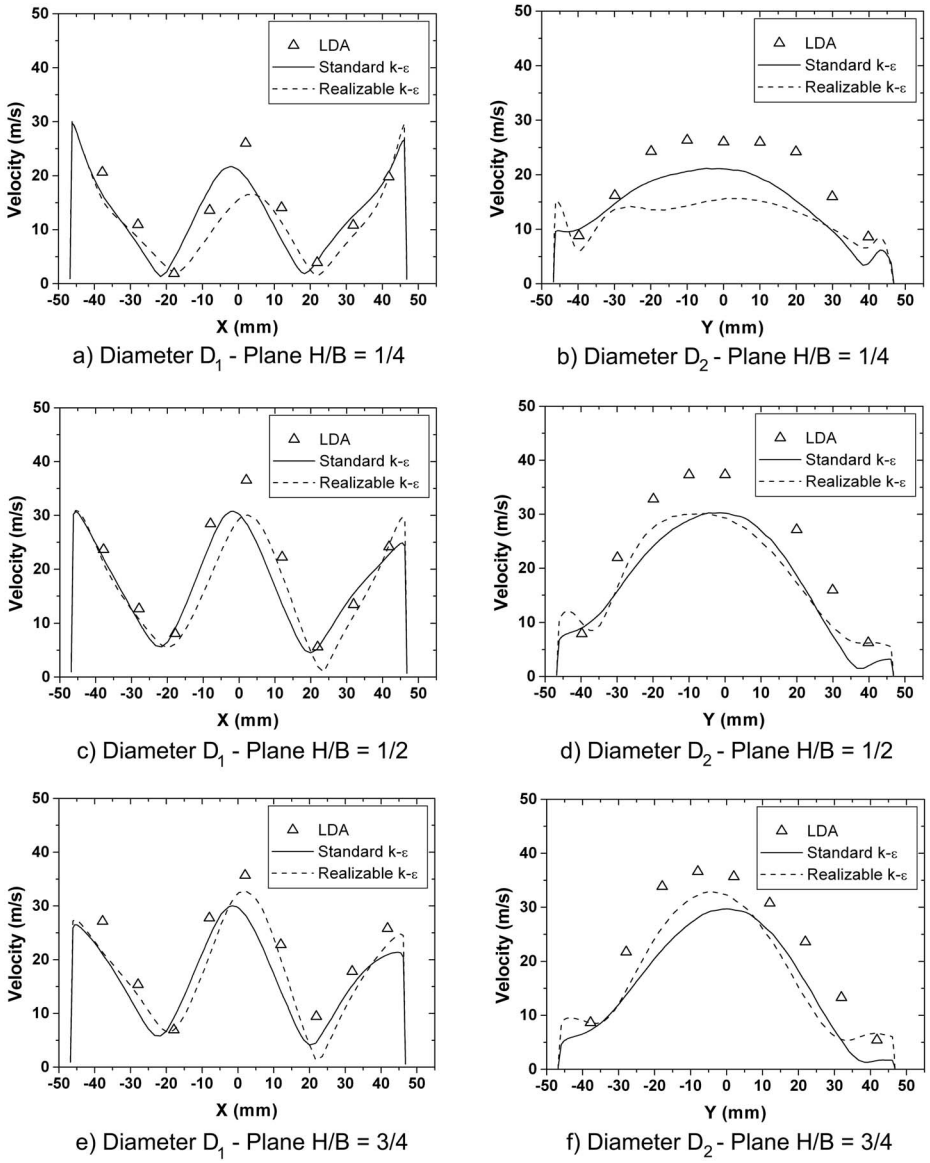

Fig. 14 ***k-ε* numerical results and LDA data comparison**

measurements and k-ω numerical results shows that in all the measuring planes the Wilcox model performs better than the other models. In particular, on the $H/B=1/2$ plane the Wilcox velocities are very close to the experimental ones for the majority of the measuring points (Figs. 15(*c*) and 15(*d*)). Some differences were registered near to the axis of the combustion chamber, nevertheless, the numerical data were perfectly aligned with respect to the LDA measurements (Fig. 15(*c*)). Larger differences are present when the SST k-ω model is used. Specifically, a wider recirculating corner vortex was computed (Fig. 7(*d*)) and a different velocity profile in the proximity of the cylinder wall ($x<-40$ mm) was evaluated. Furthermore, a slight misalignment of the SST results with respect to LDA data was observed (Fig. 15(*c*)).

Considering the $H/B=3/4$ plane, the agreement between LDA and Wilcox data is very satisfying (Figs. 15(*e*) and 15(*f*)): all the numerical data, in fact, reproduce the experimental measurements properly, while larger differences and a misalignment between experimental and numerical data is confirmed when the SST formulation is used.

Furthermore, an index was introduced to quantify the capability of the four turbulence models in reproducing the in-cylinder flow field. It was defined as:

$$\sigma = \frac{\sqrt{\sum_{i=1}^{N} (v_{LDA} - v_{CFD})_i^2}}{N} \tag{5}$$

where N is the total number of measuring points, i is the generic measuring location, v_{LDA} is the LDA velocity measurement, and v_{CFD} is the CFD velocity data.

Table 2 shows the values on the two analyzed diameters.

The previous results confirm that the Wilcox turbulence model more properly reproduces the experimental data and that the largest differences are localized on the D_2 diameter.

Finally, the CFD data were used to quantify the overall angular momentum of the flux with respect to the cylinder axis. To this purpose, the angular momentum produced by the tangential velocity v_t was combined with the axial mass flow, as [47–49]:

$$M = 2\pi \int_0^{B/2} \rho v_a v_t r^2 dr \tag{6}$$

where v_a is the axial velocity, v_t is the tangential velocity, r is the distance of the generic measuring point from the cylinder axis,

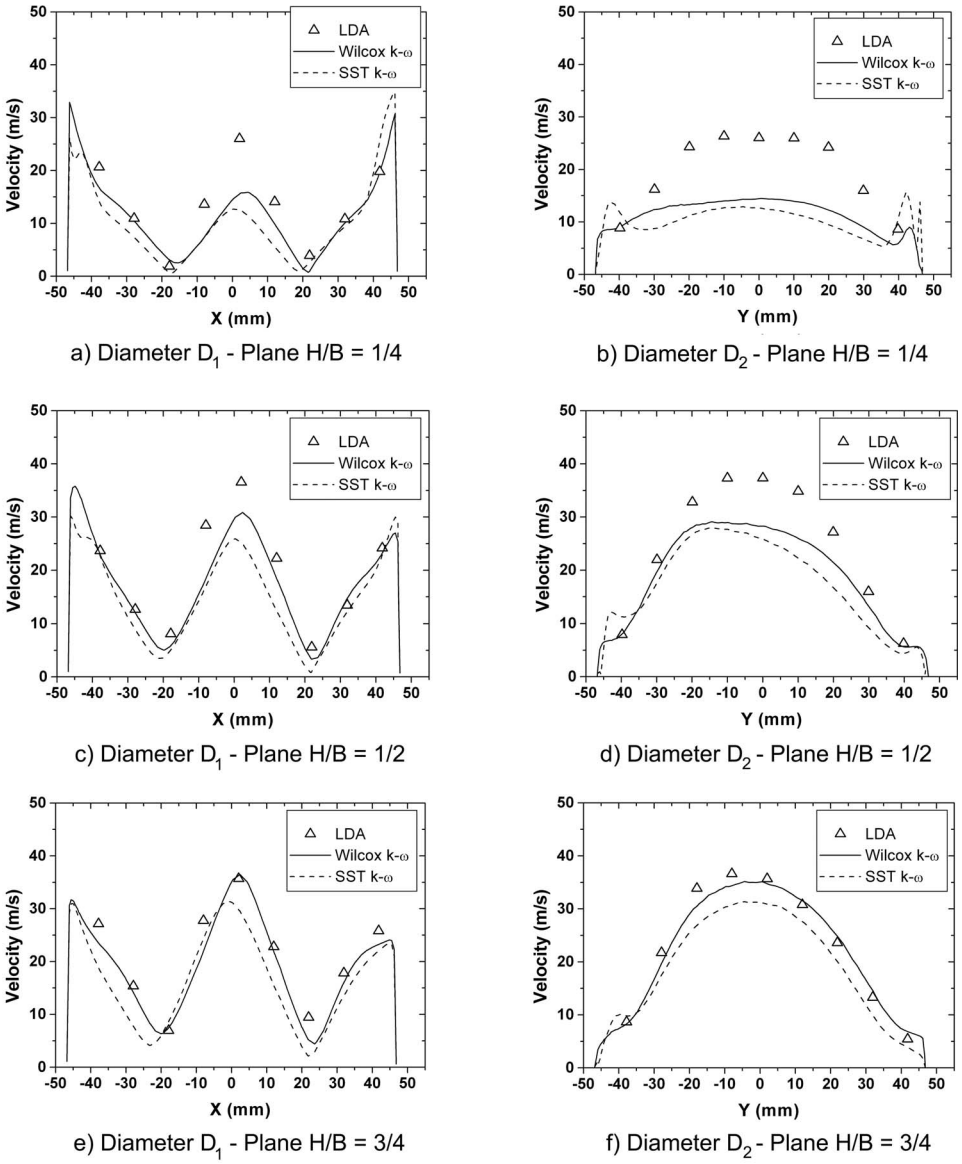

Fig. 15 ***k-ω*** **numerical results and LDA data comparison**

and ρ is the air density.

Figure 16 shows the angular momentum computed at the cylinder exit section and the value measured in a previous work using an impulse swirl meter posed at a dimensionless distance from the engine head equal to $H/B=2$ [50].

Figure 16 shows clearly that the value of the experimental angular momentum is very low and hence it is very difficult to predict accurately. In fact, the numerical angular momenta are different, nevertheless the flow fields on the planes perpendicular to the cylinder axis are very similar. The analysis depicted that the Wilcox k-ω data are in a better agreement with the experimental value than the others turbulence models.

Table 2 Sigma index values for the four turbulence models

	σ (m/s)			
Diameter	Standard k-ε	Realizable k-ε	Wilcox k-ω	SST k-ω
D_1	1.51	1.49	1.31	2.13
D_2	2.21	2.41	1.86	2.62

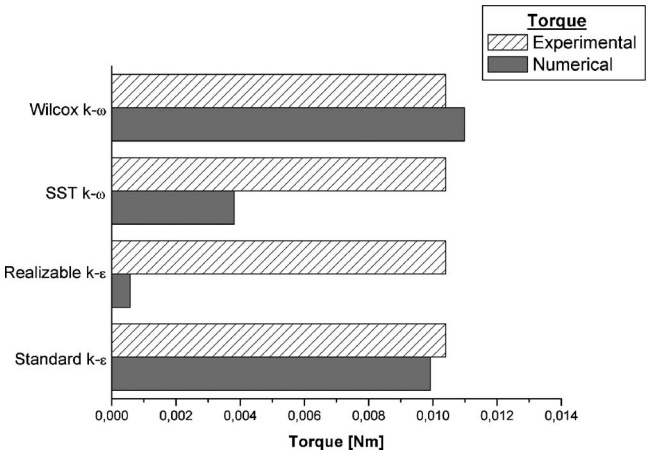

Fig. 16 Numerical and experimental torque at the outlet section

Conclusions

The fluid dynamic behavior of a high performance four-stroke motorcycle engine was examined by means of a numerical and an experimental analysis.

The experimental investigation was carried out on a steady flow rig. The global engine head breathability was characterized in terms of flow coefficient, while the LDA technique was used to define the flow field inside the combustion chamber.

The measurements were compared to the corresponding numerical results obtained by solving RANS equations for the most used two-equation turbulence models with the objective to evaluate the accuracy of the different turbulence models in defining the in-cylinder flow.

The numerical data and the experimental measurements presented a good agreement. In fact, all the turbulence models well reproduced the experimental pressure value at the exit section when the mass flow rate was imposed. The percentage differences were always lower than 2.50%, with a value lower than 0.10% obtained with the Wilcox k-ω turbulence model.

Furthermore, all the turbulence models characterized well the mean flow structure and the presence of two contrarotating vortices. Specifically, the analysis depicted that the two adopted near-wall treatments well reproduces the flow field near to the cylinder wall. Non-negligible differences between measurements and computations were found close to the cylinder head, probably due to the high complexity of the flow at the low valve lift, while an improving agreement was evident moving away from the engine head.

The comparison between the four turbulence models showed that standard k-ε model presents the largest numerical diffusivity with the flow that develops closer to the engine head, whereas the other models show an increasing vortex intensity with the distance from the head.

Furthermore, the comparison with the LDA measurements put in evidence that the Wilcox k-ω model permits the flow field inside the combustion chamber of the engine to be reproduced more properly and to quantify the overall angular momentum of the flux with respect to the cylinder axis accurately.

Acknowledgment

The authors would like to thank the Ducati Motor Ltd. for the provision of the engine components and for the technical information.

Nomenclature

A_{ref} = reference area
B = cylinder bore
C_{abs} = absolute flow coefficient
C_f = flow coefficient
C_s = swirl coefficient
D_i = ith-measuring diameter
D_v = valve diameter
D_t = throttle diameter
H = distance of the measuring plane from the head
L = stroke
L_v = valve lift
M = overall angular momentum of the flux
N = total number of measuring points
T_0 = ambient temperature
a_0 = sound speed
i = generic measuring location
k = turbulent kinetic energy
$\dot{m}$ = mass flow rate
$\dot{m}_{meas}$ = measured mass flow rate
$\dot{m}_r$ = reference mass flow rate
p_0 = ambient pressure
p_C = cylinder pressure
r = distance of the generic measuring point from the cylinder axis
r_c = compression ratio
v_a = axial velocity
v_{CFD} = CFD velocity data
v_{LDA} = LDA velocity measurement
v_t = tangential velocity
y^+ = dimensionless cell centroid-wall distance
Δp = ambient-cylinder pressure drop
ε = dissipation term
ϕ = generic variable
γ = adiabatic index
λ = wavelength of the laser beam
ρ = air density
σ = LDA-CFD agreement index
ω = turbulent specific dissipation rate
CFD = computational fluid dynamics
DNS = direct numerical simulation
HWA = hot wire anemometry
ICE = internal combustion engine
LDA = laser Doppler anemometry
LES = large eddy simulation
PIV = particle image velocimetry
RANS = Reynolds averaged Navier-Stokes
SST = shear stress transport
WOT = wide open throttle
d.c.e. = discrete conservation equation

References

[1] Bianchi, G. M., and Fontanesi, S., 2003, "On the Applications of Low-Reynolds Cubic k-ε Turbulence Models in 3D Simulations of ICE Intake Flows," SAE Paper No. 2003-01-0003.

[2] Deshmukh, D., Kumar, R., Garg, M., Nayeem, M. J., and Lakshminarasimhan, V., 2004, "Optimisation of Gas Exchange Process on a Single Cylinder Small 4-Stroke Engine by Intake and Exhaust Tuning: Experimentation and Simulation," SAE Paper No. 2004-32-0007.

[3] Blair, G. P., Mackey, D. O., and Ashle, M. C., 2002, "Exhaust Tuning on a Four-Stroke Engine; Experimentation and Simulation," SAE Paper No. 2001-01-1797.

[4] Blair, G. P., Callender, E., and Mackey, D. O., 2002, "Maps of Discharge Coefficients for Valves, Ports and Throttles," SAE Paper No. 2001-01-1798.

[5] Nonaka, Y., Horikawa, A., Nonaka, Yo., Hirokawa, M., and Noda, T., 2004, "Gas Flow Simulation and Visualization in Cylinder of Motorcycle Engine," SAE Paper No. 2004-32-0004.

[6] Hong, C.-W., and Tarng, S.-D., 2001, "In-Cylinder Tumble Flow Field Measurements and Predictions," ASME J. Eng. Gas Turbines Power, **123**(1), pp. 139–145.

[7] Blair, G. P., McBurney, D., McDonald, P., McKernan, P., and Fleck, R., 1998, "Some Fundamental Aspects of the Discharge Coefficients of Cylinder Porting and Ducting Restrictions," SAE Paper No. 980764.

[8] Bohac, S. V., and Landfahrer, K., 1999, "Effects of Pulsating Flow on Exhaust Port Flow Coefficients," SAE Paper No. 1999-01-0214.

[9] Blair, G. P., and Drouin, F. M. M., 1996, "Relationship Between Discharge Coefficients and Accuracy of Engine Simulation," SAE Paper No. 962527.

[10] Chan, V. S. S., and Turner, J. T., 2000, "Velocity Measurement Inside a Motored Internal Combustion Engine Using Three-Component Laser Doppler Anemometry," Opt. Laser Technol., **32**, pp. 557–566.

[11] Payri, F., Desantes, M., and Pastor, J. V., 1996, "LDV Measurements of the Flow Inside the Combustion Chamber of a 4-Valve D.I. Diesel Engine With Axisymmetric Piston-Bowls," Exp. Fluids, **22**, pp. 118–128.

[12] Choi, W-C., and Guezennec, Y. G., 1999, "Study of the Flow Field Development During the Intake Stroke in an IC Engine Using 2-D PIV and 3-D PTV," SAE Paper No. 1999-01-0957.

[13] Bevan, K. E., and Ghandhi, J. B., 2004, "PIV Measurements of In-Cylinder Flow in a Four-Stroke Utility Engine and Correlation With Steady Flow Results," SAE Paper No. 2004-32-0005.

[14] Zhijun, W., and Zhen, H., 2001, "In-Cylinder Swirl Formation Process In Four-Valve Diesel Engine," Exp. Fluids, **31**, pp. 467–473.

[15] El Tahry, S. H., Khalighi, B., and Kuziak, W. R. J., 1987, "Unsteady-Flow Velocity Measurements Around an Intake Valve of a Reciprocating Engine," SAE Paper No. 870593.

[16] Xu, H., 2001, "Some Critical Technical Issues on the Steady Flow Testing of Cylinder Heads," SAE Paper No. 2001-01-13.

[17] Ohm, I. Y., and Cho, Y. S., 2000, "Mechanism of Axial Stratification and Its Effect in an SI Engine," SAE Paper No. 2000-01-2843.

[18] Kang, K. Y., and Reitz, R. D., 2000, "Intake Flow Structure and Swirl Generation in a Four-Valve Heavy-Duty Diesel Engine," ASME J. Eng. Gas Turbines Power, **122**(4), pp. 570–578.

[19] Stier, B., and Koochesfahani, M. M., 1999, "Molecular Tagging Velocimetry (MTV) Measurements in Gas Phase Flows," Exp. Fluids, **26**, pp. 297–304.
[20] Hascher, H. G., Novak, M., Lee, K., Schock, H. J., Rezaei, H., and Koochesfahani, M., 1998, "An Evaluation of IC-Engine Flows With the Use of Modern In-Cylinder Measuring Techniques," *Proc. 34th AIAA/ASME/SAE/ASEE Joint Propulsion Conference and Exhibit*, July 13–15.
[21] Haworth, D. C., and Jansen, K., 2000, "Large-Eddy Simulation on Unstructured Deforming Meshes: Towards Reciprocating IC Engines," Comput. Fluids, **29**(5), pp. 493–524.
[22] Haworth, D. C., 1999, "Large-Eddy Simulation of In-Cylinder Flows," Oil Gas Sci. Technol., **54**(2), pp. 175–185.
[23] Haworth, D. C., El Tahry, S. H., and Huebler, M. S., 1993, "A Global Approach to Error Estimation and Physical Diagnostics in Multidimensional Computational Fluid Dynamics," Int. J. Numer. Methods Fluids, **17**, pp. 75–97.
[24] Amsden, A. A., O' Rourke, P. J., and Butler, T. D., 1989, "KIVA-II: A Computer Program for Chemically Reactive Flows With Sprays," Los Alamos National Laboratory Report No. LA-11560-MS.
[25] Baratta, M., Catania, A. E., Spessa, E., and Liu, R. L., 2005, "Multidimensional Predictions of In-Cylinder Turbulent Flows: Contribution to the Assessment of k-ε Turbulence Model Variants for Bowl-in-Piston Engines," ASME J. Eng. Gas Turbines Power, **127**(4), pp. 883–896.
[26] Bianchi, G. M., Cantore, G., Parmeggiani, P., and Michelassi, V., 2002, "On Application of Nonlinear k-ε Models for Internal Combustion Engine Flows," ASME J. Eng. Gas Turbines Power, **124**(3), pp. 668–677.
[27] Khalighi, B., El Tahry, S. H., Haworth, D. C., and Huebler, M. S., 1995, "Computation and Measurement of Flow and Combustion in a Four-Valve Engine With Intake Variations," SAE Paper No. 950287.
[28] Hanjalic, K., 2005, "Will RANS Survive LES? A View of Perspectives," ASME J. Fluids Eng., **127**, pp. 831–839.
[29] El Tahry, S. H., and Haworth, D. C., 1992, "Directions in Turbulence Modeling for In-Cylinder Flows in Reciprocating IC Engines," J. Propul. Power, **8**, pp. 1040–1048.
[30] El Tahry, S. H., and Haworth, D. C., 1996, "A Perspective on the State-of-the-Art in IC Engine Combustion Modeling," *Proc. SIAM Sixth International Conference on Combustion*, New Orleans, LA, March 4-6.
[31] Auriemma, M., Caputo, G., Corcione, F. E., and Valentino, G., 2003, "Fluid-Dynamic Analysis of the Intake System for a HDDI Diesel Engine by Star-CD Code and LDA Technique," SAE Paper No. 2003-01-0002.
[32] Algieri, A., Bova, S., and De Bartolo, C., 2005, "Experimental and Numerical Investigation on the Effects of the Seeding Properties on LDA Measurements," ASME J. Fluids Eng., **127**(3), pp. 514–522.
[33] Amelio, M., Bova, S., and De Bartolo, C., 2000, "The Separation Between Turbulence and Mean Flow in ICE LDV Data: The Complementary Point-of-View of Different Investigation Tools," ASME J. Eng. Gas Turbines Power, **122**(4), pp. 579–587.
[34] Algieri, A., and Bova, S., 2004, "Influence of Valve-Wall Distance on the Intake Flow in High Performance I.C.E.," SAE paper 2004-01-1922, and in Direct Fuel Injection, Engine Diagnostics, and New Developments in Powertrain Tribology, CVT, ATF & Fuel Economy, SAE Special Publication SP-1891.
[35] Heywood, J. B., 1998, *Internal Combustion Engine Fundamentals*, Mc Graw Hill, New York.
[36] Algieri, A., Amelio, M., and Bova, S., 2001, "Global and LDA Steady Flow Measurements in Two High-Performance I.C.E. Head Configurations," SAE-NA Paper No. 2001-01-20, Proc. 5th International Conference on Internal Combustion Engines - ICE2001.
[37] FLUENT v. 6.2.16, 2005, Fluent Inc., Lebanon, NH.
[38] Launder, B. E., and Spalding, D. B., 1972, *Lectures in Mathematical Models of Turbulence*, Academic, London.
[39] Wilcox, D. C., 1998, *Turbulence Modeling for CFD*, DCW Industries, Inc., La Canada, CA.
[40] Shih, T.-H., Liou, W. W., Shabbir, A., Yang, Z., and Zhu, J., 1995, "A New k-ε Eddy-Viscosity Model for High Reynolds Number Turbulent Flows—Model Development and Validation," Comput. Fluids, **24**(3), pp. 227–238.
[41] Saffman, P. G., 1970, "A Model for Inhomogeneous Turbulent Flow," Proc. R. Soc. London, **A317**(1530), pp. 417–433.
[42] Menter, F. R., 1994, "Two-Equation Eddy-Viscosity Turbulence Models for Engineering Applications," AIAA J., **32**(8), pp. 1598–1605.
[43] Kader, B., 1981, "Temperature and Concentration Profiles in Fully Turbulent Boundary Layers," Int. J. Heat Mass Transfer, **24**(9), pp. 1541–1544.
[44] Pattijn, S., 1999, "Niet lineaire, laag-Reynolds, twee-vergelijkingen turbuleti-emodellen," Ph.D. thesis, Universitet Gent, Gent.
[45] GAMBIT v. 2.2.30, 2005, Fluent Inc., Lebanon, NH.
[46] Weclas, M., Melling, A., and Durst, F., 1995, "Unsteady Intake Valve Gap Flow," SAE Paper No. 952477.
[47] Zhijun, W., and Zhen, H., 2001, "In-Cylinder Swirl Formation Process In Four-Valve Diesel Engine," Exp. Fluids, **31**, pp. 467–473.
[48] Algieri, A., Bova, S., and De Bartolo, C., 2006, "Influence of Valve Lift and Throttle Angle on Intake Flow in a High-Performance Four-Stroke Motorcycle Engine," ASME J. Eng. Gas Turbines Power, **128**(4), pp. 934–941.
[49] Crnojevic, C., Decool, F., and Florent, P., 1999, "Swirl Measurements in a Motored Cylinder," Exp. Fluids, **26**, pp. 542–548.
[50] Carrera, M. A., 2004, "Caratterizzazione fluidodinamica di teste di MCI ad elevate prestazioni," thesis (in Italian), Mechanics Department, University of Calabria, Cosenza, Italy.

The Maximum Power Operating Point for a Combustion-Driven Thermoelectric Converter With Heat Recirculation

Richard B. Peterson
Department of Mechanical Engineering,
204 Rogers Hall,
Oregon State University,
Corvallis, OR 97331
e-mail: richard.peterson@oregonstate.edu

A model is developed for determining the ideal operating point, based on maximum power output, for a thermoelectric conversion (TEC) element coupled to a combustor. In the analysis, heat recirculation from the combustor exhaust is included. Results presented here are relevant to the operating characteristics of small, combustion-driven energy systems. The model is composed of a TEC element, a combustor, a counterflow heat exchanger, and a thermal shunt resistance to the surroundings. Including the shunt is necessary due to the increased importance of this effect in small-scale thermal systems. From this combination of components, an optimal combustor operating temperature is found giving maximum power output and efficiency. The model is used to determine ideal performance figures as a function of system parameters such as the effectiveness of heat regeneration, loss of heat by conduction, and the parameters describing the thermoelectric conversion element (the so-called ZT parameter). Although a high degree of idealization is employed, the results show the importance of heat recirculation and the significance of thermal losses on system operation. [DOI: 10.1115/1.2747261]

Keywords: thermoelectric conversion, TEC, combustion, micro engine

Introduction

Future power-intensive applications in the mesoscale size regime (characteristic sizes from 1 mm to 10 cm) will require an energy source with higher performance than electrochemical batteries [1–4]. Whether the area of interest is powering handheld, multifunction electronic devices, remote unattended sensors, or for miniature autonomous vehicles for ground, air, and marine operation, both energy density and power density considerations will strain the capabilities of even the most advanced battery technology. Exploring the alternatives, liquid fuels appear to be a source rich in energy density and with potential for high power output when burned in micro engines. However, current micro engine development is challenging in the size class of 100 W and smaller. In this small-scale power regime, engine performance is poor due to heat loss to the surroundings, incomplete combustion, frictional effects, pressure drops through small passages, and problematic mechanical design outside the traditional operating parameters of current engineering practice [4]. Nevertheless, the attractive dual features of *potential* high power and energy densities continue to motivate researchers to find ways of making practical small engine operation below the 100 W level. Solid state heat engines such as those based on thermoelectric conversion (TEC) would relieve some of the complexity associated with micro engine development. Several past projects have developed small-scale systems for study [5–8]. A combustion-driven TEC would operate with acceptable efficiency if its primary descriptive parameter, that is the ZT factor, were higher than about 3 (currently not attainable). For small-scale operation, the combustion chamber could be operated continuously and with a catalyst to ensure near complete combustion. Aside from major practical aspects such as balance-of-plant componentry, the basic thermodynamics of combustion-driven TEC is of practical interest. This work presents a model for such a system operating at the point of maximum power output.

There have been many finite rate, finite time analyses of thermoelectric conversion (e.g., see [9–13] for a sampling). The majority rely on the basic configuration of a high temperature reservoir supplying heat to the conversion element through a thermal resistance. Heat rejected from the TEC can also pass through a thermal resistance to a low temperature reservoir. Within this class of problem, many variations have been studied where the heat transfer expressions take different forms, where the operating point is either at maximum power or maximum efficiency, and whether the TEC configuration is single element or multielement. Less common is an analysis of combustion powered TEC where a reactant mixture is supplied to a combustor which in turn supplies heat to the converter [14,15]. In this past work, a novel TEC configuration was examined having distributed disk-type elements integrated into the heat recovery process. Reference was also made to an "idealized" configuration where the TEC elements were exposed to a single high temperature source at the hot end of the heat exchanger. However, this past work does not employ the thermodynamic operating point (maximum power output) and does not parameterize the problem with the TEC figure-of-merit, the heat exchanger effectiveness, or other quantities important to the problem. Recently, a model has been presented [16,17] that has a combustor operating at a specified temperature (determined by the maximum power point) where thermal energy recovery from the exhaust is used to heat the incoming reactants by way of a counterflow heat exchanger. The combustor supplies heat to a Carnot engine for generating work. Depending on the effectiveness of the heat exchanger, and the operating temperature of the combustor, a *fundamental* expression can be developed for the conversion of heat-to-work in the simple Carnot-based model. The study presented here addresses the case of a TEC element coupled to a combustor. The salient features in this analysis are: (1) finding a combustor temperature giving maximum power; (2) determining efficiency for the conversion process; and (3) a parameterization of the problem.

Submitted to ASME for publication in the JOURNAL OF ENGINEERING FOR GAS TURBINES AND POWER. Manuscript received June 26, 2006; final manuscript received April 11, 2007. Review conducted by Kenneth Mark Bryden.

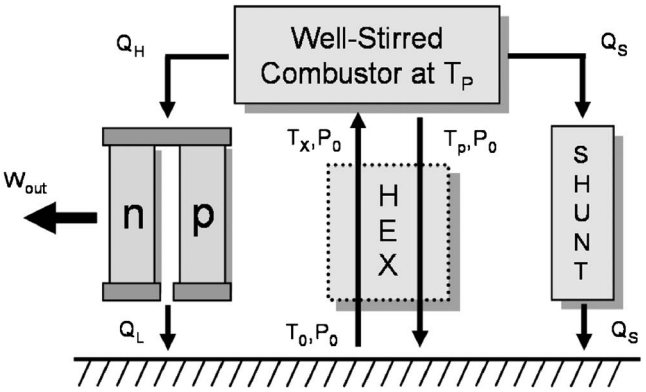

Fig. 1 System model diagram of the TEC element combined with the combustor having heat recirculation and a thermal shunt. Combustor operates as a well-stirred system with a temperature of T_p.

One cannot discuss the performance of small-scale thermal systems without examining thermal losses to the surroundings through so-called shunt effects or through insulation. Although the development here is meant to show the effects of combustor temperature on the TEC process, and to show an optimal temperature exists, the present model is also capable of assessing the conduction losses associated with small-scale energy systems. This will be a critical issue to resolve in the development of combustion driven micro engines. Our past work in related areas [18–20] has examined the effects of heat loss on reversible engines, cryocoolers, and counterflow heat exchangers (HEX). Scaling studies of these technologically useful devices have provided information on performance degradation upon a reduction in size. In addition, estimates have been obtained for ultimate size limitations (based on thermal losses) on the general type of device that relies on a temperature difference for operation. This development, in part, continues this work in the area of combustion-driven heat engines. Although many other factors will impact system efficiency in a miniaturized engine/combustion system such as pressure losses, friction, and incomplete combustion, assessing thermal losses from a small-scale device will be central for determining overall performance.

Model Development

The TEC/combustor model is shown in Fig. 1. The basic arrangement is a well-stirred combustor operating at a temperature of T_p. The reactants enter the overall system at T_0 and P_0. The counterflow heat exchanger (HEX) increases the temperature of the reactants by transferring thermal energy from the products. Heat at T_p is supplied to the TEC element while a shunt loss allows a portion of the combustor heat to escape to the surroundings. The combustor temperature, T_p, also sets the exhaust temperature of the well-stirred combustor. Thus the products enter the HEX at T_p and cool to some lower temperature dictated by the effectiveness of the thermal energy transfer. The adiabatic flame temperature (with reference to T_0) is used as a measure of the heating value supplied to the combustor. This model is similar to that presented earlier [17] where now the Carnot engine has been replaced by a TEC element.

The model shown in Fig. 1 would most likely operate at its maximum power point. This system characteristic is demonstrated as follows by examining the two operating extremes assuming the HEX has an effectiveness of zero. If the combustor operates such that T_p approaches the adiabatic flame temperature, or T_{af}, then very little thermal energy is transferred to the TEC element because the combustion products carry away most of the heating value of the fuel. Hence, the work output from the overall system is small even though the TEC element operates at high temperature with relatively high efficiency. However, if nearly all of the heating value is directed toward the conversion element, T_p approaches T_0 resulting in very low output efficiency. Between these two extremes is an optimal T_p yielding the maximum output possible for the process. It is termed the maximum power point and requires the condition, $\partial \dot{W}/\partial T_p = 0$, to be satisfied. If the HEX is now incorporated into the analysis, superadiabatic conditions can potentially be reached, but the thermal recovery afforded by the HEX does not change the character of the problem.

The analysis presented here idealizes all of the processes associated with the thermodynamics, heat transfer, TEC operation, and loss mechanisms. Furthermore, pressure drops are ignored and property variations due to temperature and/or compositional changes are assumed negligible. The reactants enter the HEX at T_0 and P_0. They emerge at a temperature T_x which is governed by the effectiveness

$$\varepsilon = \frac{T_x - T_0}{T_p - T_0} \tag{1}$$

A thermal shunt resistance is included for modeling thermal losses to the surroundings. This heat loss mechanism could be associated with the heat exchanger, or the necessary structural support connecting the hot sections of the device to the ambient temperature sections, or both mechanisms could be present. In any case, the flow of heat through the thermal shunt can be modeled as

$$\dot{Q}_S = (kA/L)(T_p - T_0) \tag{2}$$

where k is an effective thermal conductivity, A is a representative cross-sectional area for heat flow, and L is a characteristic length for the heat flow path. Noting that the heating rate of the reactant mixture entering the combustor can be expressed as $\dot{H}_p(T_{\text{af}}, P_0) - \dot{H}_p(T_0, P_0)$, rewriting this form using an average specific heat and mass flow rate yields,

$$\dot{HV} = \dot{m}\bar{c}_p(T_{\text{af}} - T_0) \tag{3}$$

where $\dot{m}$ and $\bar{c}_p$ are the product mass flow rate and specific heat, respectively, and T_{af} is the adiabatic flame temperature. This is a rather strong idealization for describing the heating value (in rate form). It does not explicitly take into account dissociation effects, product mixture composition, variations in $\bar{c}_p$ over the stated temperature range, and incomplete combustion. Equation (3), however, is meant to provide an idealized measure of the rate of heating by way of the adiabatic flame temperature in order to arrive at an analytical solution to the problem. With this qualification, writing an energy balance for the combustor of Fig. 1, the total heating rate available to both the TEC element and the thermal shunt becomes (after simplification)

$$\dot{Q}_{\text{tot}} = \dot{m}\bar{c}_p(T_{\text{af}} - T_0) + \dot{m}\bar{c}_p T_x - \dot{m}\bar{c}_p T_p \tag{4}$$

where upon using the definition for effectiveness, Eq. (4) can be rewritten as

$$\dot{Q}_{\text{tot}} = \dot{m}\bar{c}_p(T_{\text{af}} - T_p) + \dot{m}\bar{c}_p\varepsilon(T_p - T_0) \tag{5}$$

Now observe that the flow of heat to the TEC element is $\dot{Q}_H = \dot{Q}_{\text{tot}} - \dot{Q}_S$ where $\dot{Q}_S$ is given by Eq. (2), thus

$$\dot{Q}_H = \dot{m}\bar{c}_p(T_{\text{af}} - T_p) + \dot{m}\bar{c}_p\varepsilon(T_p - T_0) - \frac{kA}{L}(T_p - T_0) \tag{6}$$

At this juncture, the conversion efficiency of the TEC element can be introduced. Two choices can be considered for this analysis: efficiency can be based upon the element operating at its maximum power point, or its maximum efficiency point [21,22]. The two conditions yield operating efficiencies that are quantitatively very similar. For a geometrically optimized converter operating at its maximum efficiency,

$$\eta_{\mathrm{TEC}} = \frac{(T_H - T_0)}{T_H}\frac{(M_{\mathrm{opt}} - 1)}{(M_{\mathrm{opt}} + T_0/T_H)} \tag{7}$$

where T_H is the temperature characterizing the heat input to the TEC element and M_{opt} is a simplifying term containing the figure-of-merit, Z, and takes the form,

$$M_{\mathrm{opt}} = \left[1 + Z\left(\frac{T_H + T_0}{2}\right)\right]^{1/2} \tag{8}$$

where Z, which is geometrically optimized for maximum operating efficiency, is

$$Z = \frac{(\alpha_p - \alpha_n)^2}{[(k_p\rho_p)^{1/2} + (k_n\rho_n)^{1/2}]^2} \tag{9}$$

Note that ZT_{ave} is a characteristic parameter of the TEC element and essentially governs its internal conversion efficiency [23,24]. It is well known that the value of Z can have strong variations in temperature [21,25]. In this work, in order to gain insight into optimal combustor operating temperatures, the value of Z is assumed to be constant. Although this is a strong simplification of the actual situation, it provides tractable solutions for the combustor temperature and operating efficiency of the TEC element.

Substituting for T_H with T_p in Eqs. (7) and (8), then forming the overall output power as $\dot{W} = \dot{Q}_H \eta_{\mathrm{TEC}}$, the rate of work generated by the system becomes

$$\dot{W} = \dot{m}\bar{c}_p\left[(T_{\mathrm{af}} - T_p) + \varepsilon(T_p - T_0) - \frac{kA}{\dot{m}\bar{c}_p L}(T_p - T_0)\right] \times\left(\frac{T_p - T_0}{T_p}\right)\left(\frac{M_{\mathrm{opt}} - 1}{M_{\mathrm{opt}} + T_0/T_p}\right) \tag{10}$$

From this expression, the overall system efficiency (defined by the power output divided by the combustion heating rate) of the conversion process immediately follows by dividing Eq. (10) by the heating rate, $\dot{m}\bar{c}_p(T_{\mathrm{af}} - T_0)$, or

$$\eta_{\mathrm{sys}} = \left(\frac{1}{(T_{\mathrm{af}} - T_0)}\right)\left[(T_{\mathrm{af}} - T_p) + \varepsilon(T_p - T_0) - \frac{kA}{\dot{m}\bar{c}_p L}(T_p - T_0)\right]\eta_{\mathrm{TEC}} \tag{11}$$

Note that the TEC element efficiency has been used in place of the last two parenthetical terms of Eq. (10). The resulting expression has the same functionality as Eq. (10) since $(T_{\mathrm{af}} - T_0)$ is invariant with T_p and therefore achieves its maximum value at the same combustor temperature. In Eq. (10), M_{opt} is also a function of T_p (after substituting for T_H). In this work we will distinguish two thermal efficiencies. The first one, as defined immediately above in Eq. (11), is the overall system efficiency. The second one is the isolated TEC element efficiency from Eq. (7) where T_p substitutes for T_H.

Figure 2 shows a typical result for the power output and system efficiency as T_p is varied from T_0 to T_{af}. The case examined was for the regenerator effectiveness and conduction parameter both set to zero. Note that the power output has been normalized to give relative values since the actual output would depend on $\dot{m}\bar{c}_p$. The efficiency is directly accessible due to the fact that the mass flow rate and specific heat cancel out of the efficiency expression. From the figure, the combustor can be operated either near T_{af}, or temperatures approaching T_0, both conditions produced little generated work. As described earlier, Fig. 2 clearly shows a T_p where a maximum output is generated by the combined system. The curves shown in the figure represent a broad range of Z values—the higher ones being far beyond the current state-of-the-art for TEC materials. At the low end of the range, $Z=0.0001$ gives low efficiency for all combustor temperatures where the overall system efficiency never exceeds 1%. Successively higher Z values are used for generating each subsequent curve. For example, the third curve from the bottom (represented by open triangles) is for a Z value of 0.01. Using the average temperature between T_0 and the combustor temperature (at maximum output), a ZT_{ave} of 4.8 can be calculated. At the maximum power point, the overall efficiency approaches 16.5% and corresponds to a respectable conversion efficiency for an advanced TEC element when coupled to a combustor (although a $ZT_{\mathrm{ave}}=4.8$ is not yet attainable). As higher Z values are considered, an efficiency limit is approached which is characterized by an ideal TEC device operating with Carnot efficiency. This is very closely approximated by the top curve in Fig. 2 where a Z value of 100 was used to generate the curve giving a ZT_{ave} or 45,300 (use of such unrealistic values is for determining limiting theoretical cases only). It is interesting to distinguish the intrinsic element efficiency at the maximum power point and the overall system efficiency. For the $Z=0.01$ case, the system efficiency is near 16.5%. The intrinsic element efficiency using Eq. (7) is 26.8% which is significantly higher than the overall system value. Thus combustor operating characteristics contribute to a significant decrease in overall conversion efficiency from the intrinsic TEC element efficiency.

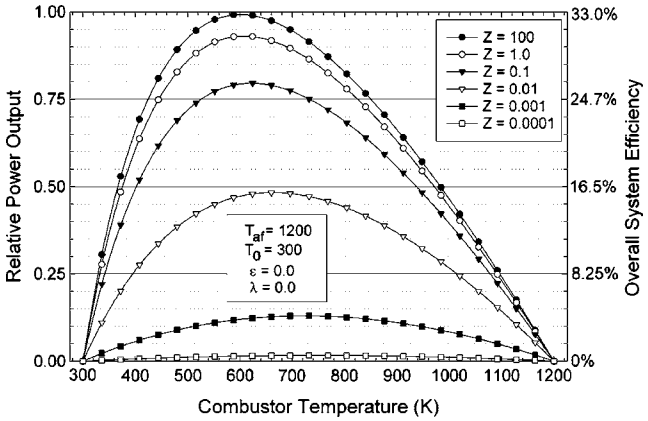

Fig. 2 Plot of the relative power output and overall system efficiency as a function of combustor temperature where $\varepsilon=0$ and $\lambda=0$. Each curve is generated using Z values that vary from 0.0001 to 100. Using the temperature average between the maximum power point and the surroundings, ZT_{ave} for each curve is (starting with the lowest ZT value): 0.0525, 0.507, 4.8, 46.2, 453, and 45,300. The last value listed gives performance that is essentially Carnot limited in converting combustor heat to power.

Figure 3 presents a different case where the HEX has an effectiveness of 0.75. As before, the conduction parameter was set to zero. Although the behavior of each curve is qualitatively similar to those of Fig. 2, because of heat regeneration, temperatures in excess of 3200 K are possible. However, combustion temperatures at the maximum power point are considerably lower. They fall into the range between 1120 K for $Z=100$ (near Carnot performance) and 1800 K for $Z=0.001$. As Z decreases, the combustor temperature at the maximum power point increases more so for this case of higher heat recirculation. This is a direct result of the wider combustor temperature range afforded by heat recovery, as evidenced by the curves in Fig. 3.

By invoking the condition for the maximum power output, $\partial\dot{W}/\partial T_p = 0$, an expression for T_p is potentially derivable. Even though the numerical procedure for generating Fig. 2 is straightforward, a general closed form solution for T_p has not been found. This also precludes finding a closed form solution for the overall system efficiency. With the lack of an analytical solution, it is instructive to examine the two limiting cases for the system thermal efficiency. For the case of $ZT \gg 1$, Eq. (7) reduces to [21]

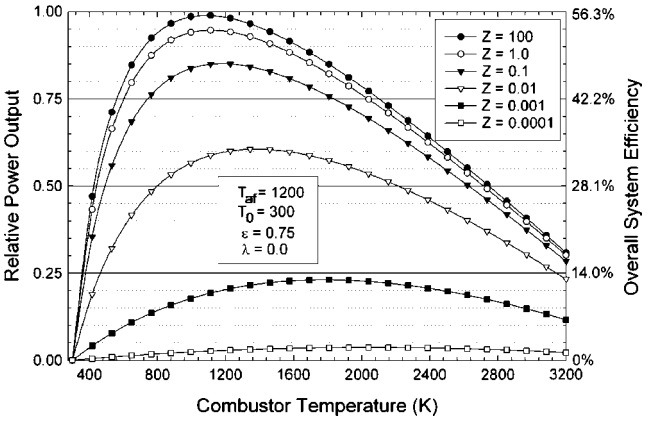

Fig. 3 Plot of the relative power output and overall system efficiency as a function of combustor temperature where ε =0.75 and λ=0. Each curve is generated using Z values that vary from 0.0001 to 100. Using the temperature average between the maximum power point and the surroundings, ZT_{ave} for each curve is (starting with the lowest ZT value): 0.117, 1.05, 8.51, 73.5, 706, and 70,600. The last value listed gives performance that is essentially Carnot limited in converting heat from the combustor to power.

$$\eta_{ZT\gg 1} = \eta_{\text{Carnot}} = 1 - \frac{T_0}{T_H} \tag{12}$$

Using this efficiency with $T_H = T_p$ in place of the final two terms in parentheses in Eq. (10), taking the derivative of the resulting expression with respect to T_p, and then setting the result to zero yields the temperature of the combustor at the maximum power point. Solving this resulting expression for T_p^* and introducing the conduction parameter

$$\lambda = \frac{kA}{\dot{m}\bar{c}_p L} \tag{13}$$

yields a closed form expression for the combustor temperature. Note that λ has been used in past studies on conduction effects in heat exchangers [26,27] and heat engines [18]. Before continuing, it is instructive to clarify the role the conduction parameters play in describing the amount of energy shunted to the surroundings. Forming the ratio between the shunt heat transfer and the total combustor heating rate yields

$$\frac{\dot{Q}_S}{\dot{H}V} = \frac{kA}{\dot{m}\bar{c}_p L}\frac{(T_p - T_0)}{(T_{\text{af}} - T_0)} = \lambda\frac{(T_p - T_0)}{(T_{\text{af}} - T_0)} \tag{14}$$

From this it is clear that the fraction of energy shunted to the surroundings depends on λ and T_p. However, T_p also depends on the value of the conduction parameter and can lie above or below T_{af} depending on the value of ε. Continuing with the development for the combustor temperature at the maximum power point, for the ideal Carnot case, the closed form expression is

$$T_p^* = \left(\frac{T_{\text{af}}T_0 - \varepsilon T_0^2 + \lambda T_0^2}{1 - \varepsilon + \lambda}\right)^{1/2} \tag{15}$$

By replacing T_p in Eq. (10) with the above derived T_p^*, the maximum work output is obtained. The TEC element efficiency at this operating point can be found by setting T_H in Eq. (12) to T_p^* yielding

$$\eta_{ZT\gg 1}^* = 1 - \left(\frac{1 - \varepsilon + \lambda}{T_{\text{af}}/T_0 - \varepsilon + \lambda}\right)^{1/2} \tag{16}$$

This is the same expression derived in previous work [17] where a combustor coupled to an ideal heat engine was examined. Note that when ε and λ are set to zero, the expression is analogous to the Curzon-Alborn equation where the adiabatic flame temperature assumes the high temperature value, but also realize that the combustor is not operating at T_{af}. That is, Eq. (16) no longer explicitly contains the combustor temperature—only the temperature of the surroundings and the adiabatic flame temperature appear. These two temperatures are the quantities that determine the combustor operating temperature at the maximum power (and efficiency) point. The efficiency given in Eq. (16) is to be distinguished from the overall system efficiency which is determined by substituting T_p^* from Eq. (15) into Eq. (11) for T_p and using the ideal element efficiency given in Eq. (12) for η_{TEC}.

The other TEC efficiency limit is when $ZT \ll 1$. In this case, the efficiency is given by [21]

$$\eta_{ZT\ll 1} = \left(1 - \frac{T_0}{T_H}\right)\left(\frac{Z(T_0 + T_H)}{4(1 + T_0/T_H)}\right) \tag{17}$$

where upon further analytical manipulation reduces to

$$\eta_{ZT\ll 1} = \frac{Z}{4}(T_H - T_0) \tag{18}$$

For deriving an analytical expression for the optimal operating temperature for this limiting case, we start by substituting the above efficiency into Eq. (10) for the last two terms in parentheses. With T_p replacing T_H, the derivative of the resulting expression is taken with respect to T_p. Finally, setting the derivative to zero and solving for T_p^* yields

$$T_p^* = \frac{1}{2}\left(\frac{T_{\text{af}} + T_0(1 - 2\varepsilon + 2\lambda)}{1 - \varepsilon + \lambda}\right) \tag{19}$$

This result can be substituted into Eq. (18) where T_p^* replaces T_H to obtain the TEC element efficiency at the maximum power point. Again, this result only holds for the case of $ZT_{\text{ave}} \ll 1$, i.e., for low performing TEC. The resulting expression is

$$\eta_{ZT\ll 1}^* = \frac{Z}{8}\left(\frac{T_{\text{af}} - T_0}{1 - \varepsilon + \lambda}\right) \tag{20}$$

The overall system efficiency (TEC plus combustor) can be found by using Eq. (11) with the efficiency and temperature as given in Eqs. (18) and (19), respectively, with the appropriate substitutions.

Results and Discussion

Once the optimal combustor temperature has been identified, the performance of the TEC element, and overall system, can be determined through their respective thermal efficiency expressions. In the discussion to follow, results are presented for performance values based on system operation at the maximum power point, hence maximum efficiency point, since this gives optimal performance for the system. It is also a unique and unambiguous operating point. It should be noted that parameter variation in the following discussion is focused on ε and λ. The adiabatic flame temperature, T_{af}, and the surroundings temperature, T_0, are held constant at 1200 K and 300 K, respectively. These can be considered as representative values characterizing lean combustion in terms of heating value. A change in T_{af} will affect the results numerically, but the overall trends and qualitative behavior of the results will be similar to those presented here.

Figure 4 shows curves for the combustor temperature at the maximum power point. Each curve is a function of ZT_{ave} and has a different HEX effectiveness. Note that T_{ave} is determined by using the sum of T_0 and T_p (not T_{af}) and then dividing by 2. Also for each curve, the conduction parameter was set to zero. Figure 4 clearly shows the effect of heat recirculation on the optimized combustor operating temperature. For effectiveness values approaching zero, little variation in combustor temperature is observed through the range of ZT_{ave} going from 0.01 to well over 1000. This does not mean that the efficiency of the conversion process remains nearly constant (as will be examined later). It

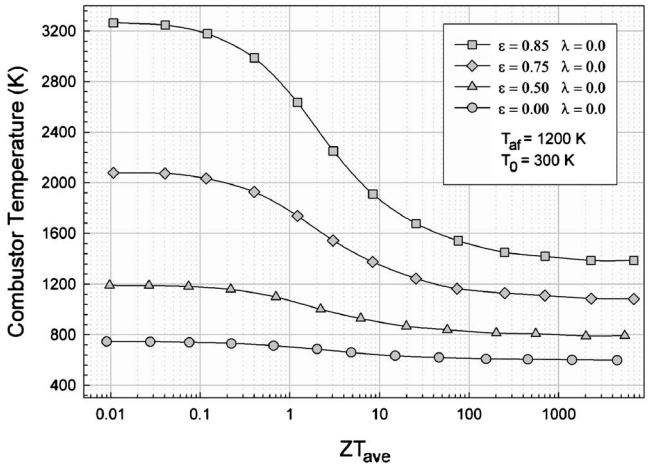

Fig. 4 Combustor temperature at the maximum power point as a function of ZT_{ave}. Curves are distinguished by the degree of heat regeneration through the HEX effectiveness. The adiabatic flame temperature and surroundings temperature are held constant at 1200 K and 300 K, respectively.

only means that for low levels of heat recirculation, moderate levels of combustor temperature must be maintained to achieve optimal conversion efficiency. As the heat recirculation increases, the combustor temperature variation becomes more pronounced. At low ZT_{ave}, the combustor must run hotter to maintain a respectable conversion efficiency, and since high HEX effectiveness opens up the higher temperature regime, the overall device will run at these elevated temperatures. As the TEC element efficiency increases with higher ZT_{ave}, the combustor temperature can be reduced thus sending more thermal energy to the TEC element and hence providing higher overall efficiency. Note that each extreme in ZT_{ave} results in a limit in the combustor temperature.

It is instructive to examine the limiting solutions for the high and low ZT_{ave} cases derived in the earlier section. The vehicle for this is through the efficiency. Figure 5 provides this comparison by plotting the efficiencies for the limiting cases and the exact case (found numerically) as a function of ZT_{ave}. The conditions

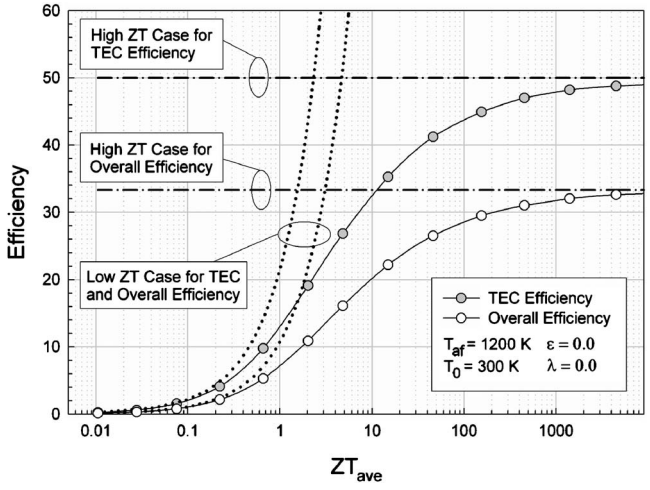

Fig. 5 Comparison of the three solutions for efficiency. In each of the three cases, the efficiency of the TEC element and the overall system efficiency are plotted as a function of ZT_{ave}. The three solutions are: (1) the exact solution, given by filled or open circles, where a numerical computation is necessary, (2) the case where $ZT \ll 1$, and (3) the case where $ZT \gg 1$. The curves are generated for the base case of $\varepsilon = 0$ and $\lambda = 0$.

used in generating Fig. 5 are $\varepsilon = 0$ and $\lambda = 0$. It should be reiterated that two efficiencies are relevant to this discussion—the thermal efficiency of the TEC element and the overall system efficiency. In Fig. 5, the full-range numerical solution for the former is given as filled circles while the latter is given as open circles. From the figure, each numerically-derived efficiency smoothly transitions from near zero at the low range of ZT_{ave} to approaching their limiting high efficiencies as ZT_{ave} exceeds 1000. For the case examined, it is clear the TEC element efficiency is significantly higher than the overall system efficiency with the former being nearly twenty percentage points higher. The high ZT_{ave} limit is well predicted by the closed form solutions given by Eqs. (14) and (15). However, this high limit is only good for ZT_{ave} exceeding approximately 1000. This is far too high to be useful for current technology in the TEC field. In fact, the most useful ZT_{ave} range is between 1 and 10. As shown in Fig. 5, neither the high nor low ZT_{ave} limiting solutions have utility in this mid-range regime. The low ZT_{ave} solution appears to be useful from about $ZT_{ave} = 0.3$ and below. The conclusion here is that although the high and low ZT_{ave} cases provide interesting theoretical results for efficiencies, they provide little utility in the most relevant regime for current technology application. All further results presented here are from the full-range numerical solution. Although some relaxation in the simplifying assumptions could be made at this point (e.g., in assuming a constant specific heat), little utility is gained from this as opposed to using an appropriately averaged value. More important would be to relax the assumption of constant $Z(T)$. However, this would preclude any use of the common equations used for modeling the TEC effect (Eqs. (7)–(9)). From these considerations, the simplifying approximations made earlier will be retained.

Figure 6 shows two graphs for the TEC element efficiency (*a*) and the overall system efficiency (*b*). The two graphs are best considered together in order to form an accurate picture of the effects of ZT_{ave} and HEX effectiveness on efficiency. The curves in each graph represent a HEX effectiveness ranging from 0 to 0.85. The latter value is probably not the ultimate achievable effectiveness (at least not by macroscale device standards), but is probably realistic of what can be attained with small-scale devices. Also, the effects of thermal shunting of heat to the surroundings are not examined until Fig. 7. Thus, for the set of conditions delineated, the curves provide a picture of how the thermal efficiency is affected by heat recovery alone. First, there is a strong general trend toward higher efficiencies with increasing ZT_{ave}. Note that from the data presented in Fig. 4, this increase in efficiency is also associated with a decrease in operating temperature. From the behavior of the curves, significant increases in efficiencies take place in the ZT_{ave} range between 1 and 10. This is the regime where a numerical solution is needed and the limiting case solutions have little utility. Still further increases in ZT_{ave} from 10 to 100 produce higher efficiencies until the high ZT_{ave} limit is approached beyond 1000. As the HEX effectiveness increases from 0 to 0.85, progressively higher TEC efficiency and overall system efficiency are achieved. Finally, the two graphs taken together show the differences between the TEC element efficiency and the lower overall system efficiency where both are based on the heating value of the fuel supplied to the combustor. For the TEC efficiency, taken in the most relevant ZT_{ave} range of from 1 to 10, values in the 20–50% range are typical. Higher HEX effectiveness leads to higher element efficiency, but for ZT_{ave} ranging from 1 to 4, effectiveness higher than approximately 0.75 is probably not justified for the marginal increase it would bring. However, heat exchanger performance significantly impacts the attainable efficiencies and would be an important feature of any combustion driven TEC device. Overall efficiencies are typically down by 10–20 percentage points from the TEC element values in the ZT_{ave} range of 1–4. This is due to thermal energy escaping in the exhaust and not being available to the TEC element for potential conversion to electrical power. As the heat exchanger effectiveness increases, this loss is reduced although as mentioned ear-

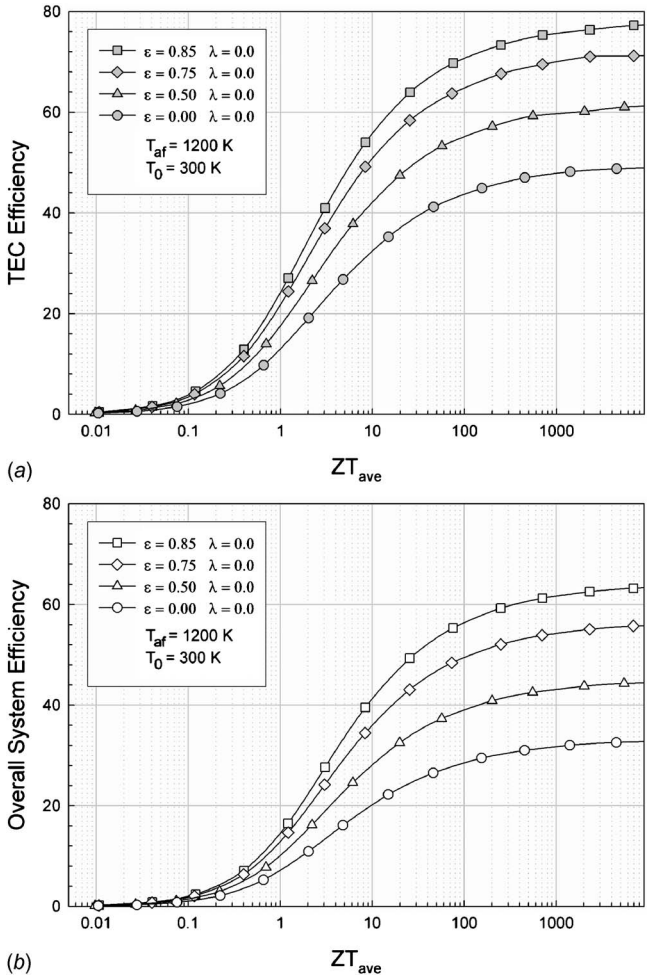

Fig. 6 TEC element efficiency (*a*) and overall system efficiency (*b*) as a function of ZT_{ave} for a range of HEX effectiveness values. The conduction parameter is set to zero.

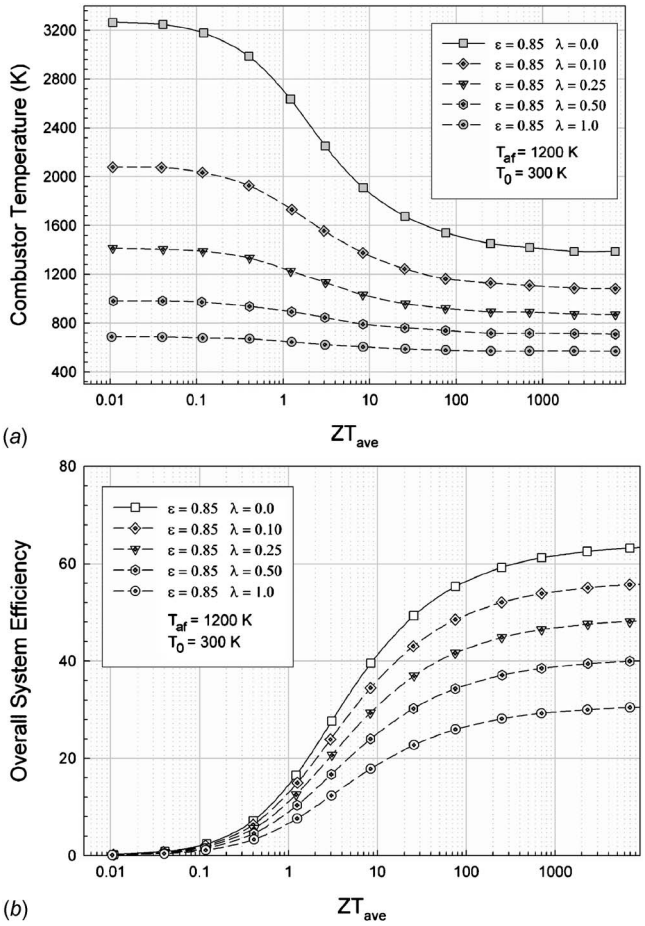

Fig. 7 Combustor temperature (*a*) and overall system efficiency (*b*) as a function of ZT_{ave} for a HEX effectiveness of 0.85. The conduction parameter varies from 0.0 to 1.0. Conductive heat loss as a percent of heating rate at the high *ZT* limit for each λ value is 0%, 8.7%, 15.9%, 22.8%, and 30.1%.

lier, ε exceeding about 0.75 is not warranted. Finally, even though the high limiting cases look impressive from an energy conversion view point, ZT_{ave} for present day thermoelectric materials (and with anticipated advancement) will only fall in the range of 1–3. From the theoretical view point of this work, there remains considerable irreversibility associated with energy conversion even at the ZT_{ave} level of 3. If breakthroughs in TEC materials occur, there is considerable up-potential existing in the type of small-scale power generators considered here.

Finally, Fig. 7 is presented as an example of how thermal conduction losses can affect overall system performance. Figure 7(*a*) gives the combustor temperature as a function of ZT_{ave} for a variety of conduction parameter values, λ. In the results presented, the HEX effectiveness was kept at 0.85. There are two interesting features displayed in the data. First, there is a marked decrease in combustor temperature with even small values in the conduction parameter. In fact, at the low ZT_{ave} range, a temperature decrease of over 1000 K results when λ increases from 0 to 0.10. At the high ZT_{ave} range, this temperature decrease is reduced to approximately 400 K, but still represents a large impact on combustor temperature. The second feature displayed in the data is the similar qualitative appearance to Fig. 4 as the conduction parameter is increased. This can be explained in terms of thermal energy loss from the combustor and its impact on the combustor operating conditions. Figure 4 shows how thermal energy recovery from the exhaust increases combustor temperature, or conversely, having low values of thermal recovery results in thermal losses from the combustor. This drives down the optimal temperature at which the combustor operates. Figure 7(*a*) shows a similar effect of conductive heat loss causing a decrease in the operating temperature. Thus both mechanisms appear to result in the same overall effect on the combustor. The lowest curve in each of the figures emphasizes this in the respect that they have very similar, i.e., flattened, shapes.

Figure 7(*b*) presents the curves for overall system efficiency corresponding to the same conditions as Fig. 7(*a*). For a HEX effectiveness of 0.85 and no thermal shunt to the surroundings, the top curve (signified by open squares) gives moderate-to-high system efficiency starting with a ZT_{ave} of about 2. As significant thermal losses begin to occur, the thermal efficiency also starts to decrease because of the increased thermal shunting to the surroundings. At the high *ZT* limit in Fig. 7, as the conduction parameter varies through its range, the shunt heat loss as a percent of heating rate takes on values of 0%, 8.7%, 15.9%, 22.8%, and 30.1%. The decrease in thermal efficiency, however, does not appear to be as precipitous as the drop off in combustor temperature. That is, the system efficiency does not look as sensitive to thermal conduction losses as the combustor temperature, but there is still considerable impact on performance. One reason for this behavior is the ability of the combustor temperature to "shift" to the value that produces a maximized power output and efficiency. Thus, if the conduction losses to the surroundings "shunt" away a quantity of heat from the TEC element, the combustor temperature can partially compensate by operating at a slightly higher temperature

to improve overall conversion efficiency. With this said, it remains important to maximize the amount of thermal energy retained by both recovering thermal energy in the exhaust and minimizing conduction losses.

Concluding Remarks

A model has been presented for a power generating device composed of a thermoelectric conversion element coupled to a combustor. A unique thermodynamic operating point, based on maximum power output, is used to determine system efficiency and combustor operating temperature. In the analysis, heat recirculation from the combustor exhaust is included as is a thermal shunt to the surroundings. This study is relevant to the operating characteristics of small, combustion-driven energy systems. Results are given in terms of both the TEC element efficiency and overall system efficiency as a function of ZT_{ave}. Even though a wide range of this parameter is used in the analysis (with a limiting case on the high side being far superior to any TEC material currently achievable), the most relevant values are of order unity based on present technology for thermoelectric materials. For a device burning a reactant mixture having an adiabatic flame temperature of 1200 K, and with an effectiveness of 0.75 for the heat recovery, the TEC efficiency is approximately 22% for a $ZT_{\text{ave}}=1$. This drops to 12% for an overall system efficiency when combustor operation is considered. Higher values of ZT_{ave} have pronounced effects on system performance in the 1–10 ZT_{ave} range. Heat loss also greatly influences the performance of the system. Based on the nondimensional conduction parameter, λ, significant decreases in system performance occur for even small values of this quantity. Thus, in the design and development of small combustion-driven thermoelectric generators, significant benefits accrue by incorporating a high degree of heat recirculation and taking care to minimize the thermal conduction losses to the surroundings.

Nomenclature

A = representative cross-sectional area for conductive heat loss, m^2

$\bar{c}_p$ = representative constant pressure specific heat, J/kg K

$\dot{H}_p$ = enthalpy flow of products out of combustor, W/kg

$\dot{H}_r$ = enthalpy flow of reactants into combustor, W/kg

$\dot{HV}$ = heating value rate, W

k = representative thermal conductivity for heat loss, W/m K

k_n = thermal conductivity of n-type material, W/m K

k_p = thermal conductivity of p-type material, W/m K

L = representative path length for conductive heat loss, m

M_{opt} = parameter for TEC element efficiency

$\dot{m}$ = mass flow rate of the products, kg/s

P_0 = pressure of the surroundings, N/m^2

$\dot{Q}_H$ = rate of heat flow to the TEC element, W

$\dot{Q}_S$ = rate of heat loss to the surroundings through the thermal shunt, W

$\dot{Q}_{\text{tot}}$ = rate of heat release within the combustor, W

T_{af} = adiabatic flame temperature of the reactants, K

T_{ave} = average temperature between surroundings and combustor, K

T_H = temperature characterizing the heat input to the TEC element, K

T_p = temperature of the well-stirred combustor and products, K

T_p^* = temperature of the combustor at the maximum power point, K

T_x = temperature of flow emerging from HEX, K

T_0 = temperature of the surroundings, K

$\dot{W}$ = rate of work by the overall system, W

Z = figure-of-merit for thermoelectric conversion, K^{-1}

Greek Symbols

α_n = Seebeck coefficient for n-type material, V/K

α_p = Seebeck coefficient for p-type material, V/K

ε = heat exchanger effectiveness

η_{Carnot} = efficiency of a reversible Carnot heat engine, $1-T_0/T_H$

η_{sys} = efficiency of the overall system

η_{TEC} = efficiency of the thermoelectric conversion element

η^* = thermal efficiency at the maximum power point

λ = conduction parameter, $kA/\dot{m}\bar{c}_pL$

ρ_n = electrical resistivity of n-type material, ohm m

ρ_p = electrical resistivity of p type material, ohm m

Abbreviations

HEX = heat exchanger

TEC = thermoelectric conversion

References

[1] Koeneman, P. B., Busch-Vishniac, I. J., and Wood, K. L., 1997, "Feasibility of Micro Power Supplies for MEMS," J. Microelectromech. Syst., **6**(4), pp. 355–362.

[2] Fernandez-Pello, A. C., 2002, "Micro-Power Generation Using Combustion: Issues and Approaches," Proceedings of the 29th International Symposium on Combustion, Sapporo, Japan, The Combustion Institute, Pittsburgh, PA.

[3] Peterson, R. B., 2003, "Miniature and Microscale Energy Systems," *Heat and Fluid Flow in Microscale and Nanoscale Structures*, M. Faghri and B. Sunden, eds., WIT P., Southampton, UK, pp. 1–43.

[4] Dunn-Rankin, D., Leal, E. M., and Walther, D. C., 2005, "Personal Power Systems," Prog. Energy Combust. Sci., **31**, pp. 422–465.

[5] Park, C.-W., and Kaviany, M., 2000, "Combustion-Thermoelectric Tube," ASME J. Heat Transfer, **122**, pp. 721–729.

[6] Katsuki, F., Tomida, T., Nakatani, H., Katoh, M., and Takata, A., 2001, "Development of a Thermoelectric Power Generation System Using Reciprocation Flow Combustion in a Porous $FeSi_2$ Element," Rev. Sci. Instrum., **72**, No. 10, pp. 3996–3999.

[7] Schaevitz, S. B., Franz, A. J., Jensen, K. F., and Schmidt, M. A., 2001, "A Combustion-Based MEMS Thermoelectric Power Generator," Proceedings of the 11th International Conference on Solid-State Sensor and Actuators (in Digest of Technical Papers, Transducers '01, Eurosensors XV), pp. 30–33.

[8] Yoshida, K., Tanaka, S., Tomonari, S., Satoh, D., and Esashi, M., 2006, "High-Energy Density Miniature Thermoelectric Generator Using Catalytic Combustion," J. Microelectromech. Syst., **15**, No. 1, pp. 195–203.

[9] Gordon, J. M., 1991, "Generalized Power Versus Efficiency Characteristics of Heat Engines: Thermoelectric Generators as an Illustration," Am. J. Phys., **59**, No. 5, pp. 551–555.

[10] Chen, J., Yan, Z., and Wu, L., 1996, "The Influence of Thomson Effect on the Maximum Power Output and Maximum Efficiency of a Thermoelectric Generator," J. Appl. Phys., **79**, No. 11, pp. 8823–8828.

[11] Bejan, A., 1997, *Advanced Engineering Thermodynamics*, 2nd ed., Wiley, New York, pp. 665–682.

[12] Agrawal, D. C., and Menon, V. J., 1997, "The Thermoelectric Generator as an Endoreversible Carnot Engine," J. Phys. D, **30**, pp. 357–359.

[13] Chen, L., Sun, F., and Wu, Chih, 2005, "Thermoelectric-Generator With Linear Phenomenological Heat-Transfer Law," Appl. Energy, **81**, pp. 358–364.

[14] Weinberg, F. J., Rowe, D. M., and Min, G., 2002, "Novel High Perfromance Small-Scale Thermoelectric Power Generation Employing Regenerative Combustion Systems," J. Phys. D, **35**, pp. L61–L63.

[15] Weinberg, F., 2004, "Optimizing Heat Recirculating Combustion Systems for Thermoelectric Converters," Combust. Flame, **138**, pp. 401–403.

[16] Peterson, R. B., 2005, "Development of an Analytical Model Useful for Micro Heat Engine Analysis," Int. Commun. Heat Mass Transfer, **32**, pp. 884–889.

[17] Peterson, R. B., 2005 "A Scaling Study of a Combined Micro Combustor and Heat Engine System," Power Eng. J., **219**, pp. 371–381.

[18] Peterson, R. B., 1998, "Size Limits for Regenerative Heat Engines," Microscale Thermophys. Eng., **2**, pp. 121–131.

[19] Peterson, R. B., and Al-Hazmy, M., 1997 "Size Limits for Stirling Cycle

Refrigerators and Cryocooler," Proceedings of the 32nd IECEC, Honolulu, HI, American Institute of Chemical Engineers, New York, pp. 997–1002.
[20] Peterson, R. B., 1999, "Numerical Modeling of Conduction Effects in Microscale Counterflow Heat Exchangers," Microscale Thermophys. Eng., **3**, pp. 17–30.
[21] Decher, R., 1997, *Direct Energy Conversion*, Oxford University Press, Oxford, England, pp. 240–252.
[22] Angrist, S. W., 1982, *Direct Energy Conversion*, 4th ed., Allyn and Bacon, Inc., Boston, MA, pp. 121–171.
[23] Goldsmid, H. J., 1995, "Conversion Efficiency and Figure-of-Merit," *CRC Handbook of Thermoelectrics*, D. M. Rowe, ed., CRC Press, Boca Raton, FL, pp. 19–25.
[24] Nolas, G. S., Sharp, J., and Goldsmid, H. J., 2001, *Thermoelectrics, Basic Principles and New Materials Development*, Springer, Berlin, pp. 178–191 and 235–254.
[25] Matsuura, K., and Rowe, D. M., 1995, "Low-Temperature Heat Conversion," *CRC Handbook of Thermoelectrics*, D. M. Rowe, ed., CRC Press, Boca Raton, FL, pp. 573–593.
[26] Bahnke, G. D., and Howard, C. P., 1964, "The Effects of Longitudinal Heat Conduction on Periodic-Flow Heat Exchanger Performance," J. Eng. Power, **86**, pp. 105–120.
[27] Peterson, R. B., and Vanderhoff, J. A., 2001, "Analysis of a Bayonet-Type Counterflow Heat Exchanger With Axial Conduction and Radiative Heat Loss," Numer. Heat Transfer, Part A, **40**, pp. 203–219.

Natural Gas Decarbonization Technologies for Advanced Power Plants

Marco Gambini
e-mail: gambini@ing.uniroma2.it

Michela Vellini
e-mail: vellini@ing.uniroma2.it

Department of Industrial Engineering,
University of Rome "Tor Vergata,"
Via del Politecnico no. 1,
00133 Rome, Italy

In this paper two options for H_2 production, by means of natural gas, are presented and their performances are evaluated when they are integrated with advanced H_2/air cycles. In this investigation two different schemes have been analyzed: an advanced combined cycle power plant (CC) and a new advanced mixed cycle power plant (AMC). The two methods for producing H_2 are as follows: (1) steam methane reforming: it is the simplest and potentially the most economic method for producing hydrogen in the foreseeable future; and (2) partial oxidation of methane: it could offer an energy advantage because this method reduces the energy requirement of the reforming process. These hydrogen production plants require material and energetic integrations with power section and the best interconnections must be investigated in order to obtain good overall performance. With reference to thermodynamic and economic performance, significant comparisons have been made between the above introduced reference plants. An efficiency decrease and an increase in the cost of electricity has been obtained when power plants are equipped with a natural gas decarbonization section. The main results of the performed investigation are quite variable among the different H_2 production technologies here considered: the efficiency decreases in a range of 5.5 percentage points to nearly 10 for the partial oxidation of the natural gas and in a range of about 9 percentage points to over 12 for the steam methane reforming. The electricity production cost increases in a range of about 41–42% for the first option and in a range of about 34–38% for the second one. The AMC, coupled with partial oxidation, stands out among the other power plant solutions here analyzed because it exhibits the highest net efficiency and the lowest final specific CO_2 emission. In addition to this, economic impact is favorable when AMC is equipped with systems for H_2 production based on partial oxidation of natural gas.
[DOI: 10.1115/1.2719266]

1 Introduction

There are various options to meet world energy demands in the next years. Conventional oil and gas resources are large and there are abundant coal resources to meet such a demand. However, reductions in fossil fuel use may occur as a response to climate change concerns: in the next years emissions from fossil fuel would have to be restricted substantially to limit climate change effects. If global warming concerns remain an issue, substantial carbon sequestration will be required.

A hydrogen economy will become even more attractive in this new situation, with sequestration of carbon it could sustain the use of fossil fuels, and hydrogen could replace oil and gas as heavily traded resource.

Hydrogen also provides an ideal complement to electricity. Both are premium quality energy carriers, do not contain carbon and generate little or non polluting emissions at the point of use. While electricity is at disadvantage when storage is required, hydrogen could be well suited for those applications. Its versatility is enhanced by the fact that it can be produced from a variety of fossil resources. For these reasons, on the initial phase of a "hydrogen economy," H_2 could be produced from the current competitive fossil fuels.

Therefore, in this paper we want to evaluate overall performance of advanced power plants, based on natural gas decarbonisation. More precisely, we want to compare two different processes, which provide hydrogen (steam reforming and partial oxidation of natural gas), and we want to study their integration with advanced power plants. In this paper a proper thermodynamic and economic analysis will be performed and the results will be compared in terms of energy efficiency, emission of CO_2 and electricity production cost.

2 Reference Power Plants

In this paper the comparison of performance decrease and electricity cost increase of two advanced power plants, equipped with hydrogen production systems, is treated. The reference power plants, analyzed here, are as follows:

- CC: combined cycle power plant, fed by natural gas,
- AMC: advanced mixed cycle power plant, fed by natural gas.

In Fig. 1 the CC plant layout is shown. There is a heavy-duty gas turbine as the topping cycle, and a three pressure level, reheat steam cycle as the bottoming cycle. In the same figure, heat and mass balance is displayed, when the working parameters, which maximize power plant efficiency, are chosen. To show these results, a numerical investigation has been performed, by using a proper numerical model, developed by the authors. This model is based on calculation procedures for conventional components (turbines, compressors, pumps, heat exchangers, etc.) and unconventional ones (for example, the water separator, which is a component of the second reference power plant). Moreover, by using a commercial numerical code (GateCycle), we have simulated some power sections and evaluated their performance (especially for the integrated solutions).

Table 1 shows the most important output parameters of this first

Submitted to ASME for publication in the JOURNAL OF ENGINEERING FOR GAS TURBINES AND POWER. Manuscript received October 13, 2006; final manuscript received January 24, 2007. Review conducted by Dilip R. Ballal. Paper presented at the ASME Power 2006 (PWR2006), May 2–4, 2006, Atlanta, GA.

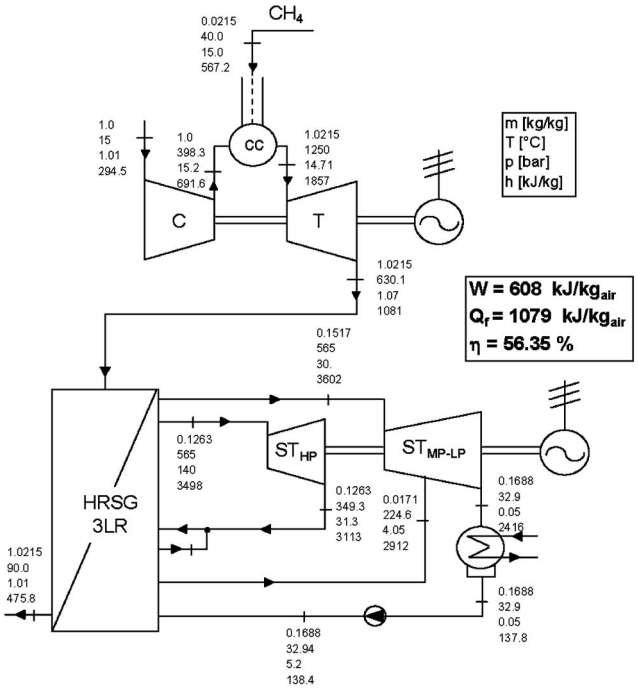

Fig. 1 CC power plant

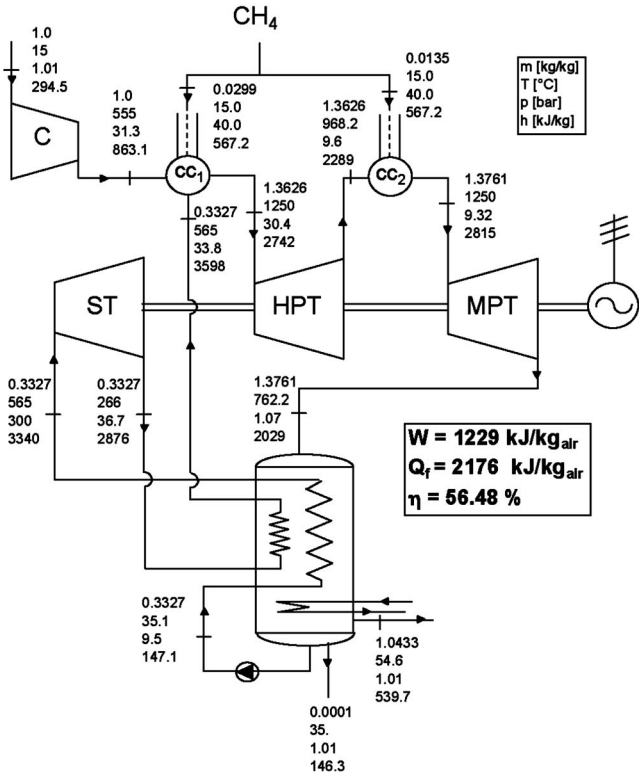

Fig. 2 AMC power plant

reference power plant; in order to compare these results with those of the second reference power plant, it is important to show the AMC plant layout (Fig. 2).

As can be seen in the plant scheme of Fig. 2, the AMC is a mixed gas-steam cycle in which steam works in a closed cycle [1,2]. There is an initial steam heating, carried out in a regenerative way, and then steam heating (SH and RH) is carried out partly in a regenerative way and partly by mixing steam with exhaust gases from the internal combustion of natural gas and compressed air in the two combustion chambers (cc_1 and cc_2). In the AMC cycle, water separation and recovery are necessary to operate in a closed steam cycle mode. In fact, in this plant solution there is a special water separation unit, consisting of a heat exchanger arrangement, where the mixture (incondensable gases and steam) is cooled below the condensation temperature of steam [3].

Waste heat flow is profitably recovered: in this plant layout there is a full regenerative steam generation. It is also necessary to point out that the steam recirculation in this cycle allows the reduction of the excess air used to limit the turbine inlet temperature. In Fig. 2, heat and material balance, evaluated by the numerical model above introduced, is shown, when the working parameters, which maximize power plant efficiency, are chosen.

Table 2 shows the most important output parameters of this second reference power plant.

In performance terms, the two reference power plants are very similar: the net efficiency attains a value of about 56.5%; in layout terms, they are quite different: while the CC power plant has a very standard gas turbine and a quite sophisticated bottoming steam cycle (there is a three pressure level heat recovery steam generator), the AMC power plant has an unusual gas turbine because there is a second combustion chamber (it is a reheat gas turbine), but, above all, there is a steam injection in the first combustion chamber. Moreover, while the steam turbine of the AMC power plant is very conventional (it is a steam turbine where steam expands from a supercritical condition—300 bars and 565°C—to the pressure of the first combustion chamber) and the

Table 1 CC mass and energetic balance and overall performance

Power plant work balance (kJ/kg_{air})	Power plant heat balance (kJ/kg_{air})
	Q_a 294.5
W_{C_GT} 401.2	Q_{fuel} (inlet+HHV) 1210
W_{T_GT} 784.7	Q_{COND} 384.5
W_{T_SC} 237.0	Q_{HRSG} 486.3
W_{p_sc} 3.35	Q_{CC} 4.77
	Q_{losses} 21.06
Net work output 607.9	$Q_{IN}-Q_{OUT}$ 607.9
Overall performance	
Fuel heat (natural gas LHV, kJ/kg_{air}) 1079	
Overall efficiency (%) 56.34	
CO_2 specific emission (kg/kWh) 0.3513	

Table 2 AMC mass and energetic balance and overall performance

Power plant work balance (kJ/kg_{air})	Power plant heat balance (kJ/kg_{air})
	Q_a 294.5
W_C 574.4	Q_{fuel} (inlet+HHV) 2440
W_{ST} 152.7	Q_{SEP} 890.4
W_{HPT} 611.1	Q_{HRSG} 563.0
W_{MPT} 1071.0	Q_{CC} 9.67
W_{aux} 12.60	Q_{losses} 42.8
Net work output 1229	$Q_{IN}-Q_{OUT}$ 1229
Overall performance	
Fuel heat (natural gas LHV, kJ/kg_{air}) 2176	
Overall efficiency (%) 56.48	
CO_2 specific emission (kg/kWh) 0.3504	

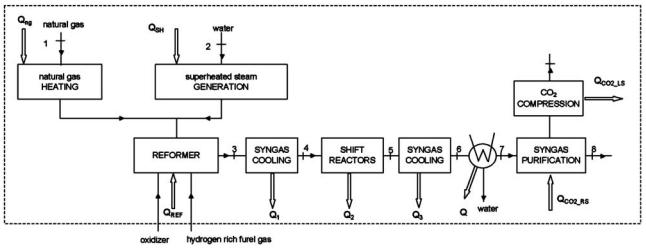

Fig. 3 Steam methane reforming process

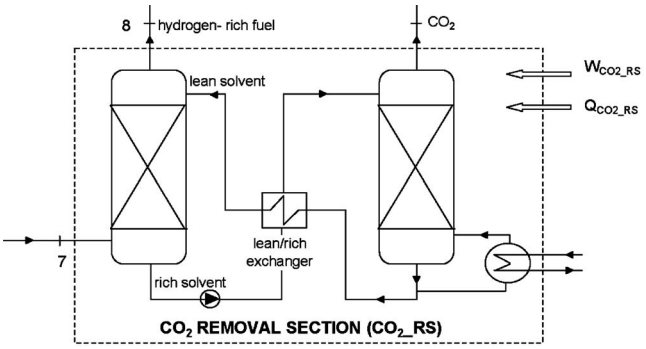

Fig. 4 Separation process of CO_2 by chemical absorption

heat recovery steam generator is very simple (only one level, even if it is supercritical), there is a particular final section: the separator. In this component, water recovery must be performed: for this reason exhaust gases must be cooled to a proper temperature in order to collect at the bottom of the separator a suitable quantity of water (equal to the steam flow rate injected in the first combustion chamber) [3]. To ensure this mass balance, an external cooling fluid is used in order to reach the required final temperature of the exhaust gases.

In spite of these considerations, the overall performance of the AMC power plant seems very interesting and worthy of further investigations.

3 Natural Gas Decarbonization Technologies

As stated above, hydrogen is an energy carrier so that it must be manufactured from other compounds, which are widely available on earth. The most attractive option is the removing of carbon from hydrocarbon feedstocks, which is the decarbonization of the fossil fuels, such as natural gas, coal, and so on.

For the natural gas, two main technologies are available in order to produce hydrogen-rich fuel gas: the steam methane reforming and the methane partial oxidation. The simplest and potentially the most economic method for producing hydrogen in the foreseeable future is the steam reforming of natural gas [4–6], but an unavoidable drawback of this process is its intensive energy requirement [7]. A possible alternative is the methane partial oxidation, in combination with steam and/or CO_2 reforming, which could offer an advantageous reduced energy requirement of the reforming process.

Therefore, in this paper we want to examine in detail these two methodologies. In this paragraph we have reported some information about their mass and energy requirements.

Steam Methane Reforming. To produce hydrogen from methane, several steps have to be performed, they are shown in Fig. 3.

First, methane and steam are introduced into a reformer where the next chemical reaction takes place:

$$CH_4 + H_2O \rightarrow CO + 3H_2, \quad \Delta h = 206.4 \text{ kJ/mol}$$

This reaction is endothermic and is favored at higher temperatures and lower pressures; another important parameter is the steam/methane ratio. A proper parametric analysis [8] showed that, with relatively low operating temperature (about 700°C), it is possible to obtain a high conversion rate (over 95%) by adopting a near-atmospheric reactor and a high steam/methane ratio (over 3). External heat, needed to drive the reaction, can be provided by the combustion between a proper oxidizer and the final fuel. Heat transfer to the reactants is accomplished indirectly through a heat exchanger. In order to limit the maximum temperature of the catalyst bed, it is possible to do some supplementary firing operations.

After reforming, the syngas is mainly composed of CO and H_2. To avoid carbon dioxide emissions from the power plants, it is necessary to produce a hydrogen rich fuel gas. Thus, the hydrogen output is increased via the following water-gas shift reaction:

$$CO + H_2O \rightarrow CO_2 + H_2, \quad \Delta h = 41.2 \text{ kJ/mol}$$

which converts CO to H_2. This reaction is exothermic and is favored at temperatures of less than about 600°C and can take place as low as 200°C, with sufficiently active catalysts. For the hydrogen production, the shift reaction is often accomplished in two stages: one at high temperature (350–450°C) accomplishes much of the conversion, and then another one, at lower temperature (200–250°C), brings the CO concentration down to a few percent by volume. During shift reaction, heat can be usefully recovered (by means of feed water preheating or low-pressure steam production, for example).

Finally, the gas exiting the shift reactors must be purified; in fact it contains not only hydrogen but also a rather large quantity of carbon dioxide, which can be considered as the main impurity, so, before the combustion in a power plant, the carbon dioxide must be separated from this fuel gas. As fuel is at atmospheric pressure, the chemical absorption is the most suitable method for CO_2 separation. Using the CO_2 separation process based on amine-water solution, a recovery factor of 90% of CO_2 in fuel gas is possible. The separation process of carbon dioxide by chemical absorption consists of two steps (Fig. 4): absorption of CO_2 by chemical solvents (usually amine-water solution) at low temperature (40–65°C) and next recovery of CO_2 from chemical solvents by using low-grade heat (temperature in the range of 100–150°C).

This process needs the two following energy requirements:

- Heat for solvent regeneration (2.75 MJ per kg of recovered carbon dioxide): this heat can be provided by low pressure steam; if the temperature for solvent regeneration is about 140°C, the steam pressure must be about 4 bars. Steam gives out its latent heat of condensation and leaves the separation plant as saturated liquid at the same pressure;
- Energy for fuel compression (in order to overcome pressure drops through the separation plant) and for amine solution pumping through the removal plant: this energy requirement is about 0.11 MJ/kg of recovered carbon dioxide.

After CO_2 separation, the removed carbon dioxide must be sequestrated. The CO_2 can be stored as liquid, so carbon dioxide must be liquefied. The liquefaction is performed (Fig. 5) in various steps, by alternately compressing and cooling. For this process an amount of energy is necessary: 0.35 MJ per kg of recovered carbon dioxide, when an intercooled compression is chosen (three steps with equal partial compression ratio until a final pressure of 80 bars, a polytropic efficiency of 0.85, and a mechanical efficiency of 0.98). No consideration has been made with regard to heat for intercooling because it is supposed that a suitable cooling fluid is easily available.

According to these assumptions, in this paper we have devel-

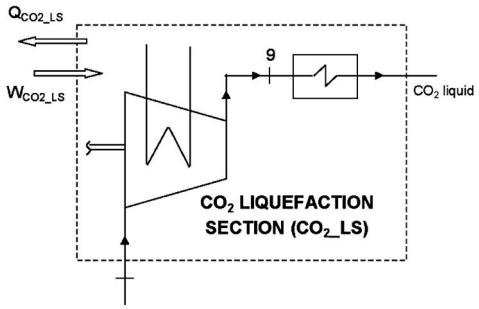

Fig. 5 CO_2 liquefaction process

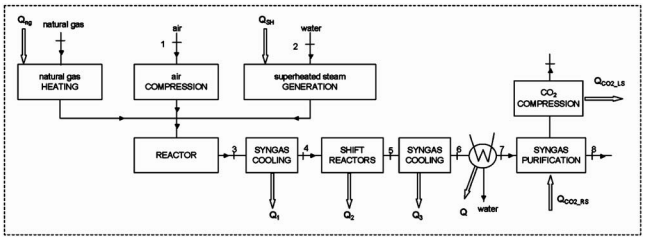

Fig. 6 Methane partial oxidation process

oped a rather simple numerical model to evaluate mass and composition of the main streams in the focal sections of the production plant (Table 3).

Methane Partial Oxidation. Hydrogen production, by means of methane partial oxidation, consists of several steps, as shown in Fig. 6.

First, methane, air, and steam are introduced into a catalytic air-blown partial oxidation reactor where different chemical reactions take place: partial and total oxidation together with steam and CO_2 reforming of methane. The most important operating parameters of the partial oxidation are the O_2/CH_4 ratio, the temperature, and the pressure. The optimal O_2/CH_4 ratio decreases with increasing temperature (it is 0.5 when temperature is greater than 800°C), the syngas yields increase with increasing temperature but with decreasing pressure, yet high temperature can suppress the pressure effect [7]. In this paper, because the optimal pressure ratio of the combined cycle, analyzed here, is about 15, we have assumed a pressurized solution with the following quantities of air and steam: 5.165 kg_{air}/kg_{ng} (it is equivalent to O_2/CH_4 molar ratio by 0.6025) and 1 kg_{steam}/kg_{ng} (ratio between steam and methane) [9].

After the partial oxidation, the syngas is composed of CO and H_2 in the presence of nitrogen, steam, and carbon dioxide. To avoid CO_2 emissions from the power plant, it is necessary to produce a hydrogen-rich fuel gas. Thus the hydrogen output is increased via the water-gas shift reaction, as in the previous case.

Finally, the gas, leaving the shift reactors, must be purified; in fact, also in this case it contains a rather large quantity of carbon dioxide, which can be considered as the largest impurity. If the syngas is at low pressure (about 15 bars) and the CO_2 fraction is small (about 15% by volume), the chemical absorption process is again the most suitable separation process.

As in the previous case, after carbon dioxide separation, CO_2 liquefaction is performed.

According to technical works [7,9–11], and on the basis of proper assumptions, we have developed a numerical model, able to evaluate mass and composition of the main streams in the focal sections of the production plant (Table 4).

4 Reference Power Plants Integrated With H_2 Production Plants

The previous paragraph has just shown how complex the hydrogen productions are, because there are a lot of energetic and material requirements and discharges.

For steam methane reforming, it is necessary to have

- a combustion in the reformer: it can take place when a proper oxidizer is provided together with the final fuel;
- a heating of the steam and methane mixture before its inlet into the reformer;
- steam for the reforming reaction and for the fuel purification;
- some mechanical energy requirements.

But the production process also releases material and energetic flows, which can be profitably used. For example, the fuel at the reformer exit is at high temperature (about 700°C), while the first shift reaction takes place at lower temperature (about 400°C). This heat, at quite high temperature, could be used to heat the mixture of steam-methane before reformer inlet (this heat can be enough to reach mixture temperature, if steam is extracted from steam turbines during the expansion at a proper pressure). Moreover, the shift reactions are slightly exothermic.

So, it is very important to choose the best integration between the power plants, analyzed here, and the hydrogen production plant.

First of all, exhaust gases, at the last gas turbine exit, can be used in the reformer as an oxidizer: in fact they contain enough oxygen to do the combustion and they are also rather hot. So, they

Table 3 Mass balance in steam methane reforming section

Stream properties				% by volume						
Point	T (°C)	p (bar)	m (kg/kg_{CH4})	CH_4	CO	CO_2	H_2	H_2O	N_2	O_2
1	15	40	1.0	100	0.0	0.0	0.0	0.0	0.0	0.0
2	15	1.5	3.10	0.0	0.0	0.0	0.0	100	0.0	0.0
3	700	1.28	4.10	0.88	16.80	0.0	50.39	31.93	0.0	0.0
4	400	1.22	4.10	0.88	16.80	0.0	50.39	31.93	0.0	0.0
5	200	1.20	4.10	0.88	0.67	16.13	66.52	15.80	0.0	0.0
6	60	1.15	4.10	0.88	0.67	16.13	66.52	15.80	0.0	0.0
7	35	1.09	3.409	1.0	0.76	18.25	74.70	5.29	0.0	0.0
8	35	1.04	1.152	1.19	0.91	2.18	89.06	6.67	0.0	0.0
9	142	80	2.257	0.0	0.0	100	0.0	0.0	0.0	0.0

Mechanical energy requirements:	$W_{CO2\_RS}+W_{CO2\_LS}$	1038 kJ/kg_{ng}
	$Q_{ng}+Q_{SH}$	12.77 MJ/kg_{ng}
Thermal energy requirements:	Q_{CO2_RS}	6.21 MJ/kg_{ng}
Thermal energy discharge:	$Q_1+Q_2+Q_3$	7.58 MJ/kg_{ng}

Table 4 Mass balance in methane partial oxidation section

Stream properties				% by volume						
Point	T (°C)	p (bar)	m (kg/kg$_{ng}$)	CH_4	CO	CO_2	H_2	H_2O	N_2	O_2
1	15	1.013	5.239	0.0	0.0	0.0	0.0	0.0	79.0	21.0
2	15	40.0	1.000	0.0	0.0	0.0	0.0	100.0	0.0	0.0
3	980	15.0	7.239	0.05	11.53	3.93	29.44	16.01	39.04	0.0
4	400	14.7	7.239	0.05	11.53	3.93	29.44	16.01	39.04	0.0
5	200	14.4	7.239	0.05	0.57	14.88	40.40	5.06	39.04	0.0
6	90	14.1	7.239	0.05	0.57	14.88	40.40	5.06	39.04	0.0
7	35	13.8	6.925	0.05	0.60	15.62	42.37	0.40	40.96	0.0
8	35	13.6	4.722	0.06	0.70	1.82	49.32	0.47	47.63	0.0
9	145	80	2.203	0.0	0.0	100.0	0.0	0.0	0.0	0.0

Mechanical energy requirements: $W_{POX}+W_{CO2\_RS}+W_{CO2\_LS}$ 2.45 MJ/kg$_{ng}$
Thermal energy requirements: $Q_{ng}+Q_{SH}$ 5.18 MJ/kg$_{ng}$
Q_{CO2_RS} 6.06 MJ/kg$_{ng}$
Thermal energy discharge: $Q_1+Q_2+Q_3$ 10.25 MJ/kg$_{ng}$

enter into the reformer and then into the HRSG: compared to the previous schemes, there is a new component before the HRSG. The fuel, used to drive the reforming reaction, is the hydrogen-rich fuel gas, obtained at the exit of the hydrogen production plant; a part of this fuel goes into the combustion chambers of the power plants and the remaining part goes into the reformer. In order to limit the maximum temperature of the catalyst bed, we have assumed to do three supplementary firing operations, and heat exchange takes place when the combustion products (which are only a part of the working fluid) cool themselves from 800°C down to 700°C. During the last cooling, instead, the gaseous stream cools until a temperature of about 600°C. These combustion products are then mixed with the exhaust gases at the exit of the last gas turbine and next all exhaust gases enter into the HRSG.

Steam, used for the reforming, is provided by the steam section of the CC and AMC: it is extracted at the pressure required by the CO_2 removal plant (we have assumed that there is only one extraction). This steam for the reforming reaction is then laminated to the atmospheric pressure and mixed with natural gas. This mixture, after heating, enters into the reformer.

The steam for the solvent stripping is extracted from the power plant steam sections at about 4 bars. The return condensate goes into the drum of HRSG together with preheated water, which must replace the steam used during the reforming. For this reason, heat released during the second syngas cooling, Q_3, is used to heat water from environmental condition up to return condensate condition.

In Figs. 7 and 8 the CC and AMC plant schemes, integrated with the H_2 production plant, based on steam methane reforming, are shown. By choosing the working parameters that maximize the power plant efficiency, it is possible to evaluate the overall performance of the CC and AMC power plants equipped with hydrogen production plant. In Figs. 7 and 8 it is possible to note the quantification of the main mass and energy integrations; Tables 5 and 6 show the most important output parameters. It is important to point out that all results are referred to the unitary mass at the compressor inlet (for both the power plants).

The good integration between the power plants, analyzed here, and H_2 production plant, based on steam-methane reforming, allows a limited consumption of hydrogen-rich fuel in the reformer. In the CC and AMC power plants over 20% and 12%, respectively, of produced hydrogen rich fuel are used to provide heat in the reformer. About CO_2 emission, it is 0.0806 and 0.0748 kg/kWh in CC and in AMC, respectively. (We must remember that, even if we have assumed a removal efficiency of 90% after the shift reactions, in the hydrogen-rich fuel gas there is some unconverted CH_4 and CO, which become oxidized in the combustion of the power plant and the reformer.)

When the AMC power plant is integrated with a steam methane reforming section, its overall performance is very interesting: an efficiency of over 47% (about 3.5 percentage points higher than CC efficiency) and a CO_2 emission of about 0.0748 kg/kWh. It is clear that the efficiency drop depends on the mass requirement of the hydrogen production plant (that is, the steam extracted for the reactor and the CO_2 stripping) as well as on the hydrogen consumption in the reformer. For the first consideration, we have seen that the hydrogen production requires a large quantity of steam and this bled steam involves a higher efficiency penalty in CC than in AMC. The explanation is the following: in the AMC

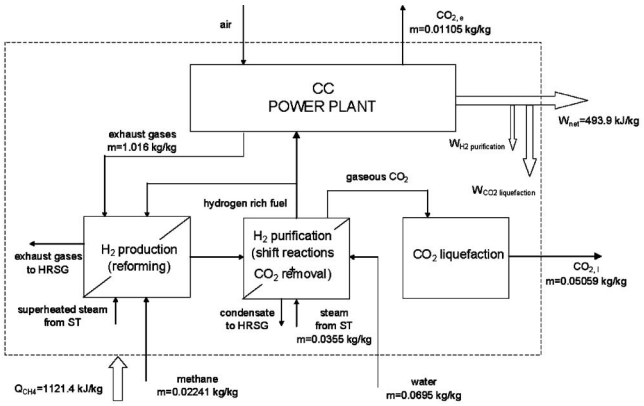

Fig. 7 CC power plant integrated with H_2 production plant (steam methane reforming)

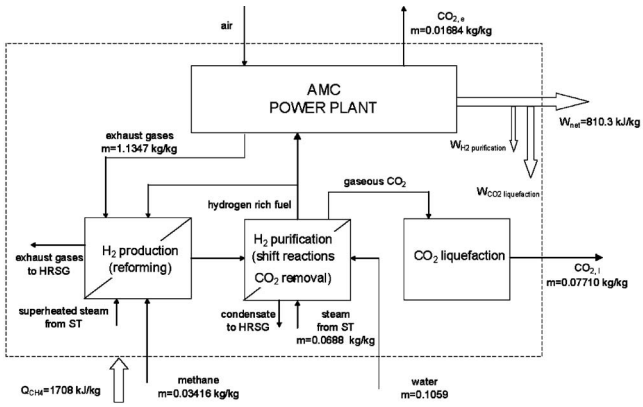

Fig. 8 AMC power plant integrated with H_2 production plant (steam methane reforming)

Table 5 CC mass and energy balance and overall performance (steam methane reforming)

CC power plant work balance (kJ/kg)	H_2 production plant works (kJ/kg)
W_{ST} 161.7	W_{CO2_RS} 5.56
W_T 811.7	W_{CO2_LS} 17.71
W_C 401.1	Total electric requirement 23.27
W_{syn} 47.52	
	Fuel mass (kg/kg)
Net work output 516.9	m_{fuel_cc} 0.02043
CC power plant heat balance (kJ/kg)	m_{fuel_ref} 0.00539
inlet	m_{CH4} 0.0224
	Fuel heat (kJ/kg)
Q_a 294.5	Q_{CH4} (LHV) (at the global plant inlet) 1121.4
Q_{fuel}(HHV) 1628	
outlet	CO_2 emission (kg/kg)
$Q_{HRSG+COND}$ 807.5	m_{CO2} (produced) 0.06164
QREF 288.9	m_{CO2} (liquefied) 0.05059
Q_{CO2} 255.5	m_{CO2} (e_CC) 0.01105
Q_{losses} 53.8	
Overall performance	
Overall efficiency (%) 44.02	
Specific CO_2 emission (kg/kWh) 0.0806	

power plant the bled steam reduces the work of gas turbine, owing to the reduction of injected steam, but this work reduction is partly recovered by a backpressure reduction of the steam turbine (from 30 to about 4-5 bars, related to the pressure of the steam feeding the stripper reboiler). In the CC power plant, instead, the bled steam involves an important work decrease of the low-pressure steam turbine, which nearly becomes a backpressure steam turbine.

For the methane partial oxidation, we want to show the best power plant performance, attained when all the possible heat, discharged by the hydrogen production plant, is profitably used. By studying the temperature profiles of heating and cooling, it is possible to come to these conclusions:

Table 6 AMC mass and energy balance and overall performance (steam methane reforming)

AMC power plant work balance (kJ/kg)	H_2 production plant works (kJ/kg)
W_{ST} 190.4	W_{CO2_RS} 8.47
W_{HPT} 668.3	W_{CO2_LS} 26.99
W_{MPT} 671.0	Total electric requirement 35.46
W_C 574.3	
W_{syn} 86.17	Fuel mass (kg/kg)
W_{aux} 10.51	m_{fuel_cc} 0.03447
Net work output 845.8	m_{fuel_ref} 0.00488
	m_{CH4} 0.03416
AMC power plant heat balance (kJ/kg)	
inlet	fuel heat (kJ/kg)
Q_a 294.6	Q_{CH4} (LHV) (at the global plant inlet) 1708
Q_{fuel}(HHV) 2482	
outlet	CO_2 emission (kg/kg)
$Q_{HRSG+SEP}$ 1076	m_{CO2} (produced) 0.09394
QREF 440.2	m_{CO2} (liquefied) 0.07710
Q_{CO2} 334.8	m_{CO2} (e_AMC) 0.01684
Q_{losses} 79.8	
Overall performance	
Overall efficiency (%) 47.45	
Specific CO_2 emission (kg/kWh) 0.0748	

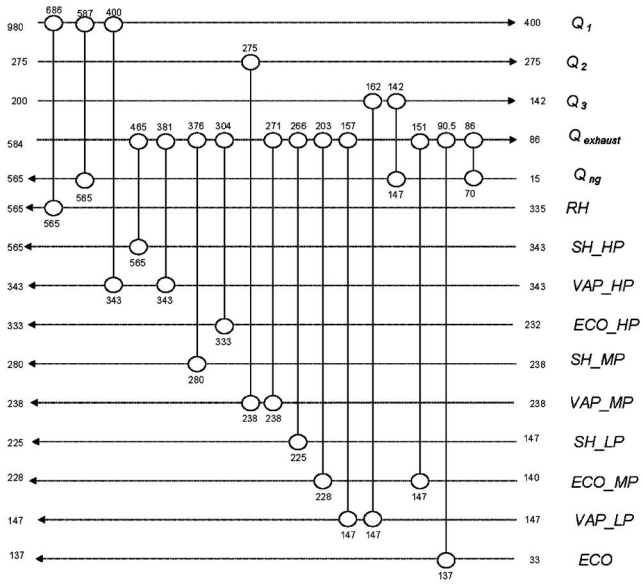

Fig. 9 Heat exchanger network (CC)

- All heat loads (Q_1, Q_2, Q_3) of the production plant can be put in the thermodynamic cycle in order to increase steam production.
- Steam, for the reactor and the CO_2 removal plant, is extracted at the suitable pressures from the steam turbines.

This analysis [12] was developed by using the calculation model SuperTarget6, which performs the pinch technology [13]. This technology, which is based on thermodynamic principles, especially the second one [13,14], provides the best design of heat exchanger networks. In fact, reference power plant performance is better if heat, discharged by the production plant, is usefully exploited in the power section for increasing the net work cycle output. Pinch technology, which is a method able to match hot and cold streams, was applied in order to define an efficient heat exchanger network [12].

The optimal heat exchanger network designs are shown in Figs. 9 and 10 for the CC and the AMC, respectively. Every horizontal line is a stream: the hot streams go from left to right, while the cold ones go from right to left. At the end of every line there are the initial and final temperatures (target temperatures). The verti-

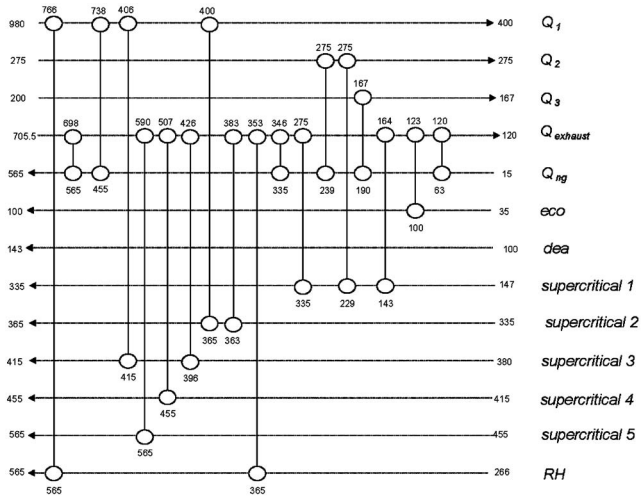

Fig. 10 Heat exchanger network (AMC)

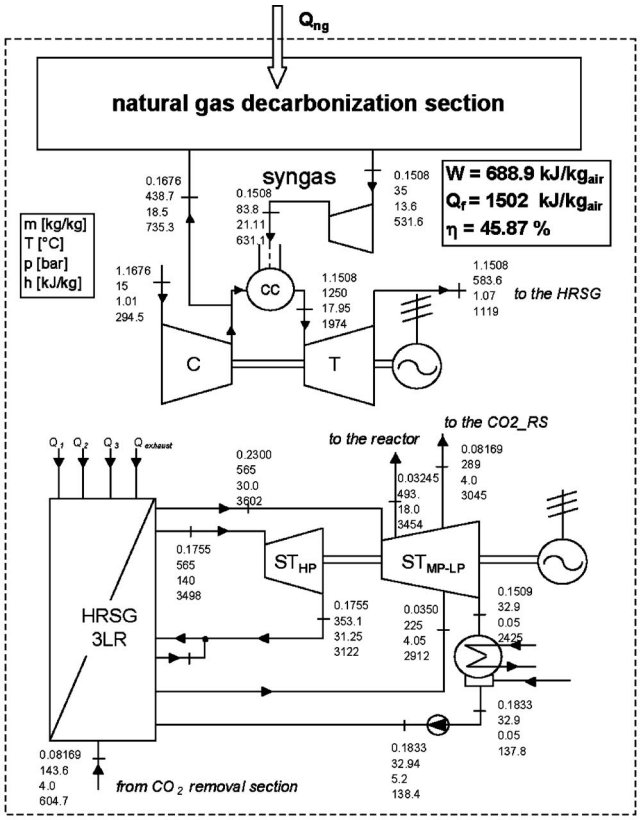

Fig. 11 Heat and mass balances (CC)

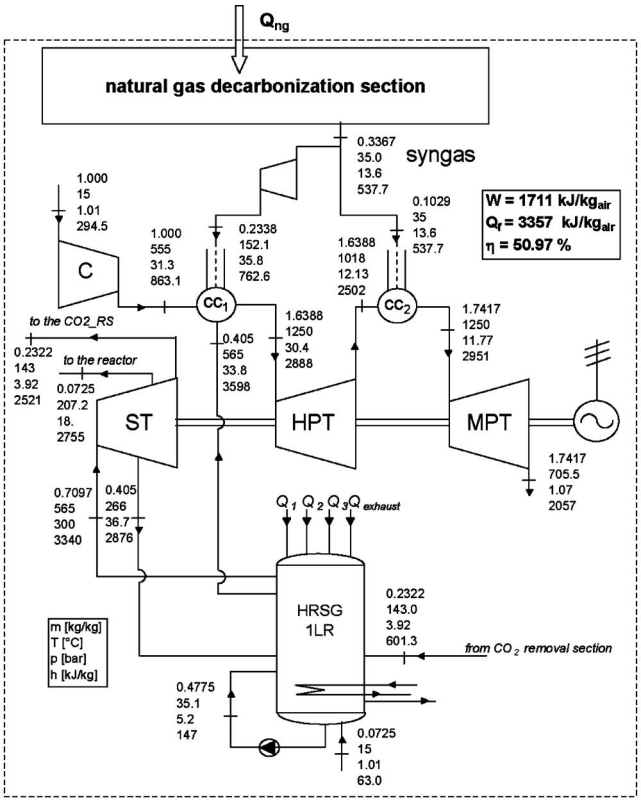

Fig. 12 Heat and mass balances (AMC)

cal segments are the heat exchangers: on the upper circle there is the temperature of the hot stream at the heat exchanger exit, while on the lower circle there is the temperature of the cold stream at the heat exchanger exit.

The steam production in the AMC is subdivided in five parts in order to take into account the real trend of the enthalpy as a function of the temperature. It is clear that such integration is quite complex and implies many heat exchangers, but all these possible schemes must be investigated because they permit us to use fossil fuel in a very clean mode.

In conclusion, it is possible to show the mass and heat balances (Figs. 11 and 12) and the overall performance (Tables 7 and 8) of this new integration.

Also in this case, it is interesting to note that, while the two power plants, without a H_2 production plant, attain similar efficiency levels, the AMC power plant attains an efficiency (about 51%) about 5 points higher than CC (about 46%), when it is integrated with the H_2 production plant. The total efficiency drop, due to H_2 production, is of about 10 percentage points for CC and over 5 percentage points for AMC. The causes, as in the previous case, must be investigated in the energy interaction between the two power plants and the H_2 production plant. Also in this case, the efficiency drop depends on the mass requirement of the hydrogen production plant (that is, the steam extracted for the reactor and the CO_2 stripping). Now the first extraction is at about 18 bars (for the reactor), while the second one is at about 4 bars (for the solvent regeneration).

Therefore, the difference in efficiency drop between the two power plants is larger: in fact the large quantity of steam extracted at high pressure penalize the CC performance while for the AMC, even if there is less steam injected in the first combustion chamber, there is a partial recovery of the work reduction because the steam for the reactor expands further (from 30 to 18 bars) as well as the steam for the solvent regeneration (from 30 to 4 bars).

Moreover, in this case the hydrogen rich fuel produced is used only in the power sections because partial oxidation is not an endothermic reaction.

5 Technical and Economic Performance

Table 9 reports the most important performance parameters (net specific work and overall efficiency), specific rate of CO_2 removed, and the final specific emission rate of carbon dioxide.

When natural gas is decarbonized, before its use in the combustion chambers of the reference power plants, there is a substantial penalty of overall efficiency; the CC-SMR is the most penalized scheme: the work output decreases by about 19% and the efficiency is over 12 percentage points lower. Moreover, the CC-SMR is the power plant with the major CO_2 emission. This plant solution exhibits a substantial decrease in its performance because the steam methane reforming is an endothermic reaction (that is,

Table 7 Overall performance (CC)

Power section work balance (kJ/kg_{air})		Production section required work (kJ/kg_{air})	
		$W_{CO2\_RS+CO2\_LS}$	10.12
W_{C_GT}	445.2	$W_{air\_compr\_POX}$	68.9
W_{syn_GT}	14.2	W_{aux}	79.02
W_{T_GT}	973.9	Fuel heat input (kJ/kg_{air})	
W_{p_SC}	4.8	Q_{fuel}	1502
W_{T_SC}	269.7	CO_2 emission (kg/kg_{air})	
$W_{power\ section}$	767.8	m_{CO2} (produced)	0.0834
		m_{CO2} (liquefied)	0.0725
		m_{CO2} (e_CC)	0.0110
Overall performance			
Net work (kJ/kg_{air})	688.8		
Overall efficiency (%)	45.86		
Specific CO_2 emission (kg/kWh)	0.0573		

Table 8 Overview performance (AMC)

Power section work balance (kJ/kg_{air})	Production section required work (kJ/kg_{air})
	$W_{CO2\_RP+CO2\_LS}$ 22.62
W_{ST} 401.3	$W_{air\_compr\ (POX)}$ 153.1
W_{HPT} 626.7	W_{aux} 175.7
W_{MPT} 1542	Fuel heat input (kJ/kg_{air})
W_C 574.4	Q_{fuel} 3357
W_{aux} 79.8	CO_2 emission (kg/kg_{air})
$W_{power\ section}$ 1887	m_{CO2} (produced) 0.1864
	m_{CO2} (liquefied) 0.1619
	m_{CO2} (e_CC) 0.0245
Overall performance	
Net work (kJ/kg_{air}) 1711	
Overall efficiency (%) 50.98	
Specific CO_2 emission (kg/kWh) 0.0515	

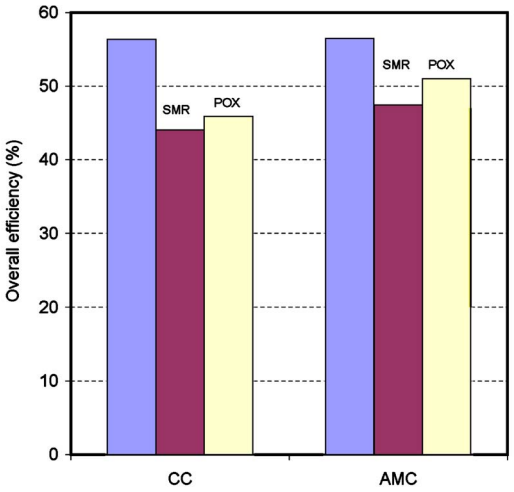

Fig. 13 The overall efficiency

some of the hydrogen, produced in the H_2 production plant, must be used to drive this reaction) and it requires a large amount of steam (both for the reforming reaction and for the purification of the syngas produced in the reformer). As the AMC-SMR is better coupled with the hydrogen production plant (the steam extraction is less penalizing), its performance is better than the CC-SMR: even if the net work output decreases by over 30% (we must remember that the net specific work is referred to the unitary mass of air at the compressor inlet), the efficiency is about 9 percentage points lower (versus 12 percentage points of the previous case).

For the second natural gas decarbonization technology (POX), the penalizations are less significant: the net specific work increases because there is additional heat (Q_1, Q_2, Q_3) that can be profitably used in the cycle, while the net efficiency is reduced between 5.5 and 10.5 percentage points. On the whole, the AMC-POX stands out because it exhibits the highest net efficiency and the lowest final specific CO_2 emission. This performance is possible because this scheme can be suitably integrated with natural gas decarbonization technology, based on methane partial oxidation, as explained above.

Finally, Figs. 13 and 14 show the penalization in efficiency level and the corresponding reduction of the CO_2 in all the power plants, analyzed here, as function of the decarbonization technologies.

To complete the evaluation of these power plants, a preliminary economic analysis has been carried out. Investment costs have been estimated by following the indications and trends reported in the literature [8,15–20].

More precisely, the CC investment cost has been elaborated by following these indications. Also the AMC investment cost has been elaborated in accordance with the same data, but with some additional hypotheses; in the AMC we have a gas reheat turbine with a high steam injection and for this reason its cost is assumed to be 50% higher than the cost of a standard turbine. The "steam cycle" (that is, high pressure steam turbine and a simple HRSG at one pressure level and RH) has also been considered as a conventional bottoming cycle: in fact, in this plant configuration, steam condensation from a gas/steam mixture is absolutely necessary, but involves some plant layout implications. Therefore, the steam cycle in the AMC is simpler than the one in the CC, but the same investment costs have been taken into consideration because of the presence of an unconventional component (the separator).

For the additional components for the natural gas decarbonization, we have adopted very rough hypotheses because technical works do not offer the same data, especially regarding the reformer. However, we have considered the two reactors (for the steam methane reforming and for the partial oxidation of the methane), the shift reactors, and the components for the syngas cooling, and finally the CO_2 removal section and CO_2 liquefaction section with all their equipment. When hydrogen-rich fuel is used in the combustion chambers, the syngas compressors must be taken into account.

Total investment costs were then obtained by a 30-fold increase in the component costs; this percentage considers the following aliquots: the balance of the plant 12%, engineering costs 8%, and contingencies 10%.

After defining investment costs, it is possible to estimate the cost of the electricity produced. In this cost, three aliquots have been envisaged:

- depreciation,
- fuel,
- operation and maintenance.

Table 9 Overall performance (AMC)

	W (kJ/kg)	η %	$CO_{2\ removed}$ (kg/kWh)	$CO_{2\ emission}$ (kg/kWh)
CC	607.9	56.35	0	0.3513
AMC	1229	56.48	0	0.3504
CC - SMR	493.9	44.02	0.3689	0.0806
AMC - SMR	855.8	47.45	0.3407	0.0748
CC - POX	688.9	45.86	0.3787	0.0573
AMC - POX	1711	50.98	0.3406	0.0515

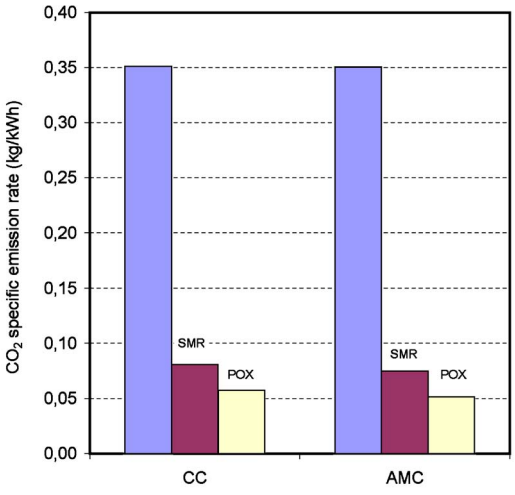

Fig. 14 The CO_2 specific emission rate

Table 10 Overview of the costs

	CC	AMC	CC-SMR	AMC-SMR	CC-POX	AMC-POX
Capital costs ($/kW)						
Power plant	540	620	690	910	650	870
Syngas production (SMR/POX)	0	0	120	110	140	125
Shift reactors and syngas cooling	0	0	40	40	40	35
Syngas purification section	0	0	60	50	65	58
CO_2 liquefaction section	0	0	10	10	2	2
Total capital cost	540	620	920	1120	897	1090
Annualized costs ($/kW*yr)						
Capital charges power plant	68.85	79.05	87.98	116.0	82.88	110.9
Capital charges H_2 production plant	0	0	29.33	26.78	31.49	28.05
O&M costs power plant	21.60	24.80	27.60	36.40	26.00	34.80
O&M costs H_2 production plant	0	0	9.20	8.40	9.88	8.80
Fuel feedstock	178.8	178.4	228.8	212.3	219.7	197.6
Total annualized costs	269.2	282.2	382.9	399.9	369.9	380.2
Electricity production cost (m/kWh)	38.46	40.31	54.71	57.13	52.84	54.31

For our calculations some assumptions have been made: a discount rate of 12% was taken and depreciation over 25 years to quantify capital charges of the power plants. With regards to fuel, an assumed natural gas price of $0.20 per kg was used. These costs are meant to represent the average trends on the European market. The operation and maintenance (O&M) costs were set at a fixed percentage of the investment cost (exactly 4.0). Finally, all the power plants analyzed were assumed to operate for 7000 hours per year.

For the size of the power plants analyzed here, we have chosen a base size of 240 MW for the gas turbine of the CC, while for the AMC we have considered the same total size of the CC: we have taken into account the different size of the reheat gas turbine with steam injection by adopting a 50% higher cost than the cost of a standard turbine. When decarbonization technologies are evaluated, we have considered a fuel thermal input (based on natural gas) of 800 MW. In this case in order to take into account the gas turbine remakes, we have increased the cost of a standard gas turbine cost by 20%.

Table 10 shows the results of the economic analysis, but it is necessary to remember that the absolute values do not inspire much confidence, considering the uncertainties of our analysis. It is important, however, to perform comparisons between the power plants and to evaluate the increase in the cost of electricity by considering that all these systems with respect to the same economic assumptions.

Figure 15 shows the cost of kWh in each scheme, while Fig. 16 reports the percentage increase in the electricity production costs.

For capital costs, we can see that, in the schemes based on CC power plants, the additional costs for natural gas decarbonization are a higher fraction in comparison with schemes based on AMC power plants. In fact, the costs of these unconventional components are added to the cost of a conventional plant solution and the final result is a fraction of about 25–27% of the total capital costs (more precisely 25% in the SMR and over 27% in the POX). The same additional costs have a different influence on the total capital costs of the AMC power plants: the fraction is about 19% for the SMR and 20% for the POX.

Fuel costs are higher when the overall efficiencies are lower, so these aliquots are higher in the SMR than those in the POX. The CC-SMR shows the highest fuel cost.

Finally, the power plants, coupled with the natural gas decarbonization technology based on steam reforming, exhibit the highest cost of kWh: this result depends on the high total capital costs of these solutions as well as on their low technical performance. If we compare CC-SMR and AMC-SMR with the same schemes but without the decarbonization section, we find an increase of the electricity production cost of over 40% (42.2% for the CC and 41.7% for the AMC).

The natural gas decarbonization, based on partial oxidation, shows important potentialities also in economic terms: the increase of the electricity production cost is lower than that of the previous case: 37.4% for the CC and 34.7% for the AMC. This result depends on the higher overall efficiencies attained. Thus, it is evident that the power plants coupled with decarbonization technology based on steam partial oxidation attain an economic performance higher than that of the same power plants but coupled with decarbonization technology based on steam methane reforming.

Although our economic calculations contain many uncertainties, the AMC seems to be the best solution both in technical performance and in economic aspects. The good energy integration between the power plant and the hydrogen production section allows the lowest efficiency decrease and the lowest electricity cost increase. So, even if the AMC is not a technological reality compared with the other conventional solution (CC), its high performance makes this power plant, in our opinion, noteworthy when it is necessary to reduce CO_2 emissions with high conversion efficiency levels and low economic impact on the electricity production cost.

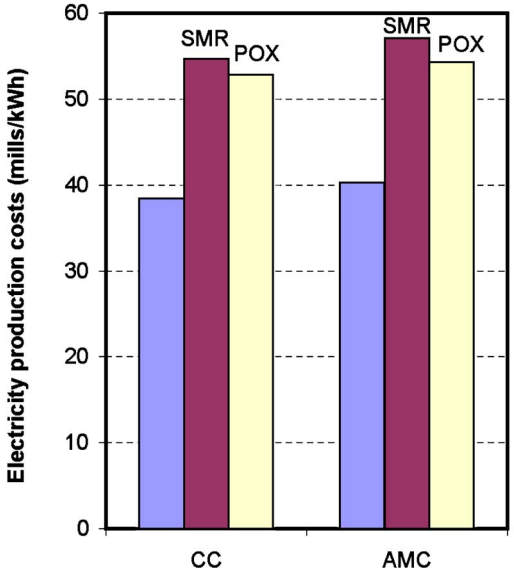

Fig. 15 Electricity production costs

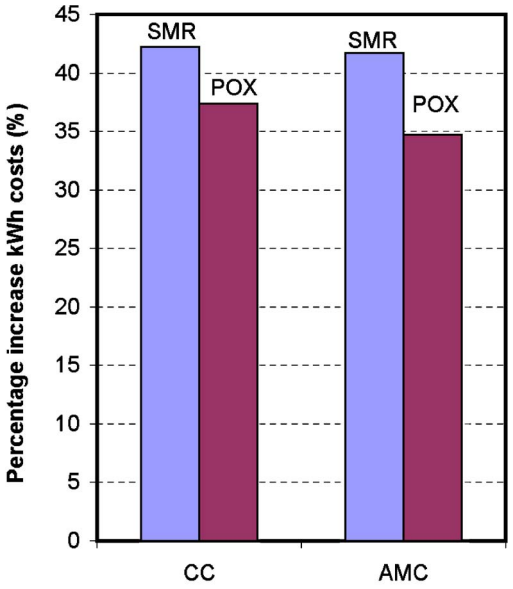

Fig. 16 The electricity production cost increase

6 Conclusions

This paper has analyzed the thermodynamic performance and the economic aspects of advanced power plants and compared the results in terms of energy efficiency, emission of CO_2, and electricity production cost. Among the different solutions analyzed here, there is a new advanced mixed cycle (AMC) proposed by the authors: it attains interesting performance with respect to the CO_2 emission abatement and to the electricity production cost when it is integrated with the decarbonization technology based on partial oxidation of the methane. It is able to achieve very limited CO_2 emissions (0.0515 kg/kWh) by converting thermal power from natural gas to electric power at an efficiency level of about 51% and increasing electricity production cost by about 35%. The second reference plant (CC), coupled with the partial oxidation of methane, has lower overall performance: a specific carbon dioxide emission of 0.0573 kg/kWh, a net efficiency of 45.9%, and a kWh cost increase of 37.4%.

With regard to the second decarbonization technology (steam methane reforming process), the efficiency penalization is 12.3 percentage points for the CC and 9.0 for the AMC.

The thermodynamic reasons for these results are amply discussed in the paper.

Regarding economic aspects, although the calculations may contain many uncertainties, all the power plants analyzed here respect the same assumptions and hypotheses so that the comparisons performed are significant. Results show that the increase of electricity production cost is variable: the first decarbonization technology, based on steam methane reforming, shows the highest increase (42.2% for the CC and 41.7% for the AMC), while the second decarbonization technology, based on partial oxidation of methane, shows a lower increase (37.4% for the CC and 34.7% for the AMC).

These results confirm that partial oxidation of natural gas could have great potential in terms of both high performance and low atmospheric impact.

Finally, we can conclude that these two power plants can be coupled to a decarbonization technology in order to reduce the specific CO_2 emissions drastically. The AMC-POX shows the best thermodynamic and economic performance. Thus, even if the AMC is not a technological reality compared with the other conventional solution (CC), its high performance makes this power plant, in our opinion, noteworthy when it is necessary to reduce CO_2 emissions with high conversion efficiency levels and low economic impact on the electricity production cost.

Nomenclature

η	=	efficiency
1LR	=	one level pressure and reheat
3LR	=	three level pressure and reheat
a	=	air
AMC	=	advanced mixed cycle
aux	=	auxiliaries
C	=	compressor
CC	=	combined cycle
cc	=	combustion chamber
CO_2_LS	=	CO_2 liquefaction section
CO_2_RS	=	CO_2 removal section
COND	=	condenser
GT	=	gas turbine
HHV	=	higher heating value
HP	=	high pressure
HPT	=	high-pressure turbine
HRSG	=	heat recovery steam generator
LHV	=	lower heating value
LP	=	low pressure
MP	=	intermediate pressure
MPT	=	intermediate pressure turbine
ng	=	natural gas
p	=	pump
POX	=	partial oxidation
Q	=	heat transfer interaction (kJ/kg)
REF	=	reforming
RH	=	re-superheating
SC	=	steam cycle
SEP	=	separator
SH	=	superheating
SMR	=	steam methane reforming
ST	=	steam turbine
syn	=	syngas
T	=	turbine
W	=	specific work (kJ/kg)

References

[1] Caputo, C., Gambini, M., and Guizzi, G. L., 1997, "Internal Combustion Steam Cycle (G.I.ST. Cycle): Thermodynamical Feasibility and Plant Lay-Out Proposals," International Conference ASME ASIA 97, Singapore, ASME Paper No. 97-AA-134.

[2] Gambini, M., and Guizzi, G. L., 1997, "Parametric Analysis on a New Hybrid Power Plant Based on Internal Combustion Steam Cycle (GIST Cycle)," *Proc. of FLOWERS'97, Florence World Energy Research Symposium*, Florence, Italy, July 30–August 1, pp. 55–64.

[3] Gambini, M., Guizzi, G. L., and Vellini, M., 1997, "Calculation Model for Unconventional Components of GIST Cycles" (in Italian)," *Proc. of 9th National Conference "Tecnologie e Sistemi Energetici Complessi*," Milan, Italy, June 26–27, pp. 495–509.

[4] Steinberg, M., 1999, "Fossil Fuel Decarbonization Technology for Mitigating Global Warming," Int. J. Hydrogen Energy, **24**, pp. 771–777.

[5] Kaarstad, O., and Audus, H., 1997, "Hydrogen and Electricity From Decarbonised Fossil Fuels," Energy Convers. Manage., **28**, pp. S431–S436.

[6] Gaudernack, B., and Lynum, S., 1998, "Hydrogen From Natural Gas Without Release of CO_2 to the Atmosphere," Int. J. Hydrogen Energy, **23**, pp. 1087–1093.

[7] Zhu, J., Zhang, D., and King, K. D., 2001, "Reforming of CH4 by Partial Oxidation: Thermodynamic and Kinetic Analyses," Fuel, **80**, pp. 899–905.

[8] Lozza, G., and Chiesa, P., 2000, "Natural Gas Decarbonization to Reduce CO_2 Emission From Combined Cycles. Part B: Steam-Methane Reforming," *Proceedings of ASME TURBO EXPO 2000*, Munich, Germany, May 8–11, ASME Paper No. 2000-GT-0164.

[9] Lozza, G., and Chiesa, P., 2000, "Natural Gas Decarbonization to Reduce CO_2 Emission From Combined Cycles. Part a A: Partial Oxidation," *Proceedings of ASME TURBO EXPO 2000*, Munich, Germany, May 8–11, ASME Paper No. 2000-GT-0163.

[10] Audus, H., and Freund, P., 1999, "Reduction of CO_2 Emissions by Decarbonisation of Natural Gas," *Proceedings of Power-Gen '99*, Messe Frankfurt, Germany, June 1–3.

[11] Freund, P., and Thambimuthu, K. V., 1999, "Options for Decarbonising Fossil

Energy Supplies," *Proceedings of Combustion Canada '99*, Calgary, Alberta, Canada, May 26–28.
[12] Gambini, M., and Vellini, M., 2006, "Performance Optimization of Advanced H_2/Air Cycle Power Plants based on Natural Gas Partial Oxidation," *Proceedings of ASME Turbo Expo 2006*, Barcelona, Spain, May 8–11, ASME Paper No. GT2006-90871.
[13] Linnhoff, M., 1998, "Introduction to Pinch Technology," available from Linnhoff March Ltd, UK.
[14] Gundersen, T., 2002, "A Process Integration PRIMER," SINTEF Energy Research.
[15] Hendriks, C. A., Blok, K., and Turkenburg, W. C., 1989, "The Recovery of Carbon Dioxide From Power Plants," in *Climate and Energy*, P. A. Okken, R., J. Swart, S. Zwerver, Eds, Kluwer, Dordrecht, The Netherlands.
[16] Hendriks, C. A., Blok, K., and Turkenburg, W. C., 1991, "Technology and Cost of Recovering and Storing Carbon Dioxide From an Integrated-Gasifier, Combined-Cycle Plant," Energy, **16**(11/12), pp. 1277–1293.
[17] Langeland, K., and Wilhelmsen, K., 1993, "A Study of the Costs and Energy Requirement for Carbon Dioxide Disposal," Energy Convers. Manage., **34**(9/11), pp. 807–814.
[18] Audus, H., Kaarstad, O., and Skinne, G., 1998, "CO_2 Capture by Precombustion Decarbonization of Natural Gas," *Proc. of 4th International Conference on Greehouse Gas Control Technologies*, Interlaken, CH, August 30–September 2.
[19] Savoldelli, P., 2000, "Evaluation of CO_2 Emission Reduction Processes by Using Fuel or Air Treatment," Research Report EMICO/GEN02/008, CESI (in Italian).
[20] Narula, R. G., Wen, H., and Himes, K., 2001, "Economics of Greenhouse Gas Reduction—The Power Generation Technology Options," *Proc. of 18th Congress World Energy Council*, Buenos Aires, Argentina, October 21–25.

H.-J. Kretzschmar
Department of Technical Thermodynamics,
Zittau/Goerlitz University of Applied Sciences,
P.O. Box 1455,
D-02754 Zittau, Germany
e-mail: hj.kretzschmar@hs-zigr.de

J. R. Cooper
Department of Engineering,
Queen Mary, University of London,
London, UK

J. S. Gallagher
Physical and Chemical Properties Division,
National Institute of Standards and Technology,
Gaithersburg, MD

A. H. Harvey
Physical and Chemical Properties Division,
National Institute of Standards and Technology,
Boulder, CO

K. Knobloch
Department of Technical Thermodynamics,
Zittau/Goerlitz University of Applied Sciences,
P.O. Box 1455,
D-02754 Zittau, Germany

R. Mareš
Department of Thermodynamics,
University of West Bohemia,
Plzeň, Czech Republic

K. Miyagawa
Tokyo, Japan

N. Okita
Thermal Plant Systems Project Department,
Toshiba Corporation,
Yokohama, Japan

R. Span
Department of Thermodynamics,
Ruhr-University of Bochum,
Bochum, Germany

I. Stöcker
Department of Technical Thermodynamics,
Zittau/Goerlitz University of Applied Sciences,
P.O. Box 1455,
D-02754 Zittau, Germany

W. Wagner
Department of Thermodynamics,
Ruhr-University of Bochum,
Bochum, Germany

I. Weber
Power Generation,
Siemens AG,
Erlangen, Germany

Supplementary Backward Equations $p(h,s)$ for the Critical and Supercritical Regions (Region 3), and Equations for the Two-Phase Region and Region Boundaries of the IAPWS Industrial Formulation 1997 for the Thermodynamic Properties of Water and Steam

When steam power cycles are modeled, thermodynamic properties as functions of enthalpy and entropy are required in the critical and supercritical regions (region 3 of IAPWS-IF97). With IAPWS-IF97, these calculations require cumbersome two-dimensional iteration of temperature T and specific volume v from specific enthalpy h and specific entropy s. While these calculations are not frequently required, the computing time can be significant. Therefore, the International Association for the Properties of Water and Steam (IAPWS) adopted backward equations for $p(h,s)$ in region 3. For calculating properties as a function of h and s in the part of the two-phase region that is important for steam-turbine calculations, a backward equation $T_{sat}(h,s)$ is provided. In order to avoid time-consuming iteration in determining the region for given values of h and s, equations for the region boundaries were developed. The numerical consistency of the equations documented here is sufficient for most applications in heat-cycle, boiler, and steam-turbine calculations. [DOI: 10.1115/1.2719267]

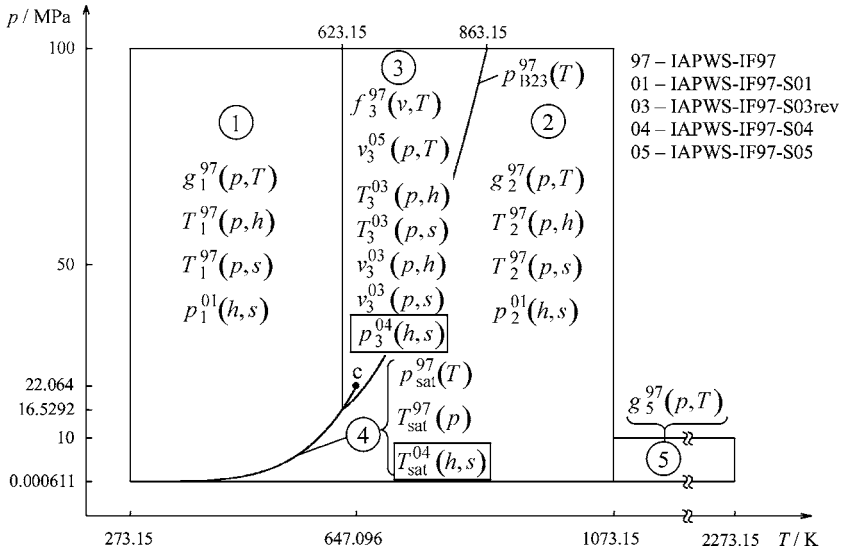

Fig. 1 Regions and equations of IAPWS-IF97, IAPWS-IF97-S01, IAPWS-IF97-S03rev, IAPWS-IF97-S05 and the backward equations $p_3^{04}(h,s)$ and $T_{sat}^{04}(h,s)$ of this work

1 Introduction

The International Association for the Properties of Water and Steam (IAPWS) has adopted the IAPWS Industrial Formulation 1997 for the Thermodynamic Properties of Water and Steam (IAPWS-IF97) [1,2] as the standard for calculation of thermodynamic properties of water and steam in the power industry. It contains basic equations, saturation equations, and equations for the commonly used "backward" functions $T(p,h)$ and $T(p,s)$ valid in the liquid region 1 and the vapor region 2 (see Fig. 1).

In 2001, IAPWS-IF97 was supplemented by "Backward Equations for Pressure as a Function of Enthalpy and Entropy $p(h,s)$ to the IAPWS Industrial Formulation 1997 for the Thermodynamic Properties of Water and Steam" [3,4], referred to here as IAPWS-IF97-S01. These equations are valid in regions 1 and 2 (see Fig. 1).

An additional supplementary release "Backward Equations for the Functions $T(p,h)$, $v(p,h)$ and $T(p,s)$, $v(p,s)$ for Region 3 of the IAPWS Industrial Formulation 1997 for the Thermodynamic Properties of Water and Steam" [5,6], referred to here as IAPWS-IF97-S03rev, was adopted by IAPWS in 2003 and revised in 2004.

In modeling steam power cycles, thermodynamic properties as a function of enthalpy and entropy (h,s) are also required in region 3. With IAPWS-IF97, these calculations require two-dimensional iteration of specific volume v and temperature T using the functions $h(v,T)$ and $s(v,T)$ that can be explicitly calculated from the basic equation of region 3, $f(v,T)$. With v and T, the other properties can be calculated. While these calculations are not frequently required, the relatively large computing time required for two-dimensional iteration can be significant. Therefore, this work provides an explicit calculation of the functions $v(h,s)$ and $T(h,s)$ in region 3. However, test calculations showed that is it not feasible to set up explicit backward equations for these functions that meet the IAPWS requirements for numerical consistency. Therefore, equations for the backward function $p_3(h,s)$ were developed (see Fig. 1). With the pressure p, the temperature can be calculated from the IAPWS-IF97-S03rev equation $T_3^{03}(p,h)$,[1] and the specific volume can be calculated from the IAPWS-IF97-S03rev equation $v_3^{03}(p,s)$.[2]

Thermodynamic properties as a function of h and s are also required for region 4, the two-phase vapor/liquid region (wet steam). These calculations require iteration using the basic equations of the adjacent single-phase regions and the saturation-pressure equation. In order to avoid such iteration, we provide an equation $T_{sat}(h,s)$ for the part of the two-phase region that is important for steam-turbine calculations. With the temperature T, the pressure p can be calculated from the IAPWS-IF97 saturation-pressure equation $p_{sat}^{97}(T)$, and the vapor fraction x can be calculated explicitly by use of the IAPWS-IF97 basic equations. The equation $T_{sat}(h,s)$ is described in Sec. 4.

Since IAPWS now provides explicit equations for independent variables (h,s) in liquid region 1, vapor region 2, critical and supercritical region 3, and the important part of region 4, these functions can be calculated efficiently. However, iteration is necessary to find the region for the given (h,s). In order to avoid such iteration, we provide equations for the region boundaries as functions of h and s. These are described in Sec. 3.

The equations described here were adopted by IAPWS in 2004 as "Supplementary Release on Backward Equations $p(h,s)$ for Region 3, Equations as a Function of h and s for the Region Boundaries, and an Equation $T_{sat}(h,s)$ for Region 4 of the IAPWS Industrial Formulation 1997 for the Thermodynamic Properties of Water and Steam" [7], referred to here as IAPWS-IF97-S04. The purpose of this paper is to fully document IAPWS-IF97-S04.

Figure 1 shows additional backward equations $v_3(p,T)$ for region 3 that were adopted as an additional supplementary release, referred to here as IAPWS-IF97-S05 [8]. These will be documented in a future paper. The entire system of supplementary backward equations adopted by IAPWS is summarized in [9] and described in detail in [10].

Submitted to the ASME for publication in the JOURNAL OF ENGINEERING FOR GAS TURBINES AND POWER. Manuscript received October 18, 2006; final manuscript received January 16, 2007. Review conducted by Dilip R. Ballal.

[1]The alternative use of the IAPWS-IF97-S03rev backward equation $T_3^{03}(p,s)$ leads to worse numerical consistency.

[2]The alternative use of the IAPWS-IF97-S03rev backward equation $v_3^{03}(p,h)$ leads to worse numerical consistency.

2 Backward Functions $p(h,s)$, $T(h,s)$, and $v(h,s)$ for Region 3

2.1 Consistency Requirements. The maximum permissible temperature difference between the backward function $T_3(h,s)$ and the basic equation $f_3^{97}(v,T)$ was set by IAPWS to $|\Delta T|_{tol}=25$ mK and corresponds to that of the backward functions $T_3^{03}(p,h)$ and $T_3^{03}(p,s)$ [11]. The tolerance $|\Delta v/v|_{tol}=0.01\%$ for the backward function $v_3(h,s)$ corresponds to the IAPWS requirement for the backward functions $v_3^{03}(p,h)$ and $v_3^{03}(p,s)$ [5,6].

In order to fulfill the required numerical consistency of the functions $T_3(h,s)$ and $v_3(h,s)$, the maximum relative deviation between the pressure calculated from the backward equation $p_3(h,s)$ and the IAPWS-IF97 basic equation $f_3^{97}(v,T)$ must be smaller than 0.01%.

2.2 Development of the Equations. A major motivation for the development of IAPWS-IF97 and its supplementary backward equations was to reduce the time for computing thermodynamic properties. As shown previously [12], the following functional form is effective for this purpose

$$\frac{Z(X,Y)}{Z^*}=\sum_i n_i\left(\frac{X}{X^*}+a\right)^{I_i}\left(\frac{Y}{Y^*}+b\right)^{J_i} \tag{1}$$

where the reducing parameters Z^*, X^*, and Y^* are maximum values of the corresponding property within the range of validity of the equation. The shifting parameters a and b were determined by nonlinear optimization. The exponents I_i, J_i, and coefficients n_i were determined from the structure optimization method of Wagner [13] and Setzmann and Wagner [14], which chooses the optimal terms from a bank of terms with various values of I_i and J_i. The final equations were developed using the approximation algorithm developed in previous work [15–18].

In the approximation process, the backward equations were fitted to *T-v-p-h* or *T-v-p-s* values, with p, h, and s calculated from the IAPWS-IF97 basic equation $f_3^{97}(v,T)$ for values of v and T distributed over the range of validity. The critical point was set as a constraint. The computing time is considered in the optimization. Details of the fitting processes are given in [15,19].

2.3 Subregions. The equation set consists of backward equations $p(h,s)$ for region 3. Region 3 is defined by

$$623.15\ \text{K}\leqslant T\leqslant 863.15\ \text{K}\quad\text{and}\quad p_{B23}^{97}(T)\leqslant p\leqslant 100\ \text{MPa}$$

where p_{B23}^{97} represents the B23-equation of IAPWS-IF97. The division of region 3 into subregions for the backward equations $p_3(h,s)$ is identical to the division for the previous region 3 backward equations [5,6] (see Fig. 2).

Table 1 shows the decision path to find the correct subregion for the function $p(h,s)$. For pressures less than the critical pressure $p_c=22.064$ MPa [20], the saturation line is the boundary between subregions 3a and 3b. If the specific enthalpy h is less than or equal to $h'_{3a}(s)$, Eq. (5), calculated from the entropy s on the saturated-liquid line, then the point to be calculated is located in subregion 3a. If h is greater than or equal to $h''_{2c3b}(s)$, Eq. (7), calculated on the saturated-vapor line, then the point is located in subregion 3b. Otherwise, the point is in the two-phase region. In this case, the saturation-pressure equation $p_{sat}^{97}(T)$ and the basic equation $f_3^{97}(v,T)$ of IAPWS-IF97 can be used to calculate the pressure from the given enthalpy and entropy.

For pressures greater than or equal to p_c, the boundary between subregions 3a and 3b corresponds to the critical isentrope $s=s_c$ (see Fig. 2). For the function $p(h,s)$, input points can be tested directly to identify the subregion, since the specific entropy is an independent variable. If the specific entropy s is less than or equal to

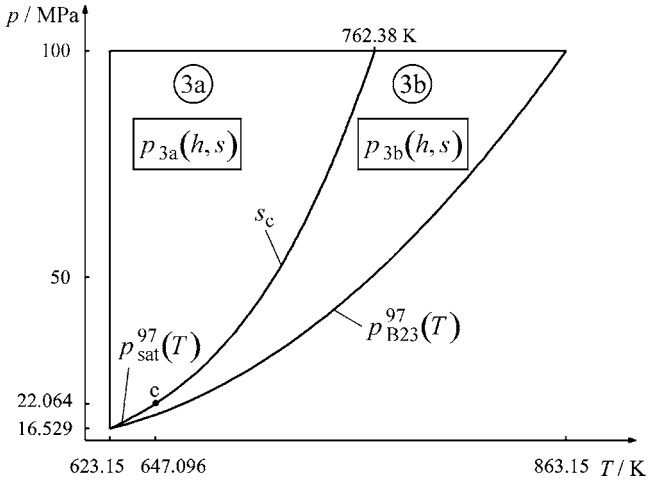

Fig. 2 Division of region 3 into two subregions 3a and 3b for the backward equations $p(h,s)$

$$s_c=4.412\ 021\ 482\ 234\ 76\ \text{kJ kg}^{-1}\ \text{K}^{-1}$$

then the point is located in subregion 3a; otherwise it is in subregion 3b. The critical entropy s_c is given with 15 digits to avoid numerical problems.

2.4 Backward Function $p(h,s)$

2.4.1 The Equations $p(h,s)$. The backward equation $p_{3a}(h,s)$ for subregion 3a has the dimensionless form

$$\frac{p_{3a}(h,s)}{p^*}=\pi(\eta,\sigma)=\sum_{i=1}^{33} n_i(\eta-1.01)^{I_i}(\sigma-0.750)^{J_i} \tag{2}$$

where $\pi=p/p^*$, $\eta=h/h^*$, and $\sigma=s/s^*$, with $p^*=99$ MPa, $h^*=2300$ kJ kg^{-1}, and $s^*=4.4$ kJ kg^{-1} K^{-1}. The coefficients n_i and exponents I_i and J_i of Eq. (2) are listed in Table 2.

$p_{3b}(h,s)$ for subregion 3b has the dimensionless form

$$\frac{p_{3b}(h,s)}{p^*}=\pi(\eta,\sigma)=\left[\sum_{i=1}^{35} n_i(\eta-0.681)^{I_i}(\sigma-0.792)^{J_i}\right]^{-1} \tag{3}$$

where $\pi=p/p^*$, $\eta=h/h^*$, and $\sigma=s/s^*$ with $p^*=16.6$ MPa, $h^*=2800$ kJ kg^{-1}, and $s^*=5.3$ kJ kg^{-1} K^{-1}. The coefficients n_i and exponents I_i and J_i of Eq. (3) are listed in Table 3.

To assist in computer-program verification of Eqs. (2) and (3), Table 4 contains test values for calculated pressures.

2.4.2 Consistency with IAPWS-IF97. The maximum and root-mean-square relative differences between the calculated pressure (Eqs. (2) and (3)) and the IAPWS-IF97 basic equation $f_3^{97}(v,T)$, together with the permissible differences, are listed in Table 5. The maximum deviations are less than the permissible value. The critical pressure is met exactly by $p_3(h,s)$.

2.4.3 Consistency at the Subregion Boundary. The maximum relative difference between the backward equations $p_{3a}(h,s)$, Eq. (2), and $p_{3b}(h,s)$, Eq. (3), along the boundary s_c, is 0.00074%,

Table 1 Criteria for finding the subregion, 3a or 3b, for the backward function $p(h,s)$

	Subregion	
	3a	3b
For $p<p_c$	$h\leqslant h'_{3a}(s)$	$h\geqslant h''_{2c3b}(s)$
For $p\geqslant p_c$	$s\leqslant s_c$	$s>s_c$

Table 2 Coefficients and exponents of the backward equation $p_{3a}(h,s)$, Eq. (2)

i	I_i	J_i	n_i
1	0	0	$0.770\,889\,828\,326\,934\times10^{1}$
2	0	1	$-0.260\,835\,009\,128\,688\times10^{2}$
3	0	5	$0.267\,416\,218\,930\,389\times10^{3}$
4	1	0	$0.172\,221\,089\,496\,844\times10^{2}$
5	1	3	$-0.293\,542\,332\,145\,970\times10^{3}$
6	1	4	$0.614\,135\,601\,882\,478\times10^{3}$
7	1	8	$-0.610\,562\,757\,725\,674\times10^{5}$
8	1	14	$-0.651\,272\,251\,118\,219\times10^{8}$
9	2	6	$0.735\,919\,313\,521\,937\times10^{5}$
10	2	16	$-0.116\,646\,505\,914\,191\times10^{11}$
11	3	0	$0.355\,267\,086\,434\,461\times10^{2}$
12	3	2	$-0.596\,144\,543\,825\,955\times10^{3}$
13	3	3	$-0.475\,842\,430\,145\,708\times10^{3}$
14	4	0	$0.696\,781\,965\,359\,503\times10^{2}$
15	4	1	$0.335\,674\,250\,377\,312\times10^{3}$
16	4	4	$0.250\,526\,809\,130\,882\times10^{5}$
17	4	5	$0.146\,997\,380\,630\,766\times10^{6}$
18	5	28	$0.538\,069\,315\,091\,534\times10^{20}$
19	6	28	$0.143\,619\,827\,291\,346\times10^{22}$
20	7	24	$0.364\,985\,866\,165\,994\times10^{20}$
21	8	1	$-0.254\,741\,561\,156\,775\times10^{4}$
22	10	32	$0.240\,120\,197\,096\,563\times10^{28}$
23	10	36	$-0.393\,847\,464\,679\,496\times10^{30}$
24	14	22	$0.147\,073\,407\,024\,852\times10^{25}$
25	18	28	$-0.426\,391\,250\,432\,059\times10^{32}$
26	20	36	$0.194\,509\,340\,621\,077\times10^{39}$
27	22	16	$0.666\,212\,132\,114\,896\times10^{24}$
28	22	28	$0.706\,777\,016\,552\,858\times10^{34}$
29	24	36	$0.175\,563\,621\,975\,576\times10^{42}$
30	28	16	$0.108\,408\,607\,429\,124\times10^{29}$
31	28	36	$0.730\,872\,705\,175\,151\times10^{44}$
32	32	10	$0.159\,145\,847\,398\,870\times10^{25}$
33	32	28	$0.377\,121\,605\,943\,324\times10^{41}$

Table 3 Coefficients and exponents of the backward equation $p_{3b}(h,s)$, Eq. (3)

i	I_i	J_i	n_i
1	−12	2	$0.125\,244\,360\,717\,979\times10^{-12}$
2	−12	10	$-0.126\,599\,322\,553\,713\times10^{-1}$
3	−12	12	$0.506\,878\,030\,140\,626\times10^{1}$
4	−12	14	$0.317\,847\,171\,154\,202\times10^{2}$
5	−12	20	$-0.391\,041\,161\,399\,932\times10^{6}$
6	−10	2	$-0.975\,733\,406\,392\,044\times10^{-10}$
7	−10	10	$-0.186\,312\,419\,488\,279\times10^{2}$
8	−10	14	$0.510\,973\,543\,414\,101\times10^{3}$
9	−10	18	$0.373\,847\,005\,822\,362\times10^{6}$
10	−8	2	$0.299\,804\,024\,666\,572\times10^{-7}$
11	−8	8	$0.200\,544\,393\,820\,342\times10^{2}$
12	−6	2	$-0.498\,030\,487\,662\,829\times10^{-5}$
13	−6	6	$-0.102\,301\,806\,360\,030\times10^{2}$
14	−6	7	$0.552\,819\,126\,990\,325\times10^{2}$
15	−6	8	$-0.206\,211\,367\,510\,878\times10^{3}$
16	−5	10	$-0.794\,012\,232\,324\,823\times10^{4}$
17	−4	4	$0.782\,248\,472\,028\,153\times10^{1}$
18	−4	5	$-0.586\,544\,326\,902\,468\times10^{2}$
19	−4	8	$0.355\,073\,647\,696\,481\times10^{4}$
20	−3	1	$-0.115\,303\,107\,290\,162\times10^{-3}$
21	−3	3	$-0.175\,092\,403\,171\,802\times10^{1}$
22	−3	5	$0.257\,981\,687\,748\,160\times10^{3}$
23	−3	6	$-0.727\,048\,374\,179\,467\times10^{3}$
24	−2	0	$0.121\,644\,822\,609\,198\times10^{-3}$
25	−2	1	$0.393\,137\,871\,762\,692\times10^{-1}$
26	−1	0	$0.704\,181\,005\,909\,296\times10^{-2}$
27	0	3	$-0.829\,108\,200\,698\,110\times10^{2}$
28	2	0	$-0.265\,178\,818\,131\,250$
29	2	1	$0.137\,531\,682\,453\,991\times10^{2}$
30	5	0	$-0.522\,394\,090\,753\,046\times10^{2}$
31	6	1	$0.240\,556\,298\,941\,048\times10^{4}$
32	8	1	$-0.227\,361\,631\,268\,929\times10^{5}$
33	10	1	$0.890\,746\,343\,932\,567\times10^{5}$
34	14	3	$-0.239\,234\,565\,822\,486\times10^{8}$
35	14	7	$0.568\,795\,808\,129\,714\times10^{10}$

which is smaller than the 0.01% consistency requirement of Eqs. (2) and (3) with the IAPWS-IF97 basic equation.

2.5 Backward Function $T(h,s)$

2.5.1 Calculation of $T(h,s)$. The $p_3(h,s)$ equations described in Sec. 2.4.1, together with the IAPWS-IF97-S03rev backward equation $T_3^{03}(p,h)$,[3] [5,6] make it possible to determine temperature T from enthalpy h and entropy s without iteration.

For calculating $T(h,s)$ in region 3, the following steps should be taken:

- Use the entropy line s_c (see Fig. 2) to identify the subregion (3a or 3b) for the given values of h and s. Then, calculate the pressure p with $p_{3a}(h,s)$, Eq. (2), or $p_{3b}(h,s)$, Eq. (3).
- Use the IAPWS-IF97-S03rev boundary equation $h_{3ab}^{03}(p)$ [5,6] to identify the subregion (3a or 3b) for the given value of h and the previously calculated value of p. Then, calculate T with the backward equation $T_{3a}^{03}(p,h)$ or $T_{3b}^{03}(p,h)$.

2.5.2 Consistency with IAPWS-IF97. Table 6 lists the maximum temperature differences and related root-mean-square differences between the temperature calculated as described in the previous section and the IAPWS-IF97 basic equation $f_3^{97}(v,T)$, together with the permissible differences. The maximum deviations are less than the tolerances. Therefore, the accuracy of pressure calculated by $p_{3a}(h,s)$ and $p_{3b}(h,s)$ (Eqs. (2) and (3)) is sufficient for calculating temperature using the backward equations $T_{3a}(p,h)$ and $T_{3b}(p,h)$.

2.5.3 Consistency at the Subregion Boundary. The subregion

Table 4 Selected pressure values calculated from Eqs. (2) and (3)

Equation	h, kJ kg^{-1}	s, kJ kg^{-1} K^{-1}	p, MPa
$p_{3a}(h,s)$, Eq. (2)	1700	3.8	$2.555\,703\,246\times10^{1}$
	2000	4.2	$4.540\,873\,468\times10^{1}$
	2100	4.3	$6.078\,123\,340\times10^{1}$
$p_{3b}(h,s)$, Eq. (3)	2500	5.1	$1.720\,612\,413\times10^{1}$
	2400	4.7	$6.363\,924\,887\times10^{1}$
	2700	5.0	$8.839\,043\,281\times10^{1}$

Table 5 Maximum and root-mean-square differences between the pressure calculated from Eqs. (2) and (3) and from the IAPWS-IF97 basic equation $f_3^{97}(v,T)$, and related permissible values

Subregion	Equation	$\lvert\Delta p/p\rvert_{tol}$	$\lvert\Delta p/p\rvert_{max}$	$\lvert\Delta p/p\rvert_{RMS}$
3a	(2)	0.01%	0.0070%	0.0030%
3b	(3)	0.01%	0.0084%	0.0036%

[3]The alternative use of the IAPWS-IF97-S03 backward equation $T_3^{03}(p,s)$ leads to worse numerical consistency.

Table 6 Maximum and root-mean-square differences between calculated temperatures and IAPWS-IF97 basic equation $f_3^{97}(v,T)$ compared with the permissible differences

Subregion	$\lvert\Delta T\rvert_{tol}$	$\lvert\Delta T\rvert_{max}$	$\lvert\Delta T\rvert_{RMS}$
3a	25 mK	23.7 mK	10.5 mK
3b	25 mK	22.4 mK	9.9 mK

Table 7 Maximum and root-mean-square relative differences between calculated specific volume and the IAPWS-IF97 basic equation $f_3^{97}(v,T)$, and related permissible values

Subregion	$\lvert\Delta v/v\rvert_{tol}$	$\lvert\Delta v/v\rvert_{max}$	$\lvert\Delta v/v\rvert_{RMS}$
3a	0.01%	0.0097%	0.0053%
3b	0.01%	0.0095%	0.0043%

boundary between the backward equations $T_{3a}^{03}(p,h)$ and $T_{3b}^{03}(p,h)$ is the boundary equation $h_{3ab}^{03}(p)$. The subregion boundary between the backward equations $p_{3a}(h,s)$ and $p_{3b}(h,s)$ is the critical isentrope $s=s_c$. These two boundaries are independent but cross each other at four points in the pressure range from p_c to 100 MPa. The greatest temperature difference at these crossings is 0.68 mK, which is considerably smaller than the 25 mK numerical consistency specified for IAPWS-IF97.

2.6 Backward Function $v(h,s)$

2.6.1 Calculation of $v(h,s)$. The $p_3(h,s)$ equations described in Sec. 2.4.1, together with the IAPWS-IF97-S03rev backward equation $v_3^{03}(p,s)$,[4] [5,6] make it possible to determine specific volume v from enthalpy h and entropy s without iteration.

For calculating $v(h,s)$ in region 3, the following steps should be taken:

- Use the entropy line s_c (see Fig. 2) to identify the subregion (3a or 3b) for the given values of h and s. Then, calculate the pressure p with $p_{3a}(h,s)$, Eq. (2), or $p_{3b}(h,s)$, Eq. (3).
- Since s_c is the subregion boundary for the backward equations $v_3^{03}(p,s)$, calculate v for the subregion identified previously with the backward equation $v_{3a}^{03}(p,s)$ or $v_{3b}^{03}(p,s)$.

2.6.2 Consistency with IAPWS-IF97. Table 7 lists the maximum relative deviations and related root-mean-square relative deviations between the specific volume calculated as described in the previous section and the IAPWS-IF97 basic equation $f_3^{97}(v,T)$, together with the permissible differences. The maximum relative deviations are less than the tolerances. Therefore, the accuracy of pressure calculated by $p_{3a}(h,s)$ and $p_{3b}(h,s)$ (Eqs. (2) and (3)) is sufficient for calculating specific volume using the backward equations $v_{3a}^{03}(p,s)$ and $v_{3b}^{03}(p,s)$.

2.6.3 Consistency at the Subregion Boundary. The maximum relative specific volume difference between the two backward equations of the adjacent subregions 3a and 3b along the boundary s_c is 0.00028%, which is considerably smaller than the 0.01% consistency requirement with the IAPWS-IF97 basic equation.

3 Equations of Enthalpy and Entropy for Region Boundaries

3.1 Introduction. IAPWS now provides [3,7] explicit equations for functions of the variables (h,s) in liquid region 1, vapor region 2, and region 3. Before calculating these equations, it must be determined in which region the given point is located for the given enthalpy and entropy. Without explicit equations for region boundaries in terms of (h,s), this involves time-consuming iterative calculations.

We therefore constructed a set of equations that allow direct determination of the region for independent variables (h,s). The boundary equations $h_1'(s)$, $h_{3a}'(s)$, $h_{2ab}''(s)$, and $h_{2c3b}''(s)$ (see Fig. 3) provided here make it possible to determine without iteration whether a given state point is located in the single-phase regions 1, 2, and 3 or in the two-phase region 4. The equation $h_{B13}(s)$ has been developed to describe the boundary between regions 1 and 3 (see Fig. 3). The new equation $T_{B23}(h,s)$, in conjunction with the existing IAPWS-IF97-S01 backward equation $p_{2c}^{01}(h,s)$, allows the determination of the boundary between regions 2 and 3 without iteration.

3.2 Consistency Requirements. The numerical consistency requirements on the equations for region boundaries result from IAPWS requirements on backward functions. These requirements are given in Table 8. Backward functions of enthalpy and entropy must meet these requirements when the equations for region boundaries are used.

3.3 Equations $h_1'(s)$ and $h_{3a}'(s)$ for the Saturated Liquid. In order to meet the requirements for numerical consistency, the saturated-liquid curve was divided into two sections. Section 1 adjoins region 1 and Section 3a adjoins subregion 3a.

The equation $h_1'(s)$ describes the saturated-liquid curve from the triple-point temperature 273.16 to 623.15 K and can be simply extrapolated to 273.15 K so that it covers the entropy range (see Fig. 3)

$$s'(273.15\ \text{K}) \leq s \leq s'(623.15\ \text{K})$$

$$\text{where } s'(273.15\ \text{K}) = -1.545\ 495\ 919 \times 10^{-4}\ \text{kJ kg}^{-1}\ \text{K}^{-1}$$

$$\text{and } s'(623.15\ \text{K}) = 3.778\ 281\ 340\ \text{kJ kg}^{-1}\ \text{K}^{-1}$$

The boundary equation $h_1'(s)$ has the dimensionless form

$$\frac{h_1'(s)}{h^*} = \eta(\sigma) = \sum_{i=1}^{27} n_i(\sigma - 1.09)^{I_i}(\sigma + 0.366 \times 10^{-4})^{J_i} \qquad (4)$$

where $\eta = h/h^*$ and $\sigma = s/s^*$, with $h^* = 1700\ \text{kJ kg}^{-1}$, and $s^* = 3.8\ \text{kJ kg}^{-1}\ \text{K}^{-1}$. The coefficients n_i and exponents I_i and J_i of Eq. (4) are listed in Table 9.

The equation $h_{3a}'(s)$ describes the saturated-liquid curve in the entropy range (see Fig. 3)

$$s'(623.15\ \text{K}) < s \leq s_c$$

$$\text{where } s'(623.15\ \text{K}) = 3.778\ 281\ 340\ \text{kJ kg}^{-1}\ \text{K}^{-1}$$

$$\text{and } s_c = 4.412\ 021\ 482\ 234\ 76\ \text{kJ kg}^{-1}\ \text{K}^{-1}$$

The boundary equation $h_{3a}'(s)$ has the dimensionless form

$$\frac{h_{3a}'(s)}{h^*} = \eta(\sigma) = \sum_{i=1}^{19} n_i(\sigma - 1.09)^{I_i}(\sigma + 0.366 \times 10^{-4})^{J_i} \qquad (5)$$

were $\eta = h/h^*$ and $\sigma = s/s^*$ with $h^* = 1700\ \text{kJ kg}^{-1}$ and $s^* = 3.8\ \text{kJ kg}^{-1}\ \text{K}^{-1}$. The coefficients n_i and exponents I_i and J_i of Eq. (5) are listed in Table 10.

If the enthalpy h is greater than $h_1'(s)$ or $h_{3a}'(s)$ calculated from the given entropy s, then the point to be calculated is located in the single-phase regions 1 or 3; otherwise it is in the two-phase region 4 (see Fig. 3).

To assist in computer-program verification of Eqs. (4) and (5), Table 11 contains test values for calculated enthalpies.

[4]The alternative use of the IAPWS-IF97-S03 backward equation $v_3^{03}(p,h)$ leads to worse numerical consistency.

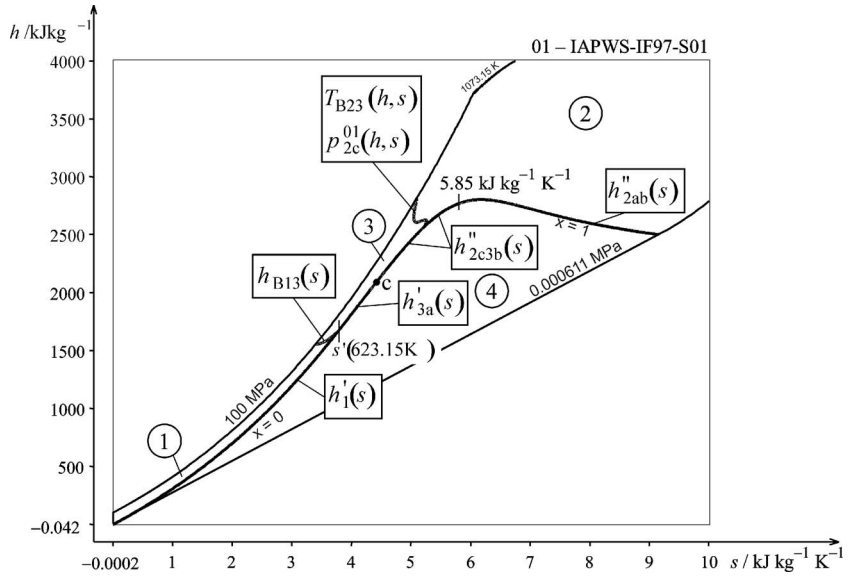

Fig. 3 Regions of IAPWS-IF97 and boundary equations $h'_1(s)$, $h'_{3a}(s)$, $h''_{2ab}(s)$, $h''_{2c3b}(s)$, $h_{B13}(s)$, and $T_{B23}(h,s)$ of this work

3.4 Equations $h''_{2ab}(s)$ and $h''_{2c3b}(s)$ for the Saturated Vapor. The saturated-vapor curve was also divided into two sections. Section 2ab adjoins subregions 2a and 2b. Section 2c3b adjoins subregion 2c and subregion 3b.

The equation $h''_{2ab}(s)$ describes the saturated-vapor curve from the triple point to 5.85 kJ kg^{-1} K^{-1} and can be simply extrapolated to 273.15 K so that it covers the entropy range (see Fig. 3)

$$5.85 \text{ kJ kg}^{-1}\text{ K}^{-1} \leq s \leq s''(273.15\text{ K})$$

$$\text{where } s''(273.15\text{ K}) = 9.155759395 \text{ kJ kg}^{-1}\text{ K}^{-1}$$

$h''_{2ab}(s)$ has the dimensionless form

$$\frac{h''_{2ab}(s)}{h^*} = \eta(\sigma) = \exp\left[\sum_{i=1}^{30} n_i(\sigma_1^{-1} - 0.513)^{I_i}(\sigma_2 - 0.524)^{J_i}\right] \quad (6)$$

where $\eta = h/h^*$, $\sigma = s/s_1^*$, and $\sigma = s/s_2^*$, with $h^* = 2800$ kJ kg^{-1}, $s_1^* = 5.21$ kJ kg^{-1} K^{-1}, and $s_2^* = 9.2$ kJ kg^{-1} K^{-1}. The coefficients n_i and exponents I_i and J_i of Eq. (6) are listed in Table 12.

The equation $h''_{2c3b}(s)$ describes the saturated-vapor curve in the entropy range (see Fig. 3)

$$s_c \leq s < 5.85 \text{ kJ kg}^{-1}\text{ K}^{-1}$$

$$\text{where } s_c = 4.412\,021\,482\,234\,76 \text{ kJ kg}^{-1}\text{ K}^{-1}$$

and has the dimensionless form

$$\frac{h''_{2c3b}(s)}{h^*} = \eta(\sigma) = \left[\sum_{i=1}^{16} n_i(\sigma - 1.02)^{I_i}(\sigma - 0.726)^{J_i}\right]^4 \quad (7)$$

where $\eta = h/h^*$ and $\sigma = s/s^*$ with $h^* = 2800$ kJ kg^{-1} and $s^* = 5.9$ kJ kg^{-1} K^{-1}. The coefficients n_i and exponents I_i and J_i of Eq. (7) are listed in Table 13.

If the enthalpy h is greater than $h''_{2ab}(s)$ or $h''_{2c3b}(s)$ calculated

Table 8 Numerical consistency requirements adopted by IAPWS for backward equations

Region	$\lvert\Delta T\rvert_{tol}$	$\lvert\Delta p/p\rvert_{tol}$		$\lvert\Delta v/v\rvert_{tol}$
1	25 mK	$p \leq 2.5$ MPa	0.6%	—
		$p > 2.5$ MPa	15 kPa	—
2				
$s \geq 5.85$ kJ kg^{-1} K^{-1}	10 mK	0.0035%		—
$s < 5.85$ kJ kg^{-1} K^{-1}	25 mK	0.0088%		—
3	25 mK	0.01%		0.01%

Table 9 Coefficients and exponents of the boundary equation $h'_1(s)$, Eq. (4)

i	I_i	J_i	n_i
1	0	14	0.332 171 191 705 237
2	0	36	$0.611\,217\,706\,323\,496 \times 10^{-3}$
3	1	3	$-0.882\,092\,478\,906\,822 \times 10^{1}$
4	1	16	−0.455 628 192 543 250
5	2	0	$-0.263\,483\,840\,850\,452 \times 10^{-4}$
6	2	5	$-0.223\,949\,661\,148\,062 \times 10^{2}$
7	3	4	$-0.428\,398\,660\,164\,013 \times 10^{1}$
8	3	36	−0.616 679 338 856 916
9	4	4	$-0.146\,823\,031\,104\,040 \times 10^{2}$
10	4	16	$0.284\,523\,138\,727\,299 \times 10^{3}$
11	4	24	$-0.113\,398\,503\,195\,444 \times 10^{3}$
12	5	18	$0.115\,671\,380\,760\,859 \times 10^{4}$
13	5	24	$0.395\,551\,267\,359\,325 \times 10^{3}$
14	7	1	$-0.154\,891\,257\,229\,285 \times 10^{1}$
15	8	4	$0.194\,486\,637\,751\,291 \times 10^{2}$
16	12	2	$-0.357\,915\,139\,457\,043 \times 10^{1}$
17	12	4	$-0.335\,369\,414\,148\,819 \times 10^{1}$
18	14	1	−0.664 426 796 332 460
19	14	22	$0.323\,321\,885\,383\,934 \times 10^{5}$
20	16	10	$0.331\,766\,744\,667\,084 \times 10^{4}$
21	20	12	$-0.223\,501\,257\,931\,087 \times 10^{5}$
22	20	28	$0.573\,953\,875\,852\,936 \times 10^{7}$
23	22	8	$0.173\,226\,193\,407\,919 \times 10^{3}$
24	24	3	$-0.363\,968\,822\,121\,321 \times 10^{-1}$
25	28	0	$0.834\,596\,332\,878\,346 \times 10^{-6}$
26	32	6	$0.503\,611\,916\,682\,674 \times 10^{1}$
27	32	8	$0.655\,444\,787\,064\,505 \times 10^{2}$

Table 10 Coefficients and exponents of the boundary equation $h'_{3a}(s)$, Eq. (5)

i	I_i	J_i	n_i
1	0	1	0.822 673 364 673 336
2	0	4	0.181 977 213 534 479
3	0	10	$-0.112\,000\,260\,313\,624\times10^{-1}$
4	0	16	$-0.746\,778\,287\,048\,033\times10^{-3}$
5	2	1	−0.179 046 263 257 381
6	3	36	$0.424\,220\,110\,836\,657\times10^{-1}$
7	4	3	−0.341 355 823 438 768
8	4	16	$-0.209\,881\,740\,853\,565\times10^{1}$
9	5	20	$-0.822\,477\,343\,323\,596\times10^{1}$
10	5	36	$-0.499\,684\,082\,076\,008\times10^{1}$
11	6	4	0.191 413 958 471 069
12	7	2	$0.581\,062\,241\,093\,136\times10^{-1}$
13	7	28	$-0.165\,505\,498\,701\,029\times10^{4}$
14	7	32	$0.158\,870\,443\,421\,201\times10^{4}$
15	10	14	$-0.850\,623\,535\,172\,818\times10^{2}$
16	10	32	$-0.317\,714\,386\,511\,207\times10^{5}$
17	10	36	$-0.945\,890\,406\,632\,871\times10^{5}$
18	32	0	$-0.139\,273\,847\,088\,690\times10^{-5}$
19	32	6	0.631 052 532 240 980

from the given entropy s, then the point is located in the single-phase regions 2 or 3; otherwise it is in the two-phase region 4 (see Fig. 3).

To assist in computer-program verification of Eqs. (6) and (7), Table 11 contains test values for calculated enthalpies.

3.5 Equation $h_{B13}(s)$ for the Boundary between Regions 1 and 3. The equation $h_{B13}(s)$ describes the enthalpy as a function of entropy for the isotherm $T=623.15$ K from the saturated liquid up to 100 MPa (see Fig. 3). The corresponding entropy range is

$$s(100\ \text{MPa}, 623.15\ \text{K}) \leqslant s \leqslant s'(623.15\ \text{K}),$$

$$\text{where } s'(623.15\ \text{K}) = 3.778\ 281\ 340\ \text{kJ kg}^{-1}\ \text{K}^{-1}$$

$$\text{and } s(100\ \text{MPa}, 623.15\ \text{K}) = 3.397\ 782\ 955\ \text{kJ kg}^{-1}\ \text{K}^{-1}$$

calculated from the IAPWS-IF97 basic equation $g_1^{97}(p,T)$. $h_{B13}(s)$ has the dimensionless form

Table 11 Selected enthalpy values calculated from Eqs. (4)–(8)

Equation	s, kJ kg^{-1} K^{-1}	h, kJ kg^{-1}
$h'_1(s)$, Eq. (4)	1.0	$3.085\,509\,647\times10^{2}$
	2.0	$7.006\,304\,472\times10^{2}$
	3.0	$1.198\,359\,754\times10^{3}$
$h'_{3a}(s)$, Eq. (5)	3.8	$1.685\,025\,565\times10^{3}$
	4.0	$1.816\,891\,476\times10^{3}$
	4.2	$1.949\,352\,563\times10^{3}$
$h''_{2ab}(s)$, Eq. (6)	7.0	$2.723\,729\,985\times10^{3}$
	8.0	$2.599\,047\,210\times10^{3}$
	9.0	$2.511\,861\,477\times10^{3}$
$h''_{2c3b}(s)$, Eq. (7)	5.5	$2.687\,693\,850\times10^{3}$
	5.0	$2.451\,623\,609\times10^{3}$
	4.5	$2.144\,360\,448\times10^{3}$
$h_{B13}(s)$, Eq. (8)	3.7	$1.632\,525\,047\times10^{3}$
	3.6	$1.593\,027\,214\times10^{3}$
	3.5	$1.566\,104\,611\times10^{3}$

Table 12 Coefficients and exponents of the boundary equation $h''_{2ab}(s)$, Eq. (6)

i	I_i	J_i	n_i
1	1	8	$-0.524\,581\,170\,928\,788\times10^{3}$
2	1	24	$-0.926\,947\,218\,142\,218\times10^{7}$
3	2	4	$-0.237\,385\,107\,491\,666\times10^{3}$
4	2	32	$0.210\,770\,155\,812\,776\times10^{11}$
5	4	1	$-0.239\,494\,562\,010\,986\times10^{2}$
6	4	2	$0.221\,802\,480\,294\,197\times10^{3}$
7	7	7	$-0.510\,472\,533\,393\,438\times10^{7}$
8	8	5	$0.124\,981\,396\,109\,147\times10^{7}$
9	8	12	$0.200\,008\,436\,996\,201\times10^{10}$
10	10	1	$-0.815\,158\,509\,791\,035\times10^{3}$
11	12	0	$-0.157\,612\,685\,637\,523\times10^{3}$
12	12	7	$-0.114\,200\,422\,332\,791\times10^{11}$
13	18	10	$0.662\,364\,680\,776\,872\times10^{16}$
14	20	12	$-0.227\,622\,818\,296\,144\times10^{19}$
15	24	32	$-0.171\,048\,081\,348\,406\times10^{32}$
16	28	8	$0.660\,788\,766\,938\,091\times10^{16}$
17	28	12	$0.166\,320\,055\,886\,021\times10^{23}$
18	28	20	$-0.218\,003\,784\,381\,501\times10^{30}$
19	28	22	$-0.787\,276\,140\,295\,618\times10^{30}$
20	28	24	$0.151\,062\,329\,700\,346\times10^{32}$
21	32	2	$0.795\,732\,170\,300\,541\times10^{7}$
22	32	7	$0.131\,957\,647\,355\,347\times10^{16}$
23	32	12	$-0.325\,097\,068\,299\,140\times10^{24}$
24	32	14	$-0.418\,600\,611\,419\,248\times10^{26}$
25	32	24	$0.297\,478\,906\,557\,467\times10^{35}$
26	36	10	$-0.953\,588\,761\,745\,473\times10^{20}$
27	36	12	$0.166\,957\,699\,620\,939\times10^{25}$
28	36	20	$-0.175\,407\,764\,869\,978\times10^{33}$
29	36	22	$0.347\,581\,490\,626\,396\times10^{35}$
30	36	28	$-0.710\,971\,318\,427\,851\times10^{39}$

$$\frac{h_{B13}(s)}{h^*} = \eta(\sigma) = \sum_{i=1}^{6} n_i(\sigma - 0.884)^{I_i}(\sigma - 0.864)^{J_i} \tag{8}$$

where $\eta=h/h^*$ and $\sigma=s/s^*$ with $h^*=1700$ kJ kg^{-1} and $s^*=3.8$ kJ kg^{-1} K^{-1}. The coefficients n_i and exponents I_i and J_i of Eq. (8) are listed in Table 14.

If the enthalpy h is greater than $h_{B13}(s)$ calculated from the given entropy s, then the point is located in region 3; otherwise it is in region 1 (see Fig. 3).

To assist computer-program verification of Eq. (7), Table 11 contains test values for calculated enthalpies.

Table 13 Coefficients and exponents of the boundary equation $h''_{2c3b}(s)$, Eq. (7)

i	I_i	J_i	n_i
1	0	0	$0.104\,351\,280\,732\,769\times10^{1}$
2	0	3	$-0.227\,807\,912\,708\,513\times10^{1}$
3	0	4	$0.180\,535\,256\,723\,202\times10^{1}$
4	1	0	0.420 440 834 792 042
5	1	12	$-0.105\,721\,244\,834\,660\times10^{6}$
6	5	36	$0.436\,911\,607\,493\,884\times10^{25}$
7	6	12	$-0.328\,032\,702\,839\,753\times10^{12}$
8	7	16	$-0.678\,686\,760\,804\,270\times10^{16}$
9	8	2	$0.743\,957\,464\,645\,363\times10^{4}$
10	8	20	$-0.356\,896\,445\,355\,761\times10^{20}$
11	12	32	$0.167\,590\,585\,186\,801\times10^{32}$
12	16	36	$-0.355\,028\,625\,419\,105\times10^{38}$
13	22	2	$0.396\,611\,982\,166\,538\times10^{12}$
14	22	32	$-0.414\,716\,268\,484\,468\times10^{41}$
15	24	7	$0.359\,080\,103\,867\,382\times10^{19}$
16	36	20	$-0.116\,994\,334\,851\,995\times10^{41}$

Table 14 Coefficients and exponents of the equation $h_{B13}(s)$, Eq. (8)

i	I_i	J_i	n_i
1	0	0	0.913 965 547 600 543
2	1	−2	$-0.430\,944\,856\,041\,991\times10^{-4}$
3	1	2	$0.603\,235\,694\,765\,419\times10^{2}$
4	3	−12	$0.117\,518\,273\,082\,168\times10^{-17}$
5	5	−4	0.220 000 904 781 292
6	6	−3	$-0.690\,815\,545\,851\,641\times10^{2}$

3.6 Equation $T_{B23}(h,s)$ for the Boundary between Regions 2 and 3. The boundary between regions 2 and 3 is defined by the B23-equation $p^{97}_{B23}(T)$ of IAPWS-IF97 (Fig. 1). Since $p^{97}_{B23}(T)$ has an S-shape in the h-s plane (see Fig. 4), it is not possible to develop $h(s)$ or $s(h)$ that meets the numerical consistency requirements. Therefore, an equation $T_{B23}(h,s)$ for this boundary was developed. $T_{B23}(h,s)$ and the IAPWS-IF97-S01 backward equation $p^{01}_{2c}(h,s)$ simplify the determination of the region for given variables h and s.

The range of validity of $T_{B23}(h,s)$ is from the saturated vapor $x=1$ calculated by the equation $h''_{2c3b}(s)$, Eq. (7), up to 100 MPa. Figure 4 shows the related entropy range

$$s^{\min}_{B23} \leqslant s \leqslant s^{\max}_{B23}$$

$$\text{where } s^{\min}_{B23} = 5.048\ 096\ 828\ \text{kJ kg}^{-1}\ \text{K}^{-1}$$

$$\text{and } s^{\max}_{B23} = 5.260\ 578\ 707\ \text{kJ kg}^{-1}\ \text{K}^{-1}$$

and enthalpy range

$$h^{\min}_{B23} \leqslant h \leqslant h^{\max}_{B23}$$

$$\text{where } h^{\min}_{B23} = h''(623.15\ \text{K}) = 2.563\ 592\ 004 \times 10^{3}\ \text{kJ kg}^{-1}$$

$$\text{and } h^{\max}_{B23} = h(100\ \text{MPa}, 863.15\ \text{K}) = 2.812\ 942\ 061 \times 10^{3}\ \text{kJ kg}^{-1}$$

The equation $T_{B23}(h,s)$ has the dimensionless form

Table 15 Coefficients and exponents of the boundary equation $T_{B23}(h,s)$, Eq. (9)

i	I_i	J_i	n_i
1	−12	10	$0.629\,096\,260\,829\,810\times10^{-3}$
2	−10	8	$-0.823\,453\,502\,583\,165\times10^{-3}$
3	−8	3	$0.515\,446\,951\,519\,474\times10^{-7}$
4	−4	4	$-0.117\,565\,945\,784\,945\times10^{1}$
5	−3	3	$0.348\,519\,684\,726\,192\times10^{1}$
6	−2	−6	$-0.507\,837\,382\,408\,313\times10^{-11}$
7	−2	2	$-0.284\,637\,670\,005\,479\times10^{1}$
8	−2	3	$-0.236\,092\,263\,939\,673\times10^{1}$
9	−2	4	$0.601\,492\,324\,973\,779\times10^{1}$
10	0	0	$0.148\,039\,650\,824\,546\times10^{1}$
11	1	−3	$0.360\,075\,182\,221\,907\times10^{-3}$
12	1	−2	$-0.126\,700\,045\,009\,952\times10^{-1}$
13	1	10	$-0.122\,184\,332\,521\,413\times10^{7}$
14	3	−2	0.149 276 502 463 272
15	3	−1	0.698 733 471 798 484
16	5	−5	$-0.252\,207\,040\,114\,321\times10^{-1}$
17	6	−6	$0.147\,151\,930\,985\,213\times10^{-1}$
18	6	−3	$-0.108\,618\,917\,681\,849\times10^{1}$
19	8	−8	$-0.936\,875\,039\,816\,322\times10^{-3}$
20	8	−2	$0.819\,877\,897\,570\,217\times10^{2}$
21	8	−1	$-0.182\,041\,861\,521\,835\times10^{3}$
22	12	−12	$0.261\,907\,376\,402\,688\times10^{-5}$
23	12	−1	$-0.291\,626\,417\,025\,961\times10^{5}$
24	14	−12	$0.140\,660\,774\,926\,165\times10^{-4}$
25	14	1	$0.783\,237\,062\,349\,385\times10^{7}$

Table 16 Selected temperature values calculated from Eq. (9)

Equations	h, kJ kg^{-1}	s, kJ kg^{-1} K^{-1}	T, K
$T_{B23}(h,s)$, Eq. (9)	2600	5.1	$7.135\,259\,364\times10^{2}$
	2700	5.15	$7.685\,345\,532\times10^{2}$
	2800	5.2	$8.176\,202\,120\times10^{2}$

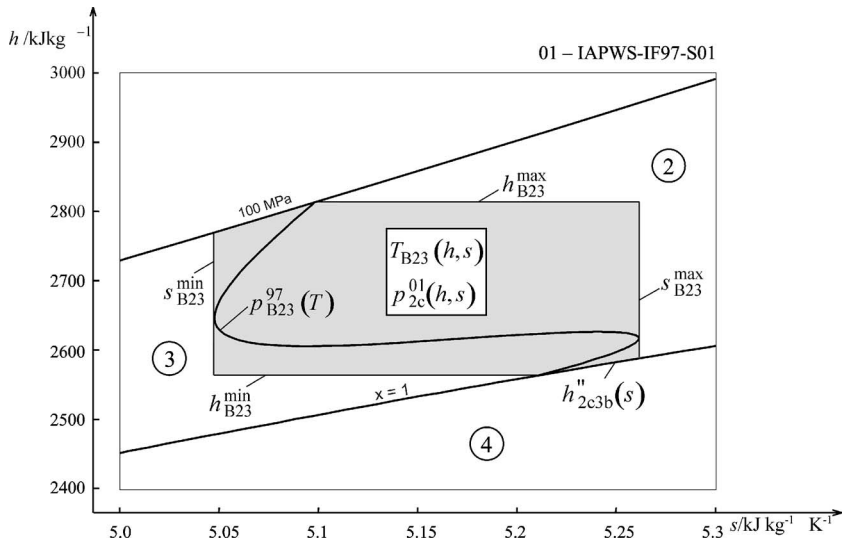

Fig. 4 Illustration of the B23-equation $p^{97}_{B23}(T)$ of IAPWS-IF97 and the range of validity of the boundary equation $T_{B23}(h,s)$ in a h-s diagram

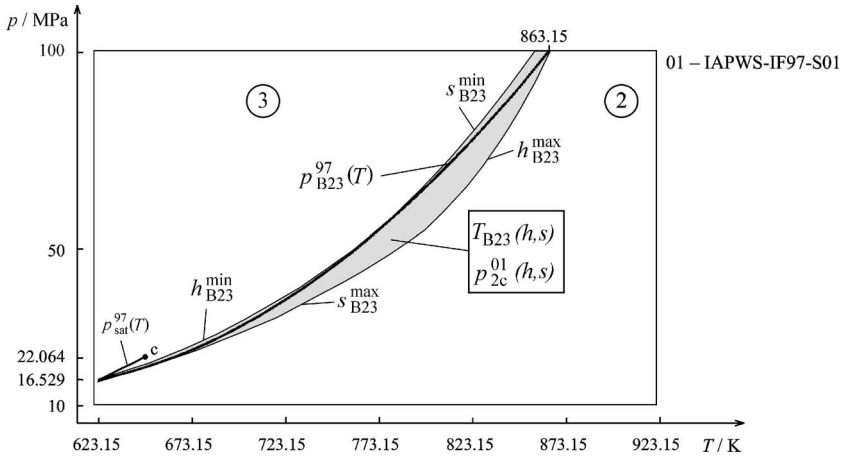

Fig. 5 Illustration of the B23-equation $p^{97}_{B23}(T)$ of IAPWS-IF97 and the range of validity of the boundary equation $T_{B23}(h,s)$ in a *p-T* diagram

Table 17 Maximum differences of pressure, temperature and specific volume between the backward equations and the IAPWS-IF97 basic equations along the region boundary equations, Eqs. (4)–(7)

Boundary equation	Region/subregion	$\lvert\Delta T\rvert_{max}$, mK	$\lvert\Delta p/p\rvert_{max}$		$\lvert\Delta v/v\rvert_{max}$
$h'_1(s)$, Eq. (4)	1	23.8	$p \leqslant 2.5$ MPa	0.59%	—
			$p > 2.5$ MPa	12.9 kPa	—
	2				
$h''_{2ab}(s)$, Eq. (6)	$s \geqslant 5.85$ kJ kg^{-1} K^{-1}	9.5	0.0027%		—
$h''_{2c3b}(s)$, Eq. (7)	$s < 5.85$ kJ kg^{-1} K^{-1}	24.1	0.0066%		—
$h'_{3a}(s)$, Eq. (5)	3a	4.8	0.0065%		0.0058%
$h''_{2c3b}(s)$, Eq. (7)	3b	6.2	0.0050%		0.0041%

$$\frac{T_{B23}(h,s)}{T^*} = \theta(\eta,\sigma) = \sum_{i=1}^{25} n_i(\eta - 0.727)^{I_i}(\sigma - 0.864)^{J_i} \qquad (9)$$

where $\theta = T/T^*$, $\eta = h/h^*$, and $\sigma = s/s^*$ with $T^* = 900$ K, $h^* = 3000$ kJ kg^{-1}, and $s^* = 5.3$ kJ kg^{-1} K^{-1}. The coefficients n_i and exponents I_i and J_i of Eq. (9) are listed in Table 15.

To assist computer-program verification of Eq. (9), Table 16 contains test values for calculated temperatures.

$T_{B23}(h,s)$, Eq. (9), and the IAPWS-IF97-S01 backward equation $p^{01}_{2c}(h,s)$ can be used as follows to determine whether a given state point (h,s) is located in region 2 or in region 3.

If the given entropy is less than or equal to s^{min}_{B23} or the given enthalpy is less than or equal to h^{min}_{B23}, then the point is in region 3. For entropies greater than or equal to s^{max}_{B23} or for enthalpies greater than or equal to h^{max}_{B23}, the point is in region 2.

For entropies $s^{min}_{B23} < s < s^{max}_{B23}$ and enthalpies $h^{min}_{B23} < h < h^{max}_{B23}$, the following steps should be taken:

- Calculate temperature T_{B23} from the given h and s with $T_{B23}(h,s)$ (Eq. (9)).
- Calculate pressure p_{B23} from the given h and s with the IAPWS-IF97-S01 backward equation $p^{01}_{2c}(h,s)$.
- Calculate pressure p^{97}_{B23} with the equation $p^{97}_{B23}(T)$ of IAPWS-IF97, where $T = T_{B23}$ was previously calculated.

If the pressure p_{B23} is greater than p^{97}_{B23}, then the point is located in region 3, otherwise it is in region 2 (see Fig. 5).

$T_{B23}(h,s)$ should only be used to determine the region for a given state point at the boundary between regions 2 and 3.

3.7 Consistency of the Backward Equations With IAPWS-IF97 Along the Region Boundaries. Table 17 lists the maximum relative pressure differences between the IAPWS-IF97-S01 backward equation $p^{01}_1(h,s)$ and the IAPWS-IF97 basic equation $g^{97}_1(p,T)$ along the boundary equation $h'_1(s)$, Eq. (4), as well as the maximum relative pressure difference between the backward equation $p_{3a}(h,s)$ (Eq. (2)) and the IAPWS-IF97 basic equation $f^{97}_3(v,T)$ along the boundary equation $h'_{3a}(s)$ (Eq. (5)).

Table 17 also shows the maximum temperature difference between the IAPWS-IF97 backward equation $T^{97}_1(p,h)$[5] and the IAPWS-IF97 basic equation $g^{97}_1(p,T)$ along the boundary equation $h'_1(s)$, Eq. (4), and the maximum temperature difference between the IAPWS-IF97-S03 backward equation $T^{03}_{3a}(p,h)$[5] and the IAPWS-IF97 basic equation $f^{97}_3(v,T)$ along the boundary equation $h'_{3a}(s)$, Eq. (5). In addition, Table 17 contains the maximum relative difference of specific volume between the IAPWS-IF97-S03 backward equation $v^{03}_{3a}(p,s)$ and the IAPWS-IF97 basic equation $f^{97}_3(v,T)$ along the boundary equation $h'_{3a}(s)$ (Eq. (5)).

Table 17 lists the maximum relative pressure differences between the IAPWS-IF97-S01 backward equations $p^{01}_2(h,s)$ and the IAPWS-IF97 basic equation $g^{97}_2(p,T)$ and between the backward equation $p_{3b}(h,s)$, Eq. (3), and the IAPWS-IF97 basic equation

[5]The alternative calculation of the temperature on the saturated-liquid line using the IAPWS-IF97 saturation-temperature equation $T^{97}_{sat}(p^{01}_1(h'_1(s),s))$ or $T^{97}_{sat}(p_{3a}(h'_{3a}(s),s))$ leads to worse numerical consistency.

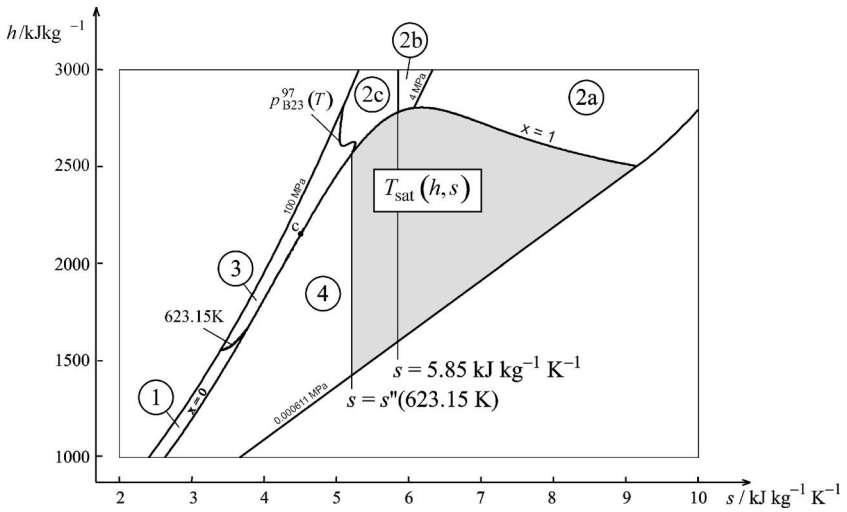

Fig. 6 Regions and subregions of IAPWS-IF97 and the backward equation $T_{sat}(h,s)$ of this work

$f_3^{97}(v,T)$ along the boundary equations $h''_{2ab}(s)$ and $p''_{2c3b}(s)$ (Eqs. (6) and (7)).

Table 17 shows the maximum temperature differences between the IAPWS-IF97 backward equations $T_2^{97}(p,h)$[6] and the IAPWS-IF97 basic equation $g_2^{97}(p,T)$, and between the IAPWS-IF97-S03 backward equation $T_{3b}^{03}(p,h)$[6] and the IAPWS-IF97 basic equation $f_3^{97}(v,T)$, along the boundary equations $h''_{2ab}(s)$ and $h''_{2c3b}(s)$ (Eqs. (6) and (7)). Table 17 also contains the maximum relative difference of specific volume between the IAPWS-IF97-S03 backward equation $v_{3b}^{03}(p,s)$ and the IAPWS-IF97 basic equation $f_3^{97}(v,T)$ along the boundary equation $h''_{2c3b}(s)$ (Eq. (7)).

The maximum pressure difference between the IAPWS-IF97-S01 backward equation $p_1^{01}(h,s)$ and the IAPWS-IF97 basic equation $g_1^{97}(p,T)$ along the boundary equation $h_{B13}(s)$ (Eq. (8)) is 14.4 kPa. The maximum temperature difference between the IAPWS-IF97 backward equation $T_1^{97}(p,h)$ and $g_1^{97}(p,T)$ along $h_{B13}(s)$ (Eq. (8)) is 24.2 mK.

Thus, the maximum differences in pressure, temperature, and specific volume are smaller than the permissible values listed in Table 8. Therefore, the accuracy of enthalpy calculated by the boundary equations (Eqs. (4)–(8)) is sufficient. The numerical consistency of these region-boundary equations with the basic equations of IAPWS-IF97 is described in detail in [7].

The maximum relative deviation between the calculated pressure $p_{2c}^{01}(h,s)$ and the IAPWS-IF97 B23-equation $p_{B23}^{97}(T)$ is 0.0045%. Thus, the combination of $T_{B23}(h,s)$ (Eq. (9)) and $p_{2c}^{01}(h,s)$ reproduces the B23-boundary of IAPWS-IF97 within the maximum allowed value 0.0088%.

The maximum relative pressure difference between the IAPWS-IF97-S01 backward equation $p_{2c}^{01}(h,s)$ and the IAPWS-IF97 basic equation $g_2^{97}(p,T)$ along the boundary, calculated as explained in Sec. 3.6, is 0.0029%. The maximum temperature difference between the IAPWS-IF97 backward equation $T_{2c}^{97}(p,h)$ and the IAPWS-IF97 basic equation $g_2^{97}(p,T)$ along the boundary is 24.1 mK. The maximum relative pressure difference is smaller than the permissible value of 0.0088% and the maximum temperature difference is smaller than the permissible value of 25 mK. Therefore, the combination of the equations $T_{B23}(h,s)$ (Eq. (9)) and $p_{2c}^{01}(h,s)$ of IAPWS-IF97-S01 is sufficiently accurate to determine the region for a given (h,s).

4 Backward Functions $T_{sat}(h,s)$, $p_{sat}(h,s)$, and $x(h,s)$ in the Two-Phase Region

4.1 Calculation of Saturation Properties From Enthalpy and Entropy. In modeling power cycles and steam turbines, thermodynamic properties as functions of the variables (h,s) are required in the two-phase (wet steam) region. The important region for steam turbine calculations is the range $s \geqslant s''(623.15\ \mathrm{K})$ (see Fig. 6), where the saturation temperature is less than 623.15 K and the two-phase region is located between regions 1 and 2. In this region, the calculation of saturation properties from h and s requires iteration using the IAPWS-IF97 basic equations $g_1^{97}(p,T)$, $g_2^{97}(p,T)$, and the saturation-pressure equation $p_{sat}^{97}(T)$. In order to avoid such iteration, IAPWS-IF97-S04 provides an equation $T_{sat}(h,s)$ for this part of the two-phase region.

4.2 Consistency Requirements. For the backward function $T_{sat}(h,s)$, the IAPWS requirements for the IAPWS-IF97 backward equations $T_2^{97}(p,h)$ and $T_2^{97}(p,s)$ (see Table 8) were adopted. Therefore, the tolerances for temperature are $|\Delta T|_{tol}=10$ mK for specific entropies greater than or equal to 5.85 kJ kg^{-1} K^{-1} and $|\Delta T|_{tol}=25$ mK for entropies less than this value.

The numerical consistency requirements for the backward function $p_{sat}(h,s)$ result from the requirements (Table 8) on the IAPWS-IF97-S01 backward equation $p_2^{01}(h,s)$. The tolerances for pressure $|\Delta p/p|_{tol}$ are 0.0035% for $s \geqslant 5.85$ kJ kg^{-1} K^{-1} and 0.0088% for $s < 5.85$ kJ kg^{-1} K^{-1}.

4.3 Backward Function $T_{sat}(h,s)$

4.3.1 The Equation $T_{sat}(h,s)$. The range of validity of $T_{sat}(h,s)$ is the two-phase region for $s \geqslant s''(623.15\ \mathrm{K})$, with $s''(623.15\ \mathrm{K})=5.210887825$ kJ kg^{-1} K^{-1} (see Fig. 6). The corresponding temperature range is $273.15\ \mathrm{K} \leqslant T \leqslant 623.15\ \mathrm{K}$.

The backward equation $T_{sat}(h,s)$ for this range has the dimensionless form

[6]The alternative calculation of the temperature on the saturated-vapor line using the saturation-temperature equation $T_{sat}^{97}(p_2^{01}(h''_{2ab}(s),s))$, $T_{sat}^{97}(p_2^{01}(h''_{2c3b}(s),s))$ or $T_{sat}^{97}(p_{3b}(h''_{2c3b}(s),s))$ of IAPWS-IF97 leads to worse numerical consistency.

Table 18 Coefficients and exponents of the equation $T_{sat}(h,s)$, Eq. (10)

i	I_i	J_i	n_i
1	0	0	0.179 882 673 606 601
2	0	3	−0.267 507 455 199 603
3	0	12	$0.116\,276\,722\,612\,600\times10^{1}$
4	1	0	0.147 545 428 713 616
5	1	1	−0.512 871 635 973 248
6	1	2	0.421 333 567 697 984
7	1	5	0.563 749 522 189 870
8	2	0	0.429 274 443 819 153
9	2	5	$-0.335\,704\,552\,142\,140\times10^{1}$
10	2	8	$0.108\,890\,916\,499\,278\times10^{2}$
11	3	0	−0.248 483 390 456 012
12	3	2	0.304 153 221 906 390
13	3	3	−0.494 819 763 939 905
14	3	4	$0.107\,551\,674\,933\,261\times10^{1}$
15	4	0	$0.733\,888\,415\,457\,688\times10^{-1}$
16	4	1	$0.140\,170\,545\,411\,085\times10^{-1}$
17	5	1	−0.106 110 975 998 808
18	5	2	$0.168\,324\,361\,811\,875\times10^{-1}$
19	5	4	$0.125\,028\,363\,714\,877\times10^{1}$
20	5	16	$0.101\,316\,840\,309\,509\times10^{4}$
21	6	6	$-0.151\,791\,558\,000\,712\times10^{1}$
22	6	8	$0.524\,277\,865\,990\,866\times10^{2}$
23	6	22	$0.230\,495\,545\,563\,912\times10^{5}$
24	8	1	$0.249\,459\,806\,365\,456\times10^{-1}$
25	10	20	$0.210\,796\,467\,412\,137\times10^{7}$
26	10	36	$0.366\,836\,848\,613\,065\times10^{9}$
27	12	24	$-0.144\,814\,105\,365\,163\times10^{9}$
28	14	1	$-0.179\,276\,373\,003\,590\times10^{-2}$
29	14	28	$0.489\,955\,602\,100\,459\times10^{10}$
30	16	12	$0.471\,262\,212\,070\,518\times10^{3}$
31	16	32	$-0.829\,294\,390\,198\,652\times10^{11}$
32	18	14	$-0.171\,545\,662\,263\,191\times10^{4}$
33	18	22	$0.355\,777\,682\,973\,575\times10^{7}$
34	18	36	$0.586\,062\,760\,258\,436\times10^{12}$
35	20	24	$-0.129\,887\,635\,078\,195\times10^{8}$
36	28	36	$0.317\,247\,449\,371\,057\times10^{11}$

$$\frac{T_{sat}(h,s)}{T^*} = \theta(\eta,\sigma) = \sum_{i=1}^{36} n_i(\eta - 0.119)^{I_i}(\sigma - 1.07)^{J_i} \qquad (10)$$

where $\theta = T/T^*$, $\eta = h/h^*$, and $\sigma = s/s^*$ with $T^* = 550$ K, $h^* = 2800$ kJ kg^{-1}, and $s^* = 9.2$ kJ kg^{-1} K^{-1}. The coefficients n_i and exponents I_i and J_i of Eq. (10) are listed in Table 18. To assist computer-program verification of Eq. (10), Table 19 contains test values for calculated temperatures.

Table 19 Selected temperature values calculated from Eq. (10)

Equation	h, kJ kg^{-1}	s, kJ kg^{-1} K^{-1}	T, K
$T_{sat}(h,s)$, Eq. (10)	1800	5.3	$3.468\,475\,498\times10^{2}$
	2400	6.0	$4.251\,373\,305\times10^{2}$
	2500	5.5	$5.225\,579\,013\times10^{2}$

Table 20 Maximum and root-mean-square differences between the temperature calculated from Eq. (10) and from the IAPWS-IF97 saturation equation $T_{sat}^{97}(p)$

Entropy range	$\lvert\Delta T\rvert_{tol}$	$\lvert\Delta T\rvert_{max}$	$\lvert\Delta T\rvert_{RMS}$
$s \geq 5.85$ kJ kg^{-1} K^{-1}	10 mK	0.67 mK	0.33 mK
$s < 5.85$ kJ kg^{-1} K^{-1}	25 mK	0.86 mK	0.45 mK

Table 21 Maximum and root-mean-square relative deviations between the pressure $p_{sat}(h,s)$ and the IAPWS-IF97 saturation equation $p_{sat}^{97}(T)$

Entropy range	$\lvert\frac{\Delta p}{p}\rvert_{tol}$	$\lvert\frac{\Delta p}{p}\rvert_{max}$	$\lvert\frac{\Delta p}{p}\rvert_{RMS}$
$s \geq 5.85$ kJ kg^{-1} K^{-1}	0.0035%	0.0029%	0.0012%
$s < 5.85$ kJ kg^{-1} K^{-1}	0.0088%	0.0034%	0.0013%

Table 22 Maximum differences of vapor fraction $x(h,s)$ from the IAPWS-IF97 basic equations $g_1^{97}(p,T)$ and $g_2^{97}(p,T)$

Entropy range	$\lvert\Delta x\rvert_{max}$	$\lvert\Delta x\rvert_{RMS}$
$s \geq 5.85$ kJ kg^{-1} K^{-1}	0.64×10^{-6}	0.25×10^{-6}
$s < 5.85$ kJ kg^{-1} K^{-1}	4.40×10^{-6}	0.57×10^{-6}

4.3.2 Consistency With the Saturation-Temperature Equation of IAPWS-IF97. The maximum and root-mean-square differences between the calculated temperature, Eq. (10), and the IAPWS-IF97 saturation equation $T_{sat}^{97}(p)$ are listed in Table 20. As can be seen, the tolerances are met.

4.4 Backward Function $p_{sat}(h,s)$

4.4.1 Calculation of $p_{sat}(h,s)$. To calculate the saturation pressure as a function of enthalpy and entropy, the following steps should be taken:

- Calculate temperature T_{sat} using $T_{sat}(h,s)$ (Eq. (10)) for the two-phase region.
- Calculate saturation pressure p_{sat} using the IAPWS-IF97 saturation equation $p_{sat}^{97}(T)$, where $T = T_{sat}$ was previously calculated.

4.4.2 Consistency With the Saturation-Pressure Equation of IAPWS-IF97. The maximum and root-mean-square relative deviations between the calculated pressure $p_{sat}(h,s)$ and the IAPWS-IF97 saturation equation $p_{sat}^{97}(T)$ are listed in Table 21. The maximum deviations are smaller than the tolerances, so the accuracy of the temperature calculated by $T_{sat}(h,s)$ (Eq. (10)) is sufficient for calculating pressure as a function of h and s.

4.5 Backward Function $x(h,s)$

4.5.1 Calculation of $x(h,s)$. To calculate the vapor fraction as a function of enthalpy and entropy, the following steps should be taken:

- Calculate temperature T_{sat} with $T_{sat}(h,s)$ (Eq. (10)) for the two-phase region.
- Calculate saturation pressure p_{sat} with the IAPWS-IF97 saturation equation $p_{sat}^{97}(T)$, where $T = T_{sat}$ was previously calculated.
- Calculate the vapor fraction x from $x = (h - h')/(h'' - h')$,[7] where $h' = h_1^{97}(p_{sat}, T_{sat})$ and $h'' = h_2^{97}(p_{sat}, T_{sat})$.

4.5.2 Consistency With the Basic Equations of IAPWS-IF97. The maximum and root-mean-square deviations between the vapor fraction $x(h,s)$, calculated as described in the previous section, and vapor fractions calculated from the IAPWS-IF97 basic equations $g_1^{97}(p,T)$, $g_2^{97}(p,T)$, and $p_{sat}^{97}(T)$, are listed in Table 22.

[7]The calculation of the vapor fraction from the saturated-liquid entropy s' and the saturated-vapor entropy s'' leads to worse numerical consistency.

The vapor fractions $x(h,s)$ agree to five significant digits. Therefore, the accuracy of temperature calculated by $T_{sat}(h,s)$ (Eq. (10)) is sufficient for calculating $x(h,s)$.

5 Computing Time Relative to IAPWS-IF97

An important motivation for this work was to reduce the computing time to obtain thermodynamic properties for a given state point (h,s). Using the $p_3(h,s)$ backward equations (Eqs. (1) and (2)) combined with the equations $T_3^{03}(p,h)$ and $v_3^{03}(p,s)$ of IAPWS-IF97-S03rev, obtaining T and v as a function of h and s is about ten times faster than that for the two-dimensional Newton method. The calculation to obtain p_{sat}, T_{sat}, and x from h and s by use of the $T_{sat}(h,s)$ backward equation combined with the IAPWS-IF97 saturation-pressure equation $p_{sat}^{97}(T)$ and the basic equations $g_1^{97}(p,T)$ and $g_2^{97}(p,T)$ is more than 14 times faster than the iterative determination from IAPWS-IF97. The region boundary equations (Eqs. (4)–(9)) allow determination of the region more quickly than iterative processes by factors ranging from 7 for $h_{B13}(s)$ to 128 for $h'_{3a}(s)$.

6 Application of the Equations

The numerical consistency of the backward equations presented in Secs. 2 or 4 and of the boundary equations presented in Sec. 3 with the IAPWS-IF97 basic equation is sufficient for most applications in heat-cycle and boiler calculations. For users not satisfied with this consistency, these equations are recommended for generating starting points to reduce the time required for convergence of an iterative process.

The backward and region-boundary equations presented here can only be used in their ranges of validity described in Secs. 2.3, 3.3–3.6, and 4.1. They should not be used for determining thermodynamic derivatives. Derivatives can be determined from the IAPWS-IF97 basic equations as described in [21]. Iteration should only be performed from the basic equations of IAPWS-IF97.

In any case, depending on the application, a conscious decision is required whether to use the backward and boundary equations or to calculate the corresponding values by iteration from the basic equation of IAPWS-IF97.

7 Summary

Backward equations $p(h,s)$ for water in IAPWS-IF97 region 3, boundary equations as functions of enthalpy and entropy, and an equation $T_{sat}(h,s)$ for the two-phase region have been developed.

The numerical consistency of pressure, temperature and specific volume calculated from the backward equations $p_{3a}(h,s)$ and $p_{3b}(h,s)$ in conjunction with $T_3^{03}(p,h)$ and $v_3^{03}(p,s)$, with the IAPWS-IF97 basic equation are sufficient for most applications in heat-cycle and boiler calculations. The new backward equations are ten times faster than iterative calculation from IAPWS-IF97.

The numerical consistency of temperature calculated by the backward equation $T_{sat}(h,s)$ with the IAPWS-IF97 basic equation is sufficient for calculating pressure and vapor fraction as a function of h and s. The calculation of these properties with $T_{sat}(h,s)$ is 14 times faster than the iterative calculation.

The consistencies of the region-boundary equations $h'_1(s)$, $h'_{3a}(s)$, $h''_{2c3b}(s)$, $h''_{2ab}(s)$, $h_{B13}(s)$, and $T_{B23}(h,s)$ with the IAPWS-IF97 basic equations are sufficient to determine the region for given state points (h,s). The boundary equations are between 7 and 128 times faster than the iterative calculation that would otherwise be needed.

For applications where the demands on numerical consistency are extremely high, iteration using the IAPWS-IF97 equations may still be necessary. In these cases, the equations presented here can be used for calculating very accurate starting values.

Further details of the numerical consistency of all backward and region-boundary equations are in the dissertation of Knobloch [19]. Computer code for the equations presented in this paper may be obtained from the corresponding author (H.-J. K.).

Acknowledgment

The authors are indebted to other members of the IAPWS Working Groups "Industrial Requirements and Solutions" and "Thermophysical Properties of Water and Steam." We are grateful to all IAPWS colleagues who contributed to the project of the development of supplementary equations for IAPWS-IF97. Two of us (H.-J. K. and K. K.) are particularly grateful to the Saxony State Ministry of Science and Art in Germany for its financial support.

Nomenclature

Quantities

- f = specific Helmholtz free energy
- h = specific enthalpy
- p = pressure
- s = specific entropy
- T = absolute temperature
- v = specific volume
- Δ = difference in any quantity
- η = reduced enthalpy, $\eta=h/h^*$
- θ = reduced temperature, $\theta=T/T^*$
- π = reduced pressure, $\pi=p/p^*$
- ρ = density
- σ = reduced entropy, $\sigma=s/s^*$
- ω = reduced volume, $\omega=v/v^*$
- x = vapor fraction

Superscripts

- 97 = quantity or equation of IAPWS-IF97
- 01 = equation of IAPWS-IF97-S01
- 03 = equation of IAPWS-IF97-S03rev
- 04 = equation of IAPWS-IF97-S04
- 05 = equation of IAPWS-IF97-S05
- * = reducing quantity
- $'$ = saturated-liquid state
- $''$ = saturated-vapor state

Subscripts

- 1 = region 1
- 2 = region 2
- 2a = subregion 2a
- 2b = subregion 2b
- 2c = subregion 2c
- 3 = region 3
- 3a = subregion 3a
- 3b = subregion 3b
- 3ab = boundary between subregions 3a and 3b
- 4 = region 4
- 5 = region 5
- B23 = boundary between regions 2 and 3
- B13 = boundary between regions 1 and 3
- c = critical point
- it = iterated quantity
- max = maximum value of a quantity
- RMS = root-mean-square value of a quantity: $\Delta z_{RMS} = \sqrt{(1/m)\Sigma_{i=1}^{m}(\Delta z_i)^2}$, where Δz_i can be either the absolute or percentage difference between the corresponding values of the quantity z; m is the number of Δz_i values (10^8 points well distributed over the range of validity)
- sat = saturation state
- tol = tolerance, range of accepted value of a quantity

References

[1] International Association for the Properties of Water and Steam, 1997, *Release on the IAPWS Industrial Formulation 1997 for the Thermodynamic Properties of Water and Steam*, IAPWS Secretariat, available at www.iapws.org.

[2] Wagner, W., Cooper, J. R., Dittmann, A., Kijima, J., Kretzschmar, H.-J., Kruse, A., Mareš, R., Oguchi, K., Sato, H., Stöcker, I., Šifner, O., Tanishita, I., Trübenbach, J., and Willkommen, Th., 2000, "The IAPWS Industrial Formulation 1997 for the Thermodynamic Properties of Water and Steam," ASME J. Eng. Gas Turbines Power, **122**, pp. 150–182.

[3] International Association for the Properties of Water and Steam, 2001, *Supplementary Release on Backward Equations for Pressure as a Function of Enthalpy and Entropy $p(h,s)$ to the IAPWS Industrial Formulation 1997 for the Thermodynamic Properties of Water and Steam*, IAPWS Secretariat, available at www.iapws.org.

[4] Kretzschmar, H.-J., Cooper, J. R., Dittmann, A., Friend, D. G., Gallagher, J. S., Knobloch, K., Mareš, R., Miyagawa, K., Stöcker, I., Trübenbach, J., Wagner, W., and Willkommen, Th., 2006, "Supplementary Backward Equations for Pressure as a Function of Enthalpy and Entropy $p(h,s)$ to the Industrial Formulation IAPWS-IF97 for Water and Steam," ASME J. Eng. Gas Turbines Power, **128**, pp. 702–713.

[5] International Association for the Properties of Water and Steam, 2003, *Supplementary Release on Backward Equations for the Functions $T(p,h)$, $v(p,h)$ and $T(p,s)$, $v(p,s)$ for Region 3 of the IAPWS Industrial Formulation 1997 for the Thermodynamic Properties of Water and Steam*, IAPWS Secretariat, available at www.iapws.org.

[6] Kretzschmar, H.-J., Cooper, J. R., Dittmann, A., Gallagher, J. S., Friend, D. G., Harvey, A. H., Knobloch, K., Mareš, R., Miyagawa, K., Okita, N., Stöcker, I., Wagner, W., and Weber, I., 2007, "Supplementary Backward Equations $T(p,h)$, $v(p,h)$, and $T(p,s)$, $v(p,s)$ for the Critical and Supercritical Regions (Region 3) of the Industrial Formulation IAPWS-IF97 for Water and Steam," ASME J. Eng. Gas Turbines Power, **129**, pp. 294–303.

[7] International Association for the Properties of Water and Steam, 2004, *Supplementary Release on Backward Equations $p(h,s)$ for Region 3, Equations as a Function of h and s for the Region Boundaries, and an Equation $T_{sat}(h,s)$ for Region 4 of the IAPWS Industrial Formulation 1997 for the Thermodynamic Properties of Water and Steam*, IAPWS Secretariat, available at www.iapws.org.

[8] International Association for the Properties of Water and Steam, 2005, *Supplementary Release on Backward Equations for Specific Volume as a Function of Pressure and Temperature $v(p,T)$ for Region 3 of the IAPWS Industrial Formulation 1997 for the Thermodynamic Properties of Water and Steam*, IAPWS Secretariat, available at www.iapws.org.

[9] Kretzschmar, H.-J., and Knobloch, K., 2005, "Supplementary Backward Equations for the Industrial Formulation IAPWS-IF97 of Water and Steam for Fast Calculations of Heat Cycles, Boilers, and Steam Turbines," in M. Nakahara et al., eds., *Water, Steam and Aqueous Solutions for Electric Power: Advances in Science and Technology*, Proc. 14th Int. Conf. on the Properties of Water and Steam, Kyoto, Japan, Maruzen Co., Ltd., pp. 34–45.

[10] Wagner, W., and Kretzschmar, H.-J., 2007, *International Steam Tables*, Springer-Verlag, Berlin, in press.

[11] Kretzschmar, H.-J., 2001, "Specifications for the Supplementary Backward Equations $T(p,h)$ and $T(p,s)$ in Region 3 of IAPWS-IF97," in B. Dooley, ed., *Minutes of the Meetings of the Executive Committee of the International Association for the Properties of Water and Steam, Gaithersburg 2001*, p. 6 and Attachment 7-Item #6.

[12] Kruse, A., and Wagner, W., 1998, "Neue Zustandsgleichungen für industrielle Anwendungen im technisch relevanten Zustandsgebiet von Wasser" ("New Equations of State for Water for Industrial Use"), Fortschr.-Ber. VDI, Series 6, No. 393, VDI-Verlag Düsseldorf.

[13] Wagner, W., 1974, "Eine mathematisch statistische Methode zum Aufstellen thermodynamischer Gleichungen—gezeigt am Beispiel der Dampfdruckkurve reiner fluider Stoffe" ("A Mathematical Statistical Method for Developing Equations of State—Demonstration With the Vapor Pressure Curves of Pure Fluids"), Fortschr.-Ber. VDI, Series 6, No. 39.

[14] Setzmann, W., and Wagner, W., 1989, "A New Method for Optimizing the Structure of Thermodynamic Correlation Equations," Int. J. Thermophys., **10**, pp. 1103–1126.

[15] Trübenbach, J., 1999, "Ein Algorithmus zur Aufstellung rechenzeitoptimierter Gleichungen für thermodynamische Zustandsgrößen" ("An Algorithm for Developing Equations of State Optimized Regarding Their Computing Time Consumption"), Fortschr.-Ber. VDI, Series 6, No. 417.

[16] Willkommen, Th., Kretzschmar, H.-J., and Dittmann, A., 1995, "An Algorithm for Setting up Numerically Consistent Forward and Backward Equations for Process Modelling," in H. J. White et al., eds., *Physical Chemistry of Aqueous Systems*, Proc. 12th Int. Conf. on the Properties of Water and Steam, Begell House, New York, pp. 194–201.

[17] Willkommen, Th., 1995, "Ein Algorithmus zur Aufstellung numerisch konsistenter Gleichungen für die in Prozessmodellierungen benötigten thermodynamischen Umkehrfunktionen" ("An Algorithm for Developing Numerically Consistent Backward Equations for Use in Process Modeling"), Dissertation, Faculty of Mechanical Engineering, Technical University of Dresden, Germany.

[18] Kretzschmar, H.-J., 1990, "Zur Aufbereitung und Darbietung thermophysikalischer Stoffdaten für die Energietechnik" ("The Preparation and Processing of Thermophysical Properties for Power Engineering"), Habilitation, Faculty of Mechanical Engineering, Technical University of Dresden, Germany.

[19] Knobloch, K., 2006, "Gleichungen für thermodynamische Umkehrfunktionen von Wasser und Wasserdampf im kritischen und überkritischen Zustandsgebiet für energietechnische Prozessberechnungen" ("Equations for Thermodynamic Backward Functions of Water in the Critical and Supercritical Regions for Power Cycle Calculations"), Fortschr.-Ber. VDI, Series 6, No. 542.

[20] International Association for the Properties of Water and Steam, 1992, *IAPWS Release on the Values of Temperature, Pressure and Density of Ordinary and Heavy Water Substances at their Respective Critical Points*, IAPWS Secretariat, available at www.iapws.org.

[21] Kretzschmar, H.-J., Stöcker, I., Klinger, J., and Dittmann, A., 2000, "Calculation of Thermodynamic Derivatives for Water and Steam Using the New Industrial Formulation IAPWS-IF97," in P. R. Tremaine et al., eds., *Steam, Water and Hydrothermal Systems: Physics and Chemistry Meeting the Needs of Industry*, Proc. 13th Int. Conf. on the Properties of Water and Steam, NRC Press, Ottawa, pp. 238–247.

Journal of Engineering for Gas Turbines and Power

Technical Brief

An Investigation Into the Application of Fuzzy Logic Control to Industrial Gas Turbines

G. M. Nelson
GE Energy Services,
General Electric Internatonal, Inc.,
G3 8BW Scotland, UK

H. Lakany[1]
University of Essex,
Wivenhoe Park,
Colchester C04 35Q, UK
e-mail: hlakany@essex.ac.uk

This paper investigates the feasibility benefits of applying fuzzy logic control (FLC) strategies for use with industrial gas turbines. Our main objective is to investigate different designs methods, design implement an FLC strategy, plant simulation in a test environment optimize the FLC, conduct tests to compare the FLC with conventional controls in scenarios relevant to the application. We have designed, implemented, and tested our simulation to the exhaust temperature control problem of a gas turbine problem. The FLC, plant simulation, existing control configuration, and integrated test environment were developed in Java. Heuristic methods were used to optimize the FLC, which proved time consuming. The paper illustrates that while implementation of the FLC is feasible, it requires more effort than the conventional controls examined. [DOI: 10.1115/1.2771568]

Keywords: fuzzy logic control, gas turbines, optimization, temperature control

1 Introduction

Gas turbines considered in this research provide mechanical energy to drive generators providing electrical power to an electrical grid system. In such systems, the fuel flow is regulated to control the turbine power output by modulating control valves in the fuel supply line to the nozzles.

Fuzzy logic control (FLC) offers an alternative to conventional control methods [1]. Lee [2] summarizes the benefits of FLC as being very useful when the processes are too complex for analysis by conventional quantitative methods. Reznick et al. [3] illustrate a combination of fuzzy logic with proportional integral differential (PID) controllers, using fuzzy logic to replace human supervision of a PID, and using established PID tuning principles to tune fuzzy logic parameters. They give possible reasons for the popularity of PID controllers as being robust and simple to design, the clear relationship between system response and the controller tuning parameters, ease of tuning, and advances in tuning and self-tuning technologies. Problems best suited to FLC applications are those which are nonlinear or where an adequate model of the process is difficult to achieve, making conventional methods difficult to apply.

2 Gas Turbine Control Problems

There are challenges ahead for gas turbine control, particularly with combustion emissions and stability in which advanced control systems may provide solutions to emerging and future issues. Docquier et al. [4] describe challenges faced by the industry in using lean premixed combustion modes to achieve NOx emissions reductions and efficiency improvements. The research describes active combustion control (ACC) methods to improve stability, emissions, or both. The authors suggest that conventional approaches with control based on lookup tables not accounting for degradation are not likely to meet demands of future emissions regulations (note however that advanced combustion systems are achieving 9 ppm NOx, 25 ppm CO to meet current US regulations with open-loop controls and off-line tuning). The required controls may include multi-input, multioutput controls, controls with time-variant response due to degradation (of plant and instrumentation), and of uncertainty in measurement signals. These would be worth considering for fuzzy logic based controls. Corbett [5] describes such a problem where a rule-based supervisory approach is adopted to minimize combustion instability in high-pressure ratio turbines.

We have reviewed existing control problems to determine whether there would be benefits from implementing a fuzzy logic control solution, investigate the feasibility, and explore designs and design methods. We considered that exhaust temperature control would be the best candidate since it is more affected by factors introducing nonlinear system response than other control loops. We base our design on the model presented by Rowen [6].

3 Methods and Experiments

The model presented by Rowen [6] is intended for dynamic power system studies. However, the representation includes a model of the temperature control system useful for this research. Rowen explains that exhaust gas temperature control is the normal means of limiting the turbine output at the optimum firing temperature. The control system determines an exhaust temperature setpoint required to achieve the optimum firing temperature based on prevailing conditions. The existing exhaust gas temperature control is a proportional plus integral (PI) controller where the input is the temperature error. The resultant fuel command signal competes in a low-value select to determine the fuel command to the valve.

[1]Corresponding author.

Submitted to ASME for publication in the JOURNAL OF ENGINEERING FOR GAS TURBINES AND POWER. Manuscript received April 22, 2007; final manuscript received May 24, 2007. Review conducted by Allan Volponi.

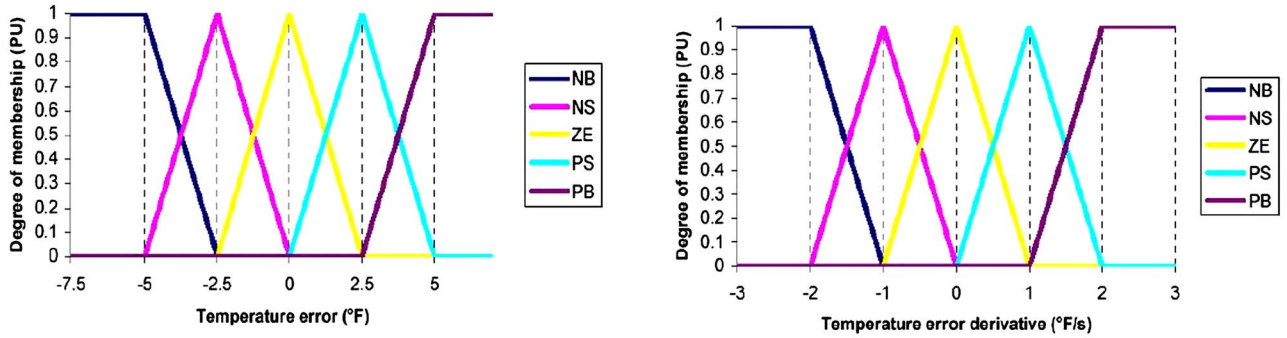

(a) Membership functions of Temperature Error E (b) Membership functions of Temperature Error Derivative $\dot{E}$

Fig. 1 Membership functions of temperature error (E) (left panel) and temperature error derivative ($\dot{E}$) (right panel)

3.1 Models Simplification. The model given shows a low-value select function to determine the fuel command signal. Inputs to the low-value select function are from the speed governor, acceleration control, and from temperature control. For this research, we are interested in temperature control. Exhaust gas temperature control takes effect when the turbine operates at maximum rated load. In this mode, the fuel command from the speed governor and from acceleration control will be greater than from temperature control. These have been omitted from our model for simplification. Typical applications for turbine generator sets are to provide power to electrical grids. In this case, the synchronous generator connects to the grid, and the speed of the turbine is determined by the system frequency. For this study, the turbine generator set is assumed to be connected to a grid of sufficient magnitude that small changes to this gas turbine output have negligible effect on the system frequency.

3.2 FLC Design. Our design choices for the FLC implementation and simulation are based on the literature where there is relevant, computational efficiency, transparency, and ease of implementation. Choices included the controller input parameters, the number, shape, distribution, and other characteristics of the membership functions (MFs), choice of inference method, aggregation, and defuzzification method.

We have chosen to use temperature error (E) and temperature error derivative ($\dot{E}$) as inputs [7–9]. We have segmented the input domain into five fuzzy sets and chose triangular and half trapezoidal to represent the membership functions [10]. The fuzzy sets were equally distributed across the input domain with crossover at 0.5 as an initial condition. The Tsukamoto type model [11] was adopted due to its transparency and simplicity. The fuzzy logic controller replaces the PI controller. The inputs to the FLC are the error E and the error derivative $\dot{E}$. The output of the FLC is an incremental change to the fuel command. The required fuel command is achieved by adding the incremental change to the previous fuel command value.

3.2.1 Fuzzification. The input space is divided into five equal fuzzy sets called (negative big) (NB), (negative small) (NS), (zero) (ZE), (positive small) (PS), and (positive big) (PB). The MFs for sets NS, ZE, and PS are triangular with half-trapezoidal sets for the extremities NB and PB. The sets are arranged with crossover at 0.5.

Figure 1 illustrates the input spaces for temperature error (E) and error derivative ($\dot{E}$), respectively, showing the fuzzy set MFs. An advantage of this simple arrangement helps in the management of the parameters associated with the input spaces. Each triangular set is defined by three parameters, with two parameters defining the half-trapezoidal sets, giving a total of 13 parameters for each input space. Given the shape of the MFs and the corner points of the NB and PB functions, we can easily derive the parameters required to define the five fuzzy sets, thus reducing the parameter count to two per input.

3.2.2 Inference Engine. The inference engine processes a complete matrix of rules for the possible combinations of inputs. The format of the rules is: **IF** E=FS1 AND $\dot{E}$=FS2 **THEN** output=FS3, where FS1 is a fuzzy set in the error input space, FS2 is a fuzzy set in the error derivative input space, and FS3 is a fuzzy set in the output space. The **AND** operator in the antecedent (**IF** E=FS1 AND $\dot{E}$=FS2) is interpreted as the taking the minimum of the membership values of E in FS1 and $\dot{E}$ in FS2 and assigning this value to the rule consequent, output=FS3. Table 1 shows a matrix of the rule consequents.

3.2.3 Defuzzification. The output space is defined by five fuzzy singleton sets, called NB, NS, ZE, PS, and PB. The crisp output values associated with each fuzzy set are initially determined based on the selected input MF parameters and on the plant model given in [6] as follows: An input error corresponding to NB corner is 5°F. The model shows a steady-state gain of $(3.3+1)/450=0.009556°F^{-1}$. According to the matrix of rule consequents, an NB error and ZE error derivative correspond to an output of NB. Thus, we set the NB singleton on the output set to correspond to $5\times0.0095556=-0.047778°F^{-1}$. The remaining sets are configured similarly, giving an equal distribution of the output sets. The results of each rule fired are aggregated such that for each rule with a given consequent fuzzy set the rule antecedents are combined with the OR operator. The combined rule based on Table 1 for the NB consequent is as follows **IF** (E=NB AND $\dot{E}$=NB) **OR** (E=NB AND $\dot{E}$=NS) **OR** (E=NB AND $\dot{E}$=ZE) **OR** (E=NB AND $\dot{E}$=PS) **OR** (E=NS AND $\dot{E}$=NB) **THEN** output =NB The **OR** operator is interpreted as taking the maximum of the values resulting from the antecedent combinations and assigning this as the output set membership value. The crisp output is derived as the weighted sum of the five output consequent values

Table 1 Matrix of rule consequents. The cell highlighted depicts the rule: IF E=NS AND $\dot{E}$=PS THEN output=NS.

	Error (E)				
Error derivative (E)	NB	NS	ZE	PS	PB
NB	NB	NB	NS	ZE	PS
NS	NB	NS	ZE	PS	PB
ZE	NB	NS	ZE	PS	PB
PS	NB	NS	ZE	PS	PB
PB	NB	ZE	PS	PB	PB

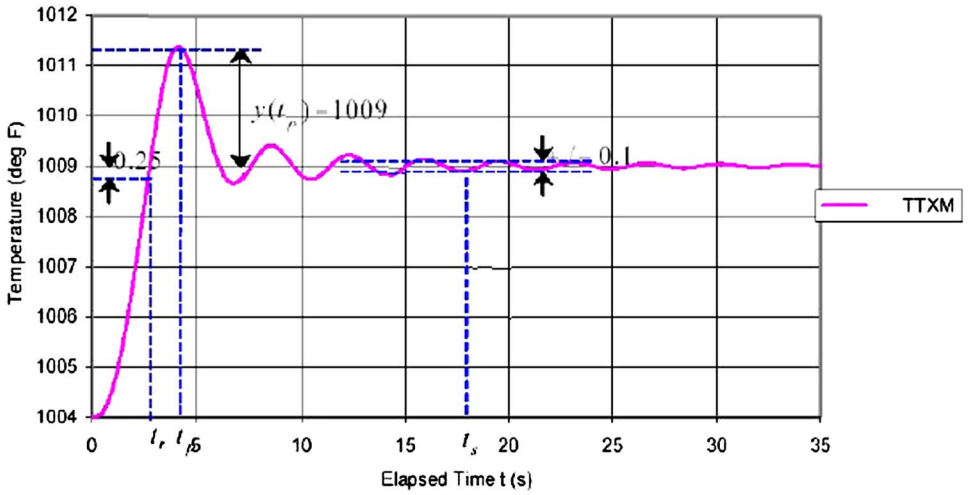

Fig. 2 Criteria used in assessment

as follows: $(\mu_{NB}\times c_{NB}+\mu_{NS}\times c_{NS}+\mu_{ZE}\times c_{ZE}+\mu_{PS}\times c_{PS}+\mu_{PB}\times c_{PB})/(\mu_{NB}+\mu_{NS}+\mu_{ZE}+\mu_{PS}+\mu_{PB})$, where μ is the membership value as determined from the aggregated rules and c is the crisp output value determined for each output set.

4 Results

4.1 Optimum FLC Configuration. The first series of tests are aimed at determining the optimum FLC configuration. Initially we test with a step change in temperature setpoint. This is an unrealistic scenario for the control system, however we expected this would be useful for assessing variations in the FLC configuration. The step was an increase from 1004°F to 1009°F in setpoint. Comparisons are based on the temperature measurement signal to the controller, TTXM. Comparisons are drawn on overshoot, rise time, and settling time. For this series of tests these are defined as shown in Fig. 2.

The assessment criteria for the test results were based on our experience as follows: (a) overshoot should be less than 1°F, (b) the process variable should settle within the test period; and (c) the optimum configuration meets the above constraints and has the shortest rise time.

We have carried out various tests to investigate the effect of variations within the rule matrix, modifying E and $\dot{E}$ data sets, changing the distribution of membership functions. We compared the performance of FLC to the existing PI controller defined by [6]. The test is based on the same +5°F step in the setpoint from steady-state conditions. Results are shown in Fig. 3. It is apparent from the above that the FLC configuration achieved thus far does not match the performance of the PI control, based on the previously defined criteria.

4.2 Realistic Test Scenarios. In this stage our objective is to test the response of the FLC configuration to disturbances that the plant and controls would be subjected to. These results are compared with those of the existing PI controls. The tests chosen were those situations envisaged to cause the greatest disturbance to the plant and controls.

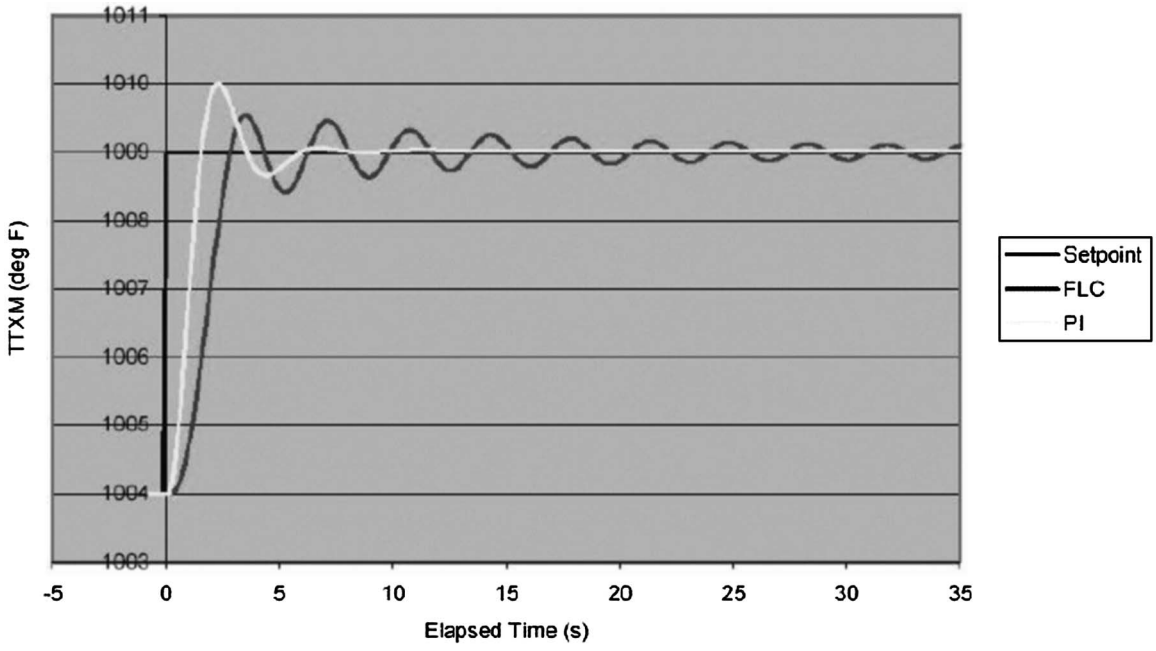

Fig. 3 Comparison of results of FLC and PI of TTXM response

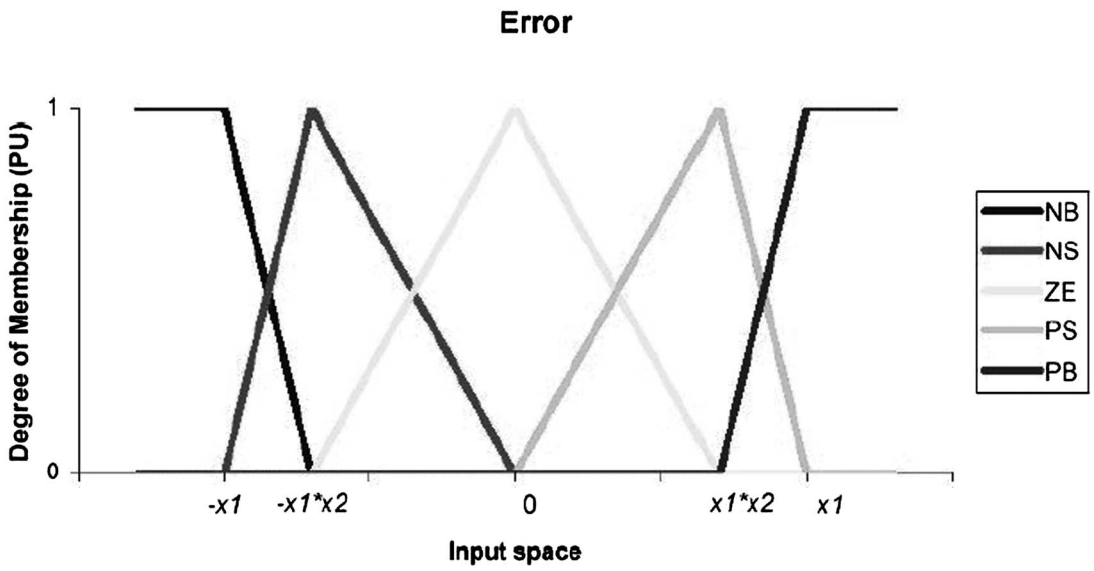

Fig. 4 Input space defined in terms of X_1 and X_2.

4.2.1 Turbine Output Increases Toward Base Load—Manual Loading Rate. Base load is the condition where the turbine operates at the nominal maximum output, limited by exhaust gas temperature control. At lower loads, fuel demand is determined by other control functions such as load control. This test considers the turbine increasing load until it reaches the nominal maximum output. Depending on operating mode, the rate at which turbine output varies under the influence of load control. The maximum loading rate for a model 7EA turbine is 0.01111 PU/s during manual load adjustments. This is the loading rate considered for the test. Recognizing this as the maximum expected loading rate we can predict the maximum rate of change of exhaust temperature from the turbine model.

1 PU change in output corresponds to 0.77 PU change in fuel flow, WF, resulting in an exhaust temperature change of 539°F. Hence, the maximum anticipated rate of change of temperature is $0.01111 \times 539 = 5.989$°F/s. A comparison of the previous test suggested that the FLC configuration achieved did not offer advantages over the PI control. This provided motivation for revisiting the configuration. Recognizing the maximum loading rate and corresponding rate of temperature rise, this formed the basis of the configuration change. A large change in output corresponds to the maximum loading rate, 0.01111 PU/s. This corresponds to a rate of change of error of 5.989°F/s. NB and PB corners for the output and $\dot{E}$ are set to 1.5 greater than these rates, allowing temperature control to increase beyond the loading rate, ensuring that temperature control does not inadvertently limit the loading rate. To determine E scaling we considered the TTXM value when FSR increased from a low steady-state value to 1.0. This was determined by setting the simulation to a steady-state value of 0.5 PU FSR by setting FSRMAN to 0.5 PU with plant simulation initial values set to corresponding fuel and temperature values. The simulation then ramps FSRMAN to 1.25 PU at the maximum rate. When FSRMAN reaches 1.0 PU TTXM reaches 968.5°F, an error of $1004 - 968.5 = 35.5$ °F. 35.5°F is then considered a large error, with NB and PB corner magnitudes set to 1.5×35.5. Initial experiments showed that it was necessary to modify the rule matrix to ensure that if the error is large then output is large, regardless of the error dot. Otherwise the temperature controller would not increase at a sufficient rate to achieve the required maximum loading rate. The tests included variations to the scaling of the NS and PS corners or the error E and error derivative E inputs. The results show that TTXM reaches the setpoint quicker with the PI control.

4.2.2 Turbine Output Increases Toward Base Load—Auto Loading Rate. The loading rate in the previous test is the maximum loading rate. The normal loading rate is the auto rate, typically 0.001375 PU/*s*. This test compares the FLC and PI in a similar scenario to the previous test except with this reduced loading rate. In this case the PI overshoot is much reduced while the response time of the FLC is greater than the PI.

4.2.3 Change in Turbine Speed. Frequency changes on the electrical grid, caused by sudden changes in load or generating capacity, cause rapid small changes in turbine speed. This test simulates an instantaneous increase of frequency from 60 Hz to 60.5 Hz, and a decrease from 60 Hz to 59.5 Hz. Results of these experiments show that the initial error is the same in both cases, however, the PI controller has a smaller overshoot on recovery and settles quicker than the FLC control. The error in the FLC is negligible after a short period.

4.2.4 Change in Fuel System Gain. The final test simulates a change in fuel gain. A step change in gain is not a realistic scenario, however the possibility of a valve calibration drift over time is considered. Assume a fuel gas valve drifts resulting in a 2% error in fuel flow. This will have negligible effect over time, however, it would create a disturbance during combustion mode changes. During normal operation at full load the turbine operates in a premix mode, where a significant proportion of fuel mixes with air before reaching the combustion zone. In the event of an abnormal condition the combustion may revert to a diffusion mode. The change in mode is achieved in part by varying the fuel split to different fuel nozzles within the combustion system. The fuel split is given as a percentage to a specific fuel nozzle, with fuel to the nozzles regulated by independent valves. With properly calibrated valves, changing the fuel split results in the same fuel flow and turbine output. However, if a valve calibration error is introduced, then a change in split will result in a change in fuel flow. Fuel splits vary from unit to unit depending on tuning, however the largest split change during such a mode change would be from ~81.5% to 60%. Assuming a 2% flow error through one valve, the flow error at 81.5% split is 1.63%, and the error at 60% split is 1.2%. The maximum rate of change of split is 20%/s, giving a transfer time of $(81.5 - 60)/20 = 1.075$ s. The rate of change of flow error is hence (1.63-1.2)/1.075 or 0.4 PU/s. The

Table 2 Definition of FLC input and output space configuration in terms of X_1 and X_2

Domain	X_1	X_2
Error input	53.25°F	0.25
Error dot input	8.9835°F/s	0.8
FSRTd output	0.016665 PU/s	0.5

results show that there is a similar overshoot in each case. Again, the PI control settles quicker, however the error in the FLC is negligible at this time.

5 Discussion

The FLC configuration involves a large number of configuration parameters compared to the PI control. Each input space requires 13 parameters to define the fuzzy set MFs, there are 25 rule consequents, and five output set values, giving a total of 56 parameters. In comparison, the PI controller has two parameters. The input and output space parameters can be reduced to an extent at the expense of flexibility. If we assume the fuzzy sets in the inputs are equally spaced around zero, then we can define the five fuzzy sets with a single parameter. Allowing for unequal distribution, but with symmetry about 0 the sets can still be defined by two parameters, e.g., as represented by X_1 and X_2 in Fig. 4. The output space can be defined similarly. Thus, the input and output spaces for the FLC configuration used in the final tests can be defined as in Table 2.

The test phase aimed to compare the performance of the FLC with PI control in scenarios likely in the exhaust gas temperature control application. The test scenarios were selected from a wider list of scenarios envisaged, considering those likely to cause the greatest disturbance.

The first scenario, increasing load toward base load at the manual loading rate, is possible but highly unlikely. Manual loading is intended to be used for smaller load changes. The normal methods of increasing to base load follow the slower auto loading rate.

Rapid changes in grid frequency of the magnitude occur in practice. Although the test depicted a step change, which is unrealistic, the rate at which the frequency could change would be sufficient that the test scenario is an adequate approximation. The resultant error in TTXM remained below 1°F.

The scenario for change in fuel system gain due to valve calibration drift showed the error below 1°F for both the FLC and PI control.

6 Conclusion

The first stage of testing implemented variations in the FLC configuration. The variations included the scaling and distribution of the fuzzy sets in the input and output spaces and variations to the rule consequents. The heuristic methods used to determine the optimum FLC configuration proved time consuming. In future work we shall investigate a more systematic way to achieve optimum configuration.

Comparisons between the performance of the FLC and the existing PI control are discussed in this paper. The comparison includes scenarios relevant to the application, however further scenarios should be considered in our future work.

The results show that the performance of the FLC is adequate, while the PI controller provides improved response and settling time in the scenarios tested. However, when the exhaust temperature is compared rather than the signal from the thermocouple, we note larger overshoot in temperature with the PI control in some scenarios.

References

[1] Bonissone, P. P., Badami, V., Chinag, K. H., Khedkar, P. S., Marcelle, K. W., and Schutten, M. J., 1995, "Industrial Applications of Fuzzy Logic at General Electric," Proc. IEEE, **83**, pp. 450–465.

[2] Lee, C. C., 1990, "Fuzzy Logic in Control Systems: Fuzzy Logic Controller, Parts I & II," IEEE Trans. Syst. Man Cybern., **20**, pp. 404–435.

[3] L. Reznik, L., Ghanayem, O., and Bourmistrov, A., 2000, "PID Plus Fuzzy Controller Structures as a Design Base for Industrial Applications," Eng. Applic. Artif. Intell., **13**, pp. 419–430.

[4] Docquier, N., and Candel, S., 2002, "Combustion Control and Sensors: A Review," Prog. Energy Combust. Sci., **28**, pp. 107–150.

[5] Corbet, N., 2001, "Remote Monitoring and Control of Advanced Gas Turbines," IEE Comp. Control Eng Journal, **12**, pp. 68–74.

[6] Rowen, W., 1983, "Simplified Mathematical Representation of Heavy-Duty Gas Turbines," ASME J. Eng. Power, **105**, pp. 865–869.

[7] Jurado, M., Ortega, M., Cano, A., and Carpio, J., 2002, "Neuro-Fuzzy Controller for Gas Turbine in Biomass-Based Electric Power Plant," Electr. Power Syst. Res., **60**, pp. 123–135.

[8] Abdennour, A., 2000, "An Intelligent Supervisory System for Drum Type Boiler During Severe Disturbances," Int. J. Electr. Power Energy Syst., **22**, pp. 213–222.

[9] Kuo, H., and Wu, L. J., 2002, "Fuzzy Control of a Heat-Bending System," J. Mater. Process. Technol., **120**, pp. 186–201.

[10] Kim, E., 2001, "A New Approach to Numerical Stability Analysis of Fuzzy Control Systems," IEEE Trans. Syst. Man Cybern., **31**, pp. 107–113.

[11] Tsukamoto, Y., 1979, "An Approach to Fuzzy Reasoning Method," *Advances in Fuzzy Set Theory and Applications*, M. M. Gupta, R. K. Ragade, and R. R. Yager, eds., North-Holland, Amesterdam, The Netherlands, pp 137–149.

Journal of Engineering for Gas Turbines and Power

Discussion

Discussion: "The Lomakin Effect in Annular Gas Seals Under Choked Flow Conditions" (Arghir, M., Defaye, C., and Frêne, F., 2007, ASME J. Eng. Gas Turbines Power, 129, pp. 1028–1034)

Dara Childs
Turbomachinery Laboratory,
Texas A&M University,
College Station, TX 77843

The authors' predictions that choked flow in an annular gas seal is likely to produce negative direct stiffness was recently borne out in tests conducted by the discussers. A smooth seal was tested in air with supply pressure 18.3 bar and discharge near atmospheric pressure. The seal has dimensions: $L=100$ mm, $D=100$ mm, and radial clearance $C_r=0.305$ mm. The measured direct static stiffness is negative, $K=-1.93$ MN/m. The model available to the discussers is based on the work of Kleynhans and Childs [1] and would not converge at the full pressure differential. The direct stiffness predicted by this model becomes negative and its magnitude increases as the input supply pressure increases from ~10 bars, but the code stops converging above a δP of ~13 bars. What do the authors predict for this seal and the test conditions provided above? Additional test results are available for the seal in [2].

Submitted to ASME for publication in the JOURNAL OF ENGINEERING FOR GAS TURBINES AND POWER. Manuscript received January 3, 2007; final manuscript received January 5, 2007. Review conducted by Dilip R. Ballal.

References

[1] Kleynhans, G., and Childs, D., 1997, "The Acoustic Influence of Cell Depth on the Rotordynamic Characteristics of Smooth-Rotor/Honeycomb-Stator Annular Gas Seals," ASME J. Eng. Gas Turbines Power, **119**(4), pp. 949–957.
[2] Zutavern, Z., 2006, "Identification of Rotordynamic Forces in a Flexible Rotor System Using Magnetic Bearings," Ph.D. dissertation, Mechanical Engineering Department, Texas A&M University.

Closure to "Discussion of 'The Lomakin Effect in Annular Gas Seals Under Choked Flow Conditions'" (2007, ASME J. Eng. Gas Turbines Power, 129, p. 1143)

Mihai Arghir
Université de Poitiers, France
e-mail: mihai.arghir@lms.univ-poitiers.fr

The authors are grateful for this experimental validation of the negative direct static stiffness of choked annular seals. For performing our own calculations, the mentioned conditions were supplemented by some additional assumptions that are somewhat usual for straight annular seals, namely, an imposed inlet pressure drop coefficient ζ_{inlet} and an exit recovery coefficient $\zeta_{exit}=1$ (complete pressure recovery). The rotation speed was $\omega=0$, and the flow regime was considered as being nonisothermal with adiabatic walls and $T_{inlet}=20°C$. Moody's friction factor was used with the possibility of bridging transition between laminar and turbulent flow. The employed grid had 16 equally spaced cells in the axial direction and 32 in the circumferential one (Fig. 1).

The first set of results was obtained for $\zeta_{inlet}=0.1$ and zero roughness. Results show a good prediction of the negative direct static stiffness at a pressure drop DP=18.3 bar and calculations could be performed for values of >20 bar. Nevertheless, the flow in the seal becomes choked at much lower pressure differences than the 10 bar announced by experiments. It was further recognized that ξ_{inlet} generally varies with the axial Reynolds number (triggered by the pressure difference); thus, a variable inlet pressure drop was used in a second set of calculations, $\xi_{inlet}=\sqrt{5.3/\log(\mathrm{Re})-1}$. The results show a larger negative value for the direct static stiffness at DP=18.3 bar but no modification of the predictions at lower pressure differences.

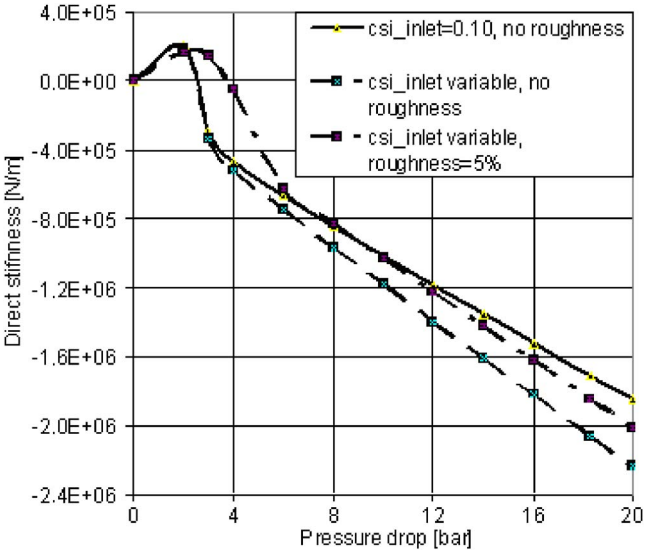

Fig. 1

A third set of results was obtained by considering the variable ξ_{inlet} and a 5% roughness of the rotor and stator surfaces. The prediction for DP=18.3 bar is very close to $K=-1.93$ MN/m, and the values of the static stiffness obtained for low-pressure drops corresponding to nonchoked flows show a tendency toward an improvement. Nevertheless, larger values of the roughness cannot be predicted by Moody's law.

Again, the authors are grateful for this discussion that evidenced that a choked exit flow of gas annular seals can lead to negative values of the static stiffness.

Submitted to ASME for publication in the JOURNAL OF ENGINEERING FOR GAS TURBINES AND POWER. Manuscript received January 3, 2007; final manuscript received January 4, 2007. Review conducted by Dilip R. Ballal.

